EUROPEAN MATERIALS RESEARCH SOCIETY SYMPOSIA PROCEEDINGS

Volume 1: Ceramic Materials Research (ed. R.J. Brook)
Volume 2: Photon, Beam and Plasma Assisted Processing (eds. I.W. Boyd and E.F. Krimmel)
Volume 3: Deep Implants (eds. G.G. Bentini, A. Golanski and S. Kalbitzer)
Volume 4: Metastable Alloys: Preparation and Properties (eds. K. Samwer, M. von Allmen, J. Bøttinger and B. Stritzker)
Volume 5: Superconducting and Low-Temperature Particle Detectors (eds. G. Waysand and G. Chardin)
Volumes 6A, 6B: High T_c Superconductors (eds. P.F. Bongers, C. Schlenker and B. Stritzker)
Volume 7: Solid State Ionics (eds. M. Balkanski and C. Julien)
Volume 8: Rare-Earth Permanent Magnets (ed. I.R. Harris)
Volume 9: Defects in Silicon (eds. C.A.J. Ammerlaan, A. Chantre and P. Wagner)
Volume 10A, 10B: Silicon Molecular Beam Epitaxy (eds. E. Kasper and E.H.C. Parker)
Volume 11: Acoustic, Thermal Wave and Optical Characterization of Materials (eds. G.M. Crean, M. Locatelli and J. McGilp)
Volume 12: Beam Processing and Laser Chemistry (eds. I.W. Boyd and E. Rimini)
Volume 13: Interfaces in Biomaterials Sciences (eds. D. Muster and G. Hastings)
Volume 14A, 14B: High T_c Superconductor Materials (eds. H.-U. Habermeier, E. Kaldis and J. Schoenes)
Volume 15: Metal Matrix Composites (eds. G. Chadwick and L. Froyen)
Volume 16: Magnetic Thin Films, Multilayers and Superlattices (eds. A. Fert, G. Güntherodt, B. Heinrich, E.E. Marinero and M. Maurer)
Volume 17: Metallurgical Coatings and Materials Surface Modifications (eds. H. Hintermann and J. Spitz)
Volume 18: Surface Processing and Laser Assisted Chemistry (eds. I.W. Boyd, E. Fogarassy and M. Stuke)
Volume 19: Materials for Optoelectronic Devices, OEICs and Photonics (eds. H. Schlötterer, M. Quillec, P.D. Greene and M. Bertolotti)
Volume 20: SiC, Natural and Synthetic Diamond and Related Materials (eds. A.A. Gippius, R. Helbig and J.P.F. Sellschop)
Volume 21: Analytical Techniques for the Characterization of Compound Semiconductors (eds. G. Bastard and H. Oppolzer)
Volume 22: Micronic Integrated Sensors (ed. J.L. Robert)
Volume 23: High Energy and High Dose Ion Implantation (eds. S.U. Campisano, J. Gyulai, P.L.F. Hemment and J.A. Kilner)
Volume 24: Laser Surface Processing and Characterization (ed. I.W. Boyd)
Volume 25: Nuclear Methods in Semiconductor Physics (eds. G. Langouche, J.C. Soares and J.P. Stoquert)
Volume 26: Clays and Hydrosilicate Gels in Nuclear Fields (ed. A. Meunier)
Volume 27: Chemistry of Cements for Nuclear Applications (eds. P. Barret and F.P. Glasser)
Volume 28: Nuclear Materials for Fission Reactors (eds. Hj. Matzke and G. Schumacher)
Volume 29: Modifications Induced by Irradiation in Glasses (ed. P. Mazzoldi)
Volume 30: Polyconjugated Materials (ed. G. Zerbi)
Volume 31: SiGe Based Technologies (eds. E. Kaspar, Y. Shiraki and T.P. Pearsall)
Volume 32: Materials Surface Processing (eds. M. Stuke, E.E. Marinero and I. Nishiyama)
Volume 33: Chemistry for Electronic Materials (eds. Y. Pauleau, G. Wahl, K.F. Jensen and T. Hirai)
Volume 34: Semiconductor Materials Analysis and Fabrication Process Control (eds. G. Crean, R. Stuck and J. Woollam)
Volume 35: Synthetic Materials for Non-Linear Optics and Electronics (eds. C. Taliani, Z.V. Vardeny and Y. Maruyama)
Volume 36: CdTe and Related Cd Rich Alloys (eds. R. Triboulet, W.R. Wilcox and O. Oda)
Volume 37: Single Chamber Processing (eds. Y.I. Nissim and A. Katz)
Volume 38: High T_c Superconductors (eds. J. Dumas, H.W. Neumüller, H.F. Braun, V.P. Seminozhenko and Yu.D. Tretyakov)
Volume 39: Materials under Extreme Conditions and Nanophase Materials (eds. G. Kostorz, I. Gorynin, V. Trevilov, H.-D. Kunze, B. Skorokhod and V. Troitsky)
Volume 40: Semiconductor Materials for Optoelectronics and LTMBE Materials (eds. J.P. Hirtz, C. Whitehouse, H.P. Meier, H.J. von Bardeleben and M.O. Manasreh)

SEMICONDUCTOR MATERIALS FOR OPTOELECTRONICS AND LTMBE MATERIALS

PROCEEDINGS OF SYMPOSIUM A ON SEMICONDUCTOR MATERIALS FOR OPTOELECTRONIC DEVICES, OEICs AND PHOTONICS AND SYMPOSIUM B ON LOW TEMPERATURE MOLECULAR BEAM EPITAXIAL III–V MATERIALS: PHYSICS AND APPLICATIONS OF THE 1993 E-MRS SPRING CONFERENCE

STRASBOURG, FRANCE, MAY 4–7, 1993

Edited by

J.P. HIRTZ
Thomson-CSF, Orsay, France

C. WHITEHOUSE
Defense Research Agency, Great Malvern, U.K.

H.P. MEIER
Rüschlikon, Switzerland

H.J. VON BARDELEBEN
Universités Paris 6 & 7, Paris, France

M.O. MANASREH
Wright Laboratory, Dayton, OH, U.S.A.

1993
NORTH-HOLLAND
AMSTERDAM-LONDON-NEW YORK-TOKYO

© 1993 ELSEVIER SEQUIOIA S.A. All rights reserved.

No part of this publication may be reproduced, stored in a retrieval system, or transmitted, in any form or by any means, electronic, mechanical, photocopying, recording or otherwise, without the prior written permission of the copyright owner, Elsevier Sequioia S.A., P.O. Box 564, 1001 Lausanne, Switzerland.

Special regulations for readers in the U.S.A. - This publication has been registered with the Copyright Clearance Center Inc. (CCC), Salem, Massachusetts. Information can be obtained from the CCC about conditions under which photocopies of parts of this publication may be made in the U.S.A. All other copyright questions, including photocopying outside of the U.S.A., should be referred to the copyright owner, Elsevier Sequioia S.A., unless otherwise specified.

No responsibility is assumed by the Publisher for any injury and/or damage to persons or property as a matter of products liability, negligence or otherwise, or from any use or operation of any methods, products, instructions or ideas contained in the material herein.

Printed on acid-free paper

ISBN: 0 444 81769 7

Published by:
North-Holland
Elsevier Science Publishers B.V.
Sara Burgerhartstraat 25
P.O. Box 211
1000 AE Amsterdam
The Netherlands

Reprinted from:
MATERIALS SCIENCE AND ENGINEERING B21 (2,3) and B22 (1)

The manuscripts for the Proceedings were received by the Publisher:
early July 1993

Printed in The Netherlands

Preface

The symposium "Materials for Optoelectronic Devices, OEICs and Photonics", held in Strasbourg, May 4–7, 1993, was part of the European Materials Research Society (E-MRS) Spring Meeting; several other symposia were devoted to the related topics of integrated processing for micro and optoelectronics, light emission in silicon and LTMBE III–V materials. This 3-day symposium was designed to provide a link between specialists coming from university or industry, and working in different fields of semiconductor optoelectronics. The main topics covered during this symposium were:

- Epitaxial growth of III–V, II–VI, IV–VI, Si-based structures
- Selective-area, localized and non-planar epitaxy, shadow-mask epitaxy
- Superlattices, quantum size structures
- Strained layer structures
- Bulk and new optoelectronic materials
- Optoelectronics on silicon
- Polymers for optoelectronics
- Optoelectronic devices

The chairmen of this symposium would like to acknowledge Dr. Schlölleter from SIEMENS and Professor Dr. G. Tränkle from the Technical University of Münich for their most valuable help in the organization of this meeting. They are also grateful to the local E-MRS organizers and to the referees who helped to prepare these proceedings.

Finally, we would like to thank the following for their financial support: the E-MRS and its President Dr. Glasgow, the E-MRS Network GaAs, particularly Professor D. G. Weimann, and finally Dr. G. Witt from the US Air Force Office for Scientific Research.

J. P. Hirtz
H. Meier
C. Whitehouse

Guest Editors

Organizers and Sponsors

Symposium Chairmen:

J. P. Hirtz
THOMSON CSF/LCR
Domaine de Corbeville
91404 Orsay Cedex
France

H. Meier
IBM Zurich Research Laboratory
Säumerstrasse 4
8803 Rüschlikon
Switzerland

C. Whitehouse
3 Christchurch Road
Malvern
Worcestershire WR14 3BH
UK

Scientific Committee

G. Tränkle (Germany)
H. Schlotterer (Germany
J. von Bardeleben (France)

Sponsors

This Conference was held under the auspices of:

The Council of Europe
The Commission of European Communities

It is our pleasure to acknowledge with gratitude the financial assistance provided by

Banque Populaire (France)
Brasserie Adelshoffen (France)
Centre de Recherches Nucléaires (France)
Centre National de la Recherche Scientifique (France)
Elsevier Science Publishers B.V. (Netherlands)
La Maison du Café - Ergersheim (France)
Office du Tourisme de la Ville de Strasbourg (France)
The Commission of European Communities
The Council of Europe
The European Parliament

Preface

Symposium B of the E-MRS Spring Meeting, 1993 was the first European meeting on the subject of III–V epitaxial layers grown by low temperature molecular beam epitaxy (LTMBE). This subject has undergone rapid development in the last three years, particularly in the USA where different MRS symposia had already been devoted to this area. The point of interest in this growth technique is that it allows the growth of layers with extremely high defect concentrations but still of excellent crystallinity. The electrical and optical properties are modified—in particular high resistive material can be elaborated—giving rise to many applications. Although up to now most of the results have been obtained for LTMBE GaAs, this technique can also be applied to all other 3–5 compounds and alloys.

At the E-MRS meeting papers were presented on the following topics:

- Growth and characterization of undoped high resistive LTMBE III–V epitaxial layers: GaAs, GaInAs, AlInAs, InP, GaP.
- Application of LTMBE III–V layers in microelectronics: MESFETS, HEMTS, MISFETS.
- Optoelectronic applications of LTMBE GaAs.

A series of six invited papers, giving an overview of the current activity in this field, was presented: "LTMBE GaAs: present status and perspectives" by G. L. Witt of AFOSR/NE, Bolling AFB (USA); "Point defects in III–V materials grown by molecular beam epitaxy at low temperature" by P. Hautojärvi, J. Mäkinen, S. Palko and K. Saarinen of Helsinki University of Technology, Espoo (Finland), C. Corbel and L. Liszkay of Centre d'Etudes Nucléaires de Saclay, Gif-sur-Yvette (France); "GaAs, AlGaAs, and InGaAs epilayers containing As clusters: semimetal/semiconductor composites" by M. R. Melloch of Purdue University, Indiana (USA), J. M. Woodall of IBM T. J. Watson Research Centre, New York (USA), N. Otsuka, K. Mahalingam, C. L. Chang and D. D. Nolte of Purdue University, Indiana (USA); "Extended defects and precipitates in LT-GaAs, LT-InAlAs and LT-InP" by A. Claverie of CEMES/LOE, Toulouse (France) and Z. Liliental-Weber, Lawrence Berkeley Laboratory, Berkeley, CA (USA); "Optoelectronic applications of LTMBE III–V materials" by J. F. Whitaker of University of Michigan, Ann Arbor, MI (USA); "Applications of GaAs grown at a low temperature by molecular beam epitaxy" by U. K. Mishra of University of California, Santa Barbara, CA (USA).

We would like to thank the US Air Force Office of Scientific Research (EOARD) for financial support.

H. J. von Bardeleben
J. P. Hirtz
M. O. Manasreh

Guest Editors

Organizers and Sponsors

Symposium Chairmen:

H. J. von Bardeleben
Groupe de Physique des Solides
Universités Paris 6&7
2 Place Jussieu
75251 Paris Cedex 05
France

M. O. Manasreh
Wright Laboratory, WL/ELRA
Wright Patterson AFB
Dayton, OH 45433-6543
USA

J. P. Hirtz
Thomson-CSF
Domain de Corbeville
91404 Orsay Cedex
France

Sponsors

This Conference was held under the auspices of:

The Council of Europe
The Commission of European Communities

It is our pleasure to acknowledge with gratitude the financial assistance provided by

Banque Populaire (France)
Brasserie Adelshoffen (France)
Centre de Recherches Nucléaires (France)
Centre National de la Recherche Scientifique (France)
Elsevier Science Publishers B.V. (Netherlands)
La Maison du Café - Ergersheim (France)
Office du Tourisme de la Ville de Strasbourg (France)
The Commission of European Communities
The Council of Europe
The European Parliament

Materials Science and Engineering, B21 (1993) 107–119

Stoichiometry of III–V compounds

Jun-ichi Nishizawa

Tohoku University, Katahira Aoba-ku 2-1-1, Sendai (Japan)

Abstract

The effects of stoichiometry on various features of III–V compounds are investigated. Application of the optimum vapour pressure of group V elements is shown to minimize the deviation from stoichiometric composition. The temperature dependence of the optimum vapour pressure is also obtained from both annealing and liquid phase epitaxial growth experiments. Vapour pressure technology is successfully applied to bulk crystal growth. In view of the defect formation mechanism, the role of the stable interstitial As atoms (I_{As}) in GaAs is emphasized. The mechanism of stoichiometry control is discussed on the basis of the equality of chemical potentials and the change in saturating solubility in the liquidus phase as a function of the vapour pressure.

1. Introduction

The most important factor to be controlled in compound semiconductor crystals is the deviation from stoichiometric composition. Since the investigation of iron pyrite in 1951 [1], annealing experiments on various III–V compound semiconductor crystals have been carried out under controlled vapour pressure of the group V element [2, 3]. It is shown that nearly perfect crystals with stoichiometric composition are produced under a specific vapour pressure and that the temperature dependence of the optimum vapour pressure is also obtained.

In view of the defect formation mechanism, the role of interstitial As atoms (I_{As}) in GaAs crystals was emphasized when GaAs was annealed under high As vapour pressure [4]. The As vapour pressure dependence on the specific weight and the intensity of anomalous X-ray transmission implies the existence of interstitial As atoms [5]. Our Rutherford-backscattering spectroscopy (RBS) experiments have also revealed interstitial As atoms in As^+-implanted GaAs and enabled us to determine the stable interstitial sites in the deformed lattice [6]. The RBS results on the stable interstitial sites are in good accordance with those of anomalous X-ray transmission measurements [5].

Photocapacitance measurements under constant-capacitance conditions have shown stoichiometry-dependent deep levels and clarified the As vapour pressure dependences of the deep level densities [7]. The formation energy of the defects was also obtained as 1.16 eV [8]. This value relates more closely to interstitial atoms than to vacancies. Recently much attention has been devoted to interstitial As atoms in GaAs as well as to antisite defects, because the so-called EL2 level relates to the excess As composition of GaAs crystals. Indeed, recent results of quasi-forbidden X-ray reflection seem to show the existence of interstitial As atoms [9].

Vapour pressure control technology has also been applied in the field of bulk crystal growth [10]. It has been shown that high purity GaAs crystals can be obtained with controlled composition and that very low dislocation densities (as low as 2000 cm^{-2}) can be achieved even in Czochralski (CZ) grown semi-insulating GaAs crystals of diameter 4 in. This enables the fabrication of superbright light-emitting diodes (LEDs) [11], including pure green LEDs without nitrogen doping in GaP [12]. Vapour pressure control during crystal growth, which enables control of the stoichiometric composition, is applied extensively not only to III–V compounds, *e.g.* InP, but also to II–VI compounds, *e.g.* ZnSe [13]. It should also be important in the research field of superconducting ceramics.

In this review the annealing effects of GaAs under arsenic vapour pressure are shown. The electrical, optical and crystallographic properties are improved under a specific arsenic vapour pressure denoted P_{opt}. In view of the stoichiometry-dependent deep levels, PHCAP results for annealed GaAs crystals are shown. The diffusion phenomenon in GaAs is closely related to the stoichiometric composition. It is shown that the amphoteric behaviour of group IV elements (Sn [14] and Si [15]) in GaAs is controlled by the application of vapour pressure during liquid phase epitaxial (LPE) growth. Results of LPE growth of GaAs by means of the temperature difference method under controlled vapour pressure (TDM-CVP) are also shown. This can

0921-5107/93/$6.00

© 1993 – Elsevier Sequoia. All rights reserved

be extended to the results of melt growth by Suzuki and Akai [16] and Parsey *et al.* [17]. Similar results are also obtained for LPE growth of GaP under controlled phosphorus vapour pressure. Vapour pressure control technology can also be extended to GaAs bulk crystal melt growth. Crystal quality is shown as a function of the arsenic vapour pressure. In view of the non-stoichiometric defect formation mechanisms, PHCAP and RBS results are shown in combination with results of crystal specific weight and anomalous X-ray transmission intensity measurements. The important role of interstitial As atoms in GaAs is emphasized. In view of the surface stoichiometry and precise control of stoichiometric composition during vapour phase epitaxial growth, experimental results of molecular layer epitaxy (MLE) of GaAs are described. The importance of surface stoichiometry is also emphasized in the research field of surface science. Finally, theoretical consideration is also shown by taking into account the deviation from stoichiometric composition.

2. Annealing effects on GaAs crystals under As vapour pressure

Annealing experiments were performed at 900–1100 °C for 67 h under various As vapour pressures. The samples used were (100)-oriented horizontal Bridgman (HB) grown GaAs with various impurity densities. The defect density introduced by annealing reaches its saturation value after 67 h of annealing. Figure 1 shows a schematic drawing of the equipment for annealing under As vapour pressure. The As vapour pressure applied on the GaAs crystals was obtained as

$$P_{\mathrm{GaAs}} = P_{\mathrm{As}}\left(\frac{T_{\mathrm{GaAs}}}{T_{\mathrm{As}}}\right)^{1/2} \qquad (1)$$

where P_{As} is the equilibrium As vapour pressure determined from the temperature of arsenic metal (T_{As}) and T_{GaAs} is the temperature of the GaAs crystals. The equilibrium As vapour pressure was obtained by Honig [18]. After annealing, the samples were cooled rapidly by plunging them into water in order to avoid any effect of slow cooling. X-ray and etching inspection revealed no slip lines even after rapid cooling.

Figure 2 shows the change in acceptor density induced by annealing as a function of the initial electron density in Te-doped GaAs after annealing. The acceptor density is almost proportional to the initial electron density. This shows that acceptor-type defects relate to both the deviation from stoichiometric composition and the dopant impurity Te. Figures 3 and 4 show the As vapour pressure dependences of the acceptor density and the lattice constant respectively.

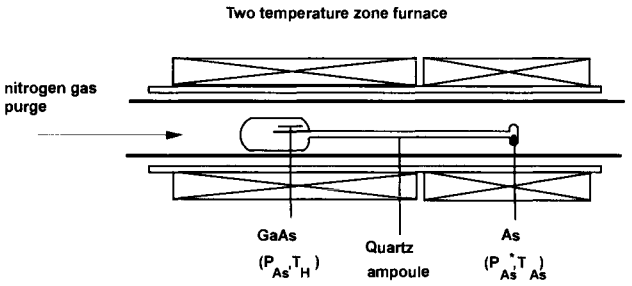

Fig. 1. Schematic drawing of the equipment for annealing under As vapour pressure.

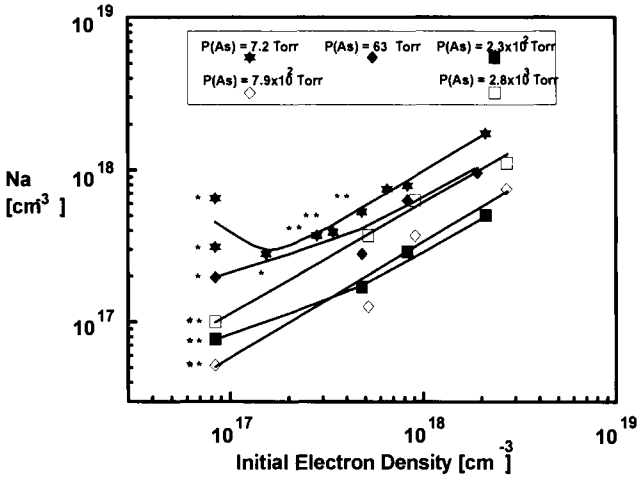

Fig. 2. Change in acceptor density induced by annealing as a function of the initial electron density in Te-doped GaAs.

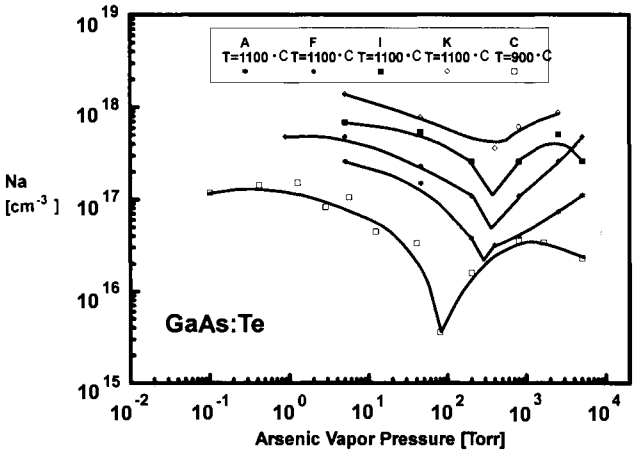

Fig. 3. Arsenic vapour pressure dependence of the acceptor density in Te-doped GaAs. Annealing was performed at 900–1100 °C for 67 h.

The lattice constant was measured using double-crystal X-ray diffraction with the (004) symmetrical configuration. The various symbols in the figures denote data obtained from crystals with different electron densities. The acceptor density shows a minimum under a

specific As vapour pressure ($P_{As,opt}$). Under almost the same As vapour pressure, the lattice constant also shows its minimum value. It seems that nearly perfect crystals with stoichiometric composition could be obtained under $P_{As,opt}$. Almost the same results were obtained for Zn-doped GaAs crystals. Therefore $P_{As,opt}$ is independent of the impurity concentration and dopant species. Almost the same results were also obtained in annealing experiments on GaP and optimum phosphorus pressure ($P_{P,opt}$) was shown to improve the crystal quality. However, in the case of GaP, the lattice constant shows its maximum value under a specific phosphorus vapour pressure.

Consequently, optimum vapour pressures were obtained as a function of annealing temperature for GaAs and GaP respectively as

$$P_{GaAs,opt} = 2.6 \times 10^6 \exp\left(-\frac{1.05\ eV}{kT}\right) \quad (2)$$

$$P_{GaP,opt} = 4.67 \times 10^6 \exp\left(-\frac{1.01\ eV}{kT}\right) \quad (3)$$

In order to investigate the deep levels in annealed GaAs crystals, PHCAP measurements [19] were carried out under constant-capacitance conditions [20]. The PHCAP method enables precise determination of the level density and activation energy, because ionization by monochromatic light irradiation at a fixed, very low temperature was used. In contrast with the conventional PHCAP method, the depletion layer thickness is kept constant regardless of the change in ion density due to light irradiation.

In order to obtain accurate values of level density and level position, fully neutralized deep levels should be ionized at each wavelength. One method of achieving this is to apply forward bias injection in the dark before each photoexcitation. In n-type GaAs bulk crystals the so-called photoquenching phenomenon [21] is observed in a specific wavelength region of about 1.0–1.5 eV below about 110 K. Therefore both the maximum and asymptotic saturation ion densities were obtained at each wavelength.

Figure 5 shows the PHCAP spectra of intentionally undoped GaAs ($n = 4 \times 10^{16}$ cm^{-3}) grown by the HB method before annealing [22]. Curves (a) and (b) show the maximum (N_{max}) and asymptotic (N_{asym}) ion densities respectively. Curve (c) represents the ion density (N_{dark}) in the dark after forward bias injection. N_{dark} corresponds to the ion density in the dark before photoexcitation. The almost constant value of N_{dark} verifies the photoexcitation of fully neutralized deep levels at each wavelength. Figure 6 shows the PHCAP spectrum obtained by subtracting N_{asym} from N_{max}. This is the deionized level density spectrum.

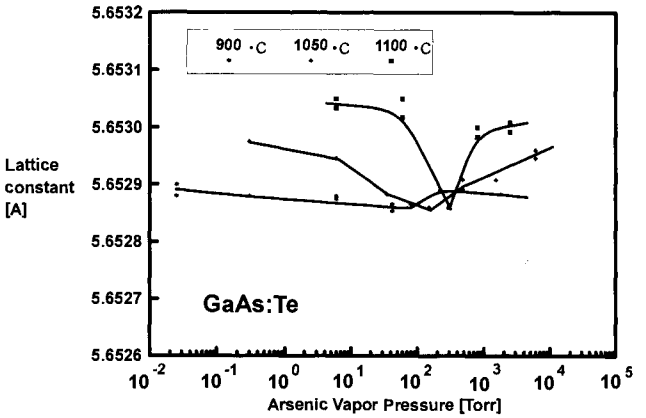

Fig. 4. Arsenic vapour pressure dependence of the lattice constant of Te-doped GaAs. The lattice constant was measured by double-crystal X-ray diffractometry.

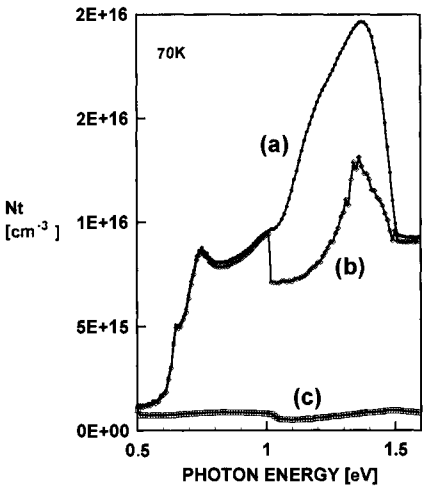

Fig. 5. Ion density PHCAP spectra of intentionally undoped GaAs ($n = 4 \times 10^{16}$ cm^{-3}) grown by the HB method before annealing: (a) and (b) show the maximum (N_{max}) and asymptotic (N_{asym}) ion densities respectively; (c) represents the ion density (N_{dark}) in the dark after forward bias injection.

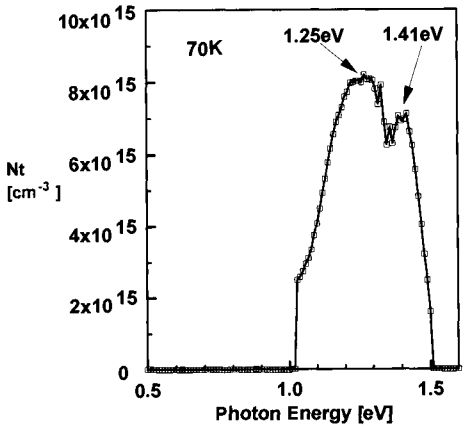

Fig. 6. Deionized level density PHCAP spectrum obtained from the subtraction of N_{asym} from N_{max}.

As seen in Fig. 5, two kinds of deep donors are clearly revealed at 0.65 and 0.72 eV below the conduction band. The deionized level density spectrum clearly shows two peaks at 1.25 and 1.41 eV respectively. The 1.25 and 1.41 eV deep levels are quite different, with different recovery temperatures and ionization levels. Figure 7 shows the PHCAP maximum ion density spectra of intentionally undoped GaAs crystals prepared by annealing under various As vapour pressures. Figure 8 shows the As vapour pressure dependence of the $E_c - 0.72$ eV level density. It is seen that the $E_c - 0.65$ eV level vanishes after annealing, perhaps owing to its thermal instability. However, the $E_c - 0.65$ eV level is stable in more strained crystals and the level density increases monotonically with increasing As vapour pressure. The level densities of the $E_c - 0.72$ eV donor and the 1.25 eV deionized level increase monotonically with increasing As vapour pressure. These deep levels are commonly detected in various GaAs bulk crystals with different dopant impurities and conductivity types [23]. The monotonic increase in level density indicates that these deep levels are closely related to the excess As composition of GaAs crystals. From the spectral correspondence among PHCAP, deep level transient spectroscopy (DLTS) and deep level photoluminescence (DLPL) [24] at 2.1 K it is seen that the $E_c - 0.65$ eV and $E - 0.72$ eV levels exhibit a larger difference between optical and thermal activation energies compared with that of the so-called EL2 level. Although both the $E_c - 0.72$ eV level and the so-called EL2 level are closely related to the excess arsenic composition of GaAs crystals, they are quite different from one another. They show different optical excitation energies and Frank–Condon shifts (d_{FC}).

The PHCAP method also revealed As-vacancy-related deep levels in heavily Te-doped GaAs prepared by annealing under As vapour pressure [25]. Figure 9 shows the As vapour pressure dependences of the 0.62 eV+E_v and 0.87 eV+E_v level densities, which were measured after 1.44 eV monochromatic light irradiation at each wavelength to empty the deep levels. The level density decreases monotonically with increasing As vapour pressure. These deep levels could also be detected in vacuum-annealed samples (500 °C for 50 h) but not in virgin samples. This confirms the close

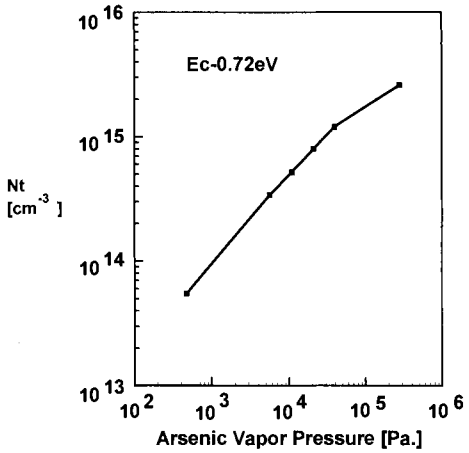

Fig. 8. Arsenic vapour pressure dependence of the $E_c - 0.72$ eV level density in intentionally undoped GaAs ($n = 4 \times 10^{16}$ cm^{-3}) grown by the HB method. Annealing was performed at 900 °C for 67 h.

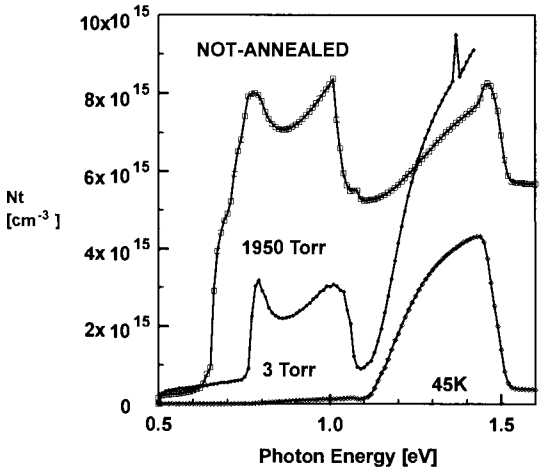

Fig. 7. Saturation ion density (N_{max}) PHCAP spectra of intentionally undoped GaAs crystals prepared by annealing under various As vapour pressures. Annealing was performed at 900 °C for 67 h.

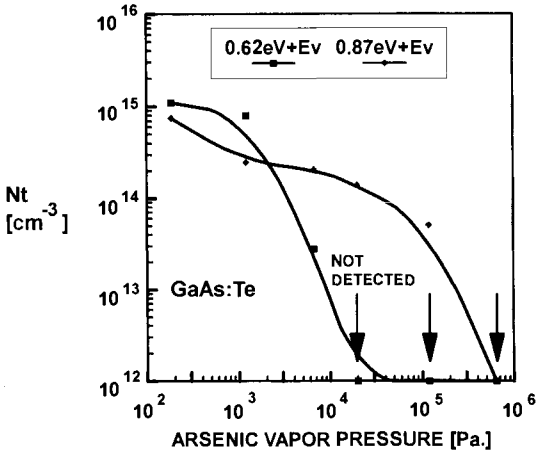

Fig. 9. Arsenic vapour pressure dependences of the 0.62 eV+E_v and 0.87 eV+E_v level densities in heavily Te-doped GaAs ($n = 7.4 \times 10^{17}$ cm^{-3}) prepared by annealing under As vapour pressure. PHCAP measurements were performed after 1.44 eV monochromatic light irradiation at each wavelength to empty the deep levels.

relation between these deep levels and the As vacancies.

Precise PHCAP measurements at 20 K revealed stoichiometry-dependent deep levels at around $E_c - 0.48$ eV in Te-doped horizontal gradient freeze (HGF) grown GaAs prepared by annealing under As vapour pressure. The level density decreases monotonically with increasing As vapour pressure. The $E_c - 0.48$ eV level was detected in Te-doped GaAs but not in intentionally undoped or Si-doped GaAs crystals. Therefore this level should relate to at least the dopant impurity Te and the As vacancies. The $E_c - 0.72$ eV deep donor was also detected in the same samples and the As vapour pressure dependence of the level density is almost the same as that in intentionally undoped HB GaAs crystals. This suggests that the $E_c - 0.72$ eV level originates from the excess-As-atom-related intrinsic defects and not from impurities.

3. Liquid phase epitaxial growth by the temperature difference method under controlled vapour pressure

The vapour pressure control technique can be successfully applied to LPE growth, enabling one to produce epitaxial layers with good crystal quality. Figure 10 shows a schematic drawing of the LPE apparatus for TDM-CVP. In contrast with the conventional slow-cooling method, crystal growth proceeds with time at a fixed substrate temperature. A temperature difference between the upper and lower parts of the solution was applied. The driving force for supersaturation at constant temperature is the difference in solubility and kinetic energy caused by the temperature difference between the lower and upper parts of the solution. Vapour pressure control of the group V element is also applied in order to control the stoichiometric composition of segregated crystals throughout the Ga–As solution.

Figure 11 shows the As vapour pressure dependences of the carrier concentration and the electron mobility. Figure 12 shows the As vapour pressure dependences of the lattice constant and the halfwidth of the X-ray rocking curve of LPE GaAs. The lattice constant was measured using the first GaAs crystal with the (004) symmetrical configuration. Therefore the halfwidth of the X-ray rocking curve is dependent on the perfection of the specimen crystals. Under a specific As vapour pressure the carrier concentration shows its minimum value and the Hall mobility shows its maximum. The lattice constant and the halfwidth of the X-ray rocking curve also show minimum values under almost the same As vapour pressure. This leads to a crucial conclusion that high purity LPE crystals with good perfection were obtained. Similar results

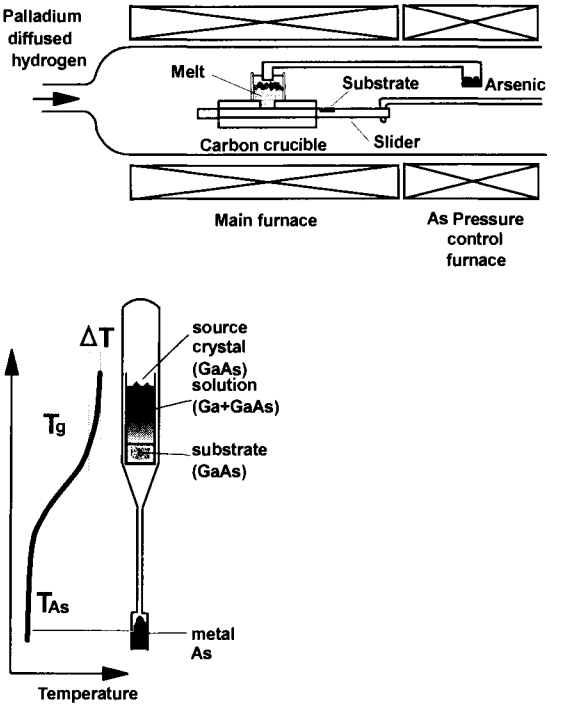

Fig. 10. Schematic drawing of the liquid phase epitaxy apparatus for the temperature difference method under controlled vapour pressure.

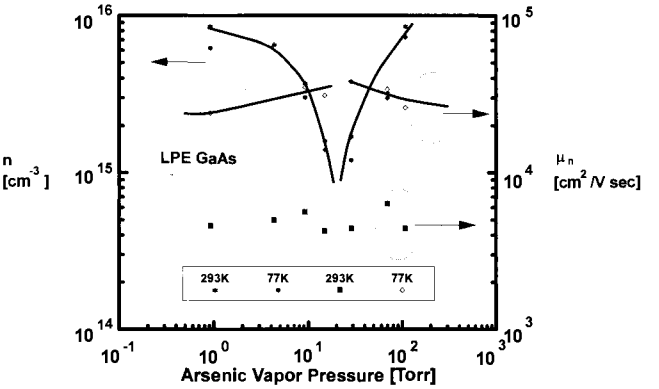

Fig. 11. Arsenic vapour pressure dependences of the carrier concentration and the electron mobility in LPE GaAs prepared by TDM-CVP.

were also obtained for LPE GaP crystals using TDM-CVP. In particular, PL measurements revealed the existence of excitons bound to shallow impurities even at room temperature. This also confirms the high crystal quality of LPE GaP grown by TDM-CVP [26].

The vapour pressure dependences of these crystal characteristics seem to be similar to those obtained from annealing experiments. Figure 13 shows the temperature dependences of the optimum As vapour pressures obtained from both LPE growth by TDM-CVP

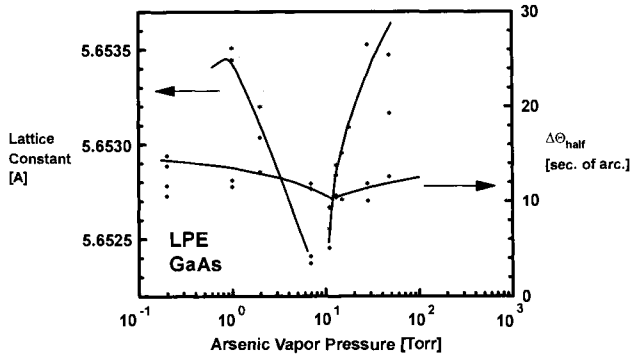

Fig. 12. Arsenic vapour pressure dependences of the lattice constant and the halfwidth of the X-ray rocking curve of LPE GaAs.

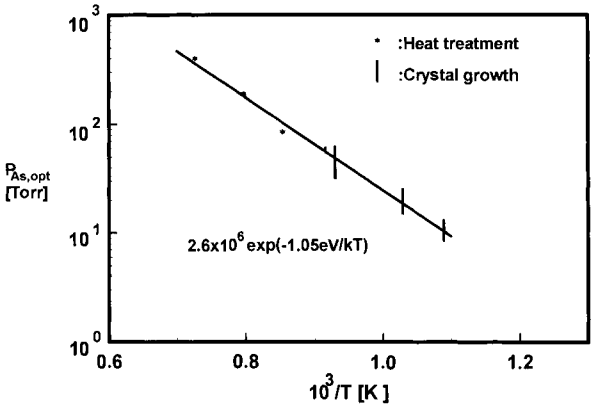

Fig. 13. Temperature dependences of the optimum As vapour pressures obtained from both LPE growth by TDM-CVP and annealing experiments under As vapour pressure.

and annealing experiments under As vapour pressure [27]. The two sets of experimental results are similar.

The deviation from stoichiometric GaAs composition influences the amphoteric behaviour of group IV elements in GaAs. As shown in Fig. 14, the diffusion phenomenon of Si in GaAs is strongly influenced by the deviation from stoichiometric composition [28]. Similar results on Si diffusion in GaAs were also reported by Omura *et al.* [29].

4. Surface treatment before regrowth of GaAs by molecular layer epitaxy and its association with the surface stoichiometry

Recent development on semiconductor devices requires extremely thin and multilayer structures. Nishizawa *et al.* applied the idea of atomic layer epitaxy (ALE) to compound semiconductor crystals and realized monomolecular layer epitaxy of single-crystal GaAs for the first time [30]. ALE was used for the

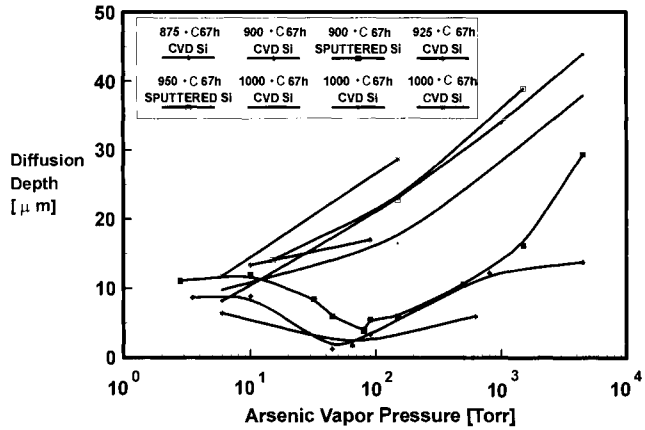

Fig. 14. Arsenic vapour pressure dependence of the diffusion depth of Si into GaAs from various diffusion sources.

preparation of II–VI compound polycrystalline films by Ahonen *et al.* [31]. This method is based on chemical reactions of adsorbates on semiconductor surfaces. In view of the growth mechanism and the resultant monomolecular crystal growth, Nishizawa *et al.* called this method molecular layer epitaxy. MLE is a promising epitaxial growth method to achieve precise thickness control with atomic accuracy (AA) and stoichiometric composition.

Figure 15 shows a schematic drawing of the MLE growth apparatus together with growth sequence diagrams of the alternate gas injection method. In the case of GaAs the source gases typically used for MLE are triethylgallium (TEG) or trimethylgallium (TMG) for gallium and AsH_3 for arsenic. A detailed description of the surface reaction mechanisms in the TMG/AsH_3 system is given elsewhere [32].

Usually, GaAs crystals are preheated just before growth to remove residual oxide and/or carbide layers. However, the pretreatment conditions, *i.e.* flush desorption conditions, have not been fully optimized yet. This is a serious problem that remains to be solved especially in ultrathin and multilayer structures with atomic accuracy.

In order to study the effects of surface treatment procedure and surface stoichiometry on the electrical properties, p^+n^- diodes were made by regrowth on commercially available metal organic chemical vapour deposition (MOCVD) grown n^-/n^+-GaAs epitaxial wafers. Defects in the interfacial region were evaluated through the current–voltage characteristics of the regrown p^+n^- diodes. The specific forward voltage (V_{fs}) at 1 μA (pad area 100 μm^2) is obtained as a function of the various pretreatment conditions for regrowth. A higher V_{fs} indicates a lower density of recombination centres.

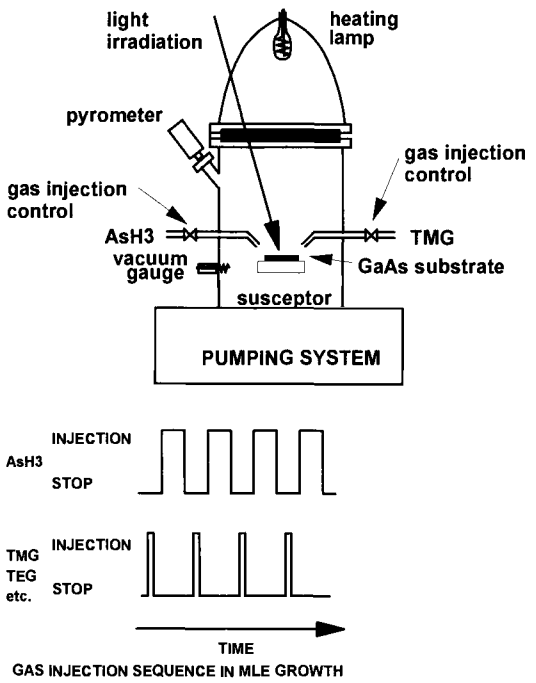

Fig. 15. Schematic drawing of the molecular layer epitaxy growth apparatus together with growth sequence diagrams of the alternate gas injection method.

The chemical treatment just before MLE was as follows. After degreasing with an organic solvent, the epitaxial wafers were chemically etched using a sulphuric-acid-based etchant to a thickness of about 1500 Å. The GaAs wafers were then dipped in HCl for a few seconds to reduce the oxide layer thickness. Even after dipping in HCl, X-ray photoelectron spectroscopy (XPS) and Auger electron spectroscopy (AES) analysis revealed a trace of thin oxide layer on the GaAs surface.

Prior to MLE growth, the substrate in the growth chamber was heated to remove the thin oxide layer and to achieve surface stoichiometry. The MLE growth temperature used was 420 °C. A mercury lamp was used to irradiate the substrate during growth. Diethylzinc (DEZn) was used for the p-type dopant in the TEG/AsH_3 system. DEZn injection was done after AsH_3 injection (mode AA) to achieve heavy acceptor doping. A detailed description of MLE doping is given elsewhere [33]. The regrown structure comprised a 100 Å Zn-doped p^{++} top contact layer with $p = 6 \times 10^{19}$ cm^{-3}, a 250 Å Zn-doped p^{+} layer with $p = 4 \times 10^{18}$ cm^{-3} and a 150 Å undoped layer with $n < 3 \times 10^{16}$ cm^{-3}. These layers were epitaxially regrown on pretreated 3500 Å n^{-} MOCVD-grown epitaxial wafers. An unalloyed Ti–Au metal electrode was applied on the p^{++} top contact layer by the conventional lift-off process without any heat treatment. The back contact was formed by AuGe–Au, also without any heat treatment. Current–voltage characteristics were measured at nominal room temperature as a function of the preheating conditions of temperature, time and AsH_3 pressure.

Recent XPS and quadrupole mass spectroscopy (QMS) results show the effect of AsH_3 on the desorption of the oxide layer from the GaAs surface [34]. In ultrahigh vacuum without AsH_3 introduction, the Ga oxide layer was desorbed from the GaAs surface at around 700 °C. Under the existence of an AsH_3 ambient the oxide layer can be safely removed at lower temperature. This can be explained by the surface reaction of the oxide layer with cracked chemical species of AsH_3.

The preheating temperature dependence of V_{fs} shows a Λ-shaped characteristic. At lower temperature the increase in V_{fs} with temperature can be explained by the removal of the residual oxide layer on GaAs. However, at higher temperature it is considered that the surface stoichiometry degrades the I–V characteristic with increasing preheating temperature. The preheating time and AsH_3 pressure dependences also confirm these results. Detailed results on the flush desorption condition are given elsewhere [34].

Stoichiometry control is also quite an important factor even in the research field of surface science.

5. Interstitial As atoms in GaAs

Figure 16 shows the As vapour pressure dependence of the crystal weight of GaAs prepared by annealing. It is seen that the crystal weight increases monotonically with increasing As vapour pressure. Figure 17 shows the results of anomalous X-ray transmission intensity measurements as a function of As vapour pressure. The intensity of anomalous X-ray transmission decreases with increasing As vapour pressure. The anomalous X-ray transmission is strongly influenced by the existence of interstitial atoms, because this phenomenon is caused by the propagation of the Poynting vector of X-rays along the diffracting lattice plane. These results seem to confirm the existence of interstitial-type defects when GaAs crystals are annealed under extremely high As vapour pressure.

Figure 18 shows the As vapour pressure dependence of the lattice constant. The samples used were Zn-doped HB-grown GaAs prepared by annealing at 900–1100 °C for 67 h under As vapour pressure. As already seen, the lattice constant shows a minimum value at the optimum As vapour pressure. In the higher As vapour pressure region the lattice constant increases monotonically with increasing As vapour

pressure and shows a saturation behaviour. From the temperature dependence of the saturation lattice constant in the high As vapour pressure region the formation energy of the defect was obtained at about 0.9 eV.

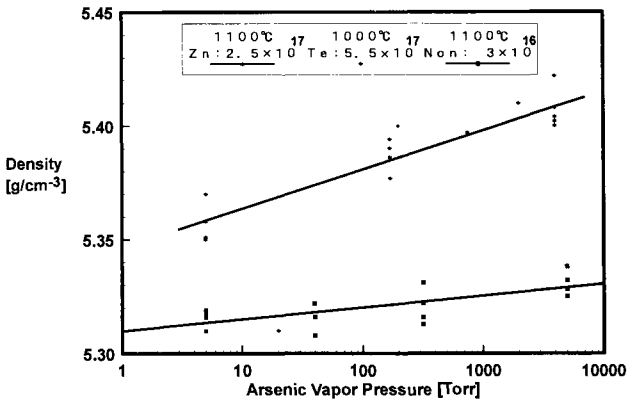

Fig. 16. Arsenic vapour pressure dependence of the crystal weight of GaAs prepared by annealing. Annealing was performed at 900–1100 °C for 67 h.

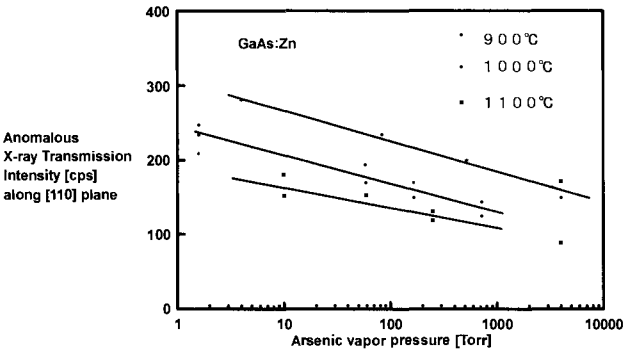

Fig. 17. Change in anomalous X-ray transmission intensity of annealed GaAs as a function of the As vapour pressure.

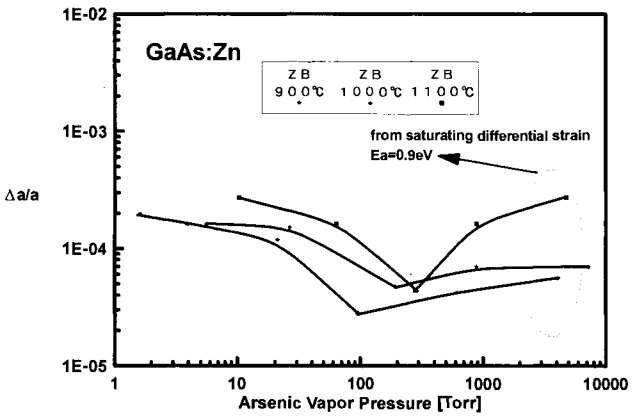

Fig. 18. Arsenic vapour pressure dependence of the lattice constant of Zn-doped HB-grown GaAs prepared by annealing at 900–1100 °C for 67 h.

Figure 19 shows the As vapour pressure dependence of the 1.25 eV level density obtained from the PHCAP measurements. This level is followed by the so-called photoquenching phenomenon. The level density increases monotonically with increasing As vapour pressure and saturates under high As vapour pressure. From the temperature dependence of the saturation level density the formation energy of the defect is determined as 1.16 eV (Fig. 20). This defect

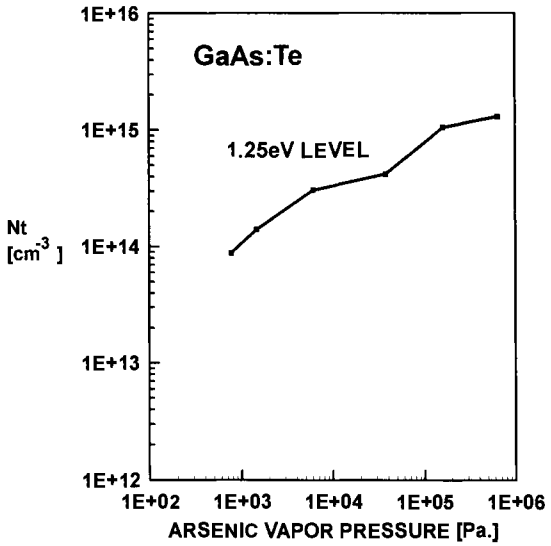

Fig. 19. Arsenic pressure dependence of the 1.25 eV deionized level density obtained from PHCAP measurements. This level is followed by the so-called photoquenching phenomenon. Samples used were intentionally undoped GaAs ($n = 4 \times 10^{16}$ cm^{-3}) grown by the HB method.

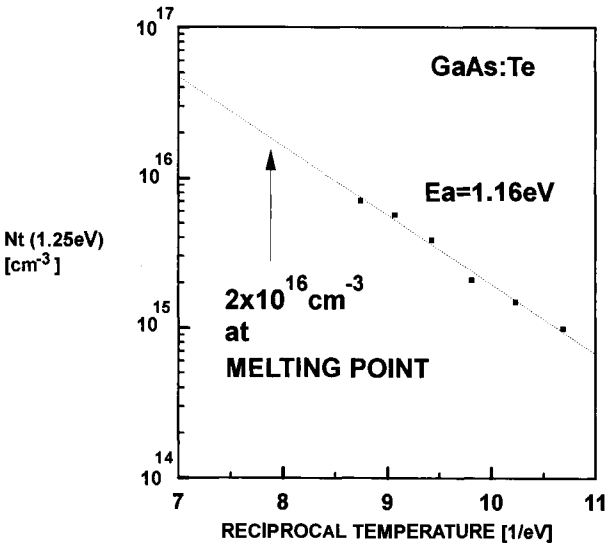

Fig. 20. Annealing temperature dependence (Arrhenius plot) of the 1.25 eV level density in n-GaAs saturated under high As vapour pressure.

formation energy is in good accordance with that obtained from the lattice constant measurements.

From the theoretical calculations of formation energy by Bennemann [36] and Swalin [37], the defect formation energy of 1.16 eV is closer to that of interstitial atoms than to that of vacancies. Therefore we consider that interstitial atoms must be introduced in the initial stage of defect formation when GaAs is annealed under high As vapour pressure.

In order to investigate the stable interstitial site, we applied the RBS technique to As^+-implanted GaAs crystals. The depth resolution was enhanced by using the grazing exit angle configuration of a silicon surface barrier (SSB) detector. From the results of multidirectional and high depth resolution RBS measurements the stable interstitial site was assumed to be ⟨100⟩-split and relaxed bond centre (r-BC) interstitialcy. This RBS result corresponds to that obtained from the anomalous X-ray transmission measurements.

6. GaAs bulk crystal growth by the vapour-pressure-controlled Czochralski (PCZ) method

The vapour pressure control technology established by our annealing and LPE experiments under controlled vapour pressure can also be extended to GaAs bulk crystal melt growth. The first application of overpressure to control GaAs solution growth was carried out by Suzuki and Akai [16] using the horizontal Bridgman method. High quality GaAs bulk crystals with very low dislocation density were grown on applying our optimum As vapour pressure of 830 Torr, where the temperature of metallic As is 617 °C. These crystals are now supplied all over the world. Thereafter this work was also reconfirmed by Parsey *et al.* [38] and it was shown that the dislocation density and defect density decreased abruptly at a specific metallic As temperature of 617 ± 1 °C. This specific As vapour pressure was set equal to that obtained from our eqn. (2) for the temperature dependence of the optimum As vapour pressure. The optimum As vapour pressure at the melting point of GaAs is obtained as 830 Torr from eqn. (2). The corresponding temperature of metallic As is 617 °C according to eqn. (1).

Whereas the dislocation density is greater than that of HB crystals owing to the large thermal strain, the conventional CZ method enables the growth of GaAs bulk crystals with large diameter compared with the HB method. By applying the vapour pressure control method to CZ growth, high quality CZ GaAs bulk crystals with very low dislocation density were obtained. As shown in Fig. 21, 2 in wafers with a dislocation density as low as 2000 cm^{-2} were grown without impurity doping under the optimum As vapour pressure. The etch pit density (EPD) of intentionally undoped LEC GaAs is about 10^5 cm^{-2}. This is higher by at least one order of magnitude than that of PCZ-grown GaAs crystals. DLTS measurements revealed three kinds of deep donors. Figure 22 shows the As vapour pressure dependence of each deep level density. It is seen that the deep level density also shows a minimum under the optimum As vapour pressure. Similar results were also obtained from the PHCAP measurements. Figure 23 shows photographs of PCZ-grown and conventional LEC-grown GaAs ingots. The surface of the PCZ GaAs crystal is seen to be very brilliant compared with that of the conventional LEC crystal.

In order to evaluate deep levels in various GaAs bulk crystals, PHCAP measurements were carried out under constant-capacitance conditions. Figure 24 shows the PHCAP spectra of various intentionally undoped n-GaAs crystals with a carrier concentration of about 4×10^{16} cm^{-3}. As reported previously, the so-

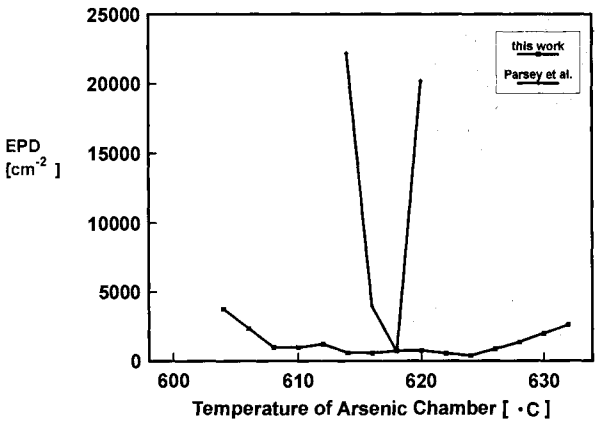

Fig. 21. Spatial distribution of the etch pit density across PCZ-grown GaAs bulk crystals. Dislocation etch pits were revealed by the molten KOH etchant.

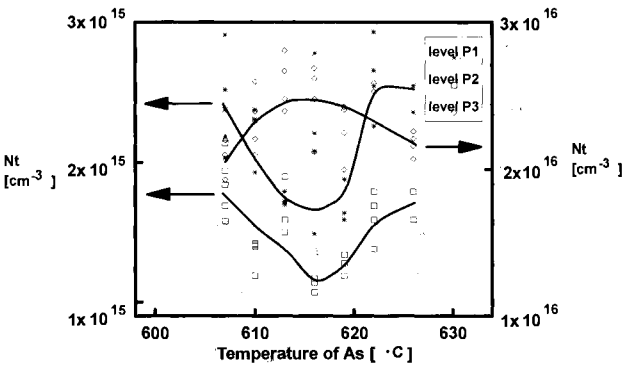

Fig. 22. Arsenic vapour pressure dependence of the deep level density of PCZ-grown GaAs bulk crystals revealed by deep level transient spectroscopy.

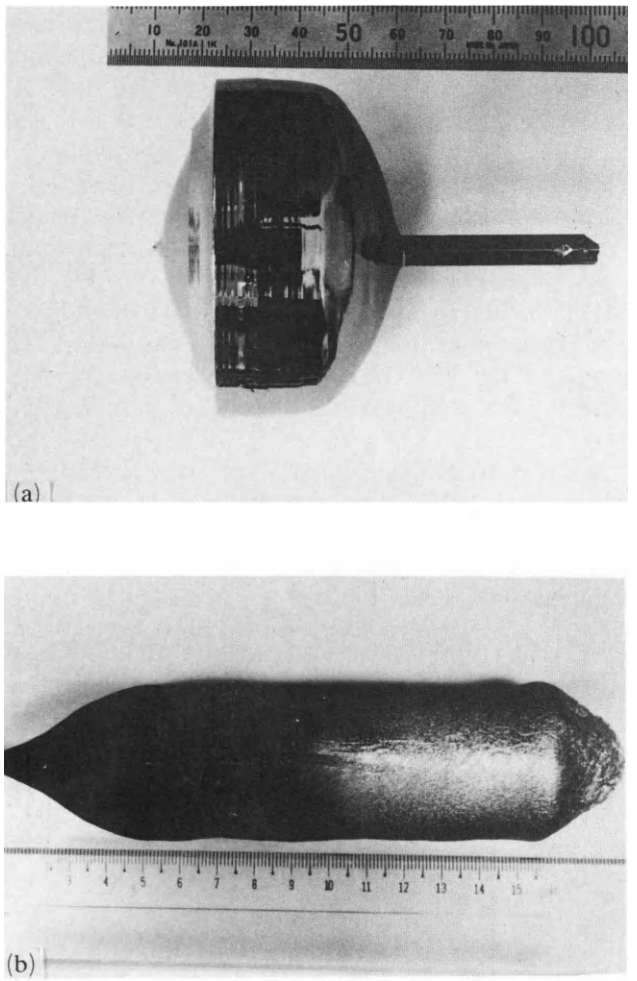

Fig. 23. Photographs of the as-grown surface of (a) PCZ-grown and (b) conventional LEC-grown GaAs ingots.

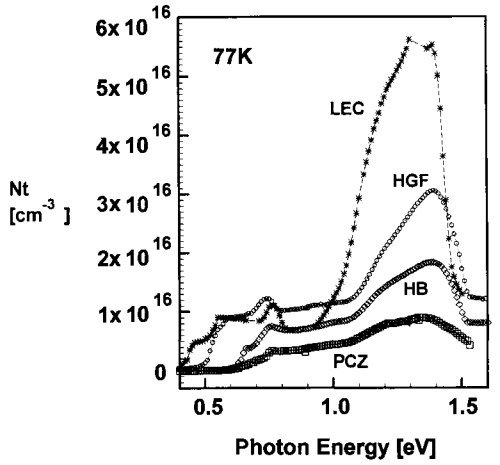

Fig. 24. Ion density PHCAP spectra of various intentionally undoped n-GaAs crystals with a carrier concentration of about 4×10^{16} cm^{-3}.

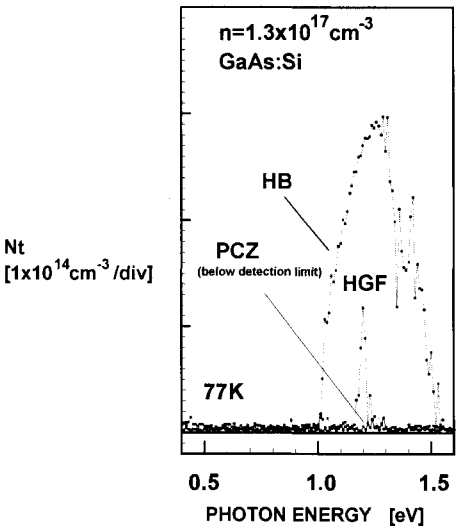

Fig. 25. Deionized level density PHCAP spectra of various n-GaAs bulk crystals. Samples used were various Si-doped GaAs bulk crystals with a carrier concentration of 1.5×10^{17} cm^{-3} grown by various methods.

called photoquenching phenomenon is observed in the spectral region of 1.0–1.50 eV below about 110 K. After irradiation with monochromatic light the ion density increases rapidly and then decreases gradually. The PCZ crystal shows a minimum deep level density compared with other crystals. This confirms the possibility of perfect crystal growth by the PCZ method. Figure 25 shows the PHCAP spectra obtained from the differences between the maximum and saturation ion densities at each wavelength. The samples used were various Si-doped GaAs bulk crystals with a carrier concentration of 1.5×10^{17} cm^{-3} grown by various methods. The PCZ crystal shows an extremely low deep level density displaying the so-called photoquenching phenomenon.

7. GaAs bulk crystal grown by the vapour-pressure-controlled float zone method

In order to obtain high purity bulk crystals with stoichiometric composition, the vapour-pressure-controlled float zone (VPC-FZ) method has been applied to GaAs bulk crystal growth*. The FZ method has the possibility to minimize the unintentional impurity contamination from the crucible. Although the growth condition has not been optimized and the As vapour pressure is not strictly controlled yet, high

*FZ-grown GaAs crystals were supplied by the Tohoku Steel Co. Ltd., Sendai, Japan.

purity p-GaAs crystals were obtained with a carrier concentration as low as about 1×10^{15} cm^{-3}. Figure 26 shows the PHCAP spectrum of a VPC-FZ-grown p-GaAs crystal. Stoichiometry-dependent deep acceptors were detected at 0.53, 0.71, 0.90 and 1.0 eV above the valence band. These deep levels were commonly detected regardless of any variation in dopant impurities and growth method. The As vapour pressure dependences of the level densities were also clarified by our PHCAP measurements. However, the level density in VPC-FZ GaAs is much lower than that in LEC-and HB-grown samples (by about three orders of magnitude). This confims the ability of the VPC-FZ method to supply high purity GaAs crystals with stoichiometric composition.

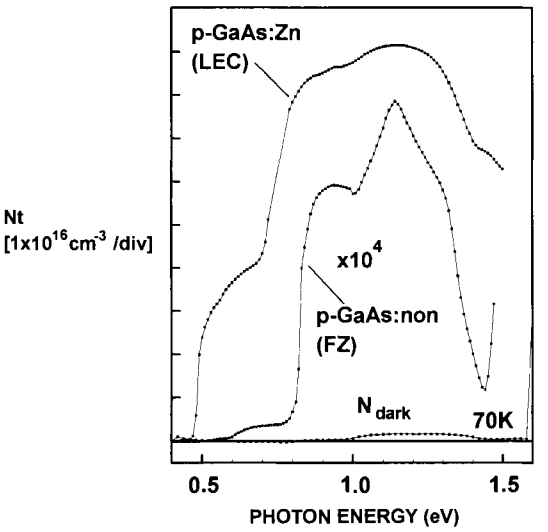

Fig. 26. Ion density PHCAP spectrum of a vapour-pressure-controlled FZ grown p-GaAs crystal, p-GaAs crystals were obtained with a carrier concentration as low as about 1×10^{15} cm^{-3}.

8. InP bulk crystal growth by the vapour-pressure-controlled zone-melting method

The vapour pressure control technique has also been applied to InP bulk crystal growth in combination with the zone-melting method. Figure 27 shows the phosphorus vapour pressure dependences of the carrier concentration and the Hall mobility. The carrier concentration and Hall mobility at 77 K show minimum and maximum values under a specific phosphorus vapour pressure of about 22.5 atm at the melting point. The present value of mobility is greater than that obtained from the conventional LEC method.

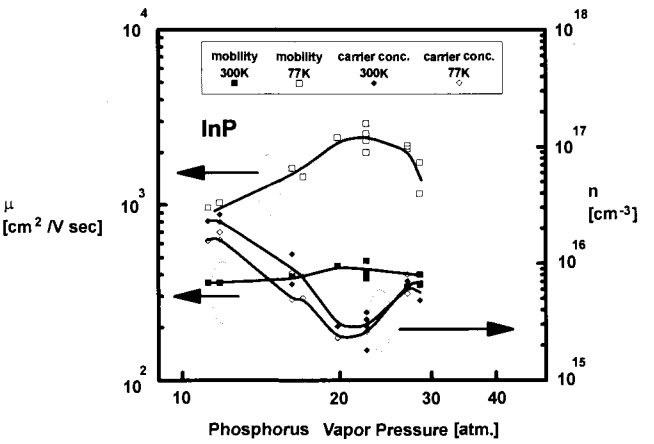

Fig. 27. Phosphorus vapour pressure dependences of the carrier concentration and the Hall mobility in vapour-pressure-controlled zone-melting grown InP.

9. GaP pure green LED without nitrogen doping

The luminous efficiency of an LED is strongly influenced by a small amount of defects. Therefore the LED characteristics are very sensitive to the crystal perfection.

It was shown that TDM-CVP yields LPE GaP almost free from dislocations and a GaP pure green LED was fabricated by this method. At that time it was believed that nitrogen should be doped to improve the luminous efficiency, because GaP has an indirect transition. However, the emission shifts to a longer wavelength on N doping and the colour of the GaP:N LED is closer to yellow than to green. The GaP LED grown by TDM-CVP exhibits a pure green emission ($\lambda = 550$ nm) with a high luminous efficiency without N doping. The wavelength of this emitted light corresponds to the direct energy gap of the GaP crystal.

Figure 28 shows the phosphorus vapour pressure dependence of the deep level density measured by the conventional PHCAP method. The deep level density shows a minimum under the optimum phosphorus vapour pressure. These levels were shown to be stoichiometry dependent and to act as non-radiative recombination centres. It is shown that TDM-CVP controls the introduction of these deep levels caused by the deviation from stoichiometric composition.

10. GaAlAs very bright LED

TDM-CVP has also been applied to LPE of AlGaAs, InGaP and AlGaAsP ternary and quaternary compound semiconductor crystals. A superbright LED has already been fabricated with a quantum efficiency of up to 30%. The temperature difference method is

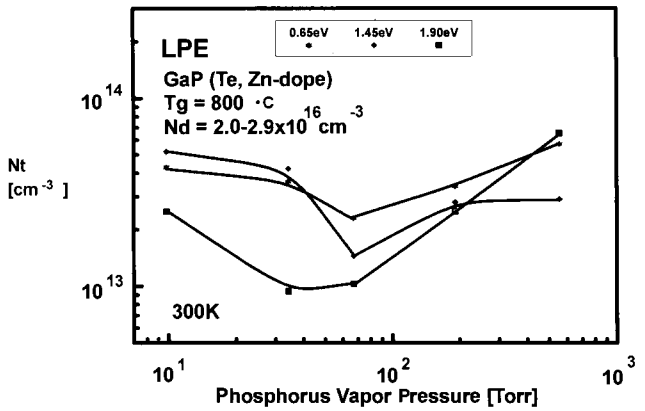

Fig. 28. Phosphorus vapour pressure dependence of the deep level density in TDM-CVP-grown LPE GaP measured by the conventional PHCAP method. The deep level density shows a minimum under a specific optimum phosphorus vapour pressure.

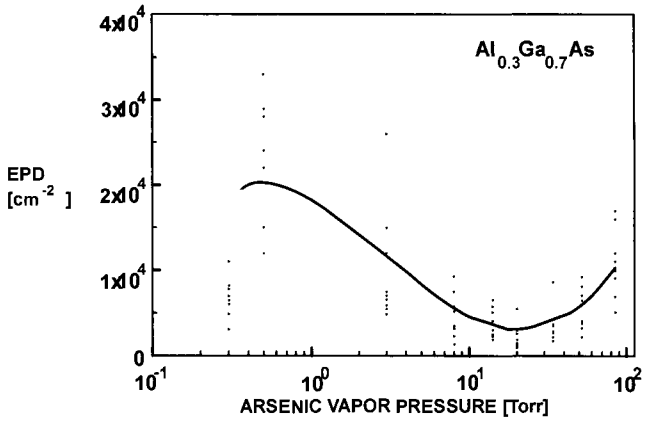

Fig. 29. Arsenic vapour pressure dependence of the etch pit density in LPE-grown $Al_xGa_{1-x}As$ ($x=0.3$). The EPD shows a minimum value under a specific As vapour pressure.

suitable for mass production of such LEDs because of its constancy of growth temperature.

Figure 29 shows the As vapour pressure dependence of the etch pit density in $Al_xGa_{1-x}As$ ($x=0.3$). The EPD shows a minimum value under a specific As vapour pressure. The optimum As vapour pressure should be dependent on the composition x. Precise control of the deviation from stoichiometric composition is expected to improve the luminous efficiency.

11. Theoretical consideration of stoichiometry control through solution

The model for the mechanism of vapour pressure control is described under the concept that the chemical potentials of As in the three phases (gas, liquid and solid) are equal to each other under the applied vapour pressure [39]. It is important that the temperature dependence of the optimum vapour pressure is the same as that of the heat treatment experiments, in which the solid phase is directly controlled by the applied vapour pressure via the equality of the chemical potentials of the solid and gas phases. The temperature difference between the molten phase and the substrate accelerates the diffusion of dissolved GaAs towards the substrate and its segregation. The growth rate is controlled by the temperature difference but not by the applied vapour pressure if the source crystals are present at the top of the molten phase. Without the temperature difference it was confirmed that the As content in the liquid reaches a balanced value depending on the applied vapour pressure after application of the vapour pressure. This means that some kind of three-phase equilibrium is established for an arbitrary value of applied vapour pressure.

The fundamental idea that the chemical potentials of As in the gas, liquid and solid phases become equal was first presented by Nishizawa in the literature. From our experimental result that the dominant non-stoichiometric defects in GaAs are As interstitial atoms at high As vapour pressure, it is assumed that these two kinds of point defects predominantly determine the chemical potentials of As as well as gallium in the solid phase. The presence of gallium vacancies and gallium interstitials is also taken into consideration, but they are assumed to be of smaller concentrations. On the other hand, the As chemical potential in the liquid phase was assumed to be determined by the GaAs molecules and some kind of As molecules or atoms in the liquid which are equilibrated with each other in order to explain the very small but finite increase in solubility under an applied vapour pressure. It is shown that the optimum vapour pressure thus calculated was in good agreement with the experimentally obtained optimum vapour pressure as a function of temperatures [39].

12. Summary

Evaluation and control of the deviation from stoichiometry have been increasingly important in the field of compound semiconductor crystals. Each device process, including crystal growth and diffusion, cannot be completed without consideration of the stoichiometry, because the compound semiconductor device requires precise control of electrical and optical characteristics. More precise control of stoichiometric composition should be required even in the field of surface science. Stoichiometry control should also be important in the field of superconducting ceramics.

References

1 Y. Watanabe, J. Nishizawa and I. Sunagawa, *Kagaku, 21* (3) (1951) 140–141.
2 H. Otsuka, K. Ishida and J. Nishizawa, *Jpn. J. Appl. Phys., 8* (1969) 632.
3 J. Nishizawa, S. Shinozaki and K. Ishida, *J. Appl. Phys., 14* (1974) 1638.
4 J. Nishizawa, H. Otsuka, S. Yamakoshi and K. Ishida, *Jpn. J. Appl. Phys., 13* (1974) 46.
5 S. Yamakoshi, *Doctoral Thesis*, Tohoku University, 1975.
6 J. Nishizawa, I. Shiota and Y. Oyama, *J. Phys. C: Solid State Phys., 9* (1986) 1.
7 J. Nishizawa, Y. Oyama and K. Dezaki, *J. Appl. Phys., 67* (4) (1990) 1884.
8 J. Nishizawa, Y. Oyama and K. Dezaki, *Phys. Rev. Lett., 65* (1990) 2555.
9 I. Fujimoto, *Jpn. J. Appl. Phys., 23* (1984) L287.
10 K. Tomizawa, K. Sassa, Y. Shimanuki and J. Nishizawa, *J. Electrochem. Soc., 131* (1984) 2394.
11 J. Nishizawa, K. Ito, Y. Okuno, F. Sakurai, M. Koike and T. Teshima, *Proc. IEEE Int. Electron. Device Meet.*, IEEE, New York, 1983, pp. 311–314.
12 J. Nishizawa, K. Itoh, Y. Okuno, M. Koike and T. Teshima, *Proc. IEEE Int. Electron. Device Meet.*, IEEE, New York, 1983, pp. 311–314.
13 J. Nishizawa, Y. Okuno, M. Koike and F. Sakurai, *Jpn. J. Appl. Phys., 19, Suppl. 19-1* (1980) 3.
14 J. Nishizawa, S. Shinozaki and K. Ishida, *J. Appl. Phys., 14* (1974) 1638.
15 J. Nishizawa and K. Inokuchi, *Proc. Int. Optoelectronics Workshop, Taiwan, 1981.*
16 T. Suzuki and S. Akai, *Bussei, 12* (1971) 144.
17 J. M. Parsey Jr., Y. Nanishi, J. Lagowski and H. C. Gatos, *J. Electrochem. Soc., 128* (1981) 937.
18 R. E. Honig, *RCA Rev., 30* (1969) 285.
19 A. Itoh, T. Sukegawa and J. Nishizawa, *Tech. Rep. Transistor Specialist Committee, IEE Japan*, 1967; *Tech. Rep. Res. Inst. Electrical Communication, Tohoku University, TR-32* (1969).
20 Y. Oyama, *Denshi Tokyo (IEEE Tokyo), 28* (1989) 130.
21 A. L. Lin, E. Omelianovski and R. H. Bube, *J. Appl. Phys., 47* (1976) 1852.
22 J. Nishizawa, Y. Oyama and K. Dezaki, *J. Appl. Phys., 67* (4) (1990) 1884.
23 J. Nishizawa, Y. Oyama and K. Dezaki, *J. Appl. Phys., 69* (3) (1991) 1446.
24 J. Nishizawa, Y. Oyama and K. Dezaki, *J. Phys. Condens. Matter, 3* (1991) 7269.
25 J. Nishizawa, Y. Oyama and K. Dezaki, *J. Appl. Phys., 70* (2) (1991) 833.
26 K. Suto and J. Nishizawa, *J. Appl. Phys., 67* (1) (1990) 459.
27 J. Nishizawa and Y. Okuno, in M. A. Herman (ed.), *Proc. 2nd Int. School on Semiconductor Optoelectronics, 28tniewo*, PWN (Polish Scientific Publishers), Warsaw, 1978, pp. 101–130.
28 Y. Kobayashi, Y. Okuno and J. Nishizawa, *Tech. Rep. Res. Inst. Electrical Communication, Tohoku University, TR-42*, 1978.
29 E. Omura, X. X. Wu, G. A. Vawter, L. Coldren, E. Hu and J. L. Merz, *Electron. Lett., 22* (1986) 496.
30 J. Nishizawa, H. Abe and T. Kurabayashi, *J. Electrochem. Soc., 132* (1983) 1197.
31 M. Ahonen, M. Pessa and T. Suntla, *Thin Solid Films, 65* (1980) 301.
32 J. Nishizawa, H. Sakuraba and Y. Oyama, *Thin Solid Films, 225* (1993) 1.
33 J. Nishizawa, H. Abe and T. Kurabayashi, *J. Electrochem. Soc., 136* (2) (1989) 478.
34 J. Nishizawa and H. Sakuraba, in preparation.
35 J. Nishizawa, in preparation.
36 K. H. Bennemann, *Phys. Rev., 137* (1961) A1497.
37 R. A. Swalin, *J. Phys. Chem. Solids, 18* (1961) 290.
38 J. M. Parsey Jr., Y. Nanishi, J. Lagowski and H. C. Gatos, *J. Electrochem. Soc., 128* (1981) 937.
39 J. Nishizawa, Y. Okuno and K. Suto, in J. Nishizawa (ed.), *Japan Annual Reviews in Electronics, Computers and Telecommunications (JARECT)*, Vol. 19, *Semiconductor Technologies*, Ohmsha and North-Holland, Tokyo, 1986, p. 17.

Materials Science and Engineering, B21 (1993) 120–129

Evaluation of III-V growth technologies for optoelectronic applications

Harald Heinecke and Eberhard Veuhoff

University of Ulm, Dept. Semiconductor Physics, P.O. Box 4066, D-W-7900 Ulm (Germany) and Siemens Corporate Research and Development, Otto-Hahn-Ring 6, D-W-8000 München 83 (Germany)

Abstract

In this review, the capabilities of molecular beam epitaxy (MBE), metalorganic vapour phase epitaxy (MOVPE) and metalorganic molecular beam epitaxy (MOMBE) or chemical beam epitaxy (CBE) for the growth of optoelectronic layered structures are evaluated. Both MBE and MOVPE are used in production of discrete devices and for future integration, MOMBE/CBE can play an increasing role due to unique features which include perfection in selective area epitaxy and environmental safety aspects. Moreover the combined multistage use of these growth technologies to generate new epitaxial device concepts offers very important potential. This is shown here by the example of a laser-amplifier/waveguide integration using MOVPE and MOMBE.

1. Introduction

The basic III–V layered structures of photonic and optoelectronic devices can be produced by several growth technologies. Nowadays, the most common processes are: molecular beam epitaxy (MBE), metal–organic vapour phase epitaxy (MOVPE), and metal–organic molecular beam epitaxy (MOMBE) or chemical beam epitaxy (CBE) [1]. In most applications, chloride vapour phase epitaxy (VPE) and liquid phase epitaxy (LPE) are being replaced by MBE, MOVPE and MOMBE. For example, novel device structures require more and more MQW layers and the overgrowth of DBR or DFB gratings on large area substrates; these requirements are difficult to achieve using VPE and LPE [2]. Furthermore, source depletion effects hinder large scale production. Consequently, this review focuses on the optoelectronic applications of MBE, MOVPE and MOMBE; after evaluating some recent achievements using these growth technologies, their application, in combination, to novel concepts will be discussed.

2. Application fields of the growth technologies

MBE and MOVPE have now been under development for more than 20 years. In the past decade both technologies have been utilized particularly in HEMT and laser production, and are competing. This situation is the driving force for further research into machines, processes and starting materials. In addition MOMBE (a combination of MBE and MOVPE) was developed, initially to study the metal–organic growth processes using surface analytical tools; however, it has now become a growth technology itself, offering new dimensions for device concepts. Each of these growth methods can be characterized by their typically strong application areas.

2.1. Molecular beam epitaxy

MBE has developed in the past five years to become a production technology for electronic and optoelectronic layered structures. Multiwafer production MBE systems first became available for commercial applications from companies such as Picogiga, Bandgap, Fujitsu and Rohm. A very famous example is the production of DH-AlGaAs lasers for use as compact disc readout lasers using a two-step MBE process [3]. With one MBE system, Rohm is able to deliver about 10^6 laser diodes (LDs) per month; this figure represents approximately 50% of the free market for the compact and video disc players.

The advance from research tool to production method included the development special effusion cell geometries to enhance operation times, good layer uniformity and low defect densities [4]. However, it is still difficult to modulate the group V fluxes quickly over a significant dynamic range. This means that the parallel use of arsenic and phosphorus to produce sharp group V switching at layer interfaces is technologically very difficult. Owing to the high molecular beam on/off ratio of the group III elements, atomically sharp interfaces in the Al–Ga–In–As material system can be achieved by using high quality materials [5].

0921-5107/93/$6.00

© 1993 – Elsevier Sequoia. All rights reserved

The outstanding performances of, for example, MBE low threshold current AlGaAs graded index separate confinement heterostructure (GRINSCH) lasers and GaAs/GaAlAs QW lasers are summarized in ref. 6. Using an AlGaInAs/InP MQW GRINSCH laser structure, Allovon *et al.* obtained a threshold current density as low as 820 Acm^{-2} on a device 1180 μm in length, with a CW threshold current of only 17 mA [7]. Recently Chen *et al.* reported submilliamp threshold currents measured on MBE-grown InGaAs/AlGaAs GRINSCH SL-SQW structures for optical interconnects [8]. Figure 1 shows the dependence of the threshold current on the optical cavity length for the as-cleaved lasers where a minimum value of 1 mA can be detected. In addition, the application of a highly refractive coating at the mirrors produced a threshold current of only 0.25 mA on a device 120 μm long.

Alternatively the optical interconnection between LSI chips or circuit boards can be achieved using vertical cavity surface emitting laser diodes (VCSELD). A schematic diagram of such a wavelength tunable three-terminal VCSELD is shown in Fig. 2, taken from ref. 9. The growth of such a structure requires an ultimate level of process control to ensure the quality of the Bragg reflectors, in this situation the MBE technique offers significant advantages. The active region has an optical thickness of $\lambda/2$ cladded by AlGaAs layers for efficient carrier confinement, whilst the bottom and top Bragg reflectors are n- and p-doped respectively [10]. Figure 3 presents a micrograph of the fully processed structure. The central top circular structure is the top reflector contact for wavelength tuning (8 μm diameter); the ring electrode is the laser p-contact.

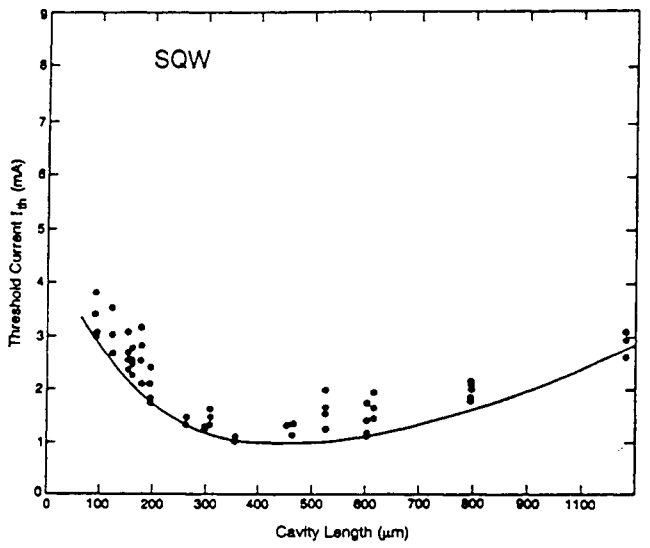

Fig. 1. Threshold current distribution *vs.* cavity length of the InGaAs SQW BH lasers; from ref. 8.

With this three-terminal device, a cw threshold current of only 0.65 mA, corresponding to a current density of 1.3 $kAcm^{-2}$, was measured with 5.6 nm continuous wavelength tuning ($\lambda = 970$ nm) by applying tuning currents of < 1 mA [10,11].

Sugimoto *et al.* optimized the VCSELD for low threshold current densities by including periodically-doped Bragg reflectors. The heavily doped regions were located at the nodes of the optical standing waves which helped to reduce the electrical resistance in the DBRs. Using a 20 μm^2 GaInAs/GaAlAs VCSELD in cw operation, the authors obtained a threshold current of 1.8 mA which corresponds to a threshold current density of 450 Acm^{-2} [12]. From Iga's very recent review of surface emitting lasers [13], it can be concluded that the state of the art results in this field are only obtained by MBE-based methods like solid-source MBE or CBE/MOMBE (see also Section 2.2). The complex, thick multilayer structures of the VCSELDs are a good example of the growth control which can be achieved using the MBE technique.

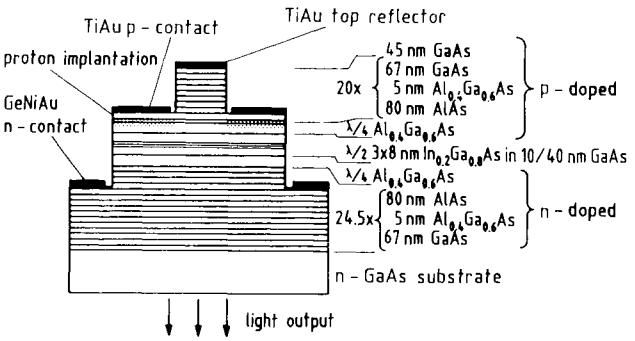

Fig. 2. Schematic diagram of the wavelength tunable vertical cavity laser diode with laser current i_c and tuning current i_T; from ref. 11.

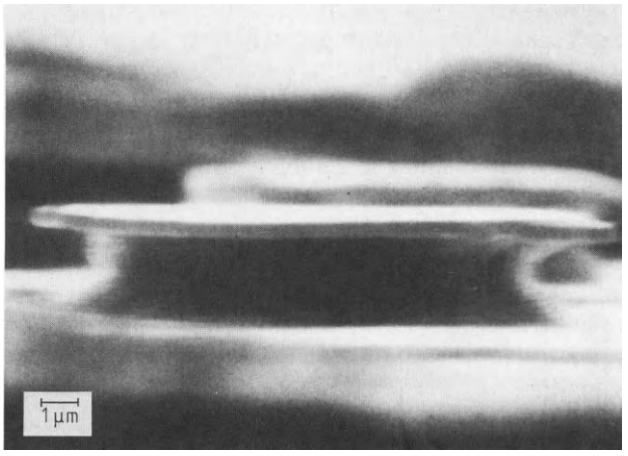

Fig. 3. Micrograph of the VCSELD from Fig. 2.

2.2. Metal-organic growth technologies

The metal-organic growth technologies use metal-organics and hydrides as starting materials. In principle, MOMBE is the MOVPE process carried out at very low total pressure. In MOVPE the material transfer is established by laminar gas flow using a carrier gas, whereas in MOMBE no carrier is required because of the nature of the molecular beams.

2.2.1. Metal-organic vapour phase epitaxy

MOVPE has been under development for about as long as MBE. The major forces behind its development were its ability to produce optical devices together with the possibility of obtaining large area growth and multiwafer processing; these characteristics are well documented [14–17]. As with MBE, there are now MOVPE production machines which are capable of multiwafer processing, including substrate rotation which improves uniformity [18–20]. High quality separate confinement QW GaAs/AlGaAs lasers with threshold current densities down to 250 Acm^{-2} for devices 500 μm long could be produced in such a production system [20]. Also, in the more complex material system, AlGaInAs on InP, excellent strained layer single quantum well 1.3 μm lasers were obtained using MOVPE [21]. A minimum threshold current density for compression-strained quantum well lasers of 100 Acm^{-2} was measured on devices 5 mm long; for tensile-strained, 188 Acm^{-2} were obtained. The type of strain determines the polarization of the light (TE for compression strain, TM for tensile strain), so polarization insensitive laser amplifiers can be produced by using combinations of compression-strained and tensile-strained MQW structures [22].

Owing to the reactivity of Al, replacing these Al-containing materials by Ga–In–As–P layers is of interest. To do this, basically any material composition between InAs and GaP can be utilized for the modulation of the bandgap structure on GaAs and InP substrates. As the sources in MOVPE are outside the reaction chamber and fast gas switching occurs, there is clear advantage in fabricating heterostructures containing As and P. As/P containing heterostructures enable strained layer (SL) system laser diodes to be produced with high modulation speed, high power [23], and high operation temperature, as well as low threshold currents. A report by Joma *et al.* shows, for example, that the application of compressive strain in GaInAsP/InP MQW lasers yields a clear advantage over bulk material lasers in terms of wavelength stability with increasing laser output power [24]. Figure 4 shows the dependence of the peak wavelength on drive current for bulk and SL-MQW lasers. The lasers with a SL active region exhibit significantly less pronounced drive current dependence.

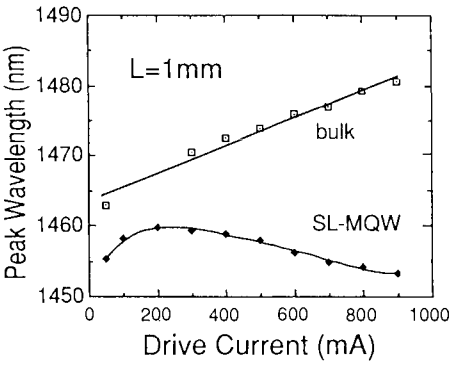

Fig. 4. Peak wavelength of the lasing spectra at several power levels, for bulk and strained GaInAsP MQW lasers; taken from ref. 24.

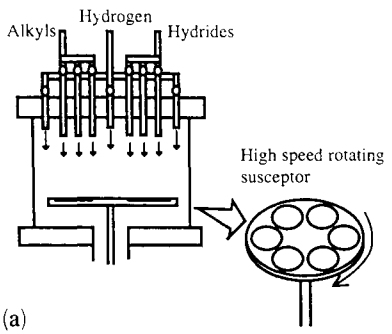

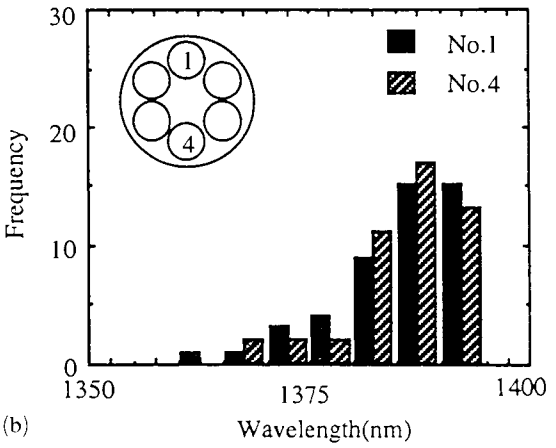

Fig. 5. (a) Schematic diagram of a multiwafer reactor. (b) Histogram of GaInAsP PL wavelength over two wafers from the same run; taken from ref. 26.

Very recently Yamamoto *et al.* reported on the growth of InAsP/GaInAsP GRINSCH-QW structures for low threshold 1.3 μm lasers [25]. A threshold current density as low as 88 Acm^{-2} was achieved on a SQW device 4 mm long.

The multiwafer MOVPE growth of SL-QW GaInAsP structures for low threshold 1.3 μm lasers was carried out in a growth system shown in Fig. 5(a)

from ref. 26. Six 2 or 3 in wafers can be processed in parallel and the fabricated laser structures, 300 μm long, exhibit low threshold currents of 2.5 mA at 25 °C and 8 mA at 80 °C. The histogram in Fig. 5(b) shows the measured GaInAsP wavelength distribution from wafer 1 and 4 of the same growth run; comparison reveals that there is good wafer–wafer reproducibility [26].

For buried heterostructure lasers the Al-free materials are attractive because the regrowth does not have to start on Al-containing surfaces, and consequently there is a move to replace the AlGaAs cladding layers in the short wavelength devices. Several groups are working in this area with excellent results; for example, 0.98 μm emitting strained QW GaInAs/GaInAsP structures with InGaP cladding layers have been reported with threshold current densities of 58 Acm^{-2} for bars 3 mm long [27]. In principle there is a general tendency to move to As/P containing systems for both the GaAs- and InP-based materials.

For device applications, the structures require increasing use of regrowth steps to provide carrier confinement and the integration of lateral heterojunctions. To achieve this, selective area epitaxy (SAE) can be utilized exploiting the fact that no material growth takes place on oxide or nitride masks. Since in solid-source MBE the adsorption–desorption processes of the group III molecules are far away from equilibrium under normal growth conditions, in general, without any additional means, polycrystalline growth occurs on the masked area. Therefore, the domain of SAE belongs to the metal–organic deposition processes like MOVPE or MOMBE where the growth parameters can be tuned so that the metal–organics do not undergo any dissociation reaction on the mask material or in the gas phase.

Total pressure in the growth system is a very influential parameter; at atmospheric pressure it is difficult to obtain true SAE because gas phase pre-reactions produce adsorption–desorption conditions similar to those found with MBE [28,29]. In MOVPE the molecules desorbing from the mask affect the concentration gradients in the reaction chamber so that the adsorption flux to open window area correlation depends on the total area masked. This lateral communication via the gas phase can often lead to non-uniformities in layer thickness and material composition [30–32]. The GaInAs and GaInAsP materials show particularly significant variations in materials composition, larger deviations are observed when more surface is masked. However, optimization of the growth conditions can improve the SAE in MOVPE significantly, especially if the results of the experiments on SAE mechanisms in MOMBE are implemented (see also next section) [33].

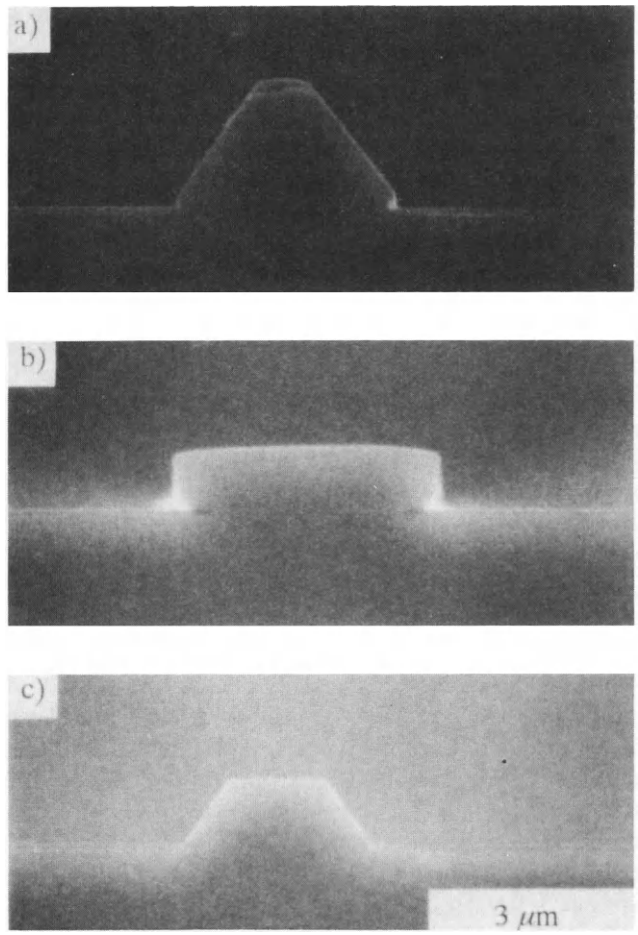

Fig. 6. Scanning electron micrographs of InP ridge cross section, view of the $(0\bar{1}1)$ plane. Ridges were grown under V/III ratios of: (a) 420; (b) 2800 on misoriented substrates; (c) as in (b), but (100) on-orientation substrate. After ref. 33.

Figure 6 shows scanning electron micrographs of InP ridge cross sections grown under different V/III ratios at a growth rate of 0.5 μmh^{-1}. The use of a higher V/III ratio (Fig. 6(b)) suppresses interfacet diffusion and decreases the kinetic barrier on the (111) planes so that planar surfaces with almost vertical sidewalls are achieved. Owing to the low effective V/III ratio for on-orientation substrates the kinetic barrier on the (111) planes can not be sufficiently reduced to suppress the formation of these planes, as observed earlier in MOMBE [34]. Under the conditions used to produce Fig. 6(b) the ridge thickness approaches the thickness found in the large area data (thickness variation between large area and SAE growth is $\Delta d/d \approx 1$ 0%). Multistage SAE processes have been used successfully for the monolithic integration of DFB lasers with ridge waveguides via a butt junction; a coupling efficiency of about 50% was achieved [35]. In addition, Wallin *et al.* report on the selective area regrowth of a butt joint coupled waveguide in a

3-electrode DBR laser [36]. They were able to show a smooth contact between the active layer and the 1.3 μm GaInAsP waveguide layer.

The major disadvantage of SAE in MOVPE is that the mask geometries can not easily be changed without affecting the material composition. In addition, the relative masked area should be as small as possible. More recent related research has concentrated on the use of alternative starting materials which are less sensitive to these parameters. Scholz *et al.* have shown that the use of dimethylaminopropyl-dimethylindium (DADI) rather than trimethylindium (TMI) reduces the communication between the masked and unmasked areas so that the growth rate enhancement and the variations in the material composition of the localized grown material are reduced [37]. It can be speculated that the higher stability and larger molecule size of DADI lead to a lower lateral diffusion flux when compared with the TMI case.

Another driving force for research into alternative starting materials is the bid to find alternatives to replace AsH_3 and PH_3 which have to be used and stored in MOVPE in relatively large quantities because of their high consumption rate [14–17]. Intensive effort is being invested in finding less toxic and dangerous starting materials for the future which comply with present safety requirements. In addition new group III starting materials, like DADI or trimethylaminealane, are under investigation for improved flux control or to achieve lower unintentional carbon and oxygen contamination. This search for new compounds is a mutual exchange between latest MOVPE and MOMBE results, since these growth technologies have significant overlap in the associated growth mechanisms.

2.2.2. *Metal–organic molecular beam epitaxy*

MOMBE of GaAs was introduced in the early 1980s [38,39] using trimethylgallium (TMG) and AsH_3 as starting materials, as in MOVPE. At first, the extremely high unintentional carbon uptake in the epilayers acting as acceptor impurities limited the applications of the method [39,40]. Subsequent selection of triethylgallium (TEG) as the group III source, however, helped to reduce the carbon uptake to approximately 10^{14} cm^{-3} [40–42]. Using mixtures of TMG and TEG, carbon concentrations of 10^{20} cm^{-3} were demonstrated [43]. Today, carbon doping is used extensively by several groups for the fabrication of GaAs-based heterojunction bipolar transistors (HBT) which require high carrier concentrations to allow for thinner base layers [44–47]. In addition, the diffusion of C is clearly lower than for other p-type dopants. However, the Al-containing materials are more difficult to grow using MOMBE or CBE because of unintentional carbon and oxygen incorporation. New Al compounds, such as trimethylaminealane, were introduced in MOMBE and these compounds have yielded carbon concentrations as much as two orders of magnitude lower [48,49]. These findings have also improved the results of GaAlAs in MOVPE [50,51].

High quality InP-based materials can be produced by MOMBE where the optical and electrical properties can compete fully with other growth technologies [1, 52, 53].

MOMBE–CBE is a relatively new growth technology and so there are fewer research groups working on MOMBE–CBE than on MOVPE. Consequently there is less work being done on device development using MOMBE material. However, Tsang [1] is very active in this field and there have been many reports, since the mid 1980s, on high quality InP-based HBTs, distributed Bragg reflector (DBR) and double heterostructure (DH) multiple quantum well lasers, avalanche photodiodes and waveguides [54,55]. Using these data, new standards of device performance have been frequently set; *e.g.* 1.5 μm wavelength strained layer GRINSCH InGaAs/InGaAsP single QW injection lasers [56]. Figure 7 demonstrates that threshold current densities as low as 172 Acm^{-2} were obtained for devices 5 mm in length with one QW. For comparison, Fig. 7 also shows the data obtained on strained and unstrained SCH MQW devices. MOVPE-grown structures yield similar results, 160 Acm^{-2} [57]. Tsang and coworkers also report about the fully CBE-grown 1.5 μm InGaAsP/InP DFB lasers [58]. CW threshold currents of 10–15 mA on bars 250 μm in length were obtained with slope efficiencies of 0.4 mWmA^{-1} and

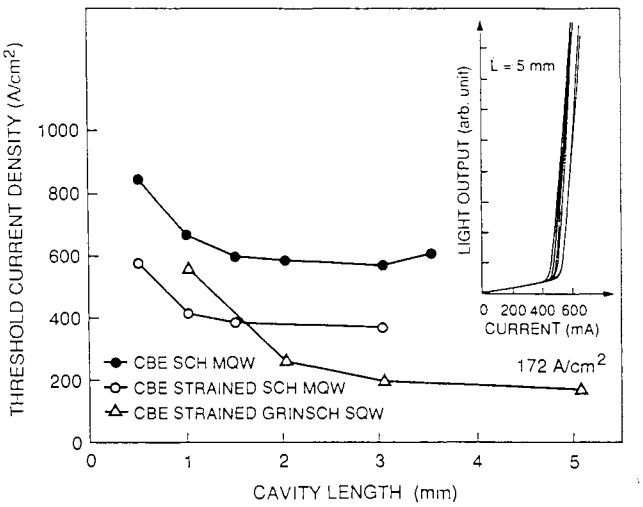

Fig. 7. Threshold current densities of CBE-grown unstrained and strained 4QW SCH lasers and strained 1 QW GRINSCH lasers plotted as a function of cavity length. The inset shows the light–current characteristics of six randomly chosen 5 mm-long GRINSCH SQW lasers; taken from ref. 1.

side-mode suppression ratios up to 52 dB [58]. Nakao *et al.* achieved threshold currents of 6 mA and slope efficiencies of 0.3 mA per facet on SL MQW 1.5 μm DFB lasers [59]. In this case the p-cladding layer and the buried heterostructure overgrowth were performed by MOVPE. Yamada *et al.* obtained threshold currents of 12 mA on 300 μm long double-channel planar buried heterostructure 1.5 μm InGaAs/InGaAsP lasers; these results demonstrate the excellent uniformity of MOMBE layers shown in the very low threshold current deviations (15 ± 3 mA) for 90% of the 50 laser structures tested [60]. Meier *et al.* found, for 1.3 μm GaInAsP/InP MQW lasers, threshold current densities of 400 Acm^{-2} measured on broad area structures 750 μm long; calculation gives an I_{th} value of 160 Acm^{-2} for infinitely long lasers [61]. MOMBE–CBE has also been used successfully to fabricate the required layer sequences for VCSELD in the GaInAsP/InP materials growth system. At 77 K, threshold currents of only 1.7 mA were achieved [13].

MOMBE–CBE material has also been used for the integration of optical devices which demand a high degree of material uniformity. Examples include GaInAs MSM–FET photoreceivers [62], monolithic p-i-n/HBT transimpedence photoreceiver circuits [1] and photodiode waveguide integration [63].

Figure 8 shows a scanning electron micrograph of a fully-processed vertically-integrated waveguide/photodiode structure working on the principle of evanescent field coupling. The GaInAs photodiode, 100 μm long, is located on the GaInAsP ($\lambda_{gap} = 1.05$ μm) straight waveguide and the contact pads can be seen in the centre of the picture. The embedded n^+ contact is on the right-hand side and the p (top) contact on the left-hand side. For diodes 100 μm long, dark currents between 130 and 600 pA were measured at 10 V reverse bias, and an absorption efficiency of higher than 96% was obtained. On the same structure, a 3 dB cut-off frequency of 9.6 GHz was found in a 50 Ω system.

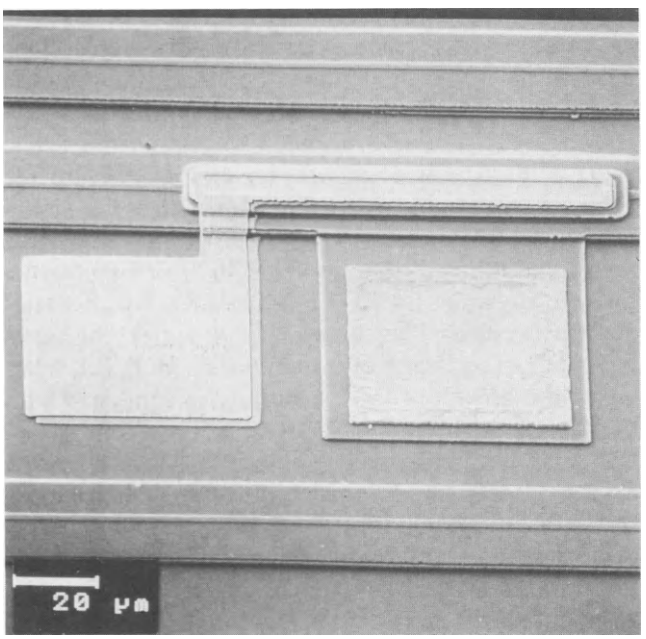

Fig. 8. Scanning electron micrograph of a processed waveguide–photodiode structure grown by MOMBE; from ref. 63.

To produce the integration of devices, selective area epitaxy is essential to the metal-organic growth technologies, as discussed above. It was first demonstrated using MOMBE that it is possible to grow InP/GaInAsP heterostructures with vertical sidewalls and lateral heterojunctions locally [29, 34, 64, 65]. These observations can be utilized in the growth of vertical superlattice and optoelectronic device structures. As discussed in the preceding section, some growth data concerning SAE can be transferred to MOVPE. However the advantage shown by MOMBE, that under the appropriate growth conditions the material composition remains nearly unaffected up to boundaries of the structure, is difficult to achieve in MOVPE [29, 34]. In MOMBE there is no lateral memory and no communication between masked and unmasked regions because there is no gas phase material transfer as found in MOVPE. Consequently, in MOMBE the results are fairly independent of the aspect ratio between masked and unmasked areas. This gives predictable results and a high degree of freedom to the designer of device structures.

Embedded localized growth using SAE enables the lateral coupling of two different DHs as required; for example, for the integration of laser and waveguides for photonic ICs. For such an application the first DH structure has to be grown, covered by the mask materials, and then selectively etched away in those areas where, in the second growth run, the second type of heterostructure has to be grown (see next section). We simulated this procedure by etching tubs, 1 μm deep, into InP. These tubs were selectively refilled by an InP (0.3 μm)/GaInAsP (0.4 μm)/InP (0.3 μm) DH structure so that a lateral InP/GaInAsP heterojunction was formed. This test structure allowed independent analysis of the selectively-grown quaternary material to be performed using focused photoluminescence without interference between a quaternary–quaternary butt contact. A scanning electron micrograph of the cross section of this test structure is shown in Fig. 9, looking on the $(01\bar{1})$ plane. The structure has been etched in order to make the heterojunctions visible. Figure 9 confirms that a smooth contact with planar surfaces can be obtained. For embedded growth it is important that the V/III ratio is not set too high because a high

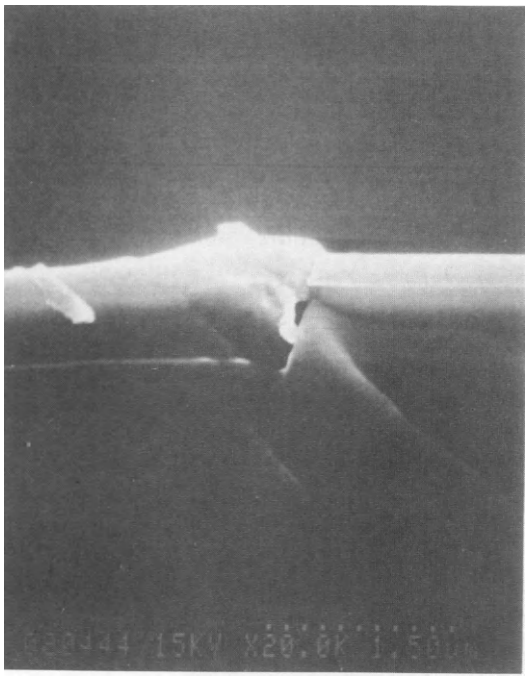

Fig. 9. Embedded growth by SAE of InP (0.3 μm)/GaInAsP (0.4 μm, $\lambda_g = 1.05$ μm)/InP (0.3 μm) in a tub etched into a InP wafer looking on the (01$\bar{1}$)plane; DH structure on the left. From ref. 34.

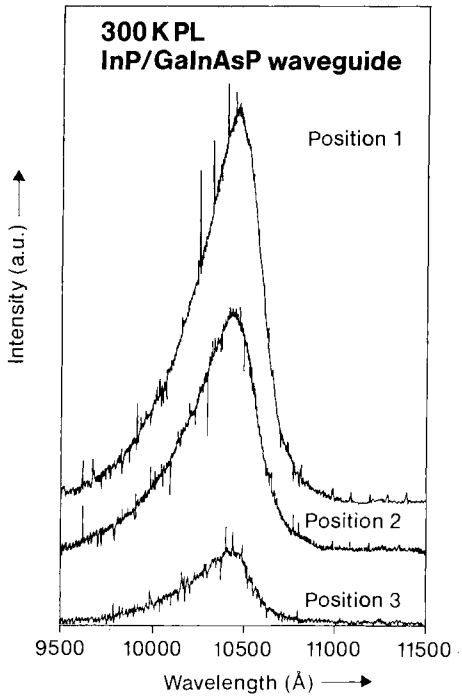

Fig. 10. Room temperature photoluminescence spectra measured at various positions on the structure in Fig. 9 (distances from the edge: Position 1, 600 μm; Position 2, approximately 5 μm; Position 3, approximately zero). Note that there is only one constant recombination wavelength, even at the edge of the oxide. From ref. 34.

V/III ratio increases the lateral growth rate (on the etched ridge) and the apparent higher vertical growth rate close to the ridge would lead to a bending in the hetero-interfaces.

Figure 10 shows the focused photoluminescence data from the structure in Fig. 9. The reference scan was recorded in the centre of the structure (about 600 μm away from the SiO_2 edge). There is no shift in the luminescence and no additional recombination lines are visible when the excitation laser spot is moved towards the SiO_2 area. Only the intensity is reduced, this is because the excitation density is lowered when the laser spot starts leaving the semiconductor area.

The data from Fig. 10 show that the extension of a vertical interlayer of another material composition can be substantially suppressed by choosing the proper epitaxial parameters so that an almost ideal butt contact between two heterostructure systems can be realized.

Owing to the high quality device results, the excellent material uniformity data [1], the low toxic material consumption and the high potential in the SAE capabilities, MOMBE–CBE is already well on the way to becoming a production tool, despite being a young technology. Nevertheless, there are still important research areas to cover, such as doping and the continuing development of alternative compounds in order to achieve further improvements in process control.

3. Integration of technologies

As discussed in the preceding section, there are differing application areas and development statuses for the various growth technologies discussed. Since modern device and integration concepts often require multistage epitaxy, which necessitates growth on processed wafers, there is no need to restrict the whole process to a single growth technology. Figure 11 presents an example of combined growth technologies where InP has been grown selectively by MOMBE around a GaInAsP long wavelength laser ridge structure grown earlier by MOVPE. The SiO_2 layer was not absolutely planar, however this did not affect the selectivity. Here the wealth of experience in MOVPE, relating to the growth of laser materials, is combined with the flexible high quality SAE capability in MOMBE. For a laser–amplifier/waveguide butt coupling in the SAE MOMBE, the InP growth is principally replaced by a $\lambda_G = 1.05$ μm GaInAsP layer. In this way, a lateral contact between the active laser–amplifier layer and the waveguide layer is established, as shown in Fig. 12(a). In a first growth run, the basic laser structure including the Q 1.56 μm layer is grown by MOVPE, followed by the SAE Q 1.05 μm MOMBE process

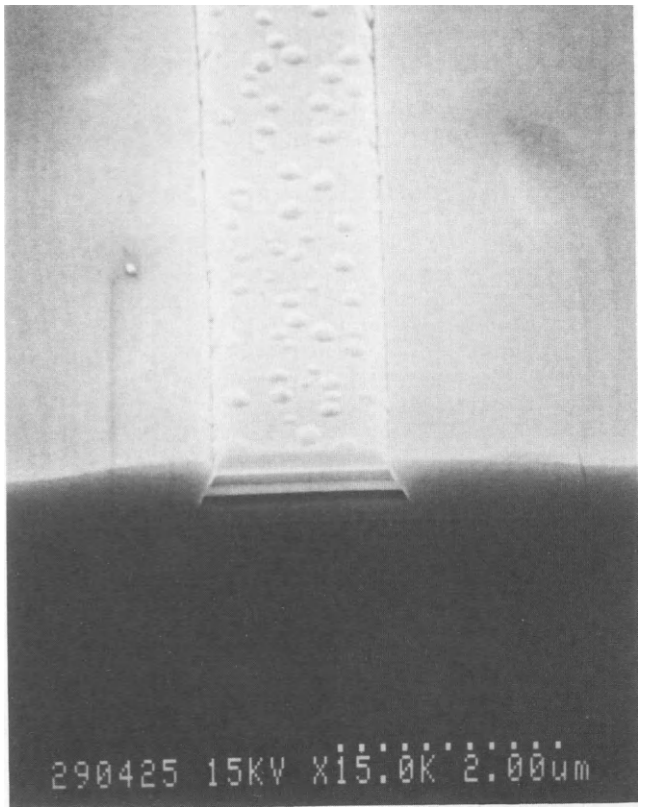

Fig. 11. Embedded InP MOMBE growth around a MOVPE grown laser structure, from ref. 29.

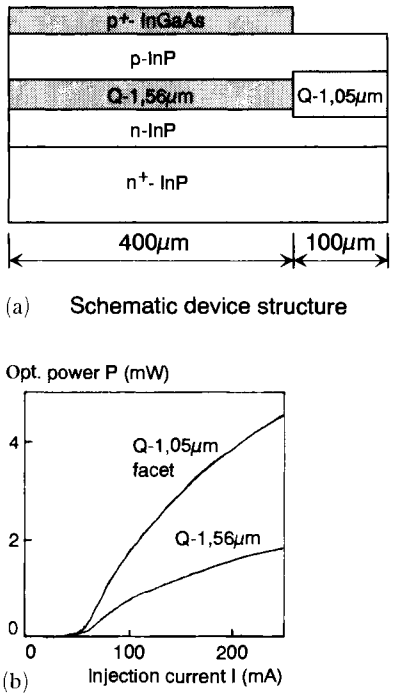

Fig. 12. SAE of MOMBE Q 1.05 μm waveguide to MOVPE laser–amplifier structure: (a) schematic device structure, from ref. 66; (b) optical output power from laser and from waveguide as a function of injection current.

around the SiO_2-covered laser amplifier region. After removing the SiO_2 layers, the whole structure was overgrown with p-InP by MOVPE (see Fig. 2(a)). Test devices, with laser amplifiers 400 μm long connected to 100 μm long quaternary 1.05 μm waveguides on one side, were prepared and characterized. Figure 12(b) shows the optical output power at the as-cleaved facet of the laser–amplifier *vs.* the injection current for operation in the lasing mode. The second trace indicates the optical output from the waveguide. From the difference in slope of the output power curves, a waveguide–amplifier coupling loss of less than 3 dB can be calculated [66].

Another field of technology integration is the combination of in-situ/in-vacuum growth and etching techniques. One example is the first demonstration of dry etching of InP in a CBE chamber using PCl_3, where crystal growth can be performed immediately after etching [67]. Another very promising method is reported by Wang *et al.* [68]. This group deposited a Si layer on an InP wafer in vacuum. A mask was then produced by focused ion beam etching followed by Cl_2 etching of the exposed InP surface. A recess area (about 3500 Å deep) was formed, and a 1.3 μm GaInAsP laser structure was then selectively filled into this groove, 6 μm wide, by MOMBE. Threshold currents of less than 40 mA were achieved on bars, 250 μm long, revealing the potential of integrated technologies [68].

4. Conclusion

MBE, as well as MOVPE, has recently developed into an established production technology. MBE is more suited to the growth of single group V element containing structures, for example, the Ga–In–Al–As systems on GaAs and InP. MOVPE and MOMBE are the best candidates for growth of Al-free material for both substrate types. If higher level integration of different device structures becomes increasingly relevant to future applications, the SAE capabilities of the metal–organic deposition technologies will play a crucial part. The relatively new MOMBE technique will have the added advantage of being a less dangerous technology; it is likely to gain a significant share in the production area.

The integration of all three growth technologies addressed here for the fabrication of novel and/or integrated electronic and optoelectronic devices combines the advantages of the individual technologies; for example, MOMBE can combine the advantages of

MBE and MOVPE. In addition, the integration of in-vacuum etching and processing technologies can facilitate the production of complex devices.

References

1 W.T. Tsang, *J. Cryst. Growth, 120* (1992) 1.
2 W. Thulke, *Mater. Sci. Eng., B9* (1991) 61.
3 H. Tonaka and M. Mushiage, *J. Cryst. Growth, 111* (1991) 1043.
4 A.Y. Cho, *J. Cryst. Growth, 111* (1991) 1.
5 C.R. Stanley, M.C. Holland, A.H. Kean, J.M. Chamberlain, R.T. Grimes and M.B. Stanaway, *J. Cryst. Growth, 111* (1991) 14.
6 H.P. Meier, *Mater. Sci. Eng., B9* (1991) 77.
7 M. Allovon, M. Quillec, M. Blez and C. Kazmierski, *J. Cryst. Growth, 111* (1991) 484.
8 T.R. Chen, B. Zhao, L. Eng, Y.H. Zhuang and A. Yariv, in *Proc. 13th IEEE Int. Sem. Laser Conf., Takamutsu, Japan, Sept. 21–25, 1992*, IEEE Lasers and Electro-Optics Society, Japan, post deadline papers p. 7.
9 T. Wipiejewski, K. Panzlaff, E. Zeeb and K.J. Ebeling, in *Proc. ECOC'92, Berlin, Sept. 1992*, VDE Berlin, p. 903.
10 T. Wipiejewski, K. Panzlaff, E. Zeeb and K.J. Ebeling, in *Proc. 6th European Conf. Integrated Optics, Neuchâtel, Switzerland, April, 1993*, pp. 7–8.
11 R. Midalzik and K.J. Ebeling, *IEEE J. Quantum Electron.*, in press.
12 M. Sugimoto, I. Ogura, H. Saito, A. Yasuda, K. Kurihara, H. Kasake, T. Numai and K. Kasahura, *J. Cryst. Growth, 127* (1993) 1.
13 K. Iga, in *Proc. 5th Int. Conf. InP and Related Materials, Paris, France, April, 1993*, p. 7.
14 Proc. III Int. Conf. MOVPE, Universal City, USA, *J. Cryst. Growth, 77* (1986).
15 Proc. IV Int. Conf. MOVPE, Hakone, Japan, *J. Cryst. Growth, 93* (1988).
16 Proc. V Int. Conf. MOVPE, Aachen, Germany, *J. Cryst. Growth, 107* (1991).
17 Proc. VI Int. Conf. MOVPE, Cambridge, MA, USA, *J. Cryst. Growth, 124* (1992).
18 J. Komeno, H. Tanaka, N. Tomesakai, H. Itoh, T. Ohori, M. Takikawa, M. Suzuki and K. Kasai, *J. Cryst. Growth, 105* (1990) 30.
19 P.M. Frijlink, J.L. Nicolas and P. Sachet, *J. Cryst. Growth, 107* (1991) 166.
20 C.J. von der Poel, H.P.M.M. Ambrosius, R.W.M. Linders, N.J. Kiwiet and J. Rijpers, *J. Cryst. Growth, 124* (1992) 300.
21 C.E. Zah, R. Bhat, F.J. Favire, M. Koza, T.P. Lee, D. Darby, D.C. Flanders and J.J. Hsieh, *Electron. Lett., 28* (1992) 2323.
22 L.F. Tiemeier, P.J.A.Thijs, T. van Dongen, R.W.M. Slootweg, J.M.M. van der Heijden, J.J. Binsma, M.P.C.M. and M.P.C.M. Krijn, *Appl. Phys. Lett., 62* (1993) 826.
23 T. Namegaya, A. Kasukawa, N. Iwai and T. Kikuta, *Electron. Lett., 29* (1993) 392.
24 M. Joma, H. Horikawa, Y. Matsui and T. Kamijoh, *Appl. Phys. Lett., 58* (1991) 2220.
25 M. Yamamoto, N. Yamamoto and J. Nakano, in *Proc. 5th Int. Conf. InP and Related Materials, Paris, France April, 1993*, IEEE catalogue no. 93CH3276-3, p. 231.
26 K. Mori, M. Takemi, T. Takiguchi, K. Goto, T. Nishimura, T. Kimura, Y. Mihashi and T. Murotami, in *Proc. 5th Int. Conf. InP and Related Materials, April, 1993, Paris, France*, IEEE catalogue no. 93CH3276-3, p. 235.
27 C.J. Chang-Hasnain, R. Bhat, H. Leblanc and M.A. Koza, *Electron. Lett., 29* (1993) 1.
28 H. Heinecke, A. Brauers, F. Grafahrend, C. Plass, N. Pütz, K. Werner, M. Weyers, H.üth and P. Balk, *J. Cryst. Growth, 77* (1986) 303.
29 H. Heinecke, A. Milde, B. Baur and R. Matz, *Semiconduct. Sci. Technol., 8* (1993) 1023.
30 G.J. Davies, W.J. Duncan, P.J. Skevington, C.L. French and J.S. Foord, *Mater. Sci. Eng., B9* (1991) 93.
31 C. Caneau, R. Bhat, M.R. Frei, C.C. Chang, R.J. Deri and M.A. Koza, *J. Cryst. Growth, 124* (1992) 243.
32 E.J. Thrush, M.A. Gibbon, J.P. Stagg, C.G. Cureton, C.J. Jones, R.E. Mallard, A.G. Norman and G.R. Booker, *J. Cryst. Growth, 124* (1992) 249.
33 E. Veuhoff, H. Heinecke, J. Rieger, H. Baumeister, R. Schimpe and S. Pröhl, in *Proc. 4th Int. Conf. InP and Related Materials, Newport, RI, USA, April, 1992*, IEEE catalogue no. 92CH3104-7, p. 210.
34 H. Heinecke, *J. Cryst. Growth, 127* (1993) 126.
35 J. Thomson, N. Carr, A.K. Wood, N. Maung, P.J. Williams, P.M. Charles and A.J. Mosely, *J. Cryst. Growth, 126* (1993) 317.
36 J. Wallin, G. Landgren, K. Streubel, S. Nilsson and M. Öberg, *J. Cryst. Growth, 124* (1992) 741.
37 F. Scholz, D. Ottenwälder, M. Eckel, K. Locke, G. Frankowsky and T. Wacher, in *Proc. 5th Int. Conf. InP and Related Materials, Paris, France, April, 1993*, p. 48.
38 E. Veuhoff, W. Pletschen, P. Balk and H. Lüth, *J. Cryst. Growth, 55* (1981) 30.
39 N. Vodjdani, A. Lemarchand and H. Paradan, *J. Phys. Colloids, C5* (12)–43 (1982) C5-C339.
40 N. Pütz, E. Veuhoff, H. Heinecke, M. Heyen, H. Lü and P. Balk, *J. Vac. Sci. Technol., B3* (1985) 671.
41 W.T. Tsang, *Appl. Phys. Lett., 45* (1984) 1234.
42 N. Pütz, H. Heinecke, M. Weyers, M. Heyen, H. Lüth and P. Balk, *J. Cryst. Growth, 74* (1986) 292.
43 H. Heinecke, K. Werner, M. Weyers, H. Lüth and P. Balk, *J. Cryst. Growth, 81* (1987) 270.
44 H. Ando, T. Fujii, A. Sandhu, T. Takahashi, H. Ishikawa, N. Okamoto and N. Yokoyama, *J. Cryst. Growth, 120* (1992) 228.
45 C.R. Abernathy, F. Ren, S.J. Pearton, T.R. Fullowan, R.K. Montgomery, P.W. Wisk, J.R. Lothian, P.R. Smith and R.N. Nottenburg, *J. Cryst. Growth, 120* (1992) 234.
46 P.A. Lane, C.R. Whitehouse, T. Martin, M. Houlton, G.M. Williams, A.G. Cullis, S.S. Gill, J.R. Dawsey, G. Ball, B.T. Hughes, M.A. Crouch and M.B. Allenson, *J. Cryst. Growth, 120* (1992) 245.
47 A. Sandhu, T. Nakamura, H. Ando, K. Domen, N. Okamoto and T. Fujii, *J. Cryst. Growth, 120* (1992) 296.
48 C.R. Abernathy, A.S. Jordan, S.J. Pearton, W.S. Hobson, D.A. Bohling and G.T. Muhr, *Appl. Phys. Lett., 56* (1990) 2654.
49 C.R. Abernathy and D.A. Bohling, *J. Cryst. Growth, 120* (1992) 195.
50 A. Kohzen, Y. Tohmori, Y.A. Katsu and H. Kamada, *J. Cryst. Growth, 124* (1992) 70.
51 G. Zimmermann, H. Protzmann, W. Stolz, E.O. Göbel, P. Gimmnich, A. Greiling, J. Lorberth, C. Thalman and K. Rademann, *J. Cryst. Growth, 124* (1992) 136.
52 H. Heinecke, B. Baur, R. Höger and A. Miklis, *J. Cryst. Growth, 105* (1990) 142.
53 T.S. Rao, C. Lacelle and A.P. Roth, *Electron. Lett., 29* (1993) 272.

54 W.T. Tsang, *J. Cryst. Growth, 95* (1989) 121.
55 W.T. Tsang, *J. Cryst. Growth, 105* (1990) 1.
56 W.T. Tsang, F.S. Choa, M.C. Wu, Y.K. Chen, A.M. Sergent and P.F. Sciortino, Jr., *Appl. Phys. Lett., 58* (1991) 2610.
57 P.J.A. Thijs, E.A. Montie and T. van Dongen, *J. Cryst. Growth, 107* (1991) 731.
58 W.T. Tsang, F.S. Choa, M.C. Wu, Y.K. Chen, R.A. Logan, S.N.G. Chu, A.M. Sergent, P. Magill, K.C. Reichmann and C.A. Burras, *J. Cryst. Growth, 124* (1992) 716.
59 M. Nakao, R. Iga, T. Yamada and H. Sugira, *Jpn. J. Appl. Phys., 31* (1992) L1549.
60 T. Yamada, R. Iga, Y. Noguchi and H. Sugiura, *J. Cryst. Growth, 120* (1992) 177.
61 H.P. Meier, R.F. Broom, P.W. Epperlein, S. Hausser, A. Jakubowicz and W. Walter, *J. Cryst. Growth, 127* (1993) 165.
62 L. Yang, A.S. Sudo, W.T. Tsang, P.A. Garbinski and R.M. Camarda, *J. Cryst. Growth, 105* (1990) 162.
63 H. Heinecke, B. Baur, N. Emeis and M. Schier, *J. Cryst. Growth, 120* (1992) 140.
64 H. Heinecke, B. Baur, R. Schimpe, R. Matz, C. Cremer, R. Höger and A. Miklis, *J. Cryst. Growth, 120* (1992) 376.
65 H. Heinecke, B. Baur, A. Miklis, R. Matz, C. Cremer and R. Höger, *J. Cryst. Growth, 124* (1992) 186.
66 A. Milde, H. Heinecke, E. Veuhoff, R. Matz, B. Baur, R. Primig, H. Baumeister, R. Schimpe and R. Kristen, in preparation.
67 W.T. Tsang, R.M. Kapre and P.F. Sciortino, Jr., in *Proc. 5th Int. Conf. InP and Related Materials, Paris, France, April, 1993*, p. 679.
68 Y.L. Wang, H. Temkin, R.A. Hamm, R.D. Yadvisch, D. Ritter, L.H. Harriot and M.B. Panish, *Electron. Lett., 27* (1991) 1324.

Materials Science and Engineering, B21 (1993) 130–146

Selective and non-planar epitaxy of InP/GaInAs(P) by MOCVD

E. J. Thrush[a], J. P. Stagg[a], M. A. Gibbon[a], R. E. Mallard[b], B. Hamilton[c], J. M. Jowett[a] and E. M. Allen[a]

[a] *BNR Europe Limited, London Road, Harlow, Essex, CM17 9NA (UK)*
[b] *Department of Materials, University of Oxford, Parks Road, Oxford, OX1 3PH (UK)*
[c] *Department of Physics, UMIST, P.O. Box 88, Sackville Street, Manchester, M60 1QD (UK)*

Abstract

Selective and non-planar epitaxy are important variants of the basic MOCVD process by which advanced III-V optoelectronics structures may be realised. This paper reviews work on the selective area growth of InP, GaInAs and GaInAsP some of which is both wide ranging and qualitative and some of which is focused and quantitative. A model has been developed which accurately describes the perturbations in material characteristics produced by selective area epitaxy. Non-planar epitaxy also is dealt with as a generic materials issue as well as attempting to relate the findings to such structures as butt coupled waveguides and buried heterostructure lasers. The exploitation of selective area epitaxy for the fabrication of a monolithically integrated laser/modulator is described and a brief account of device performance is given.

1. Introduction

The scope of the MOCVD process for the fabrication of complex III-V optoelectronics structures has been extended by the advent of selective-area and non-planar epitaxy. From the outset, the goal has been to devise processes which would lead to improved devices and, in particular, which would provide an enabling technology for device integration. During the early 1980s the first reports of selective and non-planar epitaxy of GaAs/GaAlAs began to appear in the literature [1–4] and, from the outset, application-oriented work was strongly featured. By the middle of the decade this work was being extended to InP [5, 6], and it is notable that the experiments took on a more "basic" and "generic" flavour as attempts were made to gain an improved insight into the effects produced, and the way in which these might be modified by the growth conditions.

As confidence increased, the investigations were again widened to include the InP-based alloys GaInAs and GaInAsP, and experiments were devised to reveal the evolution of the growing interface [7, 8] and the mechanisms responsible for the topology produced [9]. By this time Scott *et al.* [10] had already investigated the growth behaviour of InP and GaInAs over different crystal planes and exploited the disparity between the two alloys in the ease of nucleation on {111} facets to develop a single-step growth process for a buried heterostructure laser.

In addition to observations of, and efforts to control, the shape of features grown over patterned substrates, interest has also developed into ways in which the optical properties of III-V structures might be modified in the plane perpendicular to the growth direction. Several groups have investigated thickness and compositional perturbations occurring in the vicinity of dielectric masks with a view to quantifying the behaviour of GaInAs(P) in this respect [11–14]. These techniques have in some cases been extended to cover the lateral patterning of bandgap, by locally perturbing the quantum well thicknesses of MQW structures. The latter strategy has also been utilised to effect the monolithic integration of lasers and electroabsorption modulators [11, 15]. These devices offer great promise as the next generation of high-speed sources for optical communications systems because of their high frequency modulation capability and intrinsic low wavelength "chirp" characteristics.

During the course of our work we have become acutely aware of the complex interactions occurring between the different parameters which modify the growth habit on patterned substrates. We have therefore attempted to identify appropriate regions of parameter space using "broad brush" qualitative investigations before concentrating our effort into detailed studies under the conditions that looked most promising. This paper will briefly review our activities in both these areas and will illustrate the motivation by reference to a couple of device applications we have pursued.

0921-5107/93/$6.00

© 1993 – Elsevier Sequoia. All rights reserved

2. Experimental conditions

All structures were grown on (100)-oriented InP wafers, in horizontal RF-heated reactors, at a temperature of 650 °C and pressures between 150 and 760 Torr. Trimethyl gallium (TMG) and trimethyl indium (TMI) were used as the Group III precursors, whilst the Group V sources comprised neat arsine and phosphine. For low-pressure growth, V-III ratios of 110, 47 and 925 were used for the the deposition of InP, GaInAs and GaInAsP respectively, whilst for the atmospheric-pressure growth of InP a V-III ratio of 23 was used. Further details of the growth apparatus and procedures are given in an earlier publication [16].

A SiO_2 film 3000 Å thick, deposited by plasma-enhanced chemical vapour deposition (PECVD), was used as the masking material for selective-area epitaxy studies. This film was patterned using standard photolithography in conjunction with E-beam written masks. A similar schedule plus a reactive-ion (RIE)/wet-etch combination, and stripping of the oxide in HF, was used to prepare the samples for the generic studies of non-planar epitaxy.

The features on the mask used for the quantitative selective-area epitaxy studies (MF2 mask) were sufficiently separated to be isolated from each other in terms of their effect upon the growth process. The features consisted of pairs of parallel rectangular oxide patches with widths of 3, 7, 11, 15, 20, 25 and 30 μm separated by gaps of 6, 16 and 30 μm. These rectangles were either 600 or 800 μm long, which meant that they were effectively semi-infinite as far as their effect on layer thickness and composition was concerned. Mask patterns of this type were disposed on the wafer so that in different regions they were aligned to the two principal cleavage directions in the [011] and the [0$\bar{1}$1] directions.

3. Selective-area epitaxy

3.1. Qualitative studies

During our initial studies of selective-area epitaxy, a mask design was chosen with the aim of maximising the information which could be gathered from each growth run. This so-called "multi-feature" mask, shown in Fig.

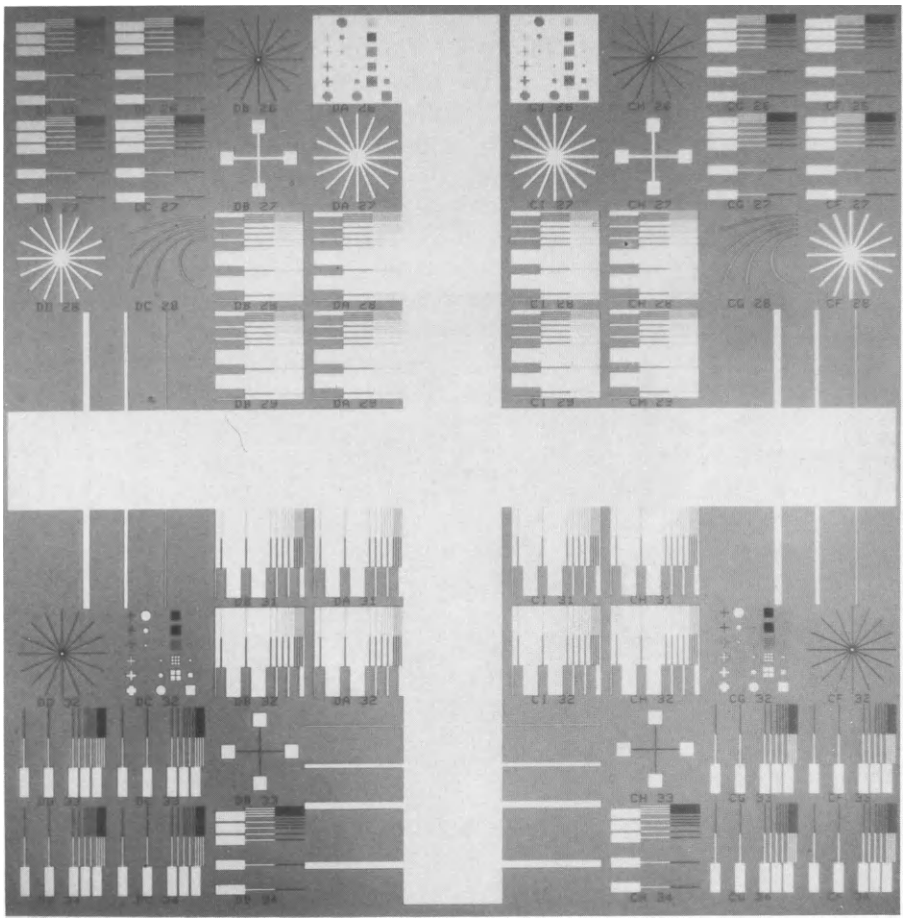

Fig. 1. Multi-feature selective-area epitaxy mask (MF1).

1, contains a wide variety of windows having geometries potentially relevant to the fabrication of optoelectronic devices. These features ranged in size from several millimetres to several microns and were positioned in a variety of locations and orientations, as shown. Of particular interest was the influence of masking density on the epitaxial habit, and for this reason identical features were provided in heavily masked (dark field) and lightly masked (light field) areas to enable this comparison to be made. The mask also provided a number of star-shaped features which simultaneously afforded variable orientation and continuously varying masking density as one progressed away from the hub of the feature to the periphery. The pattern shown in Fig. 1 represents a 1 cm × 1 cm "tile", 19 of which can be written onto a 2 in wafer. This mask was used in the usual way to photolithographically pattern silicon dioxide films deposited on the wafer surface. The patterned wafer was given a light buffered HF etch prior to epitaxy to minimise spontaneous polycrystalline nucleation on the mask.

Our first concern related to the topology, morphology and optical quality of the deposits which grew within the windows, and how these might be affected by the density of masking and the material grown. To this end we grew bulk layers of InP, GaInAs and GaInAsP on the patterned substrates, and surveyed the resulting structures using scanning electron microscopy (SEM) and photoluminescence (PL) imaging.

For large features in light-field "districts", the epitaxial layers were flat and planar and, with the exception of some thickening at the mask margin, very similar in appearance and luminescence intensity to "whole-wafer" epitaxy. Energy-dispersive X-ray analysis (EDX) measurements indicated that the indium content of GaInAs and GaInAsP layers invariably increased toward the mask margin, and it was noted, using Nomarski interference microscopy, that for large masked areas this was accompanied by a network of crystallographic slip lines adjacent to the mask edge. For some geometries a more complex pattern of structural defects prevailed, in which slip-free material was interposed between dislocated regions adjacent to the mask, and dislocated material beyond the undislocated region, some way from the mask. In contrast to the morphology seen for large features in light-field situations, it was noted that, for small features in "dark-field districts", heavy faceting occurred at the mask margin, the growth rate was substantially increased and, for the ternary and quaternary alloys, the luminescence output was generally compromised. In order to gain some insight into the latter problem, cross-sectional transmission electron microscopy (TEM) was employed. Figure 2 is a collage of TEM micrographs prepared from a GaInAsP feature grown through a window 2 μm wide in a "dark-field district" of the mask. As can be seen, a triangular central core of the feature, based upon the original window in the oxide mask, appears to be delineated by

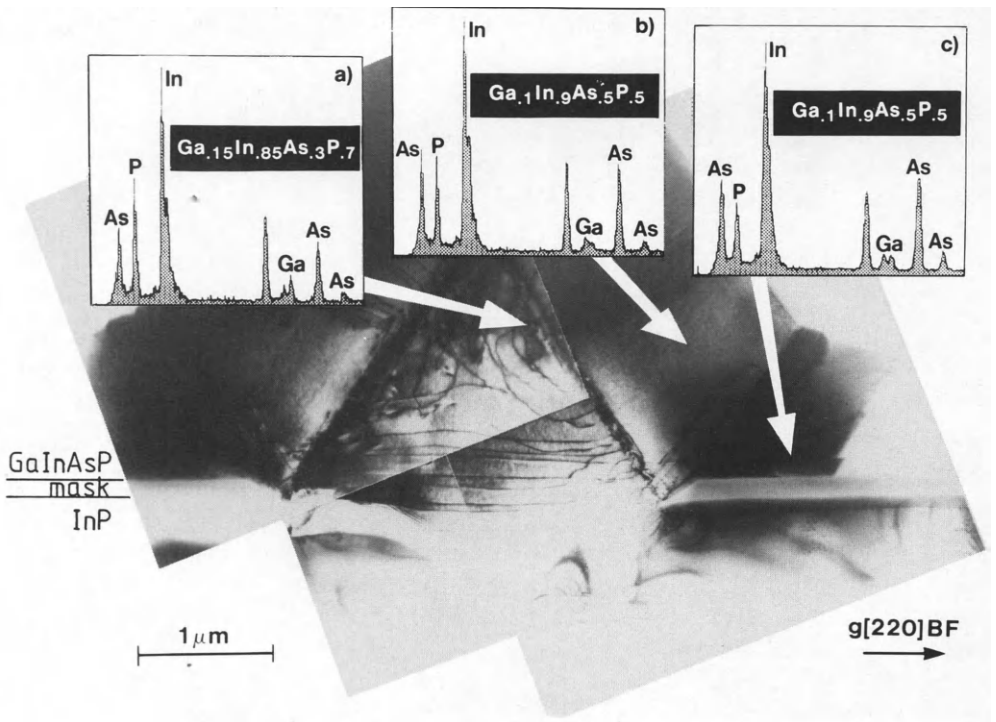

Fig. 2. TEM and EDX characterisation of selectively grown GaInAsP feature (dark-field district).

a network of dislocations, which would be consistent with luminescence quenching in the deposits. In order to check whether this dislocation network was induced by strain resulting from composition variations within the deposit, EDX measurements were performed in the TEM. The resulting spectra are also shown in Fig. 2. These measurements indicated that differences existed, on both the group III and group V sub-lattices, between material within the dislocated core (region *a*) and material outside this region (regions *b* and *c*) as indicated on the spectra. The measurements suggested that within the core the composition of the quaternary was roughly $Ga_{0.15}In_{0.85}As_{0.30}P_{0.70}$, whereas in the outer region of the deposit the composition was $Ga_{0.10}In_{0.90}As_{0.50}P_{0.50}$, and that the variation in lattice constant corresponding to these compositional differences was responsible for the non-uniform defect distribution.

The appearance of this defect structure suggested that the epitaxial deposit might be being formed by a combination of two distinct growth regimes and, to check this out, an experiment was devised to map out the evolution of the growing interface. This involved the growth of a multilayer GaInAs/GaInAsP structure which was subsequently cleaved, stained and imaged in an SEM. Figure 3 shows the result of this experiment and illustrates the form of the grown features in three regions of the mask depicted in Fig. 1. It is important to note that all three features were grown in the same run. Figure 3(a) illustrates the growth in a region remote from the influence of any masks and is provided for comparison. Figures 3(b) and 3(c) indicate the way the material grew in lightly masked and heavily masked "districts" respectively. The magnification is the same for all three photographs. As can be seen, the initial growth in all three areas takes place essentially in the [100] direction. The growth is enhanced in the two masked areas, with the more heavily masked district experiencing the greatest increase in growth rate.

From Figs. 3(b) and 3(c) it is apparent that the material growing in the [100] direction (the first regime) is bounded by {111} planes which arise due to the "casting off" of an atom per monolayer at the edge of the deposit as the layer grows. Although the mechanism for this behaviour is not fully understood, there are two possible factors which might have a bearing on the result. Firstly, the {111} planes are the most closely packed, within the lattice, so that steric hindrance could limit the growth rate in this direction. Secondly, the {111} planes uniquely present surfaces of uniform charge, rendering it difficult to incorporate both positively and negatively charged species (IIIs and Vs) necessary to sustain the growth of these polar materials. Whatever the reason, it is apparent that in the heavily masked "district" there is very rapid growth

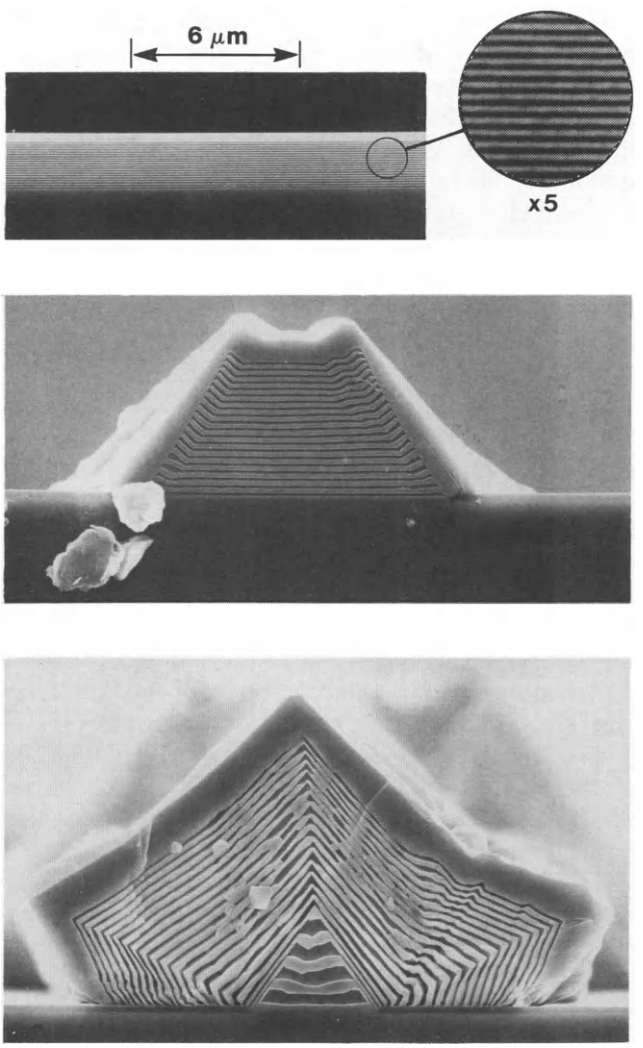

Fig. 3. Effect of masking density and feature size on evolution of selective epitaxy: (a) remote from mask; (b) lightly masked "district"; (c) heavily masked "district".

in the [100] direction which "cones off" by the formation of {111} planes at the feature edge. In the feature depicted in Fig. 3(c) the window is sufficiently small and the growth rate enhancement so great that this "cone development" proceeds to completion before the growth cycle is terminated, denying further availability of any (100)-oriented surface on which subsequent growth could take place. Once this has occurred, it can be seen that there is an acceleration of the growth occurring off the (111) plane and the deposit develops by this route (the second regime), burying the original [100] grown material. Because the feature shown in Fig. 3(b) is larger, and the growth rate enhancement more modest, growth predominantly continues in the [100] direction of the feature and does not reach the "cone-off" point before the growth cycle has been completed. It is also worth noting that the thickness of

{111} overgrowth in both areas is greatest near the base of the features (because it is here that the facet has existed for the longest time) and this causes the bounding edge to "kick out" from the {111} planes as the growth proceeds, giving rise to a concave curvature on these faces. These observations suggest that the compositional changes occurring within the deposit, shown in Fig. 2, result from a growth process which proceeds in two radically different growth directions and with markedly different growth rates. These two different regimes give rise to quaternary materials of differing composition from the same gas phase mixture.

A further detail, which can be appreciated from a close inspection of Figs. 3(b) and 3(c) is that, in addition to the "long-range" growth rate modification which arises from the different masking densities appropriate to the three regions, there is a much more localised enhancement in the growth rate in the material immediately adjacent to the {111} facets. This is thought to be due to migration of growth species off the facets themselves causing the layers to thicken and progressively bend up within a micron or so of the bounding facet. This effect can be more clearly seen in Fig. 4, which shows a magnified view of the evolution of growth at the mask margin. Here the progressive impact of the growing facet on the growth rate at the feature boundary can be clearly seen.

In experiments similar to those described above, comparisons were made between the propensities of InP, GaInAs and GaInAsP to nucleate on "non-preferred" {111} planes, and also a comparison between the characteristics of (111)A and (111)B planes in this respect was made. This is important, as the two types of plane-bound features aligned to the two principal cleavage planes, and any difference between them in terms of growth habit, may well impact decisions regarding eventual device layout on the wafer.

Although it was found that all three alloys will grow on these non-preferred {111} planes, if forced to do so by severe restriction of available (100)-oriented surfaces (either by high masking density or a large degree of facet growth), it was clear that InP did this more readily than GaInAs, with the quaternary exhibiting an intermediate characteristic. This is illustrated in Fig. 5, which compares InP and GaInAs growth at the mask margin. It can be seen that the InP has encroached significantly over the edge of the mask, whereas in the case of GaInAs very little of the oxide mask has been

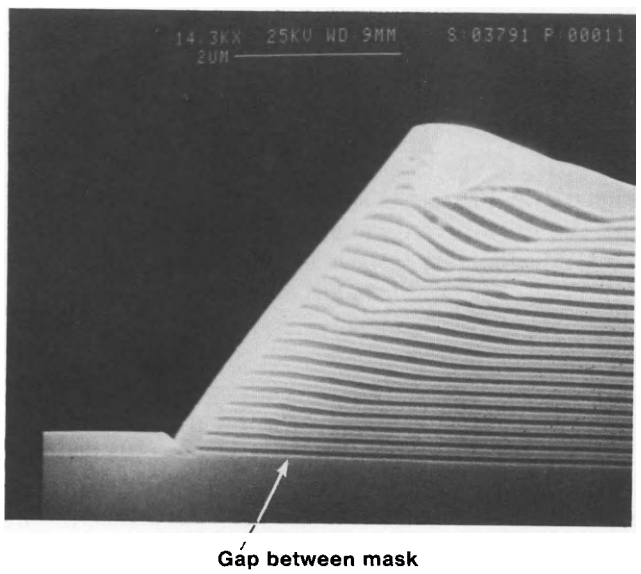

Fig. 4. GaInAsP/GaInAs marker layer growth at MF2 mask margin in light-field area. Mask width = 30 μm, gap width = 30 μm, mask aligned to [011].

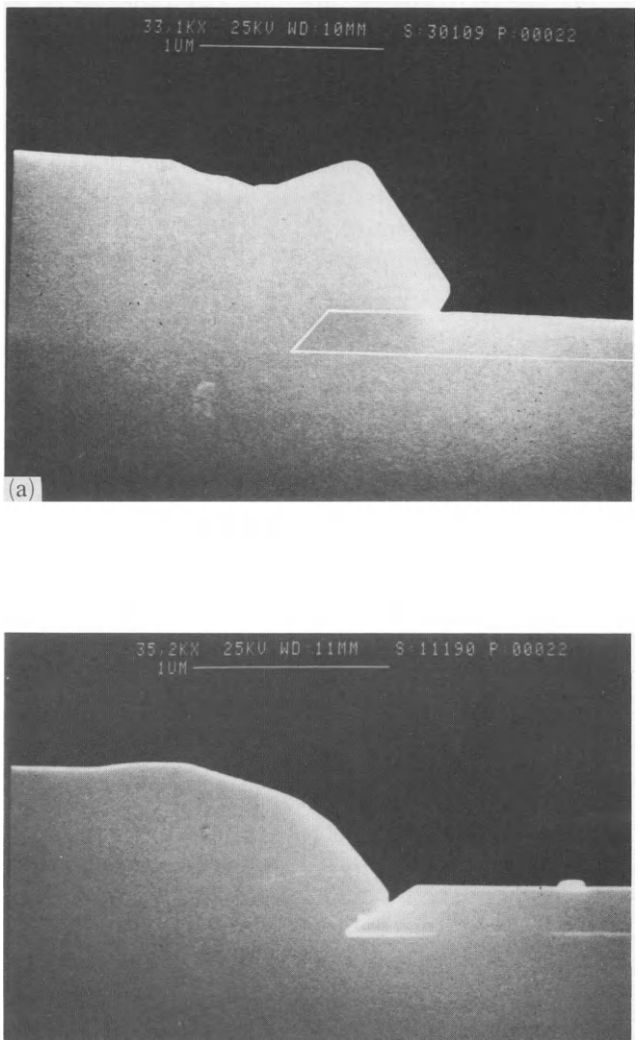

Fig. 5. Effect of material composition on growth next to mask. Mask width = 30 μm, gap width = 6 μm, mask orientation [01$\bar{1}$]: (a) InP; (b) GaInAs.

overgrown, the layer thicknesses of the two alloys being similar.

Similar observations of growth at the mask margin for star-shaped windows, where the alloy was invariant but the crystallographic orientation of the sampled feature was the variable parameter, indicated that growth off the bounding facet was a strong function of orientation, and significantly that nucleation on {111}A type facets occurred more readily than on {111}B type facets. Again the reason for this remains unproven, but one may speculate that again steric considerations may be responsible. In order to promote growth on {111}B type planes, which presents Group V atoms to the growth ambient, Group III species have to be accommodated on the surface. If, as seems most likely [17], the species responsible for growth are the partially dissociated precursors, then steric hindrance by the bulky methyl groups is likely to make nucleation more difficult than would be the case when partially dissociated Group V hydrides are incorporated on {111}A type Group III-rich surfaces to yield growth in that direction. On the other hand, the explanation may be even more simple and related to the fact that the concentration of the group III precursors is so much lower than that of the group Vs.

3.2. Quantitative measurements

As a result of the observations with the multi-feature mask, it was apparent that the closely packed, heavily masked features interacted with one another, making quantitative interpretation virtually impossible. In order to overcome this difficulty, a simpler pattern of much lower masking density was employed. This consisted of pairs of rectangular masks of varying width and separation, which were disposed in orthogonal orientations in different regions of the wafer. This pattern is depicted in Fig. 6(a). Epitaxial material deposited in the vicinity of these masks was analysed for thickness using surface profilometry and for composition using EDX measurements. Figure 6(b) shows a typical thickness measurement, indicating the way the growth rate increased toward the mask margin and between the two mask patches. In order to allow the results of different experiments to be related readily, the excess growth thickness was normalised with respect to the unperturbed growth thickness as indicated in Fig. 6(b). It was found that for InP, GaInAs and GaInAsP the layers thickened in the vicinity of the mask patches in a rational way, with the thickness in the centre of the masks increasing with mask width and decreasing with mask separation, as shown in Fig. 7, which represents data from measurements made on a GaInAs layer. Similarly the compositions of the ternary and quaternary alloys grown between the masks were found to become increasingly indium-rich as the mask

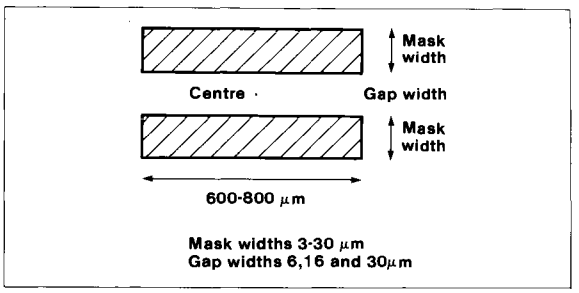

(a)

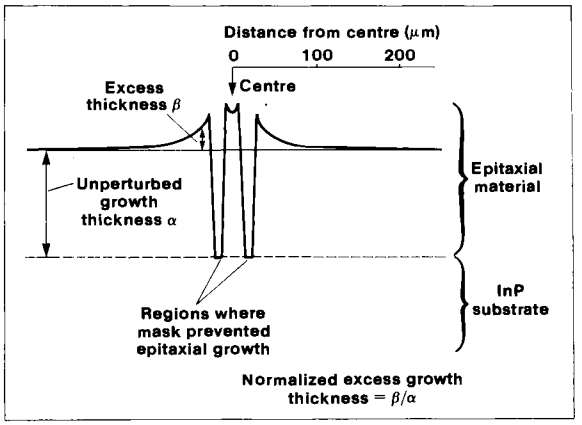

(b)

Fig. 6. Quantitative measurements of selective-area epitaxy: (a) mask arrangement; (b) typical thickness measurement.

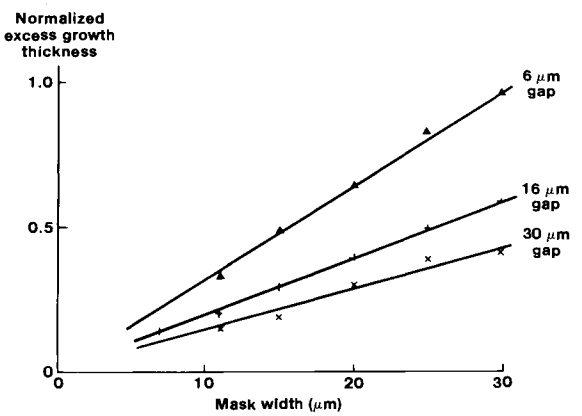

Fig. 7. Increase in GaInAs growth rate at centre of masks.

width was increased and the gap width was reduced. The form of this geometry dependence for GaInAs is shown in Fig. 8. Again the progression is seemingly predictable.

It is interesting to note that no variation in the As-to-P ratio was found for the growth of GaInAsP in the vicinity of masking features.

By combining these localised measurements of layer thickness and composition, estimations were made of

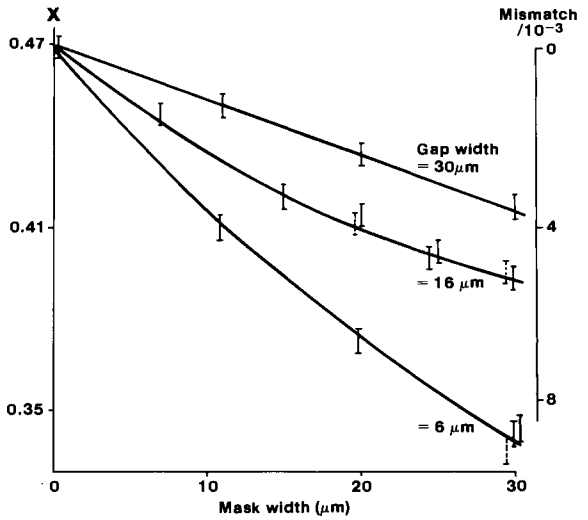

Fig. 8. Effect of masks on composition of $Ga_xIn_{1-x}As$ at centre of masks.

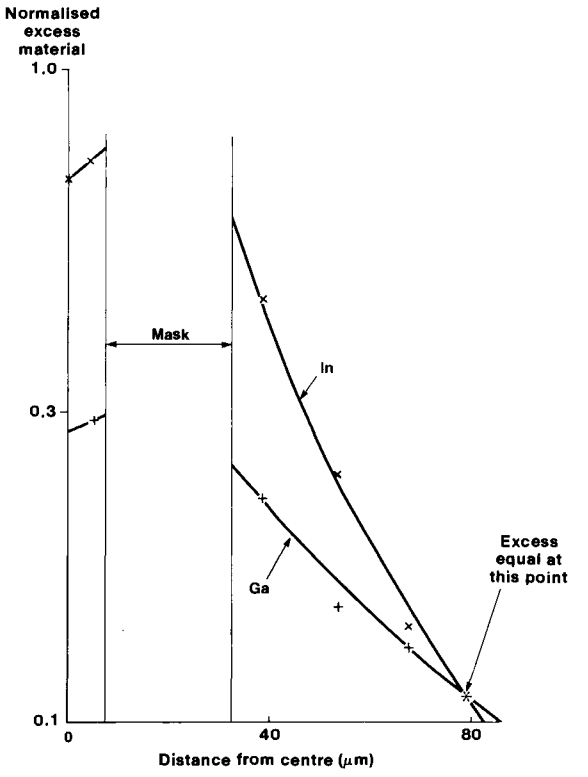

Fig. 9. Excess In and Ga species as function of distance from centre of masks.

the excess indium and gallium species responsible for growth, the distributions of which are depicted in Fig. 9.

As can be seen, the decay length of the excess gallium species exceeds that of the excess indium species, and the form of this relationship explained the previously puzzling defect distribution seen for some mask geometries, *i.e.* where non-dislocated material separated two regions of crystallographic slip in the vicinity of mask edges. This can be explained by the crossing of the indium and gallium curves, which implies that at this point (~ 80 μm from the mask edge for this particular sample), although the growth rate is enhanced, the material is growing at the unperturbed composition, as the excess concentrations are matched. Closer to the mask than 80 μm, the material is indium-rich and therefore positively mismatched, and beyond 80 μm the material is gallium-rich and therefore negatively mismatched before it asymptotically approaches the unperturbed composition beyond the influence of the masks. Bearing in mind that these decay lengths would be reflected in the scale over which device-relevant parameters vary, a cursory investigation was made of how they might be modified by the growth conditions. It was found that the decay lengths for indium during InP growth could be reduced by increasing the growth rate or the growth pressure. In round terms, doubling the TMI mole fraction (to produce a growth rate of 5.2 μm h^{-1}) caused a reduction of about 20% in the decay length, whereas doubling the growth pressure from 150 to 300 Torr reduced it by 50%. Following a detailed inspection of this derived data for the GaInAs(P) materials system, it became apparent that the decay characteristics of each excess Group III species was unaffected by the presence of the other, *i.e.* that the excess indium concentration profile was the same for indium in the growth of InP as it was for indium in the growth of GaInAs. This was an important finding, as it made the modelling of selective-area epitaxy a practical proposition.

3.3. Selective-area epitaxy model

Following the realisation that the behaviours of the Group III species controlling the growth could be treated separately, an analytical, descriptive model of the process was devised. The objective was to predict thickness and compositional perturbations resulting from selective area epitaxy, as the mask geometry was arbitrarily changed. The model assumed that the distribution of the growth species at the wafer surface was controlled by steady-state diffusion from a "nutrient" layer, remote from the surface, through a "boundary" layer interposed between it and the surface. The assumption was also made that there was no significant deposition of semiconductor upon the mask, as is found in practice.

The model operates by solving Laplace's equation for the Group III precursors separately to yield the concentration profiles of the indium, or the indium and gallium species, in the volume above the wafer, the solution being constrained by appropriate boundary conditions

The expression employed is:

$$D\left(\frac{\partial^2 n}{\partial x^2}+\frac{\partial^2 n}{\partial y^2}+\frac{\partial^2 n}{\partial z^2}\right)=0$$

which is the steady-state diffusion equation representing the conservation of the reactant species. Here D is the diffusion coefficient, n the concentration of the reactant species and x, y and z the standard Cartesian spatial coordinates. In this notation, x and y are the coordinates perpendicular to and parallel to the long axes of the masks, respectively, in the plane of the wafer, whilst z represents the coordinate perpendicular to the plane of the wafer. In fact, because the aspect ratio of the masks renders them semi-infinite in the y direction, the term $\partial^2 n/\partial y^2$ can be put to zero, reducing the problem to a two-dimensional window of width w and height d. This considerably simplifies the operation of the Fourier routine used to solve the equation. Figure 10 illustrates the form of the boundary conditions used in this modelling, which define the concentration in the "nutrient" layer as n_0, puts $\partial n/\partial x$ equal to zero at centres of symmetry within the mask pattern and puts $\partial n/\partial z$ equal to zero immediately above the oxide masks where deposition is prevented. At all other regions on the exposed surface where growth takes place, Fick's Law is invoked, which equates the product of the diffusion coefficient D and downward flux $\partial n/\partial z$ with the product of a surface incorporation coefficient k and the concentration n of the growth species. The model was operated by fixing a value of n_0 to give the appropriate growth rate remote from the masks and adjusting the value of D/k to give a fit to experimentally determined data at a single point. Thereafter the validity of the model was tested by comparing predictions derived using these input parameters with measured thickness and composition data at other locations on the mask pattern.

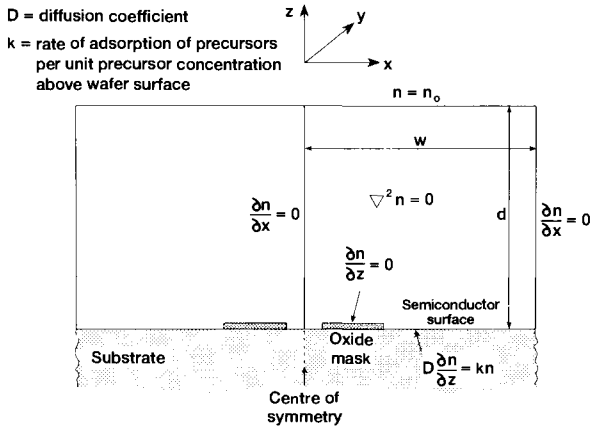

Fig. 10. Geometry and boundary conditions used in MOCVD growth model.

Figure 11 makes the comparison between practically measured, spatially resolved thickness data for selectively grown InP using a D/k value of 15 μm. Figure 12 indicates the ability of the model to cope with changes in mask geometry by charting the variation in thickness of the deposit mid-way between the mask patches as the mask width and mask separation are varied, again using the same value of D/k.

Finally, Fig. 13 illustrates the ability of the model to relate composition to position, relative to the mask, for

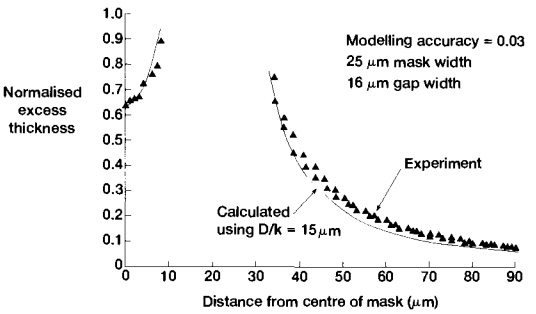

Fig. 11. Normalised excess thickness *vs.* distance from centre of masks.

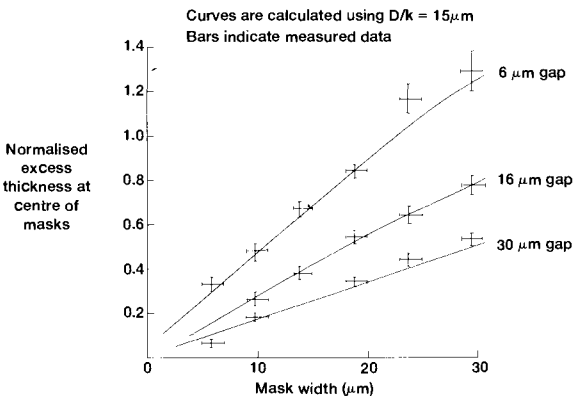
Curves are calculated using D/k = 15μm
Bars indicate measured data
Normalised excess thickness at centre of masks
6 μm gap
16 μm gap
30 μm gap
Mask width (μm)

Fig. 12. Increase in InP growth rate at centre of mask pattern.

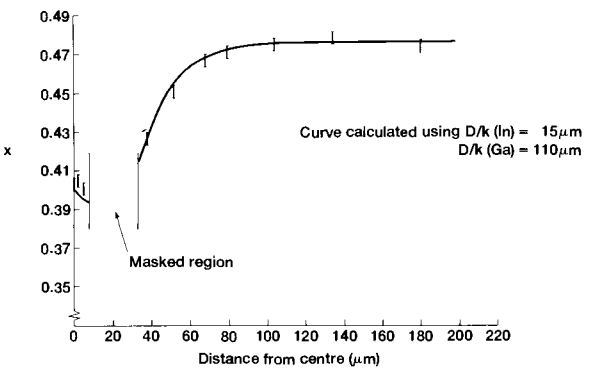

Fig. 13. $Ga_xIn_{1-x}As$ composition as a function of distance from centre of mask pattern.

GaInAs. The simulation obviously requires both the excess of the indium and gallium precursors to be modelled. Again the value of D/k used for indium was 15 μm, whilst that used for the gallium precursor was 110 μm. In all these examples the results of the model agree with the measured data to within the error bars of the measurements.

The analysis described in this section was run on an HP desktop computer and typically took up to 30 min to reach convergence.

4. Non-planar epitaxy

Non-planar epitaxy is an important technology for the fabrication of III-V optoelectronic devices and, as such, merits its generic characterisation to establish its scope, limits and amenability to optimisation. Two of the most important issues are infill control and planarisation, whilst structural and optical quality in the vicinity of step edges and butt joints is also a subject of considerable interest.

In order to gain a broad insight into the evolution of the growing interface in the vicinity of unmasked sculpted features, multilayer "marker" structures similar to those described in section 3.1 were used in conjunction with wafers which were relief-patterned using the multi-feature mask described in the same section. The relief-patterning process consisted of first coating the wafers with silicon dioxide and then photolithographically defining this oxide, as previously described, to open windows. Using the patterned oxide as a mask, the areas of substrate exposed within the windows were then etched using methane–hydrogen reactive ion etching (RIE) to produce a complex matrix of mesas and trenches, with the trenches corresponding to the open features of the original mask. About a micron of material was removed by the RIE treatment, after which any damage induced was removed by briefly etching with an appropriate wet etch (acetic/hydrochloric/peroxide/water) prior to stripping the dielectric with HF. Considerable differences were noted between the ways the overgrowth developed at different features within the mask pattern, and many of these differences were seen to be dependent upon the orientation of the etched feature relative to the crystallographic orientation.

A reasonably comprehensive picture of the variation in step-edge morphology and infill habit as a function of orientation is provided by Fig. 14, which shows isometric and cleaved edge sections of the arms of a star-shaped trench feature which has been overgrown with a GaInAs/GaInAsP marker layer structure using low-pressure MOCVD. As can be seen, there is a wide variation in side-wall morphology, with the two orientations mid-way between the [011] and [0$\bar{1}$1] principal cleavage directions, *i.e.* the [001] and [0$\bar{1}$0], giving the smoothest growth. The planarisation mechanism at the step edge is also seen to be orientation dependent. In all orientations, the initial growth on the plateaux above and below the step edge is disconnected, and little or no growth takes place off the etched sidewalls. The material growing on the upper plateau is also invariably terminated by a high-angle facet at the step edge, which becomes buried, sooner or later, by material growing on the lower plateau overhauling it. As can be seen from Fig. 14, the facet can be buried very quickly, giving rise to rapid planarisation, as for the [001] oriented step edge, or it can persist for most of the growth cycle, delaying planarisation, as is seen for the [0$\bar{1}$1]-oriented step edge.

An inspection of the marker layers suggests that there are two distinct growth habits by which the non-growing facets can be buried. The reason for the difference between these two groups can be traced back to the development of the growth at the bottom of the step. In structures which we designate type A, which are exemplified by the [001]-oriented step edge, the growth at the bottom of the step was greatly accelerated over that at locations far removed from any structure. Generally speaking, this accelerated growth took place on planes inclined at about 15° to the (100) plane, though the situation was somewhat confused in the case of channels aligned to [011]. The fast-growing planes rapidly overhauled the growth on the surrounding plateau, and terminated the high-angle facet within 2–4 periods of the marker layer structure. However, in structures of type B, which are exemplified by the [0$\bar{1}$1]-oriented step edge, the growth at the bottom of the step was inclined at 5° or less to the (100) and was only marginally accelerated. Consequently the high-angle facet was able to progress for between 12 and 14 periods of the marker layer structure without hindrance. It was eventually terminated when it was overhauled by planes which were slow growing, but which were able to climb rapidly up the facet surface by virtue of the large inclination to the (100), which they adopted in the latter stages of the growth cycle. In order to clarify the information contained in Fig. 14, Fig. 15 was constructed. This shows five "snapshots" of the layer growth in the two examples of step orientation described above. The full growth habit/orientation findings are summarised in Table 1.

It is interesting to note that in structures of type A the growth rate on the plateau next to the channel decreased slightly in the vicinity of the step. For structures of type B the reverse was true. One might speculate that, in the former case, adsorbed species are migrating off the growing plateau surface to feed adjacent fast-growing planes. Conversely, in the latter situa-

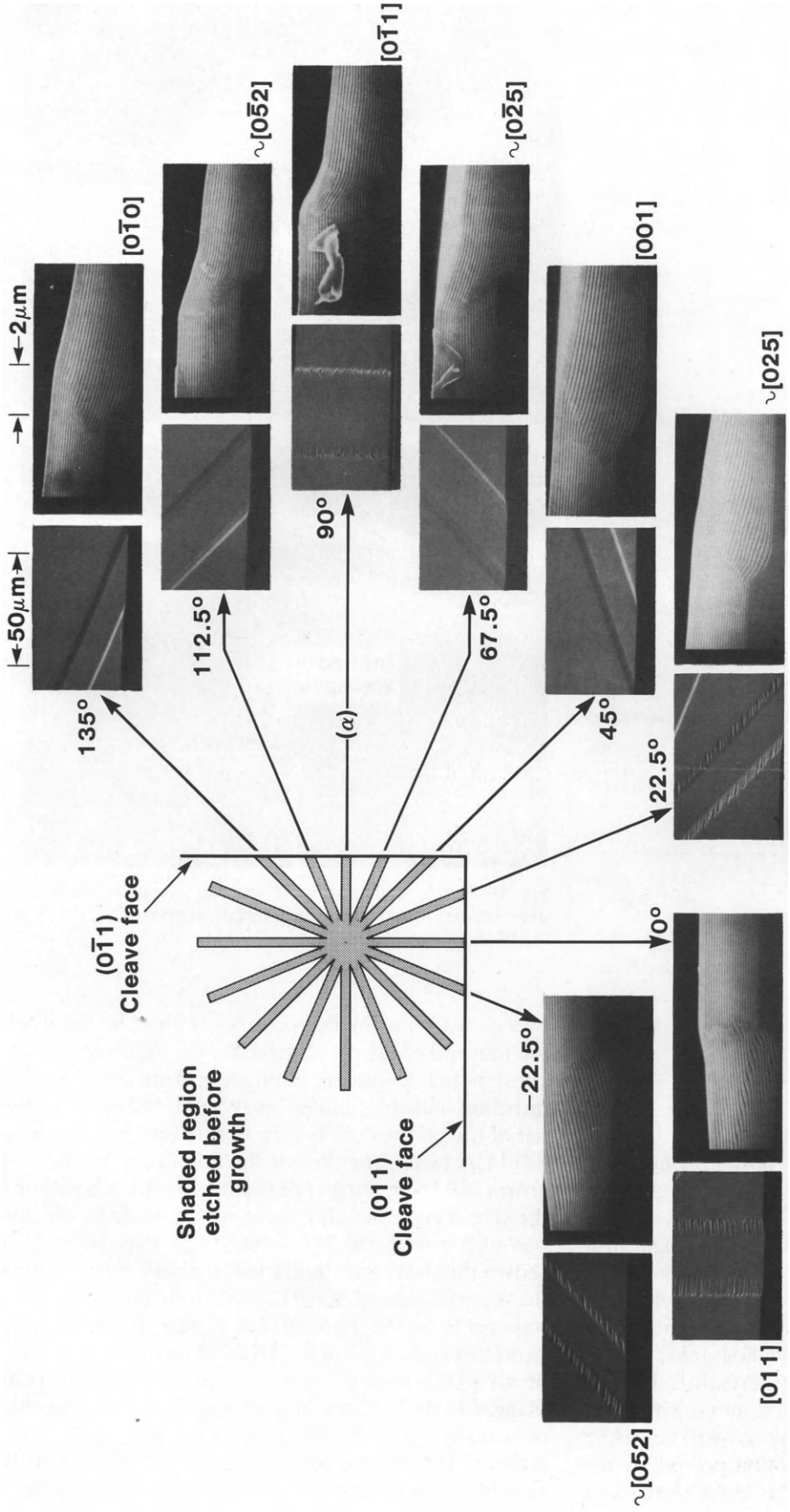

Fig. 14. Non-planar epitaxy of GaInAs/GaInAsP as a function of crystallographic orientation.

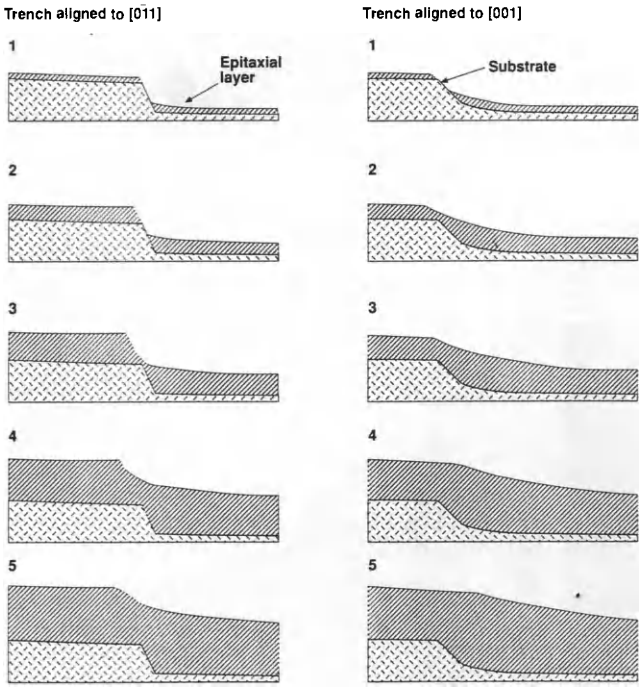

Fig. 15. Evolution of non-planar epitaxy as a function of orientation.

TABLE 1. Summary of growth habit as a function of orientation for GaInAs(P) step edge growth (see Fig. 14)

θ/ (deg)	Channel direction	Number of periods before termination of facet	Growth type
−22.5	~[0 5 2]	2	A
0	[0 1 1] or β	4	A
22.5	~[0 2 5]	2	A
45	[0 0 1]	4	A
67.5	~[0 2̄ 5]	12	B
90	[0 1 1] or α	13	B
112.5	~[0 5 2]	14	B
135	[0 1̄ 0]	4	A

tion, precursors adsorbed on the non-growing facet may be diffusing from this region to the growing plateau.

An example of the practical value of an insight into orientation-dependent non-planar growth habit is provided in Fig. 16. Figure 16 shows two cross-sections of quaternary/quaternary active/passive waveguide butt joints, formed in orthogonal crystallographic directions. The structures consist of an InP/GaInAsP composite, grown as an infill to a masked mesa, which has been etched through a previously grown GaInAsP layer of a different composition to that present in the infill. The infilled material and the mesa were then

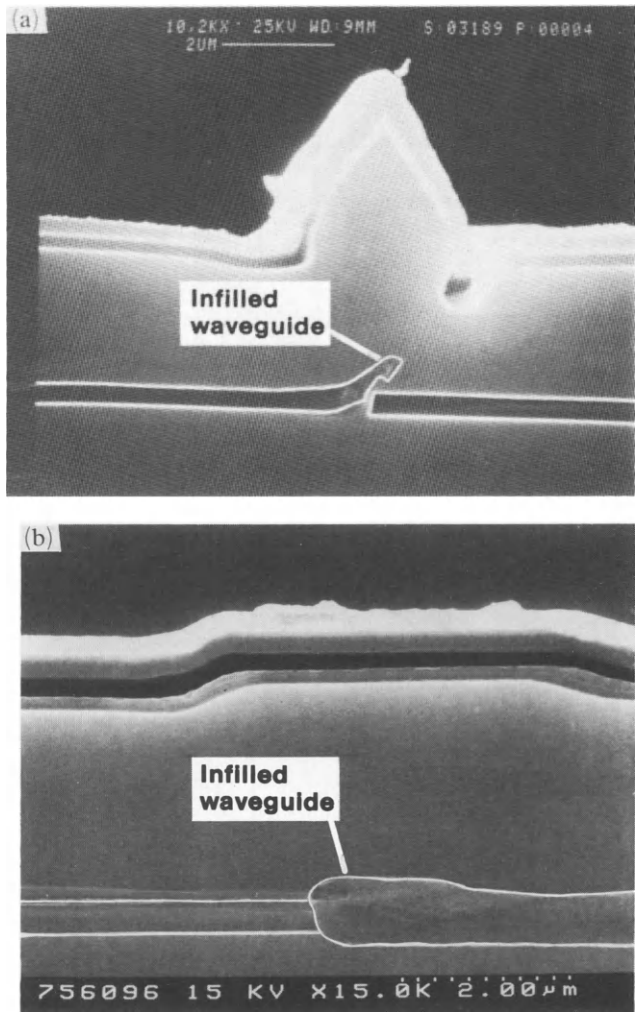

Fig. 16. Butt coupling of active/passive waveguides in orthogonal directions: active/passive interface aligned to (a) [01̄1] and (b) [011].

overgrown with an InP/GaInAs composite following the removal of the oxide mask on the mesa top. In Fig. 16(a) the active–passive interface is aligned to the [01̄1] direction and the "infilled" waveguide material on the left of the photograph is seen to ride up what would be a (111)A facet generated at the mesa edge by the first grown InP layer. Further nucleation on this facet during the subsequent thick InP layer growth leads to a highly non-planar surface. By contrast, in Fig. 16(b) it is shown that little growth has taken place on the edge of the mesa aligned to the [011] direction, and the infilled waveguide to the right of the picture is much more planar, as is the top surface. A facet forming at the edge of an [011]-oriented mesa would be in the (111)B plane, and the absence of evidence for this implies that nucleation on such planes is more difficult than for their (111)A counterparts, as previously discussed in section 3.1. It is important to note that both pictures

are taken from identical mask geometries, overgrown on the same wafer, in the same growth run with only the orientation with respect to the crystallographic axes being different.

In the context of optoelectronics an equally valid concern relates to any change in the optical properties which the non-planar growth habit might induce in the material in the region of the sculpted feature.

The first, most obvious, effect is the reduction in luminescence efficiency in the vicinity of all step edges or side walls as shown in Fig. 17. This figure comprises a collage of photoluminescence images taken from a non-planar GaInAsP layer, grown over a sculpted wafer and patterned with the multi-feature mask described earlier. The images were recorded using a lead sulphide vidicon camera whilst the sample was pumped with YAG laser light. As can be seen, the luminescence quenching is obviously fairly local to the step edge, and a broad area reduction in intensity tends to occur only where the density of step edges is high. It is also interesting to note that the degree of quenching appears to be orientation dependent, as is shown by the variation in intensity along the curved features near the centre of the picture, and by a comparison of the arms of the star-shaped features. In the latter, there is a tendency for features oriented at 22.5° to the [0$\bar{1}$1] direction to suffer less quenching than features in other orientations.

A more quantitative appraisal of such material has also been undertaken using a spatially resolved photoluminescence apparatus developed at UMIST. This machine moves the sample via a computer-controlled, stepper motor driven, translation stage and illuminates the sample with a diffraction-limited laser spot (below 2 μm). The resulting photoluminescence is analysed with a Fourier transform infra-red spectrometer which means that, because of its high optical efficiency, data can be taken rapidly and/or the pumping power can be reduced, permitting more refined spectroscopy. Owing to the use of a long working distance objective lens in this system, the sample can be mounted in a cryostat, permitting spectra to be taken down to 4 K.

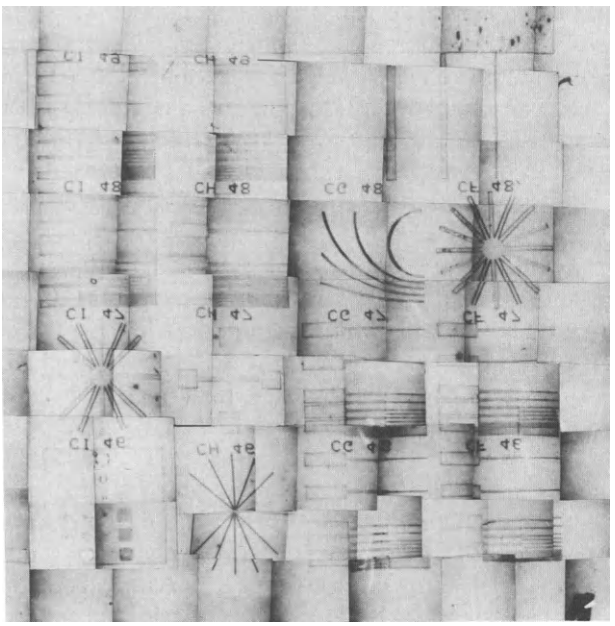

Fig. 17. Collage of photoluminescence images from non-planar epitaxy of "1.18 μm" GaInAsP.

A typical result of such studies is shown in Fig. 18, which quantifies the luminescence properties of a GaInAsP layer in the vicinity of a step edge. The sample structure is indicated in Fig. 18(a), whilst the plot of Fig. 18(b) shows how both the band gap energy changes and the luminescence intensity is quenched near the step edge. A clearer impression of the change in band gap energy is given by Fig. 18(c). It is thought that again these changes are related to compositional changes and mismatch variations that occur when growth proceeds from a number of radically different planes, as discussed in section 3.1. This type of information is obviously of considerable value, either when designing devices which have active layers close to trench or mesa edges or where passive waveguides are required to traverse such features.

5. Device applications

The way the basic materials studies described earlier have fed into our device programmes can be best understood by considering a couple of specific examples. Probably the most relevant devices to choose are buried heterostructure lasers and integrated laser/modulators. These represent examples of non-planar and selective-area epitaxy respectively.

5.1. Buried heterostructure lasers

Buried heterostructure lasers are commonly fabricated using a three-step growth process, firstly to prepare a suitable substructure, secondly to infill mesas fabricated from this substructure with appropriate current-blocking layers and thirdly to overgrow both mesa and infill with planarising p-type contact and cladding layers. The completed structure is illustrated in Fig. 19. In addition to the planar growth steps, an infill growth is required, which is both selective and non-planar, in that the top of the mesa structure is masked with silicon dioxide to prevent the nucleation of the blocking layers in that region. In our investigations we experimented with p–n blocking layers, semi-insulating blocking layers, bulk quaternary active layers, multi-quantum well active layers and growth at

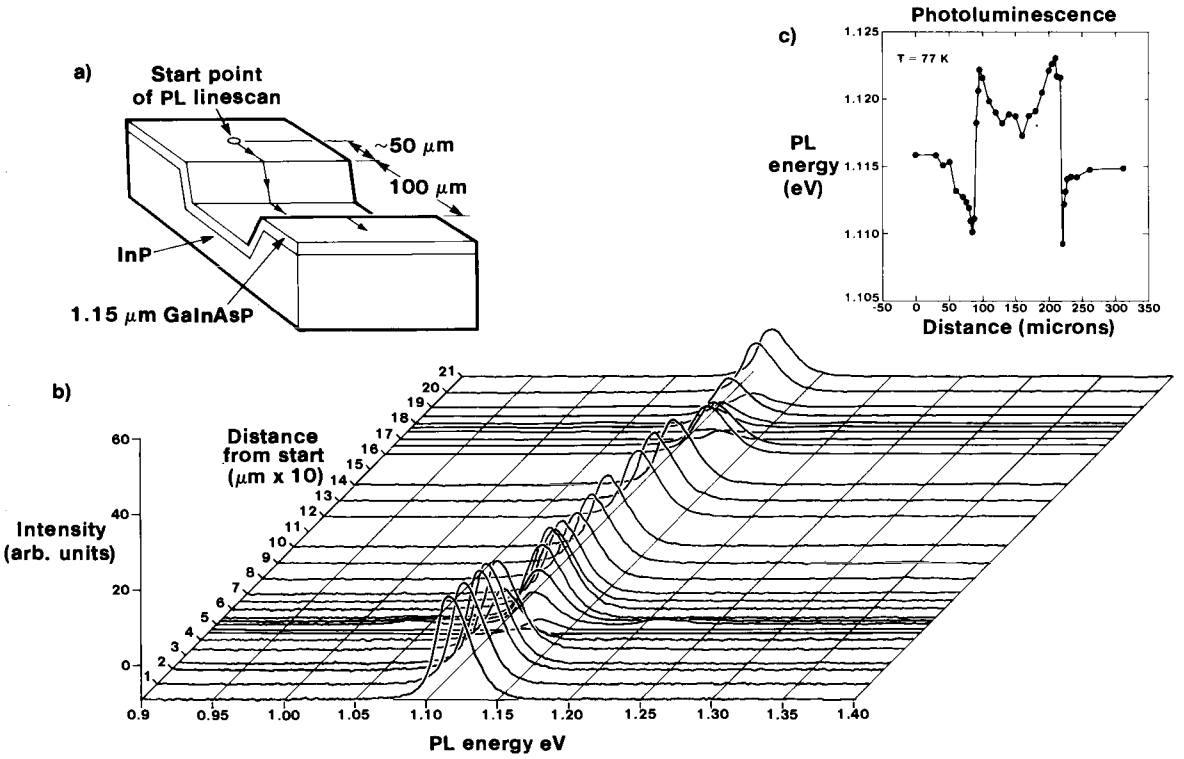

Fig. 18. 77 K PL spectra of non-planar epitaxy of GaInAsP as a function of position.

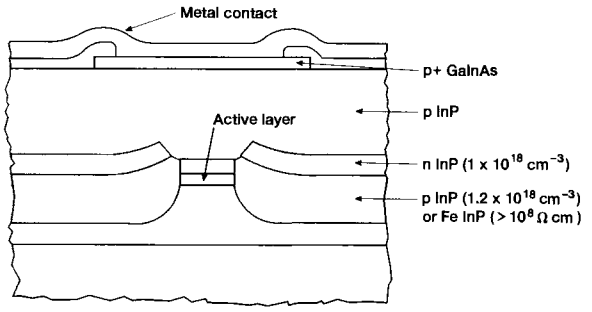

Fig. 19. Buried heterostructure laser.

both atmospheric and reduced pressure. Operation of the reactor at 150 Torr was found to facilitate the realisation of a suitable infill geometry. This infill process was again studied using marker layer techniques, this time with thick InP layers interleaved with thin GaInAs markers. In this way the optimum growth rate, growth time, mesa height, oxide overhang, etc., could be established with the minimum amount of growth effort. A graphic demonstration of the effect of growth pressure is given in Fig. 20, which compares the results of two marker layer growth cycles, at reduced and atmospheric pressure, over identical tall mesas of the type required to provide adequate current blocking with Fe-doped, semi-insulating InP. As can be seen, the structure grown at low pressure (Fig. 20(a)) yielded a coherent build-up of material adjacent to the mesa which, if growth had been terminated after the fifth GaInAs marker, would have yielded a quasi-planar structure. By comparison, the growth at atmospheric pressure (Fig. 20(b)) is singularly chaotic, with voids generated by the formation of slow growth facets extending from the mesa base and with extensive accelerated overgrowth taking place in the region of the mesa itself, causing the oxide cap on the mesa top to be virtually engulfed.

This problematic growth habit proved to be sufficiently intractable that steep-sided, high-aspect-ratio (tall) mesas could not be infilled satisfactorily at atmospheric pressure, and only shallow, gently sloping geometries could be accommodated using those growth conditions. An example of the control available with the low-pressure regime is illustrated by Fig. 21, which shows the mesa before and after the infill growth of the blocking structure.

It is interesting to note, from the shape of the marker layers abutting the mesas, that growth off the side wall was a characteristic of the low-pressure, tall-mesa scheme, whilst for the atmospheric pressure process no such evidence was found. This is considered to be an important issue, as it implies that the exposed edge of the active region is rapidly covered and protected in

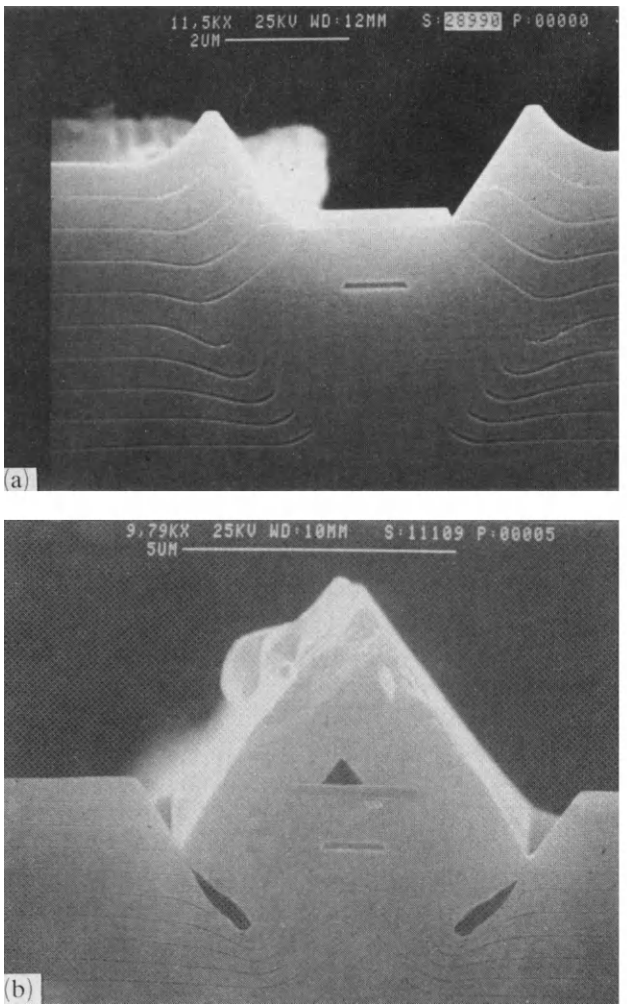

Fig. 20. Overgrowth of mesa with InP and GaInAs marker layers: (a) at low pressure; (b) at atmospheric pressure. $(0\bar{1}\bar{1})$ face; mesa height = 3.4 μm; oxide width = 2.6 μm; oxide overhang = 0.7 μm each side of mesa.

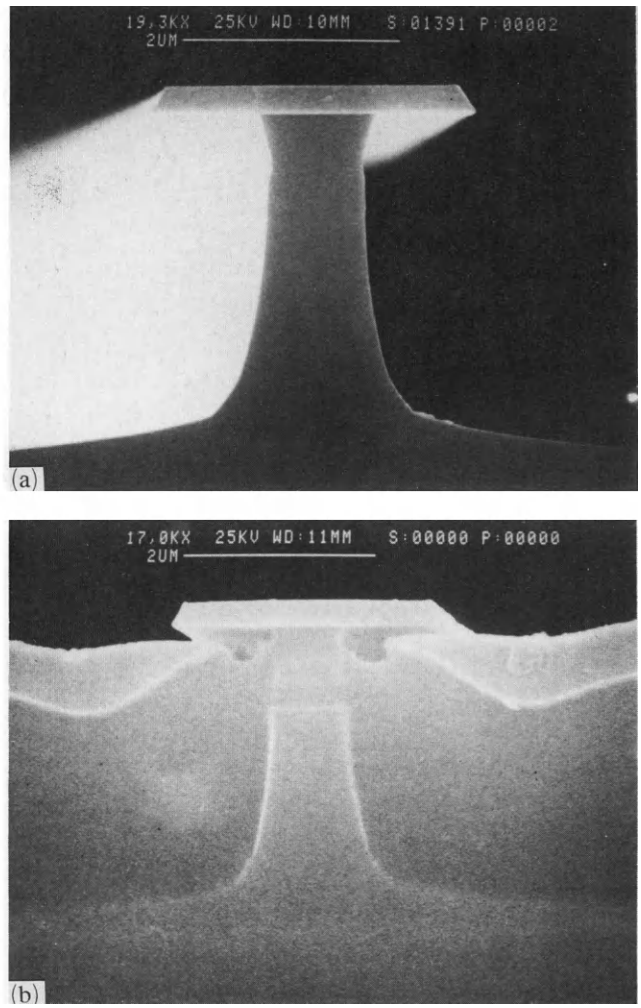

Fig. 21. Infill growth of buried heterostructure mesa: (a) substructure mesa prior to blocking-layer growth; (b) mesa region following blocking-layer growth.

the case of the tall-mesa, low-pressure growth. In the atmospheric pressure case, however, it would have remained exposed to a non-equilibrium reactor ambient until the layers advancing in the [100] direction overhauled and buried it.

Devices were fabricated using both growth regimes which gave good zero time performance with threshold currents down to 7 mA, single-mode output powers up to 20 mW and, in the case of the semi-insulating blocked devices, a 3 dB band width of 7.4 GHz. A marked difference was noted in the reliability of these lasers, with the devices infilled at low pressure exhibiting an order of magnitude lower rise in threshold current for a particular life test schedule than those devices where the blocking structure had been grown at atmospheric pressure.

In an attempt to establish the mechanism for the rapid degradation, a technique was devised for sectioning laser chips, suitable for TEM evaluation, which used a focused gallium ion beam (FIB) to erode the sample, at normal incidence to the chip surface, in the vicinity of the active region. Using this technique it was possible to produce dislocation-free, electron-transparent (~ 1000 Å) webs of material, perpendicular to the mesa direction, by the erosion of a trench behind the laser facet. Figure 22 is an isometric SEM picture illustrating a specimen thinned in this way. Using such samples, a comparison was made using TEM between un-degraded, lightly degraded and heavily degraded laser chips using both compositionally sensitive and defect-sensitive diffraction conditions. In all but the devices which showed the most severe degradation, the active regions were seen to be free of any structural defects. On the other hand, in the case of the rapidly degrading device, dislocation loops were seen at what would have been the exposed edge of the active layer

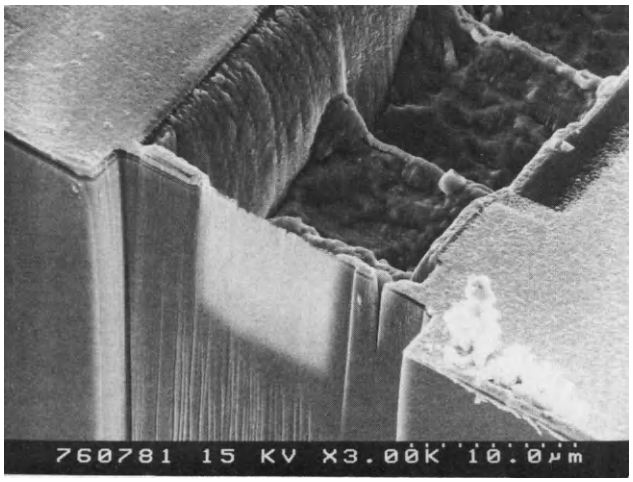

Fig. 22. Focused ion-beam thinning of buried heterostructure laser for TEM evaluation.

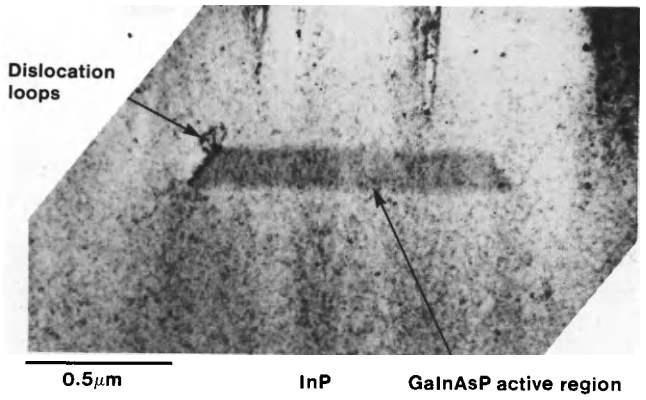

Fig. 23. Cross-sectional TEM of active region of degraded p–n blocked buried heterostructure laser.

during regrowth. Figure 23 is a TEM photograph showing such a defect. This defect structure is consistent with reports [18] that the surface of GaInAsP can be compositionally perturbed and degraded by heating to MOCVD growth temperatures under inappropriate reactor ambients, and the fact that for these rapidly degrading devices the active layer would have remained exposed for a protracted period.

5.2. Integrated laser/modulator

Probably the most interesting application of patterned growth we have so far pursued is the fabrication of an electroabsorption modulator monolithically integrated to a distributed feedback (DFB) laser. This device, which operates on the basis of the quantum-confined Stark effect, exploits the change in bandgap which can be achieved using selective-area growth to

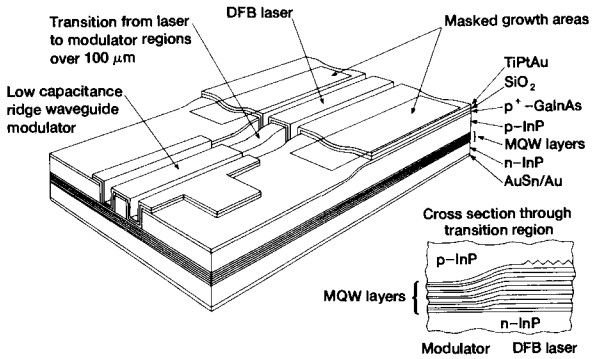

Fig. 24. Integration of laser and modulator using variable-thickness quantum wells.

perturb the thickness of GaInAs quantum wells in the vicinity of dielectric masks. In common with other workers in the field [13], we have been able to offset the band gap by more than 100 nm over a distance of about 100 μm, in layers deposited in the same growth run. This is extremely valuable in achieving a low insertion loss of the laser light into the modulator, by fabricating the laser in an area of thickened growth, such that the emission wavelength of its quantum wells is longer than that of the unperturbed material where the modulator is fabricated. A displacement of the bandgaps in the two regions is thus achieved, ensuring that very little of the laser light is absorbed by the modulator in its unbiased state. Figure 24 illustrates the basic quaternary(1)/quaternary(2) MQW structure used in this device, although additional waveguide, etch stop and undoped "dopant offset" layers are also included. These are shown in Figs. 25 and 26, which show cross-sections through the finished device in the modulator and laser regions respectively. From a comparison of Figs. 25 and 26 it is evident that an undoped InP layer and quaternary etch stop layer grown above the upper quaternary waveguide layer are removed prior to the DFB grating fabrication and overgrowth in the laser region. This is done to minimise the access resistance to the laser, but it is left in place in the modulator region to effect electrical isolation between laser and modulator and to minimise the diffusion of zinc from the p-type overgrowth into the quantum wells, which would otherwise compromise the oscillator strength of the exciton in that device. The etch stop layer is included to facilitate the fabrication of the ridge structure using selective etching techniques. As has been reported earlier [11], lasers with wavelengths shifted by between 28 and 120 nm were fabricated using different masking geometries and grating pitches. The threshold currents of these Fabry–Perot lasers varied little between different masking geometries (except for those made on the most severely perturbed material) and averaged about 27 mA. $2 \times \lambda/8$ DFB lasers were also

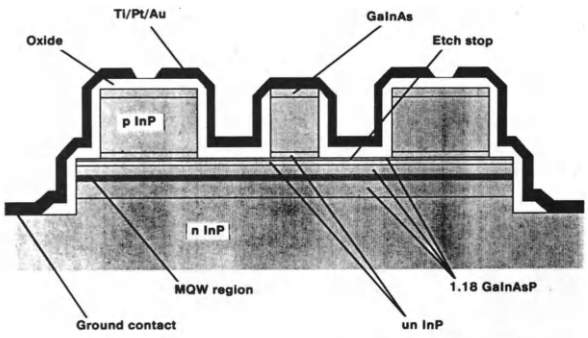

Fig. 25. Modulator part of integrated laser/modulator.

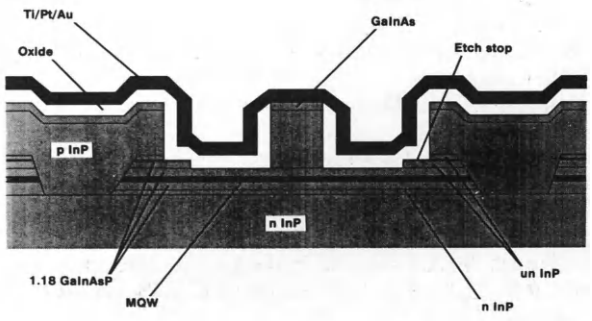

Fig. 26. Laser part of integrated laser/modulator.

produced on this selectively grown material which were indistinguishable (apart from the wavelength) from devices fabricated on unperturbed material, far from masked areas on the same wafer. The spectra of these devices showed side-mode suppression ratios of about 48 dB. Initial testing of the integrated devices involved measuring their d.c. characteristics, and this was performed on-wafer with the aid of appropriate probe cards and a semiconductor parameter analyser. Functionality of the laser was checked by monitoring the photocurrent induced in the modulator as the laser drive current was varied, and operation of the modulator was checked, in the first instance, by noting the response of the the photocurrent to changes in the modulator bias. A more realistic appraisal of the device was then undertaken by cleaving individual laser/modulator chips from the wafer, mounting them on a high-speed sub-mount and coupling the light from the output facet of the modulator into a lensed fibre. The d.c. characteristics measured using this arrangement are shown in Fig. 27, and illustrate the way in which the light coupled into the fibre varies with both laser drive current and modulator bias voltage.

High-frequency measurements were also made whilst driving the modulator with a pseudo-random bit pattern, superimposed upon a d.c. voltage designed to bias the modulator to the optimum region of its operating characteristic. The response to digital signals of this

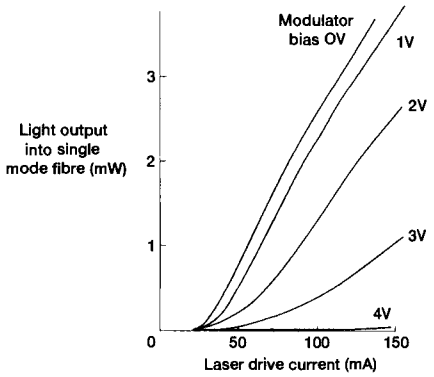

Fig. 27. Light *vs.* current characteristics from modulator end of integrated laser/modulator.

type is conveniently judged by superimposing replicas of the received signal with bit interval shifts between overlays to form an "eye" diagram. The degree to which this "eye" remains open as the frequency of operation is raised is a measure of the modulator's performance.

Devices of this type have yielded system-compatible performance to 5 Gbit s^{-1}. An estimation of the wavelength "chirp" was also made by comparing the spectra with and without modulation. As this transient change in wavelength represents one of the most important factors controlling system performance, it was gratifying to note that it was close to the measurement limit, with a value below 0.1 Å being obtained at 2.5 Gbit s^{-1}.

In designing and realising this complex device, the insight into the characteristics of selective-area epitaxy gained from the work described in section 3.2 proved invaluable.

6. Conclusions

Selective and non-planar epitaxy of InP, and its related alloys GaInAs and GaInAsP, have been studied as a function of mask geometry, orientation and, to a limited degree, growth conditions. Observations have been made of the growth habit of these different alloys on non-(100) planes, and mechanisms have been suggested which could explain the shape of the deposits seen, their crystallographic quality and their luminescence properties.

Quantitative measurements have been made of the way in which selective-area epitaxy, conducted on light-field masks, perturbs the thickness and (where appropriate) the composition of InP-based alloys. The principal effects seen can be quantitatively explained by gas-phase diffusion of the Group III growth species which produce perturbations ranging over tens of

microns, although shorter-range modifications can be related to surface migration of reactants off "non-preferred" facets.

A descriptive analytical model has been developed for the prediction of selective-area epitaxy behaviour, which provides a good fit to practical data in spite of the use of a number of simplifying assumptions. The model operates by solving Laplace's equation, describing the steady-state diffusion of reactant species above the wafer surface, under appropriate boundary conditions, using a desktop computer. The insight gained as a result of these generic investigations has proved valuable in applications relating to buried heterostructure lasers and integrated laser/modulators. A degradation problem relating to the former device has been tentatively related to the growth habit of the blocking-layer growth. The investigations into the fundamental characteristics of material grown by selective-area epitaxy have constituted a necessary stepping stone to the design of the integrated laser/modulator, which is showing significant promise as the next generation of high-speed sources.

Acknowledgments

The bulk of this work was supported, in part, by the DTI/SERC-funded LINK ASM programme. Device-related work on the integrated laser/modulator was supported in part by RACE projects 1027 and 2006 WELLCOME.

The authors are indebted to Dr. A. G. Norman of the London IRC for Semiconducting Materials, for the provision of TEM data, to Dr. B. L. Lamb of BNR Europe Ltd., for the preparation of TEM specimens by FIB thinning, and to Dr. P. D. Greene of BNR Europe Ltd. and Dr. M. E. Pemble of UMIST, Chemistry Department, for informative discussions.

References

1 R. Azoulay, N. Bouadma, J. C. Bouley and L. Dugrand, *J. Cryst. Growth, 55* (1981) 229.
2 Y. Takahashi, S. Sakai and M. Umeno, *J. Cryst. Growth, 68* (1984) 206.
3 C. Ghosh and R. L. Layman, *Appl. Phys. Lett., 45* (1984) 1229.
4 H. Ashai and S. Ando, *J. Electrochem Soc., 132* (1985) 2445.
5 C. Blaauw, A. Szaplonczay, K. Fox and B. Emmerstorfer, *J. Cryst. Growth, 77* (1986) 326.
6 A. R. Clawson, C. M. Hanson and T. T. Vu, *J. Cryst. Growth, 77* (1986) 334.
7 P. Demeester, P. Van Dael and R. Baets, *J. Appl. Phys, 63* (1988) 2284.
8 B. Garrett and E. J. Thrush, *J. Cryst. Growth, 97* (1989) 273.
9 O. Kayser, *J. Cryst. Growth, 107* (1991) 989.
10 M. D. Scott, J. R. Riffat, I. Griffith, J. I. Davies and A. C. Marshall, *J. Cryst. Growth, 93* (1988) 820.
11 E. J. Thrush, M. A. Gibbon, J. P. Stagg, C. G. Cureton, C. J. Jones, R. E. Mallard, A. G. Norman and G. R. Booker, *J. Cryst. Growth, 124* (1992) 249.
12 C. Caneau, R. Bhat, M. R. Frei, C. C. Chang, R. J. Deri and M. A. Koza, *J. Cryst. Growth, 124* (1992) 243.
13 C. H. Joyner, S. Chandrasekhar, J. W. Sulhoff and A. G. Dentai, *IEEE Photon. Lett., 4*(9) (1992) 1006.
14 J. Thompson, A. K. Wood, N. Carr, P. M. Charles, A. J. Moseley, R. Pritchard, B. Hamilton, A. Chew, D. E. Sykes and T.-Y. Seong, *J. Cryst. Growth, 124* (1992) 227.
15 M. Aoki, M. Suzuki, M. Takahashi, H. Sano, T. Ido, T. Kawano and A. Takai, *Electron. Lett., 28*(12) (1992) 1157.
16 E. J. Thrush, C. G. Cureton, J. M. Trigg, J. P. Stagg and B. R. Butler, *Chemtronics, 2*(2) (1987) 62.
17 M. E. Pemble, D. S. Buhaenko, S. M. Francis, P. A. Goulding and J. T. Allen, *J. Cryst. Growth, 107* (1991) 37.
18 N. Carr, private communication, 1993.

Materials Science and Engineering, B21 (1993) 147–152

ESPRIT MORSE: research for novel metal–organic precursors

F. Scholz

4. Phys. Institut, Universität Stuttgart, Pfaffenwaldring 57, 70550 Stuttgart (Germany)

Abstract

This paper reviews the research work done in the ESPRIT project MORSE concerning investigations of novel precursors for metal–organic vapor phase epitaxy (MOVPE) and chemical beam epitaxy (CBE) and their applications in the growth of optoelectronic device structures. Of the many compounds which have been studied, diethylaluminumhydride-trimethylamine-adduct (DEAlH-TMN), dimethylaminopropyl-dimethyl-indum (DADI), *tert*-butyl-phosphine (TBP), bis-phosphine-ethane (BPE) and *tert*-butyl-arsine (TBAs) have been found to be the best replacements for conventional precursors. Lasers emitting around 1.55 μm and 980 nm have been grown using alternative group III and group V precursors. They demonstrate that the same, or even better, performance can be obtained with these alternatives.

1. Introduction

From 1990 to 1992, the EEC supported a three year program within the framework of ESPRIT called "metal organic research for semiconductor epitaxy" (ESPRIT project 5031 MORSE), which has focused on (a) the development of new, less hazardous precursors for metal–organic vapor phase epitaxy (MOVPE) and chemical beam epitaxy (CBE, sometimes called MOMBE) and (b) the evaluation and development of the CBE growth technique. The consortium was formed by Thomson CSF (Orsay, France, main contractor), RSRE (now DRA Malvern, UK), FORTH (Heraklion, Greece), CNET (Bagneux, France), RWTH Aachen (Germany) and the University of Stuttgart (Germany) with ISA Riber (France), SMI/ENSSPICAM (France) and CNR (Italy) as associated partners (see Table 1).

This paper will focus mainly on the progress which has been achieved within MORSE in the area of novel metal–organic precursors for both group III and group V elements. A main driving force for these investigations is the potential danger of most of the precursors commonly used in MOVPE or CBE. Moreover, some of the alkyls show unwanted properties such as a high melting point or high incorporation of impurities in the epitaxial layer associated with their use. All these points have been addressed by this consortium. By the successful cooperation of chemists, epitaxial growers, and layer and device characterization people, significant development has been achieved. This has resulted in the fabrication and characterization of electronic and optoelectronic devices grown with novel precursors by MOVPE and CBE. In this paper, I shall draw more attention to the latter devices.

2. Novel aluminum precursors

2.1. Metal–organic vapor phase epitaxy

The Al precursors most widely used today, trimethyl-aluminum (TMAl) and triethyl-aluminum (TEAl), are very sensitive to oxygen (O) and similar impurities. This results in a rather high incorporation rate of O into the growing layers, which limits their electrical and optical properties [1]. Moreover, high carbon (C) concentrations can be found in MOVPE layers grown using TMAl [1] owing to incomplete elimination of the methyl groups from Al–CH_3 species [2]. Therefore, a novel saturated Al precursor dimethyl-aminopropyl-ala-cyclohexan (APAH) and the respective Ga precursor (APGH) have been investigated by RWTH (these compounds have been kindly supplied to the consortium by Dr. L. Pohl, E. Merck, Darmstadt) [3–5]. Owing to the intramolecular saturation, these compounds are chemically very stable and thus they are much safer to handle during synthesis, purification and use in epitaxy. Moreover, any tendency for parasitic side reactions to occur inside the MOVPE reactor is strongly suppressed. This has also been proved for the combination with the novel As precursor *tert*-butyl-arsine (TBAs) [6]. In fact, $Al_{0.2}Ga_{0.8}As$ layers grown with these precursors by low pressure MOVPE exhibit higher luminescence efficiency than conventionally grown layers and electrical mobilities of up to 15 000 $cm^2\ V^{-1}\ s^{-1}$. The oxygen and carbon contents can be reduced drastically for layers grown with APGH and APAH compared with those grown with TEGa and TEAl as evaluated by secondary ion mass spectrometry (SIMS) (Thomson CSF). This has resulted in the high optical quality of these layers when grown at relatively low temperatures

0921-5107/93/$6.00

© 1993 – Elsevier Sequoia. All rights reserved

TABLE 1. Key persons and main tasks of the MORSE partners

Partner	Key persons	Main task
Thomson CSF (TCSF) (main contractor)	J. P. Hirtz J. C. Garcia	CBE of GaInP/GaAs structures for transistors and lasers with conventional and novel precursors
Riber (associated to TCSF)	J. P. Delrue	Development of CBE cracker cell
DRA (former RSRE)	C. Whitehouse T. Martin P. A. Lane S. S. Gill	CBE of GaAs/AlGaAs structures for transistors with conventional, and novel precursors; growth studies; processing and characterization of transistor structures
FORTH Heraklion	G. Kiriakidis	Processing and characterization of layers and transistor structures
CNET Bagneux	A. Mircea A. Ougazzaden	MOVPE of GaInAs(P)/InP for optoelectronic devices with novel group V precursors
SMI/ENSSPICAM (associated to CNET)	D. Boyer G. Buono	Synthesis of novel In and P precursors
University of Stuttgart (UST)	F. Scholz	MOVPE of GaInAs(P)/InP with novel In precursors
CNR Padua (associated to UST)	N. Brianese	Synthesis and characterization of novel In precursors
RWTH Aachen (RWTH)	K. Heime R. Hövel	MOVPE of GaAs/AlGaAs and AlGaInAs with novel Ga and Al precursors

(*e.g.* full width at half-maximum of photoluminescence (FWHM(PL)) of 4.2 meV) (Fig. 1). Unfortunately, the variation in purity from batch to batch in combination with the rather low vapor pressure (about 1–2 Pa at 20 °C [3]) of these double ring compounds (APAH and APGH) seems to limit their importance in conventional MOVPE experiments despite their excellent chemical properties.

In some first experiments, RWTH concentrated on the diethylaluminumhydride-trimethylamine-adduct (DEAlH-TMN) after the encouraging CBE results (see Section 2.2). $Al_{0.3}Ga_{0.7}As$ has been grown by low pressure MOVPE, and carrier concentrations in the 10^{16} cm^{-3} range have been obtained in line with a narrow PL line width of 5.3 meV at 12 K.

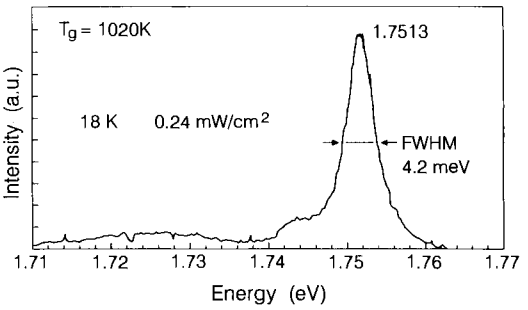

Fig. 1. Low temperature photoluminescence spectrum of an AlGaAs layer grown using APAH and APGH (RWTH).

2.2. Chemical beam epitaxy

In CBE, the problem of O and C uptake is even worse than in MOVPE [7], even when the less volatile TEAl (about 2 Pa at 20 °C) is used, which has less strong Al–C bonds. The studies within MORSE done at DRA focused on three novel compounds: triethylaluminum-trimethylamine-adduct (TEAl-TMN); diethylaluminumhydride-trimethylamine-adduct (DEAlH-TMN) and APAH. They have been carried out in a purpose designed reactor with all gaseous sources, which allows study of both conventional epitaxial growth and modulated beam reaction mechanisms [8]. The metal-organic compounds are admitted into the growth chamber without carrier gases.

As expected from the results obtained at RWTH, APAH was found to be impracticable for use in CBE owing to its low vapor pressure. By the use of the more volatile TEAl-TMN adduct (see Fig. 2), the Al source temperature could be reduced by 10 °C (compared with TEAl), and much less stringent requirements for high temperature and uniform gas line heating are necessary. In addition, the incorporation rate of O and C was found to be reduced.

DEAlH-TMN possesses a vapor pressure three times higher (Fig. 2). Now very convenient source temperatures of 20–25 °C can be used for establishing growth rates of about 0.3 $\mu m\ h^{-1}$ for AlAs. The incorporation of C and O impurities can be further reduced to levels of 1×10^{17} cm^{-3} which is comparable with the SIMS detection limit. Modulated beam mass spectroscopy (MBMS) studies have demonstrated the long-term stability of this compound.

A further significant improvement in both GaAs and AlGaAs material quality, including a major reduction in unintentional carbon impurities and a marked increase in the mobility of the two-dimensional electron gas in HEMT structures, was observed when tri-isopropyl-gallium (TiPGa) was used instead of

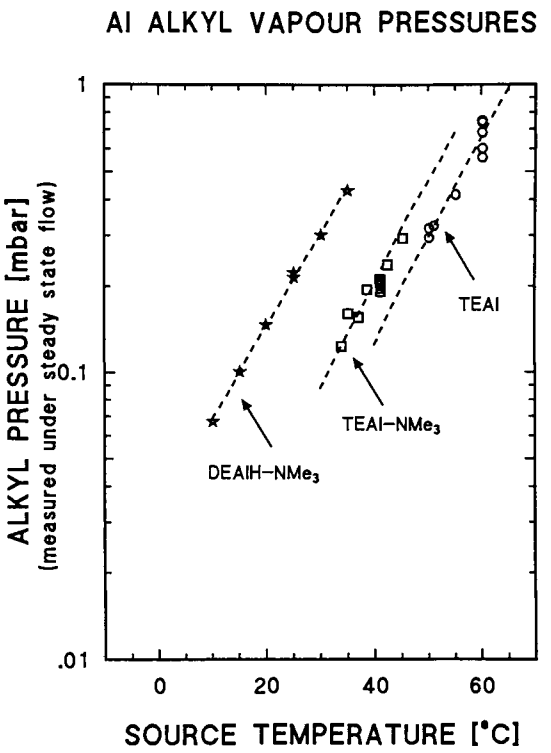

Fig. 2. Vapor pressure over temperature for TEAl, TEAl-TMN and DEAlH-TMN (DRA).

triethyl-gallium (TEGa) as the Ga precursor [9]. Thus, DEAlH-TMN has been found to be the best Al precursor for CBE studied within this project, and all further device structures have been grown with this precursor in combination with TiPGa [10].

3. Novel indium precursors

Although trimethyl-indium (TMIn) is commonly used in MOVPE and CBE when growing high quality In containing layers for optoelectronic applications, it has some unwanted properties. Its use as a solid at normal source temperatures limits the reproducibility of its evaporation rate from conventional bubblers. In addition, it is strongly pyrophoric and explosive when in contact with water and air and therefore dangerous during handling in synthesis and purification steps. Moreover, it shows the tendency to undergo parasitic side reactions with group V precursors inside the MOVPE reaction chamber.

We have studied different In pyrazoles [11] which are much less reactive than TMIn, but they suffer from very low vapor pressures. So only one compound has been tested in MOVPE resulting in very low growth rates [12].

Another way of tackling the problem involves the intermolecular or intramolecular stabilization of the In. Within MORSE, the latter has been further studied by using the compound dimethylaminopropyl-dimethyl-indium (DADI) (provided by Dr. L. Pohl, E. Merck, Darmstadt) [12], a liquid precursor with a vapor pressure similar to that of triethyl-indium (TEIn). Acceptable bubbler temperatures of 35 °C for atmospheric pressure MOVPE and 20 °C for low pressure MOVPE can be used to give growth rates of 1–2 μm h^{-1}. Studies performed at Stuttgart showed that excellent InP layers with 77 K mobilities greater than 110000 cm^2 V^{-1} s^{-1} could be grown [13] using PH_3 as the P source under otherwise standard growth conditions. Moreover, high quality GaInAs heterostructures have been grown using TEGa and AsH_3 as Ga and As precursors respectively. No indications of parasitic side reactions with either hydride could be found, even at atmospheric pressures. Quantum well structures showed monolayer peak splitting in low temperature PL spectroscopy (Fig. 3) [14], demonstrating that with DADI such structures can be grown with at least state of the art quality and interface abruptness.

The study of novel safer group V precursors was of particular interest in this project as described in Sections 4 and 5. These metal-organic P and As compounds are known to undergo parasitic side reactions with In alkyls even more readily than with the respective hydrides. However, no indications of unwanted parasitic reactions in the MOVPE reaction chamber, even under atmospheric pressure, could be detected for the combination of DADI with *tert*-butyl-phosphine (TBP) and *tert*-butyl-arsine (TBAs) [12, 13]. Although electrical and optical properties have been observed with these materials which are comparable with those of the hydride grown layers, we found that crystalline layers could still be grown at very low V-to-III ratios where only polycrystalline growth is observed when hydrides are used [13, 15]. This is probably due to the higher cracking efficiency of the *tert*-butyl compounds at a given growth temperature.

InP CBE layers grown with DADI by Thomson CSF exhibited only limited electrical properties owing to impurities in the 10^{16}–10^{17} cm^{-3} concentration range as detected by SIMS, probably owing to contamination of this specific DADI batch. The high carbon concentration of 5×10^{17} cm^{-3} found in these layers could be a direct consequence of the DADI molecule itself which obviously undergoes different cracking processes in CBE compared with MOVPE, where increased carbon uptake has never been observed.

4. Novel phosphorus precursors

A major problem in conventional MOVPE and CBE is the use of highly toxic hydrides such as PH_3,

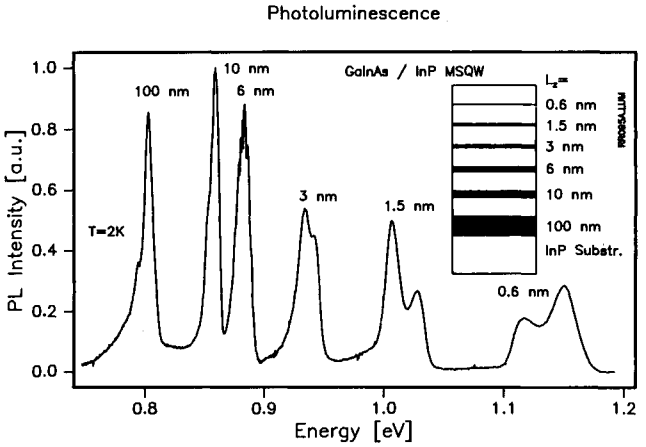

Fig. 3. Low temperature photoluminescence spectrum of a GaInAs–InP multi single quantum well structure grown by MOVPE with DADI, TEG, AsH_3 and PH_3 (Stuttgart).

AsH_3, H_2S etc., and therefore stringent safety measures are required. One of the key factors for further widespread application of these techniques will be a decrease in their potential danger and thus the development of less dangerous group V precursors. This has been attacked by the MORSE consortium by work on the larger scale production of *tert*-butylphosphine (TBP) at ENSSPICAM, where more than 500 g have already been synthesized, and by studies on its use in MOVPE and CBE (most of the epitaxy work has been done using TBP from American Cyanamid, since the ENSSPICAM material has only recently become available). This precursor has been chosen as a result of many encouraging reports worldwide (see for example ref. 16). Moreover, bis-phosphino-ethane (BPE) has been proposed as a replacement for PH_3 and has been used for MOVPE by CNET [17, 18].

4.1. Metal–organic vapor phase epitaxy

TBP was investigated at CNET by growing InP and GaInAsP layers [18, 19] and laser structures in an atmospheric pressure MOVPE system. It was found that about the same amount of P in the gas phase as used for PH_3 growth was necessary to obtain InP layers with excellent morphology. A higher As/P ratio was needed with TBP instead of PH_3 to establish the same solid composition of quaternary (GaInAsP) layers, as expected owing to the lower chemical stability of TBP, and at least the same uniformity of lateral composition was obtained as for PH_3 grown layers [18].

A further alternative to PH_3 was found to be BPE [17, 18]. This compound offers a high share of P to the molecular weight and thus a high P/C ratio. Studies done at CNET showed that the partial pressure of BPE has to be approximately half as much as that of PH_3 in order to obtain InP layers with excellent morphology, obviously owing to the fact that the BPE molecule contains two P atoms. This was confirmed when growing quaternary layers, where again half the partial pressure was necessary to obtain the same solid composition as for PH_3 grown layers. The lateral uniformity over a 2 in wafer, the run to run reproducibility, and the electrical and optical properties of the grown layers were as good as those of layers grown with the hydride.

In addition, it was observed at CNET that planarizing regrowth of a patterned substrate for buried laser structures can be realized at much lower temperatures (580 °C) with BPE than is usual when regrowing with PH_3.

4.2. Chemical beam epitaxy

InP layers grown with TBP by CBE at Thomson CSF exhibited excellent morphology and electrical data compared with those of layers grown with PH_3. SIMS studies showed about the same amount of S and Si impurities, whereas C and O were both reduced to concentrations of mid 10^{15} cm^{-3} in these layers. When growing GaInP, the same strong reduction of C uptake has been observed. The Ga/In ratio necessary to obtain lattice matching to GaAs was not influenced by the type of P precursor. Electrical and spectroscopic characterizations have proved that the layer quality compares favorably with that obtained by using PH_3.

5. Novel arsenic precursors

The reasons for the use of alternative As precursors are obviously the same as those described for the P compounds.

5.1. Metal–organic vapor phase epitaxy

GaInAs and GaInAsP layers have been grown at CNET using TBAs as the As precursor. Excellent morphology along with very good layer uniformity was obtained. The necessary molar flows for TBAs and AsH_3 for high quality layers are quite similar to those observed for TBP. Variations in composition near the wafer edge have been reduced when using TBAs + TBP [18].

5.2. Chemical beam epitaxy

The use of TBAs has been studied for the CBE growth of GaAs and AlGaAs at DRA and Thomson CSF and for the growth of GaInAs/GaInP laser structures at Thomson CSF. When using low cracker temperatures of about 500 °C, very low unintentional carbon and oxygen impurity levels, as in the case of AsH_3 grown layers, have been found in GaAs and AlGaAs. The highest electron mobility yet reported for intentionally (H_2S) doped TBAs-grown CBE GaAs

layers ($\mu_{77\,K} = 29000$ cm^2 V^{-1} s^{-1}) could be obtained. However, at this low cracker temperature, a steady and potentially dangerous accumulation of uncracked arsine in the growth reactor was observed. When the temperature is raised to about 1100 °C, a very marked increase in unintentional carbon impurity levels was detected. Thus, further studies are needed in order to optimize the cracking temperature and/or the cracker cell geometry.

Tris-dimethylamino-arsine (DMAAs) [20] has been studied in some first experiments at Thomson CSF. This precursor, having no direct C–As bonds, should lead to a reduced C uptake into the layer. This was, of course, observed in the GaAs layers grown with this precursor. Moreover, it can be noted that no precracking of this compound is needed.

6. Device results

Optoelectronic devices have been grown and processed by several groups of the consortium in order to demonstrate the compatibility of the novel precursors and growth techniques with today's device requirements.

Optical modulator structures containing five GaInAs strained quantum wells, GaInAsP layers for optical confinement, and n- and p-type doped InP cladding layers have been grown at UST using DADI as the novel In precursor [14]. Ohmic contacts have been applied following standard procedures. These devices exhibit a red shift of the excitonic transition of 6 to 11 meV when changing the internal electrical field from 4 to 7×10^4 V cm^{-1}, in good agreement with theoretical calculations [21]. Similar structures containing quaternary quantum wells have been processed into broad area laser devices. We found threshold current densities of 1 kA cm^{-2} at 0 °C, although the processing of these devices has not yet been optimized.

TBP and BPE have been used to grow 1.55 μm separate confinement multi-quantum well laser structures at CNET [17–19, 22]. Five quaternary quantum wells with $L_z = 10$ nm and a built-in compressive strain of 0.8% were positioned in the active region. Very low threshold current densities of 328 A cm^{-2} have been measured for BPE grown wafers processed into broad area lasers (Fig. 4), whereas PH_3 and TBP grown samples showed somewhat larger, but still excellent values. Probably, the better results obtained with BPE even in comparison with PH_3 are due to the lower growth temperature (610 °C instead of 660 °C) which could be used with this precursor.

At Thomson CSF, Al free GaInAs/GaAs/GaInP laser structures emitting at 980 nm have been grown by CBE using both hydride and metal-organic group V precursors [23, 24]. TMIn, TEGa, H_2S and solid Be have been used as In, Ga, n-type and p-type dopant source respectively. Broad area lasers processed from the hydride grown layers containing three 7 nm quantum wells exhibited threshold current densities of 300 A cm^{-2} and maximum power outputs per facet of 600 mW (continuous wave). A characteristic temperature $T_0 = 95$ K was deduced under pulsed operation [23].

Similar structures have been grown and processed into broad area laser devices using TBAs and TBP as group V precursors. TBP and TBAs were kept at room temperature, and no carrier gas was used owing to their high vapor pressure. Figure 5 shows pulsed light output power per facet as a function of injection current. Threshold current densities and external quantum efficiencies have been measured of 390 A cm^{-2} and 0.66 W A^{-1} respectively [24].

The power-HBT has been used as the primary electronic device demonstrator in the project, particularly seeking to exploit the ability of CBE to grow ultra-high p-type doped base regions. Following a systematic optimization (done at DRA), GaAs/AlGaAs structures with base doping of 5×10^{19} cm^{-3} and widths of 0.08 μm have yielded transit frequencies, maximum frequencies and output power values of 34 GHz, 23 GHz and 18.2 W mm^{-1} at 10 GHz respectively.

7. Summary and outlook

A large number of alternative precursors for Al, In, Ga, As and P has been studied within the ESPRIT project MORSE for their possible applications in MOVPE and CBE. We could demonstrate, that

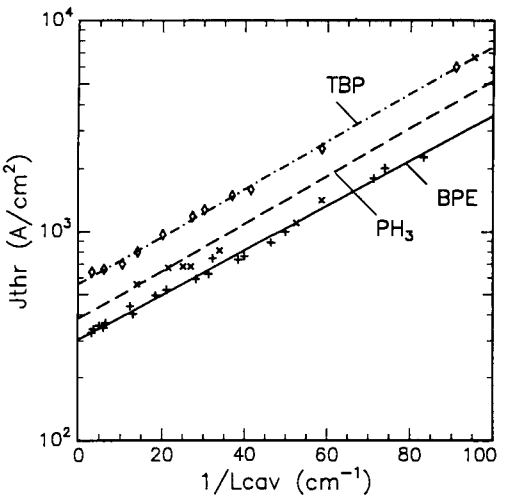

Fig. 4. Threshold current densities as a function of inverse cavity length for broad area lasers made from multi-quantum well wafers grown with TBP, BPE and PH_3 (CNET).

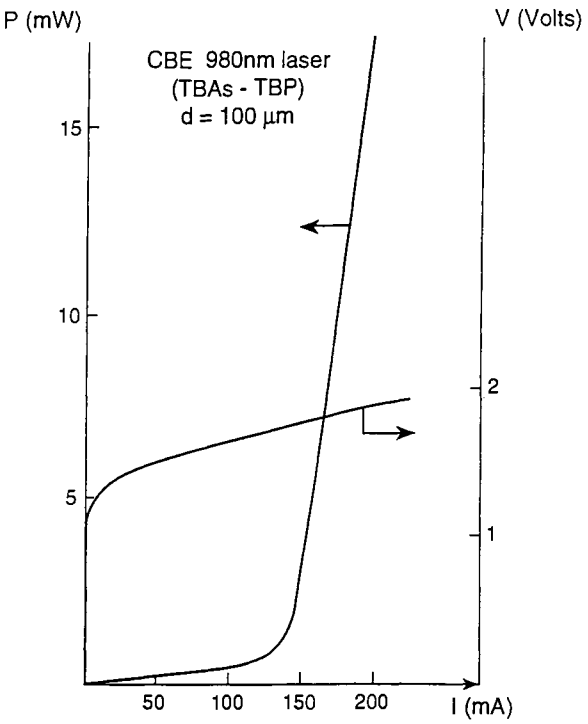

Fig. 5. Pulsed light output power per facet as a function of injection current, and current–voltage characteristic for a GaInAs/GaAs/GaInP separate confinement heterostructure multi-quantum well laser grown with TBP and TBAs (100 μm wide and 320 μm long) at 20 °C (Thomson CSF).

DEAlH-TMN, DADI, TBAs, TBP and BPE are very promising precursors for Al, In, As and P respectively, which are capable of producing at least the same quality material as conventional sources, but needing reduced safety requirements. Moreover, some of them even show better results owing to lower impurity uptake (DEAlH-TMN, TBP), higher wafer uniformity (TBP, BPE, TBAs) or advantages in regrowth over patterned substrates (TBP, BPE).

For MOVPE, very attractive alternatives to the hydrides are now available. It is mainly their comparably high price which still limits their large-scale use. However, a significant restriction for their use in CBE is the fact that most of them still have to be precracked. Further investigations seem to be necessary in particular of P precursors similar to DMAAs which do not need any precracking.

Acknowledgment

This paper has been written as a result of information given in the various MORSE discussions and reports. Therefore, I want to thank all the people who have jointly and successfully cooperated within this project under the very committed coordination of J. P. Hirtz (Thomson CSF), at least the key persons are mentioned in Table 1. Moreover, financial support by the EEC is gratefully acknowledged.

References

1 T. F. Kuech, D. J. Wolford, E. Veuhoff, V. Deline, P. M. Mooney, R. Potemski and J. Bradeley, *J. Appl. Phys., 62* (1987) 632.
2 A. C. Jones, P. J. Wright, P. E. Oliver, B. Cockayne and J. S. Roberts, *J. Cryst. Growth, 100* (1990) 395.
3 L. Pohl, M. Hostalek, H. Schumann, U. Hartmann, W. Wassermann, A. Brauers, G. K. Regel, R. Hövel, P. Balk and F. Scholz, *J. Cryst. Growth, 107* (1991) 309.
4 R. Hövel, W. Brysch, N. Neumann, K. Heime and L. Pohl, *J. Cryst. Growth, 124* (1992) 106.
5 A. Brauers, *Prog. Cryst. Growth Charact., 22* (1991) 1.
6 R. Hövel, N. Neumann and K. Heime, *J. Cryst. Growth, 124* (1992) 129.
7 C. R. Abernathy, A. S. Jordan, S. J. Pearton, W. S. Hobson, D. A. Bohling and G. T. Muhr, *Appl. Phys. Lett., 56* (1990) 2654, and references cited therein.
8 T. Martin, C. R. Whitehouse and P. A. Lane, *J. Cryst. Growth, 107* (1991) 969.
9 P. A. Lane, C. R. Whitehouse, T. Martin, M. Houlton, G. M. Williams, A. G. Cullis, S. S. Gill, J. R. Dawsey, G. Ball, B. T. Hughes, M. A. Crouch and M. B. Allenson, *J. Cryst. Growth, 120* (1992) 245.
10 P. A. Lane, T. Martin, R. W. Freer, P. D. J. Calcott, C. R. Whitehouse, A. C. Jones and S. Rushworth, *Appl. Phys. Lett., 61* (1992) 285.
11 K. Locke, J. Weidlein, F. Scholz, N. Bouanah, N. Brianese, P. Zanella and Y. Gao, *J. Organomet. Chem., 420* (1991) 1.
12 A. Molassioti, M. Moser, A. Stapor, F. Scholz, M. Hostalek and L. Pohl, *Appl. Phys. Lett., 54* (1989) 857.
13 F. Scholz, A. Molassioti, M. Moser, B. Notheisen, K. Streubel, M. Hostalek and L. Pohl, *J. Cryst. Growth, 107* (1991) 365.
14 F. Scholz, R. Rudeloff, B. Henle, V. Härle, E. Scheuble, T. Tütken, A. Hangleiter and L. Pohl, *Proc. 4th Int. Conf. on InP and Related Materials, Newport, RI, April 1992*, IEEE catalogue no. 92CH3104-7, p. 155.
15 F. Scholz, D. Ottenwälder, B. Henle, M. Eckel and K. Locke, *Proc. 5th Int. Conf. on InP and Related Materials, Paris, 1993*, IEEE catalogue no. 93CH3276-3, p. 48.
16 G. B. Stringfellow, *J. Electron. Mater., 17* (1988) 327.
17 A. Ougazzaden, A. Mircea, R. Mellet, G. Primot and C. Kazmierski, *Electron. Lett., 28* (1992) 1078.
18 A. Ougazzaden, R. Mellet, Y. Gao, K. Rao and A. Mircea, *Proc. 4th Int. Conf. on InP and Related Materials, Newport, RI, April 1992*, IEEE catalogue no. 92CH3104-7, p. 36.
19 A. Ougazzaden, R. Mellet, Y. Gao, E. V. K. Rao and A. Mircea, *Proc. 3rd Int. Conf. on InP and Related Materials, Cardiff, April 1991*, IEEE catalogue no. 91CH2950-4, p. 64.
20 C. R. Abernathy, P. W. Wisk, S. J. Pearton, F. Ren, D. A. Bohling and G. T. Muhr, *J. Cryst. Growth, 124* (1992) 64.
21 T. Tütken, G. Frankowsky, A. Hangleiter, V. Härle, K. Streubel and F. Scholz, *Superlattices and Microstructures, 7* (1990) 309.
22 A. Ougazzaden, R. Mellet, Y. Gao, C. Kazmierski, D. Robein and A. Mircea, *Electron. Lett., 27* (1991) 1005.
23 P. Maurel, J. C. Garcia, P. Regreny, J. P. Hirtz, F. Vassilakis, A. Parent, M. Baldy and C. Carriere, *Electron. Lett., 29* (1993) 91.
24 J. C. Garcia, P. Maurel and J. P. Hirtz, *Electron. Lett., 29* (1993) 432.

MBE regrowth of GaAs/AlGaAs structures on RIE patterned substrates

T. Röhr, M. Walther, S. Rochus, G. Böhm, W. Klein, G. Tränkle and G. Weimann
Walter Schottky Institut, Technische Universität München, Am Coulombwall, D-85747 Garching (Germany)

Abstract

GaAs/AlGaAs heterostructures with excellent morphology and high luminescence yield were regrown by molecular beam epitaxy on nonplanar wafers patterned by reactive ion etching with $SiCl_4$ or CCl_2F_2. Faceted growth occurs on pattern edges, depending on adatom species, crystallographic planes, growth parameters and pattern sizes. While shallow etched structures (< 100 nm) are planarized during regrowth, independent of their orientation, deep etched ridges or grooves (> 300 nm) aligned in the [011]-direction are isolated from the surrounding surface by distinct trenches due to shadowing effects. Narrow ridges (< 1 μm) with widths smaller than the migration length of the Ga atoms exhibit very smooth ($01\bar{1}$) facets at the sides and (111) B-facets on the top. This growth behaviour is applied for the direct growth of isolated nanostructures. On the other hand, the planarizing regrowth on shallow etched wafers is used to build in a thin n-AlGaAs blocking layer in the p-AlGaAs contact layer of a vertical cavity surface emitting laser diode to reduce current spreading.

1. Introduction

New concepts for devices may be realized by epitaxial regrowth on patterned substrates. Possible applications are the growth of buried structures [1], the direct growth of lasers [2], butt joints or nanostructures [3]. Molecular beam epitaxy (MBE) regrowth on nonplanar wafers has been demonstrated using various patterning techniques [4, 5], *e.g.* high quality GaAs/AlGaAs epilayers were grown on GaAs substrates and GaAs/AlGaAs epilayers patterned by optical lithography and reactive ion etching (RIE) [6].

In this paper we report on consequences of the initial surface topology on the faceted regrowth of (GaAl)As epilayers on wafers, patterned by dry etching with $SiCl_4$ or CCl_2F_2.

2. MBE regrowth on dry etched surfaces

MBE regrowth of epilayers with good morphology and high luminescence yield requires residual and damage-free surfaces after dry etching. To minimize the ion-induced damage, RIE with $SiCl_4$ or CCl_2F_2 was performed at low bias voltages (< 100 V), while maintaining etch conditions for smooth surfaces and anisotropic etching profiles on the other hand. After dry etching, the photoresist mask was removed in organic solvents (acetone, propanol). Prior to loading the wafers into the MBE system they were cleaned in an oxygen plasma and an ammonium hydroxide solution (NH_4OH 2%, H_2O 98%). The best results after regrowth, expressed in optical properties of quantum wells, are obtained for RIE with $SiCl_4$ (or CCl_2F_2) at bias voltages of about 90 V, using a gas flow rate of 25 S.C.C.M., a pressure of 20 μbar and an RF-power density of 0.1 W cm^{-2}.

The suitability of the RIE process with MBE regrowth is proven in Fig. 1, which compares the low temperature photoluminescence spectra (4.2 K) of a GaAs/AlGaAs quantum well structure for an etched and an unetched part of a patterned substrate. Two single quantum wells ($L_z = 8$ nm) were grown on a 0.3 μm thick GaAs buffer layer at a substrate temperature $T_S = 680$ °C. High luminescence yields and narrow excitonic linewidths (FWHM = 2.3 meV) are obtained for both parts, comparable to GaAs/AlGaAs quantum wells grown on planar wafers after wet chemical surface preparation.

Faceted growth on ridges and grooves is determined by the migration lengths of the adatoms on different crystallographic planes and by shadowing effects [7]. The migration lengths depend on growth parameters (T_S and V/III ratio) and on the orientation of the ridges. For structure sizes in the range of the migration lengths, the formation of (100) planes is inhibited by growth on higher indexed crystallographic planes. Hence, the surface shapes depend on the width of the ridge.

As an example of this size-dependent growth behavior, Fig. 2 shows the stain etched cross-section of

0921-5107/93/$6.00
© 1993 – Elsevier Sequoia. All rights reserved

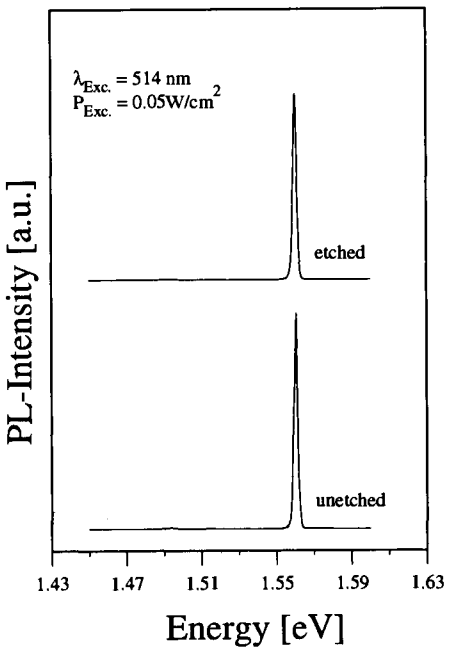

Fig. 1. Low temperature ($T = 4.2$ K) photoluminescence spectra of GaAs/AlGaAs single quantum wells ($L_z = 8$ nm) grown on an $SiCl_4$-RIE patterned substrate (top: etched region, bottom: unetched region).

0.45 μm high ridges in [011]-direction after regrowth of several GaAs and $Al_{0.3}Ga_{0.7}As$ layers (thickness: 150 nm) at $T_S = 680$ °C. Brighter areas indicate GaAs and darker ones show $Al_{0.3}Ga_{0.7}As$. The regrowth was performed after dry etching with $SiCl_4$ and thermal desorption of thin GaAs passivation layers in the UHV prior to growth. A detailed description of the thermal desorption process is given in ref. 6. (111) B-planes on both sides of the ridge can be seen, as well as the (100) facets in the center. The growth rate of GaAs on (111) B-planes is drastically reduced due to the enhanced migration of Ga atoms from (111) B-planes to (100) facets. As a result, the GaAs layers growing on the (100) planes on top of the ridge are thicker and they are completely embedded in AlGaAs. With decreasing ridge size, the (111) B-planes restrict the formation of (100) facets on top of the ridges, leading to triangular shaped structures. This is shown in Fig. 2(c) for a ridge size of 0.5 μm, where the GaAs grows preferentially at the vertex of the structure.

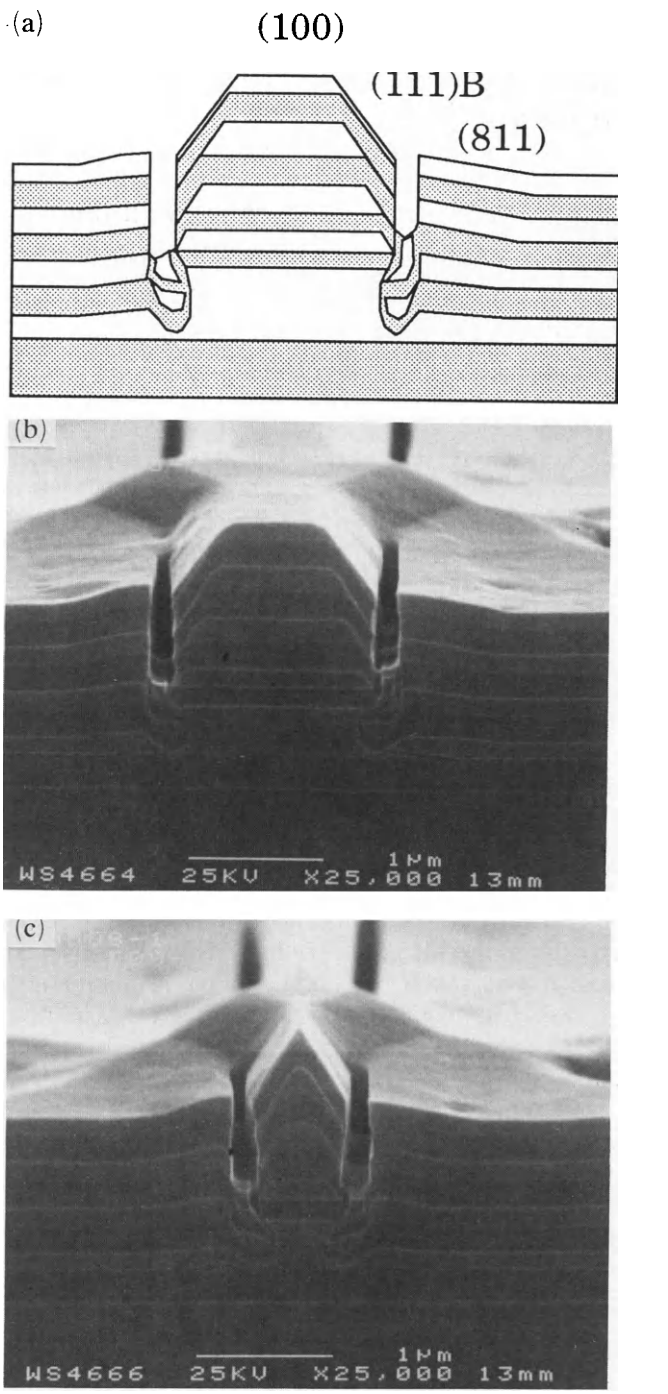

Fig. 2. Dependency of facet formation on the structure size for ridge orientation in the [011]-direction after the alternating regrowth of 150 nm thick GaAs and $Al_{0.3}Ga_{0.7}As$ layers. The shape of the etched mesas is influenced by thermal desorption of GaAs prior to growth. Bright stripes are showing GaAs, darker areas are indicating $Al_{0.3}Ga_{0.7}As$. (a) Schematic sample drawing; (b) ridge width 1.3 μm; (c) ridge width 0.5 μm.

3. Direct growth of nanostructures

It is obvious in Fig. 2, that deep etched ridges in the [011]-direction (height: 0.45 μm) are isolated from the surrounding structures by trenches due to shadowing effects. Additionally to the occurrence of crystallographic facets with high migration lengths for Ga atoms ("non-growth surfaces") and the preferential growth of GaAs on top of the triangular-shaped structures, this can be used for the direct growth of isolated nanostructures. Figure 3(a) shows the SEM picture of a 0.75 μm

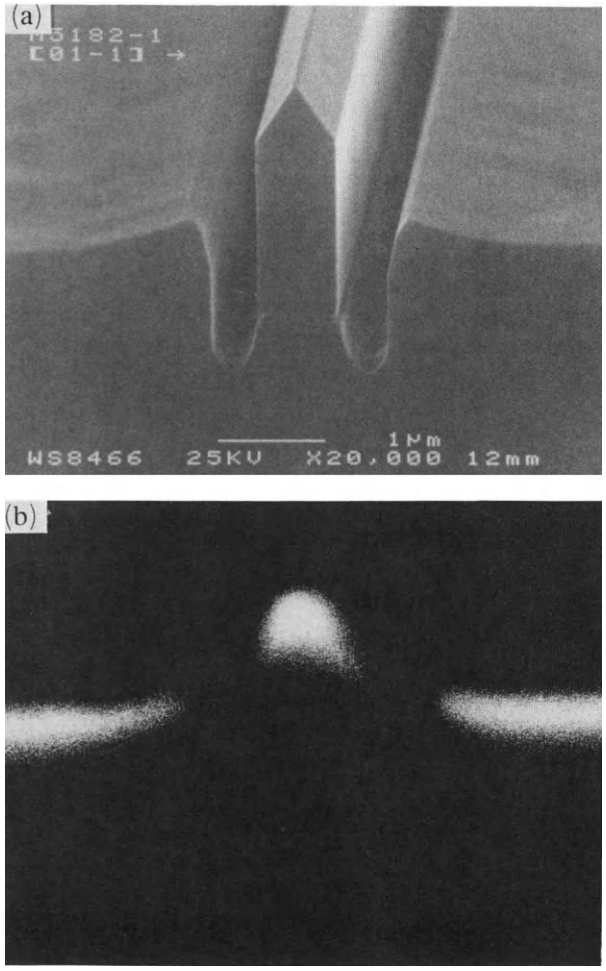

Fig. 3. SEM picture and panchromatic CL image of a 1 μm high ridge in [011] orientation, overgrown with 1.5 μm GaAs and an SQW ($L_z = 3$ nm) embedded in 30 nm thick $Al_{0.3}Ga_{0.7}As$ barriers. (a) SEM picture; (b) panchromatic CL image ($T = 85$ K).

wide and 1 μm high ridge in the [011]-direction after regrowth. The regrown layer consists of 1.5 μm GaAs and a single quantum well ($L_z = 3$ nm) embedded in 30 nm thick $Al_{0.3}Ga_{0.7}As$ barriers.

The shape of the overgrown ridge is only determined by the $(01\bar{1})$ planes at the sides and the (111) B-planes on top of the ridge. Both surfaces on the sidewalls and on top of the ridge are remarkably smooth. The inaccuracies of the patterning process are therefore completely compensated during regrowth. The self-adjusted triangular shape of the structure formed during regrowth of GaAs is the key issue for the direct growth of isolated nanostructures. Embedding a thin GaAs quantum well ($L_z = 3$ nm) between $Al_{0.3}Ga_{0.7}As$ barriers results in a direct grown quantum wire due to the enhanced migration of Ga atoms to the vertex of the ridge. Figure 3(b) shows the panchromatic spatially resolved cathodoluminescence (CL) image of the quantum wells at $T = 85$ K. The CL signal of the quantum well on each side of the ridge can be seen as well as an emission with comparable intensity from the top of the ridge.

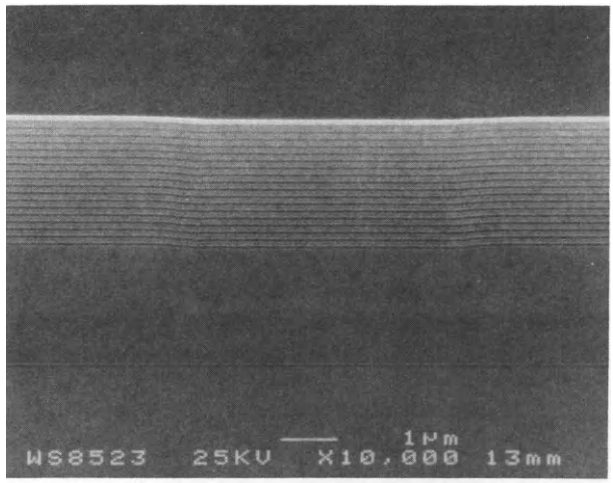

Fig. 4. Planarizing growth of an AlGaAs cladding layer and an $AlAs/Al_{0.1}Ga_{0.9}As$ high reflecting distributed Bragg reflector on a patterned epilayer (etch depth 50 nm).

4. Regrowth on shallow etched structures

In contrast to the growth of isolated structures on deep etched ridges, regrowth on shallow etched surfaces tends to planarize patterns. In Fig. 4, the cross-section of a 50 nm deep etched groove (orientation in [011]-direction) is shown after regrowth. This structure was overgrown with 880 nm Be-doped $Al_{0.35}Ga_{0.65}As$ and a high reflectivity distributed Bragg reflector (DBR). The DBR consists of 18 pairs $\lambda/4$-AlAs/$Al_{0.1}Ga_{0.9}As$ layers (63 nm/74 nm). The planarization of the initial step in the n-AlGaAs during regrowth is clearly visible; no distortion in the layer structure of the DBR is observed. This process is applied to reduce current spreading in vertical cavity surface emitting laser diodes [8].

The laser resonators with regrown top mirrors show unchanged optical properties with a reflectivity of the mirrors of more than 99.7%, comparable to resonator structures grown on planar substrates.

5. Summary

MBE regrowth on wafers patterned by RIE with $SiCl_4$ or CCl_2F_2 yields GaAs/AlGaAs epilayers with excellent optical and morphological properties. Isolated nanostructures are obtained on high and narrow

ridges in the [011]-direction due to the faceted MBE regrowth on non-planar substrates. The integration of patterned current blocking layers in VCSELs is viable by the planarization of shallow etched structures.

Acknowledgment

Financial support by the German Federal Ministry of Research and Technology (BMFT) under contract BM 117/5 is gratefully acknowledged.

References

1 J. L. Lievin, L. Le Gouezigou, D. Bonnevie, F. Gaborit, F. Poingt and F. Brillouet, *Appl. Phys. Lett., 60* (1992) 1211.
2 E. Kapon, S. Simhony, J. P. Harbison, L. T. Florez and P. Worland, *Appl. Phys. Lett., 56* (1990) 1825.
3 S. Ando and T. Fukui, *J. Cryst. Growth, 98* (1989) 646.
4 J. S. Smith, P. L. Derry, S. Margalit and A. Yariv, *Appl. Phys. Lett., 47* (1985) 712.
5 H. P. Meier, E. van Gieson, W. Walter, C. Harder, M. Krahl and D. Bimberg, *Appl. Pys. Lett., 54* (1989) 433.
6 M. Walther, T. Röhr, G. Böhm, G. Tränkle and G. Weimann, *J. Cryst. Growth, 127* (1993) 1045.
7 H. P. Meier, E. van Gieson, P. W. Epperlein, C. Harder, W. Walter, M. Krahl and D. Bimberg, *J. Cryst. Growth, 111* (1991) 1043.
8 D. G. Deppe, C. Lei, T. J. Rogers and B. G. Streetman, *Appl. Phys. Lett., 58* (1991) 2616.

Materials Science and Engineering, B21 (1993) 157–160

Improved method for GaAs-(Ga,Al)As epitaxial regrowth

E. Bedel, A. Munoz-Yague and C. Fontaine

Laboratoire d'Automatique et d'Analyse des Systèmes du CNRS, 7 Avenue du Colonel Roche, 31077 Toulouse (France)

C. Vieu

Laboratoire de Microstructures et Microélectronique du CNRS, 196 Avenue Henri Ravéra BP 107, 92225 Bagneux (France)

Abstract

UV-ozone oxidation of GaAs epitaxial layers was evaluated for GaAs molecular beam epitaxy regrowth. Auger electron spectroscopy was used to determine the conditions leading to a contaminant-free surface before epitaxy; oxide uniformity, surface roughness and crystalline defects were also studied using transmission electron microscopy. Finally, the capability of this technique was demonstrated by growing a GaAlAs-GaAs-GaAlAs quantum well on a processed GaAs epitaxial layer.

1. Introduction

Novel semiconductor device fabrication often involves epitaxial regrowth. In such a case the epitaxial structure needs to be protected during the various processing steps of the device fabrication and its surface has to be treated before regrowth. For these purposes oxides are more appropriate than surface passivation which is not a sufficient protection. Standard chemical oxidation, which is material consuming, is not suitable and alternative oxidizing methods have to be developed.

Here the UV-ozone oxidation, commonly used for GaAs substrate preparation [1–4], is studied for GaAs molecular beam epitaxy (MBE) regrowth. First C-contamination removal, thickness and uniformity of the oxide formed, as well as the crystallinity of the GaAs elaborated after regrowth, were studied by Auger electron spectrometry (AES) and transmission electron microscopy (TEM), allowing the exposure conditions to be optimized. The adequacy of this process for regrowth of quantum well (QW) structures on processed surfaces was then ascertained using photoluminescence (PL) spectroscopy.

2. Experimental details

Structure growth was carried out in a MBE system equipped with an Auger electron spectrometer with a cylindrical mirror analyzer.

First C-contamination removal was studied directly on commercial (100) substrates by means of AES. Prior to being loaded into the vacuum system, the wafers were degreased, etched in HCl, soldered with In on a Mo-block and then inserted for a variable period of time in a UV-ozone commercial apparatus equipped with a low pressure Hg lamp.

Second the efficiency of this technique for GaAs MBE regrowth was investigated by TEM in two series of samples. On the one hand oxide thickness and uniformity were characterized by elaborating, on differently oxidized surfaces, GaAs layers at 500 °C to prevent thermal oxide desorption. These structures are labelled A in the following. On the other hand the crystalline quality of GaAs epitaxial layers grown on treated surfaces was studied on two-step grown structures (labelled B). In this case, oxide desorption was obtained prior to GaAs MBE regrowth at 610 °C by heating the sample under As_4 to 615 °C.

In the first epitaxy step a 500 nm buffer layer was grown on the substrate, followed by 2 nm AlAs and 20nm GaAs; in the second step 10 nm GaAs and 2 nm AlAs were successively regrown. Finally samples A were completed by 150 nm GaAlAs (a short period superlattice), 150 nm GaAlAs and a 20 nm thick GaAs cap layer, while only the GaAs cap layer was grown for samples B. The two AlAs thin layers were used as markers for TEM observations. The numbers 0, 5, 15, written after A and B, identify the UV-ozone exposure time, expressed in minutes, applied to the corresponding samples A and B.

0921-5107/93/$6.00

© 1993 – Elsevier Sequoia. All rights reserved

With respect to the TEM analyses, the samples were prepared for cross-sectional observations using a new technique involving electron beam lithography and reactive ion etching (RIE) [5]. Observations were carried out at a voltage of 200 kV using a Philips microscope equipped with a field effect electron gun.

3. Results and discussion

3.1. Characteristics of the UV-ozone process

3.1.1. Contamination removal

C-contamination removal was followed by AES to determine the exposure time necessary for GaAs substrate surface cleaning. Figure 1 shows the decrease in C/Ga Auger signal ratio versus UV-ozone exposure time in two series of experiments. This treatment was then applied for at least 15 min to thorougly remove C residues. The Auger spectrum derived from bare GaAs substrate surfaces after thermal oxide desorption showed no trace of O and C.

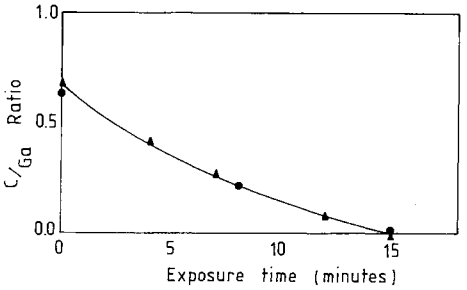

Fig. 1. Variation of the Auger signal ratio C(271 eV)/Ga(1065 eV) for a GaAs substrate exposed to UV light for different exposure times. The symbols ● and ▲ correspond to two different series of experiments.

3.1.2. Oxide characteristics

The thickness and uniformity of the oxide film were studied as a function of the UV-ozone exposure time for samples A. TEM micrographs are shown in Fig. 2.

Sample A0 yields the thickness of the native oxide as shown in Fig. 2(a). Its value (2 nm) is of the order of that found by ellipsometry. Highly interesting information can be inferred from the TEM view: apparently, the presence of the native oxide does not affect the crystallinity of the layers overgrown. Also, to interpret the cross-sectional view requires nucleation of GaAs on the native oxide with a 3D mechanism. Concurrently, a 2D nucleation was observed for AlAs, associated with the continuous white line on the TEM micrograph, covering the GaAs islands as well as the amorphous oxide. It is worth noting that $Ga_{0.7}Al_{0.3}As$ grown on AlAs recovers its standard 2D (100) growth mechanism, allowing improvement of layer surface topography, as evidenced by the upper short period superlattice marker flatness.

The results obtained from samples A5 and A15 are markedly different. As shown in Figs. 2(b) and 2(c), the oxide film is inhomogeneous. These TEM micrographs show that the bottom amorphous oxide interface is very rough. As the GaAs regrowth was carried out at 500 °C, the origin of this oxide roughness cannot be asserted: it can be related to the oxidation process [6], or to a thermal rearrangement of the species during the As oxide decomposition, which is effective at lower temperatures in the 350–400 °C range [7] or during growth of the top GaAs layer. Here semiconductor

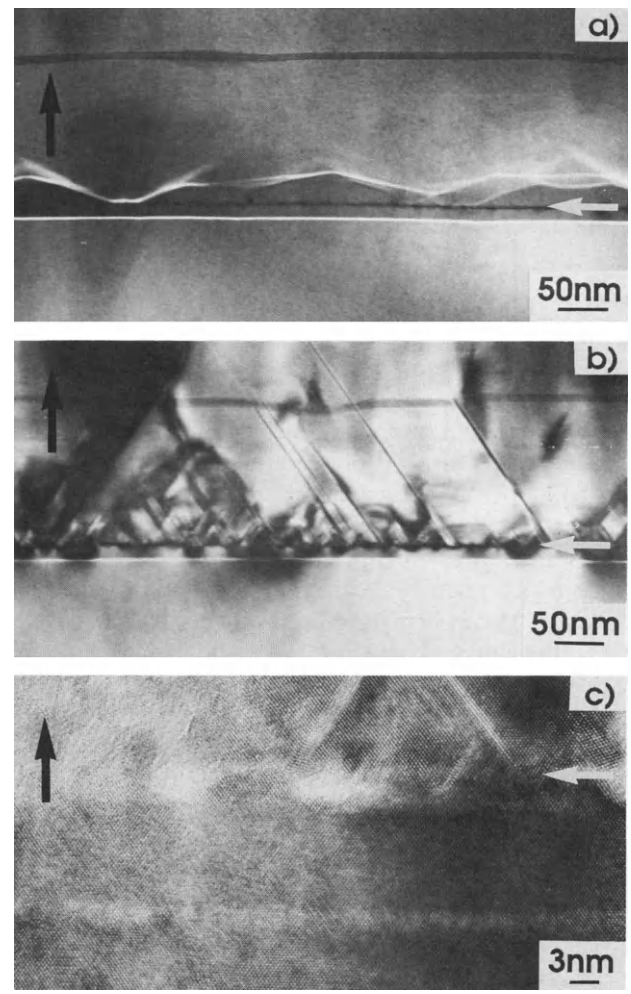

Fig. 2. TEM micrographs of samples A for increasingly long UV-ozone exposure: (a) without oxidation (dark field (DF) (220)); (b) after 5 min (DF (220)); (c) after 15 min (lattice image (LI)). Regrowth interface and growth direction are indicated by white and black arrows respectively.

layers overgrown on the oxidized surfaces exhibit a very poor crystallinity; the only differences between samples A5 and A15 lie in the average thickness of the oxide film which is more important when the surface is

exposed for a longer period of time. In the case of A15, the oxide film exhibits a pronounced roughness with amorphous oxide pockets of 4 nm diameter, as seen in Fig. 2(c).

3.2. Epitaxial regrowth

Layer crystallinity and surface flatness recovery were studied by TEM on samples B. Figure 3 shows the TEM views obtained from the three corresponding samples.

For sample B0, not subject to the oxidation process, the regrowth plane between the AlAs markers is 2 nm wide and clearly visible. "V" shaped defects are observed originating from the regrowth interface and propagating to the upper AlAs marker where they cancel. Particularly striking is the fact that some defects seem to come from the lower AlAs marker, grown before regrowth. Their origin is probably due to contamination by carbon or other impurities. Note also that no other defects, for example stacking faults and dislocations, can be observed in the layers. Finally the thin AlAs upper marker, grown 10 nm after the regrowth plane, is quite flat.

With respect to sample B5, the regrowth plane cannot be evidenced. The layer overgrown exhibits good crystallinity and no "V" defects. The AlAs marker is highly perturbed and wavy. Moreover, stacking faults originating from the upper AlAs interface are observed. Finally, in sample B15, only the irregularities, found in the AlAs upper layer, remain. No defects are present in any of the layers elaborated after regrowth. This corroborates the AES study indicating the latter exposure time needed to complete C-removal. The waviness of the AlAs layer is probably a result of the oxide roughness evidenced by TEM observations on samples A.

Finally the efficiency of the UV-ozone oxidation technique for a two-step growth with an intermediate *ex-situ* technological processing was checked. An epitaxial 800 nm GaAs layer grown in a first step was withdrawn from the MBE system and subject to RIE of the superficial 300 nanometers. The sample was then treated under the optimized conditions given above and was finally loaded again into the MBE system. After thermal oxide desorption, a GaAlAs-GaAs-GaAlAs QW was grown; the thickness of the three layers was 50, 5 and 20 nm respectively for an Al mole fraction of 0.3 for the alloy. The GaAs thin layer was grown as soon as the surface flatness was recovered, as shown by a streaky (2×4) RHEED pattern. Figure 4 shows the PL spectrum obtained at 13 K, the width (29 meV) of the peak related to the QW emission (1.5803 eV) is quite large, denoting some interface roughness. Nevertheless, the achievement of a quantum confinement at only 50 nm from the regrown interface evidences the adequacy of the technique used.

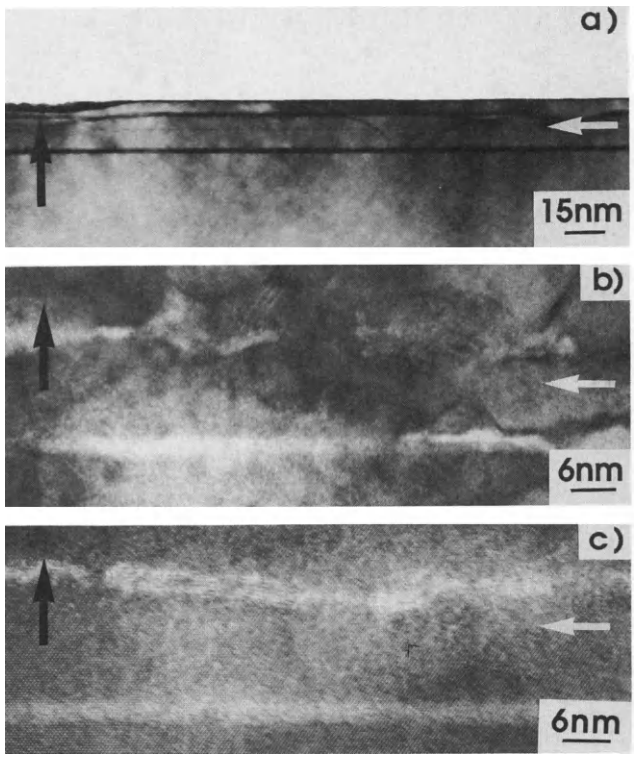

Fig. 3. TEM micrographs of samples B for increasingly long UV-ozone exposure: (a) without oxidation (low magnification bright field); (b) after 5 min (LI); (c) after 15 min (LI). Regrowth interface and growth direction are indicated by white and black arrows respectively.

4. Conclusions

GaAs UV-ozone oxidation for the preparation of surfaces prior to MBE regrowth has been studied. The exposure time needed to thoroughly eliminate C-contamination has been determined by AES. TEM obser-

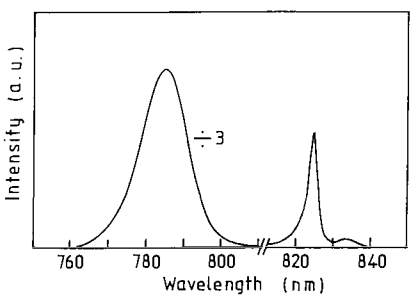

Fig. 4. Photoluminescence spectra obtained from the GaAlAs-GaAs-GaAlAs QW structure at $T = 13$ K, excited with the Ar^+ 514.5 nm line (the emission intensity from the QW has been divided by 3).

vation of oxide layers shows that a longer UV exposure degrades the flatness of the GaAs surface. GaAs layers grown after oxide desorption are free of crystalline defects if contamination has been removed, but the growth front exhibits some roughness. The surface becomes flat again after growth of 50 nm, as evidenced by the PL spectrum obtained on a QW grown under these conditions.

Acknowledgements

The authors acknowledge support from the ESPRIT–LATMIC II, project no. 6536.

References

1 J.A. McClintock, R.A. Wilson and M.E. Byer, *J. Vac. Sci. Technol., 20 (2)* (1982) 241.
2 J.R. Vig and J.W. Lebus, *IEEE Trans. Parts, Hybrids Packag. 12* (1976) 365.
3 S. Ingrey, W.M. Lau and N.S. McIntyre, *J. Vac. Sci. Technol. A4* (3) (1986) 984.
4 R.F. Kopf, P. Kinsella and C.W. Ebert, *J. Vac. Sci. Technol. B9* (1) (1991) 132.
5 J.T. Wetzel, M. Jost, S.A. Rishton, P.M. Fryer, K.T. Kwietniak, D. Klaus, J.J. Bucchignano, C.K. Hu and T.J. Brown, *Ultramicroscopy 29* (1989) 110.
6 S. Ingrey, *J. Vac. Sci. Technol. A10* (4) (1992) 829.
7 C. Lavoie, S.R. Johnson, J.A. Mackenzie, T. Tiedje and T. van Buuren, *J. Vac. Sci. Technol. A10* (4) (1992) 930.

Materials Science and Engineering, B21 (1993) 161–164

Investigation of MOVPE-grown $In_{0.53}Ga_{0.47}As$/InP multi-quantum wells by Raman spectroscopy and X-ray diffractometry

J. Finders, M. Keuter, D. Gnoth, J. Geurts and J. Woitok

I. Physikalisches Institut der RWTH Aachen, Aachen University of Technology, Sommerfeldstraße 28, W-5100 Aachen (Germany)

A. Kohl, R. Müller and K. Heime

Institut für Halbleitertechnik, RWTH Aachen, W-5100 Aachen (Germany)

Abstract

InGaAs/InP multi-quantum well structures, grown by metal–organic vapour phase-epitaxy, were investigated by Raman spectroscopy and X-ray diffractometry to analyse the influence of precursor gas switching parameters on the interface abruptness. Owing to carry-over effects, InAsP is formed at the InGaAs-to-InP interface for low PH_3 purging times (1 s), while for purging times greater than 4 s exchange of As by P leads to the formation of an InGaAsP interface layer, which for purging beyond 10 s saturates at a thickness of 1.2 nm.

1. Introduction

Lattice matched InGaAs/InP multi-quantum well structures (MQWs) are relevant for optoelectronic applications in the near-IR. Optimum device performance requires a defined InGaAs composition and also well controlled interfaces, as abrupt as possible. Total abruptness cannot be expected, since to switch between InGaAs and InP growth, the group III and group V precursor flows must be exchanged, which can induce specific effects at the InP-to-InGaAs and InGaAs-to-InP interfaces. In this study, we focus on the latter interface. A carry-over of As into the InP layer would result in an InAsP interface layer. To avoid this, purging of the reactor with PH_3 before starting the InP growth seems effective. However, during purging the As atoms in InGaAs may be substituted to some extent by P, leading to an InGaAsP interface layer. Therefore, the interface structure is expected to depend critically on the switching procedure. This dependence is the main topic of our study.

X-ray diffraction can be used for interface analysis. It is well established that the diffraction pattern of a sample with a perfect periodic sequence of layers along the growth direction shows in addition to the substrate peak a zero-order peak and a series of satellites [1], revealing the mean lattice parameter and the period thickness. The angular position of the zero-order peak corresponds to the Bragg reflection from a lattice with a lattice parameter equal to the mean value for the entire MQW stack. Therefore, the angular separation between the zero-order and the substrate peaks gives the average lattice mismatch of the MQW. In addition, the spacing of the satellites reflects the geometrical modulation, *i.e.* period thickness, of the periodic structure. Furthermore, it has been shown that the envelope of the satellite patterns is very sensitive to small fluctuations within the layer sequence of the interfaces [2, 3].

In this study we applied X-ray diffractometry and also Raman spectroscopy (inelastic light scattering) for interface analysis. In Raman spectroscopy the constituent materials of the MQW are identified by their lattice vibration eigenfrequencies. InGaAs gives rise to In *vs.* As and Ga *vs.* As vibrations, in the following denoted as In–As and Ga–As modes, respectively [4]. Their eigenfrequencies and intensity ratio characteristically depend on the ternary composition. The same applies for InAsP, showing In–As and In–P modes. For the quaternary InGaAsP even more vibration modes occur: the In–As, In–P, Ga–As, and the Ga–P modes [5]. From these modes we deduce the occurrence and composition of interface layers. The interface layer thicknesses are obtained by combining the Raman-derived data with model calculations for the measured X-ray diffraction patterns.

0921-5107/93/$6.00

© 1993 – Elsevier Sequoia. All rights reserved

2. Experimental set-up

The MQWs were grown on InP(100) substrates at 910 K with a total gas pressure of 20 hPa and a gas flux velocity of 1.2 m s^{-1} in a horizontal quartz reactor using the precursors TMIn, TMGa, PH_3 and AsH_3. The gas switching sequence at the interfaces is shown in Fig. 1. The conditions at the InP-to-InGaAs interface, most probably leading to the formation of a thin InAsP layer with a high As content, were kept constant. At the InGaAs-to-InP interface the PH_3 purging time was varied between 1 and 20 s to study the effect of purging on this interface. The MQWs consist of 10 times 2 nm $In_{0.53}Ga_{0.47}As$, separated by 6 nm InP. The InP capping layer was 12 nm. The resulting total stack thickness of 92 nm is nearly equal to the penetration depth of the 488 nm Ar^+ laser line, used for the Raman analysis. Thus, all the interfaces contribute to the Raman signal. The Raman spectra were recorded in near-backscattering geometry. The input power was 100 mW and the laser beam was focused on the sample by a cylindrical lens. In order to reduce the thermal broadening of the vibrational modes the spectra were recorded at 90 K. The scattered light was analysed using a double monochromator (Spex 1403) with an optical multichannel analyser (EG&G 1462). We used a slit width of 150 μm, giving a spectral resolution of about 1 cm^{-1}.

X-ray diffraction measurements were carried out on a home-made double-crystal diffractometer with an Si (333) first crystal. The MQWs were analysed using the symmetrical (004) substrate reflection with Cu $K\alpha_1$ radiation. Because of the Si reference crystal a slightly dispersive geometry results, leading to a small broadening of the peak widths. However, the peak positions, which are the essential results for our study, are not altered by this configuration. The data were collected in θ–2θ scans with a detector aperture of about 0.07°.

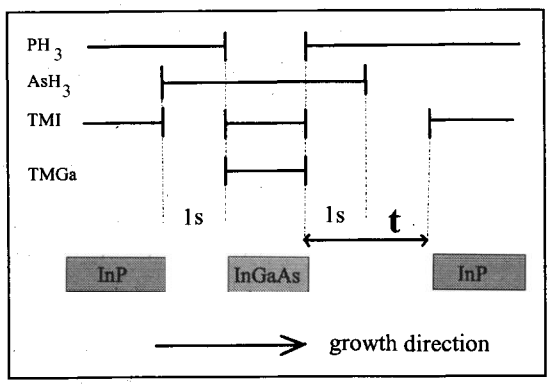

Fig. 1. Switching sequence of the precursors at the interfaces during metal-organic vapour phase epitaxy growth.

3. Results and discussion

In the Raman spectrum of the InGaAs/InP MQWs the In–As and Ga–As longitudinal optical (LO) lattice vibrations of the InGaAs layers are expected in the spectral region between 200 and 300 cm^{-1}, whereas InP gives rise to one LO mode located at 348 cm^{-1} at 90 K. Figure 2(A) shows the Raman spectrum of an MQW for a long PH_3 purging time ($t = 10$ s), recorded at crossed polarization $100(010,001)\bar{1}00$. In the InGaAs region (200–300 cm^{-1}) the dominant feature is the mode at 272 cm^{-1}, which can be attributed to the Ga–As LO mode of the $In_{0.53}Ga_{0.47}As$ layers. Its narrow halfwidth, comparable with bulk $In_{0.53}Ga_{0.47}As$, proves the good crystalline quality of these layers. The Raman spectra of bulk $In_{0.53}Ga_{0.47}As$ and InP are plotted in Fig. 2(B) for comparison. In addition to the intense Ga–As LO mode at 272 cm^{-1}, bulk $In_{0.53}Ga_{0.47}As$ essentially exhibits the In–As mode at 235 cm^{-1}, which is rather broad and weak. For bulk InP only the LO mode at 348 cm^{-1} is observed. Obviously, in the Raman spectrum of the MQW some modes appear which are not observed for bulk $In_{0.53}Ga_{0.47}As$ and bulk InP. These new features may be extracted by subtracting the bulk spectra from the MQW spectra. The result of this evaluation is shown in Fig. 2(C). We identified the new modes as LO lattice vibrations of quaternary $In_xGa_{1-x}As_{1-y}P_y$ interface layers: In–As (243 cm^{-1}), Ga–As (262 cm^{-1}), In–P (348 cm^{-1}) and Ga–P (355 cm^{-1}). Since for InGaAsP the intensity ratio of the In–As and Ga–As mode is

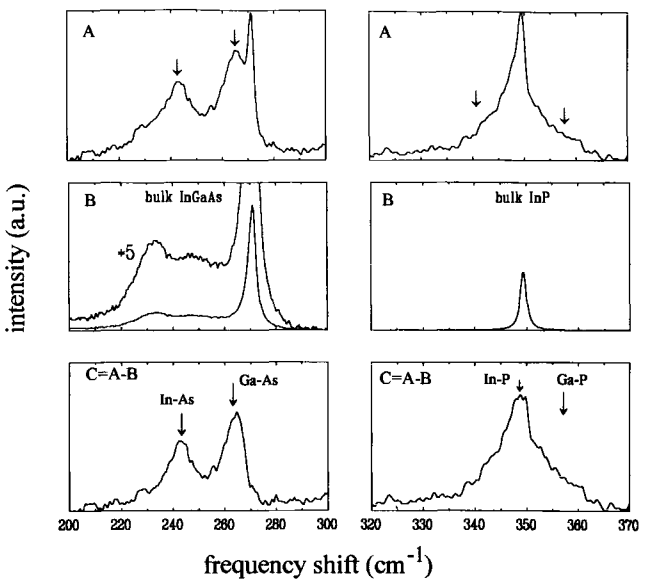

Fig. 2. (A) Raman spectrum of an InGaAs/InP MQW ($t = 10$ s), (B) Raman spectrum of bulk InGaAs (left) and bulk InP (right), and (C) evaluation of interface layer contribution (C = A-B).

proportional to the In content, the composition can be determined using the calibration of Yu *et al.* [6], yielding an In content of about 54%. Thus, within experimental accuracy, the In contents of the quaternary interface layer and the ternary $In_{0.53}Ga_{0.47}As$ well are the same. Therefore we conclude that interdiffusion plays no dominant role during growth. In the same way the P content can be derived from the intensity ratio of the As-like vibrations ($I_{In-As}+I_{Ga-As}$) and the P-like vibrations ($I_{In-P}+I_{Ga-P}$). Doing so, we obtained a P content of 54%. The quaternary layers are allocated to the InGaAs-to-InP interface, where they arise owing to a considerable exchange of As and P atoms during PH_3 purging while switching from InGaAs to InP growth [3, 7].

Raman spectra were also taken for parallel polarization: $100(010,010)\bar{1}00$. Here, the scattering signal from the InP and $In_{0.53}Ga_{0.47}As$ layers should vanish, since for this polarization the deformation potential scattering from LO phonons is symmetry forbidden [8]. Nevertheless, we observed structures which we attribute to the interface layers. These structures agree excellently with the interface signal evaluated in Fig. 2(C). The Raman spectra of the MQWs depend drastically on the PH_3 purging time at the InGaAs-to-InP interface. For $t \geqslant 10$ s the quaternary mode intensity is constant relative to the Ga–As LO mode of $In_{0.53}Ga_{0.47}As$. However, when the purging time is decreased to 4 s, the intensity of the quaternary modes decreases, as shown in Fig. 3. Since the main features of the interface layer are observed between 200 and 300 cm^{-1}, only this region is plotted. The intensity ratio of the In–As and Ga–As modes of the quaternary layer is almost independent of the purging time. This is interpreted as a constant composition of the interface layers, while their thickness decreases for decreasing purging times. For $t = 1$ s a new feature is observed in the Raman spectrum, a shoulder near 235 cm^{-1}, which we attribute to the In–As vibration of additional $InAs_yP_{1-y}$ interface layers. The formation of $InAs_yP_{1-y}$ layers is expected here, since for small purging times residual arsenic atoms are still in the reactor when the InP growth starts. No Raman peaks were resolved which could be assigned to the As-rich InAsP layers at the InP-to-InGaAs interfaces. This indicates that these layers should be extremely thin, which is confirmed by the X-ray results below.

Figure 4 shows the θ–2θ scans around the (004) Bragg reflections of the MQWs for purging times of 1 s and 10 s at the InGaAs-to-InP interface. In addition to the dominant substrate peak, the spectra exhibit a number of intense, well defined satellites. The MQW period thicknesses, obtained from the spacing of these structures, are given in Table 1. Although all samples were grown nominally lattice matched on the InP substrates, the zero-order peaks are well separated from the InP substrate peak. Furthermore, with increasing purging time they shift from one side of the substrate peak to the other. This indicates a variation in the

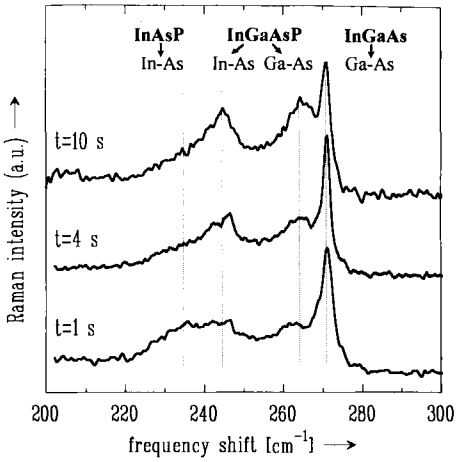

Fig. 3. Raman spectra of MQWs for different phosphine purging times.

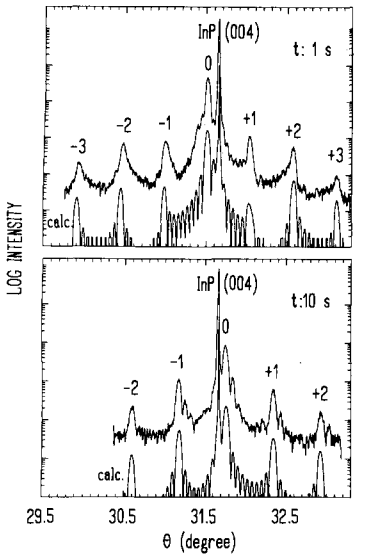

Fig. 4. Comparison of θ–2θ scans around (004) reflections for InGaAs/InP MQWs ($t = 1$ s and $t = 10$ s) and simulated spectra.

TABLE 1. MQW strain and period thickness, derived from X-ray diffractometry

t (s)	$\Delta a/a$ (%)	Period thickness (Å)
1	0.312	97.3
4	−0.107	90.9
7	0.014	94.9
10	−0.317	90.8

average vertical strain. The compressive strain, observed for the shortest purging time, decreases, leading to a nearly lattice-matched state, and finally to a tensile strain for long purging times. The strain values, calculated from the angular separation between the substrate peak and the zero-order peaks, are also given in Table 1. Because the Raman analysis gives nearly equal InGaAs composition for all samples, the zero-order peak shift has to be related to changes in the InGaAs–InP interface layers [2]. In order to evaluate the interface layer composition and thickness, the experimental data were compared with calculations based on the dynamic theory [9]. The Raman-derived InGaAs and InGaAsP compositions serve as the basis for the input parameters. A satisfactory simulation of the X-ray data requires the assumption of interface layers at each interface. For the sample with $t = 10$ s, a good fit was obtained for a structure with four monolayers $In_{0.53}Ga_{0.47}As_{0.47}P_{0.53}$ at the InGaAs-to-InP interface and one monolayer $InAs_{0.9}P_{0.1}$ at the other interface. In this case, the negatively strained InGaAsP layers ($\Delta a/a = -0.0336$) induce the observed zero-order peak shift. With decreasing purging time, the InGaAsP thickness in the fits has to be reduced, so the positive strain of the InP-to-InGaAs interface layers predominates.

4. Conclusions

In conclusion, a combination of Raman spectroscopy and X-ray diffractometry was applied to InGaAs/InP MQWs to study the influence of the PH_3 purging time at the InGaAs-to-InP interface. This combination allowed evaluation of the composition and thickness of interface layers. While interface layers were detected for all samples, the exact interface structure depends significantly on the purging time. For $t = 1$ s, ternary InAsP is formed owing to carry-over effects. For $t > 4$ s, the exchange of As and P leads to quaternary InGaAsP, whose composition is about the same for all purging times. Its thickness, however, increases with purging time until it saturates at 1.2 nm for $t > 10$ s.

References

1 M. Quillec, L. Goldstein, G. Le Roux, J. Burgeat and J. Primot, *J. Appl. Phys., 55* (1984) 2904.
2 J. M. Vandenberg, A. T. Macrander, R. A. Hamm and M. B. Panish, *Phys. Rev. B, 44* (1991) 3991.
3 R. Meyer, M. Hollfelder, H. Hardtdegen, B. Lengeler and H. Lüth, *J. Cryst. Growth, 124* (1992) 583.
4 T. P. Pearsall, R. Charles and J. C. Portal, *Appl. Phys. Lett., 42* (1983) 436.
5 R. K. Soni, S. C. Abbi, K. P. Jain, M. Balkanski, S. Slempkes and J. L. Benchimol, *J. Appl. Phys., 59* (1986) 2184.
6 S. Yu, H. Asahi, S. Emura and S. Gonda, *J. Appl. Phys., 70* (1991) 204.
7 K. Streubel, V. Härle, F. Scholz, M. Bode and M. Grundmann, *J. Appl. Phys., 71* (1992) 3300.
8 W. Richter, in G. Höhler (ed.), *Springer Tracts in Modern Physics*, Vol. 78, *Solid State Physics*, Springer, Berlin, 1976.
9 W. J. Bartels, J. Hornstra and D. J. W. Lobeek, *Acta Crystallogr. A, 42* (1986) 539.

Materials Science and Engineering, B21 (1993) 165–168

Chemical beam epitaxy of high purity InP using tertiarybutylphosphine and 1,2 bis-phosphinoethane

M. Zahzouh and G. Hincelin*

Laboratoire de Physique des Composants Electroniques, CNAM, 292 rue Saint-Martin, 75141 Paris Cedex 03 (France)

R. Mellet and A. M. Pougnet

France Telecom, CNET, Laboratoire de Bagneux, 196 Avenue Henri Ravera, 92220 Bagneux (France)

Abstract

This paper compares tertiarybutylphosphine (TBP), and 1,2 bis-phosphinoethane (BPE) as phosphorus precursors for the growth of InP in chemical beam epitaxy. The thermal decomposition of both sources in a low pressure cracking cell produces dimer P_2 and tetramer P_4 species. The P_2 to P_4 ratio is a function of the cracker temperature θ_c, the dimer P_2 is the dominant species for $\theta_c = 800$ °C. High quality InP layers, showing good surface morphology, were grown using low values of the V to III flux ratio $R_{V/III}$, leading to a very low consumption of the group V product. The lower $R_{V/III}$ value ($R_{V/III} \simeq 3$) is obtained with the BPE molecule, which contains two phosphorus atoms. 77 K Hall mobility values of 62 500 cm^2/Vs and 26 500 cm^2/Vs were obtained using TBP and BPE respectively and triethylindium as group III source. With both phosphorus sources, background carrier density levels as low as $N_D - N_A < 10^{15}$ cm^{-3} are obtained.

1. Introduction

Chemical beam epitaxy (CBE) has emerged as a promising epitaxial technique for the growth of III–V semiconductors since its introduction at the beginning of the 1980s [1–3], for it combines the major advantages of both molecular beam epitaxy (MBE) and metalorganic chemical vapour deposition (MOCVD).

There has been much interest recently in the replacement of the highly toxic and hazardous hydride group V sources used in the growth of III–V semiconductors. Other disadvantages of hydrides are the high temperature required for pyrolysis and a necessarily high $R_{V/III}$ ratio. Tertiarybutylphosphine (TBP) and 1,2 bis-phosphinoethane (BPE) are particularly attractive for phosphine replacement, because of their low vapour pressure and lower decomposition temperature. Moreover the LC_{50} TBP value is over 1100 p.p.m., while it is only 11–50 p.p.m. for phosphine [4]. No information was available regarding the toxicity of BPE though it is reasonable to assume that it is less than PH_3.

The TBP has been used successfully in MOCVD [5, 6] and more recently in CBE by D. Ritter *et al.* [7]. We have reported previously a 77 K mobility of 45 000 $cm^2\ V^{-1}\ s^{-1}$ for InP layers grown using TBP and trimethylindium (TMI) [8]. Recently, A. Chin *et al.* reported on the use of BPE for the growth of InP by CBE [9]. This new organophosphorus precursor has a favourable vapour pressure ($P_v = 20$ mbar at 25 °C); its molecule contains two phosphorus atoms, and only one carbon per phosphorus atom. In this paper, we compare the thermal decomposition processes of TBP and BPE, and their capability to grow InP layers.

2. Thermal decomposition of TBP and BPE

The CBE growth system has been described in detail elsehwere [8]. The TBP of commercial origin (Cyanamid) was melting-zone purified at CNET, while the BPE (Morton) was vacuum distilled. All gas flow is regulated by means of leak valves, the source temperature being kept constant to within 0.1 °C, and no carrier gas is used. The group V precursors are precracked in a specially designed low pressure cracking cell [8]. The thermal decomposition of TBP and BPE is studied using a quadrupole mass spectrometer (QMS) placed in the molecular beam issued from the cell.

In the cracking experiments, mass spectra are recorded at different cracking temperatures θ_c, from ambient to 1000 °C. The gas flow is kept to a constant

*Author to whom correspondence should be addressed.

0921-5107/93/$6.00

© 1993 – Elsevier Sequoia. All rights reserved

value, corresponding to an equivalent initial pressure in the 10^{-5} mbar range. For θ_c values lower than 300 °C, no cracking effect is observed and the mass spectrum displays the cracking pattern due to the spectrometer electron beam itself. For higher θ_c values, the thermal decomposition of the molecules give rise to two effects: (a) an increase of the total pressure and (b) a dramatic variation in the mass spectrum peak intensities. These variations for TBP and BPE are displayed in Figs. 1 and 2, respectively, as a function of θ_c (the data are not corrected for the apparent mass sensitivity of the QMS). Several observations can be made:

(i) For both organophosphorus compounds, the cracking occurs in the same temperature range (between 400 and 600 °C), as can be seen from the decrease of the parent peak intensity located at $m/e = 90$ amu for TBP ($C_4H_9PH_2$) and $m/e = 94$ amu for BPE ($(CH_2)_2P_2H_4$). In both cases, the decomposition efficiency is close to unity at temperatures higher than $\theta_c = 800$ °C, which is some 200 °C lower than the decomposition temperature for PH_3 in a standard commercial low pressure cracking cell.

(ii) The main phosphorus species found in the molecular beam are PH_3, P_2 and P_4 (it should be noted that the P_4 level is underestimated due to the decrease in sensitivity of our QMS *vs.* the ion mass). For $\theta_c > 600$ °C, P_4 and PH_3 results in P_2. In consequence, the dimer proportion increases as a function of θ_c and saturates at $\theta_c = 800$ °C. The production of phosphine PH_3 reaches a maximum at a temperature of about 600 °C.

(iii) The main decomposition products are H_2 and isobutene (C_4H_8) for TBP, H_2 and ethylene (C_2H_4) for BPE. At a cracking temperature greater than 800 °C, the decomposition can be described by the following overall reactions:

$$2C_4H_9PH_2 \rightarrow 2C_4H_8 + P_2 + 3H_2 \quad \text{(TBP)}$$

$$P_2C_2H_8 \rightarrow C_2H_4 + P_2 + 2H_2 \quad \text{(BPE)}$$

3. Growth and characterization of InP layers

A series of experiments were performed to determine the optimum substrate temperature θ_s and optimum $R_{V/III}$ flux ratio for InP growth using TBP or BPE. InP layers, 3 μm thick were grown at a standard growth rate of 1 μm per hour on semi-insulating Fe-doped InP substrates, misoriented 2° off towards ⟨110⟩. Triethylindium (TEI) of commercial origin and TMI synthesized at CNET were used as group III sources. θ_s was controlled by infrared pyrometry and the $R_{V/III}$ ratio was estimated according to the equilibrium pressure values of the V and III compounds in the growth

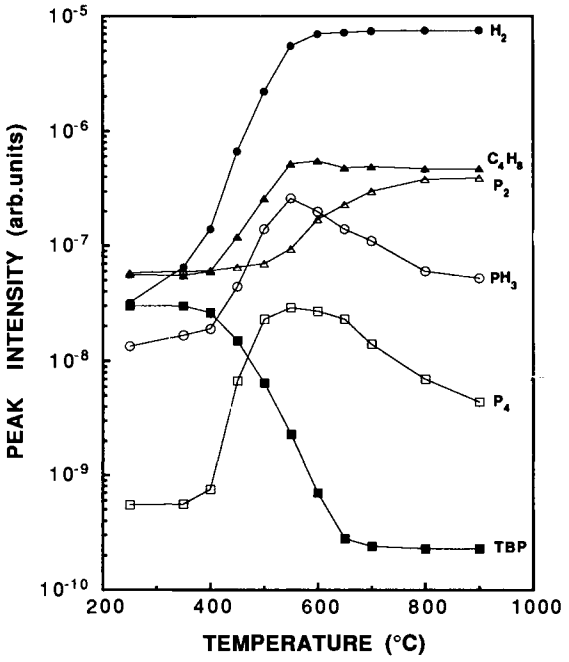

Fig. 1. Thermal decomposition of TBP: height variations (in arbitrary values) of the main species observed in the molecular beam as a function of the cracking cell, under constant gas flow conditions (initial pressure, $p = 5 \times 10^{-6}$ mbar). The curve labelled TBP relates to the parent peak $C_4H_9PH_2$ located at $m/e = 90$ amu.

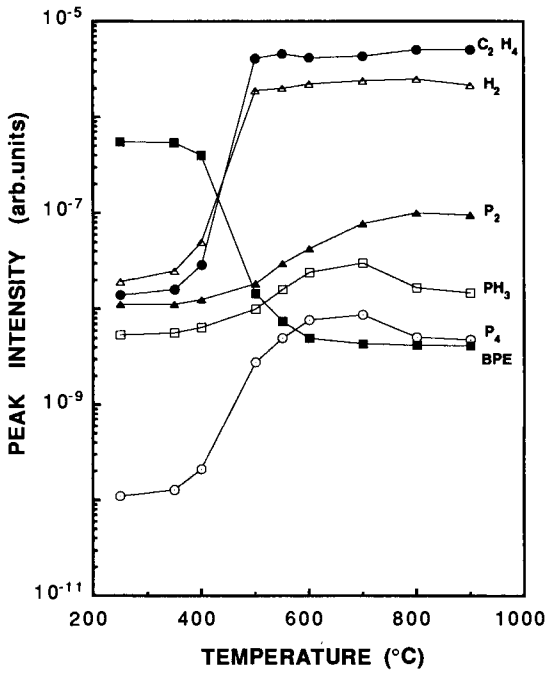

Fig. 2. Thermal decomposition of BPE: height variations of the main species observed in the molecular beam as a function of the cracking cell, under the same experimental conditions as for TBP. The parent peak $C_2H_4P_2H_4$ shows up at $m/e = 94$ amu.

chamber. The cracking temperature was set to $\theta_c = 800$ °C in order to deliver P_2. The electrical properties of the samples were analysed using conventional Hall measurements according to the Van der Pauw method. Optical characterizations were carried out by low temperature photoluminescence.

The 77 K background carrier concentration variations *vs.* growth temperature θ_s (at a constant $R_{V/III}$ ratio) are shown, using an Arrhenius plot, in Fig. 3 for InP layers grown using TBP–TMI and BPE–TEI respectively. The concentration falls readily with increasing temperature, and values as low as 4×10^{14} cm^{-3} for BPE and 10^{15} cm^{-3} for TBP are obtained. An activation energy for impurities incorporation of about $E_a = 50$ kcal mol^{-1} can be estimated from the slope of the curves. We note that this value is very close to values obtained with PH_3 and TEI by Benchimol *et al.* [10].

The Hall mobility μ_{77K} variations *vs.* the $R_{V/III}$ ratio are plotted in Fig. 4. The two upper curves are relative to TBP–TEI and TBP–TMI respectively, while the lower curve is relative to BPE–TEI. The curves show a general decrease in mobility as a function of $R_{V/III}$:

(i) The better μ_{77K} values obtained with TBP correspond to an optimum ratio close to $R_{opt} \simeq 5$. At a lower $R_{V/III}$ ratio the decrease in mobility could be ascribed to a lack of phosphorus in the layer. InP layers grown using TEI have higher mobility ($\mu_{77K} = 62\,000$ cm^2 V^{-1} s^{-1}) than those grown using TMI ($\mu_{77K} = 45\,000$ cm^2 V^{-1} s^{-1}). This is the best result obtained to date using TBP in CBE.

(ii) The mobility is lower for the layers grown with BPE. The highest value ($\mu_{77K} = 26\,500$ cm^2 V^{-1} s^{-1}) corresponds to a very low $R_{V/III}$ ratio ($R_{V/III} \simeq 3$), about half the optimum ratio for TBP. This result emphasizes that BPE is an attractive group V precursor, due to its two phosphorus atoms. On the other hand, a low mobility value, together with a low net carrier concentration $n = N_D - N_A$, indicates a high compensation ratio N_A/N_D. This is probably due to impurities in the source, and we believe that the electrical properties could be greatly improved after further purification of the BPE.

4. Conclusions

In the low pressure cell used in our laboratory, both TBP and BPE decompose totally in the temperature range 400–700 °C. For $\theta_c \geq 800$ °C, phosphorus is delivered in the dimer form P_2, with a cracking efficiency close to unity in both cases. InP layers grown with TBP or BPE show good surface morphology, good optical properties and very low background carrier concentration ($n < 10^{15}$ cm^{-3}). The highest 77 K Hall mobility ($\mu_{77K} = 62\,500$ cm^2 V^{-1} s^{-1}) is obtained with TBP–TEI, at an optimum V/III ratio

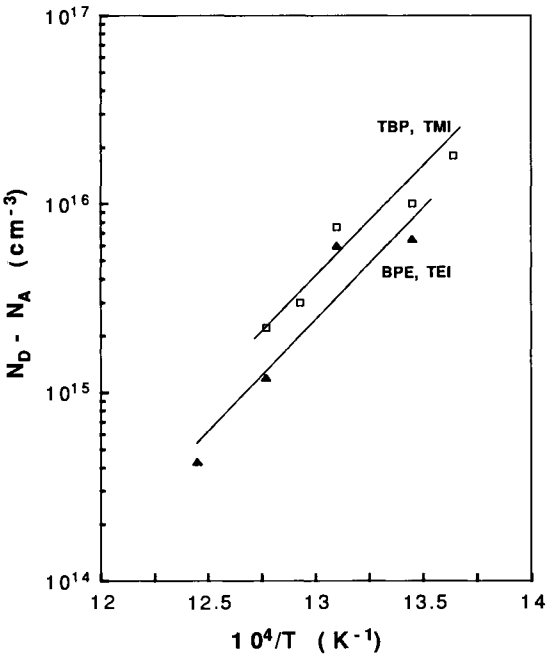

Fig. 3. Arrhenius plot of the net carrier concentration $n = N_D - N_A$ at 77 K *vs.* inverse growth temperature of InP layers grown using TBP–TMI and TBP–TEI respectively. Growth rate 1 μm h^{-1}; layer thickness 1 μm (TBP–TMI, $R_{V/III} = 3.7$) and 3 μm (TBP–TEI, $R_{V/III} = 4.4$).

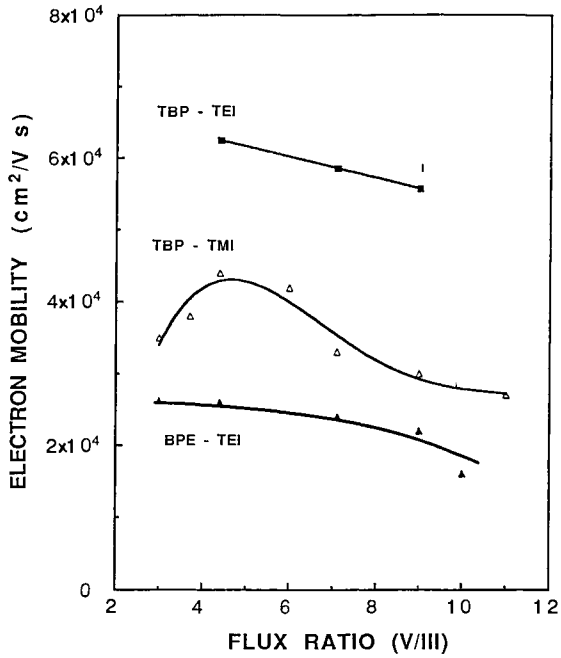

Fig. 4. 77 K Hall mobility *vs.* V/III ratio. Growth temperatures $\theta_s = 500$ °C (TBP–TEI), $\theta_s = 510$ °C (TBP–TEI and BPE–TEI).

close to $R_{opt} = 5$. As far as we are aware, this is the best result obtained with TBP in CBE. The Hall mobility of InP layers grown using BPE and TEI, $\mu_{77K} = 26\ 500$ $cm^2\ V^{-1}\ s^{-1}$, compares well with previously published values [9]. This relatively low mobility value could be explained by the presence of impurities in the BPE source, and we believe that better electrical properties would be obtained after melting-zone purification. We emphasize that a very low source V flux is needed, mainly in the case of BPE, which leads to a very low product consumption.

Acknowledgments

The authors would like to acknowledge Dr. A. Mircéa who initiated this work. They also thank Dr. J. L. Benchimol and Dr. F. Alexandre for helpful discussions. This work was partly supported by the Centre National d'Etude des Télécommunications (CNET) under contract no. 90 6D 093.

References

1 N. Vodjdani, A. Lemarchand and H. Paradan, *J. Phys. Coll., 43* (C5) (1982) 339.
2 E. Veuhoff, W. Pletschen, P. Balk and H. Luth, *J. Cryst. Growth, 55* (1981) 30.
3 W. T. Tsang, *J. Electron. Mater., 15* (1986) 235.
4 G. B. Stringfellow, *Organometallic Vapor Phase Epitaxy: Theory and Practice*, Academic Press, Boston, 1989.
5 T. Imori, T. Ninomiya, K. Ushikubo, K. Kondoh and K. Nakamura, *Appl. Phys. Lett., 59* (1991) 2862.
6 R. T. Huang, A. Appelbaum, D. Renner and S. W. Zehr, *Appl. Phys. Lett., 58* (1991) 170.
7 D. Ritter, M. B. Panish, R. A. Hamon, D. Gershoni and I. Brener, *Appl. Phys. Lett., 56* (1990) 1448.
8 G. Hincelin, M. Zahzouh, R. Mellet and A. M. Pougnet, *J. Cryst. Growth, 120* (1992) 119.
9 A. Chin, P. Martin, U. Das, J. Mazurowski and J. Ballingall, *Appl. Phys. Lett., 61* (1992) 2099.
10 J. L. Benchimol, F. Alaoui, Y. Gao, G. LeRoux, E. V. K. Rao and F. Alexandre, *J. Cryst. Growth, 105* (1990) 135.

Materials Science and Engineering, B21 (1993) 169–173

Optical characterization of extremely high purity ZnSe grown by metal–organic vapour phase epitaxy using dimethylzinc-triethylamine adduct

T. Cloitre, N. Briot, O. Briot, B. Gil and R. L. Aulombard

Groupe d'Etudes des Semiconducteurs, Université Montpellier II, Place E. Bataillon, 34095 Montpellier Cedex 5 (France)

A. C. Jones

Epichem Ltd, Power Road, Bromborough, Wirral, Merseyside, L62 3QF (UK)

Abstract

Zinc selenide (ZnSe) is now a material of established interest for the design of optoelectronic devices, following the achievement of both types of conductivity by M. Haase *et al.* (*Appl. Phys. Lett., 59* (1991) 1272). The p-type doping of this material is now well established in molecular beam epitaxy, and work is in progress in many laboratories to transpose this to metal–organic vapour phase epitaxy (MOVPE).

One of the problems to be solved in MOVPE, for the successful achievement of p-type doping, is that of obtaining a material with very low electron background concentrations, to avoid compensation effects. It has previously been demonstrated, by Jones, Wright and co-workers (*Semicond. Sci. Technol., 6* (1991) A36; *J. Cryst. Growth, 94* (1989) 441; *J. Cryst. Growth, 104* (1991) 297) that the classical zinc precursor leads to prereactions and is invariably contaminated by trace amounts of iodine. To get rid of these problems, they employ a new precursor for zinc, that is dimethylzinc triethylamine adduct (Me_2ZnEt_3). Their results demonstrate that the material purity can be increased.

Following Wright *et al.* (*J. Cryst. Growth, 94* (1989) 441; *J. Cryst. Growth, 104* (1991) 297), we have employed this original precursor to grow extremely high purity ZnSe. We investigated the growth conditions and determined the optimum growth parameters to be a growth temperature of 280 °C, a VI/II molar ratio of 5 and a reactor pressure of 40 Torr.

The samples were characterised by low temperature photoluminescence and reflectivity experiments. We observed that the use of Me_2ZnEt_3 led to a dramatic decrease of the donor bound exciton intensity in the 2 K photoluminescence spectrum, along with a correlated increase of the free exciton intensity. For the first time, free excitons and excited states up to the second (3s) were observed in reflectivity spectra. The spectra were theoretically fitted using a model similar to the one of Zheng *et al.* (*Appl. Phys. Lett., 52* (1988) 287), in the local approximation, including a "dead layer" as prescribed by Hopfield and Thomas (*Phys. Rev., 132* (1988) 563). Using this model, we accurately deduced the transition energy positions and oscillator strengths of the observed transitions. Moreover, we deduced that the damping parameter of the HH (1s) transition is 1.4 meV. Such a sharpness clearly indicates the high crystalline quality of the material.

1. Introduction

Zinc selenide (ZnSe) is a material with a direct band gap of 2.67 eV at room temperature, making it a potential candidate for blue light electroluminescence. While numerous studies have been devoted to this material, the classical problem of the II–VI compounds has remained for almost 30 years: although one type of conductivity (*i.e.* n-type) can be achieved, conversion to the other type has never been obtained. Since there is no definitive proof that this behaviour is intrinsic, many enthusiastic researchers have continued to attempt a successful p-type doping of ZnSe, using all the possible growth and doping methods, from bulk growth to more sophisticated epitaxial thin film technologies, such as molecular beam epitaxy (MBE) and metal–organic vapour phase epitaxy (MOVPE). The major breakthrough was achieved in 1991 by Haase *et al.* [1] who succeeded in the p-type doping of ZnSe grown by MBE using plasma activated nitrogen. These authors successfully employed the nitrogen-doped p-type ZnSe in the design of a blue–green laser device, changing the status of the ZnSe material from a potential candidate for blue light electroluminescence to an effective base material for a wider range of optoelectronic devices. This work has now been reproduced several times using MBE but has not yet been adapted to the MOVPE technology. The problem with MOVPE is the successful incorporation of active nitrogen in the layers, with a low compensation ratio to demonstrate efficient p-type conductivity. Since the early work of Stutius [2] and Blanconnier *et al.* [3], two

0921-5107/93/$6.00

© 1993 – Elsevier Sequoia. All rights reserved

major problems have occurred in the MOVPE growth of ZnSe. One is the occurrence of premature reactions at room temperature between the "classical" MOVPE precursors, dimethylzinc (Me_2Zn) and hydrogen selenide (H_2Se), the other is a high residual n-type contamination, which is not favourable for achieving p-type conductivity with low resistivity. This has generated an intense effort to find novel precursors to overcome these drawbacks.

For instance, the room temperature prereaction can be attributed to the facile elimination of methyl radicals from Me_2Zn by the acidic hydrogen of H_2Se. Therefore, in an effort to limit this effect, alternative group VI precursors such as dialkylselenides [4] and heterocyclic selenium compounds [5] have been investigated. Unfortunately, although this approach eliminates prereaction, it requires a higher than desirable deposition temperature (above 400 °C), which can lead to an increase in deep states [6] and to increased carbon contamination in the grown layer [4]. An alternative approach [7, 8] has been to modify the Me_2Zn source so that it is no longer susceptible to prereaction with H_2Se. In this respect, the adduct between dimethylzinc and triethylamine (Me_2ZnNET_3) has proved to be most effective [8]. This adduct has been shown virtually to eradicate prereaction with H_2Se and has allowed the growth of ZnSe of greatly improved purity at low to moderate growth temperature (250–350 °C) [8]. In addition, the presence of trialkylamine in the adduct has been shown [9] to remove unwanted alkyl iodide impurity from Me_2Zn in the form of involatile $R_3N^+I^-$ salt. This contributes to increased layer purity by removing iodine which is an efficient n-type dopant in ZnSe.

In this study, we investigated the electrical and the optical properties of ZnSe grown by MOVPE using Me_2Zn and Me_2ZnNEt_3 zinc precursors. Extremely high purity zinc selenide layers were obtained by using Me_2ZnNEt_3. In this case, the residual carrier concentration obtained was so low that no accurate electrical measurements could be made using the Hall effect. The optical properties of the layers were investigated using low temperature photoluminescence and reflectivity.

2. Experimental details

The samples were grown using an ASM France 12 MOVPE machine, with a classical horizontal reactor and a double manifold for separate injection of zinc and selenium precursors (since we also grew ZnSe using the classical combination $Me_2Zn + H_2Se$ which exhibits strong premature reactions). The Zn and Se precursors are mixed at the entrance of the reaction chamber. To avoid pollution from the selenium source, we employed exclusively H_2Se in stainless steel bottles, since the aluminium bottles may cause pollution (Al is an n-type dopant on the zinc site). The gaAs(100) substrates were cleaned with organic solvents, etched with $8H_2SO_4:1H_2O_2:1H_2O$ solution, blown dry with high purity nitrogen (99.9999%). Careful *in situ* purge (palladium purified hydrogen, 30 min) and preheating procedures were performed to remove the contaminants introduced by the substrate surface.

The photoluminescence experiments were performed at pumped liquid helium temperature using a 10 mW He–Cd laser. The reflectivity measurements were also taken at this temperature. The light emitted by a tungsten halogen lamp was focused on the entrance slit of a THR Jobin Yvon 1.5 m focal length spectrometer after being reflected by the sample and chopped. Detection was done using standard lock-in techniques.

3. Results

The growth of ZnSe using the classical combination $Me_2Zn + H_2Se$ was first performed as a reference. The MOVPE growth parameters investigated were the growth temperature T_g, the growth pressure P and the VI:II molar ratio. The optimized growth parameters were $T_g = 300$ °C, $P = 40$ Torr and a VI-to-II molar ratio of 5. The optimization was done from photoluminescence and Hall effect measurements performed on each layer.

The electron concentration was found to be extremely dependent on the growth temperature as displayed in Fig. 1. The electron concentration was as high as 10^{18} cm^{-3} for low growth temperatures and decreased below 10^{14} cm^{-3} at higher temperatures. We interpret this in terms of more efficient pyrolysis of H_2Se at high temperature, increasing the "effective" selenium concentration near the substrate surface. The iodine impurities included in the dimethylzinc are incorporated in the crystal on the selenium sublattice, and thus have a lower probability of incorporation. Unfortunately, above 400 °C the photoluminescence spectra exhibit strong "self-activated" (SA) bands, due to intrinsic defects [10]. These defects may also play a role in the free carrier reduction by trapping the electrons. The transport experiments were interpreted using a theoretical analysis [11] which offers an easy determination of the compensation ratio (the compensation ratio is $\theta = N_a/N_d$ where N_a and N_d stand for acceptor and donor impurity concentrations respectively). The result is displayed in Fig. 2 and indicates that the compensation is minimum when T_g is around 300 °C. The acceptor incorporation first decreases and then strongly increases when T_g increases above

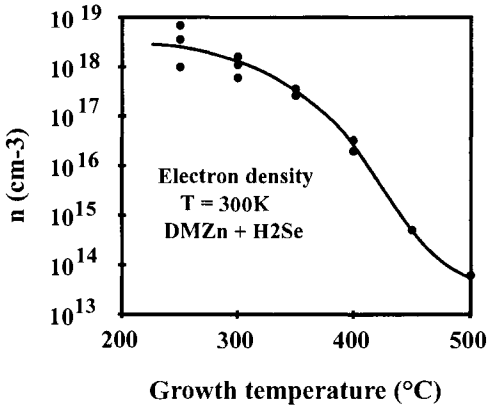

Fig. 1. Variation of the experimental electronic density measured at room temperature with the growth temperature T_g.

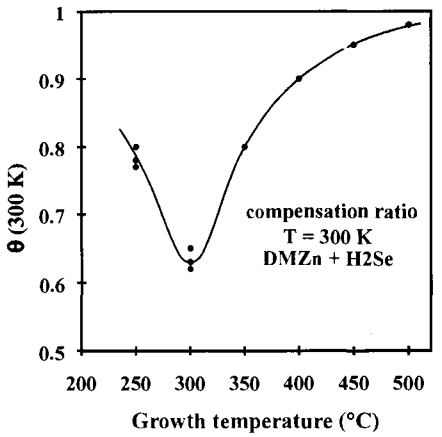

Fig. 2. Variation of the compensation ratio at room temperature ($\theta = N_d/N_a$) with the growth temperature T_g.

300 °C. This is consistent with the progressive increase in concentration of intrinsic defect which occurs when T_g is increased, if we admit that the defects trap electrons. However, the reduction in the acceptor concentration when the temperature increases from 250 °C to 300 °C could also be interpreted in terms of native defects occurring when the growth temperature is too low to allow good organization of the crystal.

For the epilayer grown under the best conditions, the photoluminescence spectrum (Fig. 3) exhibits sharp excitonic peaks, mainly donor bound exciton (I_2 at 2.789 eV) and free exciton (Ex at 2.803 eV). At lower energy we observe a weak donor–acceptor pair luminescence (DAP and DAP-LO). The absence of observable splitting of the free exciton indicates that the epilayer is relaxed, which is consistent with its thickness, $e = 1.5$ μm. The ratio between the intensities of the free exciton and the donor bound exciton lines is 0.25, and is used as a yardstick with regard to purity to discuss the photoluminescence results.

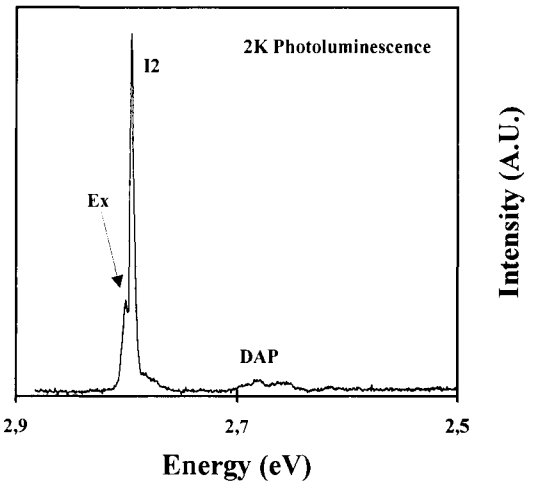

Fig. 3. 2 K photoluminescence spectrum of a 1.5 μm thck ZnSe epilayer deposited under optimal growth conditions onto a (100) GaAs substrate using H_2Se and dimethylzinc as selenium and zinc sources respectively.

Next, we investigated the growth of ZnSe epilayers using the Me_2ZnNEt_3 adduct. The residual carrier concentrations were measurable only for the first layers grown with the adduct and were around 10^{14} cm^{-3}. This is certainly due to a residual cross pollution with previous growth experiments since all the following layers became too resistive to be measured by Hall effect. The growth was optimized from the optical measurements and we found that the optimum growth conditions were the same as for the use of Me_2Zn, except for a lower growth temperature of 280 °C.

A typical photoluminescence spectrum of a sample grown under these conditions is displayed in Fig. 4. One can observe that the ratio between the donor bound exciton (I_2) and the free exciton (Ex) is now close to unity, reflecting the much lower donor content of this sample. The small peak at higher energy can be attributed to the first excited state (Ex-2s) of the free exciton. The peak at lower energy (Y_0 at 2.59 eV) is always observed in layers grown with the DMZn adduct. It was observed previously by Dean [12] and attributed to inelastic scattering of the free exciton by crystalline defects occurring in the presence of a high free exciton concentration. Such a peak would then be observed only in high quality samples.

The reflectivity spectrum of the same sample (Fig. 5) is highly structured with many transitions at high energy. In order to make an accurate analysis of the reflectivity data, we fitted the spectrum in the local approximation, using the model described by Zheng *et al.* [13] and including, as prescribed by Hopfield and Thomas [14], a "dead layer" describing the effects of the sample surface on the excitons. Four oscillators

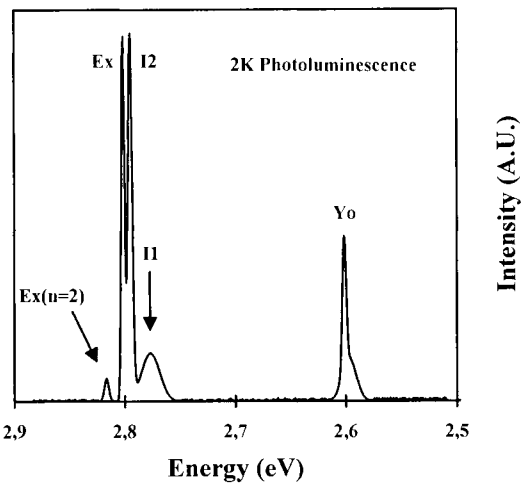

Fig. 4. 2 K photoluminescence spectrum of a 1.6 μm thick ZnSe layer grown on a (100) GaAs substrate using H_2Se and the triethylamine dimethylzinc adduct as selenium and zinc precursors respectively.

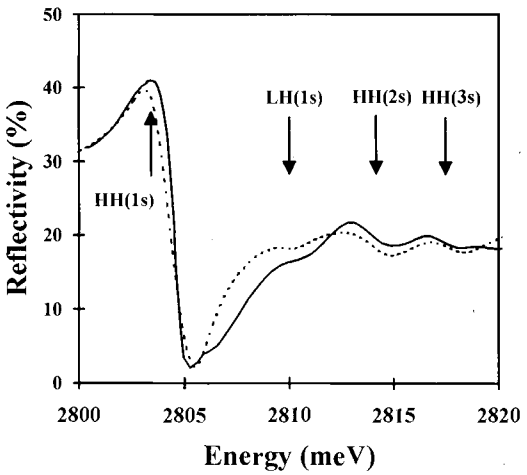

Fig. 5. Experimental 2 K reflectivity spectrum (——) and theoretical fit (– – –) obtained for a 1.6 μm thick ZnSe layer grown on a (100) GaAs substrate using H_2Se and the triethylamine dimethylzinc adduct as selenium and zinc precursors respectively.

were introduced in the calculations to account for all the structures observed. The positions, oscillator strengths and damping parameters for each transition are indicated in Table 1. The dead-layer thickness was 95 Å, in good agreement with the value of twice the excitonic Bohr radius ($a_B = 48$ Å) traditionally used. The ratio between the oscillator strengths for HH(1s)/HH(2s) transitions and HH(1s)/HH(3s) transitions are close to the theoretical values (8 and 27 respectively). From the energy separation between the 1s–2s and 1s–3s transitions, we deduce a Rydberg energy of 15 meV, in good agreement with Hölscher *et al.* [15]. The ratio between oscillators used to describe the changes in reflectivity at the energies of the 1s heavy-hole and light-hole resonances does not obey the traditional trend (a ratio of approximately 3). However, we do not describe accurately the high energy wing of the 1s heavy-hole exciton. We offer an explanation for this. Following Mitsuhashi *et al.* [16], the critical thickness for coherent growth of ZnSe on GaAs in 1500 Å. In our sample (1.6 μm), relaxation must have occurred, leading to a distribution of strain, decreasing from the ZnSe–GaAs interface to the surface. As the light-hole exciton energy shifts four times faster with strain than the heavy-hole exciton does [17], we believe that the description of the light-hole could be improved by using a series of oscillators. This could account for the discrepancy observed around the light-hole exciton between the experiment and calculations, as well as for the low value of the LH(1s) oscillator strength obtained using only one oscillator for the light-hole free exciton. In terms of material quality, the noticeable features in this reflectivity spectrum are the extreme sharpness of the transitions, the large variation of the absolute value of reflectivity coefficient between around 40% and 0%, and the 3s transition. All these observations contribute to demonstrate that the material quality and purity are extremely high.

TABLE 1. Parameters deduced from the reflectivity fitting procedure

Transition	Energy (meV)	Oscillator strength	Damping (meV)	Attribution
1	2803.5	15×10^{-3}	1.4	HH(1s)
2	2810	0.5×10^{-3}	2	LH(1s)
3	2814.2	2.2×10^{-3}	3	HH(2s)
4	2817.5	0.5×10^{-3}	3	HH(3s)

4. Conclusion

We have compared epitaxial layers obtained using the classical precursor combination $Me_2Zn + H_2Se$ with layers obtained using $Me_2ZnNETt_3 + H_2Se$. We demonstrate, by optical means (photoluminescence and reflectivity), that the triethylamine adduct leads to a highly improved purity of the layers.

Acknowledgment

This work was supported by the Commission of European Communities (CEC) under an ESPRIT III Basic Research no. 6675-MTVLE. The "Groupe d'Etudes des Semiconducteurs" is "Unité de recherche associée au CNRS" no. 357.

References

1 M. A. Haase, J. Qiu, J. M. DePuydt and H. Cheng, *Appl. Phys. Lett., 59* (1991) 1272.
2 W. Stutius, *Appl. Phys. Lett., 33* (1978) 656.
3 P. Blanconnier, M. Cerclet, P. Henoc and A. M. Jean-Louis, *Thin Solid Films, 55* (1978) 375.
4 S. Patrick, K. F. Jensen and K. P. Giapis, *J. Cryst. Growth, 107* (1991) 390.
5 P. J. Wright, R. J. M. Griffiths and B. Cockayne, *J. Cryst. Growth, 66* (1984) 26.
6 B. Cockayne, P. J. Wright, M. S. Skolnick, A. D. Pitt, J. O. Williams and T. L. Ng, *J. Cryst. Growth, 84* (1987) 552.
7 A. C. Jones, *Semicond. Sci. Technol., 6* (1991) A36.
8 P. J. Wright, P. J. Parbrook, B. Cockayne, A. C. Jones, E. D. Orrell, K. P. O'Donnell and B. Henderson, *J. Cryst. Growth, 94* (1989) 441.
9 A. C. Jones, P. J. Wright and B. Cockayne, *J. Cryst. Growth, 104* (1991) 297.
10 B. E. Ponga, J. Calas, M. Averous, T. Cloitre, O. Briot, B. Gil and R. L. Aulombard, *Mater. Res. Soc. Symp. Proc., 263* (1992) 371.
11 O. Briot, N. Briot, T. Cloitre, R. Sauvezon and R. L. Aulombard, *Semicond. Sci. Technol., 6* (1991) A24.
12 P. J. Dean, *Phys. Status Solidi, 81* (1984) 625.
13 X. L. Zheng, D. Heiman, B. Lax and F. A. Chambers, *Appl. Phys. Lett., 52* (1988) 287.
14 J. J. Hopfield and D. G. Thomas, *Phys. Rev., 132* (1988) 563.
15 H. W. Hölscher, A. Nöthe and Ch. Uihein, *Physica B, 117* (1983) 395.
16 H. Mitsuhashi, I. Mitsuishi, M. Mizuta and H. Kukimoto, *Jpn. J. Appl. Phys., 24* (1985) L578.
17 R. L. Aulombard, M. Averous, O. Briot, J. Calas, D. Coquillat, F. Hamdani, J. P. Lascaray, N. Moulin and N. Tempier, *J. Cryst. Growth, 101* (1990) 204.

Materials Science and Engineering, B21 (1993) 174–176

Spectroscopic ellipsometry: a useful tool to determine the refractive indices and interfaces of $In_{0.52}Al_{0.48}As$ and $In_{0.53}Al_xGa_{0.47-x}As$ layers on InP in the wavelength range 280–1900 nm

H. W. Dinges, H. Burkhard, R. Lösch, H. Nickel and W. Schlapp

Deutsche Bundespost Telekom Forschungs- und Technologiezentrum, Am Kavalleriesand 3, D-6100 Darmstadt (Germany)

Abstract

$In_{0.52}Al_{0.48}As$ and $In_{0.53}Al_xGa_{0.47-x}As$ layers on InP are promising quaternary materials for optoelectronic devices: lasers containing these materials have been realized and show excellent performance. The refractive indices of both $In_{0.52}Al_{0.458}Ga_{0.022}As$ and $In_{0.53}Al_{0.055}Ga_{0.415}As$ are measured for the first time with multiple angle spectroscopic ellipsometry in the wavelength range 280–1900 nm.

1. Introduction

In a previous paper the wavelength dependence of the refractive index of metal-organic vapor phase epitaxy (MOVPE) grown $In_{0.52}Al_{0.48}As$ layers on InP was shown for the first time, determined by single wavelength ellipsometry in the range 400–800 nm [1]. Spectroscopic ellipsometry (SE) is an advantageous nondestructive tool used to determine the optical properties of heterostructures. The two measured angles ψ and Δ at a single wavelength are insufficient to determine more than two unknown parameters (for example, thickness d of the natural oxide layer and refractive index $n - ik$); thus, we applied SE on thick single layer materials or multiple angle of incidence spectroscopic ellipsometry (MAISE) on 25–600 nm thick single layer materials. Using the first method we measured the ψ, Δ values of molecular beam epitaxy (MBE)-grown $In_{0.53}Ga_{0.47}As$ and $In_{0.52}Al_{0.48}As$ layers on InP in the wavelength range 245–845 nm and calculated n, k-dispersion curves and thicknesses of oxide layers [2]. The dispersion curves of $In_{0.53}Ga_{0.47}As$ layers were in very good agreement with those of Kelso *et al.* [3] and our own single wavelength measurements [4]. However, since even 2 μm thick layers of $In_{0.52}Al_{0.48}As$ are more or less transparent above a wavelength of 500 nm, it is nearly impossible to determine refractive indices by this method. Even SE at only one angle of incidence does not yield unique results. MAISE, however, is capable of exact determination of the dispersion curves and the layer thicknesses. For 0.5 μm thick layers of both ternary materials we found that an interface layer between substrate and epilayer exists. due to the exchange of phosphorus and arsenic atoms during the As_4-stabilized oxide desorption procedure prior to the MBE growth.

For exact determination of the refractive indices in the wavelength range 900–1900 nm, we investigated layers with different thicknesses. We found that beween the InP substrate and the layers of $In_{0.52}Al_{0.48}As$, $In_{0.53}Al_{0.405}Ga_{0.065}As$, $In_{0.53}Al_{0.31}Ga_{0.16}As$, $In_{0.53}Al_{0.21}Ga_{0.26}As$, $In_{0.53}Al_{0.16}Ga_{0.31}As$, $In_{0.53}Al_{0.11}Ga_{0.36}As$, and $In_{0.53}Ga_{0.47}As$ an approximately 1 nm thick interface layer exists [5–7]. This interface layer, which we assume to be InAs, was investigated in a different manner: an InP substrate was submitted to the usual desorption process in the MBE-system in the presence of an As-vapor pressure necessary for the growth of InGaAlAs. No growth on the wafer was performed. We observed the same interface layer as after growth on top of the wafer. A fit of the model to the experimenal measurements resulted in the same parameters. This means that, in the wavelength range 400–1900 nm, the interface layer can be fitted very well by the refractive index of InAs with a thickness of 0.5–1.2 nm. This interface layer of InAs was also investigated by high resolution X-ray diffraction (HRXRD) measurements [8]. The same thickness resulted.

2. MBE-growth

The layers were grown in a Varian MOD GENII MBE system on SI InP (100) substrates at growth rates between 0.2 and 0.4 nm s^{-1}. The growth temperatures varied from 500 to 530 °C and the As/(In + Al) b.e.p.

0921-5107/93/$6.00

© 1993 – Elsevier Sequoia. All rights reserved

(beam equivalent pressure) ratio varied from 50 to 70; though during one growth procedure all parameters were constant. The thicknesses of the layers were between 10 and 2000 nm.

3. Spectroscopic ellipsometry

3.1. Instrumentation and measurements

The samples were characterized by two Rudolph Research ellipsometers: the manual 436-type for the whole wavelength range 250–1900 nm with a Babinet Soleil compensator, interference filters, photomultiplier R 928 and IR detector; and the Spectro 2000 with rotating polarizer, monochromator from 250 to 865 nm and computer-assisted measurement and evaluation performance. To determine ψ and Δ with the manual ellipsometer we used the classical four quadrant method [2]. With the same method and the Babinet Soleil compensator instead of the rotating polarizer we discovered that on Spectro 2000 the true ψ, Δ angles at each wavelength are the average of the ψ, Δ values measured at positions A and B, fixed polarizer and fixed analyser [2]. Position A has a fixed polarizer angle 0° and a fixed analyser angle +45°; B has a fixed angle 0° and a fixed analyser angle −45°.

3.2. Evaluation of ellipsometric measurements

The ψ, Δ wavelength scans can be done rapidly with the Spectro 2000, though data interpretation is complex and time-consuming [2]. For determination of the n, k-graphs and thicknesses of layered structures with Fresnel formula, multiple layer models with abrupt interfaces are necessary. In our previous measurement [2, 5–7] we observed that InP has a lower refractive index than any other investigated compound, and that in the wavelength range 250–900 nm, 2 μm layers of $In_{0.53}Ga_{0.47}As$ and quaternary materials with an Al-content less than 0.11 are thick enough to absorb the light completely. For this reason the interface of the layer and the bulk material has no influence. For wavelengths greater than 1000 nm, light penetrates the interface and even reaches the bulk rear side. Therefore, the rear side of the substrate must be rough enough or inclined so that the reflected light from this side cannot influence the measurements.

For determination of the thicknesses of the oxide, quaternary, and interface layers, and the refractive index $n - ik$ of the quaternary materials, a five layer model consisting of air–oxide–quaternary material–interface layer–InP is needed. The refractive indices of the native oxide layer (1.9) [2] of InP and of InAs [3–7, 9] were known and we could determine the wavelength dependent refractive index of each quaternary layer and the three thicknesses in the whole wavelength range 280–865 nm by minimizing the quantity [3]:

$$\sum_{\lambda} [(\psi_m - \psi_c)^2 + (\Delta_m - \Delta_c)^2]$$

where m denotes measured and c denotes calculated values.

Using MAISE we measured our samples at three angles of incidence in the neighborhood of the Brewster angle (approximately 74°). Thus, we had six measured values (three Δ, ψ couples) to calculate the five unknown parameters. Figure 1 gives the n, k-dispersion curves for the quaternary materials $In_{0.52}Al_{0.458}Ga_{0.022}As$ and $In_{0.53}Al_{0.055}Ga_{0.415}As$ in the wavelength range 280–850 nm. The oxide layers were about 1.8 nm and the interface layers about 0.6 nm thick. The thickness of the quaternary layer was 120 nm in the case of $In_{0.52}Al_{0.458}Ga_{0.022}As$ and 220 nm for $In_{0.53}Al_{0.055}Ga_{0.415}As$. Figure 2 shows that, in the wavelength range 550–850 nm, the real part of the refractive

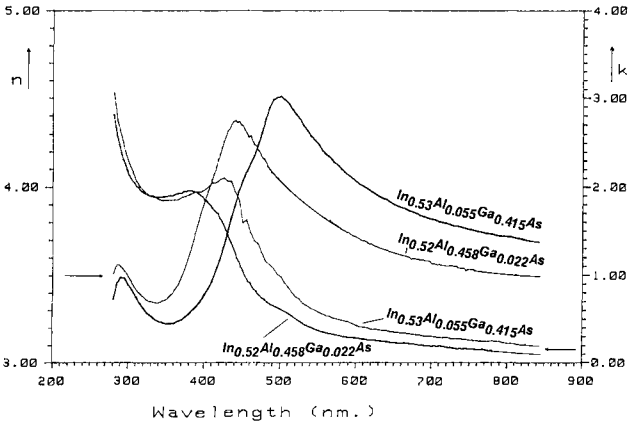

Fig. 1. n,k-Dispersion curves for $In_{0.52}Al_{0.458}Ga_{0.022}As$ and $In_{0.53}Al_{0.055}Ga_{0.415}As$ in the wavelength range 280–850 nm.

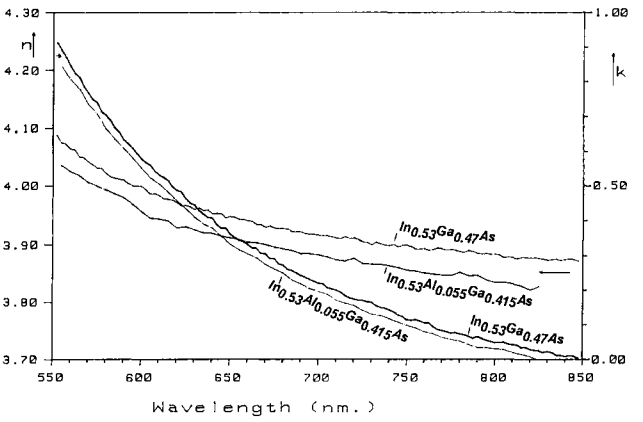

Fig. 2. n,k-Dispersion curves for $In_{0.53}Ga_{0.47}As$ and $In_{0.53}Al_{0.055}Ga_{0.415}As$ in the wavelength range 550–850 nm.

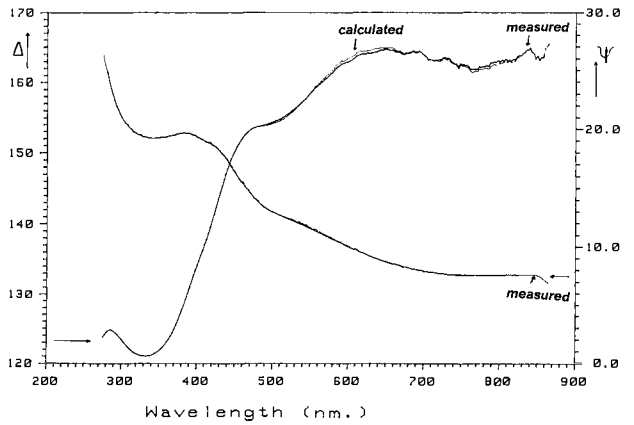

Fig. 3. Calculated and measured Δ, ψ curves at 70°.

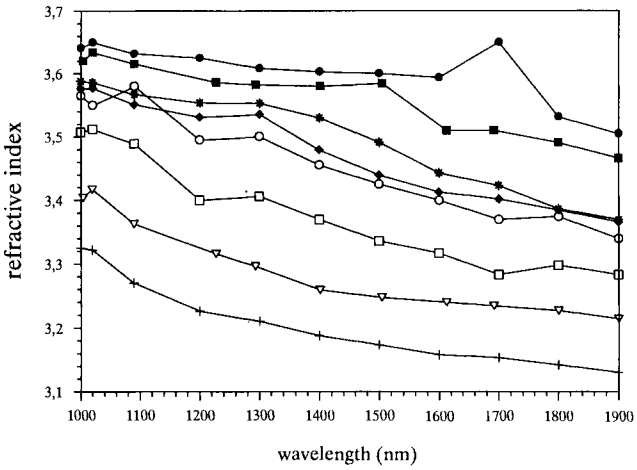

Fig. 4. Refractive indices of $In_{0.53}Ga_{0.47}As$ (●), $In_{0.53}Al_{0.055}Ga_{0.415}As$ (■), $In_{0.53}Al_{0.11}Ga_{0.36}As$ (*), $In_{0.53}Al_{0.16}Ga_{0.31}As$ (◆), $In_{0.53}Al_{0.21}Ga_{0.26}As$ (○), $In_{0.53}Al_{0.31}Ga_{0.16}As$ (□), $In_{0.52}Al_{0.458}Ga_{0.022}As$ (▽) and InP (+) in the wavelength range 1000–1900 nm.

index of $In_{0.53}Al_{0.055}Ga_{0.415}As$ is about 0.03 smaller than that of the ternary $In_{0.53}Ga_{0.47}As$. We controlled our *n*, *k*-dispersion fit by calculating and measuring the sample of 70° and comparing the two Δ, ψ curves, as shown in Fig. 3: the self consistency of the results is demonstrated. Since our investigations on semi-insulating InP and GaAs bulk samples in the IR wavelength regime [2] show very good agreement with the results of Palik [9] for GaAs and those of Pettit and Turner [10] for InP, we believe that our measurements on these materials under investigation are accurate too.

Figure 4 shows the refractive indices in $In_{0.53}Ga_{0.47}As$, $In_{0.53}Al_{0.055}Ga_{0.415}As$, $In_{0.53}Al_{0.11}Ga_{0.36}As$, $In_{0.53}Al_{0.16}Ga_{0.31}As$, $In_{0.53}Al_{0.21}Ga_{0.26}As$, $In_{0.53}Al_{0.31}Ga_{0.16}As$, $In_{0.52}Al_{0.458}Ga_{0.022}As$ and InP in the wavelength range 1000–1900 nm. The refractive indices of all quaternary compositions are higher than those of InP throughout the wavelength range, but lower than those of $In_{0.53}Ga_{0.47}As$. At a wavelength of 1500 nm, for example, the refractive index of $In_{0.53}Al_{0.055}Ga_{0.415}As$ is 3.580 ± 0.005, whereas that of $In_{0.52}Al_{0.458}Ga_{0.022}As$ is 3.250 ± 0.005.

4. Conclusions

The refractive indices of $In_{0.53}Al_{0.055}Ga_{0.415}As$ and $In_{0.52}Al_{0.458}Ga_{0.022}As$ on InP are measured for the first time in the wavelength range 280–1900 nm by spectroscopic ellipsometry. Our results on InP and GaAs are in good agreement with the measurements of Kelso *et al.* [3], Palik [9] and Pettit and Turner [10], but for InAs further measurements must be done. The interface layer which results from the exchange of phosphorus and arsenic atoms during the desorption procedure of the MBE-growth exists and was also found by high resolution X-ray diffraction.

References

1 J. Krauser, C. Bornholdt, H. Künzel, H. W. Dinges, M. Druminski, R. Gessner and K.-H. Zschauer, *Proc. 4th Eur. Conf. Int. Optics*, SETG, Glasgow, 1987, pp. 75–77.
2 H. W. Dinges, H. Burkhard, R. Lösch, H. Nickel and W. Schlapp, *Appl. Surf. Sci., 54* (1992) 477–481.
3 S. M. Kelso, D. E. Aspnes, M. A. Pollack and R. E. Nahory, *Phys. Rev. B, 26* (1982) 6669–6681.
4 H. Burkhard, H. W. Dinges and E. Kuphal, *J. Appl. Phys., 53* (1982) 655–662.
5 H. W. Dinges, H. Burkhard, R. Lösch, H. Nickel and W. Schlapp, *Mater. Sci. Eng. B, 20* (1993) 180–182.
6 H. W. Dinges, H. Burkhard, R. Lösch, H. Nickel and W. Schlapp, ICSFS-6 Paris, 29 June–3 July 1992, *Appl. Surf. Sci., 65/66* (1993) 442–446.
7 H. W. Dinges, H. Burkhard, R. Lösche, H. Nickel and W. Schlapp, ICSE 93, Paris, 11–14 January 1993, *Thin Solid Films*, in press.
8 A. Pöcker and H. W. Dinges, in preparation.
9 E. D. Palik, *Handbook of Optical Constants of Solids*, Academic Press, Orlando, FL, 1985.
10 G. D. Pettit and W. J. Turner, *J. Appl. Phys., 36* (1965) 2081.

Materials Science and Engineering, B21 (1993) 177–180

Room temperature photoreflectance as a powerful tool to characterize the crystalline quality of InAlAs layers grown on InP substrates

S. Monéger, A. Tabata, C. Bru and G. Guillot

Laboratoire de Physique de la Matière (URA CNRS 358), Institut National des Sciences Appliquées de Lyon, Bât 502, 20 Avenue Albert Einstein, 69621 Villeurbanne (France)

A. Georgakilas, K. Zekentes and G. Halkias

Foundation for Research and Technology-Hellas, Institute of Electronic Structure & Laser, PO Box 1527, 711 10 Heraklion, Crete (Greece)

Abstract

The aim of this work is to show that room temperature photoreflectance can give the same indications as low temperature photoluminescence about the crystalline quality of both layers and interfaces. Our samples consist of molecular beam epitaxy InAlAs layers lattice-matched to InP substrates, grown at different growth temperatures and using different InP cleaning temperatures. The photoreflectance broadening parameter (Γ) has been determined and compared with the well-known linewidth broadening of the photoluminescence. Both methods indicate that the best InAlAs crystalline quality is obtained for a growth temperature of 530 °C and an InP surface cleaning temperature of 530 °C.

1. Introduction

During the past decade, InGaAs/InAlAs structures (lattice-matched or strained) grown on InP substrates have been subject of extensive studies for applications in opto-electronic devices and high electron mobility transistors (HEMTs). Opto-electronic applications of this system rely on the small energy band gap of the InGaAs well in InAlAs/InGaAs quantum well structures. The excellent electron transport properties (electron mobility and peak velocity) of the InGaAs and the large conduction-band discontinuity between InAlAs and InGaAs are the main reasons for the high performance of HEMTs fabricated so far.

Looking through the literature, two kinds of material problems appear to be the predominant obstacles for further development of such structures: structural quality of the hetero-interfaces and crystalline quality of the InAlAs layer. Particularly in HEMT structures, where a high resistivity InAlAs buffer layer separates the InGaAs channel from the InP substrate [1, 2], the growth of a high quality InAlAs buffer is essential for the transistor performance. The quality of the InAlAs layer depends strongly on the molecular beam epitaxy (MBE) growth conditions [3–5], and non-optimized growth temperatures seem to cause cluster formation and high concentrations of point defects which degrade the electrical and optical properties. Clustering in the InAlAs layer is attributed to the large difference in the migration rates of the cations [6], and a critical growth temperature under which immiscibility occurs is predicted [7].

Among the various characterization techniques used for the study of the InAlAs crystalline quality, photoluminescence (PL) spectroscopy is one of the most extensively used. For bulk InAlAs, photoreflectance (PR) spectroscopy has been used, to our knowledge, only for the determination of the band gap energy at room temperature [8]. This PR technique is extremely sensitive to interband electronic transitions due to the derivative nature of spectral line shapes [9–11]. Indeed, even at room temperature, it can provide as much information as photoluminescence and photoluminescence excitation which are usually performed at low temperatures.

Hence, the aim of the present work is to use photoreflectance as a tool for systematic evaluation of material quality. The PR broadening parameter (Γ) is compared with corresponding photoluminescence full-width at half-maximum (FWHM) data obtained at low temperature.

2. Experimental details

Our PR experimental arrangement consists of an excitation source of 150 W quartz Wolfram halogen lamp dispersed through a 0.64 m monochromator,

0921-5107/93/$6.00

© 1993 – Elsevier Sequoia. All rights reserved

operating in the 0.5–1.8 μm wavelength range. The monochromatic light is focused onto the semiconductor sample (1×0.6 mm^2 spot), with an energy density up to 3 mW cm^{-2}. The modulation source is provided by a 12 mW He–Ne laser (632.8 nm) and the reflected beam is detected by Si photodiode, operating in photovoltaic mode and connected to a current-to-voltage converter. Low temperature PL measurements have been performed using an argon laser (514.5 nm) with power excitation of 5 W cm^{-2}, focused into a 150 μm diameter spot. Luminescence, analysed through a 0.60 m monochromator, is detected by a liquid nitrogen cooled Ge cell and amplified by conventional lock-in system. For low temperature measurements the samples are mounted within a variable temperature helium cryostat. Both PR and PL setups are driven by a computerized data acquisition and control system.

The analysed samples have been grown by molecular beam epitaxy on semi-insulating InP (100) substrates using a range of growth temperatures, T_g. The undoped 1.5–2.0 μm thick $In_xAl_{1-x}As$ layers have been grown with an indium composition close to the lattice-matched to InP substrate ($x_{In} = 0.52$). The InP surface-cleaning procedure used had been previously optimized in order to increase the smoothness of the etched surface and the reproducibility in oxide desorption [12]. The last stage of the InP surface preparation, prior to InAlAs growth, consisted in a thermal cleaning treatment performed either at 500 °C or at 530 °C. The InP surface-cleaning temperature T_T and the InAlAs growth temperature T_g are listed in Table 1 for each of the samples studied.

3. Fitting procedure

In order to obtain the precise values of the energy transitions and of the broadening parameters, the low-field PR data were fitted with an Aspnes third-derivative functional form (TDFF) [13]. The TDFF relation has the following form:

$$\frac{\Delta R}{R}(E) = Re[C\,e^{i\theta}(E - E_g + i\Gamma)^{-n}] \qquad (1)$$

where C, θ, E_g and Γ are amplitude, phase, critical point energy and broadening parameters, respectively. The broadening parameter Γ is defined as $h/2\pi\tau$, where h is the Planck constant and τ is the finite lifetime of the photogenerated carriers. An energy uncertainty is produced by this finite lifetime, resulting in a broadening of the singularities in the optical spectra. The coefficient n is a factor used to specify the critical point dimension and the perturbation type. Γ is particularly sensitive to the choice of n. For a three-dimensional critical point, such as for a direct band gap semiconductor, n is 2.5 [9] and the modulation spectra are directly related to the third derivatives of the unperturbed dielectric function.

TABLE 1. Growth parameters and PR, PL results on InAlAs layers

Sample	T_T (°C)	T_g (°C)	d (μm)	E_{PR} (eV)	x_{In}	Γ (meV)	FWHM (meV)
A	500	300	2.00	1.485	0.51	32	35
B	500	440	1.65	1.415	0.54	16	28
C	530	480	1.40	1.432	0.53	13	22
D	500	500	2.00	1.382	0.55	18	33
E	530	530	1.65	1.382	0.55	16	15

4. Results and discussion

In bulk InAlAs material, the dominant peak in low temperature photoluminescence measurements arises from the near band gap edge. The position of this PL energy peak is then lower than the band gap E_g by the bound exciton binding energy which is of the order of 3–5 meV [14].

In Fig. 1 we show the PR experimental data and the least-squares fit spectrum for the sample E. As can be seen, the fit obtained with the TDFF is in excellent agreement with the experimental spectrum. The 300 K photoreflectance parameters obtained by the fit, and the corresponding 5 K PL linewidths of the analysed samples are reported in Table 1. The indium composition x_{In} is derived from E_g obtained by PR at 300 K, using the energy band gap composition relation given by Gaskill *et al.* [8] and is in accordance with double-crystal X-ray diffractometry measurements.

Several physical mechanisms can contribute to the spectral broadening observed in PR and PL measurements, such as dislocations, impurities, alloy scattering and phonon absorption processes. For 300 K measurements, the last phenomenon plays a dominant role in pure and perfect crystals. In this way, the parameter Γ can provide indications about the crystalline quality. The evolution of the photoreflectance linewidths (Γ) as well as the PL full-width at half-maximum (FWHM), as a function of the growth temperature, is presented in Fig. 2. This figure indicates that an increase of the growth temperature T_g results in a decrease of the PR linewidth for T_g values below 530 °C. For InAlAs, previous investigations showed that the use of relatively low growth temperatures limits the surface mobility of Al atoms and degrades the crystalline quality [5, 6, 14]. Some theor-

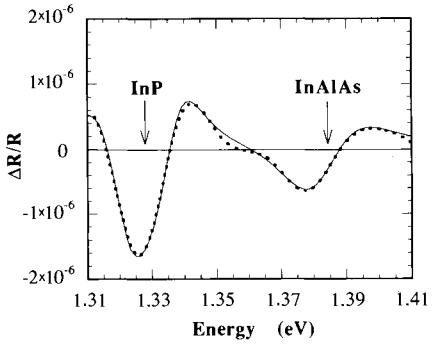

Fig. 1. Room temperature photoreflectance spectrum of sample E. (---) Experimental data, (——) least-squares fit using TDFF formalism.

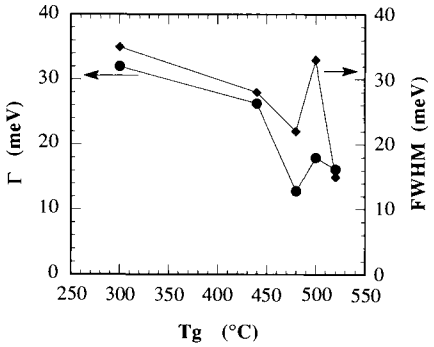

Fig. 2. Variations of the photoreflectance broadening parameter Γ (●) and of the photoluminescence FWHM (◆) *vs.* InAlAs growth temperature T_g.

etical calculations showed that at higher growth temperatures the alloy clustering is reduced [15].

We do not have any clear evidence that the reduction of the linewidth broadening is only related to the alloy homogeneity. The behaviour of the data presented in Fig. 2 is probably related to the decrease of the InAlAs crystalline defects (dislocation, stacking faults) and/or to the improvement of the alloy homogeneity. Transmission electron microscopy (TEM) observations show that the increase of growth temperature up to 530 °C improves the crystalline quality of InAlAs [12]. However, it is worth noting that when the growth temperature is increased beyond 530 °C, a broadening of the PL linewidth was observed [5]. This observation is more likely to be related to the desorption of As atoms from the surface, resulting in the incorporation of As vacancies. The abnormally high value of FWHM (and Γ) for sample D can be explained by an insufficient cleaning of the InP surface, which is supported by previously reported TEM observations [12].

Double crystal X-ray diffractometry measurements have also been performed on these samples. A very strong signal intensity and the lowest FWHM of 33 arcsec were obtained for sample E. On the contrary, a broad weak peak appeared for the low temperature grown sample A. These results give the same indications as PR and PL studies, and confirm our results.

All the samples exhibited very high resistivity, therefore electrical measurements (Hall effect, C–V profile characterization etc.) were not feasible. However, transport properties have been determined on another set of samples Si-doped at 2.5×10^{16} cm^{-3} and a higher mobility μ of 1030 cm^2 V^{-1} s^{-1} has been obtained for $T_g = 530$ °C [16].

The influence of the InP cleaning temperature T_T is not so evident, although we have to notice that the best values of Γ and FWHM are obtained for the two samples C and E which were grown on InP substrates cleaned at $T_T = 530$ °C. Therefore, the trend is to improve the material quality when the InP cleaning temperature is increased to 530 °C. Finally, sample E, which was grown using optimum temperatures ($T_T = 530$ °C and $T_g = 530$ °C), exhibits a state-of-the-art 5 K photoluminescence FWHM of 15 meV, and a PR broadening parameter at 300 K of 16 meV.

5. Conclusions

In this work we have performed PR and PL measurements in InAlAs bulk material grown by MBE on (100) InP substrates using different growth and thermal cleaning temperatures. We have confirmed the trend for InAlAs crystalline quality to improve with increasing growth temperature up to 530 °C, in agreement with previous works. Nevertheless, the importance of this paper was to illustrate that photoreflectance can provide as much information as low-temperature PL, showing that photoreflectance spectroscopy can be a powerful tool for the rapid evaluation of material quality.

Acknowledgments

This work was partially supported by the European Economic Community through ESPRIT Basic Research 3086 project. The authors would like to thank Dr. T. Benyattou and Y. Baltagi for useful discussions.

References

1 G. J. Davies, T. Kerr, C. G. Tuppen, B. Wakefield and D. A. Andrews, *J. Vac. Sci. Technol. B, 2* (1984) 219.
2 J. Massies, J. F. Rochette, P. Etienne, P. Delescluse, A. M. Huber and J. Chevrier, *J. Cryst. Growth, 64* (1983) 101.

3 A. Chin, P. Bhattacharya, W. P. Hong and W. Q. Li, *J. Vac. Sci. Technol. B, 6* (1988) 665.
4 A. S. Brown, M. J. Delaney and J. Singh, *J. Vac. Sci. Technol. B, 7* (1989) 384.
5 D. F. Welch, G. W. Wicks, L. F. Eastman, P. Parayanthal and F. H. Pollak, *Appl. Phys. Lett., 46* (1985) 169.
6 J. Singh, S. Dudley, B. Davies and K. K. Bajaj, *J. Appl. Phys., 60* (1986) 3167.
7 G. B. Stringfellow, *J. Cryst. Growth, 58* (1982) 194 and references cited therein.
8 D. K. Gaskill, N. Bottka, L. Aina and M. Mattingly, *Appl. Phys. Lett., 56* (1990) 1269.
9 F. H. Pollak and O. J. Glembocki, *Proc. Soc. Photo-Optical Instrumentation Engineers*, SPIE, Bellingham, vol. 2, *946*, 1988, p. 2.
10 O. J. Glembocki and B. V. Shanabrook, *Superlattices & Microstructures, 5* (1989) 603.
11 N. Bottka, D. K. Gaskill, R. S. Sillmon, R. Henry and R. Glosser, *J. Electron. Mater., 17* (1988) 2.
12 F. Peiro, A. Cornet, A. Herms, J. R. Morante, A. Georgakilas and G. Halkias, *J. Vac. Sci. Technol. B, 10* (1992) 2148.
13 D. E. Aspnes, *Surf. Sci., 37* (1973) 418.
14 E. Tournié, Y. H. Zhang, N. J. Pulsford and K. Ploog, *J. Appl. Phys., 70* (1991) 7362.
15 J. E. Oh, P. K. Bhattacharya, Y. C. Chen, O. Aina and M. Mattingly, *J. Electron. Mater., 19* (1990) 435.
16 A. Georgakilas, A. Christou, G. Halkias, K. Zakentes, N. Kornilios, C. Papavassiliou, A. Dimoulas, F. Peiro, A. Cornet, S. Ababou, A. Tabata and G. Guillot, in D. N. Buckley and V. Swaminathan (eds.), *Proc. 16th State-of-the-Art Program on Compound Semiconductors (SOTAPOCS), 181st Electrochemical Society Fall Meeting*, St. Louis, USA, 1992, vol. 20, p. 141.

Materials Science and Engineering, B21 (1993) 181–184

Effects of deep levels and Si-doping on GaInP material properties investigated by means of optical methods

Q. Liu, U. Quedeweit, F. Scheffer, A. Lindner, W. Prost and F. J. Tegude

Solid State Electronics Department, SFB 254, Duisburg University, Kommandantenstr. 60, W-4100 Duisburg 1 (Germany)

Abstract

Deep level characteristics in undoped and Si-doped $Ga_{0.51}In_{0.49}P$ layers has been investigated using photocapacitance and photoluminescence (PL) methods. $Ga_{0.51}In_{0.49}P$ layers were grown by metalorganic vapor-phase epitaxy in the temperature range 600–730 °C and with doping levels from 3.9×10^{17} cm^{-3} to 1×10^{19} cm^{-3}. A dominant deep level with an activation energy of about 0.98 eV was observed in all undoped samples. Further deep levels have been found with activation energies in the range 0.43–0.50 eV. Undoped samples grown at 650 °C exhibit the lowest trap concentration, with one remaining level at 0.89 eV only. A direct link of PL intensity to non-radiative recombination due to deep centers is demonstrated. Undoped samples exhibit the highest PL intensity at the growth temperature of lowest deep level density. Si doping suppresses the main deep level at $\Delta E_T = 0.89$ eV and results in an increase of PL intensity up to $N_D = 2 \times 10^{18}$ cm^{-3}. Only deep levels in the energy range 0.41–0.50 eV were detectable. No DX-like effects due to Si doping were observed.

1. Introduction

$Ga_{0.51}In_{0.49}P$ alloys lattice matched to GaAs substrates have a band gap up to 1.9 eV at room temperature, a low surface recombination velocity [1], and exhibit a decreased oxidation tendency in comparison to AlGaAs [2]. Therefore they are excellent candidates for visible-light emitting as well as high-speed device applications. It is expected that the DX and other deep centers associated with Al-containing semiconductors must be significantly reduced in this material. There are some reports about deep level investigation in GaInP by means of the DLTS (deep level transient spectroscopy) measurements and PPC (persistent photoconductivity) [3–6]. There is no detailed work on the relationship between deep levels and the optical quality of this material in term of (non-)radiative recombination. It was already known that the photoluminescence (PL) intensity is sensitive to the non-radiative recombination associated with deep levels. The non-radiative recombination in PL will be emphasized by using low excitation power and increases with increasing the sample temperature. PL measurements were preponderantly made on undoped and p-type GaInP [7–10]. In this paper, the photocapacitance method was used to study the deep level characteristics of Si-doped and undoped $Ga_{0.51}In_{0.49}P$ layers grown under various growth conditions. PL measurements at room temperature were carried out in order to examine their optical quality in dependence of deep centers. We present the connection between the different deep center properties measured by photocapacitance and photoluminescence results.

2. Experimental details

$Ga_{0.51}In_{0.49}P$ layers used in this study were grown by low-pressure metalorganic vapor-phase epitaxy on exactly (001) oriented semi-insulating GaAs substrates. Growth was performed at a rate of 1.4 μm h^{-1} with substrate temperatures from 600 to 730 °C and V/III ratios of 190 or 380. The GaInP epilayer thickness is in the range 0.7–1.4 μm. The source materials were trimethylgallium (TMGa), trimethylindium (TMIn), arsine (AsH_3) and phosphine (PH_3). For all samples reported here, the lattice mismatch was found to be less than $\pm 2 \times 10^{-3}$ by use of X-ray diffraction analysis. Following the suggestion of Paloura *et al.* [4] that Si is better than S in suppressing the DX-like center in GaInP, Si doping was carried out [11] with disilane (Si_2H_6) diluted in hydrogen (H_2). Samples with Si doping [11] in the range 10^{17}–10^{19} cm^{-3} were investigated in this study. Capacitance-voltage (C–V) and van de Pauw Hall measurements were used to determine the carrier concentration. For the purpose of photocapacitance measurements Ge/Au/Ni/Au was used for ohmic contacts and gold semi-transparent

0921-5107/93/$6.00

© 1993 – Elsevier Sequoia. All rights reserved

Schottky barriers were prepared using electron-beam evaporation. The area of the diodes was 200×200 μm^2.

The photocapacitance measurements were carried out on reverse biased Schottky diodes at about 80 K in order to neglect the thermal emission of deep centers. The change of the capacitance (ΔC) in the space charge zone beneath the anode is measured during illumination with monochromatic light. The trap concentration N_T can be derived using the following relationship:

$$N_T \approx 2 \cdot n \cdot \Delta C / C_0$$

where n and C_0 are the free-carrier concentration and steady-state capacitance in the dark, respectively. The activation energies (ΔE_T) of deep centers can be obtained by determining the threshold energy, where the capacitance signal begins to change. The photoluminescence measurements were performed using Ar^+ laser excitation. The emission spectra were analyzed by a 0.64 m monochromator and GaAs photomultiplier.

3. Results and discussion

Figures 1(a) and 1(b) show the typical photocapacitance spectra of a reverse biased GaInP/GaAs diode in the wavelength ranges 1800–500 nm (0.69–2.48 eV) and 3600–1500 mm (0.345–0.828 eV), respectively. The spectrum shown in Fig. 1(a) was recorded on an undoped sample grown at 650 °C with a V/III ratio of 190, while that shown in Fig. 1(b) was recorded on a Si-doped sample with an electron concentration of 1.6×10^{18} cm^{-3}. The labels D and A in the figures indicate the type of traps: donor and acceptor, respectively. The changes in capacitance at about 932 nm in Fig. 1(a) and 1820 nm in Fig. 1(b), labelled F, are caused by optical filters.

The photocapacitance results on the undoped samples grown at various temperatures show generally very low deep center concentrations. A dominant deep level with an activation energy $\Delta E_T = 0.89$ eV and trap concentrations in the range 2.6×10^{13}–5×10^{14} cm^{-3} was observed in all undoped samples. Samples grown at 650 °C and below exhibit only this deep level. The lowest trap concentration of 2.6×10^{13} cm^{-3} was obtained on the sample grown at 650 °C. Lower or higher growth temperatures result in a higher trap concentration. Further deep levels with activation energies in the range 0.43–0.50 eV and trap concentrations in the range 3×10^{13}–2×10^{14} cm^{-3} were observed on samples grown at higher temperatures. Si-doped samples with the doping range 3.9×10^{17}–1×10^{19} cm^{-3} were also studied. The deep level at 0.89 eV is

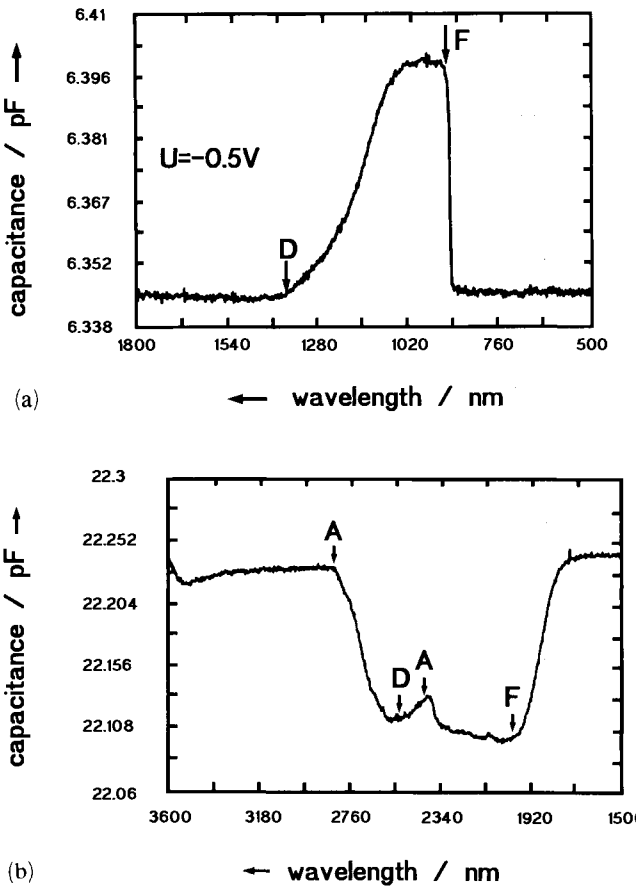

Fig. 1. Photocapacitance spectra of $Ga_{0.51}In_{0.49}P$ layers. (a) Undoped sample with the diode reverse biased at −0.5V in the wavelength range of 1800–500 nm. (b) Si-doped sample with the diode reverse biased at −1.0V in the wavelength range of 3600–1500 nm. The label F indicates the optical filter.

suppressed by Si doping. Only levels with activation energies in the range 0.41–0.50 eV were observed. No PPC was detectable in Si-doped samples as shown elsewhere [11]. The Si-related deep levels or DX centers well known in n-AlGaAs epilayers [12], the typical characteristics of which are an increase of shallow donor-induced deep level concentration with increasing shallow donor concentration and persistent photoconductivity effect, were not found in this material.

The optical quality is investigated by room temperature PL measurements on Si-doped $Ga_{0.51}In_{0.49}P$ samples and undoped samples grown under various temperatures. It was known that deep centers can bring about a quick drop of PL intensity [13]. Figure 2 shows the PL intensity of non-intentionally doped samples as a function of growth temperature. We have found the PL intensity to be maximum for the sample grown at 650 °C. The sample grown at 730 °C has no room temperature PL signals at all. This agrees with the photo-

capacitance results, where the sample grown at 650 °C exhibits the lowest and the sample grown at 730 °C exhibits the highest deep center concentration. Figure 3 shows the PL results of Si-doped $Ga_{0.51}In_{0.49}P$ measured at room temperature. The blue-shift of the peak wavelength in highly doped samples contributes to the Burstein–Moss effect but not to the disordering due to Si doping [14]. The FWHM of PL peaks increased monotonely as the Si doping increased. The PL intensity dependence on Si-doping is shown in more detail in Fig. 4. In contrast to the expected behavior, we found an increase of PL intensity as the Si doping increased up to 2×10^{18} cm^{-3}. A similar effect was also observed on Te-doped $Ga_{0.68}In_{0.32}P$ grown by liquid phase epitaxy (LPE) [10]. This behavior is attributed to the fact that, up to this Si-doping level, the radiative recombination is governed by the deep level at the activation energy $\Delta E_T = 0.89$ eV. This level, however, is suppressed by Si doping, as shown by our photocapacitance measurements. As a result, the radiative recombination increases. Above 10^{18} cm^{-3} the expected drop in PL intensity with increasing carrier concentration occurs, although up to $N_D = 1 \times 10^{19}$ cm^{-3} a distinct PL peak at room temperature can be observed (see Fig. 3).

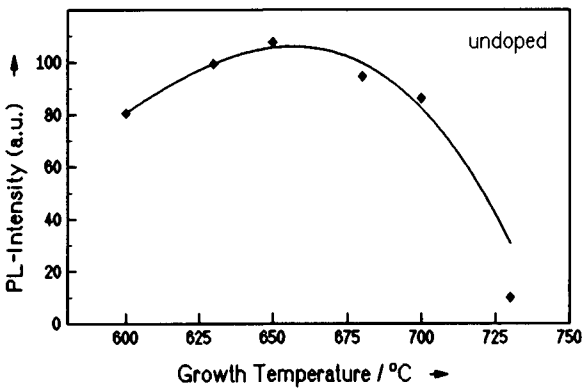

Fig. 2. PL intensity of undoped $Ga_{0.51}In_{0.49}P$ at room temperature as a function of growth temperature.

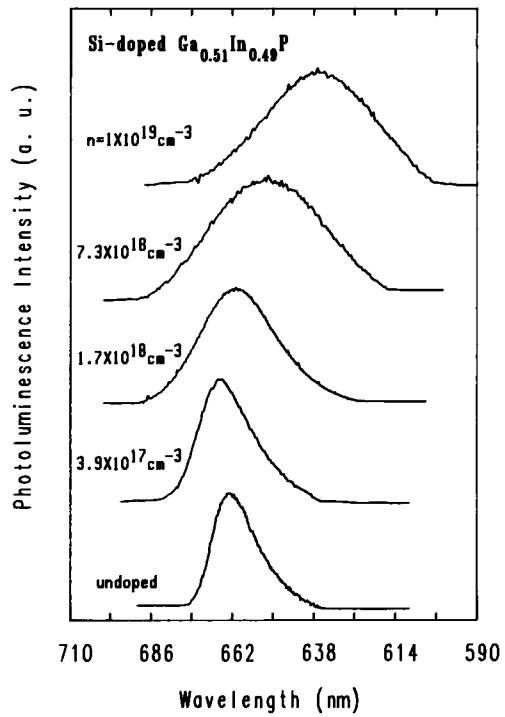

Fig. 3. Photoluminescence spectra of Si-doped $Ga_{0.51}In_{0.49}P$ at room temperature in the region of the GaInP exciton emission. The excitation power density was 3.6 W cm^2. The peak intensities are normalized.

4. Conclusions

Deep levels and their relations to growth parameters in $Ga_{0.51}In_{0.49}P$ layers were analyzed using photocapacitance and photoluminescence measurements. A dominant deep level in undoped GaInP was found at $\Delta E_T = 0.89$ eV, while in Si-doped samples, deep levels with activation energies in the range 0.43–0.50 eV were observed. We have also found a close connection between deep centers and the optical quality referred to as the (non-)radiative recombination in this material. The sample with the lowest trap concentration, grown at 650 °C, exhibits the highest PL intensity. Lower or higher growth temperatures result in higher trap concentrations. The absence of the deep level at 0.89 eV in Si-doped GaInP improved the PL quality. No DX-like effects due to Si doping have been observed either in photocapacitance or PL results. A distinct PL peak at room temperature can be observed even in the highly doped sample with an electron concentration up to 1×10^{19} cm^{-3}.

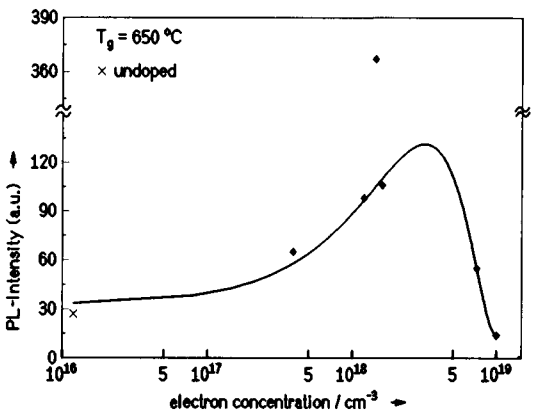

Fig. 4. PL intensity at room temperature as a function of Si-doping level in $Ga_{0.51}In_{0.49}P$. The excitation power density was 1.5 W cm^2.

Acknowledgment

This work was supported by Ministerium für Wissenschaft und Forschung des Landes Nordrhein-Westfalen.

References

1 J. M. Olsen, R. K. Ahrankiel, D. L. Dunlavy, B. Keys and A. E. Kibbler, *Appl. Phys. Lett.*, *55* (12) (1989) 1208.
2 D. Biswas, N. Debbar, P. Bhattacharya, M. Razeghi, M. Defour and F. Omnes, *Appl. Phys. Lett.*, *56* (9) (1990) 833.
3 S. Ben Amor, L. Dmowski, J. C. Portal, N. J. Pulsford, R. J. Nicholas, J. Singleton and M. Razeghi, *J. Appl. Phys.*, *65* (7) (1989) 2756.
4 E. C. Paloura, A. Ginoudi, G. Kiriakidis and A. Christou, *Appl. Phys. Lett.*, *59* (24) (1991) 3127.
5 K. Sugiura, K. Doman, M. Sugawara, C. Anayama, M. Kondo, T. Tanahashi and K. Nakajima, *J. Appl. Phys.*, *70* (9) (1991) 4946.
6 E. C. Paloura, A. Ginoudi, G. Kiriakidis, N. Frangis, F. Scholz, M. Moser and A. Christou, *Appl. Phys. Lett.*, *60* (22) (1992) 2749.
7 S. Naritsuka, Y. Nishikawa, H. Sugawara, M. Ishikawa and Y. Kokubun, *J. Electron Mater.*, *20* (9) (1991) 687.
8 S. C. Lu, M. C. Wu, C. Y. Lee and Y. C. Yang, *J. Appl. Phys.*, *70* (4) (1991) 2309.
9 M. C. DeLong, W. D. Ohlsen, I. Viohl, P. C. Taylor and J. M. Olsen, *J. Appl. Phys.*, *70* (5) (1991) 2780.
10 Chyuan-Wei Chen and Meng-Chyi Wu, *J. Appl. Phys.*, *70* (9) (1991) 5040.
11 F. Scheffer, F. Buchali, A. Lindner, Q. Liu, A. Wiersch and W. Prost, *J. Cryst. Growth*, *124* (1992) 475–482.
12 T. Ishikawa, T. Yamanoto and K. Kondo, *Jpn. J. Appl. Phys.*, *25* (6) (1986) L484–L486.
13 C. J. Nuese, A. G. Sigai, M. S. Abrahams and J. J. Gannon, *J. Electrochem. Soc.*, *120* (1973) 956.
14 Q. Liu, H. Lakner, F. Scheffer, A. Lindner and W. Prost, *J. Appl. Phys.*, *73* (6) (1993) 2770.

Optical properties of GaSb–AlSb heterostructures grown by molecular beam epitaxy

B. Lambert, Y. Toudic, Y. Rouillard, M. Baudet, B. Guenais, B. Deveaud, I. Valiente and J. C. Simon

France Telecom, CNET/LAB/OCM, BP 40 Route de Trégastel, 22301 Lannion (France)

Abstract

In the first part of this paper we discuss the optimization of the growth conditions of molecular beam epitaxy GaSb layers. Then we present preliminary results for GaSb–AlSb multiple quantum wells which have one excitonic absorption line peaking at about 1.5 μm at room temperature. Finally we present a 10 pair Bragg reflector which shows 97% reflectivity. These preliminary results allow the GaSb–AlSb system to be considered for optoelectronic devices.

1. Introduction

In this communication we report the properties of antimonide heterostructures. These structures are interesting owing to their optoelectronic properties near 1.5 μm. In the first part of this paper we discuss the optimization of homoepitaxied GaSb layers, then we study the properties of GaSb–AlSb multiple quantum wells (MQWs), and finally we report the performance of an (Al)GaSb–AlSb Bragg mirror.

2. Experimental details

The layers were grown on a (100) GaSb substrate (or on semi-insulating GaAs wafers) in a 32P molecular beam epitaxy (MBE) Riber chamber equipped with an antimony cracker cell for Sb and a valved arsenic cracker cell for As. Thus the majority of molecules created are As_2 and Sb_2. The growth temperature was 550 °C which is considered to be optimum for GaSb growth [1, 2]. Photoluminescence experiments (continuous wave PL) were performed using an Ar^+ laser operating at 514.5 nm and a cooled Ge photodetector with conventional lock-in detection. The excitation density reaching the layer was about 10 W cm^{-2}. X-ray data were collected using two different experimental techniques: a θ–2θ goniometer and a double-crystal diffractometer (DDX). Transmission electron microscopy (TEM) was performed with a JEOL 1200 EX operating at 120 keV on (110) cross-sections.

3. Homoepitaxy

The GaSb layers were grown at a substrate temperature of 550 °C [1, 2]. As already checked by Lee *et al.* [3], it is very important to obtain good quality GaSb samples to determine the boundary between the "Ga-rich" and the "Sb-rich" growth conditions. In our case, where Sb_2 molecules are obtained preferentially (owing to the use of a cracker cell) a $P(Sb_2)/P(Ga)$ ratio of 10 has been found to be the best value for a growth rate of 0.5 μm h^{-1}. The optical properties were characterized by PL experiments performed at $T = 2$ K. In Fig. 1 we observe narrow (full-width at half-maximum (FWHM) of 1.7 meV for Be_4) and intense excitonic lines (Be_n with $n = 1$, 2, 3 and 4). To our knowledge this FWHM value is the narrowest ever published for layers grown in MBE chambers [3]. Under "Ga-rich" growth condi-

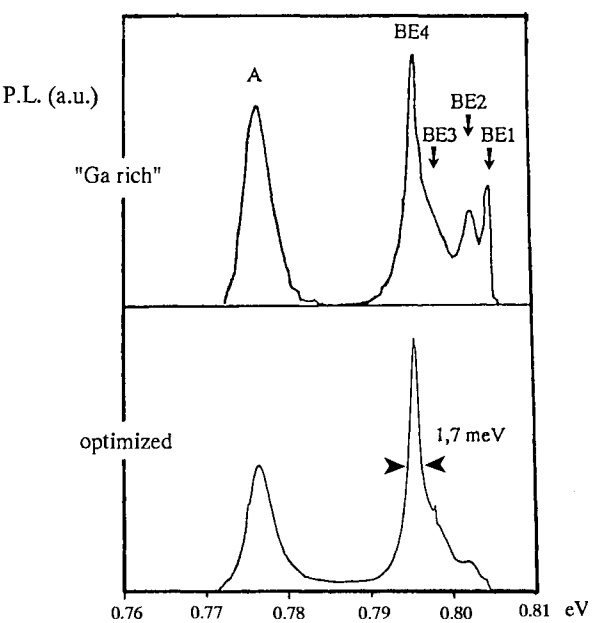

Fig. 1. Photoluminescence spectra of homoepitaxied GaSb at 2 K showing the transitions discussed in the text.

0921-5107/93/$6.00

© 1993 – Elsevier Sequoia. All rights reserved

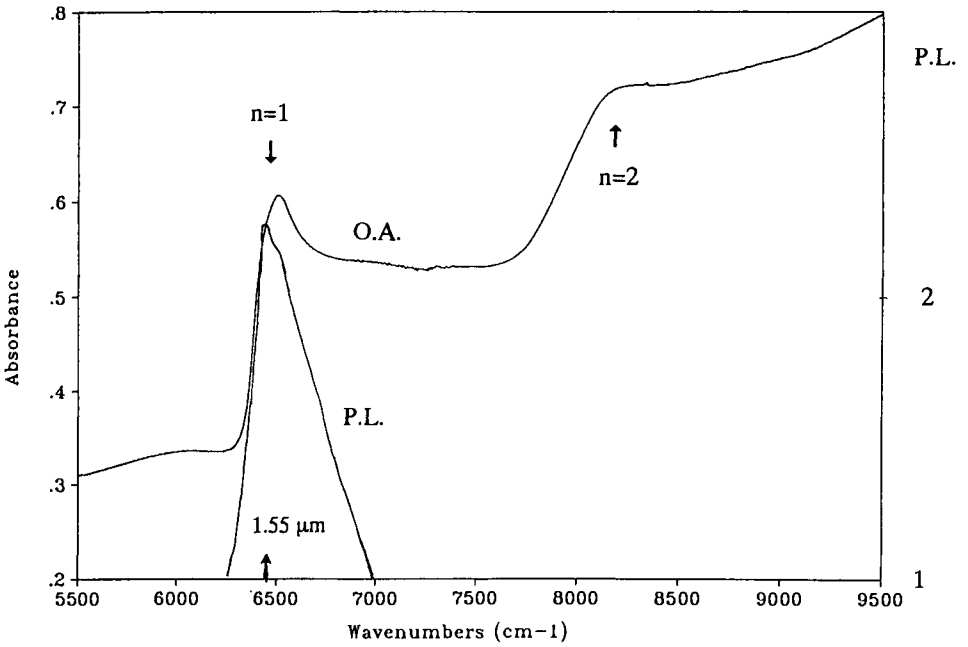

Fig. 2. Optical absorption (OA) and photoluminescence (PL) spectra at 290 K of a MQW epitaxied on a GaAs substrate.

tions we observe the different BE_n exciton lines. At the boundary we observe only the BE_4 line [4] and the A line intensity corresponding to the recombination electron–"structural" acceptor is minimized. Under "Sb-rich" conditions the intensity of every line is decreased (not shown in Fig. 1) owing to degradation of the crystallographic properties of the GaSb layer [3, 4]. Hall effect measurements of GaSb layers grown on a semi-insulating GaAs substrate give approximately the following results at room temperature: $N_A - N_D = 10^{16}\ cm^{-3}$ and $\mu = 800\ cm^2\ V^{-1}\ s^{-1}$.

Time resolved PL experiments performed on a 1 μm width double heterostructure (DHS) cladded with two thin AlGaSb barriers indicate a non-radiative time $\tau_{nr} = 3$ ns. Such values are typically obtained on GaAs DHS grown by MBE.

4. GaSb–AlSb multiple quantum well on GaAs substrate

The GaSb–AlSb MQWs are interesting because they show, for a well width L_Z of about 100 Å, one excitonic line peaking at about 1.5 μm at room temperature (Fig. 2). We grew these MQWs on both (100) GaSb and GaAs substrates. The latter substrate is transparent at 1.5 μm and so it is possible to work in the transmission mode (Fig. 2, OA). Moreover, the technological processes are now well established for GaAs substrates and so, for example, it is now possible to obtain good quality bistable microresonators [5]. The optical absorption (OA) spectrum is typical of MQWs with 2D

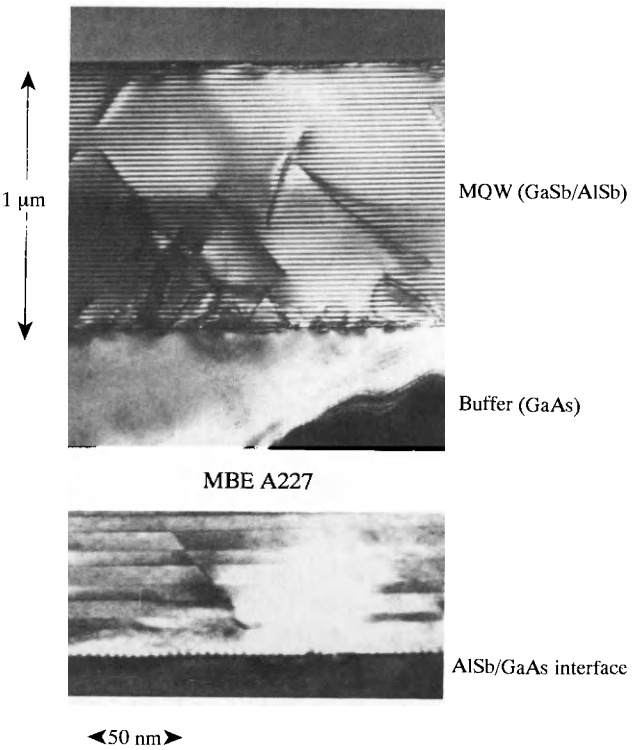

Fig. 3. TEM image of a GaSb–AlSb MQW.

state density and excitonic peaks (labelled $n = 1$ and $n = 2$). The arrows correspond to a simple envelope function type calculation for a well width $L_Z = 95$ Å.

Analysis of transmission electron micrographs indicates that relaxation occurs mainly by misfit disloca-

tions lying in the first GaSb–GaAs interface [6] and that the density of threading dislocations tends to decrease as a function of the MQW thickness (Fig. 3). Also revealed in Fig. 3 is the flatness of the GaSb–AlSb interfaces. Double diffraction X-ray diagrams show that the quality of the "relaxed" MQW is similar to that of the "strained" MQW grown on a GaSb substrate. Moreover the θ–2θ diagram (Fig. 4) shows different superlattice related satellites (up to the sixth order). From simulations [7] we have predicted the positions and the relative intensities of the lines and deduced the structural parameters ($L_Z = 95.5$ Å and $L_B = 117$ Å). We also deduced the "residual" strain parallel to the interfaces ($\varepsilon_{//\mathrm{AlSb}} = -3.398 \times 10^{-3}$ and $\varepsilon_{//\mathrm{GaSb}} = 3.071 \times 10^{-3}$).

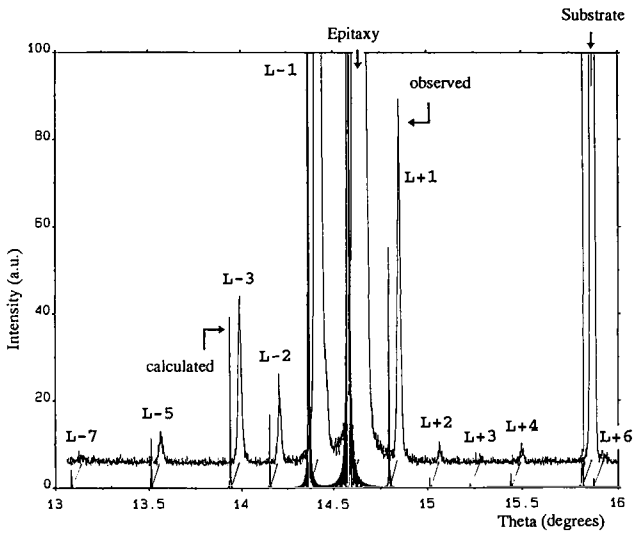

Fig. 4. X-ray θ–2θ diagram of a GaSb–AlSb MQW. The lines correspond to calculations.

Continuous photoluminescence experiments performed at 290 K indicate that there is no shift between the PL and the OA peaks (Fig. 2, PL). Time resolved PL experiments give us a non-radiative time $\tau_{nr} = 1$ ns at 290 K. The FWHM values of excitonic lines observed in continuous wave PL at liquid He temperatures *vs.* the well width L_Z are shown in Fig. 5. The full lines correspond to a simple calculation where we take into account one and two monolayer interface fluctuation respectively. A comparison with the results collected in the literature [8–14] indicates that our "relaxed" MQW structures on GaAs substrates are as good as the "matched" structures on GaSb substrates. This is stimulating because we only have preliminary results and the growth conditions have to be optimized for relaxed structures, as reported recently by Ivanov *et al.* [15].

These different results on GaSb–AlSb MQWs indicate that antimonides are "good relaxed systems" and that the MQW structures grown on GaAs substrates are of good optoelectronic quality.

5. (Al)GaSb–AlSb Bragg mirror on GaAs substrate

The difference in optical index of GaSb and AlSb [16] is about a factor of two better than beween InP and InGaAsP quaternary alloy. It is known that it requires 20 pairs of InP/InGaAsP layers to achieve a reflectivity of only 95% [17]. In order to test the suitability of the (Al)GaSb–AlSb system for obtaining effi-

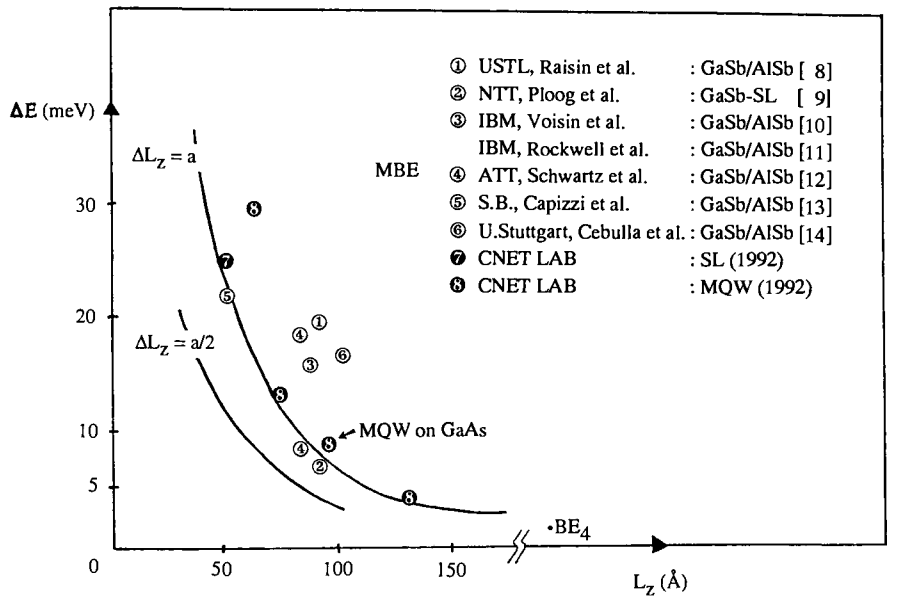
ΔE (meV)
ΔLz = a
ΔLz = a/2
MBE
① USTL, Raisin et al. : GaSb/AlSb [8]
② NTT, Ploog et al. : GaSb-SL [9]
③ IBM, Voisin et al. : GaSb/AlSb [10]
IBM, Rockwell et al. : GaSb/AlSb [11]
④ ATT, Schwartz et al. : GaSb/AlSb [12]
⑤ S.B., Capizzi et al. : GaSb/AlSb [13]
⑥ U.Stuttgart, Cebulla et al. : GaSb/AlSb [14]
⑦ CNET LAB : SL (1992)
⑧ CNET LAB : MQW (1992)
MQW on GaAs
•BE4
Lz (Å)

Fig. 5. FWHM of excitonic lines in different MQW samples [8–14] *vs.* the well width L_Z at liquid He temperatures.

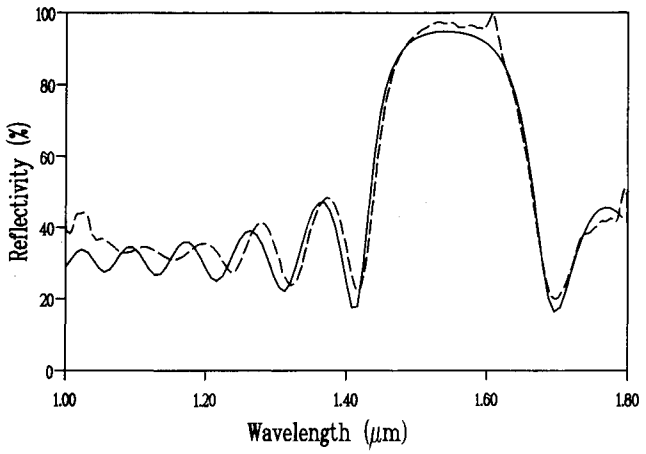

Fig. 6. Reflectivity *vs.* wavelength: experimental results (– – –) and simulation (——).

cient Bragg reflectors, we grew a structure with 10 pairs of (Al)GaSb/AlSb layers on a GaAs substrate. To decrease the dislocation concentration in the layer we grew a GaSb–AlSb MQW buffer layer with a thickness of 1122 Å. Low temperature PL shows an intense peak at 1.082 eV with an FWHM of 8 meV. This result indicates the good quality of the (Al)GaSb layers. Optical absorption measurements taken at room temperature allow us to measure an optical band gap energy of 1.016 eV (1.22 μm) for the (Al)GaSb layer. This gap value could be adjusted in the future to 1.45 μm to increase the index difference between the $\lambda/4n$ layers.

The DDX diagrams, as already mentioned above, show the good quality of these "relaxed" structures. From the θ–2θ diagram and simulations, we have measured structural parameters $L_Z = 1051 \pm 20$ Å and $L_B = 1213 \pm 20$ Å. Figure 6 shows the results of spectral reflectivity (dashed line) and theoretical calculation (full line). For the calculation we used refractive index measurements reported in ref. 16 and thickness values given above. Calculated and measured maximum reflectivities are 96% and 97% ± 2% respectively.

6. Conclusion

Various devices have been investigated in the literature to take advantage of both the MQW and vertical cavity properties (MQW vertical cavity structure). We have shown in this article that with an MQW layer as the "active" layer and efficient Bragg mirrors used to form a "cavity" it is possible to realize optical devices working at about 1.5 μm in the GaSb–AlSb system epitaxied on GaAs wafers.

References

1 J. R. Söderström, D. H. Chow and T. C. McGill, *Mater. Res. Soc. Symp. Proc., 145* (1989) 409.
2 S. V. Ivanov, A. A. Budza, A. A. Dzamasvili, P. S. Kop'ev, B. Ya Melster, V. M. Ustinov and S. V. Shapodnikov, *Proc. 6th European Conf. on Molecular Beam Epitaxy, 1991*, Tampere University of Technology, Tampere, p. EP5.
3 M. Lee, D. J. Nocholas, K. E. Singer and B. Hamilton, *J. Appl. Phys., 59* (1986) 2895.
4 E. T. R. Chidley, S. K. Haywood, A. B. Henriques, N. J. Mason, R. J. Nicholas and P. J. Walker, *Semicond. Sci. Technol., 6* (1991) 45.
5 J. L. Oudar, R. Kuozelewicz, B. Sfez, D. Pellat and R. Azoulay, *Superlattice & Microstructures, 12* (1992) 89.
6 A. Rocher, F. W. O. Da Silva and C. Raison, *Rev. Phys. Appl., 25* (1990) 957 (in French).
7 P. Auvray, M. Baudet and A. Regreny, *J. Appl. Phys., 62* (1987) 456.
8 C. Raisin, L. Lassabatère, C. Allibert, B. Girault, G. Abdel-Fattah and P. Voisin, *Solid State Commun., 61* (1987) 17.
9 K. Ploog, Y. Ohmori, H. Okamoto, W. Stolz and J. Wagner, *Appl. Phys. Lett., 47* (1985) 384.
10 P. Voisin, C. Delalande, M. Voos, L. L. Chang, A. Segmuller, C. A. Chang and L. Esaki, *Phys. Rev. B, 30* (1984) 2276.
11 B. Rockwell, H. R. Chandrascktar, M. Chandrasktar, F. H. Pollark, H. Shen, L. L. Chang, W. I. Wang and L. Esaki, *Surf. Sci., 228* (1990) 332.
12 G. P. Schwartz, G. J. Gualtieri and W. A. Sunder, *J. Cryst. Growth, 102* (1990) 147.
13 M. Capizzi, C. Coluzza, A. Frova, U. Cebulla and A. Forchel, *Appl. Phys. Lett., 55* (1989) 772.
14 U. Cebulla, A. Forchel, G. Tränkle, G. Güffiths, S. Subbanna and H. Kroemer, *Superlattices & Microstructures, 3* (1987) 429.
15 S. V. Ivanov, P. D. Altukhov, T. S. Argunova, A. A. Bakunand and A. A. Budza, *Semicond. Sci. Technol., 8* (1993) 347.
16 C. Alibert, M. Skouri, A. Joullié and M. Benouna, *J. Appl. Phys., 69* (1991) 3208.
17 F. S. Choa, K. Tai, W. T. Tsang and S. N. G. Chu, *Appl. Phys. Lett., 59* (1991) 2820.

Absorption coefficient and exciton oscillator strengths in InGaAs/InP multi-quantum wells

C. Arena and L. Tarricone*
Dipartimento di Fisica, viale delle Scienze, 43100 Parma (Italy)
F. Genova and C. Rigo
CSELT, via G. Reiss Romoli 274, 10184 Torino (Italy)

Abstract

The excitonic properties of InGaAs/InP multi-quantum-well systems grown by chemical beam epitaxy have been investigated with absorption measurements in the temperature range 8–300 K and in the spectral region 0.775–1.550 eV. In this region, the excitonic resonances corresponding to $n=1$, $n=2$ interband transitions, and the steplike behaviour of the two-dimensional density of states have been clearly observed. By fitting the lineshape of the excitonic features with Gaussian functions the most noteworthy parameters are discussed. The energy position of the peak changes as a function of temperature, according to the relation known for the InGaAs energy gap. Moreover, the full width at half maximum is deduced and is discussed in terms of an intrinsic contribution plus a thermal broadening due to the interaction with LO phonons. The integrated area of the excitonic peak examined seems to be temperature independent. On the other hand, the integrated area decreases when the well width increases, because of the shrinkage of the 1s exciton wave function. A ratio of the oscillator strengths related to light, and heavy hole excitons equal to 0.6 has been determined, in accordance with the theoretical prediction.

1. Introduction

One of the more remarkable consequences of the two-dimensional confinement provided by quantum well structures is the high enhancement of excitonic absorption. In addition, the application of a moderate electric field results in considerable wavelength shift (quantum Stark effect) and an overall increase in the absorption coefficient. These effects, first extensively studied in GaAs quantum well structures, find applications in optical fibre communication systems. Recently GaAs matched to InP has appeared as a promising system for applications in the near-IR region. In fact, the ground state exciton energy can be tuned within the wavelength region 1.30–1.55 μm by controlling structural parameters such as well width and composition of the ternary alloy.

Since the first report of InGaAs/InP quantum wells grown by low pressure metal-organic chemical vapour deposition (LPMOCVD) [1], the need to increase the structural quality of these materials has led to the use of a number of different growth techniques [2, 3]. Indeed an accurate control of thickness and composition, and an improvement in the interface abruptness can influence significantly the electrical and optical properties of the structures. In particular, chemical beam epitaxy (CBE) emerges as one of the more successful growth techniques [4]. In this work InGaAs/InP quantum well structures grown by CBE have been characterized in detail by optical measurements and the results show the superior quality of CBE.

2. Experimental details

The InGaAs/InP multi-quantum well (MQW) heterostructures, nominally undoped and prepared by CBE were grown by alternating $In_xGa_{1-x}As$ and InP layers onto an S-doped InP substrate. A nominal indium molar fraction $x=0.51$ was used. This composition corresponds to lattice mismatch (0.17%) and gives rise to strain effects in the wells, as discussed later.

In Table 1 the most important parameters of the MQW structures are reported, where n is the number of periods, L_w is the well width and L_b is the barrier width.

The MQW region is sandwiched between undoped buffer and cladding InP layers of 0.3 μm thickness. Details on the specimen growths are given in ref. 5. The

*Author to whom correspondence should be addressed.

0921-5107/93/$6.00
© 1993 – Elsevier Sequoia. All rights reserved

TABLE 1. Characteristic parameters of MQW structures used

Sample	n	L_w(Å)	L_b(Å)	x_{In}
qw191	66	94	80	51
qw300	40	63	100	51
qw370	12	68	250	51
qw371	22	25	385	51

InP substrate and buffer layers were not removed, because of their transparency near the fundamental edge of the InGaAs. This fact is an advantage since no etching is required to open an optical access through the substrate and so possible stresses to the structure are avoided. In order to perform optical measurements in the temperature range 8–300 K, a close cycle Cryophysics cold-tip cryostat was used.

The absorption coefficient spectra of all the samples studied were deduced both from transmission and absorbance measurements. For the transmission measurements, the exciting beam of a halogen lamp, chopped at a frequency of 120 Hz and dispersed by a 0.5 m Spex monochromator, was focused on the MQW samples. The light transmitted through the samples was detected using a PbS detector and the signals processed by conventional lock-in technique. Wavelength scanning and data acquisition were controlled by an Apple 2E computer. A Varian 2390 spectrophotometer was used to perform absorbance measurements and data were collected on an Olivetti computer.

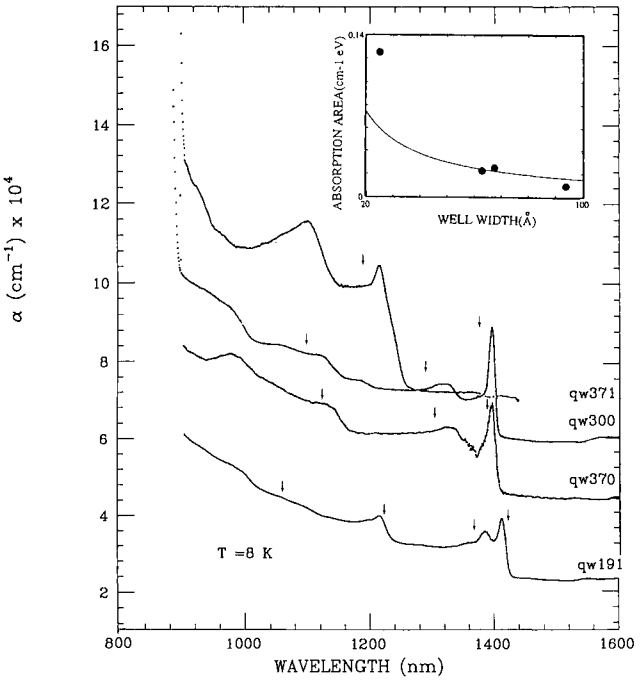

Fig. 1. Optical absorption coefficient spectra at $T = 9$ K as calculated from transmission and absorbance measurements for all the samples. The vertical arrows show the energy position of the main peaks as deduced by theory. In the inset the shrinkage of the 1s exciton with well width decrease is shown.

3. Results and discussion

Transmission and absorbance measurements in the spectral region between the absorption edge of InGaAs and InP have been performed. The absorption curves were calculated from the transmission and/or absorbance experiments according to the relation given in ref. 6, and assuming an equal reflectivity for the two facets (30%). The internal reflections at the InGaAs/InP interfaces were neglected since the refractive index of these materials is quite similar. Figure 1 shows the absorption spectra obtained at 8 K on all the samples. The absorption coefficient spectra exhibit the steplike behaviour characteristic of the two-dimensional density of states and excitonic resonances at the onset of the steps. Besides, the electron-heavy hole $n = 2$ exciton peak E_{2hh-e} becomes less well defined as the temperature increases, while electron-light and heavy hole $n = 1$ excitonic peaks ($E_{1lh-e}E_{1hh-e}$) are clearly observed up to 300 K. Sometimes in the high energy region of the spectra, the free exciton absorption peak of InP is observed also up to relatively high temperature (200 K). This latter experiment provided clear evidence of the high quality of the present materials. As expected, the number of excitonic peaks increases with increasing well width. The attribution of the peaks has been possible by comparing the calculated band-to-band energy transitions with the experimental values, having considered the influence of the excitonic binding energy [7]. The calculation was carried out by solving the Schrödinger equation for a particle in a finite potential well within an effective mass approximation. The band non-parabolicity was taken into account by considering the Luttinger parameters; the contribution due to the strain was calculated to be of 6.64 meV. The details of the calculations are given elsewhere [8].

Actually the well is not rectangular in shape but somewhat trapezoidal because of fluctuation of the composition at the interface. In fact, incorporation of As in the barriers and formation of InGaAsP at the interfaces occurs even using a very fast flux switching system [9]. Moreover, a valence band discontinuity $\Delta = 0.55$ has been assumed, even though several values of the conduction-valence band offset between InGaAs/InP are reported in literature [7].

However, a satisfactory agreement between theoretical and experimental transition energies is observed for all samples, as shown by vertical arrows in Fig. 1. In

fact, the comparison between the experimental and theoretical results gives an uncertainty of about 1% in the energy peak position. It is also possible to determine from the experimental data the quantum well width to an accuracy of about 10%.

Using Gaussian lineshape modelling for the $n=1$ hh–e exciton, a semiempirical fit has been performed on the low energy side of the absorption peaks. In addition, a best fit of the absorption spectra over the temperature range studied for sample qw191 has been made by considering Gaussian functions for the peaks related to the $n=1$hh–e and lh–e transitions respectively, superimposed on a more or less broadened two-dimensional continuum, as given by the relation reported in ref. 10.

In Fig. 2 the energy peak position is given as a function of temperature for all the samples, and it is shown that the temperature dependence of InGaAs bulk gap is followed (solid line). In the inset all the main exciton peak positions of sample qw191 are reported as a function of temperature.

Figure 3 shows the values of the full width at half-maximum (FWHM) for temperatures varying between 8 K and room temperature. It may be noted that in general the FWHM gradually increases as the well width decreases. Using the semiempirical law proposed by Chemla [11], the experimental data have been fitted (solid lines). Thus the FWHM may be taken to be composed of two main terms: a constant Γ_0 plus a contribution $\Gamma(T)$ proportional to the density of thermal LO phonons with proportionality constant Γ_1, *i.e.*

$$\Gamma=\Gamma_0+\Gamma_1/[\exp(\hbar\omega/kT)-1]$$

where an appropriate LO phonon energy $\hbar\omega=32.2$ meV [12] has been assumed. The Γ_0 parameter is primarily made up of three broadening factors, *i.e.* composition fluctuations, interface roughness and non-periodicity. The relatively large Γ_0 value of the structure with thinner wells (qw371) is due to the large influence of monolayer thickness fluctuations at the heterointerfaces.

If a comparison is made with the GaAs/GaAlAs system, the values $\Gamma_0=4.7$ meV, $\Gamma(300\text{ K})=9$ meV are usually reported for GaAs MQW samples [10], and excitonic absorption peaks are narrower than in InGaAs MQW structures. This fact is probably explained by the increased difficulty encountered in growing ternary compound layers, compared with the binary ones. The effects of dimensionality on the oscillator strength of the $n=1$ exciton have been considered. When L_w is smaller than the exciton Bohr radius a_b (which in the InGaAs system is about 178.4 Å [7]), the overlap amplitude of the electron and hole generally increases with the decrease of the well layer thickness L_w. Consequently the oscillator strength of excitons will rapidly increase. In addition, the area of

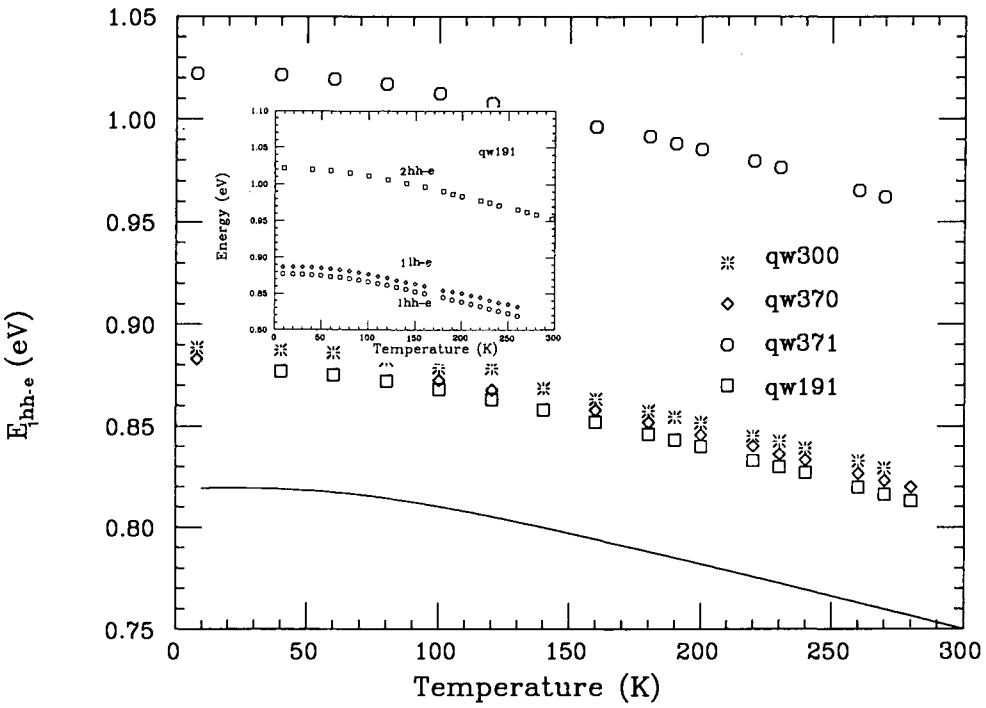

Fig. 2. Energy location of the E_{1hh-e} peak for all the samples as a function of temperature. The solid line concerns the InGaAs energy gap. In the inset the main peak positions of sample qw191 are shown.

the absorption peak is proportional to the oscillator strength. In the inset of Fig. 1, the values of the integrated area are reported as a function of the well width. In agreement with experiments first performed for the GaAs/AlAs system [13], it is evident that the area of the heavy exciton peak does not follow the $1/L_w$ dependence (solid line). Finally, in Fig. 4, the thermal behaviour of the integrated area of the main exciton peak (E_{1hh-e}) is shown for all the samples measured and is seen to be almost constant over the temperature range studied. In the inset of Fig. 4, the ratio of the absorption area of the $n=1$ light and heavy excitons, reported as a function of temperature, shows a constant behaviour. The ratio of the oscillator strengths can be expressed as:

$$f_{lh}/f_{hh} = \|M_{cv}\|^2_{lh}/\|M_{cv}\|^2_{hh}(\mu^2_{lh}/\mu^2_{hh})$$

where μ_{lh} and μ_{hh} are respectively the reduced mass of light and heavy exciton, and $\|M_{cv}\|_{lh}$ and $\|M_{cv}\|_{hh}$ are the matrix elements between conduction and light and heavy valence band states. By assuming $\|M_{cv}\|_{lh}/\|M_{cv}\|_{hh} = \frac{1}{3}$ [14], it can be proven that the experimental value of the ratio $f_{lh}/f_{hh} = 0.6$ is in good agreement with the theoretical prediction.

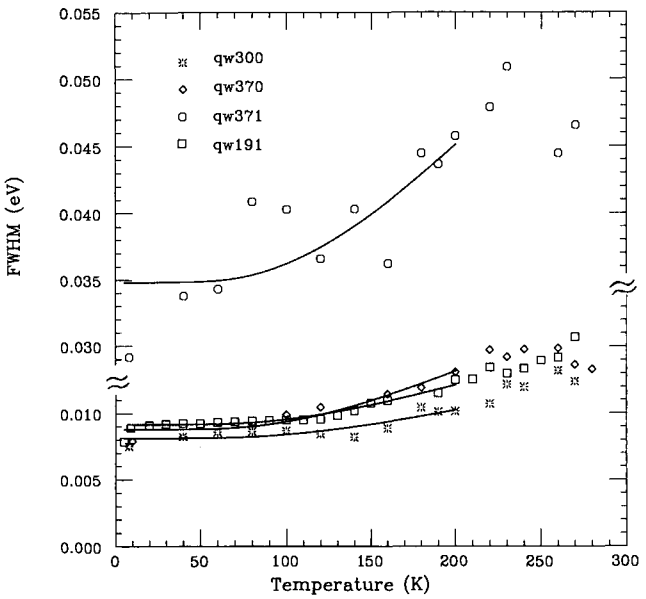

Fig. 3. The full width at half-maximum (FWHM) of the E_{1hh-e} peak as deduced from a Gaussian lineshape of the excitonic peak; the best fits, assuming $\hbar\omega = 32.2$ meV are the solid lines.

4. Conclusions

Transmission spectroscopy applied to InGaAs/InP heterostructures is confirmed as a powerful technique in investigating the MQW electronic properties which are strongly related to the two-dimensional excitonic features. With a lineshape modelling, parameters related to the structural and compositional quality are deduced, and the shrinkage of the 1s wave function is

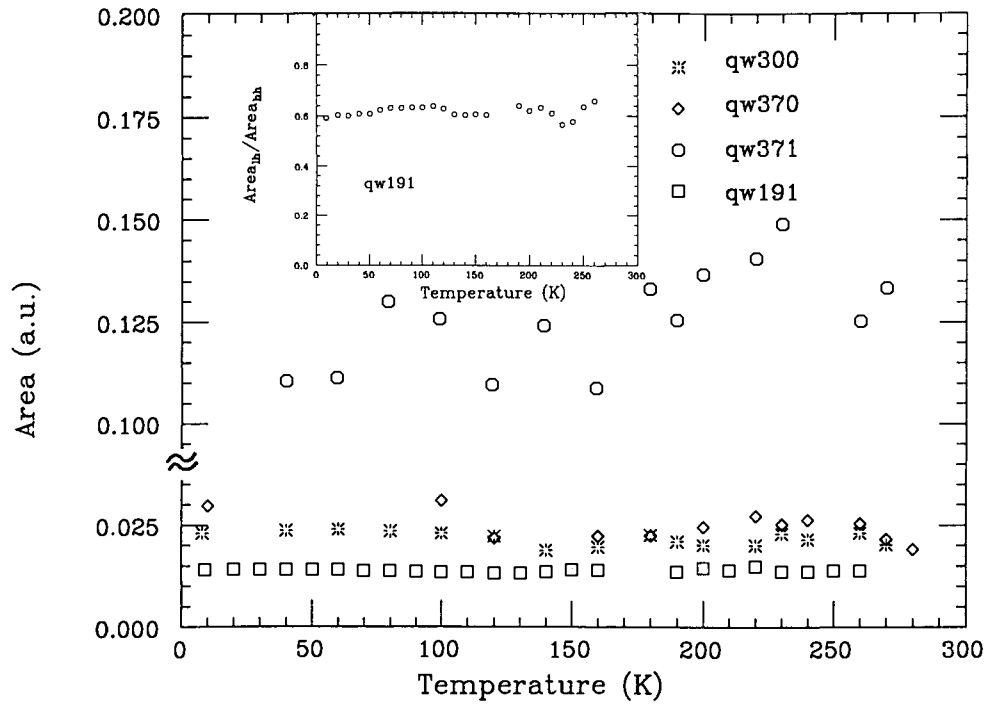

Fig. 4. Temperature dependence of the integrated area of the E_{1hh-e} absorption peak; in the inset the ratio $Area_{lh}/Area_{hh}$ is plotted.

shown. A satisfactory agreement between experimental and calculated energy of excitonic transitions supports the quality of this theoretical approach. The meaning of the ratio of the oscillator strengths of light and heavy excitons is briefly discussed and the experimental value $f_{lh}/f_{hh} = 0.6$ seems to be consistent with the theoretical one. These considerations prove also the excellent performance of CBE.

Acknowledgments

This work has been partially supported by the Progetto Strategico Elettronica dello Stato Solido-CNR. The authors wish to thank Professor R. Capelletti for her collaboration in the absorbance experiments and B. Rotelli for her help with the measurements. One of the authors (C.A.) wishes to thank CSELT which finances her fellowship.

References

1 M. Razeghi, J. P. Hirtz, U. O. Ziemelis, C. Delalande, B. Etienne and M. Voos, *Appl. Phys. Lett., 43* (1983) 585.
2 M. S. Skolnick, L. L. Taylor, S. J. Bass, A. D. Pitt, D. J. Mowbray, A. G. Cullis and N. G. Chew, *Appl. Phys. Lett., 51* (1987) 24.
3 D. J. Westland, A. M. Fox, A. C. Maciel and J. F. Ryan, *Appl. Phys. Lett., 50* (1987) 839.
4 W. T. Tsang, E. F. Schubert, S. N. G. Chu, K. Tai and R. Sauer, *Appl. Phys. Lett., 50* (1987) 540.
5 F. Genova, A. Antolini, L. Francesio, L. Gastaldi, C. Lamberti, C. Papuzza and C. Rigo, *J. Cryst. Growth, 120* (1992) 333.
6 J. Filipowicz, C. Ghezzi and L. Tarricone, *Solid State Commun., 74* (1990) 533.
7 J. P. Pocholle, M. Razeghi, J. Raffy, M. Papuchon, C. Weisbuch, C. Puech, A. Vandenborre, J. L. Bezy, L. Heinrich and J. E. Vimont, *Rev. Phys. Appl., 22* (1987) 1239.
8 S. H. Pan, H. Shen, Z. Hang, F. H. Pollak, W. Zhuang, Q. Xu, A. P. Roth, R. A. Masut, C. Lacelle and D. Morris, *Phys. Rev. B, 38* (1988) 3375.
9 G. Salviati, C. Ferrari, L. Lazzarini, F. Genova, C. Rigo, G. M. Schiavini and F. Taiariol, *VIII Conf. on Microscopy of Semiconducting Materials, Oxford, 1993, Inst. Phys. Conf. Serv.*, in press.
10 D. S. Chemla, D. A. B. Miller, P. W. Smith, A. C. Gossard and W. Wiegmann, *IEEE J. Quantum Electron., 20* (1984) 265.
11 D. S. Chemla and D. A. B. Miller, *J. Opt. Soc. Am. B, 2* (1985) 1155.
12 S. Selci, A. Cricenti, M. Righini, C. Petrillo, F. Sacchetti, F. Alexandre and G. Chiarotti, *Solid State Commun., 79* (1991) 561.
13 Y. Masumoto, M. Matsuura, S. Tarucha and H. Okamoto, *Phys. Rev. B, 32* (1985) 4275.
14 Y. Masumoto, M. Matsuura, S. Tarucha and H. Okamoto, *Surf. Sci., 170* (1986) 635.

Materials Science and Engineering, B21 (1993) 194–197

MBE growth and properties of high quality Al(Ga)InAs/GaInAs MQW structures

H. Künzel, J. Böttcher, A. Hase* and C. Schramm

Heinrich-Hertz-Institut für Nachrichtentechnik Berlin GmbH, D-10587 Berlin (Germany)

Abstract

Molecular beam epitaxy-grown Al(Ga)InAs/GaInAs single quantum well and multiple quantum well structures, comprising ternary and quaternary barriers, were investigated for laser device applications. Barrier materials of excellent lateral uniformity and high optical and crystalline quality, as well as low interface charge densities of the Al(Ga)InAs/GaInAs heterojunctions, were achieved. The influence of buffer configuration and barrier composition on the well emission properties was studied.

1. Introduction

The realization of advanced laser structures is favored by the use of quantum well (QW) structures to form the active region. Besides the necessity of low band gap material of high optical quality for the well layers, the optical quality of the barrier material and cladding layers as well as the interface properties of the QWs play an important role for the achievement of high laser performance. This study presents results on Al(Ga)InAs/GaInAs QW structures lattice-matched to InP using elemental source molecular beam epitaxy (MBE) growth which is much less developed for laser materials than for electronic devices such as HEMTs.

2. MBE growth procedure

The samples were grown in an MBE system configured for independent growth of AlInAs and GaInAs lattice-matched to InP by application of two In effusion cells. Growth of AlGaInAs of any composition can therefore be accomplished by superposition of the two ternary materials by adjusting the growth rates [1]. The typical growth rate for the ternary constituents was 1 μm h^{-1}. Growth was performed under slightly As-stabilized conditions with the As flux adjusted according to ref. 2, *e.g.* a BEP(V/III)-ratio of 15 was used in conjunction with a growth temperature of 500 °C. Owing to the two In cells used no growth interruptions at heterointerfaces were necessary, but were optionally applied for smoothing the growth front.

3. Characteristics of Al(Ga)InAs layers

For a standard growth temperature (T_s) of 500 °C, GaInAs and AlGaInAs (x_{Ga} = 0.05/0.14/0.18/0.24) layers with microscopically smooth surfaces have been obtained. Only the ternary AlInAs layers exhibit some slight characteristic surface roughness [3]. Nevertheless, the full-width at half-maximum (FWHM) values of the DCXRD spectra amounting to 17, 18 and 20 arcsec for GaInAs, Al(Ga)InAs and AlInAs, respectively, are indicative of high crystalline quality for all material compositions. These values measured on 1.5 μm thick layers agree with the best published values and theoretical expectations [4].

The optical properties of the materials were characterized by 10 K photoluminescence (PL) measurements. Single emission peak spectra were obtained irrespective of alloy composition. The FWHM values monotonously decrease from 17 meV to 14–12 meV and to 4.5 meV for AlInAs, Al(Ga)InAs with increasing Ga-content (x_{Ga} = 0.14–0.24) and GaInAs, respectively. Moreover, the FWHM values were found to be constant for growth temperatures between 500 and 570 °C indicating bound exciton emission. For growth temperatures below 500 °C spectral broadening due to band-to-acceptor transitions occurs [3], with the integral PL intensity being only moderately dependent on T_s. Figure 1 shows corresponding results for AlInAs and AlGaInAs (x_{Ga} = 0.24). An increase of the PL intensity by a factor of roughly 10 can be achieved

*On leave from: Universität Stuttgart, Pfaffenwaldring 57, D-70550 Stuttgart, Germany.

0921-5107/93/$6.00

© 1993 – Elsevier Sequoia. All rights reserved

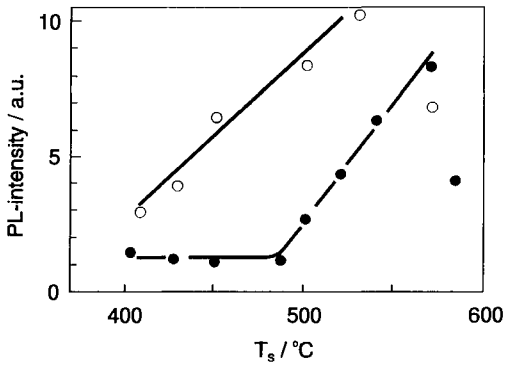

Fig. 1. Growth temperature dependence of 10 K integral PL intensity of Al(Ga)InAs layers. ○, $Al_{0.24}Ga_{0.24}In_{0.52}As$; ●, $Al_{0.48}In_{0.52}As$.

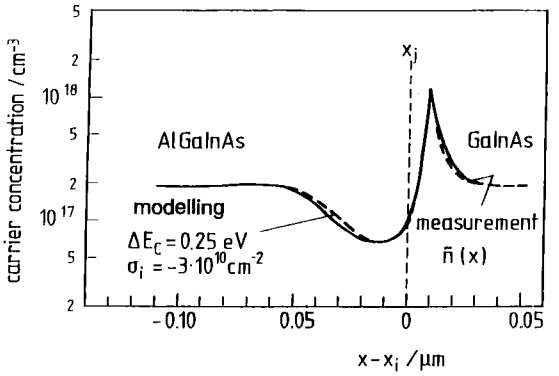

Fig. 2. Measured and calculated carrier profiles across an isotype N-AlGaInAs/n-GaInAs heterojunction with $x_{Ga} = 0.18$.

by increasing T_s from 500 to 570 °C. Further increase causes the PL intensity and FWHM to degrade due to an increasing incorporation of In-vacancy related defects [3]. The only moderate improvement attainable with increasing T_s as compared to AlGaAs indicates that the Al migration rate at 570 °C may not be sufficient to fully suppress point defects acting as non-radiative recombination centers.

4. Interface properties of Al(Ga)InAs/GaInAs heterojunctions

C/V profiling measurements on isotype n-doped heterojunctions were performed to evaluate the fixed interface charge density as a measure of the interface quality. Al(Ga)InAs/GaInAs structures were used with the Al-containing material on top to facilitate the formation of Schottky contacts. The measured carrier distribution across the heterojunction was fitted using a method as described in [5]. An optimum fit was obtained by using the interface charge density and the conduction band discontinuity as the only fitting parameters. A representative example for an Al(Ga)InAs/GaInAs junction with $x_{Ga} = 0.18$ is shown in Fig. 2. Excellent agreement between the measured and the calculated carrier distribution is obtained with a fixed interface charge density of -3×10^{10} cm^{-2} and $\Delta E_c = 0.25$ eV corresponding to 60% of the band gap difference. Similar results have been obtained for ternary AlInAs/GaInAs junctions. In this case, however, the fixed interface charge density was determined to be higher by roughly a factor of five which nevertheless is still indicative of high quality interfaces. This higher interface density may be attributed to either some small amount of alloy clustering present in AlInAs grown at 500 °C, or to slight surface roughness observed, or to alloy composition fluctuations near the interface.

The influence of the MBE growth conditions on the interface properties was studied on ternary junctions. The interface density seems to be hardly affected by T_s as long as growth is carried out above 450 °C. Below this value a trend towards higher interface charge densities can be noticed. Furthermore, growth interruptions at the heterojunction interface do not deteriorate the interface quality. Interruption times as long as 20 min were applied without systematically affecting the interface properties. The interface charge density remained below 2×10^{11} cm^{-2} in all cases. Flux transients, on the other hand, were found to have a strong effect on the interface quality indicating that compositional fluctuations near the interface are of major importance. Suppression of flux transients led to a reduction of the interface charge density by one order of magnitude.

5. Optical quality of Al(Ga)InAs/GaInAs quantum well structures

To ensure high PL yield of all QW structures investigated growth was performed at 550 °C. SQW structures with either ternary or quaternary barriers were composed of 8.5, 6.2, 3.5 and 1.8 nm thick wells (multiples of the monolayer thickness) separated by 100 nm thick barriers. Buffer layers of different design were employed. In Fig. 3 the emission spectra of SQWs with quaternary barriers with $x_{Al} = 0.24$ are depicted; the three different spectra refer to different buffer layers. Four emission lines centered at 0.88, 0.915, 0.985 and 1.13 eV corresponding to the well thicknesses given above are detected. The weak structure at 1.17 eV is due to emission from the barrier material. The spectrum shown in Fig. 3(a) was taken from a sample grown without any buffer directly onto the substrate. In this case the 8.5 nm well, which is located at the bottom of the structure, appears to be even more strongly deteri-

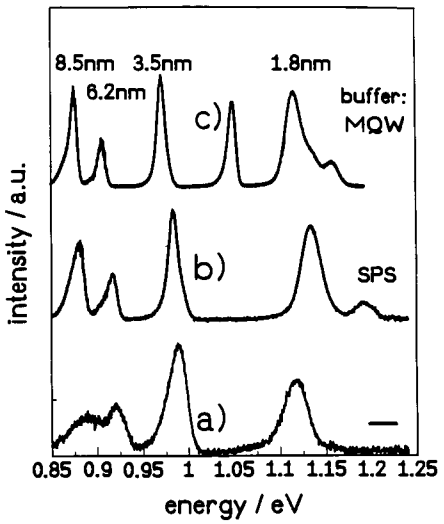

Fig. 3. 10 K PL spectra of GaInAs/AlGaInAs SQWs grown on different buffer layers: (a) no buffer (directly on the InP substrate), (b) 10 period GaInAs/AlInAs SL (2.5 nm/2.5 nm), and (c) 20 period GaInAs/AlInAs MQW (2.5 nm/25 nm).

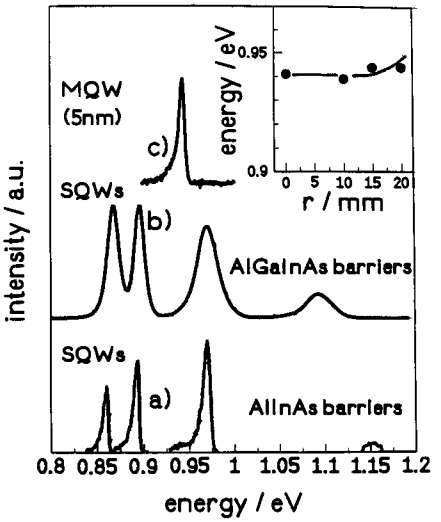

Fig. 4. 10 K PL spectra of (a) GaInAs/AlInAs SQWs, (b) GaInAs/Al(Ga)InAs SQWs (poor quality barriers), and (c) 5 period GaInAs/Al(Ga)InAs MQW. The inset shows the lateral emission uniformity of the MQW sample.

orated than the thinner SQWs in this layer sequence. Introduction of a thin superlattice GaInAs/AlInAs buffer structure, which does not give rise to any additional emission peak, strongly improves the SQW emission. The FWHM values of the individual peaks decrease and the peak intensities increase correspondingly (Fig. 3(b)). The integral intensity remains almost unchanged. In Fig. 3(c) the PL spectra can be seen to be further improved by replacing the superlattice by a QW structure with a twofold number of periods as compared to the superlattice buffer. The related emission from this buffer incorporating nominally 2.5 nm thick well appears at 1.05 eV. Using this optimum buffer configuration the FWHM value for the 3.5 nm SQW is reduced typically from 25 meV for the unbuffered structure to 10 meV though the integral PL intensity is not affected. This improvement may be attributed to the smoother growth surface of the QW buffer giving rise to very abrupt SQWs. In addition, the comparison of Figs. 3(a) and 3(b) clearly shows that the first SQW is strongly deteriorated if no pre-well is grown. Incorporating additional AlInAs layers in the buffer layer was found not to further improve the emission properties of the SQWs.

In all spectra, no splitting of the SQW emission was observed, suggesting the absence of long-range monolayer fluctuations. Furthermore growth interruptions up to 120 s either at both interfaces or at only the GaInAs/Al(Ga)InAs interface did not cause spectral splitting effects. An indication that the interfaces consist of islands much smaller than the exciton radius is also given by the fact that the small lateral thickness variation existing across the wafer results only in a shift of the emission energy.

In Fig. 4 the emission spectra of SQWs with ternary and quaternary barriers, with $x_{Al} = 0.24$, are compared. In Fig. 4(a) the PL spectrum of a sample with ternary barriers is depicted. All SQW peaks are intense and narrow except for the 1.8 nm SQW emission at 1.13 eV. Owing to the vertical homogeneity of the ternary barriers, the interface quality, and an appropriate buffer the FWHM values for the PL peaks are as small as 5.6, 6.9, 7.8 and 14 meV for the 8.5, 6.2, 3.5 and 1.8 nm SQWs and are comparable to the best published values [6, 7]. Excellent agreement with the data given in [6] is obtained even though no suppression of flux transients, in contrast to [6], was applied. Since well material composition fluctuations present in our samples due to flux transients do not broaden the PL lines compared to suppressed transients [6], it can be concluded that this effect is masked by a different dominating broadening mechanism. The record data of Mishima *et al.* [7] demonstrate that the use of specially refined In and Al sources has an additional positive effect on the FWHM values. This suggests that the barrier material is the dominant source for the linewidth broadening observed on the GaInAs/AlInAs SQW structures in this work.

Replacement of the ternary barriers by quaternary barriers led to a broadening of the SQW emission peaks in the early stage of our investigation. A corresponding spectrum is shown in Fig. 4(b). While the FWHM values for the thicker SQWs (8.5 and 6.2 nm) are only moderately increased to approximately 14

meV, drastically larger values are obtained for the narrower wells (28 meV for the 3.5 nm well). The emission line of the 1.8 nm thick well overlaps with that of the barrier material. As indicated by a smeared onset of the barrier emission in photoluminescence excitation measurements [8] and by broad DCXRD layer reflects, the poor quality of the barrier material in terms of vertical homogeneity is considered responsible for the broadened SQW emission. As a result of the developed high quality barrier material as described above, spectra as shown in Fig. 3(c) could be achieved. The FWHM values routinely amount to 10 meV for all SQWs investigated except for the 1.8 nm well (22 meV). The best values achieved are even equivalent to those for ternary barriers (*e.g.* 6.7 meV for a 3.5 nm well) in agreement with the best published values given in ref. 9.

For use of GaInAs/Al(Ga)InAs QWs as the active region in laser structures, high lateral and vertical homogeneity is a stringent requirement to precisely control the emission wavelength. The PL spectrum of an MQW structure composed of five 5 nm thick wells (suited for 1.3 μm emission) separated by 10 nm barriers is shown in Fig. 4(c). An FWHM value of the MQW luminescence at 10 K of 6.7 meV is achieved in agreement with ref. 9. The inset shows the lateral uniformity of the PL peak emission energy which can be seen to be constant to within 5 meV across a 2 in wafer. From a comparison with a GaInAs reference layer the PL shift can be inferred to be almost exclusively due to thickness variation which is calculated to be $< 3\%$.

6. Summary

Based on Al(Ga)InAs materials of high crystalline and optical quality as well as excellent interface properties as indicated by a low interface charge density, high quality QWs with ternary as well as quaternary barriers have been developed. FWHM values were found to be mainly determined by the barrier material. Virtually identical values were achieved for QW structures comprising AlInAs and AlGaInAs barriers, respectively. Excellent homogeneity of the QW emission properties was demonstrated.

Acknowledgment

This work was partially funded by the German Ministry of Research and Technology, BMFT, under contract no. TK 0571/3.

References

1 J. P. Praseuth, M. C. Joncour, J. M. Gerard, P. Henoc and M. Quillec, *J. Appl. Phys., 63* (1988) 400.
2 J. P. Praseuth, L. Goldstein, P. Henoch, J. Primot and G. Danan, *J. Appl. Phys., 61* (1987) 215.
3 A. Hase, H. Künzel, D. R. T. Zahn and W. Richter, *J. Appl. Phys.*, submitted for publication.
4 C. Ferrari, P. Franzosi, L. Gastaldi and F. Taiariol, *J. Appl. Phys., 63* (1988) 2628.
5 J. E. A. Whiteaway and C. Eng, *IEEE Proc., 130* (1983) 165.
6 E. G. Scott, S. T. Davey and G. J. Davies, *Electron. Lett., 23* (1987) 761.
7 T. Mishima, J. Kasai, Y. Uchida and S. Takahashi, *J. Cryst. Growth, 95* (1989) 338.
8 A. Hase, E. Lach and H. Künzel, unpublished results, 1992.
9 T. Fujii, Y. Nakata, S. Muto and S. Hiyamizu, *Jpn. J. Appl. Phys., 25* (1986) L598.

Materials Science and Engineering, B21 (1993) 198-200

Influence of the cap layer thickness on the optical properties of near surface GaInAs/GaAs quantum wells

J. Dreybrodt*, F. Faller, A. Forchel and J. P. Reithmaier

Technische Physik, University of Würzburg, Am Hubland, 97074 Würzburg (Germany)

Abstract

We present photoluminescence investigations of GaInAs/GaAs quantum wells with thin cap layers ranging from 20 nm in thickness down to a complete cap layer removal. We observe a strong blue shift of up to 35 meV for an uncovered surface quantum well. A further shift up to the GaAs band edge can be obtained by thinning the GaInAs layer itself. To vary the cap layer thickness we used a highly diluted H_2SO_4 etchant. Quantum mechanical calculations using finite cap layer thicknesses and a vacuum potential of 5 eV on the surface are in good agreement with the measured data, showing the strong influence of the vacuum potential. Furthermore, we observe a large step-like decrease in the photoluminescence intensity at a cap layer thickness of around 10 nm.

In spite of the many varied investigations of quantum wells (QWs) for more than two decades [1], almost all results have been devoted to QWs with thick barriers. Influence of the surface has been neglected. Only a few publications report on the influence of the surface on the optical properties of QWs [2-4].

The optical properties of near surface quantum wells are important for an understanding of the physical behaviour of laterally structured low dimensional systems such as quantum wires and dots. Most commonly these structures are defined by lateral surfaces. We investigated GaInAs/GaAs QWs at the transition from a conventional QW with effectively infinitely thick barrier layers to a surface QW strongly determined by the influence of the vacuum potential on the surface. To study the influence of the cap layer thickness on the optical properties, we used a wet etch process which allows us to control cap layer thinning on a nanometre scale. We report photoluminescence (PL) results of the dependence of the transition energies and PL intensities on the cap layer thickness, as well as a comparison with theoretical predictions.

The samples consisted of a 5 nm $Ga_{0.80}In_{0.20}As$ QW with a cap layer thickness of 16 nm, and a 7 nm $Ga_{0.81}In_{0.19}As$ QW with a cap layer thickness of 20 nm on top of 600 nm GaAs buffers. The samples were grown by molecular beam epitaxy (MBE) on [100] orientated GaAs substrates without any intentional doping. The growth temperature was 580 °C for GaAs and was reduced to 520 °C for GaInAs and the GaAs cap layer. The growth rate was 0.25 nm s^{-1}. Controlled etching was obtained with a highly diluted H_2SO_4:H_2O_2:H_2O etchant (1:10:6000). Every sample was half covered with PMMA resist, which was removed after the etch process. The etch depth was checked on each sample by a surface profiler with an accuracy of ±1 nm. Figure 1 shows the results of a series of etches at a temperature of 25 °C. The measured etch depths are plotted against the etch time. The data points are all close to the solid line representing an etch rate of 0.25 nm s^{-1}. The small deviation, caused mainly by the residual surface roughness of the etched samples, demonstrates the suitability of the etchant for our investigations. The PL investigations

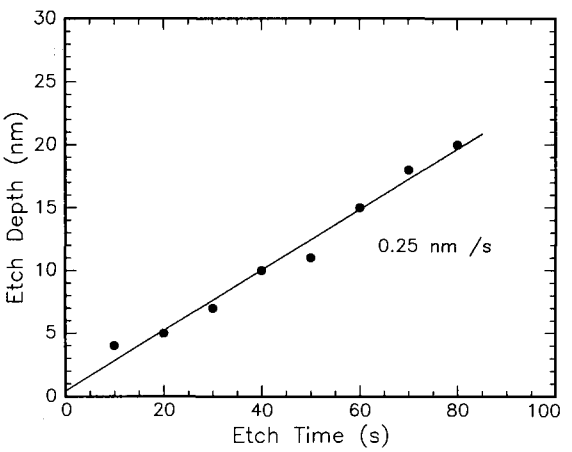

Fig. 1. Etch rate in GaAs obtained with a highly diluted H_2SO_4:H_2O_2:H_2O etchant (1:10:6000), T = 25 °C.

*Author to whom correspondence should be addressed.

0921-5107/93/$6.00

© 1993 - Elsevier Sequoia. All rights reserved

were performed with an Ar laser (514 nm) at a temperature of 5 K. The excitation density was about 10 W cm^{-2}. The PL signal was detected with a liquid N_2 cooled CCD-chip.

Figure 2 displays PL spectra of the etched 5 nm GaInAs QW at a temperature of 5 K. The spectrum of the unetched reference sample with a 16 nm thick cap layer is shown at the top. With decreasing cap layer thickness we observe a distinct shift of the PL line to higher energies. The energy shift is within etch accuracy about 35 meV for the surface QW without a cap layer. Further etching leads to a reduction in the GaInAs layer thickness and yields a shift of the emission almost up to the GaAs barrier edge (lower spectrum). For etch depths larger than 20 nm only the 3D GaAs signal is detectable.

In Fig. 3 we show the dependence of the PL transition energy of the etched samples on the cap layer thickness. We observe a shift to higher energies beginning for a cap layer less than approximately 5 nm thick. We are able to explain the blue shift with a simple quantum mechanical model. The solid line represents results from calculated transition energies. Our model uses a rectangular well with a finite GaAs cap layer thickness. We assume a 5 eV vacuum potential due to electron affinity for the conduction band and an infinite potential for the valence band on the surface. The GaAs buffer thickness is assumed to be infinite. An exciton binding energy of 8 meV is considered [5]. The effective electron mass in the vacuum is set equal to the free electron mass. The effects of the strained GaInAs layer on effective mass and band gap are included in the calculations. The schematic band diagram in the inset of Fig. 3 describes the situation.

The agreement between experiment and the calculation using finite cap layers and a vacuum potential of 5 eV is good. It reproduces the beginning of the increase in the blue shift. The deviation is mainly caused by the uncertainty of the thickness measurement. Comparison with the model demonstrates the importance of the influence of the surface. The observed behaviour leads us to recognize two effects. The blue shift already observed for GaAs cap layer thicknesses below 5 nm is only caused by the influence of the high 5 eV vacuum potential on the surface. If the GaInAs layer is thinned (data below "0 nm" in Fig. 3), the blue shift is due to the reduced thickness in conjunction with enhancement of the confinement by the vacuum potential.

Previous experiments on GaAs/AlGaAs and InP/GaInP QWs revealed a red shift [2, 4] instead of a blue shift. This was partially attributed to the interaction of carriers with surface states resulting in a reduction in energy or band bending near the surface. Our results and the good agreement with the quantum mechanical calculation imply a different situation for GaInAs/GaAs QWs. Influences such as band bending [6] and electric fields [7] in the surface region can only cause a

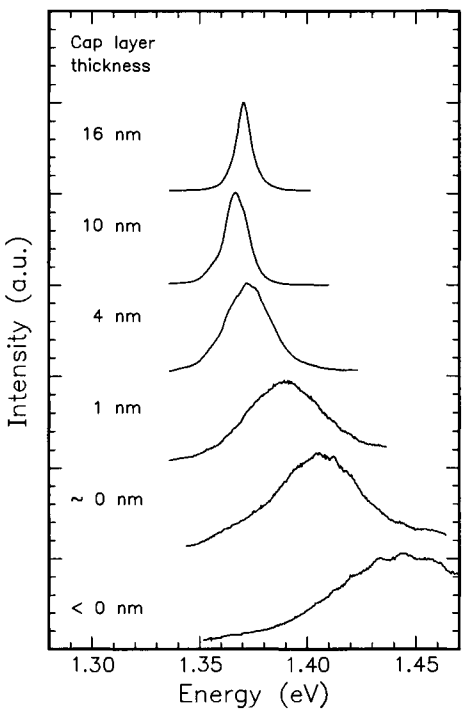

Fig. 2. 5 K PL spectra from a 5 nm $Ga_{0.80}In_{0.20}As/GaAs$ QW with different GaAs cap layer thicknesses. The cap layer thickness is given for each spectrum, $T = 5$ K.

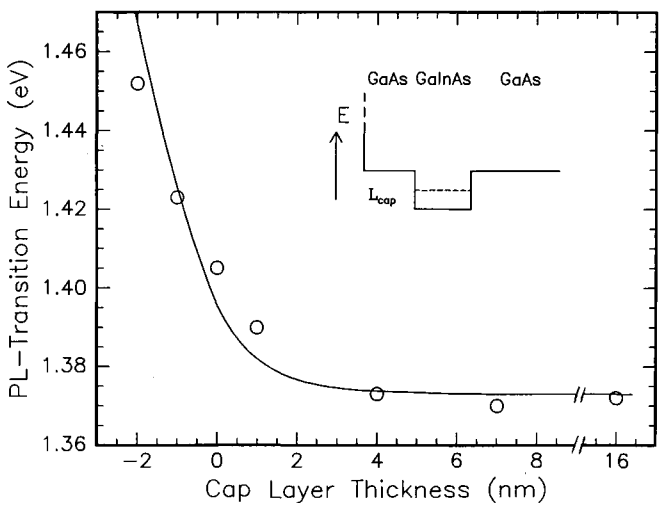

Fig. 3. PL transition energies (o) as a function of the cap layer thickness. The solid line represents a quantum mechanical calculation assuming a finite GaAs cap layer with a 5 eV vacuum potential on the surface. An exciton binding energy of 8 meV is considered. The schematic band diagram in the inset describes the situation.

red shift. Investigations of continuum states above the GaAs barrier have not provided any evidence of field effects in GaInAs/GaAs QWs [8]. The blue shift shows that there is an enhancement of confinement in GaInAs surface and near surface QWs through the vacuum potential. This for example confirms the new concept of quantum wire preparation by barrier modulation introduced by Gréus *et al.* [9]. They confine carriers laterally in quantum wires between regions consisting of surface quantum wells. The energetic difference between surface QWs and QWs with cap layers represents the laterally confining potential.

Figure 4 shows the evolution of the PL intensity as a function of the cap layer thickness. The plot displays the integrated PL intensities normalized to the intensity of an unetched reference sample. Data of two etch series are shown (closed circles, 5 nm $Ga_{0.80}In_{0.20}As$ QW; open circles, 7 nm $Ga_{0.81}In_{0.19}As$ QW). The data sets show identical behaviour. For cap layer thicknesses of more than 12 nm the intensity does not improve, indicating a fully passivated QW with no influence from the surface. A strong step-like decrease of three orders of magnitude occurs below 12 nm in a very small interval. The PL intensity is approximately constant for cap layer thicknesses below 7 nm. The anomalous high intensity difference between surface QWs and the fully passivated QWs implies a strong reduction in the surface recombination [10]. GaAs has a high density of mid-gap surface states [11]. Similar behaviour is expected for GaInAs surfaces. This leads to non-radiative recombination of carriers for the surface QW, which can explain the decrease in intensity of about three orders of magnitude. This recombination process dominates owing to the large surface recombination velocity on Ga(In)As surfaces, resulting in a low radiative recombination probability and thus low PL intensity. If the surface QW is covered with GaAs, tunnelling of electrons to surface states through the GaAs cap layer is in principle possible [12]. A decrease in the tunnelling probability with increasing cap layer thickness is expected. The observed step-like behaviour of the PL intensity may be caused by a tunnelling process.

In summary our investigations have shown that the surface strongly influences the excitonic transitions in GaInAs/GaAs surface QWs. We observe a PL line shift to higher energies, indicating enhancement of confinement by the vacuum potential with decreasing cap layer thickness. This behaviour can be described by a simple

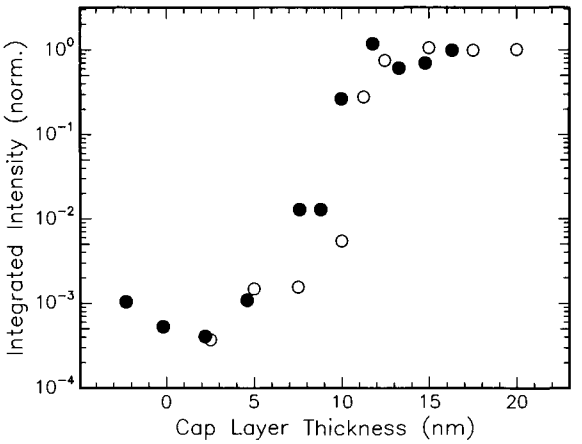

Fig. 4. Integrated density *vs.* cap layer thickness for a 5 nm $Ga_{0.80}In_{0.20}As/GaAs$ QW (●) and a 7 nm $Ga_{0.81}In_{0.19}As/GaAs$ QW (○), $T = 5$ K.

quantum mechanical model assuming a rectangular well with a finite cap layer and a 5 eV surface potential. Also a strong intensity decrease of three orders of magnitude for a surface QW is observed at a cap layer thickness of about 10 nm. Above 12 nm the QW is completely passivated and no further improvement in intensity is observed.

References

1 R. Dingle, W. Wiegmann and C. Henry, *Phys. Rev. Lett., 14* (1974) 827.
2 J. M. Moison, K. Elcess, F. Houzay, J. Y. Marzin, J. M. Gerard, F. Barthe and M. Bensoussan, *Phys. Rev. B, 41* (1990) 12945.
3 E. Yablonovitch, H. M. Cox and T. J. Gmitter, *Appl. Phys. Lett., 52* (1988) 1002.
4 R. M. Cohen, M. Kitamura and Z. M. Fang, *Appl. Phys. Lett., 50* (1987) 1675.
5 J. P. Reithmaier, R. Höger and H. Riechert, *Phys. Rev. B, 43* (1991) 4933.
6 E. Yablonovitch, B. J. Skromme, R. Bhat, J. P. Harbison and T. J. Gmitter, *Appl. Phys. Lett., 54* (1989) 555.
7 D. A. B. Miller, D. S. Chemla, T. C. Damen, A. C. Gossard, W. Wiegmann, T. H. Wood and C. A. Burrus, *Phys. Rev. B, 32* (1985) 1043.
8 S. Fafard and E. Fortin, *Phys. Rev. B, 45* (1992) 13769.
9 C. Gréus, A. Forchel, J. Straka, K. Pieger and M. Emmerling, *Appl. Phys. Lett., 61* (1992) 1199.
10 B. J. Skromme, C. J. Sandroff, E. Yablonovitch and T. Gmitter, *Appl. Phys. Lett., 51* (1987) 2022.
11 T. Saitoh, H. Iwadate and H. Hasegawa, *Jpn. J. Appl. Phys., 30* (1991) 3750.
12 C. J. Sandroff, F. S. Turco-Sandroff, L. T. Florez and J. P. Harbison, *J. Appl. Phys., 70* (1991) 3632.

Materials Science and Engineering, B21 (1993) 201–204

Intersubband transitions in InAs/AlSb quantum wells

A. Simon, J. Scriba, C. Gauer, A. Wixforth and J. P. Kotthaus
Sektion Physik, Ludwig-Maximilians-Universität, 8000 München 22 (Germany)
C. R. Bolognesi, C. Nguyen, G. Tuttle and H. Kroemer
Department of Electrical and Computer Engineering, University of California, Santa Barbara, CA 93106 (USA)

Abstract

Collective intersubband resonances in InAs/AlSb single quantum wells are studied in terms of their dependence on the well width and the electron density. The transitions are found to lie within the atmospheric windows of 8–12 μm and 3–5 μm, respectively.

Optical detectors and modulators based on intersubband transitions have been widely discussed since the first experimental observation of such transitions in GaAs quantum wells [1]. So far, the experiments and theoretical investigations have concentrated on GaAs/AlGaAs heterostructures, for a recent review see ref. 2. In this system, device parameters for detector applications matching those of commercially available HgCdTe or InSb detectors [3] have been demonstrated. There are, however, a number of drawbacks of GaAs/AlGaAs quantum wells inherent in their bandstructure, such as a limited spectral range. Therefore efforts have been made to grow material systems which combine the mature processing technology of III-V semiconductors with a band alignment allowing for detectors with a larger frequency range.

InAs quantum wells stacked between AlSb barriers represent such a novel heterostructure. The electrically active layers are grown on GaAs substrates so that GaAs technology can be used to integrate the structures. Despite a lattice mismatch of about 7% between the active layers and the substrate, low temperature mobilities reach values as high as 800 000 $cm^2 V^{-1} s^{-1}$. The effective electron mass of InAs is only 0.023 m_0 and the AlSb barriers have a height of 2.1 eV at the Γ point, so that large subband quantization energies are expected. The oscillator strength of the intersubband transition is also larger than in the case of GaAs/AlGaAs, since it is proportional to the inverse of the effective mass [1]. Excitations from higher subbands with even greater transition probabilities can be realized because high electron densities, on the order of 5×10^{12} cm^{-2}, are readily achieved [4]. The origin of the electrons in such not intentionally doped structures is discussed in ref. 5. Another interesting feature of the system is that the subband spacing of narrow wells may become larger than the band gap, so that the advantages of an intersubband- and interband-detector may be combined in the same device.

Here we report on the observation of intersubband resonances (ISR) in InAs/AlSb quantum wells. Samples with well widths of 150, 120, 96 and 82 Å are investigated. The layer sequence is as follows: on top of a GaAs substrate a sequence of buffer layers is grown as described in ref. 6; the InAs quantum well is clad by two 200 Å AlSb barriers, and a 50 Å GaSb cap layer terminates the growth sequence.

To induce intersubband transitions the incident light should be polarized along the direction of confinement. We use the strip line geometry to realize this polarization and to enhance the signal by multiple passes through the sample [7]. The top of the sample is metallized so that it can serve as a gate electrode and ensures an electric field component perpendicular to the two-dimensional electron gas (2DEG). The back of the sample is polished in order to minimize losses caused by diffuse scattering from the surface. Our sample geometry is shown as an inset to Fig. 1.

All experiments are carried out in a low-temperature cryostat containing a superconducting solenoid providing a maximum field of 15 T. The far-infrared spectra are taken with a rapid-scan Fourier transform spectrometer. Experimentally, we determine the relative change in transmisssion $-\Delta T/T=(T-T_0)/T_0$, where T_0 denotes the transmission of a reference spectrum, taken either at a different carrier density or at a different magnetic field.

In Fig. 1 we show relative transmittance spectra measured at different gate voltages, *i.e.* carrier densities, in a quantum well 150 Å wide. The reference spec-

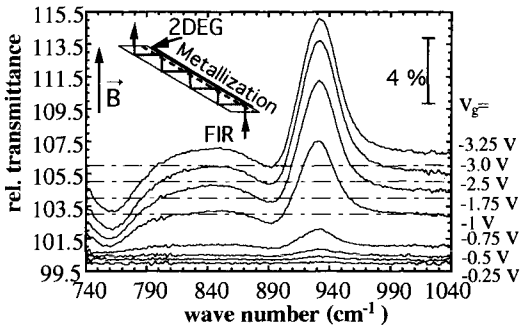

Fig. 1. Relative change of the infrared transmission taken at different carrier densities. The inset shows the experimental geometry.

trum is taken at $V_g = 0$ V. The carrier density in these structures cannot be tuned by simply evaporating a Schottky gate directly on top. Therefore we deposit a 1500 Å silicon layer before evaporating the gate electrode. It is found in Shubnikov-de Haas measurements that the number of carriers in this sample is reduced by about 20% at $V_g = -3.25$ V as compared to $V_g = 0$ V. As the electron density decreases with more negative gate bias, a peak in the relative transmission (caused by the absorption in the reference spectrum) at about 930 cm^{-1} gains strength. On the low-energy side a dip appears and deepens with decreasing carrier density. For gate voltages smaller than $V_g \leqslant -1$ V an additional minimum arises at about 760 cm^{-1}.

Tuning the electron density modifies the spectra in two ways. The absorption is proportional to the number of carriers, so that weak absorption is expected when the carrier density is low. Furthermore, many-body effects such as the depolarization and the exciton shift depend on the carrier density [8]. Finally, the self-consistent potential and effects caused by the non-parabolicity of the InAs conduction band both influence the transition energy and the line shape of the resonance [9]. The prominent peak found at $V_g < -0.5$ V is thus identified as being induced by the intersubband transition at the highest carrier density at $V_g = 0$. The dip on the low-energy side of this maximum is an artefact caused by the division of two spectra of different line shapes. A similar effect will be discussed in detail in the next paragraph. Because of the silicon layer between the metal gate and the sample, the parallel component of the infrared electric field in the plane of the quantum well is finite, so that in this setup parallel-excited intersubband absorption may be detected [10]. This excitation mechanism is found in the intersubband resonance on non-parabolic semiconductors, and its oscillator strength is approximately 10% of the perpendicular excitation under the same experimental conditions [11]. We thus interpret the minimum at around 760 cm^{-1} as the parallel-excited intersubband transition. The energetic difference between the two excitation mechanisms is mainly determined by the depolarization shift $E_{dep} = E_{12\perp} - E_{12\parallel}$. Calculating the depolarization effect for an infinitely high square well gives a shift of $E_{dep} = 140$ cm^{-1}, which is in good agreement with the one determined experimentally.

We now focus on the spectra obtained from the magnetic field ratio. In these experiments the magnetic field is oriented at an angle of 45° with respect to the sample, as shown in the inset to Fig. 1. Dividing the spectra at $B \neq 0$ T by the reference spectrum measured at $B = 0$ T gives the relative spectra in Fig. 2 for the same 150 Å wide quantum well. In these plots the strength of the relative signal increases non-linearly with the strength of the magnetic field. The spectrum at 15.3 T exhibits a prominent peak at about 910 cm^{-1} and two minima on either side. This signature is also seen in the 12 T spectrum, even though not that pronounced. The structure of the spectra taken at lower fields exhibits a minimum at high energies and a maximum at low energies. The positions of these extrema shift with the variation of the magnetic field.

In tilted magnetic fields the electric and magnetic quantizations are coupled, for a recent review see ref. 12. The component of the magnetic field $B_\parallel$ parallel to the 2DEG induces a diamagnetic shift on the subband energies

$$E_{n,dia} = \frac{e^2 B_\parallel^2}{2m^*}[(z_{nn}^2) - (z_{nn})^2] \quad (1)$$

Here, z_{nn} denotes the matrix element defined by

$$(z^x)_{ij} = \int dz \phi_i z^x \phi_j$$

whereas the other symbols have their usual meaning. Furthermore, in parallel magnetic fields the subband separation depends on k_x:

$$E_{10}(k_x) = E_{10} + \frac{e^2 B_\parallel^2}{2m^*}[(z_{11}^2) - (z_{00}^2)] + \frac{\hbar e B_\parallel}{m^*} k_x (z_{11} - z_{00})$$

According to eqn. (1) the component $B_\parallel$ influences the energy of the second subband more strongly than the energy of the first. Thus the division of two spectra taken at different magnetic fields results in a relative spectrum as shown in Fig. 2. The maxima are related to the intersubband transition at $B = 0$ T while the minima are caused by the absorption at $B \neq 0$ T. The non-linear variation of the signal with the magnetic field can be explained by the B^2 dependence of the diamagnetic shift and the division of the spectra. To study the line shape of the spectra in detail, we calculate the real part of the dynamic conductivity given by

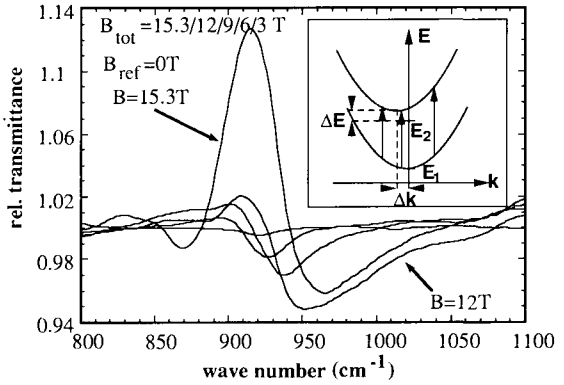

Fig. 2. Relative change of the infrared transmission taken at different magnetic fields. Note that the position of the maximum of the spectrum $B = 15.3$ T / 0 T approximately coincides with the maximum of the spectrum taken at $V_g = 0$ and $B = 0$ T in the density ratio. The inset shows the shift of the subband parabolae caused by the in-plane component of the magnetic field.

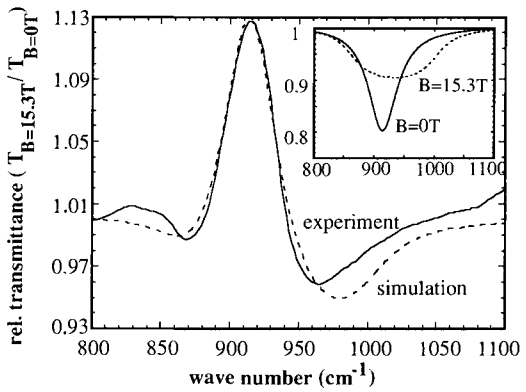

Fig. 3. Fit to the spectrum 15.3 T / 0 T. The curves in the inset represent the line shape of the resonances as obtained by fitting the dynamic conductivity to the relative spectrum.

ref. 13:

$$\mathrm{Re}(\sigma_{zz}(\omega)) = A\frac{\omega^2}{\tau}\sum_{-k_F}^{+k_F}\frac{1}{\left(\hbar^2\omega^2 - \frac{\hbar^2}{\tau^2} - E_{12}^2(k)\right)^2 - \frac{4\hbar^2\omega^2}{\tau^2}}$$

The resonance curves shown in Fig. 3 are obtained by adjusting the oscillator strength, linewidth and transition energy to the relative spectrum at 15.3 T / 0 T. As can be seen, the calculated resonance at $B = 15.3$ T is shifted to higher energies and it is considerably broader than the resonance at $B = 0$. We also simulate the spectra of the narrower wells with the same fit. The single-particle intersubband spacings for the four different InAs quantum well widths are approximated by subtracting the depolarization shift as calculated for an infinitely high square well. According to ref. 9 the exciton shift may be neglected in this calculation. The values deduced from the ISR measurements deviate only negligibly from the values derived from cyclotron resonance measurements in tilted magnetic fields [14] that will be described elsewhere. Table 1 lists the values of ISR and E_{12} energies extracted for the four different InAs quantum well widths, along with the corresponding 2DEG concentrations N_s.

In summary, we have measured bound-to-bound intersubband transitions in single InAs quantum wells demonstrating the wide frequency range (113–246 meV) that can be attained in such heterostructures. So far, no theoretical approach for calculating the subband energies in strongly non-parabolic systems gives subband separations in quantitative agreement with the experiment. Our experiments prove that InAs/AlSb quantum wells indeed offer great promise as novel infrared detectors.

TABLE 1. Intersubband resonances, E_{12} energies and 2DEG concentration (N_s) values for different InAs quantum well widths

Well width (Å)	ISR (cm^{-1})	E_{12}[a] (cm^{-1})	N_s (10^{12} cm^{-2})
150	910	770	1.5
120	1360	980	1.0
96	1680	1630	0.7
82	1980	1960	0.4

[a]The single particle level spacings E_{12} are derived from the experimentally determined transition energies by subtracting the depolarization shift calculated for an infinitely high square well.

Acknowledgments

We gratefully acknowledge financial support from the Volkswagen Stiftung. The work in Santa Barbara was supported in part by the Offfice of Naval Research, in part by QUEST, the NSF Science and Technology Center for Quantized Electronic Structures (Grant DMR 91-20007).

References

1 L.C. West and S.J. Eglash, *Appl. Phys. Lett., 46* (1985) 1156.
2 E. Rosencher *et al.* (eds.), *Intersubband Transitions in Quantum Wells*, Plenum Press, New York, 1992.
3 S.C. Shen, *Semicond. Sci. Techn., 8*(1993) 400.
4 4 C. Nguyen, B. Brar, C.R. Bolognesi, J.J. Pekarik and J.H. English, *J. Electron. Mater., 22* (1993) 255.
5 C. Nguyen, B. Brar, H. Kroemer and J.H. English, *J. Vac. Sci. Technol. B, 10* (2) (1993) 898.
6 G. Tuttle, H. Kroemer and J.H. English, *J. Appl. Phys., 65* (1989) 5239.
7 P. Kneschaurek, A. Kamgar and J.F. Koch, *Phys. Rev. B, 14* (1976) 1610.

8 T. Ando, A.B. Fowler and V. Stern, *Rev. Mod. Phys., 54* (1982) 473.
9 M. Zaluzny, *Phys. Rev. B, 47* (1993) 3995.
10 M. von Ortenberg, *Infrared Physics, 18* (1978) 735.
11 W. Zawadzki, *J. Phys. C, 16* (1983) 229.
12 E. Batke, *Festkörperprobleme, 31* (1991) 297.
13 J. Scriba, *Doctoral Thesis*, Ludwig-Maximilians-Universität München, 1993 (unpublished).
14 S. Oelting, A.D. Wieck, E. Batke and U. Merkt, *Surf. Sci., 196* (1986) 273.

Materials Science and Engineering, B21 (1993) 205–210

Blue diode lasers and visible optoelectronic devices

B. C. Cavenett, K. A. Prior and S. Y. Wang
Heriot-Watt University, Edinburgh EH14 4AS (UK)

Abstract

The recent control of both n- and p-type doping in ZnSe and related II–VI alloys has resulted in the development of the first blue diode lasers by the 3M Company and a range of modulator and optical switching devices at Heriot-Watt University. This paper briefly reviews the important steps which were taken towards these new optoelectronic devices that are important for future optical recording, printing and display systems operating in the visible spectrum.

1. Introduction

A new generation of devices based on II–VI semiconductors is being developed for visible optoelectronic systems including high density video compact discs, colour printing and displays. Blue diode lasers were first demonstrated by Haase *et al.* [1] and since then many new reports on the development of visible lasers have been published [2–5]. Currently, these lasers can only operate in continuous wave mode at low temperatures though room temperature pulsed lasers have been reported [6] but the lifetime of these devices is measured in minutes and so considerable advances in the materials technology must take place before practical devices are realized. Alternative technologies such as frequency doubling near-IR lasers and up conversion in fibre lasers can already produce continuous wave room temperature emission but in the long term the need is for cheap, compact semiconductor devices.

The II–VI semiconductors have been investigated for many years as potential materials for devices operating in the visible since the band gaps vary from the IR to the UV spectral regions as shown schematically in Fig. 1 where the band gaps are plotted against lattice constant for the so-called wide band gap II–VI materials. The historical problems with the development of II–VI materials have been the very poor crystal quality of the bulk material and the difficulty in doping the materials both n and p type. However, it was expected that the development of epitaxial growth techniques such as molecular beam epitaxy (MBE) and metal–organic chemical vapour deposition (MOCVD) would solve these problems but epitaxy needs good bulk substrates and so it has been necessary to use III–V substrates which immediately leads to the problems of growing mismatched or strained layers. Figure 1 also shows the lattice constants for GaAs, InP, GaP and Si. Also, despite optimism that these non-equilibrium growth techniques might solve the doping problems, it was almost 10 years before the first breakthrough came with the successful p-type doping of ZnSe by Ohkawa *et al.* [7] and Park *et al.* [8].

The ability to fabricate p–n junctions in ZnSe led immediately to the development of laser diodes as discussed above but, in parallel, it has also been possible to explore modulator and optical switch structures which form part of the package of visible optoelectronic devices. The first p–i–n quantum confined Stark effect modulators were fabricated by Kawakami *et al.* [9] and Wang *et al.* [10] and the first optical switch based on the self electro-optic effect device (SEED) has recently been demonstrated by Wang *et al.* [11].

2. Doping of ZnSe

At present the fabrication of ZnSe p–n junctions can only be achieved by MBE. We use a VG Semicon MBE growth kit at Heriot-Watt and in common with most groups the ZnSe layers are grown on GaAs substrates at a temperature around 280 °C using elemental Zn and Se sources. The most common n-type dopant for ZnSe is chlorine from a $ZnCl_2$ Knudsen source [12] but iodine is also an excellent dopant and we have developed an electrochemical source using ionic conductivity in AgI [13]. In order to characterize the electrical properties of the doped ZnSe material we have developed a suitable electrolyte for the Biorad electrochemical C–V profiler [14]. Using an $NaSO_3$:NaOH solution it is possible to carry out the required depth etching procedure with illumination and then measure the carrier concentration from a

0921-5107/93/$6.00

© 1993 – Elsevier Sequoia. All rights reserved

C–V measurement with the electrolyte forming the Schottky contact. Figure 2 illustrates a typical C–V carrier concentration profile for a sample where the iodine flux has been changed by adjusting the current in the electrochemical iodine cell. The rapid response of the iodine source allows a staircase doping structure to be grown as shown.

The p-type doping is achieved using nitrogen from an Oxford Applied Research plasma source. Nitrogen gas is flowed through an r.f. plasma discharge and the resulting beam of excited nitrogen molecules and nitrogen atoms is directed at the substrate. Although it has not been established which of the nitrogen species from the source is active in the doping process, p-type doping can be achieved up to concentrations of approximately 10^{18} cm^{-3}.

Qiu *et al.* [15] have shown that even if more nitrogen is incorporated, as shown by secondary ion mass spectrometry measurements, the active nitrogen concentration saturates. Hauksson *et al.* [16] have discussed these effects in terms of a vacancy associated single donor, V_{Sc}–Zn–N_{Se}, which would act as a compensating centre with a concentration which would increase with the nitrogen concentration. A model of this centre which involves the double V_{Se} donor is shown in Fig. 3. Recent optically detected magnetic resonance measurements show the presence of a deep donor supporting this compensation model.

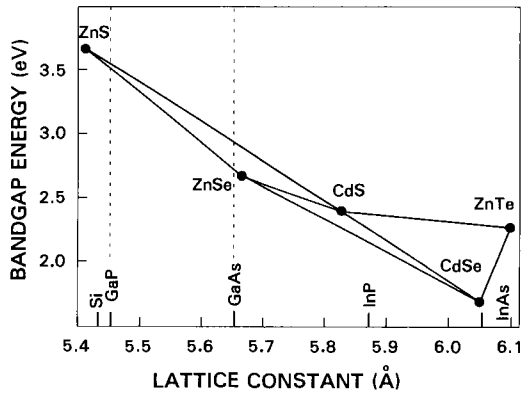

Fig. 1. Band gap *vs.* lattice constant for II–VI semiconductors showing possible substrates.

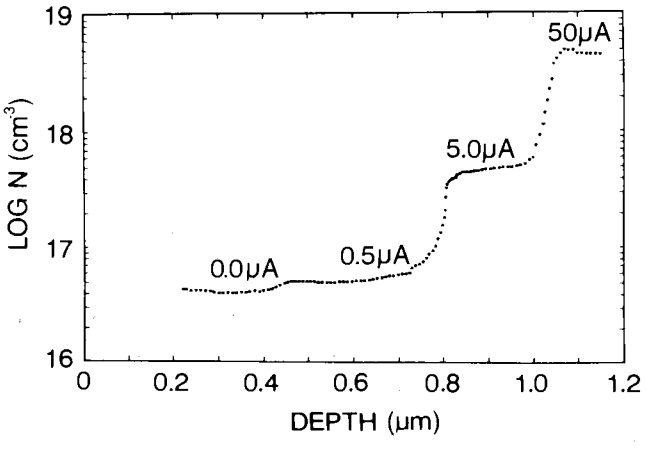

Fig. 2. Electrochemical profile of ZnSe:I n-type material where the iodine flux has been changed by adjusting the current (in microamps) through the electrochemical iodine cell.

3. Quantum well structures

Quantum well structures have high radiative efficiency and for the II–VI semiconductors it has been important to identify suitable well and barrier materials. Figure 1 shows that the addition of sulphur to ZnSe increases the band gap but Shahzad *et al.* [17] have shown that the conduction band offset is very small for the ZnSSe/ZnSe quantum wells, this being an example of the common cation rule. Samarth *et al.* [18] showed that the ZnSe/ZnCdSe quantum well structure has both conduction and valence band offsets and despite the fact that CdSe usually has an hexagonal crystal structure (Wurtzite), the alloy has excellent crystal quality. The addition of cadmium decreases the band gap energy and increases the lattice constant so that within a ZnSe structure the wells are strained and in compression.

4. Light emitting diodes

Detailed studies of light emitting diodes (LEDs) have been carried out by 3M [17] and the Purdue–Brown collaboration [19, 20] and, in particular, Hagerott *et al.* [21] have demonstrated an alphanumeric display using a quantum well structure and a transparent conducting top conduct. Walker *et al.* [22]

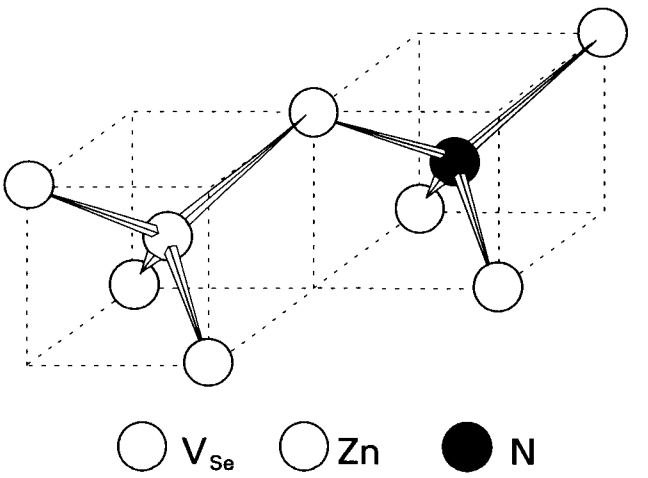

Fig. 3. Schematic model of the nitrogen associated single donor compensating centre in highly doped ZnSe:N.

have investigated the degradation processes in LEDs by observing the electroluminescence with an optical microscope as a function of operating time. In particular, they observed dark spots that elongated into a strong dark line ⟨100⟩ grid pattern during operation but devices with a lattice matched buffer layer had lifetimes which were greater by several orders of magnitude.

Figure 4 shows the room temperature blue emission from a ZnSe p–n junction fabricated at Heriot-Watt. The details of the structure are shown in the inset. An electrochemical profile through the diode showed that $n = 10^{18}$ cm^{-3} and $N_A - N_D = 4 \times 10^{17}$ cm^{-3}. Stimulated emission from this junction was observed when a conventional stripe laser structure was fabricated [23].

5. Laser diodes

A schematic diagram of a typical 3M type laser diode [1] is shown in Fig. 5. The structure consists of one or more $Cd_{0.2}Zn_{0.8}Se$ quantum wells with ZnSe barriers set at the centre of a doped ZnSe waveguide (approximately 1 μm wide). The waveguide is isolated from the absorptive GaAs substrate by a lattice matched $ZnS_{0.06}Se_{0.94}$ n-type layer and capped by a $ZnS_{0.6}Se_{0.94}$ p-type layer. The top contact is usually Au or Au–Pt alloy. The original laser devices were grown on a GaAs epitaxial buffer layer which was grown in a separate chamber in order to improve the GaAs–ZnSe interface.

InGaAs buffer layers which are lattice matched to ZnSe have also been used for laser structures [24] though, currently, many lasers are being fabricated without III–V buffer layers. We have fabricated ZnSe/$Zn_{0.8}Cd_{0.2}Se$ quantum well lasers as shown in Fig. 6.

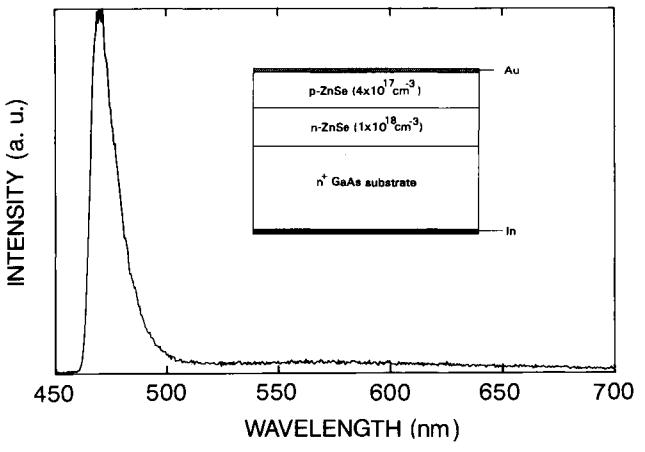

Fig. 4. Blue room temperature electroluminescence from a ZnSe p–n junction with the structure shown in the inset.

The structure consists of four quantum wells, each 60 Å wide with 80-Å barriers which were grown within a ZnSe p–n junction [5]. In order to characterize the devices, the carrier concentration was electrochemically profiled giving n- and p-doping levels of $n = 2 \times 10^{17}$ cm^{-3} and $N_A - N_D = 2 \times 10^{17}$ cm^{-3} respectively, and at the same time the photovoltage signal was monitored showing the quantum well subband absorptions.

Laser structures were fabricated with a top 100 μm Au contact and an In ohmic contact was made to the GaAs substrate. The output of the laser using 400 ns pulses at a repetition rate of 1 kHz is shown, for a temperature of 77 K, in Fig. 7. A very narrow single mode is observed at a threshold current density of 800 A cm^{-2} and at lower temperatures the longitudinal mode spacing was clearly observed with a spacing of 0.026 nm corresponding to the 0.95 mm laser structure.

Several groups have demonstrated continuous wave laser operation at 77 K [6] and pulsed operation at room temperature, though in general it is necessary to coat the laser facets since the reflectivity ($R \approx 0.21$) is much lower than in GaAs ($R \approx 0.3$).

The quantum well lasers based on $Cd_{0.2}Zn_{0.8}Se$ wells are blue at low temperature but blue–green (about 500 nm) at room temperature. More recently the group at

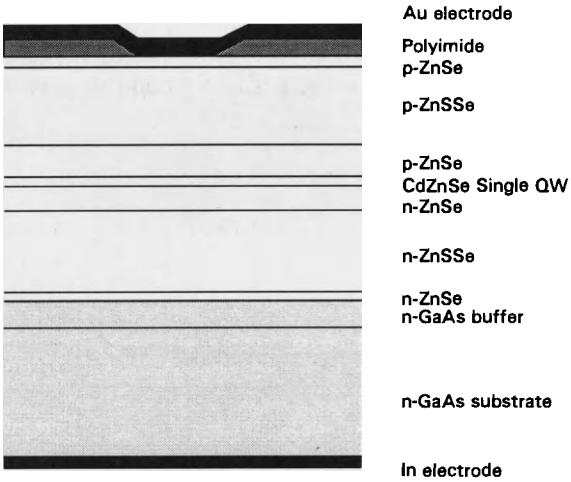

Fig. 5. Schematic diagram of the 3M type laser structure using one or more $Cd_{0.2}Zn_{0.8}Se$ quantum wells.

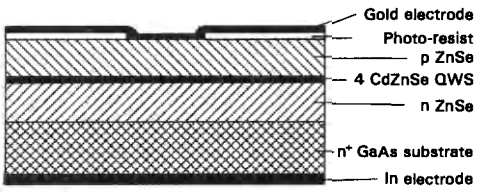

Fig. 6. Heriot-Watt quantum well laser structure.

Sony have reported the use of ZnSe wells in a laser with ZnMgSSe quaternary cladding layers [25]. This has resulted in the shortest wavelength semiconductor laser demonstrated so far. This quaternary material is attractive since it can be lattice matched to GaAs over a range of band gaps up to the UV. An alternative quaternary material CdZnSSe has been explored for blue and UV lasers by Ichino *et al.* [26] though growth on GaP would be necessary for UV lasers. However, in both the above cases, the doping properties are still unexplored and so it remains to be seen whether p–n junctions can be fabricated over a wide alloy range.

6. Optoelectronic devices

In III–V technology the device most commonly associated and integrated with a laser is the optical modulator. These devices are based on the quantum confined Stark effect where an electric field is applied to a set of quantum wells within a reverse biased p–n junction. The sub-band energy shifts result in the exciton absorption moving to longer wavelengths and at high electric fields the absorption is quenched. This change in the absorption is used to modulate the laser beam.

We have demonstrated the operation of the first II–VI quantum confined Stark effect modulator based on a $Cd_{0.2}Zn_{0.8}Se$ quantum well structure as shown in Fig. 8. The 20 quantum wells are set within a ZnSe p–n junction and a top n^+-ZnSe layer is added to make a forward biased contact to the p-ZnSe when the device is in reverse bias. A window is etched in the GaAs substrate for the absorption measurements. The response of the modulator to an electric field is shown in Fig. 9 where in (a) the light and heavy hole excitons can be observed directly in the absorption and these shift with increasing reverse bias. In Fig. 9(b) it can be seen that at the heavy hole exciton absorption a modulation of approximately 10% is obtained.

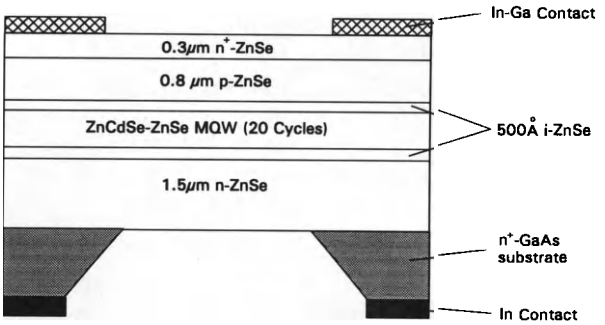

Fig. 8. Schematic diagram of a quantum confined Stark effect modulator.

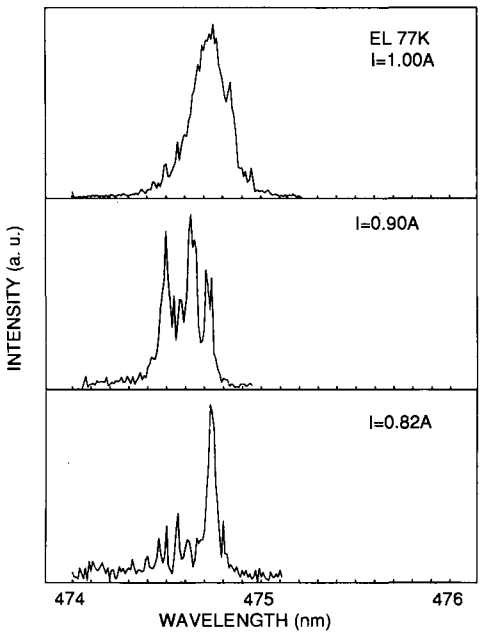

Fig. 7. Laser emission at 77 K from the structure shown in Fig. 6.

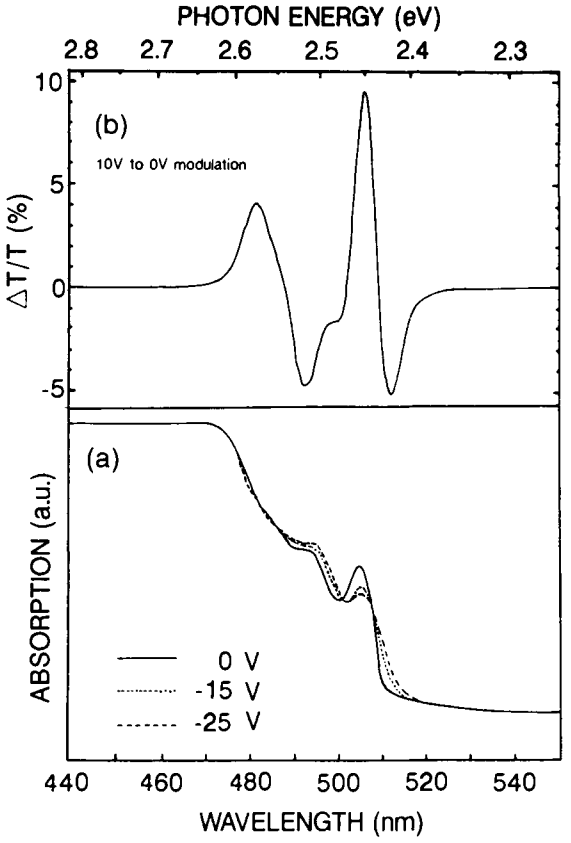

Fig. 9. (a) Absorption of the structure in Fig. 8 showing the shift of light and heavy hole excitons with increasing reverse bias. (b) Differential transmission through the modulator.

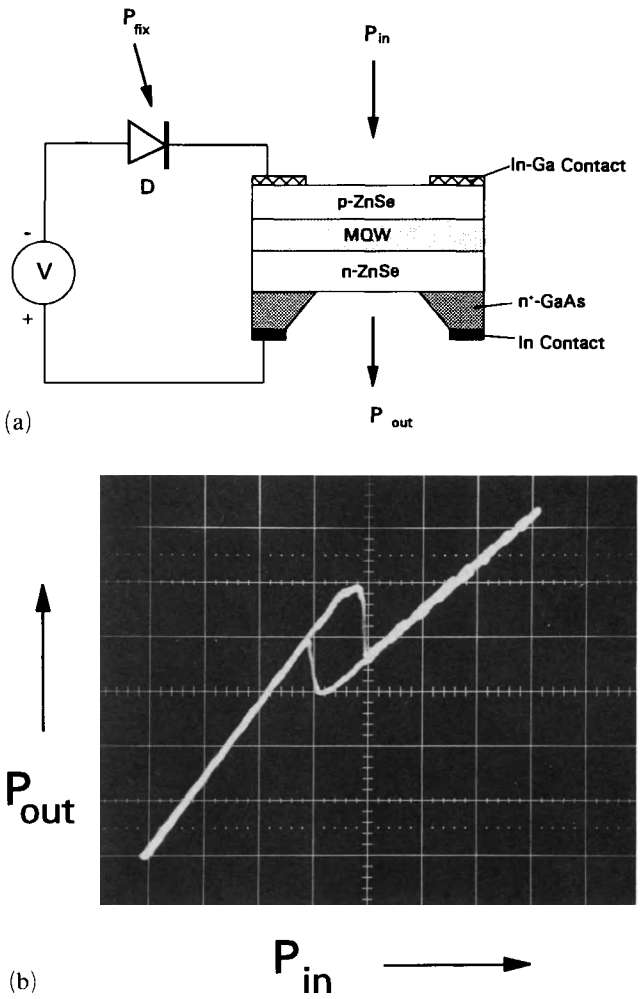

Fig. 10. (a) Schematic diagram of a D-SEED circuit showing the bias voltage V, the series photodiode D, and the modulator structure. (b) Plot of P_{out} *vs.* P_{in} for the bistable D-SEED operation.

Finally, the modulator structure can be used as the basis of an optical bistable switch which would have applications in optical processing. Developments in III–V technology have resulted in the self-electro-optic effect device or SEED which consists of a modulator structure with electrical bias. We have demonstrated the first II–VI SEED device based on a modulator with a 30 period quantum well structure consisting of ZnSe(60 Å)/$Zn_{0.8}Cd_{0.2}Se$(40 Å) [11]. The circuit is shown in Fig. 10(a) where a bias voltage is applied to the modulator via a silicon diode which is illuminated by an LED with a fixed power P_{fix}. The photoconductive response of the modulator results in bistable operation of the circuit so that the modulator has two stable transmission states as shown in Fig. 10(b) where the output power is plotted against the input power at 488 nm, in the blue-green spectral region.

7. Conclusions

The development of II–VI laser diodes and optoelectronic devices is proceeding rapidly and in the near future we can expect prototype devices which will be used in practical optoelectronic systems.

Acknowledgments

We are grateful to SERC and VG Semicon for continued support and we thank Dr. J. Simpson, Dr. M. Taghizadeh, Dr. J. Mullins, Mr. I. Hauksson and Mr. G. Horsburgh for their contributions to these studies.

References

1 M. A. Haase, J. Qiu, J. M. DePuydt and H. Cheng, *Appl. Phys. Lett., 59* (1991) 1272.
2 H. Jeon, J. Ding, A. V. Nurmikko, W. Xie, D. C. Grillo, M. Kobayashi, R. L. Gunshor, G. C. Hua and N. Otsuka, *Appl. Phys. Lett., 60* (1992) 2045.
3 Z. Yu, J. Ren, B. Sneed, K. A. Bowers, K. J. Gossett, C. Boney, Y. Lansari, J. W. Cook, J. F. Schetzina, G. C. Hua and N. Otsuka, *Appl. Phys. Lett., 61* (1992) 1266.
4 K. Ohkawa, A. Tsujimura, S. Hayshi, S. Yoshii and T. Mitsuyu, *Physica B, 185* (1993) 112.
5 S. Y. Wang, J. Simpson, H. Stewart, S. J. A. Adams, I. Hauksson, Y. Kawakami, M. R. Taghizadeh, K. A. Prior and B. C. Cavenett, *Physica B, 185* (1993) 508.
6 M. A. Haase, J. Qiu, J. M. DePuydt and H. Cheng, *Proc. Int. Symp. on GaAs and Related Compounds, Seattle, WA, 1991, Inst. Phys. Conf. Ser. No. 120*, 1992, p. 9.
7 K. Ohkawa, T. Karasawa and T. Mitsuyu, *J. Cryst. Growth, 111* (1991) 797.
8 R. M. Park, M. B. Troffer, C. M. Rouleau, J. M. DePuydt and M. A. Haase, *Appl. Phys. Lett., 57* (1990) 2127.
9 Y. Kawakami, S. Y. Wang, J. Simpson, I. Hauksson, S. J. A. Adams, B. C. Cavenett and K. A. Prior, *Physica B, 185* (1993) 496.
10 S. Y. Wang, Y. Kawakami, J. Simpson, K. A. Prior and B. C. Cavenett, *Appl. Phys. Lett., 62* (1992) 1715.
11 S. Y. Wang, G. Horsburgh, P. Thompson, I. Hauksson, J. Mullins, K. A. Prior and B. C. Cavenett, *Appl. Phys. Lett., 62* (1993) 1715.
12 K. Ohkawa, T. Mitsuyu and O. Yamazaki, *J. Appl. Phys., 62* (1987) 3216.
13 J. M. Wallace, J. Simpson, S. Y. Wang, H. Stewart, J. J. Hunter, S. J. A. Adams, K. A. Prior and B. C. Cavenett, *J. Cryst. Growth, 117* (1992) 320.
14 S. Y. Wang, J. Simpson, K. A. Prior and B. C. Cavenett, *J. Appl. Phys., 72* (1992) 5311.
15 J. Qiu, J. M. DePuydt, H. Cheng and M. A. Haase, *Appl. Phys. Lett., 59* (1991) 2992.
16 I. Hauksson, J. Simpson, S. Y. Wang, Y. Kawakami, K. A. Prior and B. C. Cavenett, *Appl. Phys. Lett., 61* (1992) 2208.
17 K. Shahzad, D. J. Olego and C. G. Van de Walle, *Phys. Rev. B, 38* (1988) 1417.
18 N. Samarth, H. Luo, J. K. Furdyna, R. G. Alonso, Y. R. Lee, A. K. Ramdas, S. B. Qadri and N. Otsuka, *Appl. Phys. Lett., 56* (1990) 1663.

19 H. Jeon, J. Ding, A. V. Nurmikko, W. Xie, D. C. Grillo, M. Kobayashi, R. L. Gunshor, G. C. Hua and N. Otsuka, *Appl. Phys. Lett., 60* (1992) 2045.
20 M. Hagerott, J. Ding, H. Jeon, A. V. Nurmikko, Y. Fau, L. He, J. Han, J. Saraie, R. L. Gunshor, C. G. Hua and N. Otsuka, *Appl. Phys. Lett., 62* (1993) 2108.
21 M. Hagerott, H. Jeon, A. V. Nurmikko, W. Xie, D. C. Grillo, M. Kobayashi and R. L. Gunshor, *Appl. Phys. Lett., 60* (1992) 2825.
22 C. T. Walker, J. M. DePuydt, M. A. Haase, J. Qiu and H. Cheng, *Physica B, 185* (1993) 27.
23 S. Y. Wang, I. Hauksson, J. Simpson, H. Stewart, S. J. A. Adams, J. M. Wallace, Y. Kawakami, K. A. Prior and B. C. Cavenett, *Appl. Phys. Lett., 61* (1992) 506.
24 A. V. Nurmikko and R. L. Gunshor, *J. Lumin., 52* (1992) 89.
25 H. Okuyama, T. Miyajima, Y. Morinaga, F. Hiei, M. Ozawa and K. Akimoto, *Electron. Lett., 28* (1992) 1798.
26 K. Ichino, K. Iwami, Y. Kawakami, Sz. Fujita and Sg. Fujita, in preparation.

Materials Science and Engineering, B21 (1993) 211–216

Aluminium-free 980 nm laser diodes

M. Pessa, J. Näppi, G. Zhang, A. Ovtchinnikov and H. Asonen

Department of Physics, Tampere University of Technology, P.O. Box 692, 33101 Tampere (Finland)

Abstract

This paper reports on material structures and device properties of GaInAs–Ga(In)As(P) semiconductor lasers intended for pumping erbium-doped fiber amplifiers at $\lambda = 0.98$ μm. The layers of these devices can be grown to high structural perfection. The lasers processed from GaInAs–Ga(In)As(P) exhibit very good performance characteristics. The best lasers have threshold current densities as low as 70 A cm^{-2}, internal quantum efficiency of 90%, external differential efficiency of 0.7 mW/mA, and internal waveguide loss well below 10 cm^{-1}. The ridge waveguide lasers operate in fundamental lateral mode to a power level of over 150 mW. They launch a wave power of 400 mW in multi-mode operation and 800 mW in pulse mode. They produce a far-field width of less than 30° perpendicular to the junction and about 10° parallel to the junction. A power of up to 50 mW at 180 mA drive current has been coupled into a single mode fiber, corresponding to 50% coupling efficiency.

1. Introduction

The optimum wavelengths for pumping erbium-doped silica fiber amplifiers (EDFAs), the repeaters in a communication system, are 1.48 and 0.98 μm [1, 2]. The pumping bandwidths of the Er^{+3} 1.48 and 0.98 μm bands are narrow, ± 10 and ± 6 nm at 3 dB compression, respectively, which require a precise wavelength control to attain stable amplification. Therefore, to practical EDFAs with compact and efficient pumps, semiconductor lasers are indispensable. Of the two wavelengths, 0.98 μm is more interesting because it corresponds to the principal Er^{3+} absorption band in terms of gain per input optical power. In addition, an EDFA pumped with a 0.98 μm source introduces less noise to the amplified network signal and less temperature-induced variation in amplification than does a 1.48 μm source [3–6].

Recently, optical amplifiers using a praseodymium-doped fiber have been demonstrated as being capable of high gain at $\lambda = 1.3$ μm. When co-doped with ytterbium, this amplifier can also be pumped at 0.98 μm [7].

Emission at 0.98 μm is achieved with various kinds of quantum well (QW) laser diodes, mostly with "conventional" AlGaAs–GaAs–GaInAs lasers (see for example ref. 8). However, AlGaAs tends to oxidize during both fabrication and operation. Oxidation-induced facet degradation is the major cause of failure of these lasers. Thus eliminating Al may enhance the useful lifetime of the device [9].

$Ga_xIn_{1-x}As_yP_{1-y}$ offers a variable alternative to AlGaAs [10]. Though the quaternaries which are lattice-matched to GaAs are more difficult to grow than AlGaAs, they offer distinct advantages [11–14]. Besides diminishing the facet oxidation, GaInAsP lends itself more readily to device fabrication by selective etching and epitaxial regrowth. It has higher ohmic and thermal conductivities than those of AlGaAs [15], and it has low surface recombination velocities (< 1.5 cm s^{-1}) [16]. All these features are supposed to enhance the maximum power level and threshold for catastrophical optical mirror damage (COD). However, these Al-free lasers have not yet been studied thoroughly. Surface compositional and structural changes, due to desorption of phosphorus, and a tendency of GaInP to form growth-dependent long range atomic ordering [17] are important reliability issues which must be examined carefully before one can move from the development phase into deployment in transmission systems.

2. Layer structures

2.1. $Ga_xIn_{1-x}As_yP_{1-y}$ lattice-matched to GaAs

$Ga_xIn_{1-x}As_yP_{1-y}$ QW layers grown on a GaAs substrate may remain under biaxial compressive strain or tensile strain or they may be unrestrained. Alloying phosphorus with GaAs opens up the band gap E_g and reduces the lattice constant a, yielding tensile strain in GaAsP. Alloying indium with GaAs decreases E_g and increases a, yielding compressive strain in GaInAs. Alloying both indium and phosphorus can result in unstrained quaternaries.

The lattice constant $a(x,y)$ of $Ga_xIn_{1-x}As_yP_{1-y}$ is approximately

0921-5107/93/$6.00

© 1993 – Elsevier Sequoia. All rights reserved

$$a(x,y) = 0.01894y - 0.0418x + 0.0013xy + 0.58696$$

in units of nm. Lattice matching to GaAs is obtained if

$$x = (0.01894y + 0.02166)/(0.0418 - 0.0013y)$$

The band gap can be estimated from the equation [18]

$$E_g \approx 1.35 + 0.68x - 1.17y + 0.758x^2 + 0.18y^2 + 0.75xy - 1.14x^2y - 0.789xy^2 + 0.819x^2y^2$$

Figure 1 shows E_g as a function of In concentration throughout the entire range of composition for lattice-matched $Ga_xIn_{1-x}As_yP_{1-y}$ at room temperature ($-1000 \leqslant \Delta a/a \leqslant 200$ p.p.m.). Our experimental results are obtained for the layers grown by gas-source molecular beam epitaxy; the other experimental results are obtained using LPE and MOCVD methods.

2.2. *Strained-layer quantum wells*

Conventional wisdom has reversed its view on the disadvantages of strained layers in semiconductor devices. It has turned out that lattice-mismatched pseudomorphic layers are very beneficial in quantum well devices, particularly in laser diodes [21].

The density of states (DOS) in the conduction band for an unstrained layer is much smaller than the DOS in the valence band which is dominated by the large curvature of the light hole (LH) and heavy hole (HH) bands around the Brillouin zone center. Biaxial compressive strain splits the LH and HH energy states. The magnitude of the splitting is a direct measure of pseudomorphic strain to which the layer is subjected. Strain modifies the band structure in such a way that the DOS of the valence band becomes small, resembling more the DOS of the conduction band. At the same time, direct intervalence band absorption and Auger recombination are reduced, due to an increased strained-induced LH–HH energy splitting. As compared to an unstrained QW laser, a compressively strained laser (emitting in TE polarization mode) exhibits a small threshold current I_{th} and current density J_{th}, low internal optical loss α_i, enhanced external differential efficiency η_e, high characteristic temperature T_o, and small linewidth enhancement factor.

Tensilely strained GaInAsP–InP QW lasers emitting a 1.5 μm also have better laser characteristics than those of unstrained lasers. Their J_{th} is even lower than that of compressively strained lasers, in contrast to the original theoretical expectations. Good lasing characteristics of these devices can mainly be attributed to strongly enhanced optical gain for the TM mode. The TM mode is increased from zero for the quantum confined states of unstrained and compressively strained wells to a value proportional to 2/3 MO^2 for the tensilely stained wells, while TE = 1/6 MO^2 (MO^2 is a transition matrix element) [20]. No similar studies have been reported for 0.98 μm lasers; we shall briefly discuss our preliminary results of such studies in Section 3.3.

The energy bands $E(\boldsymbol{k})$ of strained and unstrained quantum wells are schematically shown in Fig. 2. It should be emphasized that there exists no LH–HH degeneracy in a (thin) well layer even for the unstrained case because of the quantum confined effect and, therefore, the well emits light in pure TE mode.

To assess the quality of $Ga_xIn_{1-x}As_yP_{1-y}$ quantum wells, we grew samples with various QW structures and measured photoluminescence (PL) and X-ray diffraction (XRD). The line shape and full width at half maximum of PL were comparable to those of high-quality AlGaAs–GaInAs samples. X-ray diffraction from superlattices, shown in Fig. 3, exhibits sharp and well-

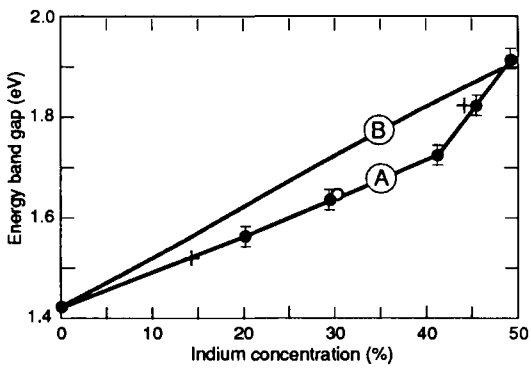

Fig. 1. Room-temperature band gaps of $Ga_xI_{1-x}As_xP_{1-x}$ lattice-matched to GaAs. Curve A: experimental, curve B: theoretical. The curve drawn through the experimental points is a guide to the eye and has no theoretical significance. o MOCVD growth by S. H. Groves [19]; + LPE growth by D. Garbuzov *et al.* [20].

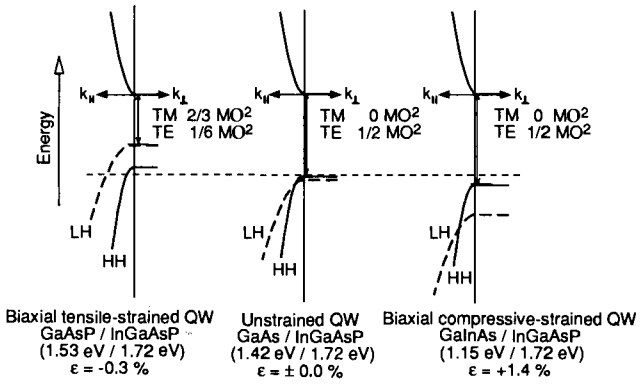

Fig. 2. Schematic diagram of energy bands $E(k_\parallel, k_\perp)$ in quantum wells. Oscillator strengths for TM and TE polarizations are proportional to the transition matrix element MO^2. For illustration, various strained-layer systems used in actual laser structures are also shown. The band gaps of the wells are not drawn on scale in this example.

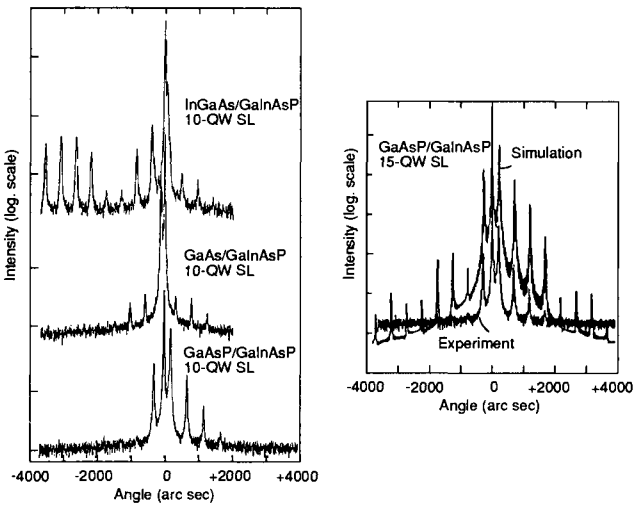

Fig. 3. X-ray diffraction from 10-period superlattices consisting of $Ga_{0.8}In_{0.2}As$(10 nm)-GaInAsP(30 nm, $E_g = 1.57$ eV), GaAs(10nm)-GaInAsP (30 nm, $E_g = 1.57$ eV), and $GaAs_{0.92}P_{0.08}$(12 nm)-GaInAsP(30 nm, $E_g = 1.57$ eV) quantum well structures. Right panel: Measured and calculated XRD rocking curves for a 15-period $GaAs_{0.92}P_{0.08}$(12 nm)-GaAs(27 nm) superlattice.

resolved peaks. By way of example, an experimental XRD in Fig. 3 is compared with a calculated XRD obtained by dynamic simulation on the assumption that the heterointerfaces are abrupt. The agreement between theory and experiment is excellent.

There exists a large valence band discontinuity ΔE_v at the $Ga_xIn_{1-x}As_yP_{1-y}$-$Ga_xIn_{1-x}As$ interface. The conduction band offset ratio [22, 23] $\Delta E_c/\Delta E_g$ of the $Ga_xIn_{1-x}As$-GaAs interface is about 0.6 for $0.75 \leqslant x \leqslant 0.93$. For $Ga_{0.51}In_{0.49}P$-GaAs, which represents the extreme combination of the band gaps ($\Delta E_g \approx 1.90 - 1.42 = 0.48$ eV), ΔE_v of 0.24 eV has been reported [24], suggesting $\Delta E_c/\Delta E_g \approx 0.5$. It is therefore likely that $\Delta E_c/\Delta E_g$ of GaInAsP–GaInAs lies between 0.5 and 0.6 independent of x.

While the confinement behavior of the HH states is generally well understood in the $Ga_xIn_{1-x}As$-GaAs quantum wells, the confinement of the LH state is not. Recent experiments have clarified this question to some extent [23]. In GaInAs-GaAs wells of 10 to 15 nm in thickness (L_z), the LH state is weakly bound at an In concentration of 7% but is not confined at higher In concentration. It is possible that the stronger confinement of the LH state in a (wide) well with a small amount of In is due to a reduction in strained-induced LH–HH band splitting. In addition to this intrinsic effect, there may also exist extrinsic effects which influence the LH states, caused by an increased number of interface defects at a high In concentration [23]. On the other hand, our PL and XRD measurements on pseudomorphic quantum wells having $L_z < 15$ nm indicate no remarkable difference in the quality of the interfaces, as In concentration is varied ($x > 0.8$).

The number of subbands in the well influences laser action at threshold [25]. Radiative transitions between higher order subbands, e-HH ($n = 2$), make a significant contribution to J_{th} and T_0 of GaInAs–GaAs lasers. For a thin well ($L_z \approx 5$ nm) there is only one HH band, but as L_z is increased, higher states are bound within the wells. These states become increasingly populated as the energy separation decreases with increasing L_z. Consequently, the e-HH ($n = 2$) transitions make an increasing contribution to the radiative recombination current even though the dominant e-HH ($n = 1$) transitions continue to provide the optical gain [25]. Association with the presence of e-HH ($n = 2$) transitions is a remarkable increase in J_{th} and a decrease in T_0 and η_e.

On the basis of the above results and our own experience it seems likely that thin GaInAs–GaAs wells ($L_z < 8$ nm) with high In concentration ($\approx 20\%$) offer advantages over broad wells with low In concentration when designing the lasers for $\lambda = 0.98$ μm.

3. Laser diodes

3.1. General considerations

Crucial to the realization of pump lasers for the EDFA are the control of a stable fundamental mode at very high power levels, the protection of the laser mirrors, the total electrical-to-optical power conversion, and the control of the far-field pattern. Of course, the ultimate goal is to achieve a maximum output power from a fiber-coupled device at drive currents where the packaged device appears reliable.

The fast development of Al-free 0.98 μm lasers in the past two years has increased the output power from a few tens to several hundred milliwatts, emitted to free space, and tens of milliwatts obtained from the fiber-pigtailed device. The reliability of these lasers is expected to be at least comparable to that of AlGaAs–GaInAs lasers but has not yet been proved for certainty. It is worth noticing that because λ is inherently related to the gain profile that varies with optical losses and degradation during operation, any reliability and lifetime projection should be considered both in terms of light *vs.* current characteristics and emission wavelength.

3.2. Device structures

A number of versions of high-output fundamental transverse mode lasers have been developed, notably, those with ridge waveguide structures, buried heterostuctures and self-aligned structures. Apart from its structural simplicity, the ridge waveguide design is very attractive because it can keep the optical wavefronts in

the device planar and exhibit low J_{th} and very high η_e. The planar wavefront results in a small, almost power-independent astigmatism and negligible phase-front distortions in the beam. The near-field spread in the vertical direction can be controlled by the structure and composition of layers. The near-field in the lateral direction can be controlled by the ridge geometry. There are also detrimental effects due to refractive index changes (δn) at a high carrier injection level, non-uniform light intensity in the cavity, local thermal heating, etc., which modify the waveguide dielectric properties. Self-consistent calculation of these detrimental effects in the active waveguide laser model has turned out difficult. Therefore, passive waveguide approximations are often used for modelling the ridge waveguide lasers, and the detrimental effects are taken into account as second-order disturbances in a non-self-consistent way [26].

A large optical field inside the cavity reduces the optical flux density in the lasing mode and helps avoiding spatial hole burning. The vertical field spread depends on an effective refractive index step, Δn_{eff}, between the active and passive parts of the structure. Small Δn_{eff} yields weak optical confinement. Although this design—small Δn_{eff} and a shallow ridge—a kind of mixed index-guiding and anti-guiding structure, increases the threshold current of the device, it increases the maximum output power attainable in single mode operation and generates a narrow vertical far-field.

The mode stability plots in (w–t) parameter space calculated for passive ridge waveguide 3-QW $Ga_{0.8}In_{0.2}As$–GaAs–GaInAsP($E_g = 1.72$ eV)–$Ga_{0.51}In_{0.49}P$ lasers are shown [27] in Fig. 4. Here, w denotes the ridge width and t the distance from the bottom of the ridge to the center of the well region. Our calculation predicts that fundamental lateral single mode operation only occurs in a limited region of (w–t) space. Apparently, lasers with relatively wide shallow ridges and weak optical confinement are desired for the EDFAs.

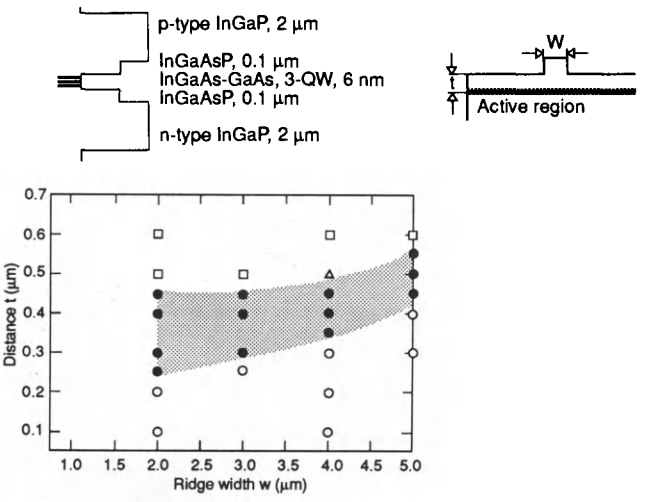

Fig. 4. Schematic real-space band structure diagram for a modelled 3-QW GaInAsP–GaInAs–GaAs–GaInP quantum well laser. Lower panel: Modal behavior for the passive waveguide structure [27]. The shaded area indicates the (w–t) space where single mode operation is predicted to occur. Here, t refers to the distance from the ridge bottom to the center of the well region. ● Single mode operation; ○ multi-mode operation; □ cut-off, no confined modes; △ transitional region, operational status unclear.

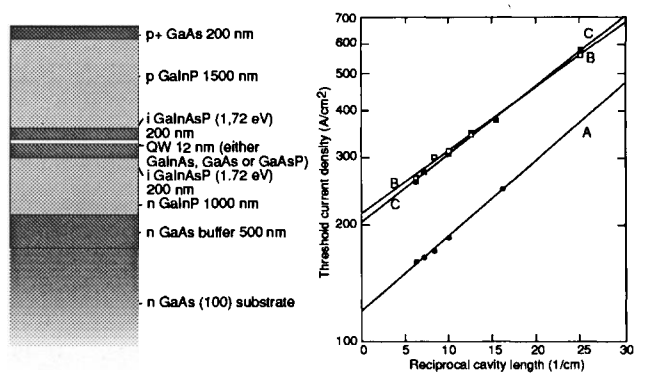
p+ GaAs 200 nm
p GaInP 1500 nm
i GaInAsP (1,72 eV) 200 nm
QW 12 nm (either GaInAs, GaAs or GaAsP)
i GaInAsP (1.72 eV) 200 nm
n GaInP 1000 nm
n GaAs buffer 500 nm
n GaAs (100) substrate
Threshold current density (A/cm²)
Reciprocal cavity length (1/cm)
A
B
C

Fig. 5. Left: layer structure of the tested lasers with different quantum well compositions; the other layers are kept unchanged. Right: threshold current density plotted against reciprocal cavity length [26]. A. GaInAs QW ($\varepsilon = 1.4\%$); B. GaAs QW ($\varepsilon = 0.0\%$); C. GaAsP QW ($\varepsilon = -0.3\%$).

3.3. *Effects of lattice strain on lasing performance*

Practically all 0.98 μm lasers reported in the literature contain compressively strained GaInAs quantum wells. Very little is known about tensilely strained lasers in this wavelength region.

We have tentatively studied strain effects on lasing characteristics [28]. Figure 5 shows J_{th} as a function of reciprocal cavity length ($1/L_c$) for the three different cases of strain. The lowest J_{th} is obtained with the compressively strained wells. One may expect, however, that the tensilely strained lasers would be better than the unstrained lasers if the quantum well had more strain (more P) and the waveguiding GaInAsP layer had higher E_g to improve optical confinement.

Figure 6 displays the continuous wave (cw) output power per facet as a function of injection current for three lasers. Although these preliminary experiments do not allow any detailed conclusions to be drawn they imply that the laser with a GaAs well has somewhat smaller η_i and η_e than the others. Optical losses are extremely small for all the devices. It can also be seen that $\lambda = 0.98$ μm can only be reached by using a GaInAs well.

4. Very high power lasers

In this section we present high-power pump lasers having GaInP cladding layers. The quantum wells are under compressive strain, while the barriers, confinement and cladding layers are lattice-matched to GaAs. These devices and their properties are compiled in Tables 1 and 2. One may see that the lasers exhibit outstanding performances which are comparable to those of the best AlGaAs–GaInAs lasers.

A representative of ridge waveguide pump lasers is illustrated in Fig. 7. This laser, recently made by our Tampere group, launches a cw output power of 430 mW in multi-mode operation and sustains single mode operation to powers higher than 150 mW. In pulsed mode, it reaches a power level of 780 mW before COD

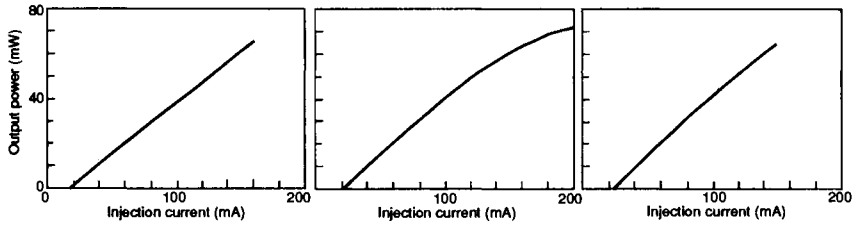

Fig. 6. Output power per facet *vs.* injection current for strained and unstrained broad-area lasers with layer structures shown in Fig. 5. (a) GaInAsP–GaInAs ($\varepsilon = 1.4\%$), $L = 1600$, $\eta_d = 73\%$, $\eta_i = 94\%$, $\alpha_j = 2.4\ \mathrm{cm}^{-1}$, $\lambda = 983$ nm at 20 mW; (b) GaInAsP–GaAs ($\varepsilon = 0.0\%$), $L = 500$, $\eta_d = 72\%$, $\eta_i = 83\%$, $\alpha_j = 3.3\ \mathrm{cm}^{-1}$, $\lambda = 875$ nm at 20 mW; (c) GaInAsP–GaAsP ($\varepsilon = -0.3\%$), $L = 800$, $\eta_d = 76\%$, $\eta_i = 93\%$, $\alpha_j = 3.3\ \mathrm{cm}^{-1}$, $\lambda = 838$ nm at 20 mW.

TABLE 1. Characteristics of broad-area Al-free lasers. N = number of quantum wells, L_c = cavity length (mm), J_{th} = threshold current density (A cm^{-2}), J_0 = transparency current (A cm^{-2}), T_0 = characteristic temperature (K), η_i = internal quantum efficiency (%), α_i = internal loss (cm^{-1}), λ = lasing wavelength (nm)

Laser structure	N	L_c	J_{th}	J_0	T_0	η_i	α_i	λ	Reference
GaInAs–GaAs	1	1.2	72	29	140	91	8.8		29, 30
	3	1.2	165						29, 30
	1	1.5	293	131		78	9.5	980	31
	1	1.5	70					980	32
	3	1.5	170					980	32
	1	2.5	72	25			6.4		33
	1	1.0	177			91	9.1		34
GaInAs–GaInAsP	3	1.2	169		235	83	5	980	35
	3	0.4	225		213			980	35

TABLE 2. Characteristics of ridge waveguide (RW), buried heterostructures (BH), and channel guided (CG) lasers. N = number of quantum wells, W = ridge width (μm), I_{th} = threshold current (mA), P_{cw} = cw output power (mW), P_p = output power in pulse mode (mW), P_{sm} = output power in single mode (mW), η_e = slope efficiency (mW mA^{-1}), Θ_{ver} = vertical beam divergence (arc ceg), Θ_{lat} = lateral beam divergence (arc deg). AR/HR refers to anti-reflection/high reflection mirror facet coatings

Laser structure	N	W	L_c	I_{th}	P_{cw}	P_p	P_{sm}	T_0	η_e	α_i	Θ_{ver}	Θ_{lat}	λ	References
GaInAs–GaAs, RW														
(AR/HR)	1	4	0.5	8	100								980	32
(uncoated)	1		1.5	22	118			130			60	20	1000	33
(AR/HR)	1	3	0.5	12	160									34
(AR/HR)	1	3	0.25	7			90	180	0.9	7.7	40	13	1000	34
GaInAs–GaAs, CG														
(uncoated)	1	6	0.75	20	125				0.28				980	10
GaInAs–GaInAsP, RW														
(AR/HR)	1	5	1.6	30	430	780	>150		0.7	3	<30	10	980	36
(uncoated)	3	5	0.8	21			25		0.37		47		980	35
GaInAsP–GaIn(As)P, BH														
(HR)	1	7	0.8		500	1200							780	31

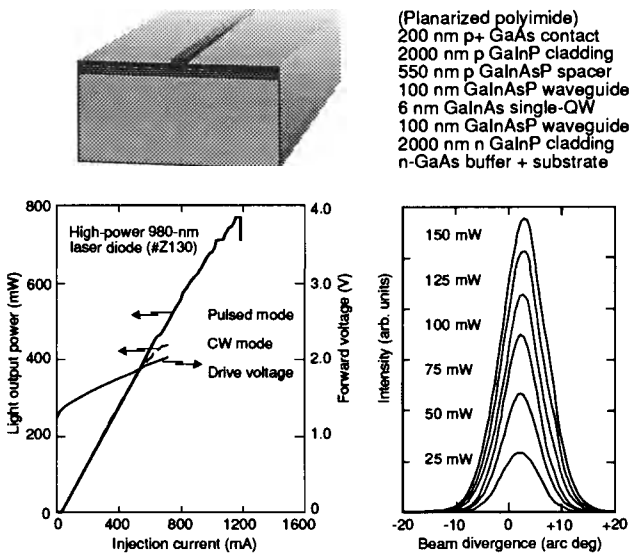

Fig. 7. Light *vs.* current curves and lateral far-field spread of a ridge waveguide GaInAs-GaInAsP-GaInP separate confinement heterostructure single quantum well laser ($L_c = 1.6$ mm) with AR/HR facet coatings, emitting at 0.98 μm.

takes place (the facet melts). The threshold current is about 30 mA, $\eta_i \approx 91\%$, $\eta_e \approx 0.7$ mW mA^{-1} and $\alpha_i \approx 3$ cm^{-1}. The beam divergence in the lateral direction varies between 8° and 11°, as the output power is varied between 25 and 150 mW. The vertical far-field spread remains below 30°. In preliminary fiber coupling tests, a power of 50 mW at drive current 180 mA has been coupled into a single mode fiber, corresponding to an overall coupling efficiency of about 50%.

Acknowledgments

This work was supported by the Technology Development Centre (TEKES) and The Academy of Finland. It was carried out, in part, within the framework of the EC RACE WELCOME #R2006 programme.

References

1 E. Snitzer, H. Po, F. Hakimi, R. Tumminelli and B. C. McCollum, *Proc. OFC'88*, PD2, (1988).
2 R. I. Laming, M. C. Farries, P. R. Morkel, L. Reekie, D. N. Payne, P. L. Scrivener, F. Fontana and A. Rihetti, *Electron. Lett.*, *52* (1989) 12.
3 M. Yamada, M. Shimizu, M. Okayasu, T. Takeshita, M. Horiguchi, Y. Tachikawa and E. Sugita, *IEEE Photon. Technol. Lett.*, *2* (1990) 205.
4 M. Shimizu, M. Horiguchi, M. Yamada, M. Okayasu, T. Takeshita, I. Nishi, S. Uehara, J. Noda and E. Sugita, *Electron. Lett.*, *26* (1990) 498.
5 B. Pederson, B. A. Thompson, S. Zemon, W. J. Miniscalco and T. Wei, *IEEE Photon. Technol. Lett.*, *PTL-4* (1992) 46.
6 E. Desurvire, *IEEE Photon. Technol. Lett.*, *2* (1990) 208.
7 M. Yamada, M. Shimizu, Y. Ohishi, J. Temmyo, M. Wada, T. Kanamori, M. Horiguchi and S. Takahashi, *IEEE Photon. Technol. Lett.*, *4* (1992) 1041.
8 A. Larsson, J. Cody, S. Forouhar and R. J. Lang, *Appl. Phys. Lett.*, *56* (1990) 1731.
9 Y. K. Sin, H. Horikawa and T. Kamijoh, *J. Appl. Phys.*, *72* (1992) 3212.
10 T. Ijichi, M. Ohkubo, N. Matsuoto and H. Okamoto, in *Proc. 12th IEEE Int. Semiconductor Laser Conf., Davos, September 1990*, p. 44.
11 Y. J. Chan, D. Pavlidis, M. Razeghi and F. Omnes, *IEEE Trans. Electron. Devices*, *37* (1990) 2141.
12 S. L. Yellen, A. H. Shepard, C. M. Harding, J. A. Baumann, R. G. Waters, D. Z. Garbuzov, V. Pjataev, V. Kochergin and P. Zory, *IEEE Photon. Technol. Lett.*, *4* (1992) 1531.
13 Y. J. Chan, D. Pavlidis, M. Razeghi and F. Omnes, *IEEE Trans. Electron. Devices*, *37* (1990) 2141.
14 G. Zhang, A. Ovtchinnikov, J. Näppi, H. Asonen and M. Pessa, *J. Quantum Electron.*, *QE-29* (June 1993).
15 W. Nakwaski, *J. Appl. Phys.*, *64* (1988) 159.
16 J. M. Olson, R. K. Ahrenkiel, D. J. Dunlavy, B. Keyes and A. E. Kibbler, *Appl. Phys. Lett.*, *55* (1989) 1208.
17 Q. Liu, H. Lakner, F. Scheffer, A. Lindner and W. Prost, *J. Appl. Phys.*, *73* (1993) 2770.
18 T. Iwamoto, K. Mori, M. Mizuta and H. Kukimoto, *Jpn. J. Appl. Phys.*, *22* (1983) L191.
19 S. H. Groves, *J. Cryst. Growth*, *124* (1992) 747.
20 D. Garbuzov, N. Yu. Antonishkis, A. D. Bondarev, A. B. Galarkov, S. N. Zhigulin, N. I. Katsavets, A. V. Kochergin and E. V. Rafailov, *IEEE J. Quantum Electron.*, *27* (1991) 1531.
21 E. Yablonovitch and E. O. Kane, *J. Lightwave Technol.*, *LT-4* (1986) 504.
22 D. Ahn, S. L. Chuang and Y. C. Chang, *J. Appl. Phys.*, *64* (1988) 4056; D. Ahn and S. L. Chuang, *IEEE J. Quantum Electron*, in press.
23 J.-P. Reithmaier, R. Hger and H. Riechert, *Appl. Phys. Lett.*, *57* (1990) 957.
24 M. A. Rao, E. J. Caine, H. Kroemer, S. I. Long and D. I. Babic, *J. Appl. Phys.*, *61* (1987) 643.
25 P. Blood, E. D. Fletcher, K. Woodbridge and M. Vening, *Appl. Phys. Lett.*, *57* (1990) 1482.
26 H. Jaeckel, G.-L. Bona, P. Buchmann, H. Meier, P. Vettiger, W. J. Kozlovsky and W., Lenth, *IEEE J. Quantum Electron.*, *27* (1991) 1560.
27 J. Näppi, A. Ovtchinnikov, H. Asonen, P. Savolainen, M. Korteoja and M. Pessa, to be presented at *ECOC '93, Switzerland, September, 1993.*
28 G. Zhang, Applications of molecular beam epitaxy grown III-V compound semiconductors in optoelectronic devices, *PhD Thesis*, Tampere University of Technology, 1993.
29 G. Zhang, *Appl. Phys. Lett.*, *62* (1993) 1405.
30 G. Zhang, J. Näppi, K. Vänttinen, H. Asonen and M. Pessa, *Appl. Phys. Lett.*, *61* (1992) 96.
31 D. Z. Garbuzov, N. Ju. Antonishkis, S. N. Zhigulin, N. D. Ilinskaya, A. V. Kochergin, D. A. Lifshitz, E. U. Railov and M. V. Fuksman, *Appl. Phys. Lett.*, *62* (1993) 1062.
32 Y. K. Sin, H. Horikawa and T. Kamojoh, *J. Appl. Phys.*, *72* (1992) 3212.
33 R. M. Kapre, W. T. Tsang, Y. K. Chen, M. C. Wu, M. A. Chin and F. S. Choa, *J. Cryst. Growth*, *124* (1992) 176.
34 J. M. Kuo, Y. K. Chen, M. C. Wu and M. A. Chin, *Appl. Phys. Lett.*, *59* (1991) 2781.
35 J. Näppi, A. Ovtchinnikov, P. Savolainen, G. Zhang and H. Asonen (to be published in 1993).
36 H. Asonen, J. Näppi, A. Ovtchinnikov, P. Savolainen, G. Zhang, R. Ries and M. Pessa, *IEEE Photon. Technol. Lett.* (June 1993).

Materials Science and Engineering, B21 (1993) 217–223

Shadow mask MBE for the fabrication of lead chalcogenide buried heterostructure lasers

A. Lambrecht, R. Kurbel and M. Agne

Fraunhofer Institute for Physical Measurement Techniques (IPM), Heidenhofstr. 8, D-79110 Freiburg (Germany)

Abstract

Laser diodes based on IV-VI-compounds are important sources for tunable infrared radiation in the 3 to 20 μm spectral region. A major application is trace gas analysis of atmospheric pollutants. Fabrication of buried heterostructure (BH) lasers by molecular beam epitaxy (MBE) improves the spectral and farfield emission properties.

Using the materials PbSe, PbEuSe, PbSrSe and PbSnSe, BH lasers were fabricated by directly growing the active stripe through a shadow mask with reduced process duration. The shadow masks were prepared by anisotropic chemical etching of Si(100). The lasers show reduced threshold currents when compared to DH lasers, similar to BH lasers made by a photolithographic technique and also improved radiation patterns.

Due to their smooth shape and less surface contamination as compared to their photolithographic counterparts, the overgrowth results show a reduced amount of material discontinuities for the shadow mask lasers.

1. Introduction

Laser diodes based on IV-VI compounds are important sources for tunable infrared radiation in the 3–20 μm spectral region. Major applications are trace gas analysis of atmospheric pollutants [1] and fast automotive exhaust analysis [2]. These mid-infrared lasers have to be operated at low temperatures, usually with liquid nitrogen coolers. A widespread use of mid-infrared laser spectrometer systems is hampered by the still-insufficient state of development of these laser diodes. For example, if a laser diode needs to be changed, the user frequently has to face a tedious optical readjustment of the system since present state-of-the-art laser diodes do not have uniform, device-independent radiation patterns. Depending on the diode used, the user may not even recover the former gas detection limits achieved with another diode.

Buried heterostructure (BH) devices are expected to be better suited for spectroscopic applications than the double heterostructure (DH) lasers usually employed. These lasers are commonly made by molecular beam epitaxy (MBE). Details of the basic DH structures and fabrication techniques are given elsewhere [3,4]. For a BH laser a narrow active stripe has to be formed; this is usually done using etching techniques [5]. This stripe has to be buried within the confinement material. Shape and surface quality of the active ridge determine the overgrowth quality. Successful MBE overgrowth of 2–5 μm wide lateral structures is also a prerequisite for the future fabrication of advanced submicrometer structures as distributed feedback lasers [6].

In the following, two techniques for BH lead salt lasers are explained: a conventional photolithographic process for reference, and the new shadow mask technique (Fig. 1).

2. Technology

Usually the active stripe for a BH laser is made by a destructive technique, *i.e.* by photolithography and some wet [7,8] or dry [5] etching process.

Wet etching is probably less destructive. However, for the rather large range of ternary material compositions to be covered during the fabrication of spectroscopically relevant lasers, the etch rates turn out to be very different. On the one hand, the etching solutions we used for the materials PbSe, PbEuSe, PbSnSe and PbSrSe gave strongly composition-dependent etch rates and could not be sufficiently reproduced during subsequent experiments. On the other hand, the strong selectivity of these etchants can be used as a preparation tool to reveal different material compositions of a given MBE structure using scanning electron microscopy (SEM). This method was used to reveal the active layer of the laser shown in Fig. 2.

Dry etching gives stable etch rates which depend only weakly on the materials used. We were using Ar^+ ion beam etching with the above-mentioned materials.

0921-5107/93/$6.00

© 1993 – Elsevier Sequoia. All rights reserved

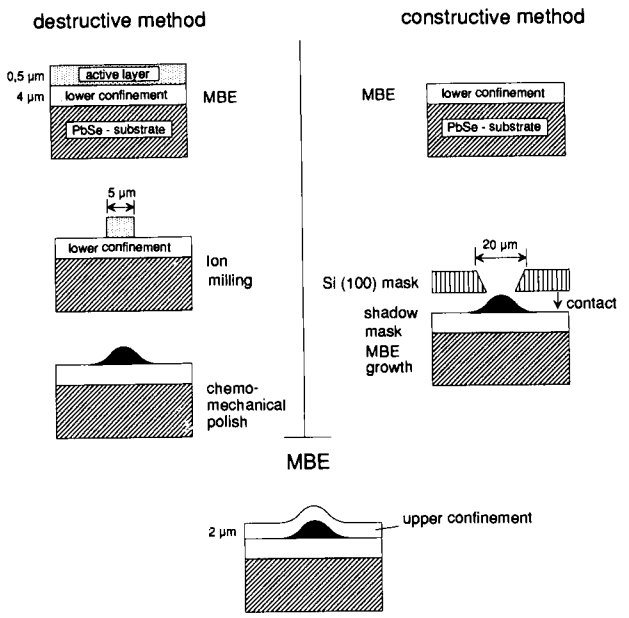

Fig. 1. Fabrication steps for a BH laser by photolithography (destructive technique) or by shadow mask growth (constructive technique).

Dry etching yields a well-defined geometry of the etched stripe and can be applied down to submicrometer dimensions, for example for the fabrication of DBR lasers [9].

However, dry etching damages the material and causes additional surface contamination by polymerized photoresist residues which can barely be removed before overgrowth. We recently reported on the use of a chemico-mechanical etching process to improve the shape and surface quality of dry etched active BH ridges [10] (see Fig. 1). With this additional process step we obtained a smooth shape and reasonable surface quality suitable for the subsequent MBE overgrowth. Following this procedure a series of photolithographic BH lasers that match the maximum operation temperatures of DH lasers had been made, as shown in Fig. 3. This technology is reproducible and material independent; however, it needs many intermediate process steps. Furthermore, it turned out that many steps have to be controlled by SEM analysis to ensure a reasonable yield and quality. Therefore it takes at least a full day to process a wafer with the active layer until it can enter the MBE apparatus again for the final overgrowth.

The shadow mask technique described here is a constructive method. It should be better adapted to a small-volume production since it needs less equipment to make reasonable mid-infrared BH lasers.

Shadow mask growth for III–V compounds has already been reported by Tsang and Ilegems [11]. Following this technique (see Fig. 1) an Si shadow mask is placed on top of (and in contact with) the lower confinement layer of a DH laser structure. With a second MBE step the active layer is grown through the slits in the mask. The width, shape and composition of the active stripe obtained depend on the mask geometry, the position of the MBE furnaces, and other growth parameters (substrate and mask temperatures, substrate rotation). It is geometrically evident that the distance between mask and substrate is a very critical parameter. Therefore, we decided to place the mask in contact with the substrate. In most cases we obtained stripes as illustrated by the dark area in Fig. 2. They have tailed edges suitable for subsequent overgrowth. However, with some samples we observed an increased thickness of the ridge at the edges, which might be an indication for re-evaporation of material from the Si mask. Re-evaporation will probably depend on the growth temperature. In this work we used the same growth temperatures as for DH structures and did not optimize this parameter for shadow mask growth.

The chemico-mechanical etching successfully employed for photolithographically obtained stripes [10] can also be used with the active ridges made by shadow mask growth. We used this method once to improve further the surface. However, laser data did not show a difference between etched and original wafers.

After growth of the active stripe, the mask is removed, and in the final MBE step the upper confinement layer is grown. In our case we removed the substrate holder from the MBE chamber to fix/detach the masks in a flow box. Evidently one can develop a complete *in vacuo* process where the mask can be fixed or removed within an MBE chamber. In our case the whole process of mask mounting/removal takes about 10 min, so we can easily perform the whole three-step MBE process during one day.

Compared with the photolithographic technique, difficulties shift towards the fabrication and use of proper masks. Our masks are made by anisotropic etching of Si(100) by KOH [12]. We started with 380-μm-thick wafers polished on both sides. Thermal SiO_2 was used as a mask material. Using standard photolithography, properly designed slits are opened by HF etching. V-groove etching through the wafer was performed in several steps to control the etch rate. The total wafer thickness is critical if one wants to end at slits in the 10 μm range. The final etching step is quite difficult using this method; when the slits begin to appear, they tend to open rapidly. However, we were able to obtain a series of masks with slits 15–20 μm wide and 10 mm long by this method. With these masks the BH lasers shown here are fabricated. In Fig. 4 an SEM side view of a mask with an 80-μm-wide slit is shown.

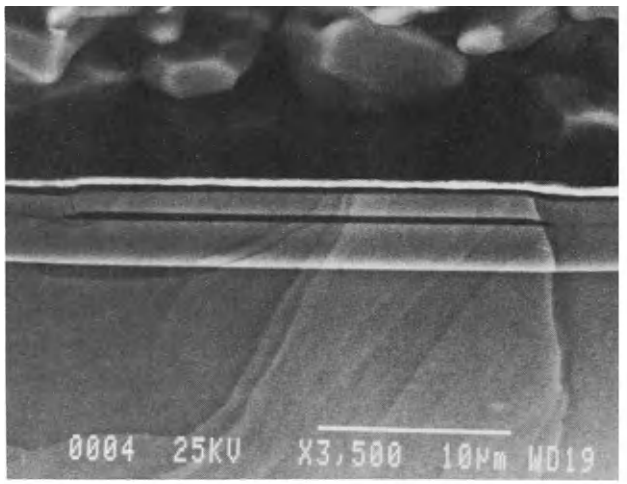

Fig. 2. SEM image of a contacted and mounted PbSnSe shadow mask laser (MBE 1447). The active layer is shown by the darker area.

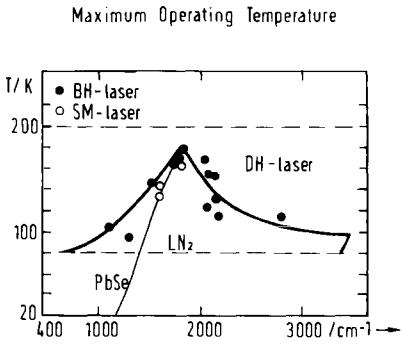

Fig. 3. Maximum operating temperatures of PbSe-based DH lasers (line), photolithographically obtained BH lasers (full circles), and shadow mask BH lasers (open circles).

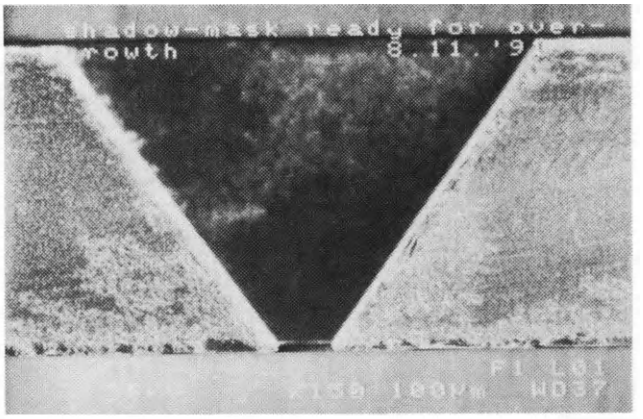

Fig. 4. SEM side view of a 80-μm-wide slit in an Si(100) wafer obtained by anisotropic etching with KOH.

As an alternative approach we stopped the Si etching just before opening the slits to get a thin (diameter 10 μm) Si diaphragm. By cutting it with a KrF eximer laser at 248 nm we obtained long and 4.3-μm-wide slits (see Fig. 5). We also tried ion-beam etching for the final slit formation, which gave similar widths but less uniform edges compared with laser cutting.

Mask generation may be further simplified by the use of more advanced processing methods, for example the use of plasma-enhanced chemical vapor deposition-grown Si-oxide or -nitride passivation layers, or the use of one-side boron-implanted Si wafers to stop KOH etching at a 1–2-μm-thick diaphragm.

As IV–VI wafers are quite small (less than 1 cm^2) a large number of shadow masks can be obtained from a single Si wafer. Hence a mask may be disposed of after a single MBE run. However, the masks may be used repeatedly. During our experiments we used one mask three times without cleaning, but cleaning of the Si masks seems to be possible, and they may be baked at high temperatures after processing.

When growing the active layer through the mask, two different methods can be used. If the substrate rotates during growth of the active layer, a rather broad stripe will be obtained. This method was used for laser 1415 of Table 1. For ternary active layers this is necessary to obtain reasonable homogeneity across the stripe to get emission at a predetermined wavelength. If the substrate does not rotate during active layer growth the stripes can be narrower, but an inhomogeneous concentration profile will result. Emission may then occur from a quite narrow region with the lowest gap value. This method was used for lasers 1447 and 1460 in Table 1.

3. Results

In Fig. 2 a PbSnSe shadow mask BH laser (MBE 1447) is shown. This laser has PbEuSe confinement layers. The active layer is about 20 μm wide. Obviously this is larger than the width obtainable by the photolithographic method. A closer inspection of the selectively etched cleavage plane shows that the MBE overgrowth of the shadow mask laser is better than in the case of photolithographically obtained BH lasers. The smooth edges of the active stripe caused by the shadow mask method favour a crack-free overgrowth. It is difficult to obtain such a shape by etching techniques [10].

Figure 6 shows a comparison of the threshold currents of three different laser structures. The lasers emit at about 7.5 μm at $T=80$ K in cw mode, as expected from the active layer composition. The lasers are a DH stripe contact laser, a photolithographically

TABLE 1. Data of shadow mask lasers

MBE run	Materials	Active width (SEM) (μm)	Ith (80 K) (mA)	ν (80 K) (cm^{-1})	T_{max} (K)	Rotation (+/−)
1415	PbEuSe(c) PbSe(a)	30	101	1372	140	+
1447	PbEuSe(c) PbSnSe(a)	23[a]	18	1335	140	−
1460	PbSrSe(c) PbSrSe(a)	23[a]	20	1386	160	−

[a]Effective active width possibly thinner owing to inhomogeneities.
Ith (80 K), threshold current in cw mode at $T = 80$ K.
ν (80 K), emission wavelength at threshold at $T = 80$ K.
T_{max}, maximum operation temperature obtained in cw mode.
c = confinement; a = active layer.

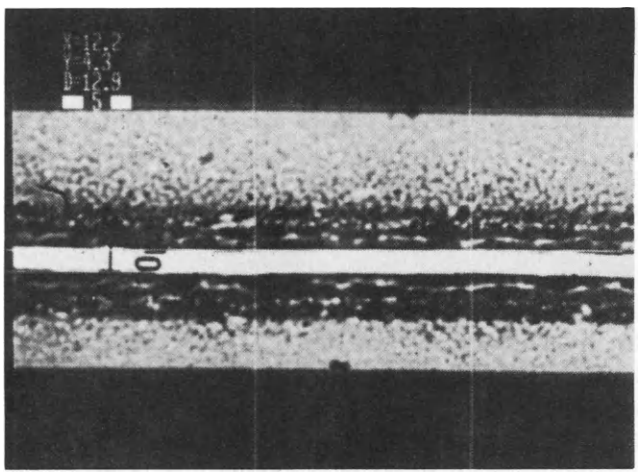

Fig. 5. 4.3-μm-wide slit in an Si(100) diaphragm obtained by eximer laser cutting.

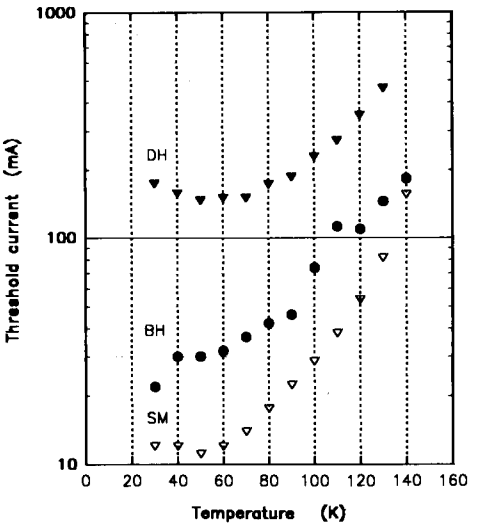

Fig. 6. Threshold currents observed for PbSnSe BH lasers: (top) stripe contact DH laser, (middle) 10-μm-wide photolithographically made BH laser, (bottom) shadow mask (SM) laser (MBE 1447). DH and BH lasers are processed from the same MBE run. The threshold data are obtained with an automatic system which causes some scatter in the data points, especially for the BH laser.

obtained 10-μm-wide BH laser (both were fabricated from the same MBE wafer), and a shadow mask (SM) laser with about the same active layer composition. The SM laser reaches even lower threshold currents than the BH laser.

The modal intensity distributions of these SM lasers are quite similar to 20-μm BH lasers or to DH lasers. Narrow BH lasers with an active width of 5 μm generally have quite regular mode distributions with no high order lateral modes, but the disadvantage is less modal power.

The main advantage of IV–VI BH lasers was found to lie in their improved far-field characteristics. As was pointed out by spectroscopists [13], the far-field emission pattern strongly influences the achievable sensitivity limits. Therefore we investigated the far-field distributions in more detail.The far-field patterns are measured by stepping an HgCdTe detector across the intensity distribution in front of the laser diode [10,14]. The commonly used DH lasers have multi-lobe far fields that change their distribution with operating temperatures and currents. BH lasers have well-defined far fields which are more stable to variations in the operating parameters. For 5-μm BH lasers we usually find single fundamental lateral mode emission [10,14], but even the two-lobe emission generally found for wider active stripes will be more reliable and useful for spectroscopic applications than the changing emission patterns found with DH lasers. The observed far fields of BH lasers agree quite well with calculated emission

patterns from a multilayer waveguide model [14] and hence can be predetermined by the design parameters.

The far-field pattern of the rather broad SM laser 1415, which has an active layer of PbSe (see Table 1), is given in Fig. 7(a). It has a two-lobe emission. The far-field distribution agrees quite well with the calculated pattern of the TE_{10} mode (Fig. 7(b)). The calculation for SM structures used the effective index method as described in ref. 14.

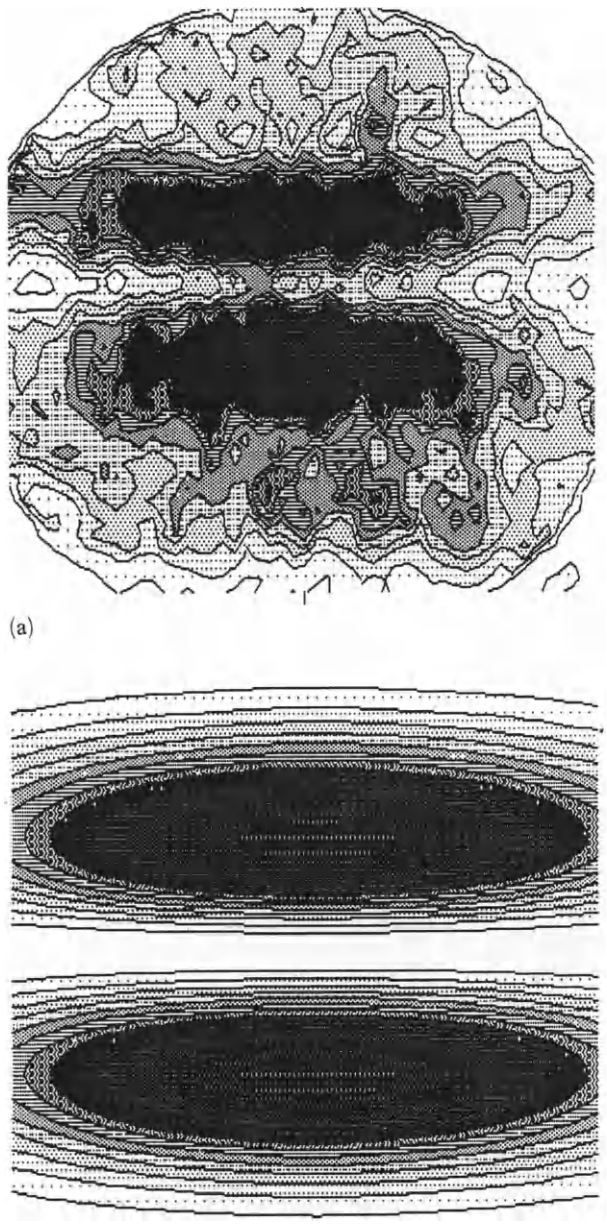

(a)

(b)

Fig. 7. (a) Far-field pattern of laser 1415-1-3 at $T=80$ K and $I=500$ mA. The p/n junction plane is oriented vertically. The scanned field is $51° \times 51°$. (b) Calculated TE_{10}-mode pattern with same orientation and angular range as in (a).

In Fig. 8 the far-field distributions of some lasers of Fig. 6 are shown: Fig. 8(a) shows high-order lateral modes typical of the DH laser. Figure 8(b) shows the far-field of a 20-μm BH laser having a first-order lateral TE_{10} pattern. It is similar to the far-field pattern of the SM laser (Fig. 8(c)). The 10-μm BH laser presented in Fig. 6 has a single-lobe far field at $T=30$ K, but then shifts to higher-order transverse modes at higher temperatures that cannot be explained theoretically at present [14].

The improvement of laser far fields by shadow mask growth is even more pronounced in the case of laser 1460 (Table 1). Here the emission at $T=80$ K does not occur at the anticipated wavelength of 5.0 μm (as planned from the composition of the active layer), but only at a slighly shorter wavelength than the emission of a PbSe layer. However, driving the laser with short current pulses of about 500 mA produces additionally the anticipated emission wavelength. This indicates that by growth without rotation we have formed a narrow stripe of material with very low Sr concentration caused by the orientation of the MBE furnaces towards the substrate. This narrow stripe width explains the low threshold current of this laser. The overall stripe width of the PbSrSe layer is about the same as for the laser in Fig. 6. The far-field emission pattern (Fig. 9) found for this laser is TE_{00}, as observed with 5-μm BH lasers [10,14]. This indicates that the optical confinement of the guided wave is made by the large-gap PbSrSe active stripe material, together with the even higher Sr concentration in the cladding layers. The modal power distribution of this laser also comes quite close to that of narrow stripe BH lasers and shows almost negligible power in high-order lateral modes.

4. Conclusions

It has been shown that by shadow mask growth lead salt BH lasers can easily be prepared. The lasers have properties similar to those of photolithographically obtained BH lasers, especially in the case of the observed far-field distributions.

Growing the active stripe through a shadow mask which has contact with the laser wafer does not appear to affect the laser properties. Investigation by SEM shows similar growth on wafer regions covered by the mask and on the active stripes. Whether transfer of contaminants from the shadow mask occurs by contact is not known at present, and should be further investigated. The threshold current data for SM lasers are from the start better than the values obtained for ion-beam-etched BH lasers of the same active width. This gives a clear hint that photolithographic technology

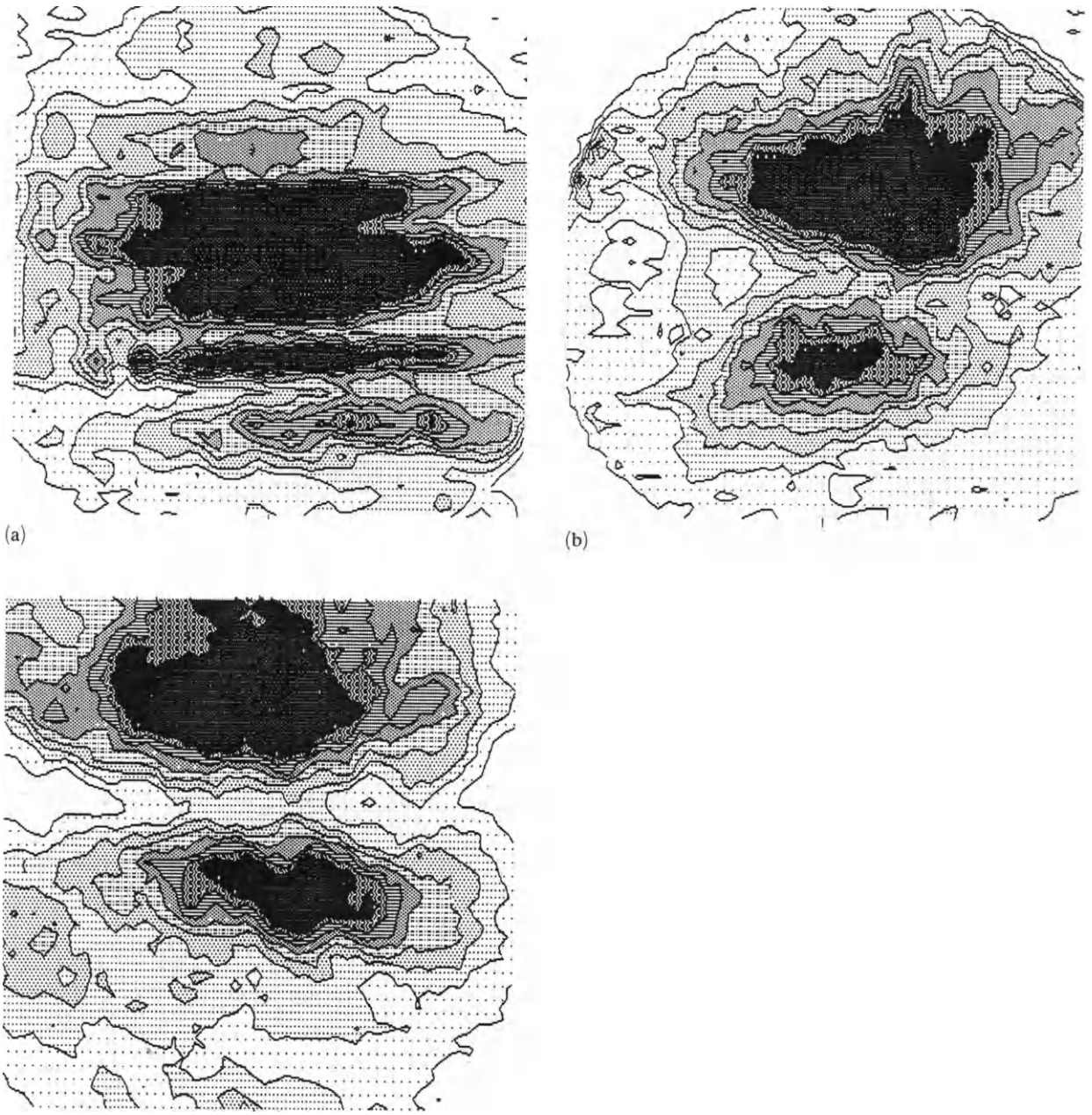

Fig. 8. (a) Far-field pattern of the DH laser of Fig. 6 (top) at $T = 80$ K, $I = 300$ mA. (b) Far-field pattern of an etched 20-μm-wide BH laser from the same wafer as the 10-μm BH laser of Fig. 6 (middle) at $T = 90$ K and $I = 100$ mA. (c) Far-field pattern of the shadow mask laser given in Fig. 2 and Fig. 6 (bottom) at $T = 80$ K, $I = 200$ mA. The p/n junction plane is oriented vertically. The scanned field is $51° \times 51°$ for (a) and (b), but $44° \times 44°$ for (c).

using dry etching can be further improved, since defects and contamination limit the quality of those BH lasers.

Our work has resulted in some promising suggestions for improvements in the mask fabrication process. Therefore, narrow stripes at least 5 μm wide seem to be obtainable by this method on a routine basis. This will yield improved BH properties. Mounting and removal of the mask under ultrahigh vacuum conditions will further improve the quality of the structures.

To cover reproducibly the mid-infrared range the ternary composition must be varied with SM lasers. This may be difficult since the growth process within the slit is not yet clear. We do not know to what extent molecules or atoms re-evaporate from the mask or how far they diffuse on the surface shadowed by the mask.

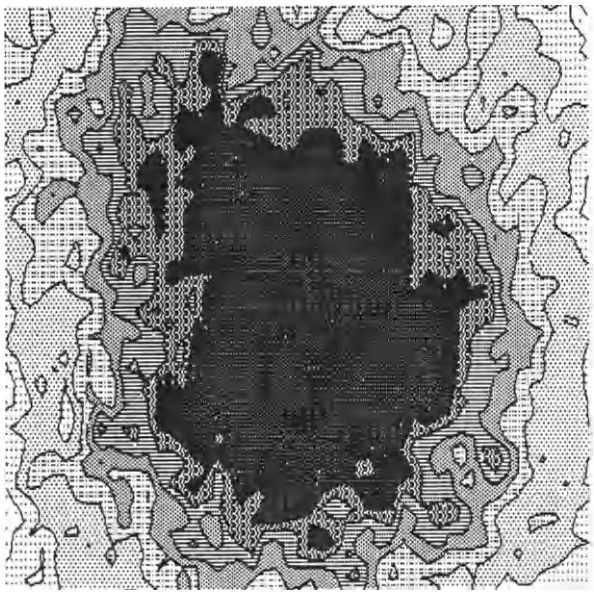

Fig. 9. Far-field pattern of laser 1460-1-5 at $T = 80$ K, $I = 60$ mA. The p/n junction plane is oriented vertically. The scanned field is 44° × 44°.

These processes may be composition dependent. Hence, suitable MBE parameters have to be found to grow the required ternary active layer concentrations reproducibly. Moreover, there is an additional degree of freedom in these structures since by stopping the substrate rotation with suitable geometrical conditions submicrometer active wire structures embedded in large-gap material are obtainable. Here too the detailed concentration profile is as yet unknown.

A combination of the shadow mask process with the recently described embossing technique [6] for fabrication of IV-VI-DFB lasers will give spectroscopists total lateral and longitudinal mode control to yield monomode BH-DFB lasers with superior properties. This can be done without the use of any costly photolithographic equipment.

Apart from the physical aspects, shadow mask fabrication might be especially interesting for those enterprises making mid-infrared lasers. The mid-term development of this market section will not allow the introduction of difficult production techniques at present.

Acknowledgments

This work was supported by the BMFT as part of the JETDLAG program (grant no. 7Eu733). The help of H. Böttner with SEM investigations, and of Mrs. G. Uptmoor and Mrs. Ch. Vogel with the fabrication of the shadow masks, is gratefully acknowledged. The authors would like to thank M. Tacke for critical reading of the manuscript. Laser cutting experiments on masks were performed by P. Bizenberger. Special thanks are due to U. Schieβl for his help with the laser characterization.

References

1 R.Grisar, H.Böttner, M.Tacke and G.Restelli (eds.), *Proc. 3rd Int. Symp. on monitoring of gaseous pollutants by tunable diode lasers, Freiburg, 17–18 October 1991*, Kluwer, Dordrecht, 1992, pp.3–60.

2 R.Grisar, H.Böttner, M.Tacke and G.Restelli (eds.), *Proc. 3rd Int. Symp. on monitoring of gaseous pollutants by tunable diode lasers, Freiburg, 17–18 October 1991*, Kluwer, Dordrecht, 1992, pp.319–324.

3 M.Tacke, B.Spanger, A.Lambrecht, P.R.Norton and H.Böttner,Infrared double-heterostructure diode lasers made by molecular beam epitaxy of $Pb_{1-x}Eu_xSe$, *Appl. Phys. Lett., 53* (23) (1988) 2260–2262.

4 B.Spanger, U.Schiessl, A.Lambrecht, H.Böttner and M.Tacke, Near-room-temperature operation of $Pb_{1-x}Sr_xSe$ infrared diode lasers using molecular beam epitaxy growth techniques, *Appl. Phys. Lett., 53* (26) (1988) 2582–2583.

5 K.-H.Schlereth, B.Spanger, H.Böttner, A.Lambrecht and M.Tacke, Buried waveguide double heterostructure PbEuSe lasers grown by MBE, *Infrared Phys., 30* (5) (1990) 449–454.

6 K.H.Schlereth and H.Böttner, Embossed grating lead chalcogenide distributed-feedback lasers, *J. Vac. Sci. Technol., B10* (1) (1992) 114–117.

7 Z.Feit, D.Kostyk, R.J.Woods and P.Mak, Molecular beam epitaxy-grown PbSnTe–PbEuSeTe buried heterostructure lasers, *IEEE Photonics Technol. Lett., 2* (12), (1990) 860.

8 Z.Feit, D.Kostyk, R.J.Woods and P.Mak, Single-mode molecular beam epitaxy grown PbEuSeTe/PbTe buried heterostructure diode lasers for CO_2 high-resolution spectroscopy, *Appl. Phys. Lett., 58* (4) (1991) 343.

9 Y.Shani, A.Katzir, M.Tacke and H.M.Preier, PbSnSe/PbEuSnSe corrugated lasers, *IEEE J. Quant. Electron., QE-25* (1989) 1828.

10 A.Lambrecht, H.Böttner, M.Agne, R.Kurbel, A.Fach, B.Halford, U.Schiessl and M.Tacke, Molecular beam epitaxy of laterally structured lead chalcogenides for the fabrication of buried heterostructure lasers, *Semicond. Sci. Technol., 8* (1993) S334–336.

11 W.T.Tsang and M.Ilegems, Selective area growth of GaAs/$Al_xGa_{1-x}As$ multilayer structures with molecular beam epitaxy using Si shadow masks (for integrated optics), *Appl. Phys. Lett., 31* (1977) 301–304.

12 A.Heuberger (ed.), *Mikromechanik: Mikrofertigung mit Methoden der Halbleitertechnologie*, Springer, Berlin, 1989 (in German).

13 G. Schmidtke, W.Kohn, U.Klocke, M.Knothe, W.J.Riedel and H.Wolf, Diode laser spectrometer for monitoring up to five atmospheric trace gases in unattended operation, *Appl.Opt., 28* (17) (1989) 3665.

14 M.Agne, A.Lambrecht, U.Schieβl and M.Tacke, Guided modes and far-field patterns of lead chalcogenide buried heterostructure laser diodes, submitted to *Infrared Phys.*

Materials Science and Engineering, B21 (1993) 224–227

Quantum confined Stark effect (QCSE) and self-electro-optic effect device (SEED) in II–VI heterostructures

H. Haas, P. Gentile, N. Magnea and J. L. Pautrat

CEA/Departement Recherche Fondamentale, Service Materiaux et Microstructures, 85X, 38041 Grenoble (France)

Le Si Dang

Laboratoire de Spectrométrie Physique, CNRS, Université J. Fourier, 38047 Saint Martin d'Hères (France)

N. T. Pelekanos

CNET Lannion B, OCM, BP 40, 22301 Lannion (France)

Abstract

We report on the first observation of the self-electro-optic effect in II–VI CdTe/CdZnTe heterostructures. At low temperature, wide modulation of the excitonic absorption is produced by applying an electric field of 5×10^4 V cm^{-1}. This makes possible the realization of a self-electro-optic effect device working at 774 nm with a switching power of hundreds of microwatts.

1. Introduction

II–VI compounds should possess unique electro-optical properties, but observation of these properties has been hindered by the difficulty of growing perfect materials. However, the development of new epitaxial techniques such as molecular beam epitaxy (MBE) now allows II–VI heterostructures of high quality with controlled p- or n-type conductivity to be produced. The realization of optical devices operating from the IR to the UV thus becomes possible. As we have shown elsewhere, excitonic absorption at room temperature in CdTe/CdZnTe quantum wells (QWs) is possible owing to an increase in the exciton binding energy over the LO-phonon energy, so future devices will work at room temperature [1].

Because of the high structural quality of multiple quantum wells (MQWs) and the possibility of high n-type doping (up to 10^{18} cm^{-3}) we have been able to develop a Schottky-diode device which allows an electric field up to 10^5 V cm^{-1} to be applied.

The present work is the first report of a self-electro-optic effect device (SEED) in II–VI heterostructures. This SEED is based on the quantum confined Stark effect (QCSE) on excitonic CdTe/CdZnTe MQWs.

The experimental features are detailed in section 2. In section 3 we present low temperature electro-absorption data related to the quantum Stark effect. The last section is devoted to the SEED data obtained at 2 K. Optical and electrical bistability are observed for wavelengths around 774 nm.

2. Experiments and device specifications

The Schottky contact diode was grown on CdZnTe (4% = Zn) by MBE. The strain symmetrized quantum well (QW) region with five periods of 13 nm/20 nm CdTe/CdZnTe (21% = Zn) with a cap layer of 85 nm was grown on an n^+ (4×10^{17} cm^{-3}) indium doped buffer layer with 15% zinc. This configuration allows a potential barrier of 90 meV for electrons and of 30 meV for heavy holes. The calculated exciton binding energy for the e_1hh_1 transition is around 16 meV. The device is shown in Fig. 1(a).

The optical active layers were partially removed to give access to the highly doped contact layer. A 600 nm indium contact was evaporated on top of the n^+ layer for ohmic contacts. To ensure good electrical properties and mechanical strength of the Schottky contact, a Cr/Au (4 nm/250 nm) metallization island (400 μm diameter) was evaporated onto the optical active region which permits gold wire bonding and electrical contact to a semitransparent gold area of 1 mm diameter which was deposited for the transmission of light under an electric field.

0921-5107/93/$6.00

© 1993 - Elsevier Sequoia. All rights reserved

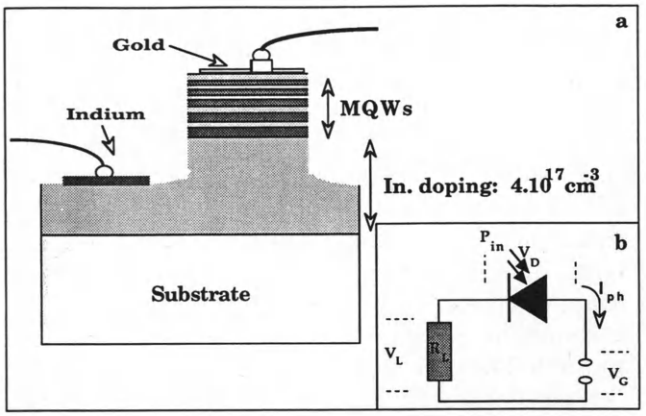

Fig. 1. (a) Schematic diagram of the sample showing the layered structure. The five CdTe quantum wells of 13 nm between 20 nm $Cd_{0.8}Zn_{0.2}Te$ barriers on a 2 μm $Cd_{0.85}Zn_{0.15}Te$ n-type buffer layer are grown on a $Cd_{0.96}Zn_{0.04}Te$ substrate. (b) Schematic diagram of the elecronic circuit for SEED configurations. V_G, V_D, V_l are the voltages of the generator, the diode and the resistor load R_L respectively.

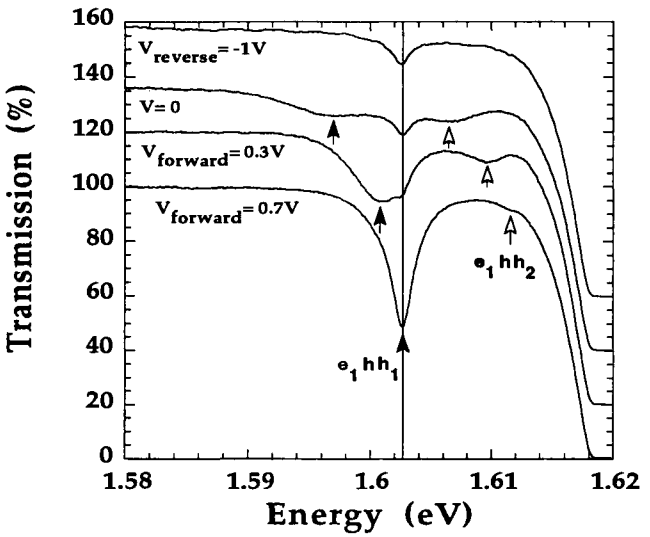

Fig. 2. Transmission spectra of the sample for different bias voltages V_D. The straight line corresponds to exciton absorption in a region not perturbed by the field. The high energy absorption is due to the substrate.

Measurements of the QCSE were taken by analysing the transmitted light of a broad band lamp placed behind the sample with the beam covering an area of the sample larger than the semitransparent gold area. The SEED worked with a Ti/sapphire laser pumped by an argon laser. All the experiments were performed at 2 K.

3. The quantum confined Stark effect

The transmission characteristics (Fig. 2) show large modulations when applying an external bias on the diode. The absorption feature indicated by the straight line and which does not move corresponds to the e_1hh_1 exciton absorption in a region surrounding the diode where the excitons are not in interaction with the field.

At forward bias near to the built-in voltage of the diode V_{bi} we approach flat band conditions. The hole and the electron wave functions are nearly centred in the QW region to give maximum overlap and oscillator strength. When the field is increased going to reverse bias, the electron wave function shifts towards the barrier and the hole wave function shifts in the opposite direction which lowers the transition energy and the wavefunctions overlap [2].

As the holes are confined by low barriers (30 meV) they can easily tunnel through the triangular barriers. The hole leakage decreases the exciton lifetime and leads to exciton ionization at high fields. This phenomenon leads to a broadening of excitonic transitions and a loss of oscillator strength.

When applying a reverse bias of 1 V corresponding to a field of 6×10^4 V cm^{-1} the absorption peaks of the shifted transitions disappear and cannot be distinguished from the slight absorbing continuum. This effect is interesting because it provides a large modulation of the electro-optic properties (absorption, refractive index) for low bias [3].

On the high energy tail of the transmission spectra we observe the symmetry forbidden e_1hh_2 excitonic transition at the position expected from the calculations. At low field the transition is weakly absorbing but with increasing fields the oscillator strength becomes comparable with and even exceeds that of the e_1hh_1 transition.

In Fig. 3 we compare the experimental QCSE shift of the e_1hh_1 and e_1hh_2 excitonic lines with the calculations as a function of the electric field. The electric field was estimated by assuming a built-in voltage $V_{bi} = 0.65$ V and a 250 nm wide QW region with a low doping level (10^{14} cm^{-3}). The Stark shift was calculated within the envelope function approximation using the band parameters of CdTe/CdZnTe heterojunctions given in ref. 4. Good agreement is obtained for the e_1hh_1 transition. For the parity forbidden e_1hh_2 line the experimental curve does not fit the calculations very well. This discrepancy could be due to excitonic effects which are not included in the model.

The observation of efficient modulation of the e_1hh_1 excitonic absorption peak is the starting point for optoelectronic modulators as the SEED which is presented in the next section.

4. Self-electro-optic effect device

The operative principle of the SEED is based on self modification of the voltage across the device V_D when a photocurrent I_{ph} created by resonant light absorption passes through the electronic circuit (Fig. 1(b)). This voltage variation will in turn modify the absorption strength through the QCSE, then the photocurrent will modify the diode voltage again, and so on. The feedback provided by the resistive load R_L can be positive and bistability can be observed [5].

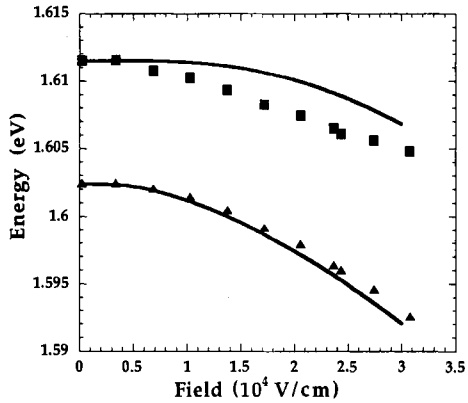

Fig. 3. Comparison between experimental Stark shift (▲ e_1hh_1, ■ e_1hh_2) and calculated shift (——) of a 13 nm wide QW.

In our experiments the diode is loaded with a 5.7 kΩ resistor and biased with a constant source voltage V_D. Light from the Ti/sapphire laser is focused on the Schottky contact at a wavelength (774 nm) close to the maximum of e_1hh_1 absorption obtained for zero electric field. The optical power can be varied continuously between 0.2 and 2 mW. Figure 4(a) shows the variation of I_{ph} with the bias voltage V_D (the electric field on the MQWs increases from the right to the left). Strong negative differential conductance is observed beginning at $V_D = 0.36$ V ($E = 1.1 \times 10^4$ V cm^{-1}). At this critical point the dissipated power in the circuit is maximum and any increase in the bias voltage will make the system switch to the low absorption state associated with high electric field on the diode. When the bias is

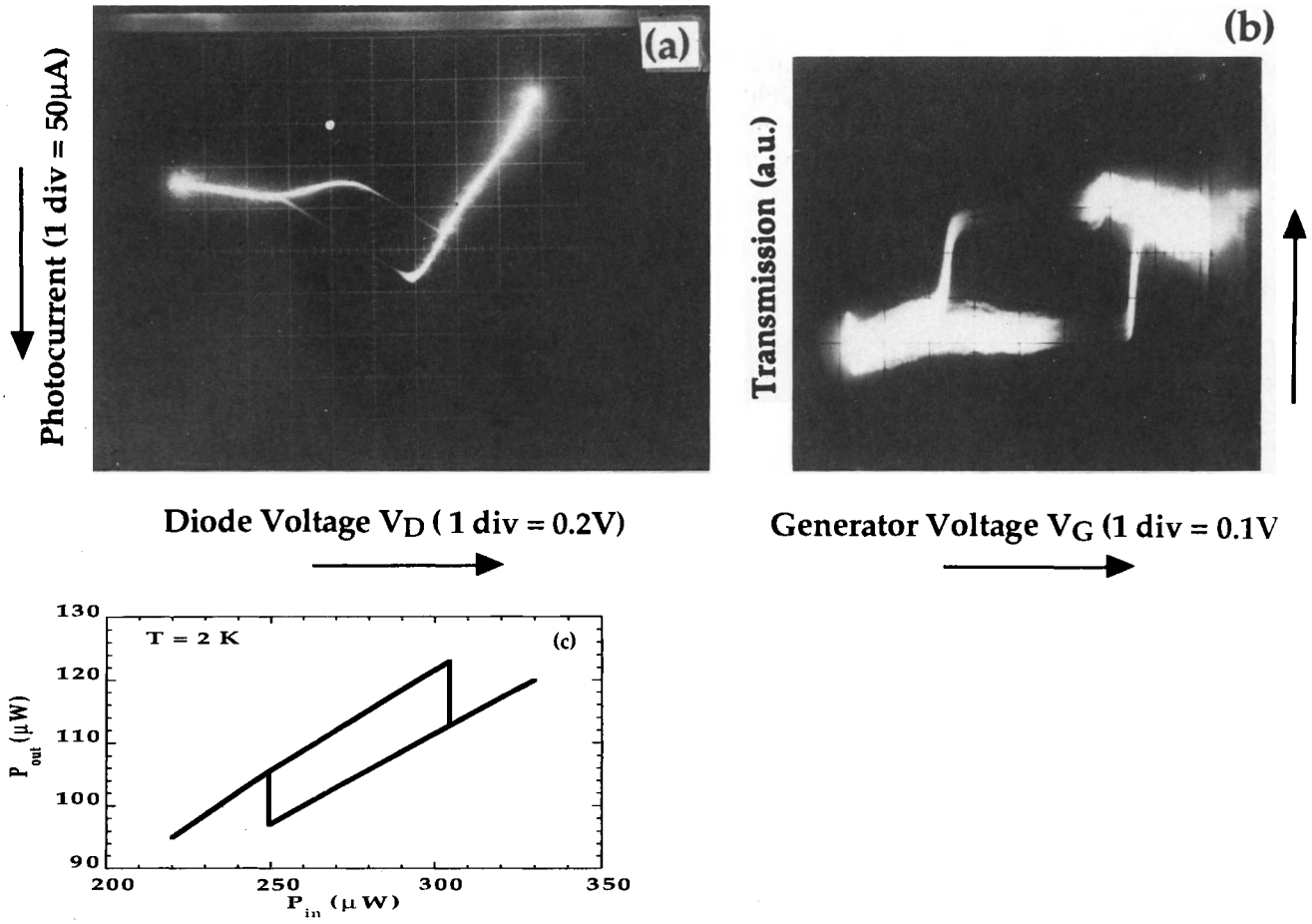

Fig. 4. (a) Photocurrent variations as a function of the diode bias voltage V_D for an incident power $P_{in} = 1$ mW at 774 nm and a load resistor $R_L = 5.7$ kΩ. The white point corresponds to the origin. (b) Bistability curve obtained on the transmitted beam by sweeping the generator voltage V_G. (c) Optical input over output P_{in}/P_{out} characteristic of the SEED at $\lambda = 774$ nm and $V_G = -0.5$ V.

swept from a reverse towards a forward voltage the system is locked in the low absorption state. We observe a second critical point at $V_D = 0.12$ V giving a wide hysteretic loop.

At the same time the transmitted light is modulated as shown in Fig. 4(b). The switching is obtained for generator voltages V_G corresponding to the critical points of the $I(V_D)$ curve in Fig. 4(a).

As stated by Miller *et al.* [5], the criterion for bistability of the electronic circuit is given by

$$P_{in} \frac{\partial S(V)}{\partial V} \leqslant \frac{\partial I}{\partial V} \leqslant 0$$

where $S(V)$ is the response function giving the current per incident photon. This relation expressed in terms of resistance leads to $R_D \leqslant -R_L$ where R_D is the differential resistance of the diode. Then bistaility can be obtained either by modulating $\partial S/\partial V$ with the bias voltage as shown in Fig. 4(a) or by varying P_{in}.

This effect is shown in Fig. 4(c) where we plot the intensity of the measured transmitted light P_{out} as a function of the input power P_{in} for a constant bias $V_G = 0.5$ V. Switching is observed for $P_{in} = 300$ μW with an on–off ratio of 10%.

5. Conclusion

The quantum Stark effect and SEED operation have been observed in CdTe/CdZnTe quantum wells. The effect of the electric field on the excitonic transitions is a red shift and an efficient field ionization of the exciton giving strong modulation of the absorption coefficiednt. When the diode is loaded with a resistor the optoelectronic feedback induces optical and electrical bistability. The device we have studied works at low temperature but high temperature operation is possible as room temperature exciton absorption can be observed using more confined structures. These results open the way for optical modulators based on II–VI compound quantum device working in the IR as well as in the blue.

Acknowledgments

Special thanks are due to F. Bassani, K. Saminadayar and S. Tatarenko for their expertise in the growth of doped layers.

References

1 N. T. Pelekanos, H. Haas, N. Magnea, H. Mariette and A. Wasiela, *Appl. Phys. Lett.*, 61 (1992) 3154.
2 G. Bastard, E. E. Mendez, L. L. Chang and L. Esaki, *Phys. Rev. B*, 28 (1983) 3241.
3 R. A. Morgan, M. T. Asom, L. M. F. Chirovsky and K. W. Goossen, *Appl. Phys. Lett.*, 59 (1991) 1049.
4 H. Tuffigo, N. Magnea, H. Mariette, A. Wasiela and Y. Merle D'Aubigné, *Phys. Rev. B*, 43 (1991) 1049.
5 D. A. B. Miller, D. S. Chemla, T. C. Damen, T. H. Wood, C. A. Burrus, A. C. Gossard and W. Wiegmann, *IEEE J. Quantum Electron.*, 21 (1985) 1462.

Materials Science and Engineering, B21 (1993) 228–231

Growth of InAlGaAs multilayer structures for high power and submilliamp vertical cavity lasers

K. Panzlaff[a], T. Hackbarth[b], E. Zeeb[a], T. Wipiejewski[a] and K. J. Ebeling[a]

[a] *Univ. Ulm, Dept. of Optoelectronics, POB 4066, W-7900 Ulm (Germany)*

[b] *Daimler Benz Research Center, Ulm (Germany)*

Abstract

We have used solid source molecular beam epitaxy (MBE) with As_4 to grow multilayer structures for vertical cavity surface emitting laser diodes (VCSEL) on n-GaAs substrates. Processed wafers with strained InGaAs active layers show a record low threshold current of 650 μA for 8 μm devices at an emission wavelength of 970 nm. In larger devices of 95 μm diameter we obtain 20 mW maximal cw output power applying proper heat sinking. Using strained InAlGaAs quantum wells with 25% In and 35% Al we observe a threshold current density of 1.1 kAcm^{-2} at an emission wavelength of 747 nm for broad area in-plane lasers.

1. Introduction

High quality InAlGaAs–GaAs multilayer structures are critical to the performance of vertical cavity surface emitting laser diodes (VCSEL). These lasers are of increasing importance because of their single longitudinal and transversal mode emission [1], highly efficient fibre coupling [2], on-wafer testing, and potential two-dimensional array formation. Advanced growth techniques are required to optimise device properties. High optical gain in active quantum well layers, suitable cladding layer configurations, low loss and low resistive Bragg reflectors are all features of well developed devices.

We used solid source molecular beam epitaxy (MBE) with As_4 to fabricate VCSELs with a record low threshold current of 650 μA in devices with an active diameter of 8 μm [3]. Independent wavelength tuning is achieved by a third terminal on top of the reflector mesa. High power devices of 95 μm diameter show a maximum output power of 20 mW when properly soldered with AuSn onto a MoW heat sink in an upside down configuration.

To reduce the emission wavelength we introduced strained InAlGaAs quantum wells with AlGaAs barriers. Efficient visible room temperature photoluminescence is obtained from $In_{0.1}Al_{0.42}Ga_{0.48}$ quantum wells emitting at 643 nm. A GRINSCH laser structure employing three strained $In_{0.25}Al_{0.35}Ga_{0.4}$ quantum wells was grown. The output power characteristics of a broad area laser (50 μm wide and 400 μm long) emitting at 747 nm have a threshold current of 220 mA corresponding to a threshold current density of 1.1 kAcm^{-2}.

2. Growth of epitaxial layers and device processing

Figure 1 illustrates the multilayer structure as well as the contact configuration of the submilliamp threshold device. Solid source MBE with As_4 is used for growth on n-GaAs substrates. Three 8 nm thick $In_{0.2}Ga_{0.8}As$ quantum wells are embedded in 10 nm GaAs barriers and surrounded by 40 nm GaAs and 75 nm $Al_{0.4}Ga_{0.6}As$ layers for efficient carrier confinement. The top as well as the bottom Bragg reflectors consist of stacks of 80 nm AlAs and 67 nm GaAs of quarter wavelength thickness. One-sided 5 nm thick intermediate layers of $Al_{0.4}Ga_{0.6}As$ provide a reduced electrical resistance [4]. The top reflector is p-doped (Be, $p = 5 \times 10^{18}$ cm^{-3}) and has 20 pairs, the lower is n-doped (Si, $n = 5 \times 10^{18}$ cm^{-3}) and is made of 24.5 pairs. A 45 nm thick GaAs layer provides optical phase matching to the Au top reflector. To achieve high output power levels a slightly different structure was used employing 18 pairs for the top and 22.5 pairs for the bottom reflector. Two one-sided intermediate layers with different Al contents are used to further decrease the resistivity of the Bragg reflectors.

The growth conditions of the complete structure were particularly optimised in terms of substrate temperature. Previous experiments showed that the crystal quality of the barrier layers is extremely important. Therefore, we chose a temperature of 630 °C for the

0921-5107/93/$6.00

© 1993 – Elsevier Sequoia. All rights reserved

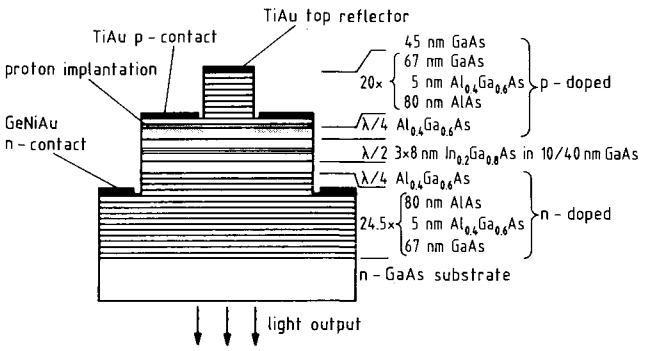

Fig. 1. Mulitilayer structure and contact configuration of a low threshold double mesa vertical cavity laser.

growth of the quarter wavelength thick $Al_{0.4}Ga_{0.6}As$ layers as well as for the innermost Bragg reflector pairs. Efficient photoluminescence in $In_{0.2}Ga_{0.8}As$ quantum wells is obtained at 520 °C, and the rest of the structure was grown at 580 °C.

Proton implantation is employed for lateral device formation. In low threshold devices a total dose of 10^{15} cm^{-2} at varying ion energies from 40 up to 300 keV is used to achieve lateral current confinement in the active region. TiAu contacts for tuning on the top Bragg reflector are defined by the standard lift-off technique and serve as an etch mask for wet chemical mesa etching which is stopped after etching of 17 reflector pairs. TiAu contacts are deposited at the bottom of the mesas that serve as common ground for tuning and laser currents. Finally, broad area mesas of 100 μm diameter are etched to apply the lower AuGeNi n-contacts as well as to electrically insulate individual lasers.

High power device wafers are thinned to 90 μm after a deep proton implantation at 300 keV with a dose of 5×10^{14} cm^{-2}. AuGeNi backside n-contacts contain 100 μm holes for light output. The Au reflector on top of the non-implanted area is formed by standard lift-off technique and the following complete covering with TiPtAu constitutes the p-contact. Dices of 500 μm × 500 μm are cleaved and soldered upside down with AuSn onto a MoW heat sink.

3. VCSEL characteristics

Light output of the lasers occurs via the GaAs substrate. Figure 2 shows the cw output characteristics of 8 and 12 μm low threshold devices when applying no tuning current. The threshold currents are 650 μA and 1.35 mA, respectively; these correspond to a threshold current density of 1.3 $kAcm^{-2}$ for both sizes. The differential quantum efficiency slightly above threshold is approximately 5%. For these devices without a heat sink, the output power saturates at 170 and 230 μW

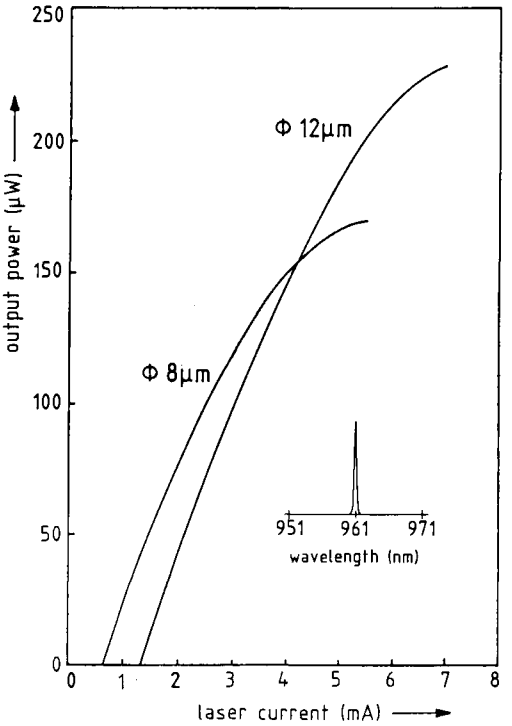

Fig. 2. Cw output power characteristics of low threshold devices for 8 and 12 μm diameter VCSELs.

owing to thermal heating. The maximum pulsed output power (not shown) is 0.4 and 1.85 mW (50 ns pulses, 10 kHz repetition rate) for 8 and 12 μm lasers, respectively.

Laser emission is both longitudinal and transversal single mode at 970 nm (see inset of Fig. 2). Larger devices also emit in higher transversal modes. The mode profile is determined by the gain guiding of the injection current in the active region as well as by the index guiding induced by the top reflector mesa. The polarisation is linear but varies for different devices on the wafer.

The emission wavelength can be tuned independently from the output power by injecting a current into the top reflector mesa. Both laser and tuning currents cause local heating of the devices resulting in a refractive index change which increases the optical length of the cavity. We observe a normalised wavelength shift of 1.0 nm mA^{-1} for the laser current and 3.7 nm mA^{-1} for the tuning current indicating efficient heating of the small top reflector. The tuning time constant is less than 2 μs.

Figure 3 shows the cw output characteristics of different high output power devices. We obtain threshold currents of 55 and 95 mA and, at room temperature, maximum output powers of 17 and 19 mW for 75 and 95 μm devices, respectively. A slight cooling of the heat sink to 5 °C raises the output power to > 20 mW.

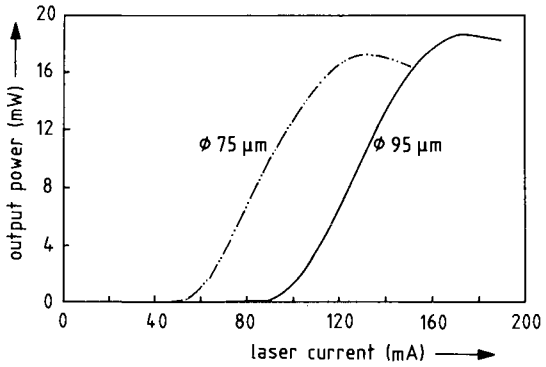

Fig. 3. High cw output power characteristics for 75 and 95 μm diameter devices.

For both devices the threshold current density is 1.3 kAcm^{-2} and a differential quantum efficiency of 25% is achieved.

4. Short wavelength InAlGaAs quantum well laser diodes

Theoretical studies show that compressive strain enhances the heavy-hole light-hole energy band splitting and reduces the effective mass resulting in improved threshold current density and differential gain [5]. For the InGaAsP–InP system it is shown that strained quantum wells can lead to superior devices with high output power as well as low threshold currents [6]. We introduced InAlGaAs instead of AlGaAs quantum wells to reduce the emission wavelength of the lasers since investigations indicated a similar improvement of device performance for this system [7].

To optimise photoluminescence efficiency and optical gain we grew several InAlGaAs quantum wells with various layer structures as shown in Fig. 4(a). Growth conditions were similar to those for VCSELs. Figure 4(b) shows the maximum photoluminescence intensity as a function of temperature. The roll-off of the intensity is essentially determined by the cladding layer configuration. It is seen that the decrease for the $In_{0.25}Al_{0.35}Ga_{0.4}As$ quantum wells can be kept almost as small as for the $In_{0.2}Ga_{0.8}As$ quantum wells. At low temperatures, the efficiency of very short wavelength $In_{0.1}Al_{0.42}Ga_{0.48}As$ quantum wells is comparable, but this similarity decreases with increasing temperature owing to inefficient barriers. Nevertheless, emission at 643 nm is still clearly visible at room temperature and indicates high quality layers.

We fabricated GRINSCH lasers for approximately 745 nm emission wavelength quantum wells based on $In_{0.25}Al_{0.35}Ga_{0.4}As$. Details of the layer structure are shown in Fig. 5(a). Broad area in-plane lasers of 50 μm × 400 μm size were processed by wet chemical

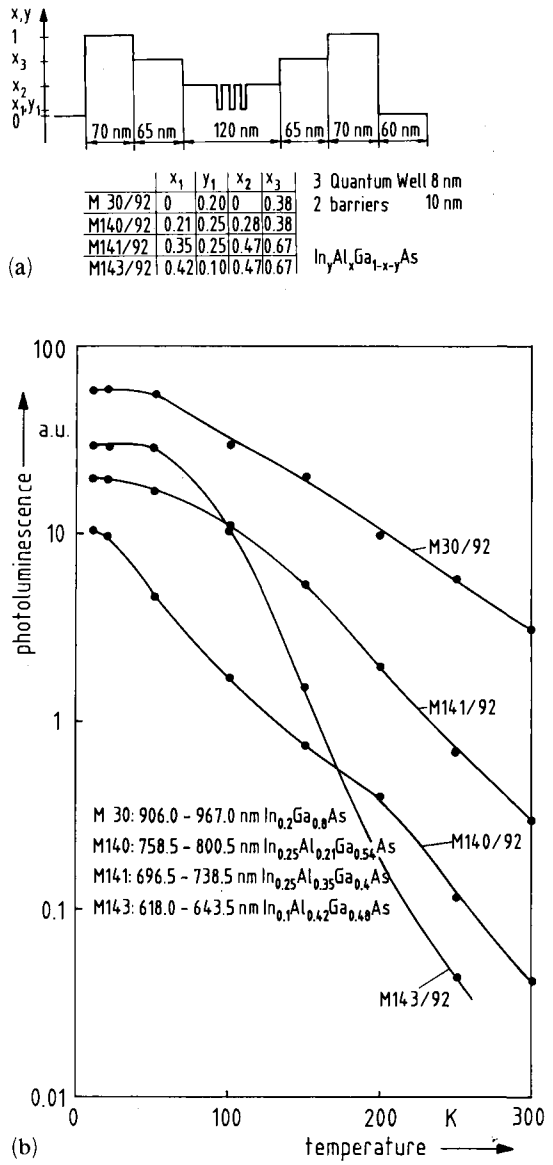

Fig. 4. (a) The various InAlGaAs quantum well structures investigated. (b) Temperature dependence of maximum photoluminescence intensity for the various InAlGaAs structures shown in (a).

etching with TiAu contacts used as an etch mask. The corresponding room temperature output power characteristics are shown in Fig. 5(b). The one-sided differential quantum efficiency is 19% and the threshold current of 220 mA corresponds to a threshold current density of 1.1 kAcm^{-2} or 370 Acm^{-2} per quantum well.

5. Conclusion

We used solid source MBE to grow multilayer InAlGaAs structures for 980 nm wavelength VCSELs.

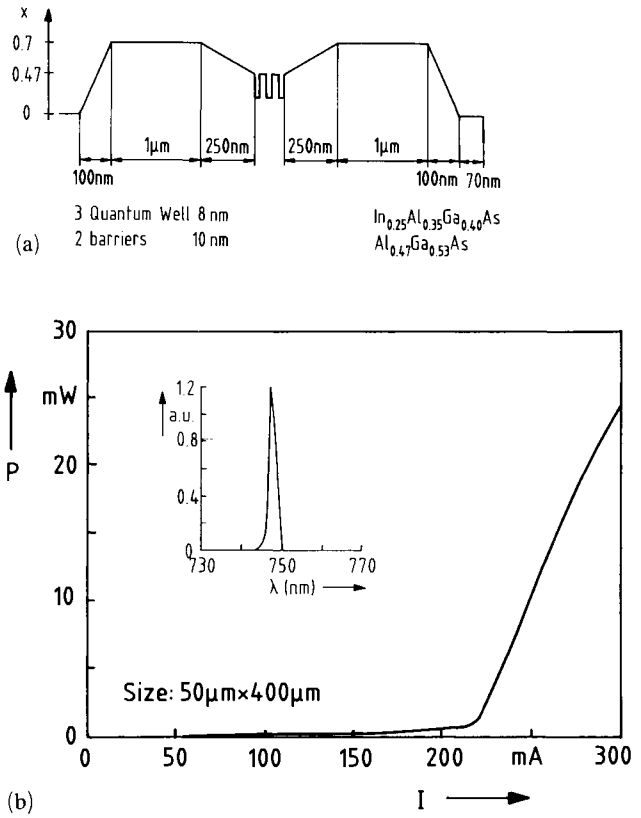

Fig. 5. (a) The GRINSCH laser structure with InAlGaAs quantum wells. (b) Pulsed output characteristics of a broad area InAlGaAs GRINSCH laser diode.

By optimising growth conditions and processing techniques we produced devices with a record low threshold current of 650 μA for small size VCSELs and high output power of up to 20 mW for broad area VCSELs. The shorter wavelength operation, employing strained InAlGaAs quantum wells, looks very attractive. Broad area in-plane lasers for 747 nm operation showed a threshold current of 1.1 kAcm^{-2}, or 370 Acm^{-2} per quantum well when providing optimised carrier confinement.

Acknowledgement

Support from DFG and Daimler Benz Research Center, Ulm is gratefully acknowledged.

References

1 J. Jewell, A. Scherer, S.L. McCall, Y.H. Lee, S. Walker, J.P. Harbison and L.T. Florez, Low threshold electrically pumped vertical-cavity surface-emitting microlasers, *Electron Lett., 25* (1989) 1123.

2 K. Tai, G. Hasnain, J.D. Wynn, R.J. Fischer, Y.H. Wang, B. Weir, J. Gamelin and A.Y. Cho, 90% coupling of top surface emitting GaAs/AlGaAs quantum well laser output into 8 μm diameter core fiber, *Electron Lett., 26* (1990) 1628.

3 T. Wipiejewski, K. Panzlaff, E. Zeeb and K.J. Ebeling, Submilliamp vertical cavity laser diode structure with 2.2 nm continuous tuning, *Proc. 18th Euro. Conf. Opt. Comm., Berlin* (1992) 903.

4 E. Zeeb and K.J. Ebeling, Potential barriers and current-voltage characteristics of p-doped graded AlAs-GaAs heterojunctions, *J. Appl. Phys., 72* (1992) 993.

5 E. Yablonovitch and E.O. Kane, Reduction of lasing threshold current density by the lowering of valence band effective mass, *J. Lightwave Technol., LT-4* (1986) 504.

6 P.J.A. Thijs, T. van Dongen, L.F. Tiemeijer, R.W.M. Slootweg and J.J.M. Binsma, High output power (380 mW), low threshold current (1.3 mA), low linewidth enhancement factor ($\leqslant 2$) $\lambda = 1.3$ μm strained quantum well lasers, *Proc. 17th Euro. Conf. Opt. Comm.* (1991) 48.

7 W.D. Goodhue, J.P. Donnelly, C.A. Wang, G.A. Lincoln, K. Rauschenbach, R.J. Bailey and G.D. Johnson, Monolithic two-dimensional surface-emitting strained-layer InGaAs/AlGaAs and AlInGaAs/AlGaAs diode laser arrays with over 50% differential quantum efficiencies, *Appl. Phys. Lett., 59* (1991) 632.

Materials Science and Engineering, B21 (1993) 232–236

p-Dopant incorporation and influence on gain and damping behaviour in high-speed GaAs-based strained MQW lasers

J. D. Ralston, S. Weisser, I. Esquivias*, A. Schönfelder, E. C. Larkins, J. Rosenzweig, P. J. Tasker, M. Maier and J. Fleissner

Fraunhofer-Institut für Angewandte Festkörperphysik, Tullastrasse 72, D-79108 Freiburg (Germany)

Abstract

We investigate p-dopant incorporation and the influence of p-doping on the gain and damping behaviour in GaAs-based strained multiple quantum well lasers. By adding 5×10^{18}–2×10^{19} cm^{-3} beryllium doping to the active region of $In_{0.35}Ga_{0.65}As$/GaAs strained multiple quantum well lasers (4 QW's), we are able to demonstrate both very efficient high-speed modulation (20 GHz at a DC bias current of 50 mA) and the first semiconductor lasers to achieve a direct modulation bandwidth of 30 GHz under DC bias (heat-sink temperature = 25°C).

1. Introduction

The high-speed performance of unstrained GaAs/AlGaAs multiple quantum well (MQW) lasers has been shown experimentally to be enhanced by the addition of p-doping in the active region [1]. A simple theoretical treatment of these results [2] attributed the increase in the relaxation oscillation frequency, f_r, to a large increase in the differential gain, $\partial g/\partial n$. Such behavior arises from a doping-induced compensation of the asymmetry in the density of states between the conduction and valence bands. More recent experimental results have demonstrated that the combination of p-doping and strain in the active region leads to further enhancements in the high-frequency performance of both GaAs-based InGaAs MQW lasers [3] and InP-based GaInAsP MQW lasers [4]; such devices have to date achieved 3 dB modulation bandwidths, f_{3dB}, of 30 GHz [3] and 25 GHz [4], respectively. Recent theoretical results indicate that p-doped strained MQW distributed feedback lasers may also offer the possiblity of chirp-free direct modulation [5]. Previously, we have shown experimentally that the modulation bandwidth enhancements in p-doped strained InGaAs/GaAs MQW lasers arise from the combination of an increase in $\partial g/\partial n$ and a decrease in the non-linear gain coefficient, ε [6]. In the present paper we review more detailed investigations of p-dopant incorporation and the influence of p-doping on the gain and damping behavior in strained InGaAs/GaAs MQW lasers.

2. Epitaxial layer structures

Figure 1 shows schematically the epitaxial layer design of the lasers, all containing four 5.7 nm $In_{0.35}Ga_{0.65}AS$ QWs separated by 20 nm GaAs barriers in the active region of a vertically compact, separate confinement, double heterostructure (SCDH) waveguide with $Al_{0.8}Ga_{0.2}As$ cladding layers. The cladding layers have been realized using GaAs/AlAs binary short-period superlattices. Structures with five different doping configurations in the active region were grown by molecular-beam epitaxy (MBE) on undoped GaAs substrates: (i) undoped QWS, (ii) 4.5 nm, 5×10^{18} cm^{-3} Be-doped regions centered in the InGaAs QWs, or (iii) placed in the GaAs barriers above each of the QWs, separated by a 3 nm undoped GaAs spacer, (iv) 4.5 nm, 2×10^{19} cm^{-3} Be-doped regions centered in the InGaAs QWs, or (v) placed in the GaAs barriers above each of the QWs, separated by a 3 nm undoped GaAs spacer. The design and epitaxial growth of the laser structures is discussed in more detail elsewhere [6, 7].

High depth-resolution secondary ion mass spectrometry (SIMS) profiles of the epitaxial layer structures reveal that, at the substrate temperatures used for the above structures [6, 7], redistribution of the Be-doping spikes occurs during MBE growth. Figure 2, for example, presents In, Al, Be and Si depth profiles of structure (iv), containing 2×10^{19} cm^{-3} Be-doping spikes centered in the InGaAs QWs. In Fig.

*On leave from the Department of Electronic Technology at the Polytechnical University of Madrid.

0921-5107/93/$6.00

© 1993 – Elsevier Sequoia. All rights reserved

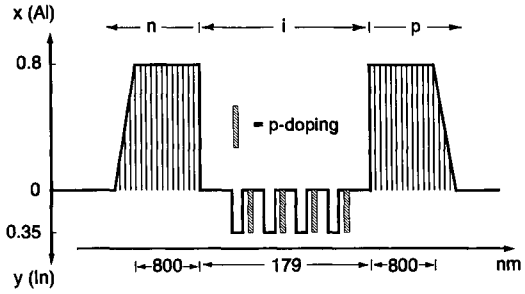

Fig. 1. Layer structure of vertically compact, ungraded SCDH MQW lasers, containing four 5.7 nm $In_{0.35}Ga_{0.65}As$/20 nm GaAs QWs in the active region. Undoped, QW-doped and barrier-doped active regions have been investigated.

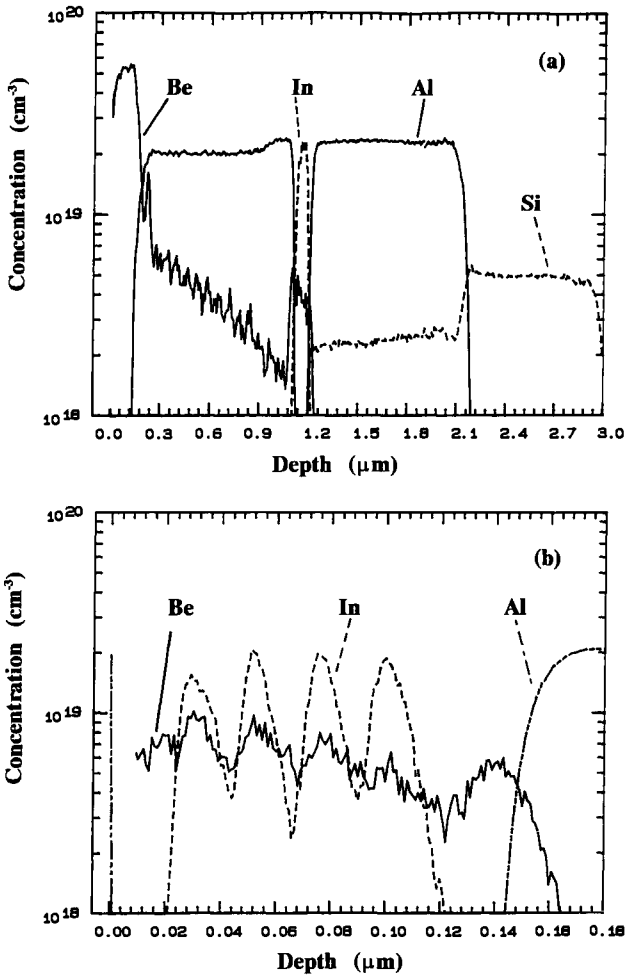

Fig. 2. SIMS profiles of laser structure with 2×10^{19} cm^{-3} Be-doped regions centered in the QWs: (a) profile through complete epitaxial layer structure, (b) profile through structure which has first been etched down to the GaAs/InGaAs core region. The concentration scales on the left correspond only to the Be and Si profiles.

2(a), the entire epitaxial layer is profiled, revealing the overall AlGaAs/GaAs/InGaAs waveguide design. In Fig. 2(b), the epitaxial layers have first been etched away to a point just above the InGaAs/GaAs core region, in order to allow high resolution profiling of the four p-doped QWs. The Be depth profiles of the barrier-doped samples are also very similar to those of the QW-doped samples shown in Fig. 2(b); both show substantial diffusion of the p-dopant throughout the core region, with small residual peaks in the QWs. These peaks are attributed to a SIMS matrix effect (higher Be yield from the InGaAs layers than from the GaAs layers). The SIMS depth profiles also reveal that the Be diffusion is contained between the $Al_{0.8}Ga_{0.2}As$ cladding layers, and that the effective p–n junction is on the substrate side of the core region. Due to the above Be diffusion, there is actually very little difference between the final doping profiles in the QW-doped and the barrier-doped structures, for both doping levels. This behavior is mirrored in both the DC and high-frequency lasing characteristics of the devices. The above acceptor redistribution can be avoided by replacing Be with carbon, as has been demonstrated both in npn GaAs/AlGaAs heterostructure bipolar transistors (HBTs) [8] and in AlAs/GaAs Bragg reflector structures [9] grown by MBE.

3. Laser fabrication and characterization

Lasers were fabricated with 3 μm wide mesas, cleaved to lengths of 200–900 μm, and indium-soldered onto copper heat-sinks. A coplanar ground–signal–ground laser contact geometry [6, 7, 10] was used in the present work, eliminating the need for bonding and reducing parasitic impedances. The four laser structures were first characterized in terms of threshold current, I_{th}, lasing wavelength at threshold, λ_{th}, internal quantum efficiency, η_i, and internal laser loss, α_i; the latter two parameters were obtained from plots of reciprocal external quantum efficiency as a function of cavity length. Small-signal direct modulation response measurements were carried out using DC bias currents at a heat-sink temperature of 25 °C. Parasitic-free relative intensity noise (RIN) power spectra measurements were utilized to determine $\partial g/\partial n$, the damping factor K, the non-linear grain coefficient, ε, and the effective carrier lifetime, τ_c. As previously discussed [6], this technique is better suited than direct modulation response measurements for determining the intrinsic gain and damping behavior of semiconductor lasers. The DC and high frequency measurement results are summarized in Table 1.

Figure 3 compares typical single-facet P–I curves of the five different devices (3×200 μm^2). The threshold current, I_{th}, initially decreases at a doping level of

TABLE 1. Summary of DC and high-frequency measurement results for $3 \times 200\ \mu m^2$ laser structures

Active region	I_{th}, best (mA)	λ_{th} (nm)	η_i (%)	α_i (cm^{-1})	J_{trans} (A/cm^2)	τ_c (ns)	$\partial g/\partial n$ (cm^2)	K (ns)	ε (cm^3)	f_{3dB}^{max} (GHz)	I_{20GHz} (mA)
4-QW Undoped	17	1082	67	26	360	0.38	2.2×10^{-15}	0.26	8.6×10^{-17}	34	60
4-QW $5 \times 10^{18}\ cm^{-3}$	14	1089	66	32	140	0.39	2.0×10^{-15}	0.23	6.4×10^{-17}	38	50
4-QW $2 \times 10^{19}\ cm^{-3}$	17	1095	63	53	285	0.17	2.5×10^{-15}	0.14	4.6×10^{-17}	63	50

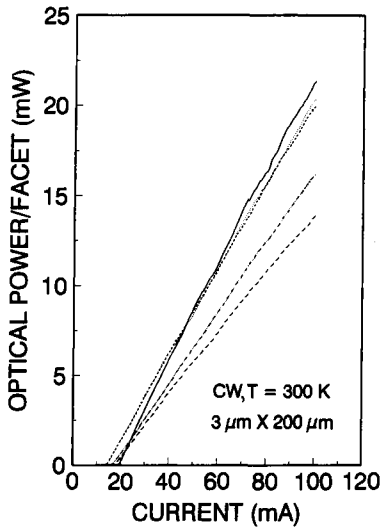

Fig. 3. Single-facet output power *vs.* current characteristics (CW, room-temperature) for $3 \times 200\ \mu m^2$ mesa-geometry lasers with five different doping configurations in the active region (QW = direct doping in QWs, MD = modulation doping in barriers). ——— undoped, - - - QW $5 \times 10^{18}\ cm^{-3}$, ····· MD $5 \times 10^{18}\ cm^{-3}$, ——— QW $2 \times 10^{19}\ cm^{-3}$, —·····— MD $2 \times 10^{19}\ cm^{-3}$.

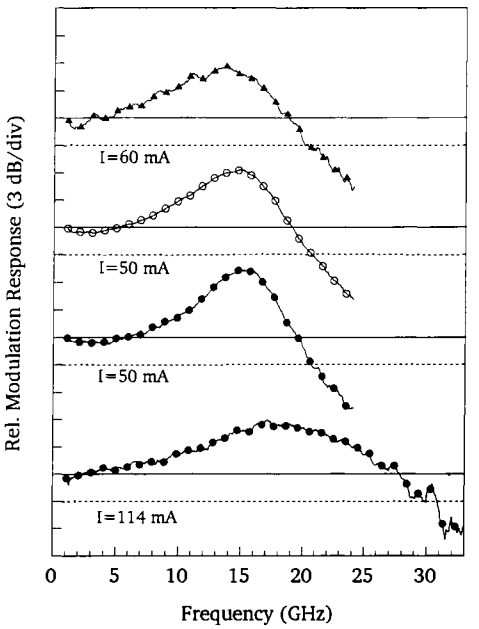

Fig. 4. Small-signal direct modulation response (DC bias, heat-sink temperature 25 °C) of $3 \times 200\ \mu m^2$ $In_{0.35}Ga_{0.65}As$ MQW lasers with three different doping levels in the active region. The bottom curve demonstrates a 3 dB modulation frequency of 30 GHz at a bias current of 114 mA. ▲ Undoped, ○ $5 \times 10^{18}\ cm^{-3}$, ● $2 \times 10^{19}\ cm^{-3}$.

$5 \times 10^{18}\ cm^{-3}$, but then increases again as the doping level is increased to $2 \times 10^{19}\ cm^{-3}$. A doping-induced increase in λ_{th} is observed, from 1082 (undoped) to 1095 nm ($2 \times 10^{19}\ cm^{-3}$). The internal quantum efficiency, η_i, is not strongly affected by the doping level. However, the internal loss, α_i, increases substantially, most likely due to free-carrier absorption. As can be seen in Fig. 3, the increased internal loss leads to a decrease in the external quantum efficiency with increasing doping level.

Figure 4 presents a series of small-signal direct modulation response spectra for $3 \times 200\ \mu m^2$ lasers with undoped active regions, along with devices doped at 5×10^{18} and $2 \times 10^{19}\ cm^{-3}$; no difference was observed between direct doping in the wells and doping in the barriers. The bias current required to achieve $f_{3dB} > 20$ GHz decreases from 60 to 50 mA with the addition of p-doping, as shown in the upper three curves in Fig. 4. These bias currents are substantially lower than those previously required in order to achieve similar modulation bandwidths in a semiconductor laser. The measured f_{3dB} saturates at high photon densities, giving rise to maximum values of 21 GHz (undoped), 24 GHz ($5 \times 10^{18}\ cm^{-3}$) and 30 GHz ($2 \times 10^{19}\ cm^{-3}$). These are the first semiconductor lasers to achieve a direct modulation bandwidth of 30 GHz under DC bias (Fig. 4, bottom curve). The modulation bandwidths were found to be limited by the appearance of higher order lateral modes in the strongly index-guided mesa waveguide structure at DC bias currents above roughly 60 mA, as revealed by far-field measurements (Fig. 5). This problem can be overcome by using a ridge waveguide structure.

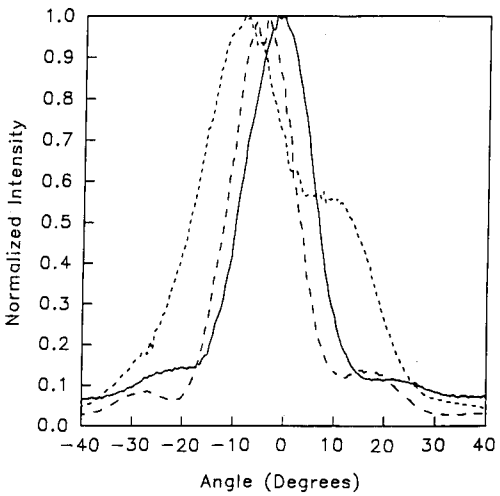

Fig. 5. Measured far-field patterns, at various bias currents, of $3 \times 200\ \mu m^2$ laser structure with 2×10^{19} cm^{-3} Be-doping in the active region. Higher order lateral modes appear in the mesa waveguide structure at DC bias currents above roughly 60 mA. —— $I = 20$ mA, - - - $I = 50$ mA, ----- $I = 80$ mA.

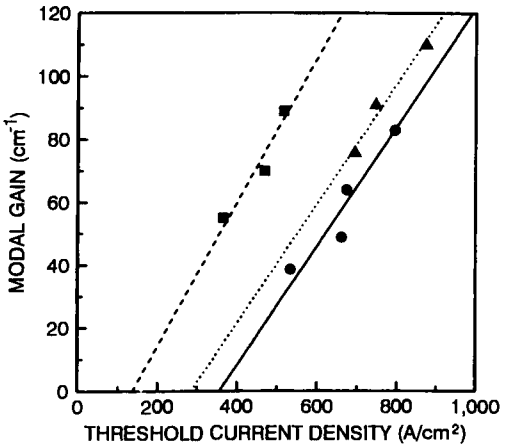

Fig. 6. Experimental modal gain *vs.* threshold current density for $In_{0.35}Ga_{0.65}As/GaAs$ MQW lasers with three different doping levels in the active region. —●— Undoped, - -□- - 5×10^{18} cm^{-3} Be, ···▲··· 2×10^{19} cm^{-3} Be.

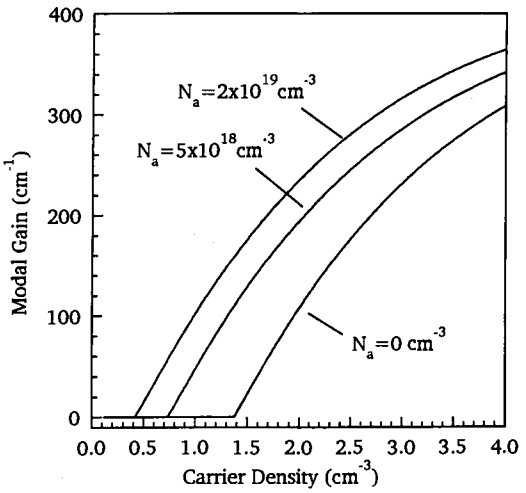

Fig. 7. Theoretical modal gain *vs.* carrier density for $In_{0.35}Ga_{0.65}As/GaAs$ QW lasers with three different doping levels in the active region.

As shown in Table 1, the enhanced high-frequency performance in the p-doped devices is due to a small increase in the differential gain, coupled with a large decrease in the non-linear gain coefficient. Since the very narrow core region in the present lasers is expected to eliminate carrier-transport-induced damping effects [11], the measured K factor implies a maximum intrinsic 3 dB modulation bandwidth, $f_{3\,dB}^{max}$, of 63 GHz for the devices doped at 2×10^{19} cm^{-3} in the active region [6]. The role of p-doping in reducing ε remains the subject of intense experimental and theoretical debate. Possible explanations include a counteraction of strain-enhanced spectral hole-burning effects [12] (resulting from a doping-induced decrease in the intraband relaxation time, τ_{in}), improved hole transport in the core region, and more uniform pumping of the MQWs.

4. Gain spectra

In Figs. 6 and 7, experimental and theoretical modal gain (g_{mod}) spectra are compared for the three different doping levels. The experimental values of g_{mod} (Fig. 6) are calculated as a function of the threshold current density, J_{th}, from the total losses, $g_{mod} = \alpha_i + \alpha_m$, where α_m is the mirror loss. The transparency current density, J_{trans}, was estimated by extrapolating to $g_{mod} = 0$ (see Table 1). The theoretical gain, as a function of injected carrier density (Fig. 7), has been calculated using a model which includes both the strain-induced non-parabolicity of the valence subbands and carrier-density-dependent intrasubband scattering. The experimental and theoretical doping dependencies of the differential gain are in good agreement; a p-doping level of 2×10^{19} cm^{-3} is predicted to increase $\partial g/\partial n$ from 1.9×10^{-15} cm^2 (undoped) to 2.1×10^{-15} cm^2. In Fig. 7, the transparency carrier density is predicted to decrease monotonically with increasing active region doping level. However, as was observed for I_{th} in Fig. 3, J_{trans} first decreases in the devices doped at 5×10^{18} cm^{-3}, and then increases at the higher doping level. This increase is attributed to a decrease in the carrier lifetime in the laser. The doping-induced decrease in τ_c shown in Table 1, may lead to a decrease in the turn-on delay time of the lasers, which is expected to improve the large-signal digital modulation performance [13].

5. Conclusions

We have investigated p-dopant incorporation and the influence of p-doping on the gain and damping behavior of GaAs-based strained multiple quantum well lasers. By adding 2×10^{19} cm^{-3} beryllium doping to the active region of $In_{0.35}Ga_{0.65}As/GaAs$ strained MQW lasers, we have been able to demonstrate both very efficient high-speed modulation (20 GHz at a DC bias current of 50 mA) and the first semiconductor lasers to achieve a direct modulation bandwidth of 30 GHz under DC bias. Further device improvements may be possible by replacing Be with carbon as the p-dopant in the core region. Together with the inherent advantages of our vertically compact laser structure for monolithic integration with GaAs-based electronics, the performance enhancements reported here demonstrate the potential of utilizing p-doped strained-layer GaAs-based MQW lasers for analog optical links out to millimeter wave frequencies and for digital transmission at data rates exceeding 20 Gbit s^{-1}.

Acknowledgments

The authors wish to thank W. Benz, T. Fuchs, C. Hoffmann, W. Jantz, B. Matthes, K. Räuber and J. Seibel, for their assistance with sample preparation and characterization. We also wish to thank G. Grau and H. Rupprecht for their continuing support and encouragement, and H. Ennen for his role in initiating this project. This work was supported by the Bundesministerium für Forschung und Technologie.

References

1 K. Uomi, T. Mishima and N. Chinone, *Jpn. J. Appl. Phys., 29* (1990) 88.
2 K. Uomi, *Jpn. J. Appl. Phys., 29* (1990) 81.
3 S. Weisser, J. D. Ralston, E. C. Larkins, I. Esquivias, P. J. Tasker, J. Fleissner and J. Rosenzweig, *Electron. Lett., 28* (1992) 2141.
4 P. A. Morton, R. A. Logan, T. Tanbun-Ek, P. F. Sciortino Jr., A. M. Sergent, R. K. Montgomery and B. T. Lee, *Electron. Lett., 28* (1992) 2156.
5 T. Yamanaka, Y. Yoshikuni, W. Lui, K. Yokoyama and S. Seki, *IEEE Photon. Technol. Lett., 4* (1992) 1318.
6 J. D. Ralston, S. Weisser, I. Esquivias, E. C. Larkins, J. Rosenzweig, P. J. Tasker and J. Fleissner, *IEEE J. Quantum Electron., 29* (1993) 1648.
7 J. D. Ralston, E. C. Larkins, W. Rothemund, I. Esquivias, S. Weisser, J. Rosenzweig and J. Fleissner, *J. Cryst. Growth, 127* (1993) 19.
8 R. J. Malik, R. N. Nottenberg, E. F. Schubert, J. F. Walker and R. W. Ryan, *Appl. Phys. Lett., 53* (1988) 2661.
9 R. F. Kopf, E. F. Schubert, S. W. Downey and A. B. Emerson, *Appl. Phys. Lett., 61* (1992) 1820.
10 S. D. Offsey, W. J. Schaff, P. J. Tasker and L. F. Eastman, *IEEE Photon. Technol. Lett., 2* (1990) 9.
11 R. Nagarajan, T. Fukushima, M. Ishikawa, J. E. Bowers, R. E. Geels and L. A. Coldren, *IEEE Photon. Technol. Lett., 4* (1992) 121.
12 S. Seki, P. Sotirelis, K. Hess, T. Yamanaka and K. Yokoyama, *Appl. Phys. Lett., 61* (1992) 2147.
13 K. Y. Lau, N. Bar-Chaim, P. L. Derry and A. Yariv, *Appl. Phys. Lett., 51* (1987) 69.

Materials Science and Engineering, B21 (1993) 237–240

Experimental and theoretical studies of multi-quantum well structures for unipolar avalanche multiplication

Mika Toivonen, Marko Jalonen and Markus Pessa
Department of Physics, Tampere University of Technology, PO Box 692, FIN-33101 Tampere (Finland)
Kevin R. Lefebvre and Neal G. Anderson
Department of Electrical and Computer Engineering, University of Massachusetts at Amherst, Amherst 01003 (USA)

Abstract

Multi-quantum well structures exhibiting intraband impact ionization were studied. Fabricated devices consisted of donor doped GaAs or $In_{0.20}Ga_{0.80}As$ quantum wells and undoped $Al_xGa_{1-x}As$ barrier regions. Effective gain-per-stage was found to be strongly dependent on structure design and measurement conditions (incident light intensity, chopping frequency and temperature). The limits of the validity of the current single-valley model for these structures are discussed.

1. Introduction

Multi-quantum well avalanche photodiodes (MQW APDs) have been widely studied because they have the potential of minimizing avalanche multiplication noise. However, MQW APDs have so far been based on multiplicative gain via interband impact ionization and their operation naturally involves both holes and electrons. Therefore, an alternative avalanche multiplication mechanism, impact ionization of electrons out of confined quantum states, has been introduced because of its highly unipolar nature, *i.e.* the gain is derived from the multiplication of only one carrier species [1]. This approach should lead to much lower noise operation than in conventional APDs.

In principle unipolar ionization is feasible in a properly designed MQW system in which quantum wells filled with electrons by impurity doping can act as sources of electrons. In these devices, electrons generated by photon absorption and accelerated by the applied electric field in the undoped barrier region can scatter bound electrons from the wells (Fig. 1). Consequently, the multiplication of photoelectrons can be derived from the successive scattering events in the MQW region. Recent experimental measurements of carrier multiplication in GaInAs/AlInAs, GaSb/AlSb and AlGaAs/GaAs MQW structures have verified the existence of this highly unipolar multiplication process [2, 3].

There are, however, some specific problems which impose rigorous limitations on the design of unipolar APDs [4]. Dark currents increase rapidly with gain owing to thermal ionization and tunnelling. Also, the wells quickly become depleted of carriers when the multiplication is started. Therefore, in order to sustain the impact ionization process, the wells need to be continuously replenished with electrons. This can occur via thermal generation, optical generation, or separate ohmic contacts to each well.

In this paper, we present the main results from experimental studies of GaAs/AlGaAs and strained InGaAs/AlGaAs MQW structures grown by molecular beam epitaxy. The structures consisted of donor doped GaAs or $In_{0.20}Ga_{0.8}As$ wells and undoped $Al_xGa_{1-x}As$ barrier regions. Results from these experiments are compared with calculations, and general issues regarding the modelling of these devices are discussed.

2. Experimental results and discussion

Details of the structures studied are summarized in Table 1 and Fig. 1. The devices were cooled to cryogenic temperature during measurements. Chopped light of $\lambda = 420$ nm from a monochromator was focused on the active area of the devices (0.125 mm^2) and the resulting photocurrent I_{ph} was measured using a lock-in amplifier. By changing the temperature with a heating resistor and by regulating the illumination to suitable intensity levels we were able to obtain direct information on the operation of our MQW structures.

The photocurrent multiplication factors M and dark currents I_d for devices SPPM07, SSPM19, SSPM23 and SSPM32 respectively, are given in Fig. 2 as a function of electric field E in the MQW region at a

0921-5107/93/$6.00

© 1993 – Elsevier Sequoia. All rights reserved

temperature of 98 K. Devices exhibited a strong roll-off of gain as a function of chopping frequency owing to the quantum well depletion effect [2, 3]. A low chopping frequency of 20 Hz was usually used to maintain a reasonable level in multiplication. The total effective gain M in these unipolar devices can be given by the aid of average gain-per-period g and number of periods N: $M = I_{ph}/I_{prim} = g^N$. It should be noted that g reflects the relative rates of electron capture, ballistic transport through the well and ionization processes [7]. We obtained $g \approx 1.13$ for SSPM19 ($N = 20$) and $g \approx 1.23$ for SSPM32 ($N = 10$) at a field of about 160 kV cm^{-1}. The smaller g in SSPM19 can be attributed to faster depletion of electrons out of quantum wells via the impact ionization due to the larger number of periods. In the same way, g decreased in all structures with increasing primary photocurrent I_{prim}.

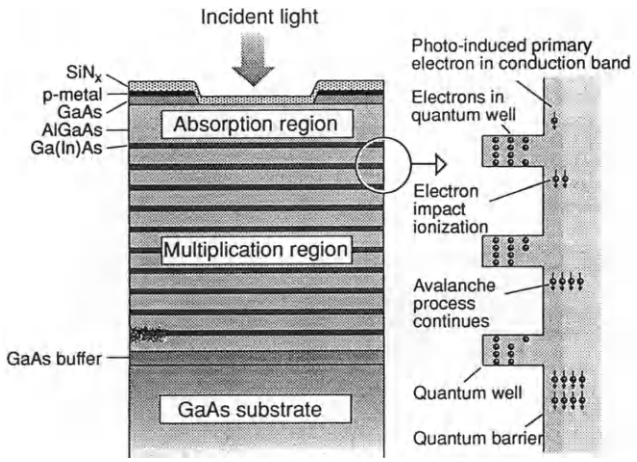

Fig. 1. Schematic cross-section of a unipolar avalanche photodetector made of Ga(In)As and AlGaAs layers. When a photon is absorbed in the absorption layer an electron–hole pair is formed but only electrons are injected in the MQW multiplication region where they ionize more electrons out of the quantum wells.

The onset of multiplication in SSPM19 and SSPM32 occurred at an electric field of about 3.8 kV cm^{-1}. At this field the ionization process on average starts to dominate the capture in each well. This value of E is much smaller than the threshold field for impact ionization across the band gap. Calculations for the threshold field in SSPM19 or in SSPM32 which include the effects of carrier capture [7] yield a threshold field roughly 10 times the experimental value. This may suggest the importance of tunnelling [8] and/or other mechanisms in the multiplication process, as are discussed later.

The behaviour of multiplication in SSPM07 differed clearly from that in other GaAs/AlGaAs structures. The total gain was already about 18 at a field of about 90 kV cm^{-1} and was not saturated even at fields twice as high. For example the total gain in SSPM19 was only about 12 at the same field and strongly saturated above a field of 20 kV cm^{-1}. Because of the indirect band gap in the barriers of SSPM07 ($x = 0.71$) we assume that, at least at high fields, this different type of behaviour is strongly affected by the fractional carrier occupations of the various valleys.

SSPM23 had the deepest wells in the MQW region and direct gap barriers. The calculations including capture but excluding tunnelling effects gave a threshold field of 60–80 kV cm^{-1}, while in our experimental studies the field yielding unity gain occurred at about 27 kV cm^{-1}. This decreased onset may again suggest that tunnelling-assisted impact ionization is important. We observed the maximum total gain of about 26 and $g \approx 1.18$ ($N = 20$) at a field of about 70 kV cm^{-1}. This seems to indicate that accelerated electrons in the barriers above the threshold energy have a much larger probability of impacting electrons out of $In_{0.2}Ga_{0.8}As$ wells than out of GaAs wells. Above 70 kV cm^{-1} the I_{ph} of SSPM23 started to decrease and fluctuate strongly.

All devices exhibited dark currents several orders of magnitude higher than the photocurrents at reasonable

TABLE 1. Composition and multi-quantum well dimensions of studied devices

Device	x	y	N	L_{QW} (nm)	L_B (nm)	N_d ($\times 10^{18}$ cm^{-3})	ΔE_c (eV)	$E_{g,QW}$ (eV)
SSPM07	0.71	0	20	10	100	4	0.3[a]	1.42
SSPM19	0.32	0	20	10	100	4	0.25	1.42
SSPM23	0.30	0.20	20	10	100	4	0.39[b]	1.19[b]
SSPM32	0.32	0	10	10	100	4	0.25	1.42

x is the Al molar fraction in barriers, y is the In molar fraction in wells, N is the number of periods, L_{QW} is the quantum well width, L_B is the barrier width, N_d is the doping concentration in the well layers, ΔE_c is the conduction band offset, and $E_{g,QW}$ is the band gap of the well region.

[a] Γ–X separation, ref. 5.

[b] Strained structure, ref. 6.

multiplication levels with the illumination conditions used. Although the dark currents are much too high for any practical applications, I_d could be decreased to some extent through structure design. For example in SSPM07 I_d is already 10^6 times larger than the photocurrent at 6 kV cm^{-1} while in SSPM23 the corresponding value is "only" about 550 at 10 times higher field.

We also varied the temperature of the devices step-by-step from 98 K to 163 K. In the case of SSPM19, M increased with temperature until at 143 K it started to turn down. This strongly suggests that first electron occupation increases in upper sub-bands in wells with increasing T. Then the depletion of wells by the dark current decreases the multiplication at higher temperature. This kind of increased multiplication is in sharp contrast to the case of band-to-band ionization.

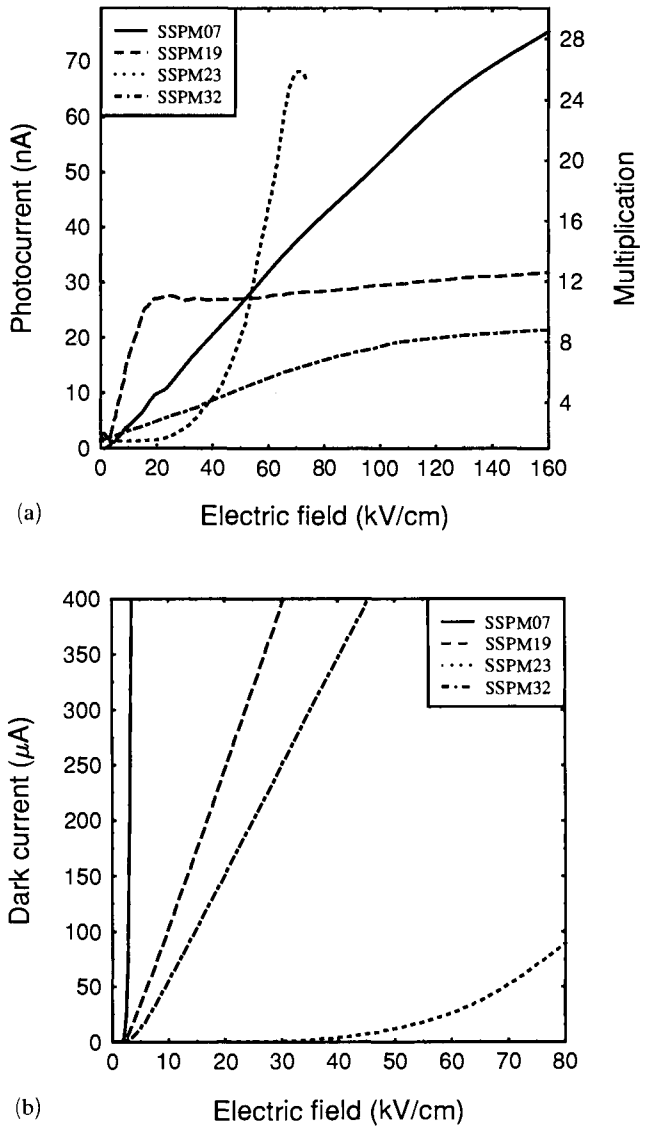

Fig. 2. (a) Photocurrent and multiplication *vs.* electric field in the MQW region for SSPM07, SSPM19, SSPM23 and SSPM32 (I_{prim} = 2.65 nA, chopping frequency 20 Hz, T = 98 K). (b) Dark current *vs.* electric field in the MQW region for SSPM07, SSPM19, SSPM23 and SSPM32 (T = 98 K).

3. Theoretical background

Several final remarks are in order regarding comparison of experimental and theoretical values for solid-state photomultipliers. Current models for these devices [4, 7], including the model used for the theoretical predictions presented in this paper [7], are based on the fundamental approach introduced by Chuang and Hess [1]. In these models, carriers incident on the well are assumed to occupy a single conduction band valley centred at $k = 0$ and are assumed to be distributed according to a drifted Maxwellian function. Those carriers above the threshold energy for intra-band ionization are then assumed to interact with bound electrons in the well via a two-particle Coulomb potential, yielding carrier ejection from the well at a rate specified by Fermi's golden rule including both energy and momentum conservation. Tunnelling out of the well is not considered.

While this approach is reasonable for low fields, it is probably of limited use for quantitative calculations at fields as high as those required to operate devices which have been experimentally demonstrated to date. In $Al_xGa_{1-x}As$ with $x \approx 0.3$, the barrier material used in all of the devices reported in this work except SSPM07, significant intervally transfer of carriers to higher conduction band valleys occurs at fields above roughly 5 kV cm^{-1} [9]. This limits the validity of the single-valley model in this field regime both because a significant fraction of the carriers resides in the valleys with different energy–momentum relationships and because the distribution function in the central valley can be expected to become highly non-Maxwellian in the range of fields where intervalley scattering becomes active. Increased fields also increase tunnelling-assisted ionization rates.

It is interesting to note that the approximate 5 kV cm^{-1} limit on the validity of the single-valley model for these structures nearly coincides with the 3.8 kV cm^{-1} field at which appreciable ionization is observed in the structures with the GaAs wells (SSPM19 and SSPM32). The single-valley model of ref. 7 indeed predicts a significant increase in the fraction of carriers about the threshold energy at fields in this regime, but the multiplication is not predicted to overcome capture until fields of 30–35 kV cm^{-1} are reached. Single-stage multiplication factors (*i.e.* $g-1$) calculated for the central valley, which are of similar magnitudes to those

obtained by others [4] for similar structures, are as much as two orders of magnitude too small to result in the observed current gains at high fields (greater than 5 kV cm^{-1}) even if capture is neglected. While errors induced by the drifted Maxwellian approximation, three-dimensional screening of the electron–electron interaction, and other simplifications in the single-valley models may account for some of the error, it seems unlikely that they could be entirely responsible for such large discrepancies in calculated and measured gains. This may indicate that, coincidentally, tunnelling commences in that same range of fields in which the single-valley approximation breaks down.

An alternative explanation for this behaviour is that multiplication rates are significantly higher for the indirect minima, thus increasing gain significantly in the 3–5 kV cm^{-1} range where intervalley scattering commences. Such an interpretation would be consistent with the fact that the gain observed in SSPM07, which is similar to SSPM19 but with high-mass indirect $Al_{0.71}Ga_{0.29}As$ barriers, turns on more slowly but ultimately yields a substantially higher gain. (Large effective masses at the barrier band edge would be expected to increase the field required to accelerate carriers above a fixed threshold, which is consistent with a relatively gradual increase in gain with field.) The development of multi-valley models for unipolar multiplication will aid in understanding the nature of the gain at high fields, and will probably be required to resolve this issue.

References

1 S. L. Chuang and K. Hess, *J. Appl. Phys., 59* (1986) 2885.
2 F. Capasso, J. Allam, A. Y. Cho, K. Mohammed, R. J. Malik, A. L. Hutchinson and D. Sivco, *Appl. Phys. Lett., 48* (1986) 1294.
3 M. Toivonen, M. Jalonen, A. Salokatve and M. Pessa, *Appl. Phys. Lett., 62* (1993) 1664.
4 Y. Wang, D. H. Park and K. F. Brennan, *IEEE J. Quantum Electron., 26* (1990) 285.
5 A. J. Hill and P. H. Ladbrooke, *Electron. Lett., 22* (1986) 218.
6 S. Niki, C. L. Lin, W. S. C. Chang and H. H. Wieder, *Appl. Phys. Lett., 55* (1989) 1339.
7 K. R. Lefebvre and N. G. Anderson, *Appl. Phys. Lett., 61* (1992) 282.
8 S. L. Chuang and K. Hess, *J. Appl. Phys., 61* (1987) 1510.
9 H. Hjelmgren, unpublished Monte Carlo results, 1993.

Materials Science and Engineering, B21 (1993) 241-243

Lateral thickness modulations in alternate tensile-compressive strained GaInAsP multilayers grown by gas source molecular beam epitaxy

A. Ponchet and A. Rocher
CEMES-LOE/CNRS, 29 rue Jeanne Marvig, BP 4347, 31055 Toulouse (France)
J. Y. Emery, C. Starck and L. Goldstein
Alcatel Alsthom Recherche, Route de Nozay, 91460 Marcoussis (France)

Abstract

Compressive GaInAsP multiple quantum wells (MQWs) grown on (001)InP have demonstrated high potential for the production of lasers emitting at 1.5 μm. A GaInAsP tensile barrier is now used instead of a lattice matched barrier to compensate for the compressive strain. However, zero-net strained MWQs grown at 500 °C by gas source molecular beam epitaxy show a decrease in structural and optical quality. A structural investigation of two MQWs using a -0.5% mismatched barrier was performed using transmission electron microscopy to understand why using a tensile barrier induces such degradation. All the samples studied show a lateral quasi-periodic thickness modulation which is strongly anisotropic with a periodicity of about 50 nm along the [110] direction, while no modulation occurs along the [1$\bar{1}$0] direction. Since the growth is easier on relaxed areas than on strained areas, we deduce that the thicker parts of the layer are more relaxed than the thinner parts. Moreover, the average period of 50 nm is found to be independent of both the barrier thickness and the mismatch of the compressive well, while the amplitude of the modulation is drastically enhanced when the barrier thickness increases. This confirms that the phenomenon is controlled by the partial elastic relaxation of tensile layers.

1. Introduction

Compressive multiple quantum wells (MQWs) have demonstrated good potential in the design of GaInAsP based lasers emitting at 1.5 μm [1]. However, the total thickness of the MQWs is limited by a critical thickness related to the creation of misfit dislocations. Use of tensile rather than lattice matched barriers is expected to allow the total MQW thickness to be increased by stabilizing the whole structure. However, macroscopic characterizations of gas source molecular beam epitaxy (GSMBE) MQWs have shown that the introduction of tensile barriers instead of lattice matched barriers causes a decrease in the optical and structural quality [2]. The purpose of the structural study reported here was to determine the role of the tensile barrier in such degradation.

2. Experimental details

A zero-net strained $Ga_{0.18}In_{0.82}As_yP_{1-y}$ MQW (sample A) was grown on (001) InP by GSMBE at a substrate temperature of 500 °C. The quantum well used to obtain a 1.5 μm laser ($y=0.7$) presents a lattice mismatch with InP of $\Delta a/a=1\%$ and is 8 nm thick. Because the lattice mismatch of the tensile GaInAsP used as barrier ($y=0.2$) is -0.5%, its thickness was adjusted to 16 nm to obtain a zero-net strained structure. Another sample (B) was grown under the same conditions with the same tensile barrier composition but another thickness (24 nm) and a different composition of compressive well ($y=0.8$ and $\Delta a/a=1.5\%$). Because these thicknesses are lower than the critical thickness, the MQWs are expected to be tetragonally distorted. The [110] and [1$\bar{1}$0] directions were revealed by chemical etching figures.

Samples A and B were characterized by *in situ* reflection high energy electron diffraction (RHEED), X-ray double diffraction (XRD) and room-temperature photoluminescence (PL). The transmission electron microscopy (TEM) study was performed at 200 kV on a Philips CM20 microscope using both cross-sectional and plan view observations. Thin specimens were obtained by mechanical polishing followed by Ar^+ beam milling with liquid nitrogen cooling. Dark field (DF) images were taken with $g=\{002\}$, which is highly sensitive to variations in chemical composition, while DF images were taken with $g=\{220\}$ which is highly sensitive to strain fields.

0921-5107/93/$6.00

© 1993 - Elsevier Sequoia. All rights reserved

3. Results

RHEED, XRD and PL characterizations of sample A showed a drastic decrease in the optical and structural properties of studied samples compared with similar MQWs with lattice matched barriers [2]. The degradation is increased with a thicker barrier as seen in sample B. The effect of growth conditions (temperature, V-to-III ratio and growth interruption) has been reported previously [2].

In both samples, $(\bar{1}10)$ TEM cross-sectional observations revealed a quasi-periodic undulation of interfaces (Fig. 1). Undulation starts first at the barrier–well interface, while the growth of the compressive layer tends to smooth the reverse interface. However, after a few periods, both interfaces become more and more undulated. As soon as it occurs, the modulation has a columnar structure throughout the whole multilayer with a lateral periodicity of about 50 nm. Undulations of the well–barrier interface and of the reverse interface spread out with phase opposition, as seen in Fig. 1.

Plan-view observations (Fig. 2) demonstrate that the thickness modulation is strongly anisotropic. Irrespective of the diffraction vector, only modulated contrasts parallel to the $[\bar{1}10]$ direction are observed. The average period measured in plan views was 50 nm along the [110] direction for both samples, and the coherent length of modulation in the $[\bar{1}10]$ direction is greater than 200 nm. A (100) cross-sectional observation of sample A reported previously [3, 4] gave the same results concerning anisotropy.

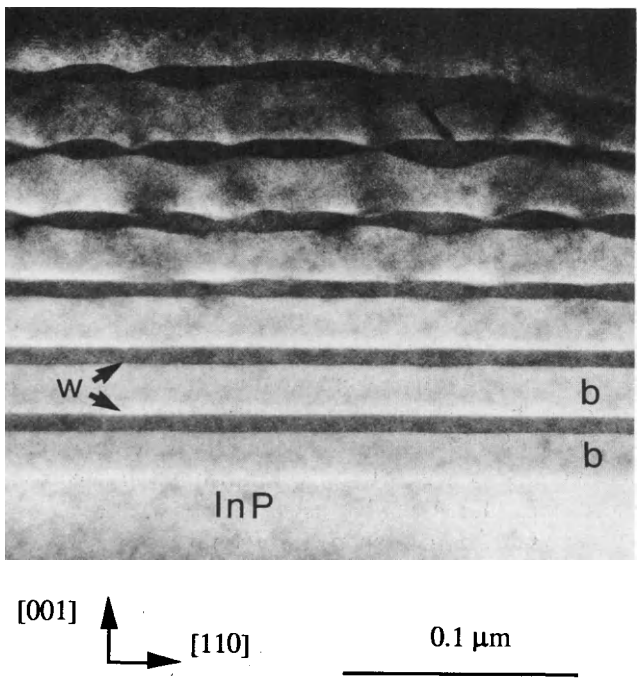

Fig. 1. $g=002$ DF (110) cross-sectional micrograph of sample B. The epitaxed structure is composed of an InP buffer layer, tensile barriers (b) and compressive quantum wells (w).

Observations made on $(\bar{1}10)$ cross-section specimens [4] with $g=220$ showed systematically a columnar structure with a lateral periodicity well correlated with the thickness modulation described above. Moreover, while $g=220$ plane-view micrographs present a periodic contrast (Fig. 2(b)), $g=\bar{2}20$ micrographs present complete extinction of significant modulated contrast (Fig. 2(c)). These results are consistent with a displacive modulation along the [110] direction but not along the $[\bar{1}10]$ direction: (110) interplanar distances are modulated while $(\bar{1}10)$ interplanar distances are not.

Although both samples present quite similar morphology, some quantitative differences can be reported and can be used to explain the degradation of MQW properties in sample B relative to sample A (a more detailed report of sample A has previously been reported [4, 5]). Undulation of barrier–well interfaces for the same number of wells increases more rapidly in sample B than in sample A. Many extended defects are more rapidly developed in sample B than in sample A. Dislocations appear as early as the fifth period as seen on cross-sectional specimens, while dislocations were observed only from the eighth period in sample A. However, asymmetry of morphology between the barrier–well interface and the reverse interface, which exhibits facets rather than rounded undulations, is observed in sample B (Fig. 1). This will be reported elsewhere.

In fact, the progressive increase in undulation and the creation of extended defects appear to be a function of the cumulative thickness of the tensile barrier, and are independent of the nature of the compressive well.

4. Discussion

It can be deduced from our observations that the tensile layer is responsible for starting the modulation. Firstly, similar MQWs using lattice matched barriers do not exhibit such modulations. Secondly, the barrier–well interface develops undulation before the reverse interface, and its amplitude is only a function of the total thickness of the tensile layer. Finally, the modulation wavelength which is the same in both samples is independent of the compressive well mismatch.

According to comparison with other strained systems [5, 6] and considering the fact that relaxation could occur by three-dimensional growth before the creation of interfacial dislocation, we propose that the

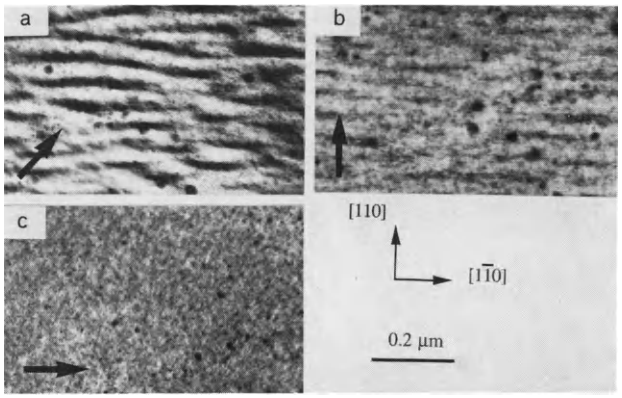

Fig. 2. DF plan view micrographs of sample A: (a) $g=200$; (b) $g=220$; (c) $g=2\bar{2}0$. In the last case, there is no significant modulated contrast. The directions of the diffraction vectors are indicated by arrows.

lateral modulation is a way of producing a partial elastic relaxation of the tensile layer. Some models have recently been developed to show this [7, 8].

In the case described here, the phase opposition and amplification of the modulation can easily be accounted for by the assumption that growth is easier on the more relaxed zones than on the more strained zones. Then it is deduced that the thickest zones are partially relaxed compared with the thinnest zones. Because the sign of lattice mismatch is reversed, the zones which are favourable for growing tensile GaInAsP are unfavourable for the compressive GaInAsP, so that the interfaces are in phase opposition. A more detailed model of lateral interplanar distance modulation has been proposed and discussed previously [3, 4].

5. Conclusions

Two different compressive MQWs present a lateral modulation of thickness and strain within the layers, when the same tensile GaInAsP ($\Delta a/a=-0.5\%$) is used as barrier instead of a lattice matched barrier. The modulation is periodic with a wavelength of 50 nm and is strongly anisotropic: (110) plane spacings are modulated while ($\bar{1}10$) ones are not. Increasing the barrier thickness increases the amplitude of modulation.

Comparison of the samples shows that the tensile layers are responsible for starting the phenomenon. From these experiments and according to recent models, we suggest that the modulation is induced by a partial elastic relaxation of strained layers. The observed morphology is well accounted for by this hypothesis.

References

1 C. Starck, J.-Y. Emery, R. J. Simes, L. Goldstein and J. Barrau, *J. Cryst. Growth, 120* (1992) 180.
2 J.-Y. Emery, C. Starck, L. Goldstein, A. Ponchet and A. Rocher, *Proc. 7th Conf. on Molecular Beam Epitaxy, 1992, J. Cryst. Growth*, in press.
3 A. Ponchet, A. Rocher, J.-Y. Emery, C. Starck and L. Goldstein, *Proc. 8th Microsc. Semicond. Mater. Conf., Oxford, 1993, Inst. Phys. Conf. Ser.*, in press.
4 A. Ponchet, A. Rocher, J.-Y. Emery, G. Starck and L. Goldstein, *J. Appl. Phys.*, in press.
5 K. Y. Cheng, K. C. Hsieh and J. N. Baillargeon, *Appl. Phys. Lett., 60* (1992) 2892.
6 A. G. Cullis, D. J. Robbins, A. J. Pidduck and P. W. Smith, *J. Cryst. Growth, 123* (1992) 333.
7 F. Glas, *J. Appl. Phys., 62* (1987) 3201.
8 J. Grilhé, *Acta Metall. Mater., 41* (1993) 909.

Growth and characterization of $In_{0.53}Ga_{0.47}As/In_xGa_{1-x}As$ strained-layer superlattices

A. Kohl[a], S. Juillaguet[b], B. Fraisse[c], R. Schwedler[a], F. Royo[b], H. Peyre[b], F. Bruggeman[a], K. Wolter[a], K. Leo[a], H. Kurz[a] and J. Camassel[b]*

[a]*Institute of Semiconductor Electronics I and II - RWTH, 5100 Aachen (Germany)*
[b]*GES-USTL, 34095 Montpellier cedex 5 (France)*
[c]*LAMMI-CNRS, Université de Montpellier 2, 34095 Montpellier cedex 5 (France)*

Abstract

Since the early proposal that InGaAs/InGaAs strained-layer superlattices (SLSs) should constitute a new class of optoelectronic materials, very little work has been done to master the growth conditions and optimize the resulting superlattice properties. In this work, we present the results of a preliminary investigation of SLSs grown by low-pressure metal-organic vapour phase epitaxy. Two different series of samples were grown to check independently the effect of well thickness and barrier composition. In both cases, in order to conserve one layer nominally lattice-matched to InP, the wells had a standard composition $In_{0.53}Ga_{0.47}As$.

1. Introduction

In the range of 1.3 and 1.55 μm wavelengths, strained-layer superlattices (SLSs) made of various arrangements of InGaAsP/InGaAsP wells and barriers have specific advantages over the more classical (and much more investigated) InGaAs/InP system. First is the great variety of band gaps and band line-ups which can be achieved by changing independently the respective compositions of the different layers. Second is the possibility to introduce opposite strains in the wells and barriers. When the strain components are cancelled over a superlattice period, this results in the so-called strain-compensated (SC) structures. They give additional degrees of freedom to adjust for the in-plane dispersion of the topmost (confined) level associated with the valence band (effective mass) and have been shown to result in increased laser efficiency [1].

A particular type of SC structure is very important for optical device applications. This is the case where a constant arsenic-to-phosphorus ratio (in both the wells and barriers) is used. The corresponding structures are known as "constant-y" (also called CY) and have been recently introduced by Mircea and coworkers [2, 3]. Their specific advantages include the following:

(i) improved interface properties (with respect to the standard InGaAs/InP), mainly because there is no group V concentration gradient at the interface;

(ii) improved thermal stability, again because there is no gradient of concentration (driving force) to trigger the interdiffusion of group V species and, second, because the wells can be designed large enough to make the effect of group III interdiffusion negligible [4, 5].

When no phosphorus is present in the active layers (wells *and* barriers), one reaches the limiting case of InGaAs/InGaAs superlattices. In this case, all unwanted exchange of phosphorus by arsenic during the switching sequences [6] is completely avoided. This should result in even better interfaces compared with standard CY structures and both SL and SC structures can be easily designed.

Historically, InGaAs/InGaAs SLSs were first discussed (theoretically) by Osbourn [7] and subsequently investigated by Quillec *et al.* [8] after which no further investigation was done. Recently, there has been renewed interest because of the potential for polarization insensitive optoelectronic devices [9–12] including lasers, amplifiers and modulators. However, because one can tune separately the barrier *and* the well compositions *and* thicknesses, very broad ranges of layer design can be considered. This makes it difficult to compare different data reported by different groups.

In this work, we present systematic results of the growth and characterization of two different series of InGaAs/InGaAs SLSs grown by low-pressure metal-organic vapour phase epitaxy on sulphur-doped InP

*Author to whom correspondence should be addressed.

0921-5107/93/$6.00
© 1993 - Elsevier Sequoia. All rights reserved

substrates. One series was designed to investigate the effect of well thickness, the other to investigate the effect of barrier composition.

2. Growth technique and corresponding results

We used a horizontal reactor with a total gas pressure of 20 hPa. The growth temperature was 640 °C. To allow for fast exchange of the gas phase composition, the apparatus was equipped with a vent-run switching manifold. Trimethylindium (TMI), trimethylgallium (TMG), undiluted phosphine (PH_3) and arsine (AsH_3) were used as group III and group V precursors respectively. H_2 carrier gas served to keep the gas flow velocity constant at 1.3 m s^{-1}.

The compositional changes in the superlattice layers were monitored by switching two TMI lines with different fluxes. The TMG and AsH_3 fluxes were kept constant. The growth rate was about 2 μm h^{-1} (2 monolayers per second) but varied slightly from well to barrier (it decreases when decreasing the indium content). A growth interruption sequence of 3 s under arsine was introduced after the growth of each InGaAs layer to ensure an abrupt change in layer composition and to allow for smoothing of the interfaces. More systematic investigations along this line have still to be conducted.

Only $In_{0.53}Ga_{0.47}As$ wells (active layers) were considered. The first series of samples (grown to investigate the effect of changing the well thickness at constant barrier composition and thickness) consisted of 10 layers of InGaAs (wells) with thicknesses of 120, 80 and 40 Å sandwiched between 11 barriers of gallium composition 0.60 and thickness 100 Å. For calibration purposes, a reference layer was systematically embedded inside the InP buffer. In the following, these samples are referred to as series A. Preliminary results concerning the optical properties of samples from series A have already been reported [13]. The second series of samples (series B) was grown to investigate the effect of barrier composition at constant thickness. These SLS structures consisted of 10 layers of InGaAs (wells) with thicknesses 120 Å (and of course constant gallium composition 0.47) sandwiched between 11 layers of InGaAs (barriers) with thicknesses of 100 Å and gallium compositions of 0.48, 0.52 and 0.60 respectively. In this case, no reference layer was deposited.

We collected double X-ray diffraction spectra for all samples of series A and B. In most cases, we obtained good superlattice features. In Table 1, we compare the SLS period obtained from the X-ray data with that deduced from the nominal growth parameters. Within 5%, they agree satisfactorily.

In Fig. 1 we compare two different spectra (log scale) collected for samples A1 and B3. Except for the introduction of a reference layer in sample A1, both had nominally identical growth parameters. In fact, they show (slightly) different periods: 255 Å for sample A1 against 211 Å for sample B3. Moreover, two points should be emphasized.

(i) Introducing a reference layer (sample A1) smears out many significant features of the superlattice structure. This should be systematically avoided.

(ii) When no reference layer is included (sample B3), there is still one additional feature (marked with an asterisk) close to the central InP diffraction peak. This is an effect of arsenic memory: after growth of the 10 period InGaAs superlattice, and despite the growth interruption sequence, there is enough arsenic left in the reactor to enter the topmost InP cap and change the nominal composition from InP to InAsP.

This was confirmed independently by examining sputtered neutral mass spectroscopy (SNMS) data collected in ref. 13 for sample A2 (Fig. 2). It is interesting to note that, both after growth of the reference layer (sputtering time 300 s) and of the superlattice structure

TABLE 1. Comparison of nominal growth parameters and superlattice periods deduced from the X-ray diffraction spectra

Sample	Reference layer	Well		Barrier		X-rays (L_W+L_B) (Å)
		Gallium composition	L_W (Å)	Gallium composition	L_B (Å)	
A1	Yes (1000 Å)	0.47	120	0.6	100	225
A2	Yes (1000 Å)	0.47	80	0.6	100	185
A4	Yes (1000 Å)	0.47	40	0.6	100	135
B0	No	0.47	120	0.48	100	Unresolved
B1	No	0.47	120	0.52	100	212
B2	No	0.47	120	0.56	100	210
B3	No	0.47	120	0.6	100	211

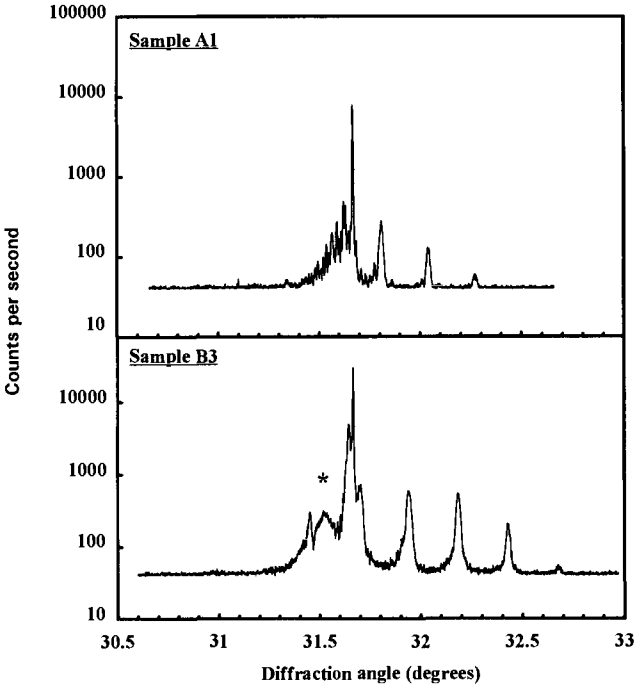

Fig. 1. Comparison of X-ray spectra collected for two different samples with nominally identical growth parameters. Sample A1 had a reference layer embedded in the InP buffer. Sample B3 did not have a reference layer but exhibited an extra feature (*) which corresponds to an arsenic memory effect (see text).

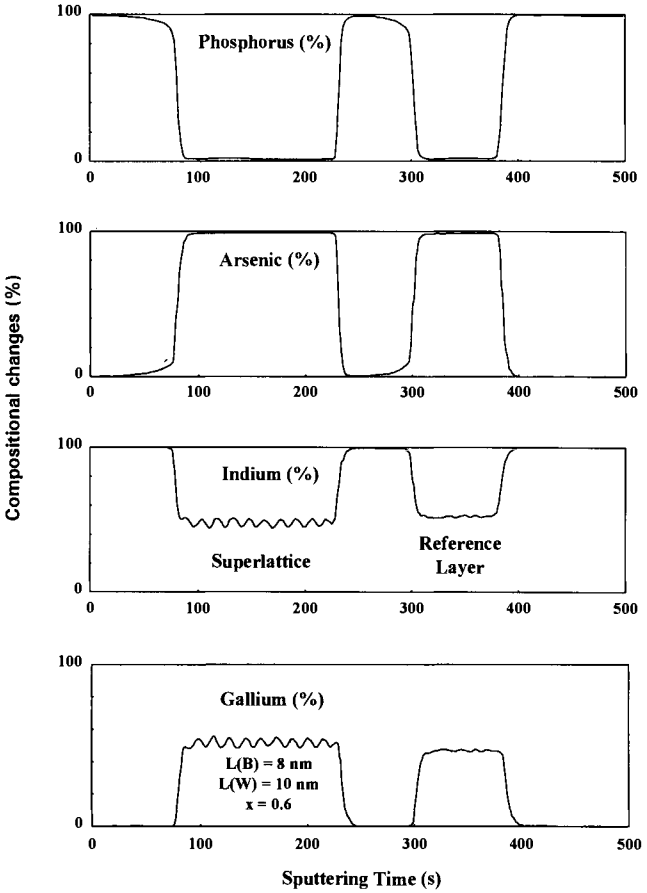

Fig. 2. SNMS data collected for sample A2. The features of interest are the long arsenic tails which appear after about 80 and 300 s sputtering time respectively.

(sputtering time 80 s) there is a long arsenic tail which is due to unwanted incorporation of phosphorus in the following InP layer.

To determine quantitatively the amount of arsenic which enters the cap, we used a simple kinematic model. We followed the path described in ref. 14 and computed theoretical diffraction spectra to compare with the experimental spectra. The results are shown for sample B3 (linear scale) in Fig. 3. Figure 3(a) shows the experimental data, and Fig. 3(b) shows the results of our simulation for the SLS features. No account is taken of the InP substrate. For completeness, a comparison of experimental and estimated peak amplitudes is given in Table 2. The overall agreement is very satisfactory and supports the following values of structural parameters:

(i) SLS period 211 Å;

(ii) width of wells 115 Å, with a gallium composition 0.469;

(iii) width of barriers 96 Å, with a gallium composition 0.564.

Finally, in Fig. 3(c), the diffraction profile computed for a single layer (marked with an asterisk) of InAsP with 6% arsenic and typical thickness of 250 Å is given. Obviously, the overall agreement is very satisfactory.

3. Computational results

We performed a standard computation of confinement energies as a function of well thickness and barrier composition. The results are shown in Figs. 4(a) and 4(b) respectively. We find the usual type I/type II behaviour [7] (where both the electrons and heavy holes localize in the wells, while the light holes localize in the barriers) and some unusual results.

The relationship obtained as a function of quantum well thickness (Fig. 4(a)) reveals peculiar behaviour. Because the change in transition energy for E_1-L_1 is due only to the increase in electron confinement energy, it is *lower* than the change expected for E_1-H_1. This is opposite to the effect expected for more standard systems. The same is true of the change in confinement energy *vs.* barrier composition (Fig. 4(b)). We predict again a high sensitivity of E_1-H_1 while the type II transition (E_1-L_1) stays more constant. This is now a complex effect of relative thicknesses, strain and band offsets.

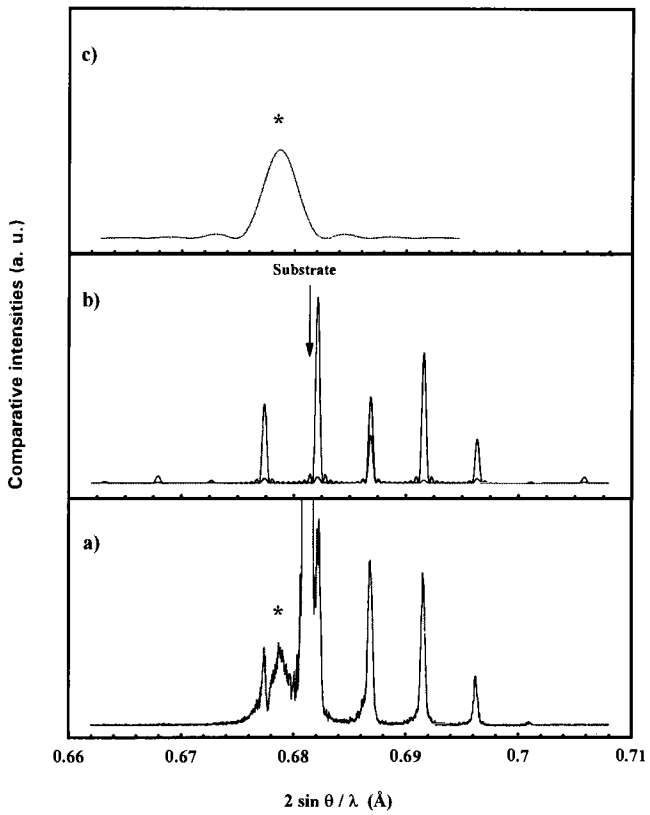

Fig. 3. Comparison of experimental and simulated X-ray diffraction peaks for sample B3.

TABLE 2. Comparison of experimental diffraction peaks and the results of our computation

SLS order	I/I_{max} (experimental)	I/I_{max} (theoretical)
143	41.52	42.63
144	100	100
145	81.35	72.58
146	75.42	71.06
147	28.81	24.36

The nominal growth parameters are listed in Table 1 (sample B3). The X-ray data give $L_W = 115$ Å with gallium composition 0.469, and $L_B = 96$ Å, with gallium composition 0.564.

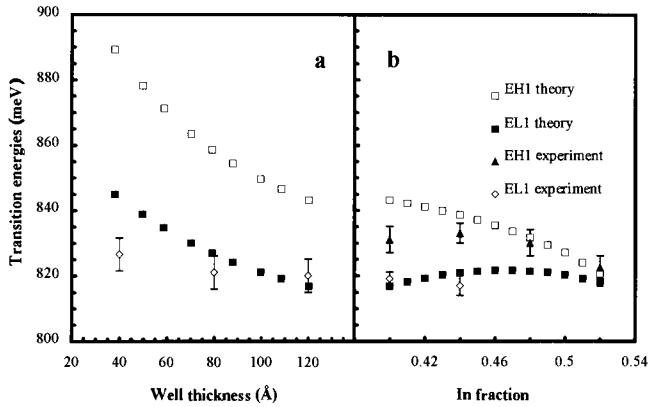

Fig. 4. Theoretical interband transitions computed for $In_{0.53}Ga_{0.47}As/InGaAs$: (a) relationship *vs.* well width, the barrier width was 100 Å with gallium composition 0.60; (b) relationship *vs.* barrier composition, the barrier width was 100 Å. The well width was kept constant at 120 Å. For clarity, the experimental results are displayed as a function of the nominal growth parameters.

4. Optical data

Results for samples from series A have already been given [13]. They are indicated as open diamonds in Fig. 4(a). Concentrating on samples from series B, we find the following.

(i) From the absorption spectra collected at 2 K, there is strong evidence of increased localization of the *electrons* and *heavy holes* in the same layers (wells). This is the expected type I behaviour. As a function of band offset (barrier composition), this results in more and more easily resolved excitonic peaks when the gallium composition is increased from 0.48 to 0.60. The corresponding energies are displayed as black triangles in Fig. 4(b).

(ii) In all samples the photoluminescence (PL) line is shifted to lower energy by typically 10–20 meV with respect to the main excitonic peak resolved in absorption. As a matter of fact, in the transmission spectra the PL peak corresponds to a weak shoulder which develops on the low energy side of the strong E_1–H_1 transition. This is shown in Fig. 5 for sample B3. As a consequence, we associate both the PL *and* the shoulder to the weaker (type II) *electron–light hole* transition.

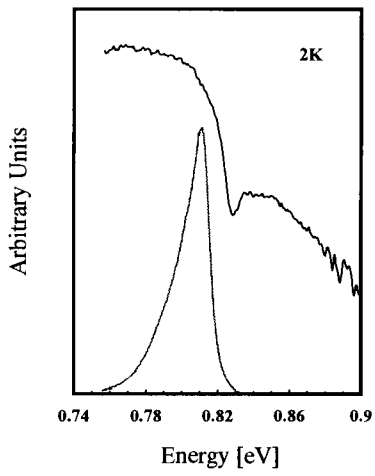

Fig. 5. Comparison of PL and transition spectra collected at 2 K for sample B3. Notice the small shoulder on the low energy side of the main E_1–H_1 transition.

(iii) Finally, all theoretical results suggest that the E_1–L_1 transition energy is fairly insensitive to the fluctuations in barrier composition and well thickness. This is what is found from a consideration of the experimental data displayed in Figs. 4(a) and 4(b). To some extent this accounts for the very small full width at half-maximum observed from PL. Indeed, experimental values as low as 2 meV at 2 K have been observed. Still, the effect of small band gap discontinuities and small interface roughness has to be clarified.

5. Conclusion

We have reported on the growth, X-ray diffraction spectra and optical properties of InGaAs/InGaAs SLS structures. From analysis of the X-ray data, we have found good overall agreement with the nominal values of structural parameters. Some evidence of artefacts, such as an arsenic memory effect, was also found. Our spectroscopic data support qualitatively the predicted type I/type II behaviour. However, more detailed investigations have to be carried out before perfect quantitative agreement can be obtained.

References

1 B. J. Miller, U. Koren, M. G. Young and M. D. Chien, *Appl. Phys. Lett.*, *58* (1991) 1952.
2 A. Mircea, A. Ougazzaden, G. Primot and C. Kazmierski, *J. Cryst. Growth*, *124* (1992) 737.
3 A. Mircea, A. Ougazzaden, J. Barrau, J. C. Bouley, B. Calvas, J. Charil, C. Kazmierski and G. Leroux, *Proc. 5th Int. Conf. on Indium Phosphide and Related Materials, IPRM '93, Paris*, IEEE-cat: 93 CH 3276-3, post-deadline papers series p. 41.
4 H. Peye, F. Alsina, J. Camassel, J. Pascual and R. Glew, *J. Appl. Phys.*, *73* (1993) 3760.
5 J. Camassel, H. Peyre and R. Glew, *Proc. 5th Int. Conf. on Indium Phosphide and Related Materials, IPRM '93, Paris*, IEEE-cat: 93 CH 3276-3, p. 36.
6 J. Camassel, J. P. Laurenti, S. Juillaguet, F. Reinhardt, K. Wolter, H. Kurz and D. Grützmacher, *J. Cryst. Growth*, *107* (1991) 543.
7 G. C. Osbourn, *Pnys. Rev. B*, *27* (1983) 5126.
8 M. Quillec, J. Y. Marzin, J. Primot, G. Le Roux, J. L. Benchimol and J. Burgeat, *J. Appl. Phys.*, *58* (1986) 2447.
9 K. Magari, M. Okamoto and Y. Nogushi, *IEEE Trans. Photon. Lett.*, *3* (1991) 998.
10 M. Okamoto, K. Sato, M. Mawatari, F. Kano, K. Magari, Y. Kondo and Y. Itaya, *IEEE J. Quantum Electron.*, *27* (1991) 1463.
11 J. E. Zucker, C. H. Joiner and A. G. Dentai, *IEEE Photon. Technol. Lett.*, *4* (1992) 432.
12 A. Godefroy, A. Le Corre and F. Clerot, *5th Int. Conf. on Indium Phosphide and Related Materials, IPRM '93, Paris*, IEEE-cat: 93 CH 3276-3, p. 143.
13 R. Schwedler, F. Bruggemann, K. Wolter, Ch. Jeakel, R. Kersting, A. Kohl, K. Leo and H. Kurtz, *Proc. 5th Int. Conf. on Indium Phosphide and Related Materials, IPRM '93, Paris*, IEEE-cat: 93 CH 3276-3, p. 656.
14 M. Quillec, L. Goldstein, G. Leroux, G. Burgeat and J. Primot, *J. Appl. Phys.*, *55* (1984) 2904.

Materials Science and Engineering, B21 (1993) 249–252

Metal–organic vapour-phase epitaxial growth of symmetrically strained (GaIn)As/Ga(PAs) superlattices

S. Lutgen, T. Marschner, T. F. Albrecht, W. Stolz* and E. O. Göbel
Materials Sciences Center and Department of Physics, Philipps-University, D-35032 Marburg (Germany)
L. Tapfer
C.N.R.S.M., I-72100 Brindisi (Italy)

Abstract

Novel symmetrically strained (GaIn)As/Ga(PAs) superlattices (symm. SLS) are realized by metal–organic vapour-phase epitaxy (MOVPE). The structural and optical properties of the symm. SLS are determined by means of high-resolution X-ray diffraction (XRD) as well as by photoluminescence (PL) and excitation spectroscopy (PLE) and are compared also to one-side strained (GaIn)As/GaAs as well as Ga(PAs)/GaAs SLS. The optimization of growth conditions with respect to substrate misorientation and growth temperature is presented and discussed. In order to realize high-quality symm. SLS, it is important to avoid growth surface irregularities, i.e. steps introduced by substrate misorientation, or rough surface morphologies, leading to an enhanced strain relaxation. The residual average lattice mismatch is below 5×10^{-4} for 50 period SLS layers, having lattice mismatches of up to $\pm 2.4 \times 10^{-2}$ in the individual layers. Because of this almost perfect symmetric strain profile, the SL critical thickness becomes much larger than the typical layer thickness. Narrow XRD linewidths for the superlattice satellite peaks of 20″ to 30″ (FWHM) are obtained. First PL and PLE studies are briefly described and discussed with respect to the exciton binding energy in this system, providing indication of a considerably reduced in-plane hole mass in these symm. SLS.

1. Introduction

Strained III/V-semiconductor heterostructures are becoming increasingly important, particularly for applications in optoelectronic devices [1], primarily due to the possibility of designing the valence band structure as a function of the incorporated strain. In strained layer superlattices (SLS), however, two critical layer thickness types exist with respect to strain relaxation by incorporation of misfit dislocations, one being the critical thickness of the individual layers, the other the critical thickness of the total superlattice layer structure. Therefore, severe limitations exist for the strain level and/or thickness of the individual layers as well as for the number of periods in the superlattice structure.

So far, most of the work has concentrated on structures containing one-side strained epitaxial layers, as in the case of the (GaIn)As/GaAs material system. In order to overcome the limitations with respect to the superlattice critical thickness, the growth of symmetrically strained layer superlattices (symm. SLS), *i.e.* alternating layers with built-in compressive and tensile strain, by metal–organic vapour-phase epitaxy (MOVPE) has been studied for the (GaIn)As/Ga(PAs) material system on GaAs substrate. First reports on symm. SLS systems have recently been published for modulator structures in the (GaIn)As/Ga(PAs) on GaAs material system, grown by gas source molecular beam epitaxy (GSMBE) [2] as well as in the In(PAs)(GaIn)P on InP system, grown by chemical beam epitaxy (CBE) [3] and for laser applications in the (GaIn)(PAs)/(GaIn)(PAs) on InP system grown by MOVPE [4]. In the present work, the optimization of the MOVPE growth conditions of (GaIn)As/Ga(PAs) symm. SLS with respect to substrate misorientation and growth temperature, as well as the first investigations of structural and optical properties, are reported and discussed. They indicate the high-crystalline quality achievable with these novel symm. SLS in comparison to one-side strained SLS.

2. Experimental details

The MOVPE growth studies have been performed using commercial equipment (Aix 200, Aixtron Corp.) at a reactor pressure of 100 mbar for growth tempera-

*Author to whom correspondence should be addressed.

0921-5107/93/$6.00

© 1993 – Elsevier Sequoia. All rights reserved

tures in the range of 600 °C to 700 °C using the standard precursors trimethylgallium (TMGa), solution trimethylindium (TMIn, Billiton Precursors) in combination with AsH_3 and PH_3. The (100) GaAs substrates were either exactly oriented or off-oriented by 2° in the [011] direction. The sample structure for the growth investigations consisted of a 50 period 9.5 nm (GaIn)As/1.5 nm GaAs/9.5 nm Ga(PAs)/1.5 nm GaAs superlattice layer structure with varying In- and P-concentrations. In order to avoid problems associated with strained interfaces, 1.5 nm thin GaAs layers were deposited between the respective ternary layers. No growth interruption schemes were applied at the different interfaces. High-resolution X-ray diffraction (XRD) investigations were performed in a standard three crystal diffraction set-up. Photoluminescence (PL) and excitation spectroscopy (PLE) were studied using standard equipment with either an Ar-ion or a Ti:sapphire laser as excitation source.

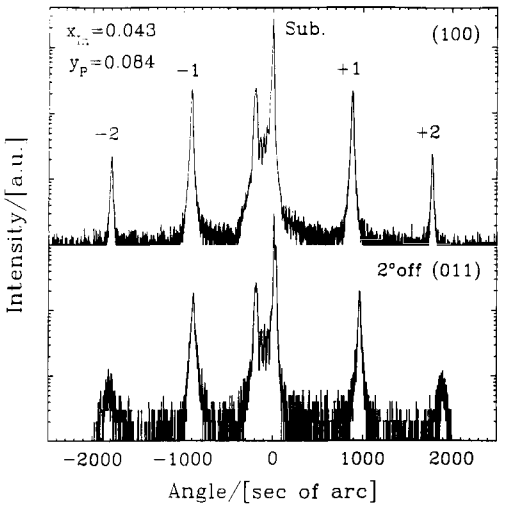

Fig. 1. High-resolution X-ray diffraction patterns (log. scale) of (GaIn)As/Ga(PAs) symm. SLS grown on a (100) exactly oriented substrate (top) and on a substrate oriented 2° off towards [011] in the vicinity of the 400-reflection of GaAs ($CuK_{\alpha 1}$-radiation). The patterns are shifted in intensity for clarity.

3. Results and discussion

In this, the main section, we first describe the optimization of growth conditions for the SLS. The structural properties, as a function of strain, of the (GaIn)As/Ga(PAs) symm. SLS are then compared to (GaIn)As/GaAs- as well as GaAs/Ga(PAs) one-side strained SLS, clearly revealing the improvements in layer quality obtained when using the symmetrical strain profile in the SLS. Finally, the exciton properties in the symm. SLS are briefly described.

In the course of the optimization of MOVPE growth conditions for these SLS, substrate temperatures have been investigated in the range of 600 to 700 °C. For temperatures higher than 675 °C, strong In-desorption is observed for the (GaIn)As layers. At the other end of the scale, for growth temperatures below 625 °C it becomes increasingly difficult to control the P-content in the Ga(PAs) layers, particularly for high P-concentrations [5], because of the thermal stability of PH_3. Therefore, a growth temperature of 650 °C has been selected for the major part of this study.

In order to realize high-quality strained layers, it is important to avoid any surface irregularities, *i.e.* surface steps introduced by substrate misorientation, or atomically unsmooth growth surfaces, during deposition. This is demonstrated by comparing the high-resolution XRD pattern of (GaIn)As/Ga(PAs) symm. SLS (Fig. 1.) grown simultaneously on an exactly oriented substrate (top) and on a 2° off-oriented one (bottom) for $x_{In} = 0.043$ and $y_P = 0.084$, respectively. Both structures exhibit a symmetric intensity profile of the superlattice satellite peaks, while the main superlattice reflection coincides with the GaAs substrate peak, indicating the perfect strain balancing in these structures, with a residual average lattice mismatch below about 2×10^{-4} in this case. However, while for the symm. SLS grown on the exactly oriented substrate the linewidth of the higher order satellites also stays constant, a significant broadening is observed in the case of the structure grown on off-oriented substrates. This broadening of the XRD pattern is a clear indication of deteriorated interfaces.

This deterioration in crystalline quality is especially noticeable in structures with even higher strain values, as shown in Fig. 1., where further broadening of the XRD pattern is observed for structures grown on off-oriented substrates. This behaviour is due to an enhanced strain relaxation for SLS structures grown on misoriented substrates. In the case of misoriented substrates and/or rough surface morphologies, a large number of steps exist on the growth surface. The cause of the enhanced strain relaxation is assumed to be the reduction in activation energy for dislocation nucleation on the growth surface if a surface step is annihilated in this process [6]. Detailed investigations using transmission electron microscopy (TEM) are underway to clarify the precise strain relaxation mechanism in these structures. In order to improve the smoothness of the growth surface, all of the SLS structures are grown on a buffer layer consisting of an (AlGa)As layer and a short period (AlGa)As/GaAs SL. For this buffer structure both XRD patterns can be seen at a diffraction angle of $-200''$ with respect to the GaAs substrate reflection in Fig. 1.

The superior concept of using a symmetric strain profile in highly strained SLS is demonstrated by comparison of the crystalline quality with one-side strained systems. The XRD patterns of three 50 period SLS ((GaIn)As/Ga(PAs) symm. SLS (top), (GaIn)As/GaAs SLS (middle) and GaAs/Ga(PAs) SLS (bottom)) with comparable strain values in the respective layers are depicted in Fig. 2. A distinct broadening of the XRD pattern is observed for both one-side strained systems, presumably due to the incorporation of misfit dislocations, as compared to the symm. SLS. This behaviour is shown in Fig. 3 as a function of varying In- and P-concentration, respectively, where the linewidth of the first order satellite peak (FWHM) is shown as a function of the composition of the respective SLS. While for the one-side strained SLS an increase in XRD linewidth is observed with increasing strain in the layers, the linewidth in the symm. SLS case stays constant at values between 20″ and 30″ (FWHM) for x_{In} up to 0.17 (x_P up to 0.36). For these structures the incorporated strain is still below the critical value of the individual layers for misfit dislocation formation. These linewidths, which approach the theoretical value of about 18″ (FWHM) for this total SLS layer thickness and are narrower than those reported in the literature [2, 3], clearly demonstrate the high-crystalline quality achieved in these structures.

It is important to note that, because of the symmetric strain profile in these structures, the real incorporated strain, and thus the respective concentrations in the individual layers, cannot be extracted as easily from the XRD pattern as in the case of the one-side SLS, where the angular distance from the main superlattice peak to the substrate reflection determines the average strain in the SLS. For symm. SLS these reflections coincide. Therefore, the real incorporated strain of the individual compressive and tensile strained layers in these structures has to be determined from the intensity distribution of the symm. SLS satellite reflections in comparison to a full dynamical simulation [7, 8, 9] of the XRD pattern. In Fig. 4. the comparison of the experimental XRD pattern of a (GaIn)As/Ga(PAs) symm. SLS (top) shows the nearly perfect agreement with the simulation (bottom), again proving the high-crystalline quality of symm. SLS achieved. Details of these investigations will be published separately.

Finally, the optical properties of these heterostructures are briefly discussed. The excitonic resonances in the PLE spectra with typical linewidths of 4–6 meV (FWHM) are clearly resolved from the subband transition. The excitonic recombination lines, with linewidths of 3–4 meV (FWHM), show a "Stokes-shift" of 2–3 meV. A detailed description of the luminescence properties, as a function of strain, will be published

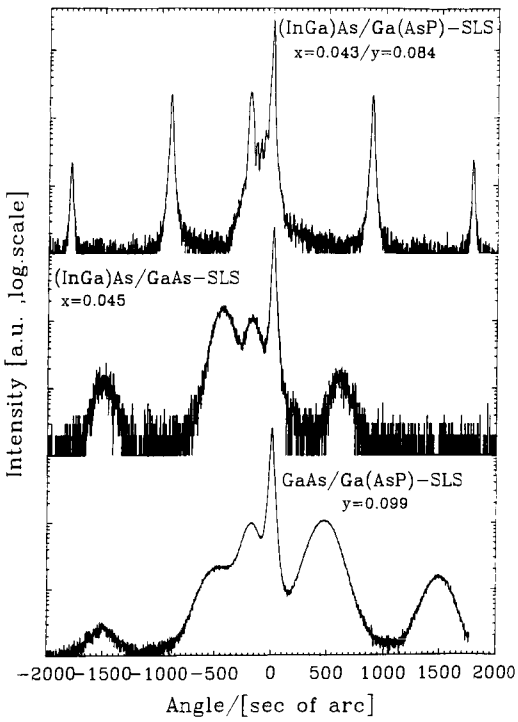

Fig. 2. High-resolution X-ray diffraction patterns (log. scale) of (GaIn)As/Ga(PAs) symm. SLS (top), (GaIn)As/GaAs (middle) and GaAs/Ga(PAs) one-side SLS (bottom) in the vicinity of the 400-reflection of GaAs ($CuK_{\alpha 1}$-radiation). The patterns are shifted in intensity for clarity.

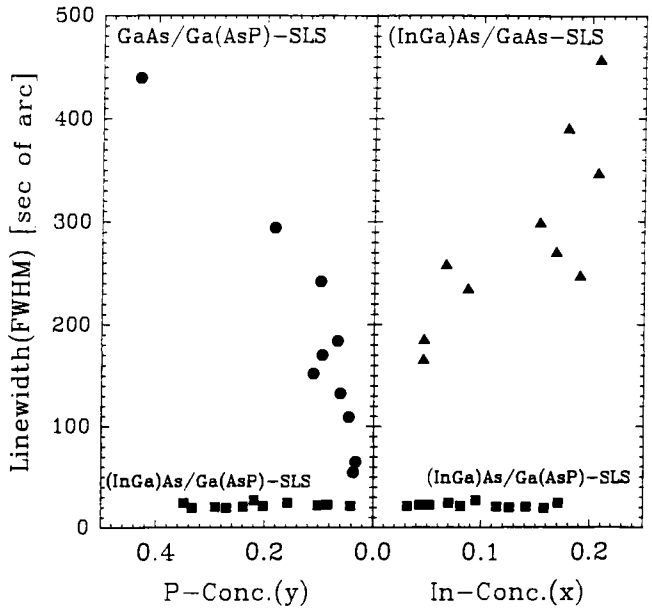

Fig. 3. X-ray diffraction linewidth of the first order satellite peak (FWHM) as a function of In- and P-concentration respectively for 50 period (GaIn)As/Ga(PAs) symm. SLS (■), (GaIn)As/GaAs (▲) and GaAs/Ga(PAs) one-side SLS (●).

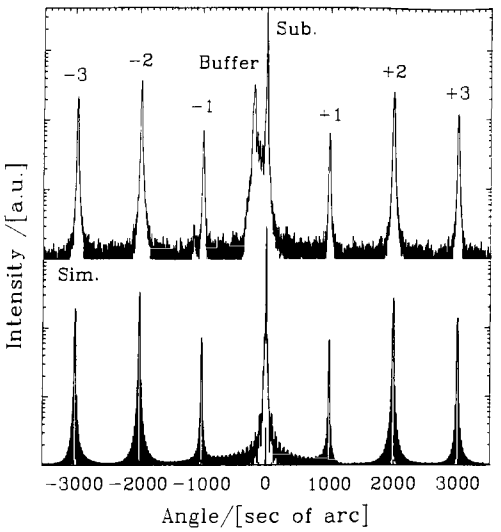

Fig. 4. Experimental (top) and theoretical (bottom) X-ray diffraction patterns (log. scale) of a (GaIn)As/Ga(PAs) symm. SLS in the vicinity of the 400-reflection of GaAs ($CuK_{\alpha 1}$-radiation). The patterns are shifted in intensity for clarity.

elsewhere. Using a theoretical description of the absorption spectrum of a two-dimensional system [10, 11, 12] for the PLE spectra the lowest E_{1h} subband transition, and thus the exciton binding energy, is determined. A significantly reduced exciton binding energy in the symm. SLS is observed in the range of 5-6meV (as compared to a value of 10 meV for unstrained GaAs quantum wells of similar well width [13]). This reduction in exciton binding energy as a function of strain is a clear indication of the reduced in-plane mass of the participating hole in contrast to the case of unstrained quantum wells [13]. An estimate of the in-plane hole mass, obtained from the exciton binding energy using the model of Mathieu *et al.* [14] for infinite barrier height, leads to a value for the hole masses comparable to the electron mass in these structures.

4. Summary

In conclusion, high-quality (GaIn)As/Ga(PAs) symm. SLS, as revealed by sharp XRD patterns (linewidth of 20″ to 30″ (FWHM) of SL satellite reflections), and PL as well as PLE studies, have been realized by MOVPE. The optimized growth conditions have been presented and discussed. The average lattice mismatches of these symm. SLS are below 5×10^{-4} for lattice mismatches of up to $\pm 2.4 \times 10^{-2}$ in the individual (GaIn)As and Ga(PAs) layers respectively. Because of the symmetric strain profile, the superlattice critical thickness limitations with respect to strain level and/or total thickness (number of periods) of the symm. SLS are removed, this is in contrast to one-side (GaIn)As/GaAs and GaAs/Ga(PAs) SLS. Initial PLE studies are briefly discussed, with respect to the exciton binding energy in this strained system, indicating a considerably reduced in-plane hole mass in these symm. SLS.

Acknowledgments

Expert technical support has been provided by T. Ochs. Financial support from the Deutsche Forschungsgemeinschaft (DFG) is gratefully acknowledged.

References

1 *Proc. 13th Int. Conf. Semiconductor Lasers, Takamatsu (1992), IEEE J. Quantum Electronics*, in press.
2 J.E. Cunningham, K.W. Goossen, M. Williams and W.Y. Jan, *Appl. Phys. Lett. 60* (1992) 727.
3 T.H. Chiu, J.E. Cunningham, T.K. Woodward and T. Sizer II, *Appl. Phys. Lett. 62* (1993) 340.
4 A. Mircea, A. Ougazzaden, G. Primot and C. Kazmierski, *Proc. 6th Int. Conf. Metalorganic Vapour Phase Epitaxy, Cambridge MA (1992), J. Crystal Growth 124* (1992) 737.
5 L. Samuelson, P. Omling, H. Titze and H.R. Grimmeiss, *J. Physique 43* (1982) C5-C323
6 J.W. Matthews, *J. Vac. Sci. Technol. 12* (1975) 126.
7 Yu.N. Belyaev and A.V. Kolpakov, *Phys. Status Solidi A76* (1983) 641.
8 D.M. Vardanyan, H.M. Manoukyan and H.M. Petrosyan, *Acta Crystallogr. A41* (1985) 212.
9 L. Tapfer, M. Ospelt and H. von Känel, *J. Appl. Phys. 67* (1990) 1298.
10 M. Shinada and S. Sugano, *J. Phys. Soc. Japan 21* (1966) 1936.
11 H. Iwamura, H. Kobayashi and H. Okamoto, *Jap. J. Appl. Phys. 23* (1984) L795.
12 W. Stolz, J.C. Maan, M. Altarelli, L. Tapfer and K. Ploog, *Phys. Rev. B36* (1987) 4301.
13 J.C. Maan, G. Belle, A. Fasolino, M. Altarelli and K. Ploog, *Phys. Rev. B30* (1984) 2253.
14 H. Mathieu, P. Lefebre and P. Christol, *J. Appl. Phys. 72* (1992) 300.

Materials Science and Engineering, B21 (1993) 253–256

Strain effects on carrier lifetimes in InGaAs/(Al)GaAs multiple quantum wells

M. H. Moloney* and J. Hegarty

Optronics Ireland Research Centre, Department of Pure and Applied Physics, Trinity College, Dublin 2 (Ireland)

L. Buydens and P. Demeester

IMEC-Gent, Laboratory of Electromagnetism and Acoustics, Rijkuniversiteit Gent, Sint-Pietersnieuwstraat 41, B-9000 Gent (Belgium)

R. Grey and J. Woodhead

Department of Electrical and Electronic Engineering, University of Sheffield, Mappin Street, Sheffield S1 3JD (UK)

Abstract

Lifetimes were measured in several InGaAs/(Al)GaAs samples with various levels of strain and strain relief, with thick barriers and with GaAs barriers. Lifetimes of the order of 0.5 ns were measured. We have found that the introduction of indium, to obtain InGaAs wells, causes a dramatic decrease in the carrier lifetime by an order of magnitude, as compared with similar GaAs wells. Once indium is present in the wells then the dominant carrier loss–recombination process in the InGaAs multiple quantum well materials is unaffected by the strain, strain relief or barrier design.

1. Introduction

Many optical devices such as diode lasers, electro-optic modulators [1, 2] and all-optical modulators [3] have been demonstrated with InGaAs grown on GaAs as the active layer. Despite the considerable lattice mismatch inherent in their growth and the short carrier lifetimes that have been recorded [4, 5] these devices have very good operating characteristics. Strained lasers in particular have shown very low threshold currents [6, 7]. Short lifetimes may be expected to be a result of strain or strain relief, through lattice dislocations, but despite the growing importance of these materials very little effort has been made to understand the carrier dynamics in InGaAs quantum wells. In this paper a systematic investigation of carrier lifetimes as a function of strain, through varying the indium concentration from 0% to 15%, and as a function of strain relief and barrier design is presented. The lifetimes are very sensitive to the initial introduction of indium into the wells but particularly insensitive to the strain or strain relief. In particular drastic changes in the material structure, as indicated by changes in low temperature photoluminescence spectra, are not reflected in changes in the room temperature lifetime. The lifetimes measured for the InGaAs/(Al)GaAs wells are all of the order of 0.5 ns.

Six InGaAs/AlGaAs multiple quantum well (MQW) samples were designed for this investigation, with the seventh sample being an InGaAs/GaAs asymmetric Fabry–Perot modulator (AFPM) [2, 3]. We shall refer to the samples as S1 to S7, as detailed in Table 1. Samples S1–S6 were grown by metal-organic vapour phase epitaxy (MOVPE) on an undoped GaAs substrate. The first epitaxial layer was 0.5 μm of GaAs followed by 0.5 μm $Al_{0.35}Ga_{0.65}As$ and 0.5 μm $Al_{0.2}Ga_{0.8}As$, the last 1 μm AlGaAs acting as an etch stop. On top of these lattice matched layers were grown P periods of strained 8 nm/8 nm $In_xGa_{1-x}As/Al_{0.2}Ga_{0.8}As$ well/barrier pairs. Values for P and x for each of the samples are listed in Table 1. S6 had thicker barriers of 25 nm $Al_{0.2}Ga_{0.8}As$. The wafers were capped with 0.5 μm $Al_{0.2}Ga_{0.8}As$ and the whole structure was intrinsically doped. The AFPM (S7) was grown as an electro-optic modulator by molecular beam epitaxy (MBE) with a 15.5 period n-type GaAs/AlAs dielectric stack on top of which were grown 29.5 periods of intrinsic 15 nm/15 nm $In_{0.1}Ga_{0.9}As$/GaAs quantum well/barrier pairs followed by a 0.2 μm p-type GaAs cap.

Samples S1, S2, S3 and S4 were designed to investigate the effect of strain on lifetimes with indium con-

*Author to whom correspondence should be addressed.

0921-5107/93/$6.00

© 1993 – Elsevier Sequoia. All rights reserved

TABLE 1. Design details, photoluminescence results and lifetimes of samples investigated, the PL results shown are averaged at several points across the samples, no PL data were available for sample S7

Sample	Indium concentration x	Number of periods P	Well/barrier width (nm)	Barrier composition	PL position (eV)	PL linewidth (meV)	Pump-probe wavelength (nm)	Lifetime (ns)
S1	0.00	10	8/8	$Al_{0.2}Ga_{0.8}As$	1.5603	6.88	839.5	3.98
S2	0.05	10	8/8	$Al_{0.2}Ga_{0.8}As$	1.5321	6.82	857.5	0.440
S3	0.10	10	8/8	$Al_{0.2}Ga_{0.8}As$	1.4688	8.52	892.5	0.558
S4	0.15	10	8/8	$Al_{0.2}Ga_{0.8}As$	1.4169	8.52	927	0.553 (a) 0.552 (b)
S5	0.15	40	8/8	$Al_{0.2}Ga_{0.8}As$	1.4144	15.5	933	0.564
S6	0.15	40	8/25	$Al_{0.2}Ga_{0.8}As$	1.4145	7.54	933	0.570
S7	0.10	29.5	15/15	GaAs	—	—	950	0.440

centrations of 0%–15% and lattice mismatches estimated to be 0%, 0.36%, 0.71% and 1.06% respectively. Samples S4 and S5 were grown to investigate the effects of strain relief which results from the thicker structure approaching the critical thickness [8]. The advantageous effects on photoluminescence data of having thicker barrier structures, as described later, dictated the design of sample S6. For the samples with 10% indium or less, namely samples S1, S2 and S3, the 8 nm wells result in the exciton feature at room temperature being buried in the GaAs substrate residual absorption, necessitating the removal of the substrate using a freon plasma etching system. In samples S4, S5 and S6 the exciton was clearly visible through the substrate, allowing non-linear measurements to be made without etching. To assess the effects of etching the strained layer S4 was cleaved into S4a and S4b, with S4a etched and S4b left unetched. Measurements on the AFPM were taken in reflection.

A pump and probe technique [9] was used to measure the lifetimes. A frequency doubled Nd:YAG, running at 76 MHz, pumps a dye laser yielding an output of typically 6–7 ps pulses over a tuning range from around 800 nm to 960 nm. The dye laser output is split into pump and probe beams with the latter travelling along a path which includes a variable delay line under computer control. This system allows the arrival time of the probe pulse at the sample to be controlled from -1 ns before, to 8 ns after the arrival of the pump pulse, which excites the non-linearity. The pump and probe are chopped at different frequencies and the non-linear signal is detected with a photodiode and two lock-in amplifiers in series. The non-linear signal arises from the change in probe transmission as carriers are injected into the wells by the pump pulse. The carriers in the MQW layer cause a change in the exciton absorption at the band edge through non-linear effects [10] such as fermion exchange, Coulomb screening and phase space filling. In Fig. 1 typical pump-probe signals can be seen to rise from a thermal

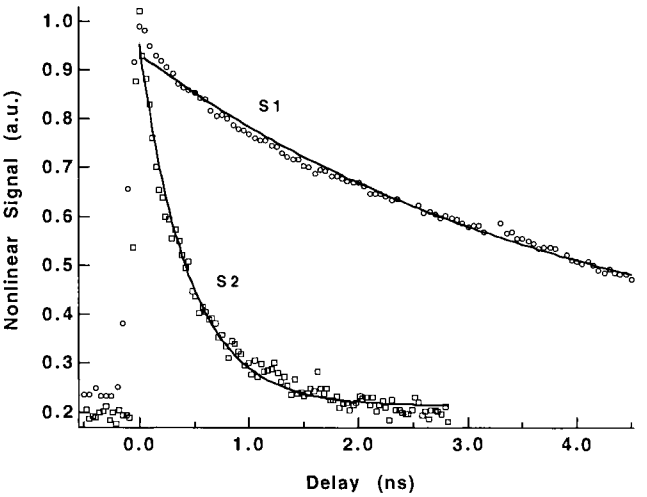

Fig. 1. Non-linear pump-probe decays for samples S1 (○) and S2 (□) for pump powers less than 1 mW. The signals can be seen to rise at zero delay, from the thermal background signal at negative delay, and subsequently decay back to the background level. The data were fitted to exponential decays, shown with a solid line, of 3.98 ns and 0.44 ns for samples S1 and S2 respectively.

background signal at negative delays, to a peak at zero delay, followed by a decay back towards the background signal. The background thermal signal has been measured as constant over the repetition rate of the laser. In the low carrier density regime the transmission recovers exponentially with carrier density, allowing the lifetime to be estimated. The data for samples S1 and S2, as in Fig. 1, fit to decays yielding 3.98 ns and 0.44 ns respectively. The lifetimes measured for samples S1–S7 are shown in Table 1.

It is a valid concern that etching the substrate from a strained material may seriously affect the strain. Any change in strain will show up in transmission measurements since a decrease in strain leads to a red shift in the absorption edge [11]. Transmission measurements of samples S4a and S4b, etched and

unetched respectively, show the exciton to be present at 927 nm, indicating no change in strain due to etching. There is also no change in lifetime measured for samples S4a and S4b, with values of 553 ps and 552 ps respectively. We can conclude that for the 10 period samples etching does not adversely affect the strain or the lifetime measurements. None of the 40 period samples was etched.

The main focus of this study was to investigate the effect of strain and strain relief on the carrier lifetime in InGaAs quantum wells. Although the lifetime of sample S1 is relatively short, as compared with typical GaAs samples, when indium is introduced into the wells the lifetime decreases by an order of magnitude, approximately 4 ns to 0.5 ns. Although the lifetime sample S2 is shorter than that of in S3 or S4a/S4b, as there is no definite trend with indium concentration, we conclude that once the indium is present there are no further strain or indium concentration dependent changes in the lifetime of samples S2, S3 or S4a/S4b.

As the number of periods is increased from 10 (S4) to 40 (S5), the presence of strain relief is demonstrated by a red shift of the exciton in transmission from 927 nm (S4) to 933 nm (S5). Low temperature photoluminescence (PL) measurements also show a marked decrease, by an order of magnitude, in the PL efficiency from samples S4 to S5, see Fig. 2, even though sample S5 has four times as many wells as sample S4. There is also a substantial increase in the linewidth for the 40 period sample (S5). The relevance of the line positions in Fig. 2 is difficult to determine owing to sample non-uniformity, which becomes significant when only a small spot on the sample is excited in the PL experiment. However, when several PL spectra are taken across the samples, the red shift in average PL position, see Table 1, would again imply a reduction in the strain from samples S4 to S5. The efficiencies and linewidths do not vary substantially across the samples. The decrease in PL efficiency and increase in linewidth are taken as an indication of the presence of dislocations in the MQW layer [8]. However, the room temperature lifetimes in samples S4 and S5 are 552 ps and 564 ps respectively. There would seem to be a contradiction here as a decrease in PL efficiency would usually imply a decrease in lifetime but in this case the lifetimes are unchanged. The answer may lie in the fact that the PL was excited at 10 K and the lifetimes measured at room temperature. It is possible that the dominant free carrier recombination process at room temperature, which seems unaffected by the onset of dislocation production, is no longer dominant at 10 K where the radiative recombination becomes sensitive to the presence of dislocations. However, the low temperature PL does inform us of the presence of dislocations and leads to the important

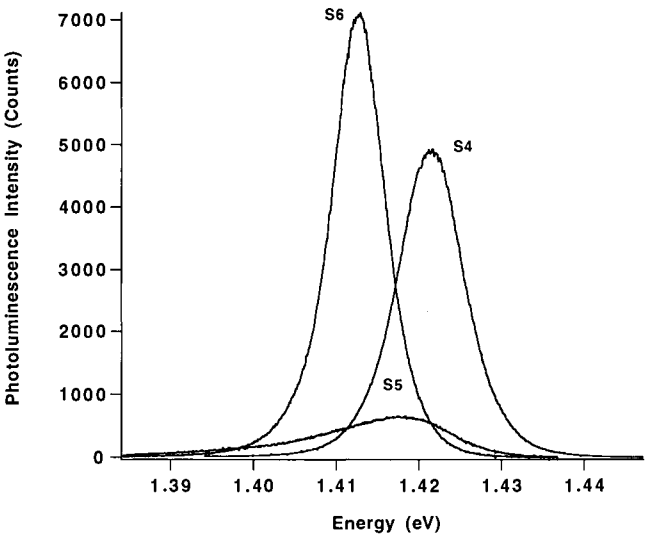

Fig. 2. Typical low temperature (10 K) photoluminescence spectra for samples S4, S5 and S6. Luminescence was excited with 5 μW from an argon ion laser. Samples were cooled to 10 K in a helium closed cycle refrigerator and luminescence was detected with a CCD camera. Some sample non-uniformity was evident in the position of the PL peaks. Average values for the PL peak positions from several spectra are shown in Table 1. The ratio of the average linewidths is 0.549:1:0.486 for S4:S5:S6 and the ratio of the average PL intensities is 7.78:1:11.14 for S4:S5:S6, averaged across the samples.

and surprising result that at room temperature the lifetime is not affected by dislocation production.

The effect of barrier thickness is demonstrated by samples S5 and S6, with sample S6 grown with thicker barriers of 25 nm as opposed to 8 nm in samples S1–S5. Thicker barrier structures are generally grown because of the improvements in low temperature PL that are reported for such samples [12]. In Fig. 2 such PL improvements can be seen with an increase of an order of magnitude in PL efficiency, from samples S5 and S6, and a decrease in the PL linewidths. The average PL positions, see Table 1, and room temperature transmission measurements of samples S5 and S6, which show the exciton in both samples to be at 933 nm, imply no difference in the strain for samples S5 and S6. These PL and transmission results would imply that the thicker barrier design is not preventing strain relief but is hindering the production of dislocations in the wells and/or their ability to thread into the wells. The thicker barrier structure does not affect the room temperature lifetime in sample S6, yielding a value of 570 ps.

In general, low GaAs barriers with InGaAs wells result in thermal loss from the well into the barriers being a significant loss mechanism. More recently AlGaAs barriers have been used, as in samples S2–S6, to provide much deeper wells and minimize thermal

loss. The lifetime was measured in the AFPM, sample S7, to determine the influence of having shallow wells on the lifetime. The mirror layers do not affect the measurements apart from the pump-probe experiment being carried out in reflection. The lifetime measured in this sample was 440 ps, essentially the same as for the deeper InGaAs/AlGaAs wells.

In conclusion we have shown that InGaAs/(Al)GaAs MQW layers have significantly shorter lifetimes than similar GaAs/AlGaAs MQW layers. Contrary to what might be expected for non-lattice matched material, the dominant carrier loss-recombination process in the InGaAs MQW materials is unaffected by the level of strain, the depth of the wells and, most surprisingly, the extent of strain relief. Drastic changes in low temperature PL properties, indicating changes in the dislocation density in the quantum wells, are not reflected in any change in room temperature lifetime. To gain a complete understanding of the different recombination processes involved at low temperature and room temperature, measurements of the low temperature lifetimes and the room temperature PL efficiencies will be necessary. Possible recombination paths include defect centres, as a result of the presence of indium, or recombination centres at the well-barrier interfaces. Further investigations are planned to discover whether the dramatic change in lifetime occurs for indium concentrations in the impurity or alloy range, and to measure the density and distribution of dislocations in these samples using electron microscopy. The results presented here are of great importance as they show that it is possible to design and grow strained layer devices that may require large numbers of wells, resulting in strain relief, without adversely affecting the carrier lifetime. The removal of any defects and a resultant increase in carrier lifetime may lead to much better device operating characteristics.

Acknowledgments

This work was carried out as part of FOCUS, ESPRIT project 3180. The authors would like to thank Dr. Garreth Parry and Kevin Lee, of the technical staff, at the Digital Optics Group of University College London for their assistance with the sample etching.

References

1 B. Pezeshki, D. Thomas and J. S. Harris, *IEEE Photon. Technol. Lett., 2* (1990) 807.
2 T. E. Sale, J. Woodehead, A. S. Pabla, R. Grey, P. A. Claxton, P. N. Robson, M. H. Moloney and J. Hegarty, *Appl. Phys. Lett., 59* (1991) 1670.
3 M. H. Moloney, J. F. Heffernan, J. Hegarty, J. Woodhead, P. A. Claxton and R. Grey, *Conf. on Lasers and Electro-Optics, Baltimore, MA, 1991*, OSA Technical Digest Series, Vol. 10, 1991, p. 46.
4 P. L. Gourley, J. J. Wiczer, T. E. Zipperian and L. R. Dawson, *Appl. Phys. Lett., 49* (1986) 100.
5 R. Jin, K. Okada, G. Khitrova, H. M. Gibbs, M. Pereira, S. W. Koch and N. Peyghambarian, *Appl. Phys. Lett., 61* (1992) 1745.
6 E. Yablonovitch and E. O. Kane, *J. Lightwave Technol., 6* (1988) 1292.
7 R. L. Williams, M. Dion, F. Chatenoud and K. Dzurko, *Appl. Phys. Lett., 58* (1991) 1816.
8 T. G. Andersson, Z. G. Chen, V. D. Kulakovskii, A. Uddin and J. T. Vallin, *Appl. Phys. Lett., 51* (1987) 752.
9 W. H. Knox, R. L. Fork, M. C. Downer, D. A. B. Miller, D. S. Chemla, C. V. Shank, A. C. Gossard and W. Wiegmann, *Phys. Rev. Lett., 54* (1985) 1306.
10 S. Schmitt-Rink, D. S. Chemla and D. A. B. Miller, *Adv. Phys., 38* (1989) 89.
11 H. Asai and K. Oe, *J. Appl. Phys., 54* (1983) 2052.
12 R. Grey, J. P. R. David, P. A. Claxton, F. Gonzalez Sanz and J. Woodhead, *J. Appl. Phys., 66* (1989) 975.

Determination of residual strain by reflectivity, X-ray diffraction and Raman spectroscopy in ZnSe epilayers grown on GaAs(001), InP(001) and GaSb(001) by metal–organic vapor phase epitaxy

M. Stoehr* and M. Maurin

Laboratoire de Physicochimie des Matériaux Solides, Université Montpellier II, Place E. Bataillon, 34095 Montpellier Cedex 05 (France)

F. Hamdani and J. P. Lascaray

Groupe d'Etude des Semiconducteurs, Université Montpellier II, Place E. Bataillon, 34095 Montpellier Cedex 05 (France)

D. Barbusse, B. Fraisse and R. Fourcade

Laboratoire des Agrégats Moléculaires et des Matériaux Inorganiques, Université Montpellier II, Place E. Bataillon, 34095 Montpellier Cedex 05 (France)

P. Abraham and Y. Monteil

Laboratoire de Physicochimie Minérale, Université C. Bernard, 43 bd du 11 novembre 1918, 69622 Villeurbanne (France)

Abstract

Reflectivity, X-ray diffraction and Raman spectroscopy allowed determination of the residual strain in ZnSe epilayers grown on different substrates such as GaAs(001), InP(001) and GaSb(001) by metal–organic vapor phase epitaxy. The lattice mismatch as well as the difference in thermal expansion coefficients induced a residual strain in the layer. In ZnSe/GaAs(001) heterostructures both compressive and tensile strains were observed owing to the lattice mismatch (0.27%) and to the difference in thermal expansion coefficients between the layer and the substrate. ZnSe epilayers grown on InP(001) (lattice mismatch −3.5%) and grown on GaSb(001) (lattice mismatch −7%) are under tensile strain owing to the difference in thermal expansion coefficients. A relaxation of thermal strain is observed in both cases when the layer thickness is increased from 0.2 to 2 μm (ZnSe/InP) and from 1 to 7 μm (ZnSe/GaSb).

In spite of the difference in measurement temperature and also in the thickness range analyzed by reflectivity, X-ray diffraction and Raman spectroscopy, the strain determined using these methods is of the same order of magnitude.

1. Introduction

With a direct band gap of 2.7 eV at room temperature, ZnSe has attracted much attention owing to its potential application in blue light emitting devices. The optical properties of the heterostructures are greatly influenced by the residual strain in the epilayer induced by the lattice mismatch as well as the difference in thermal expansion coefficients. To obtain a better understanding of the variation of the residual strain, ZnSe epilayers with different thicknesses were grown on three different substrates (GaAs, InP and GaSb (001)). These samples present different lattice mismatches (0.27%– −7%) and also variation of the difference in thermal expansion coefficients. For epitaxial growth of ZnSe by molecular beam epitaxy (MBE) [1, 2] or metal–organic vapor phase epitaxy (MOVPE) [3], GaAs has mostly been used as substrate material because of its small lattice mismatch (0.27%) and the high quality of available substrates. In this paper, we report results of an investigation of the residual strain in ZnSe/GaAs, and in the less studied ZnSe/InP and ZnSe/GaSb heterostructures, by reflectivity at low temperature (1.8 K), X-ray diffraction and Raman spectroscopy at room temperature.

*Present address: Laboratoire de Physique et de Spectroscopie Electronique, Faculté des Sciences et Techniques, 4 rue des frères Lumière, 68093 Mulhouse, France.

0921-5107/93/$6.00

© 1993 – Elsevier Sequoia. All rights reserved

2. Experimental details

The epitaxial layers were grown at atmospheric pressure by MOVPE at different growth temperatures. The substrates were cleaned by solvent and etched following different procedures described previously for GaAs [4], InP [5] and GaSb (001) [6]. After being loaded into the reactor, the substrates were thermally etched for about 10 min in hydrogen at 600 °C for GaAs, 550 °C for InP and 500 °C for GaSb. Dimethylzinc at a molar flow rate of 23 μmol min^{-1} and diethylselenide were used as source materials with a II-to-VI ratio of 0.24 for growth on GaAs at 530 °C, and of 0.12 for growth on GaSb and InP at 500 and 425 °C, respectively.

The standard reflectance technique was used to study excitonic transitions in the band edge (4350–4550 Å) and in the region above the band edge (3750–3950 Å). Light from a tungsten lamp was focussed on the epilayer surface at normal incidence. The samples were immersed in liquid helium which was pumped below its λ point.

The X-ray analyses were performed either with a simple diffractometer or a double-crystal diffractometer and $\Delta d/d$ was determined with an accuracy of 5×10^{-3} and 2×10^{-5} respectively (d is the distance between the observed planes).

Raman spectra were obtained at room temperature using the 476.5 nm line of an Ar^+ laser as the excitation source. Scattered light was analysed with a double monochromator (JY U-1000) and detected using a photon counting system.

3. Results and discussion

3.1. Reflectivity

Figure 1 shows the reflectance spectra at 1.8 K of ZnSe epilayers for different thicknesses grown on InP and GaSb in the spectral region of the ZnSe band edge. Two excitonic resonances assigned to the light-hole and heavy-hole transitions split by tensile strain are observed at a lower energy than the free-exciton transition of the bulk material. The decrease in the splitting between these transitions with increasing layer thickness from 0.2 to 2 μm indicates a decrease in stress and also a relaxation of the tensile stress in the ZnSe epilayer grown on InP. In ZnSe/GaSb heterostructures the same relaxation of strain is observed for a layer thickness varying from 1.6 to 7 μm. In this thickness range, these layers are thicker than the critical thickness estimated at a few monolayers [7] because of a lattice mismatch of more than 3.5% in both heterostructures. At the growth temperature these layers are relaxed by the creation of dislocations at the interface,

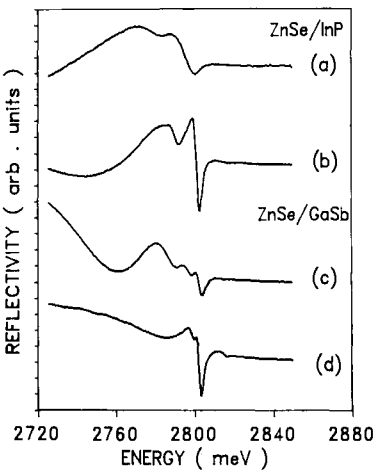

Fig. 1. Reflectivity spectra at 1.8 K of 0.2 μm (a) and 2 μm (b) ZnSe epilayers grown on InP(001) and of 1.6 μm (c) and 7 μm (d) ZnSe epilayers grown on GaSb(001).

but suffer a two-dimensional tensile strain due to the difference in thermal expansion coefficients between the layer (α(ZnSe)$=11.62\times10^{-6}$ K^{-1} at 530 °C [8]) and the substrates (α(InP)$=4.6\times10^{-6}$ K^{-1} at 425 °C [9], α(GaSb)$=10\times10^{-6}$ K^{-1} at 500 °C [10]) on cooling. For a 0.15 μm thick ZnSe epilayer grown on GaAs, we have previously reported [11] a shift of the heavy hole and light hole transitions to a higher energy than the free-exciton transition in bulk ZnSe, indicating a compressive stress in the epilayer. Layers thicker than 1.5 μm are under tensile stress owing to the thermal strain (α(GaAs)$=7.6\times10^{-6}$ K^{-1} at 530 °C [12]) and a decrease in the thermal strain is also observed on increasing the layer thickness from 1.5 to 14 μm [11]. For the 2 and 7 μm ZnSe epilayers grown on InP and GaSb respectively, the reflectance spectra reveal an additional signature at 13 meV higher than the heavy hole ground state free-exciton, related to the first excited state of the heavy hole exciton. In ZnSe/GaAs layers thicker than 2 μm the same signature is observed [11]. Observation of this feature indicates the good crystalline quality of the epilayer after relaxation. Shifts of the two free-exciton transitions under biaxial in-plane stress σ are given by

$$\Delta E_{\pm}=[2a/(C_{11}+2C_{12})]\sigma\pm[b/(C_{11}-C_{12})]\sigma \qquad (1)$$

where the + and − signs correspond to the light hole and heavy hole excitons respectively, a is the hydrostatic deformation potential, b is the shear deformation potential and C_{ij} are the elastic stiffness constants. The stress splitting δE is then given by

$$\delta E=\Delta E_{+}-\Delta E_{-}=[2b/(C_{11}-C_{12})]\sigma \qquad (2)$$

From the measured exciton splitting $\delta E=-17$ meV for a 0.2 μm ZnSe/InP, and from the value

$\delta E = -6.7$ meV for the 1.6 μm thick ZnSe/GaSb sample and taking $b = -1.19$ eV [13], $C_{11} = 8.72 \times 10^6$ and $C_{12} = 5.24 \times 10^6$ N cm^{-2}, eqn. (2) gives stress values $\sigma = 248$ MPa and $\sigma = 97$ MPa respectively. Figure 2 shows a reflectance spectrum in the region above the band gap edge of ZnSe/InP. The resonance dip is associated with the excitonic transition from the Γ_7 (spin-orbit split) valence band to the conduction band of ZnSe. The transition energy is taken from the inflection point of the structure. In spite of a broadened line characteristic of the $E_0 + \Delta_0$ transition, the red shift of the transition energy clearly indicates a tensile stress in the epilayer, and also allows determination of the stress. The energy shift with respect to the zero stress value is given by

$$\Delta(E_0 + \Delta_0) = [2a/(C_{11} + 2C_{12})]\sigma \quad (3)$$

For the 1 μm thick ZnSe epilayer grown on InP, this transition observed at 3220 meV is shifted by 5 meV compared with the energy of the $E_0 + \Delta_0$ transition in bulk ZnSe. With $a = -5.4$ eV [14], eqn. (3) gives $\sigma = 88$ MPa. This is in good agreement with the value determined from splitting of the E_0 transition.

3.2. X-ray diffraction

The lattice parameters of the layer perpendicular to the interface were obtained using simple or double X-ray diffraction measurements. Figure 3 shows the rocking curve in logarithmic scale for the (004) reflection on a 2 μm thick ZnSe epilayer grown on InP obtained using double X-ray diffraction. The value of the lattice parameter perpendicular to the interface ($a_{ZnSe} = 5.6615$ Å) which is shorter than the lattice parameter of bulk material, indicates that the layer is under tensile stress. Taking into account Hooke's law assuming that layers are under elastic stress in this thickness range, the stress is determined using

$$\sigma = -[(C_{11} - C_{12})(C_{11} + 2C_{12})/2C_{12}]\varepsilon \quad (4)$$

where ε is the strain perpendicular to the interface. Using eqn. (4), the stress is estimated at 76 MPa for the 2 μm thick ZnSe epilayer grown on InP. The weak (004) ZnSe diffraction peak observed using a linear scale is probably due to the small value of thickness, and does not allow estimation of the crystalline quality of the epilayer. Figure 4 shows a simple diffraction pattern of a 7 μm ZnSe epilayer grown on GaSb. The (004) Cu Kα_1 and Cu Kα_2 diffraction lines of both ZnSe and GaSb are observed. The (004) Cu Kα_1 ZnSe line is observed at 32.95°. The value of strain is estimated at 35 MPa. ZnSe/GaAs heterostructures were previously investigated by double X-ray diffraction [15]. The layers were of high crystalline quality.

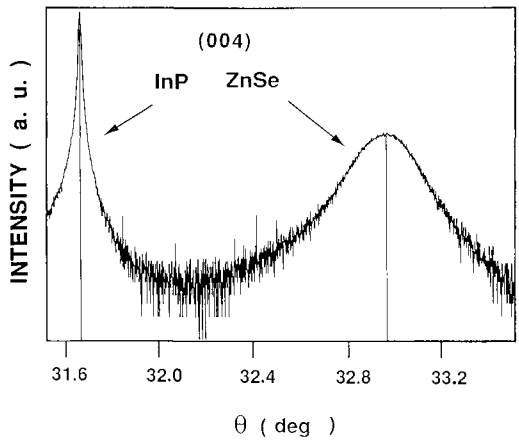

Fig. 3. Double X-ray diffraction pattern of a 2 μm thick ZnSe epilayer grown on InP(001) with the diffraction intensity on a logarithmic scale.

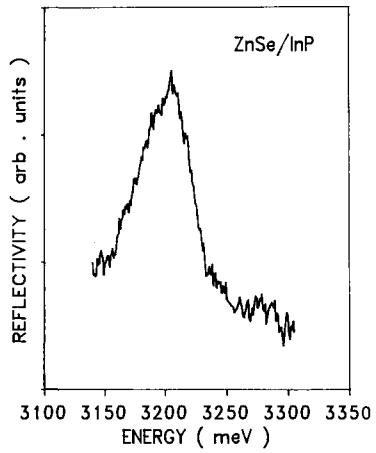

Fig. 2. Reflectivity spectrum at 1.8 K of a 1 μm ZnSe epilayer grown on InP(001) above the band gap edge.

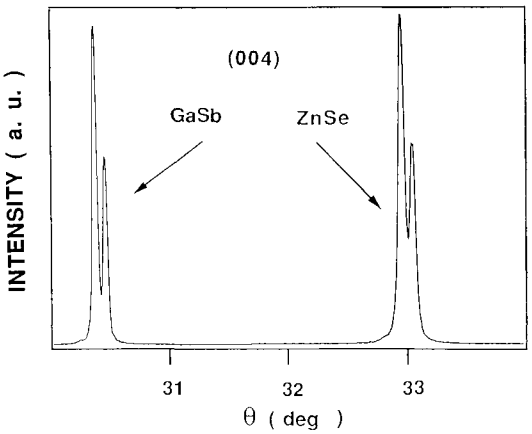

Fig. 4. X-ray diffraction pattern of a 7 μm ZnSe epilayer grown on GaSb(001).

3.3. Raman spectroscopy

The Raman spectrum of a 0.2 μm ZnSe layer grown on InP is presented in Fig. 5. The peak at 251 cm^{-1} is attributed to the longitudinal optical phonon (LO) mode of the ZnSe epilayer and its position is shifted with respect to the bulk value which is at $\omega_0 = 253\ cm^{-1}$ [16]. A biaxial strain in the epilayer has induced a displacement of the (LO) phonon. The shift of the LO peak induced by the stress is given by

$$\Delta\omega = \omega - \omega_0 = [[(p+2q)(S_{11}+2S_{12})/3\omega_0] - [(p-q)(S_{11}-S_{12})/3\omega_0]]\sigma \quad (5)$$

where ω is the frequency of the ZnSe LO phonon in the epilayer, ω_0 is the zero strain frequency of the ZnSe LO phonon, p and q are parameters related to the third elastic coefficients [17], S_{11} and S_{12} are the elastic compliances and σ the stress. For a shift of 2 cm^{-1}, the stress was estimated at 380 MPa using eqn. (5). Figure 6 shows the Raman spectra of 0.15 and 3.5 μm thick ZnSe layers grown on GaAs with the frequency of the ZnSe LO phonon at 253.8 and 252.7 cm^{-1} respectively. The sign of the LO phonon energy shift ($\Delta\omega$) indicates clearly the sign of the stress in the epilayer. The stress values of -153 MPa and 61 MPa indicate a biaxial compressive and biaxial tensile stress respectively and are in accordance with the stress values previously obtained by X-ray diffraction and reflectivity.

4. Conclusion

In this study we investigated the stress variation in different ZnSe/III–V heterostructures using different experimental techniques. In Figs. 7 and 8, we present the variation in stress as a function of the layer thickness for ZnSe/GaAs and ZnSe/InP heterostructures analysed by reflectivity, X-ray diffraction and Raman spectroscopy. In all these heterostructures the stress

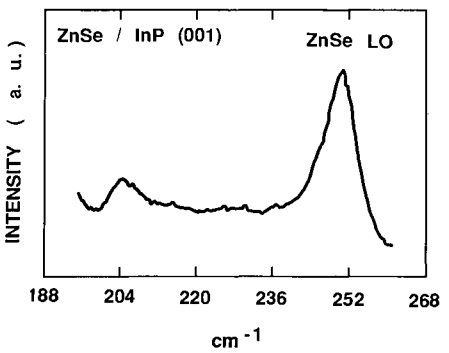

Fig. 5. Raman spectrum of a 0.2 μm thick ZnSe epilayer grown on InP(001).

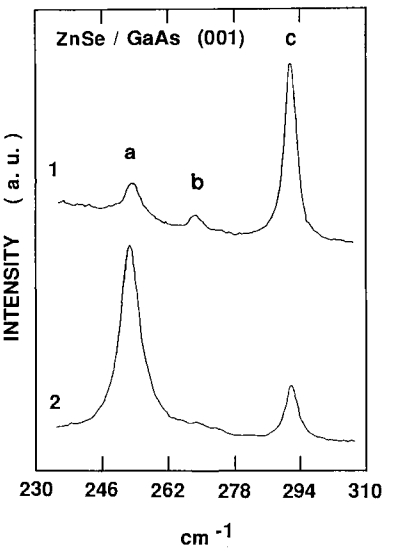

Fig. 6. Raman spectra of 0.15 (1) and 6 μm (2) ZnSe epilayers grown on GaAs(001). a, b and c correspond to the ZnSe LO peak, GaAs TO peak and GaAs LO peak respectively.

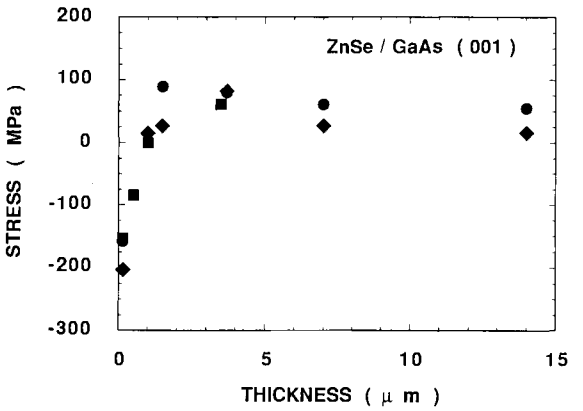

Fig. 7. Stress variation in ZnSe epilayers grown on GaAs(001) determined using reflectivity (●), double X-ray diffraction (◆) and Raman spectroscopy (■) as a function of the layer thickness.

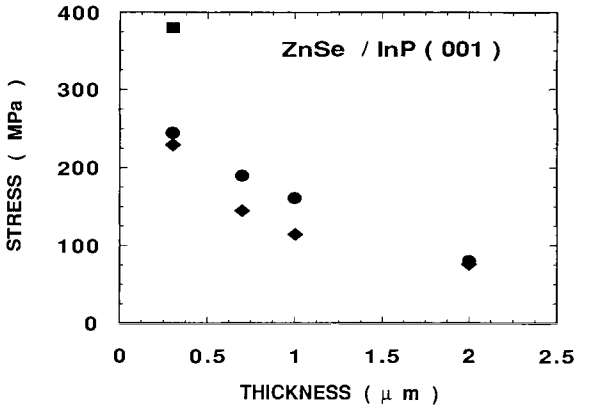

Fig. 8. Stress variation in ZnSe epilayers grown on InP(001) determined using reflectivity (●), X-ray diffraction (◆) and Raman spectroscopy (■) as a function of the layer thickness.

values determined by these techniques are of the same order of magnitude.

References

1 T. Yao, Y. Odaka, S. Matsui, K. Ishida and I. Fujimoto, *J. Cryst. Growth, 81* (1987) 518.
2 Y. R. Lee, A. K. Ramdas, L. A. Kolodziejski and R. L. Gunshor, *Phys. Rev. B, 38* (1988) 13143.
3 A. Ohki, N. Shibata and S. Zembtsu, *J. Appl.Phys., 64* (1988) 694.
4 T. Imai, S. Fuke, M. Izawa and K. Kuwahara, *J. Appl. Phys., 64* (1988) 1245.
5 K. Y. Cheng, A. Y. Cho, W. R. Wagner and W. A. Bonner, *J. Appl. Phys., 52* (1981) 1015.
6 H. P. Wagner, W. Kuhn and W. Gebhardt, *J. Cryst. Growth, 101* (1990) 119.
7 J. H. van der Merwe and W. A. Jesser, *J. Appl. Phys., 63* (1988) 1509.
8 H. P. Singh and B. Dayal, *Phys. Status Solidi, 23* (1967) K93.
9 S. I. Novikova, in R. K. Willardson (ed.), *Semiconductors and Semimetals*, Vol. 3, Academic Press, New York, 1967.
10 S. I. Novikova and N. K. Abrikosov, *Sov. Phys. Solid State, 5* (1964) 1558.
11 M. Stoehr, F. Hamdani, J. P. Lascaray and M. Maurin, *Phys. Rev. B, 44* (1991) 8912.
12 A. S. Jordan, *J. Cryst. Growth, 49* (1980) 631.
13 J. Gutowski, N. Presser and G. Kudleck, *Phys. Status Solidi B, 120* (1990) 11.
14 A. Blacha, H. Presting and M. Cardona, *Phys. Status Solidi B, 126* (1984) 11.
15 M. Stoehr, M. Maurin, D. Barbusse and R. Fourcade, *Eur. J. Solid. State Inorg. Chem., 29* (1992) 1145.
16 T. Matsumoto, A. Fujii, K. Mizogushi, A. Mitsuichi and K. Yoneda, *Jpn. J. Appl. Phys., 27* (1988) 1327.
17 F. Cerdeira, C. J. Buchenauer, F. H. Pollack and M. Cardona, *Phys. Rev. B, 5* (1977) 580.

Materials Science and Engineering, B21 (1993) 262–265

Characterization of heterointerfaces and surfaces in InSb on GaAs and in InAs/AlSb quantum wells

J. Wagner, J. Schmitz, A.-L. Alvarez*, P. Koidl and J. D. Ralston

Fraunhofer-Institut für Angewandte Festkörperphysik, Tullastrasse 72, D-79108 Freiburg (Germany)

Abstract

Resonant Raman scattering by longitudinal optical (LO) phonons and by interface modes was used to study InSb/GaAs and InAs/AlSb heterointerfaces for InSb on GaAs and for InAs/AlSb quantum wells respectively, grown by molecular beam epitaxy. Raman spectra recorded from samples with InSb layers ranging in thickness from 10 to 300 monolayers indicate that, to achieve two-dimensional growth of InSb on GaAs with good crystalline quality, the layer thickness must exceed around 100 monolayers. From the dependence on excitation power of electric-field-induced LO phonon scattering measured for a series of n- and p-type doped thick InSb layers, it is concluded that the surface Fermi level is pinned at the valence band edge. In InAs/AlSb quantum wells, scattering by an InSb-like interface mode is observed which resonates at approximately the InAs E_1 energy gap.

There is considerable current interest in the narrow band gap III–V semiconductors InSb and InAs, and in related heterostructures such as InAs/AlSb quantum wells (see for example ref. 1). There is a variety of potential applications for these heterostructures in electronic and IR optoelectronic devices [1]. The fabrication of such devices requires epitaxial growth of the above III–V materials. For technological reasons heteroepitaxy on GaAs substrates is advantageous [2, 3]. The critical layer thickness for the growth of, for example, InSb on GaAs is below two monolayers, which reflects the large lattice mismatch between these two materials. It has been shown that heteroepitaxial growth of InSb on GaAs starts with the nucleation of three-dimensional islands and complete coverage of the GaAs substrate is only obtained for equivalent layer thicknesses exceeding 100 monolayers (ML) [4]. In InAs/AlSb heterostructures the lattice mismatch is much smaller than in the InSb/GaAs system. Also, in these heterostructures there is no common anion or cation across the heterointerface which results in two different types of interface, either InSb- or AlAs-like. It has been shown that the in-plane electronic transport properties of the two-dimensional electron gas formed in the InAs channel of an InAs/AlSb quantum well depend critically on the type of heterointerface [5].

In the present study we used resonant Raman scattering by longitudinal optical (LO) phonons and by interface modes to study the heteroepitaxial growth of InSb on GaAs, including the Fermi level position at the InSb surface, and the interface formation in InAs/AlSb quantum wells. The samples were grown by solid-source molecular beam epitaxy (MBE) on (100) GaAs substrates. Growth of InSb was performed using an Sb_2 molecular beam with an In-to-Sb flux ratio close to unity. The substrate temperatures were in the range 400–450 °C. Si and Be were used as n- and p-type dopants respectively. Undoped layers showed residual p-type conductivity at low-temperatures, with a hole concentration of approximately 10^{16} cm^{-3}. The thickness of the layers was typically 1 μm. InAs/AlSb single quantum wells with a width of 15 nm were grown on a 1 μm thick AlSb buffer layer followed by a GaSb/AlSb 2.5 nm/2.5 nm superlattice. The InAs quantum well was sandwiched between a 40 nm wide AlSb barrier on the substrate side and a 10 nm wide AlSb layer on the surface side. The shutter sequence for the growth of the InAs/AlSb heterointerfaces was chosen to promote the formation of InSb-like interfaces [5]. The whole structure was capped with 10 nm GaSb. Growth of the quantum well structure was performed at 500 °C.

Figure 1 shows a series of low-temperature Raman spectra of InSb layers grown on GaAs substrates with equivalent layer thicknesses of 10, 40, and 300 ML. Here the equivalent layer thickness was determined from the deposition time, based on growth rate calibration using reflection high-energy electron diffraction (RHEED) oscillations. The spectra were recorded in backscattering mode from the (100) growth surface with the polarization of the incident and scattered light

*Permanent address: ETSI Telecommunicación, Universidad Politécnica, E-28040 Madrid, Spain.

0921-5107/93/$6.00

© 1993 – Elsevier Sequoia. All rights reserved

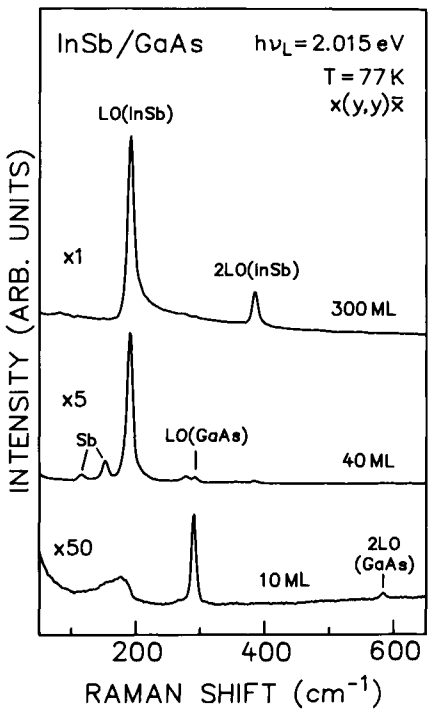

Fig. 1. Low-temperature (77 K) Raman spectra of InSb grown on (100) GaAs for different equivalent InSb layer thicknesses ranging from 10 to 300 monolayers (ML). The spectra were excited at 2.015 eV in resonance with the InSb E_1 band gap energy. Polarization of both incident and scattered light was parallel to the same (100) crystallographic direction.

parallel to the same (100) crystallographic direction $[x(y,y)\bar{x}]$. Optical excitation was at 2.015 eV in resonance with the E_1 band gap energy of InSb [6]. For the present scattering configuration intrinsic two-LO phonon scattering is allowed, whereas one-LO phonon scattering by the deformation mechanism is symmetry forbidden. For resonant excitation, however, intrinsic one-LO phonon scattering via the Fröhlich mechanism as well as defect-induced and electric-field-induced one-LO phonon scattering contribute to the Raman spectrum [7].

The present Raman spectra show that equivalent layer thicknesses of several tens of monolayers are required to produce films which exhibit the one-LO phonon line of crystalline InSb. In addition, scattering by crystalline Sb is observed, with two lines resolved at 116 and 153 cm^{-1} [8], for an equivalent layer thickness of 40 ML. For a film thickness of 10 ML only a broad peak at 150–200 cm^{-1} is observed, other than the one-LO and two-LO phonon scattering from the GaAs substrate [9]. This broad peak can be assigned to scattering by highly disordered or amorphous InSb, and possibly by amorphous Sb. For a thickness of 300 ML both the InSb one-LO and two-LO phonon lines are well resolved and there is no further change in the Raman spectrum when the InSb layer thickness is increased up to the micrometre range. The observation of comparatively strong two-LO phonon scattering from InSb for layer thicknesses greater than or equal to 300 ML indicates the good crystalline quality of the fully relaxed InSb film [10] despite the large dislocation density arising from the lattice mismatch to the GaAs substrate.

If we combine the present findings with results reported by Zhang *et al.* [4], which were obtained by transmission electron microscopy and RHEED, the following picture can be constructed. For equivalent InSb layer thicknesses of the order of 10 ML, small islands about 10 nm in height are present with a surface coverage of about 25% [4]. These islands give rise to the broad Raman peak observed in the lowest curve of Fig. 1. With increasing equivalent layer thickness the surface coverage and the island size both increase, forming a connected InSb network [4]. As a consequence, the phonon coherence length also increases leading to the appearance of mainly defect-induced one-LO phonon scattering from crystalline InSb. At this stage also crystalline Sb is present, possibly on the uncovered GaAs surface. Equivalent layer thicknesses exceeding 100 ML are required to achieve complete coverage with InSb [4] and to observe the intrinsic InSb two-LO phonon line, which is indicative of the good crystalline quality of the grown material, along with dominantly intrinsic one-LO phonon scattering.

In Fig. 2 the intensity of one-LO phonon scattering, normalized to the strength of the purely intrinsic two-LO phonon signal, is plotted *vs.* the optical power density for a series of approximately 1 μm thick n- and p-type doped InSb layers. The data were again recorded in the $x(y,y)\bar{x}$ scattering configuration. Both the nominally undoped, but residually p-type, and the intentionally p-type doped layers show a comparatively low one-LO phonon intensity which shows very little variation with power density. The homogeneously n-type doped sample exhibits a much larger one-LO phonon intensity at low power densities along with a marked decrease in intensity with increasing excitation power density. An InSb n–i–p–i structure was also analysed, consisting of 10 nm thick Si and Be doped layers separated by 40 nm wide undoped spacers. Proceeding from the epilayer surface back towards the substrate, the layer sequence starts with a 40 nm thick undoped InSb cap layer followed by the first Be-doped layer. The donor N_D and acceptor N_A concentrations were in the 10^{18} cm^{-3} range with $N_D > 2N_A$. Similar to the homogeneously n-type doped layer, the residual n-type n–i–p–i structure also shows a large relative

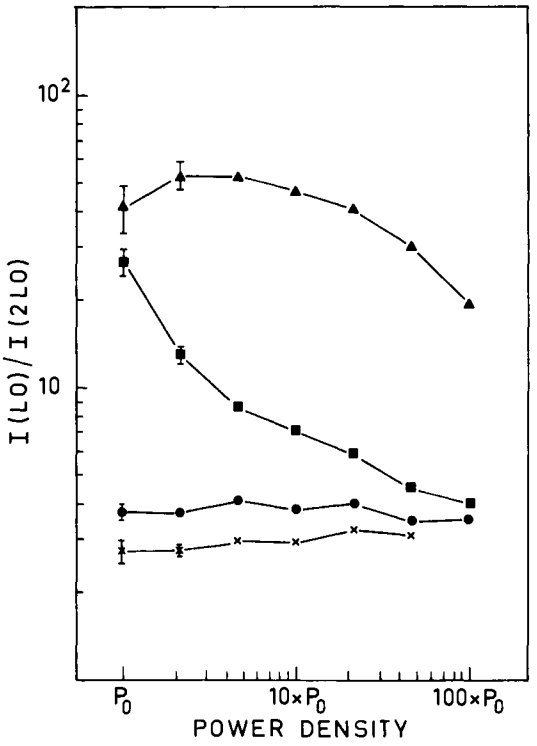

Fig. 2. Normalized LO phonon scattering strength $I(LO)/I(2LO)$ *vs.* optical power density. P_0 corresponds to a power density of approximately 10 W cm^{-2}. Data are shown for undoped InSb (×), p-type InSb:Be (●) with a low-temperature hole concentration of 9.1×10^{17} cm^{-3}, an InSb n-i-p-i doping superlattice (■), and n-type InSb:Si (▲) with a low-temperature electron concentration of 1.6×10^{17} cm^{-3}. Error bars are indicated for the data points recorded at the lowest power densities.

one-LO phonon intensity at low power densities followed by a very pronounced decrease in that intensity for increasing power density.

The above findings can be explained by the presence of a surface electric field in the n-type samples which leads to electric-field-induced Raman scattering by the one-LO phonon. The intensity of this scattering is proportional to the square of the strength of the surface electric field averaged over the probing depth in the Raman experiment of about 14 nm. (This value is based on room-temperature ellipsometry data [11] which have been shifted in energy to account for the temperature induced variation in band gap energy.) The surface electric field is progressively screened by photogenerated carriers with increasing optical power density. The slight decrease in relative LO phonon intensity, observed in the homogeneously doped n-type InSb:Si layer at the lowest excitation power density, is within experimental error. The surface electric field, the presence of which has been confirmed by the observation of interference effects between dipole-allowed and electric-field-induced LO phonon scattering [12], is caused by pinning of the surface Fermi level at the valence band edge [13, 14]. For this situation we expect a surface electric field of the order of 10^5 V cm^{-1} for n-type InSb with a carrier concentration of 10^{17} cm^{-3} [15], but a negligible electric field in p-type material. Thus the present experiment demonstrates how resonant LO phonon Raman scattering can be used to study surface Fermi level pinning in III–V semiconductors such as InSb via the resulting surface electric field, as well as the effects of optical excitation on this surface field.

We turn now to the resonant Raman scattering from InAs/AlSb heterostructures. Figure 3 shows a low-temperature Raman spectra of a 15 nm wide InAs/AlSb single quantum well. The spectra were excited at 2.71 eV, close to the E_1 band gap resonance of bulk InAs [16]. The polarization of the scattered light was either parallel $[x(z,z)\bar{x}]$ (top curve) or perpendicular $[x(y,z)\bar{x}]$ (bottom curve) to the polarization of the incident light. The spectra show one-LO phonon scattering by the InAs quantum well and by the AlSb barriers as well as two-LO phonon scattering from InAs. The presence of an InAs two-LO phonon signal, and the observation that InAs one-LO phonon scattering is stronger for parallel than for crossed polarizations, show clearly the resonant enhancement of LO phonon scattering from the InAs quantum well [16]. The non-resonantly excited AlSb one-LO phonon signal, in contrast, is as expected [7, 9] most intense for crossed polarizations. Non-resonant one-LO phonon scattering from the GaSb capping layer overlaps with the InAs one-LO phonon signal [17] and is just resolved, for crossed polarizations, as shoulders on the high- and low-frequency sides of the InAs one-LO phonon line. This observation proves the high sensitivity to scattering from the InAs quantum well achieved in the present experiment by resonant excitation, despite the strong absorption of the incident and the scattered light in the GaSb cap and the AlSb top barrier layer [17]. In the present sample the GaSb one-LO phonon line is split into a GaSb-like and a GaAs-like mode [18] owing to the unintentional incorporation of As [19]. The effect of As incorporation on the AlSb LO phonon is to shift this mode to higher frequencies; $AlAs_xSb_{1-x}$ displays a single-mode behaviour [20].

In the low-frequency range the Raman spectra of the InAs/AlSb quantum well (Fig. 3) show second-order acoustic phonon scattering from the AlSb barriers [2TA(AlSb)] [21] which is strongest for parallel polarizations, and a peak at about 190 cm^{-1} [IF(InSb)] which is most intense for crossed polarizations. The latter peak is assigned to a longitudinal InSb interface mode [17, 22]. Scattering by the 190 cm^{-1} mode was found to resonate at approximately the InAs E_1 gap energy and *not* at the corresponding gap energy of InSb (see

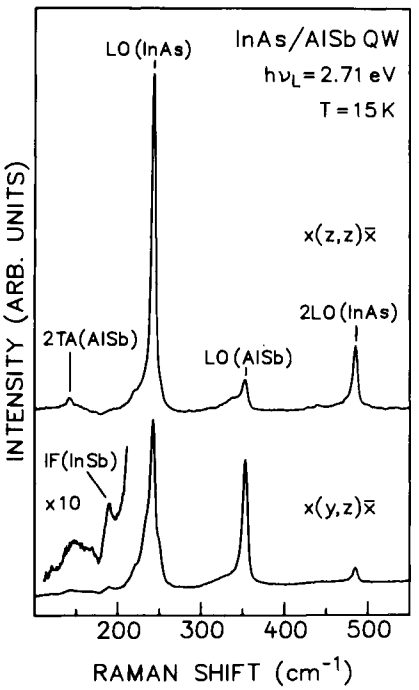

Fig. 3. Low-temperature (15 K) Raman spectra of an InAs/AlSb single quantum well. The spectra, excited in resonance with the InAs E_1 band gap energy, were recorded with polarization of the scattered light either parallel $[x(z,z)\bar{x}]$ (top) or perpendicular $[x(y,z)\bar{x}]$ (bottom) to that of the incident light. Here x, y, and z denote (100) crystallographic directions.

above), which gives additional support to the assignment of this peak to an interface mode [19].

In conclusion, we have shown how resonant Raman scattering by LO phonons and by interface modes can be used to analyse heterointerfaces and surface Fermi level pinning in InSb/GaAs and InAs/AlSb heterostructures. Tuning the incident photon energy into resonance with an appropriate band gap energy of one of the constituents allows the vibrational properties of that particular layer to be probed with a high degree of selectivity.

Acknowledgments

We would like to thank G. Bihlmann for valuable technical assistance in MBE growth and P. Hiesinger for performing the Hall effect measurements. A.-L.A. wishes to thank the Comunidad Autónoma de Madrid for financial support.

References

1 *Proc. 6th Int. Conf. on Narrow Gap Semiconductors, Semicond. Sci. Technol., 8* (1990) S102–S137, S183–S225.
2 R. A. Stradling, *Semicond. Sci. Technol., 6* (1991) C52.
3 J. R. Söderström, M. M. Cumming, J.-Y. Yao and T. G. Anderson, *Semicond. Sci. Technol., 7* (1992) 337.
4 X. Zhang, A. E. Staton-Bevan, D. W. Pashley, S. D. Parker, R. Droopad, R. L. Williams and R. C. Newman, *J. Appl. Phys., 67* (1990) 800.
5 G. Tuttle, H. Kroemer and J. H. English, *J. Appl. Phys., 67* (1990) 3032.
6 W. Dreybrodt, W. Richter and M. Cardona, *Solid State Commun., 11* (1972) 1127.
7 J. Menéndez and M. Cardona, *Phys. Rev. B, 31* (1985) 3696. J. Menéndez, L. Vina, M. Cardona and E. Anastassakis, *Phys. Rev. B, 32* (1985) 3966.
8 M. Hünermann, W. Pletschen, U. Resch, U. Rettweiler, W. Richter, J. Geurts and P. Lautenschlager, *Surf. Sci., 189–190* (1987) 322.
9 R. Trommer and M. Cardona, *Phys. Rev. B, 17* (1978) 1865.
10 J. Wagner and Ch. Hoffmann, *Appl. Phys. Lett., 50* (1987) 682.
J. Wagner, *Appl. Phys. Lett., 52* (1988) 1158.
11 D. E. Aspnes and A. A. Studna, *Phys. Rev. B, 27* (1983) 985.
12 J. Wagner, A.-L. Alvarez, J. Schmitz, J. D. Ralston and P. Koidl, *Appl. Phys. Lett., 63* (1993) 349.
13 C. A. Mead and W. G. Spitzer, *Phys. Rev., 134* (1964) A713.
14 J. Geurts, W. Pletschen and W. Richter, *Surf. Sci., 152–153* (1985) 1123.
15 J. Geurts, *PhD Thesis*, Technical University of Aachen, 1984.
16 R. Carles, N. Saint-Cricq, J. B. Renucci, A. Zwick and M. A. Renucci, *Phys. Rev. B, 22* (1980) 6129.
17 I. Sela, C. R. Bolognesi, L. A. Samoska and H. Kroemer, *Appl. Phys. Lett., 60* (1992) 3283.
18 D. H. Jaw, D. S. Cao and G. B. Stringfellow, *J. Appl. Phys., 69* (1991) 2552.
19 J. Wagner, J. Schmitz, M. Maier, J. D. Ralston and P. Koidl, submitted to *Appl. Phys. Lett.*
20 I. Sela, C. R. Bolognesi and H. Kroemer, *Phys. Rev. B, 46* (1992) 16142.
21 Y. S. Raptis, E. Anastassakis and G. Kanellis, *Phys. Rev. B, 46* (1992) 15801.
22 M. Inoue, M. Yano, H. Furuse, N. Nasu and Y. Iwai, *Semicond. Sci. Technol., 8* (1993) S121.

Materials Science and Engineering, B21 (1993) 266–269

Improvements in the heteroepitaxial growth of GaAs on Si by MOVPE

T. Marschner, W. Stolz and E. O. Göbel

Materials Science Center and Department of Physics, Philipps-University, D-35032 Marburg (Germany)

F. Phillipp

Max Planck Institute for Metal Research, D-7000 Stuttgart 80 (Germany)

M. Müller and J. Lorberth

Department of Chemistry and Materials Sciences Center, Philipps University, D-35032 Marburg (Germany)

Abstract

We describe methods of improving the metalorganic vapour phase epitaxy (MOVPE) growth of heteroepitaxial GaAs on Si. The low temperature growth step at the start is optimized by using the new alternative group III precursor dimethyl-ethyl-amine-gallane ($GaH_3{\cdot}N(CH_3)_2C_2H_5$ (DMEAGa)) as a substitute for the conventional group III compound TMGa. Further improvements in surface morphology and X-ray diffraction linewidth are obtained by applying the modulated atomic layer epitaxy (ALE) for this growth step. Thermal cycle annealing which is much more effective in dislocation reduction than constant temperature annealing has been optimized with respect to the high as well as the low temperature steps. We present a model of low temperature behaviour of dislocations to explain the role of cooling the samples during thermal cycle annealing. An additional improvement of layer quality is achieved by introducing a thin (AlGa)As-layer after the low-temperature-GaAs-layer leading to a confinement of dislocations after performing thermal cycle annealing as established by TEM-investigations.

1. Introduction

The growth of heteroepitaxial GaAs on Si substrates has attracted great attention during recent years because of the advantages offered by integrating Si and GaAs-based device structures. In addition, the GaAs on Si material system has become a model system for studying the influence of strain properties on the mechanism of epitaxial growth. The main problems when growing GaAs on Si heteroepitaxially are the large lattice mismatch of 4% and the difference in thermal expansion coefficients between the materials.

In order to realize high quality device structures like laser diodes it is necessary to optimize the nucleation of GaAs on Si and to reduce the density of dislocations in the epitaxial layer that act as recombination centres. Several methods for reducing the dislocation density have been reported; *e.g.* growth of strained layers to bend or confine dislocations, or thermal cycle annealing (TC). TC has been shown to be much more effective than constant temperature annealing [1]. However, the role of cooling during thermal cycle annealing as well as the influence of strained layers on the dislocations is largely unexplained.

In this work we describe methods of improving the metal-organic vapour phase epitaxy (MOVPE) of GaAs on Si. The low temperature growth step at the start of the conventional two step growth mode of GaAs on Si [2] has been improved using a new alternative group III precursor and by applying the modulated atomic layer epitaxy (ALE). The structural properties of the grown samples before and after thermal cycle annealing are presented and discussed with respect to the low annealing temperature. In particular, the role of cooling of the samples during thermal cycle annealing is explained. In addition we present a model that confines the dislocations to the low temperature GaAs layer after thermal cycle annealing influenced by a thin (AlGa)As layer introduced after the low temperature GaAs layer as established by transmission electron microscopy (TEM) investigations.

2. Experimental details

Epitaxial growth was performed by MOVPE using a commercial system with a horizontal reactor (AIX 200, Aixtron Corporation). The Si substrates were (100) oriented 1.7° off in the [011] direction. Prior to growth, the substrates were prepared using a chemical cleaning procedure, described by Ishizaka and Shiraki [3], without the degreasing and HNO_3 boiling steps.

Before moving the samples to the reactor the liner and the susceptor were cleaned and heated at 850 °C to remove any traces of As. In order to evaporate the thin oxide layer the substrates were annealed at 975 °C for 30 min. Growth was performed at 50 mbar using the conventional two step mode of GaAs on Si. The low temperature growth was performed using either the new alternative group III precursor dimethyl-ethyl-amine-gallane ($GaH_3{\cdot}N(CH_3)_2C_2H_5$ (DMEAGa)) [4] at 450 °C or TMGa at 400 °C in combination with AsH_3.

For one series of samples the ALE deposition technique was applied for the low temperature GaAs layer using DMEAGa. After the low temperature growth step the temperature was raised to 600 °C and 70 nm (AlGa)As was deposited followed by 2 μm GaAs. The grown samples were annealed by TC performed under As overpressure to prevent incongruent As evaporation from the sample. The annealing time for the low as well as the high temperature annealing step was 5 min. The number of thermal cycles was limited to four because no evidence of further changes in the dislocation density as a result of a larger numbers of cycles was observed, in accordance with the data in the literature [5]. The structural properties of the grown as well as of the annealed samples were investigated by using high resolution X-ray diffraction (XRD), molten KOH etching at 400 °C to estimate the dislocation density [6] and TEM. After optimization of the KOH etching process, good correlations were observed between the dislocation densities determined by XRD, KOH etch pit density (EPD) and plane-view TEM techniques.

3. Results and discussion

In this section we describe the optimization of the starting step for the growth of GaAs on Si and then discuss the optimization of the thermal cycle annealing of the grown samples. Confirmation of the confinement of dislocations to the low temperature GaAs layer is presented using TEM evidence. This behaviour is explained by the bending of threading dislocations at the GaAs/(AlGa)As interface during thermal cycle annealing.

The advantages of the alternative group III precursor DMEAGa over TMGa, especially in the low temperature growth step, are the lower decomposition temperature and the lack of direct metal–carbon bonds (Fig. 1) preventing the incorporation of carbon during GaAs growth nucleation. TMGa decomposes via an intramolecular hydrogen transfer yielding methane and an adsorbed GaCH group leading to the incorporation of carbon at the GaAs/Si interface [7]. This results in the formation of SiC on the Si surface which might cause 3D GaAs growth nucleation. The ALE technique, using DMEAGa during the low temperature growth step, leads to a further improvement of layer quality at low temperatures when compared with the results of the standard MOVPE growth process. We observe an improvement of surface morphology as well as a reduction in XRD linewidth from 180 s of arc to 150 s of arc for thermally-annealed GaAs on Si layers of 2 μm thickness. These results agree with those obtained by molecular beam epitaxy (MBE) and modulated migration enhanced epitaxy (MEE) [8].

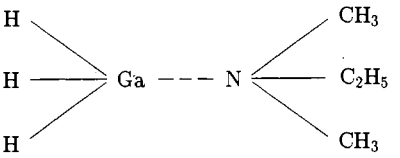

Fig. 1. Schematic molecular structure of the alternative group III compound dimethyl-ethyl-amine-gallane ($GaH_3{\cdot}N(CH_3)_2C_2H_5$ (DMEAGa)).

In order to understand the underlying mechanism of dislocation motion the thermal cycle annealing step has been optimized with respect to the high and low annealing temperature. At high annealing temperatures dislocation annihilation is caused by the motion of dislocations towards the edge and interface and by dislocation coalescence. The driving force for the motion of dislocations is thought to be the thermally-induced stress because this would explain the difference in thermal expansion coefficients of GaAs and Si. Raising the annealing temperature beyond 850 °C has no influence on dislocation reduction, see also ref. 9. Therefore, the high annealing temperature was fixed at 875 °C for the present work.

To investigate the influence of cooling during thermal cycle annealing on the grown samples, the low annealing temperature (T_{low}) was varied. Lowering T_{low} leads to a strong decrease in the XRD linewidth and a decrease in the EPD. Below a low annealing temperature of approximately 350 °C a saturation of XRD linewidth (Fig. 2(a)) and of EPD (Fig. 2(b)) is observed. This effect can be explained by the bending of dislocations along surface steps introduced by the substrate misorientation. Detailed experiments to investigate this mechanism of saturation and reduction of dislocation density at low temperatures are underway and will be published [10].

Finally, the influence of a thin $(Al_xGa_{1-x})As$ layer ($x = 0.5$) placed near the GaAs/Si interface on the motion of dislocations is discussed. Figure 3 shows two transmission electron micrographs of epitaxial GaAs layers on Si before (top) and after thermal cycle annealing (bottom). A large number of dislocations is observed threading through the whole layer structure

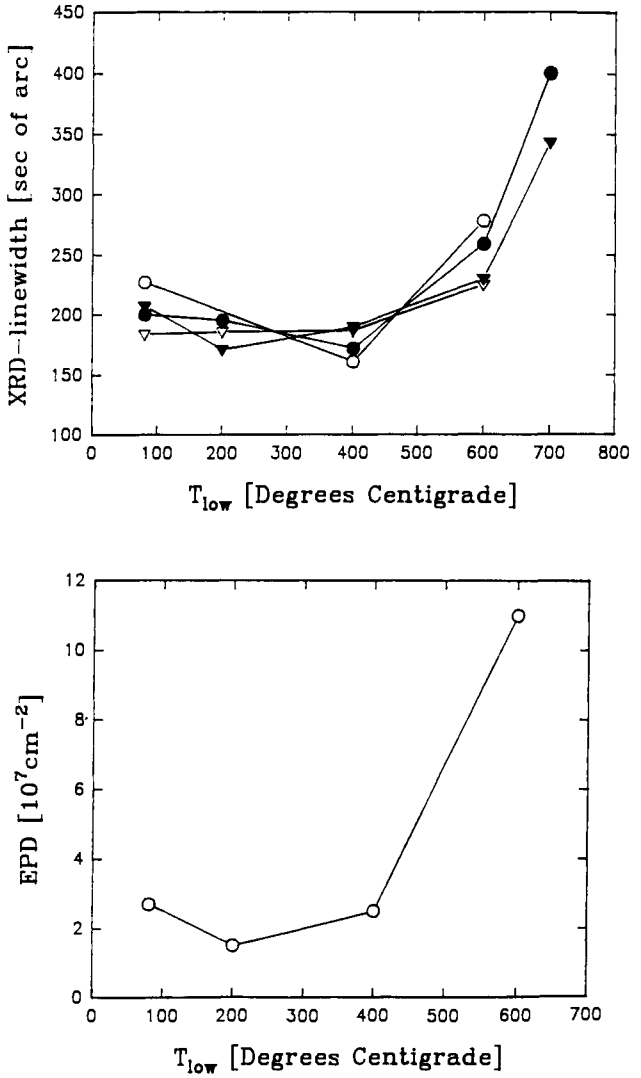

Fig. 2. Dependence of XRD linewidth (top) and EPD (bottom) as a function of the low annealing temperature in the thermal cycle annealing step.

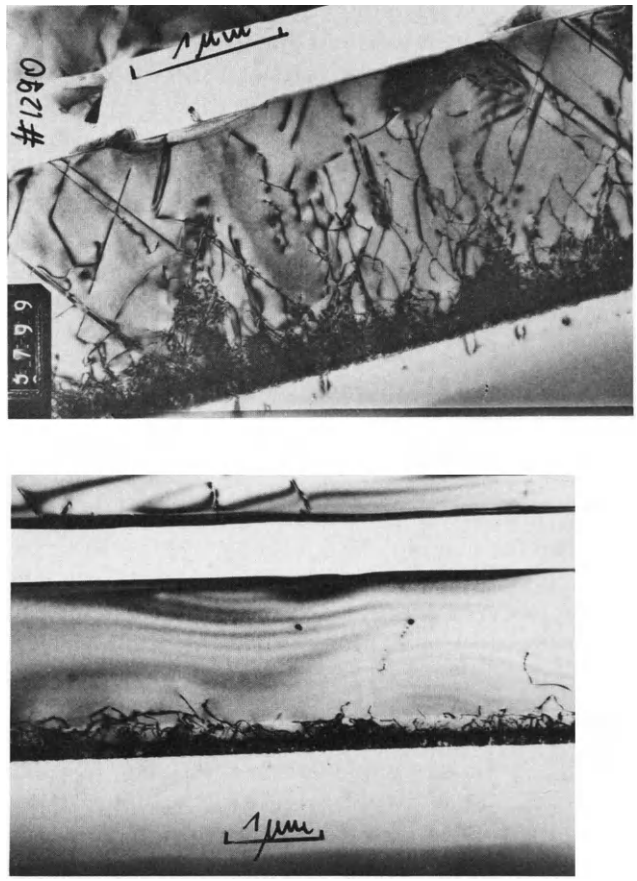

Fig. 3. Transmission electron micrographs (cross section) of heteroepitaxial GaAs layers on Si samples before (top) and after (bottom) thermal cycle annealing.

prior to TC. After TC the dislocations are confined to the low temperature GaAs layer. This behaviour can be explained by a model, as schematically shown in Fig. 4. Two mechanisms (indicated in the bottom part of Fig. 4) might be responsible for this observation: (i) the extension of a misfit dislocation segment along the interface after the low temperature GaAs layer during TC; (ii) the blocking of dislocation halfloops re-emitted from the GaAs/Si interface in the TC annealing step [11]. The re-emission of dislocation halfloops from the GaAs/Si interface would eventually lead to additional threading dislocations in the GaAs layer structure. The first mechanism should, in principle, be also observed during normal MOVPE growth. However, no indication for dislocation bending after the low temperature GaAs layer is observed in as grown samples. Therefore, we assume that the second mechanism of blocking of re-emitted dislocation halfloops is responsible for the experimental observations.

Further studies are underway to combine these improvements; in particular for structured GaAs/Si layers in order to try to reduce the dislocation density to values acceptable for optoelectronic device applications.

4. Summary

The MOVPE growth of GaAs on Si has been optimized with respect to the low temperature growth step at the start by using the alternative group III precursor DMEAGa and by applying the ALE growth technique. DMEAGa offers distinct advantages over TMGa; *e.g.* a lower decomposition temperature and lack of direct metal carbon bonds which prevents the formation of SiC on the Si surface. Thermal cycle annealing of the grown samples has been investigated especially with

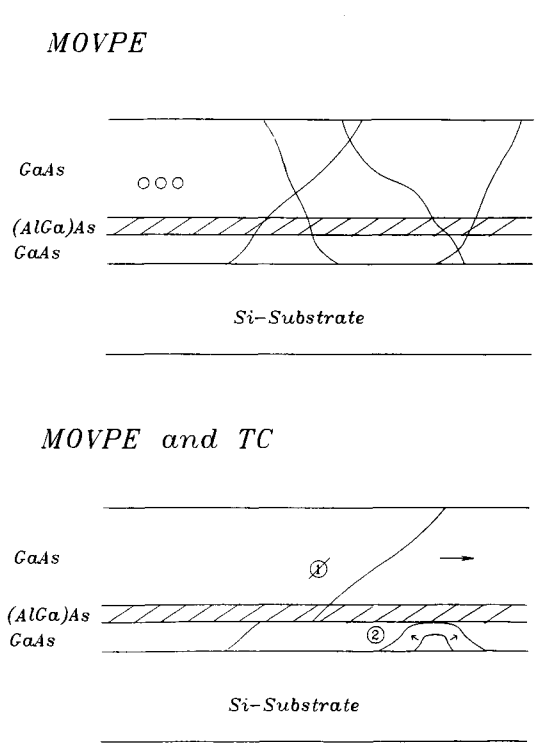

Fig. 4. Model to show the confinement of dislocations to the near interface GaAs layer by introducing a thin (AlGa)As layer (top, as grown; bottom, after thermal cycle annealing). For details see text.

respect to the low annealing temperature. Lowering T_{low} below 350 °C leads to a saturation of XRD linewidth as well as of EPD which is explained by the bending of dislocations along surface steps introduced by the substrate misorientation. Introducing a thin (AlGa)As layer after the low temperature growth step leads to a further improvement of layer quality because of the confinement of dislocations to the low temperature GaAs layer after thermal cycle annealing. This behaviour is discussed in conjunction with a model for blocking of dislocations using a thin (AlGa)As layer.

Acknowledgments

The authors would like to thank T. Ochs for expert technical support during MOVPE. This work was sponsored by the Deutsche Forschungsgemeinschaft (DFG).

References

1 S.F. Fang, K. Adomi, S. Iyer, H. Morkoc and H. Zabel, *J. Appl. Phys., 68* (1990) R31.
2 M. Akiyama, Y. Kawarada, T. Ueda, S. Nishi and K. Kaminishi, *J. Cryst. Growth, 77* (1986) 490.
3 A. Ishizaka and Y. Shiraki, *J. Electrochem. Soc., 33* (1986) 666.
4 H. Protzmann, T. Marschner, O. Zsebök, W. Stolz, E.O. Göbel, R. Dorn and J. Lorberth, *J. Cryst. Growth, 115* (1991) 248.
5 H. Okamoto, Y. Watanabe, Y. Kadota and Y. Ohmachi, *Jpn. J. Appl. Phys., 26* (1987) L1950.
6 J.G. Grabmeier and C.B. Watson, *Phys. Stat. Sol., 32* (1969) K13.
7 F. Lin and R.I. Masel, *Surf. Sci., 258* (1991) 225.
8 W. Stolz, M. Naganuma and Y. Horikoshi, *Jpn. J. Appl. Phys., 27* (1988) L283.
9 M. Yamaguchi, M. Tachikawa, Y. Itoh, M. Sugo and S. Kondo, *J. Appl. Phys., 68* (1990) 4518.
10 T. Marschner, W. Stolz, E.O. Göbel, Y. Horikoshi and K. Nozawa, unpublished, 1993.
11 H.L. Tsai and Y.C. Kao, *J. Appl. Phys., 67* (1990) 2862.

Characterization of the heterostructure between heteroepitaxially grown β-$FeSi_2$ and (111) silicon

M. Pauli, M. Dücker, M. Döscher and J. Müller
Technical University Hamburg-Harburg, Eißendorferstrasse 42, 2100 Hamburg 90 (Germany)
W. Henrion and H. Lange
Hahn-Meitner Institut, Rudower Chaussee 5, O-1199 Berlin (Germany)

Abstract

A new method was developed to grow β-$FeSi_2$ thin films heteroepitaxially on (111) silicon in a two-step process by first depositing an amorphous but stoichiometric Fe + 2Si film on a (111) silicon substrate and a subsequent crystallization using a rapid thermal and large area process. The potential of this method for the fabrication of β-$FeSi_2$ films was investigated as the heterostructure was characterized by transmission and reflection measurements, by infrared spectroscopy, and by Rutherford backscattering. The specific resistivity, the carrier type and concentration, and the mobility of the heteroepitaxially grown β-$FeSi_2$ were measured taking into account the influence of the n-doped silicon substrate. The measured values are 164 $(\Omega\ cm)^{-1}$, p-type with $p = 8 \times 10^{18}\ cm^{-3}$, and 128 $cm^2\ V^{-1}\ s^{-1}$ respectively. The I–V characteristics of the β-$FeSi_2$/Si heterojunction show rectifying behaviour.

1. Introduction

Semiconducting β-iron disilicide (β-$FeSi_2$) is a promising material for light-absorbing thin films as β-$FeSi_2$ has been identified by optical measurements to be a semiconductor with a direct band gap [1, 2]. The band gap was measured to be 0.85 eV. This band gap enables the β-$FeSi_2$ to absorb light to the near infrared. Furthermore β-$FeSi_2$ shows the ability to grow heteroepitaxially on (111)-oriented silicon [3, 4].

This paper investigates the potential of a new method to form β-$FeSi_2$ films in a two-step process. First an amorphous but stoichiometric Fe + 2Si film is deposited on a (111) 3 inch silicon substrate by sputtering a stoichiometric Fe + 2Si target in an argon plasma. Subsequently this amorphous film is crystallized in a rapid thermal and large area process by local heating with a line electron beam. The maximum temperature in the Fe + 2Si film is about 450 °C [5]. During the rapid heating process the amorphous Fe + 2Si film not only crystallizes to form β-$FeSi_2$ but also shows heteroepitaxial grain growth on the underlying (111) silicon substrate, as was proven by the X-ray diffraction pattern of the crystallized film which exhibit only the (110) reflection of the β-$FeSi_2$. It was also proven by the electron diffraction pattern of the β-$FeSi_2$ grains with the underlying silicon substrate obtained from transmission electron microscopy (TEM) cross-sectional investigations [6]. This two-step process offers the following advantages as the crystallization temperature can be kept as low as 450 °C for only 70 s.

(1) The number of iron atoms dissolved in the silicon substrate can be minimized as the solubility decreases with decreasing temperature.

(2) Impurity diffusion from the deposited film to the forming β-$FeSi_2$/Si interface can also be minimized as the diffusion coefficients also decrease with decreasing temperature.

The purpose of this paper is to present the results of optical measurements obtained from the as-deposited and the crystallized β-$FeSi_2$ films, to present the carrier type, concentration and mobility of the heteroepitaxially grown β-$FeSi_2$ regarding the silicon substrate and to present the I–V characteristics of the β-$FeSi_2$/Si heterojunction.

2. Sample preparation

The (111) silicon substrate was cleaned by HNO_3 etching followed by a HF dip. The native oxide on the silicon substrate was removed in the sputtering chamber by plasma etching. The amorphous but stoichiometric Fe + 2Si film was deposited on the substrate by sputtering a stoichiometric Fe + 2Si target in an argon plasma. The film thickness was varied between 0.1 and 1 μm. On some samples the β-$FeSi_2$ film was structured with the van der Pauw pattern shown in Fig.

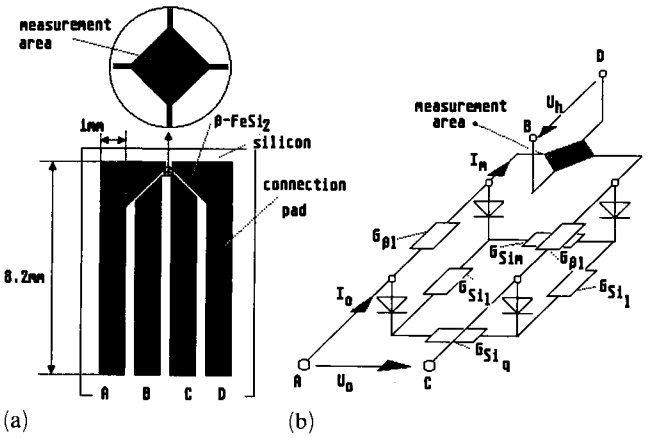

Fig. 1. Structured β-$FeSi_2$ film in plane view used for measurement of the specific conductance and the Hall voltage (a) and the equivalent electrical circuit (b) of the structured β-$FeSi_2$ and the underlying silicon substrate.

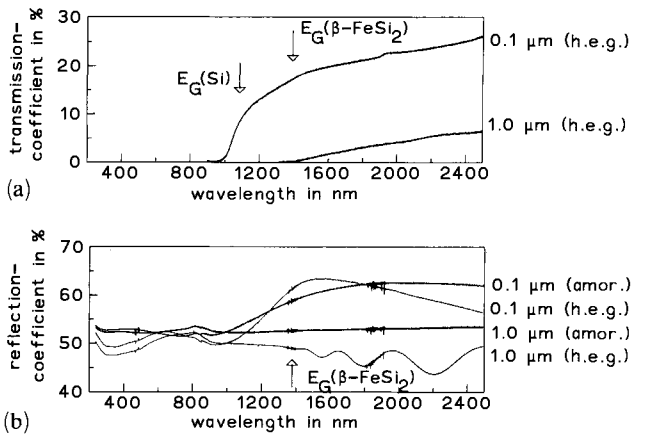

Fig. 3. Optical transmission (a) and reflection (b) spectra of amorphous (amor.) Fe + 2Si and heteroepitaxially grown (h.e.g.) β-$FeSi_2$ films on (111) silicon substrates for two film thicknesses.

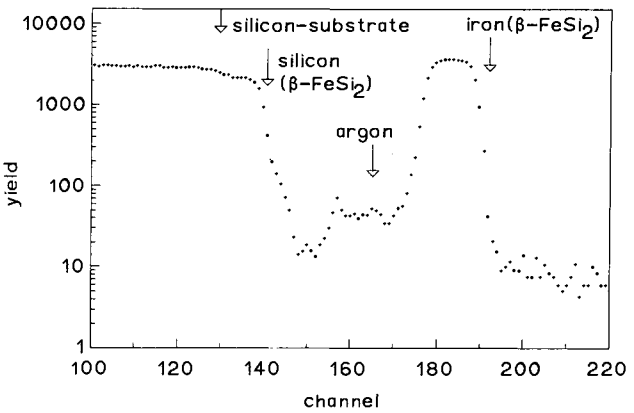

Fig. 2. Rutherford backscattering intensity as a function of the energy of the backscattered ions for a crystallized β-$FeSi_2$ film (thickness 1 µm) on a silicon substrate.

1(a). For this purpose a chromium layer deposited on the amorphous Fe + 2Si film was structured by photolithography. The structured chromium was used as the mask to etch the amorphous Fe + 2Si film in a buffered $HF + HNO_3$ solution and was removed after etching. At last the amorphous Fe + 2Si films were crystallized to β-$FeSi_2$.

3. Characterization of the β-$FeSi_2$–silicon heterostructure

Figure 2 shows the results obtained from Rutherford backscattering (RBS) of a 1 µm thick β-$FeSi_2$ film on a silicon substrate. The signal resulting from substrate silicon atoms is clearly separated from the silicon atoms of the β-$FeSi_2$ film. From the width of the latter signal, the β-$FeSi_2$ film thickness can be evaluated to be 1 µm, which corresponds to the value measured by a thickness profiler. Comparing the backscattering yield resulting from iron atoms to the yield resulting from silicon atoms of the β-$FeSi_2$ film gives the stoichiometry of the crystallized film to be $n_{Si}/n_{Fe} = 1.95$. The iron content in the β-$FeSi_2$ film exceeds the right stoichiometric ratio. During the sputtering of the Fe + 2Si target in the argon plasma, argon atoms are incorporated into the amorphous Fe + 2Si film as the RBS measurements show that argon atoms are incorporated into the crystallized β-$FeSi_2$ film.

Figure 3 depicts the results obtained from optical transmission (a) and reflection spectroscopy measurements (b) of amorphous Fe + 2Si and crystallized β-$FeSi_2$ films with a film thickness of 0.1 and 1 µm. Amorphous Fe + 2Si films do not transmit light due to a semi-metallic absorption behaviour. The β-$FeSi_2$ film of 0.1 µm thickness exhibits two discontinuities in the curve of the transmission coefficient as a function of the wavelength. The first discontinuity at $\lambda = 1.4$ µm can be assigned to the absorption edge of the β-$FeSi_2$ film ($E_G = 0.85$ eV) and the second at $\lambda = 1.1$ µm to the absorption edge of the silicon substrate ($E_G = 1.14$ eV). The β-$FeSi_2$ film of 1 µm thickness shows a stronger absorption compared to the thinner film and only the absorption edge at $\lambda = 1.4$ µm is visible.

The reflection behaviour of the amorphous films does not show any dependence on the wavelength. The crystallized β-$FeSi_2$ films is transparent for wavelengths less than $\lambda = 1.4$ µm as the reflected intensity varies with the wavelength due to constructive or destructive interference of the light reflected directly at the surface and the light reflected at the interface of the β-$FeSi_2$ film and the silicon substrate. At shorter wavelengths the increasing light absorption in the β-$FeSi_2$ film leads to a decrease of the transmitted intensity and

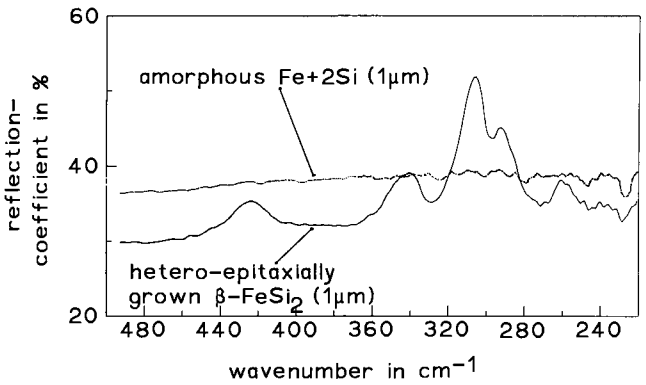

Fig. 4. Infrared spectrograph of an amorphous Fe + 2Si film and a heteroepitaxially grown β-$FeSi_2$ film on a (111) silicon substrate.

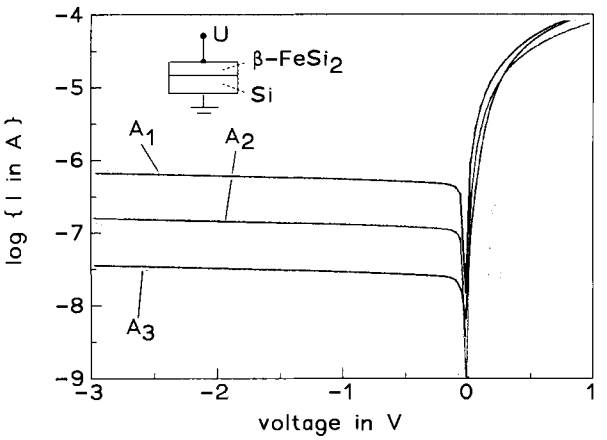

Fig. 5. Logarithm of the current flowing through the β-$FeSi_2$/Si heterostructure as a function of the applied voltage for three contact areas ($A_1 = 7.96 \times 10^{-4}$ cm^2, $A_2 = 1.98 \times 10^{-4}$ cm^2 and $A_3 = 0.49 \times 10^{-4}$ cm^2).

a variation of the reflected intensity due to constructive or destructive interference can no longer be observed.

Figure 4 shows the results of the infrared spectroscopy for an amorphous Fe + 2Si and a crystallized β-$FeSi_2$ film. The amorphous film does not show any variation of the reflected light intensity with the wavenumber whereas the reflected intensity of the crystallized film clearly reveals the excitation states of the β-$FeSi_2$.

4. Electrical properties of the heteroepitaxially grown β-$FeSi_2$ film

The van der Pauw structure shown in Fig. 1(a) was used to measure the specific conductivity and the carrier type and concentration by the van der Pauw method [7, 8] at room temperature. The thickness d of the investigated β-$FeSi_2$ film is 0.1 μm. The silicon substrate is n-doped ($n = 2 \times 10^{15}$ cm^{-3}) and has a specific conductivity $\sigma = 0.5\ (\Omega\ \text{cm})^{-1}$.

As the β-$FeSi_2$ film is electrically connected to the silicon substrate, the influence of the silicon substrate must be taken into account. The equivalent electrical circuit resulting from the geometry and the electrical properties of the structure is shown in Fig. 1(b). A voltage U_0 is applied to the connection pads A and B to measure the specific conductivity or A and C to measure the Hall voltage. The voltage U_0 causes a current I_0 to flow into the connection pad. Due to the large area of the connection pad most of the current I_0 will flow across the heterostructure into the silicon along the conductance G_{Siq}. This current is limited by the rectifying characteristic of the heterostructure (compare with Fig. 5) but nevertheless it significantly reduces the current I_{AB} which flows laterally to the measurement area. The voltage U_{CD} which drops across the other two connection pads of the measurement area is measured by a high impedance voltage analyser.

To a first approximation, the measurement current I_{AB} can be evaluated as the product of the induced voltage U_0 and the lateral conductivity of the connection pads, as the voltage drop across the measurement field is negligible due to geometric reasons. The lateral conductance of the connection pad G_{cp} consists of $G_{\beta l}$ parallel to G_{Sil} which will be reduced by the current limiting heterostructure. G_{cp} was evaluated experimentally to be 30 μs. The measured values for U_{CD} and U_0 are 11.2 mV and 5.57 V respectively. Taking the van der Pauw formula for the specific conductivity and replacing I_{AB} by $0.5 \times G_{cp} \times U_0$ leads to:

$$\sigma_{\beta\text{-}FeSi_2} = \frac{\ln 2}{2\pi} \frac{G_{cp} U_0}{U_{CD}} \frac{1}{d} = 165 \frac{1}{\Omega\ \text{cm}} \qquad (1)$$

The influence of the silicon substrate on the calculation of specific conductivity is neglected because of the following reasons:

(i) the specific conductivity of silicon is much lower than the one evaluated in eqn. (1);

(ii) in the silicon substrate, the current distribution will spread with increasing distance from the β-$FeSi_2$ film. Thus the measured voltage drop is little influenced by the current flowing laterally through the silicon substrate.

For measuring the Hall voltage the considerations given above are still valid. The sign and the value of the Hall voltage was calculated from the difference of the voltage drop across connection pads B and D when the magnetic field ($B = 0.7$ T) applied perpendicular to the measurement field, is reversed. The sign of the Hall voltage identifies the carrier of the β-$FeSi_2$ to be holes. Taking van der Pauw's formula to calculate the carrier

concentration with the measured Hall voltage, $U_h = 1.84$ mV, the measured induced voltage $U_0 = 5.59$ V, and the elementary charge q leads to:

$$p_{\beta\text{-}FeSi_2} = \frac{BG_{cd}U_0}{qU_h d} = 8 \times 10^{18}\ \text{cm}^{-3} \quad (2)$$

The Hall mobility $\mu_{h\beta\text{-}FeSi_2}$ can be calculated from the specific conductivity and the carrier concentration:

$$\mu_{h\beta\text{-}FeSi_2} = \frac{\sigma_{\beta\text{-}FeSi_2}}{qp_{\beta\text{-}FeSi_2}} = 128\ \text{cm}^2\ \text{V}^{-1}\ \text{s}^{-1} \quad (3)$$

5. Electrical characterization of the β-$FeSi_2$/Si heterostructure

To determine the I–V characteristics of the β-$FeSi_2$/Si heterojunction, the β-$FeSi_2$ film was structured into circular-shaped β-$FeSi_2$ areas having three different diameters $d_1 = 25$ μm, $d_2 = 50$ μm and $d_3 = 100$ μm. Figure 5 shows the logarithm of the measured current across the heterojunction as a function of the applied voltage for the three different diameters. The heterojunction shows a rectifying behaviour and the diffusion voltage across the space charge of the heterojunction is oriented from the silicon substrate to the β-$FeSi_2$ film. The reverse current scales with the cross-sectional area of the heterojunction. The forward current increases slower than exponential with the applied voltage. Consequently the ideality factor increases from 1.2 at 100 mV to 2.24 at 200 mV.

6. Summary and conclusions

The method of forming β-$FeSi_2$ films by heteroepitaxial grain growth from the amorphous but stoichiometric phase using a rapid thermal and large area crystallization process leads very reliably to β-$FeSi_2$ films of high crystalline quality and good electrical properties. Optical measurements revealed the heterostructure properties of the heteroepitaxially grown β-$FeSi_2$ film and the silicon substrate. The specific resistivity, the carrier type and concentration, and the mobility of the heteroepitaxially grown β-$FeSi_2$ were measured to be 164 $(\Omega\ \text{cm})^{-1}$, p-type with $p = 8 \times 10^{18}$ cm^{-3} and 128 $\text{cm}^2\ \text{V}^{-1}\ \text{s}^{-1}$ respectively.

The measurement set-up to determine the electrical properties of the heteroepitaxially grown β-$FeSi_2$ will be improved to make these parameters more directly accessible to the measurement as the measurement principle presented here still leads to results which contain an uncertainty of about 20%. The characteristics of the β-$FeSi_2$/Si heterostructure will be investigated more precisely by I–V, CV and $I(T)V$ measurements.

References

1 S. S. Lau, S. Y. Feng, J. O. Olowolafe and M. A. Nicolet, *Thin Solid Films, 25* (1975) 415.
2 M. C. Bost and J. E. Mahan, *J. Appl. Phys., 58* (7) (1985) 2696.
3 N. Cherief, C. D'Anterroches, R. C. Cinti, T. A. Nguyen Tan and J. Derrien, *Appl. Phys. Lett., 55* (16) (1989) 1671.
4 H. C. Cheng, L. J. Chen and T. R. Your, *Mater. Res. Soc. Proc., 25* (1984) 441.
5 M. Pauli, G. Dähn, J. Müller and M. Döscher, *Appl. Surf. Sci., 69* (1993) 398.
6 M. Pauli, M. Döscher, G. Dähn and J. Müller, *Appl. Surf. Sci., 65/66* (1993) 525.
7 L. J. van der Pauw, *Philips Research Reports, 13* (1958) 1.
8 R. L. Pertritz, *Phys. Rev., 110* (1958) 1254.

Optical investigation of interdiffusion in CdTe/CdMnTe quantum wells

D. Tönnies, G. Bacher, A. Forchel, A. Waag and G. Landwehr
Physikalisches Institut der Universität Würzburg, Am Hubland, D-97074 Würzburg (Germany)

Abstract

We investigated thermally induced interdiffusion in CdTe/CdMnTe quantum wells by luminescence spectroscopy. CdTe/CdMnTe quantum wells grown by molecular beam epitaxy were annealed by rapid thermal annealing for 1 min at temperatures between 380 and 550 °C. We observed simple diffusion behaviour in this temperature region, offering the possibility of shifting the luminescence spectrum up the barrier energy. Our results are discussed using an interdiffusion model.

In recent years nanofabrication of semiconductor heterostructures has become a wide field of research activity. A very promising technology for structuring semiconductors is selective ion implantation and subsequent annealing to induce interdiffusion between the quantum well (QW) and the barrier material. So far essentially III–V semiconductors have been studied in detail. Recently, II–VI semiconductors have become of interest for optoelectronic devices, because they offer a wide range of energy band gaps. However, there is only little information about the potential of these materials for microstructured systems.

In this paper we report on a low temperature photoluminescence (PL) investigation of diffusion effects in thermally processed $CdTe/Cd_{1-x}Mn_xTe$ quantum wells. Thermal annealing causes interdiffusion of Mn and Cd ions and thus alters the composition profile of the QW. Mn ions diffuse into the well region and the Mn content in the barrier layers is changed. This leads to a different quantum well shape and in consequence to an increase in the band gap. Therefore a blue shift of the characteristic emission spectrum of annealed samples is expected [1].

Nominally undoped $CdTe/Cd_{1-x}Mn_xTe$ single QWs were grown by molecular beam epitaxy (MBE) on a 100-oriented CdTe substrate with a 0.2 μm CdTe buffer. We investigated samples of different QW thickness. The Mn content in the barrier was chosen between 12% and 14%. The CdTe QW layers were sandwiched between a 0.4 μm thick CdMnTe buffer and a 0.2 μm top layer.

We used rapid thermal annealing (RTA) to induce interdiffusion. The annealing time was 1 min for each sample and the temperatures were chosen between 380 and 550 °C. During the annealing process the samples were under a continuous flux of N_2 to avoid oxidation of the surfaces and to allow the samples to cool down rapidly after annealing.

Figure 1 presents PL spectra of a 4.0 nm QW (measured at 5 K) annealed at different temperatures. We observe a small blue shift at an annealing temperature of 400 °C (for comparison the growth temperature was 230 °C). Further increasing the annealing temperature to 500 °C leads to a blue shift of 150 meV corresponding to the energy of the barrier, *i.e.* the Cd and Mn ions have almost totally interdiffused.

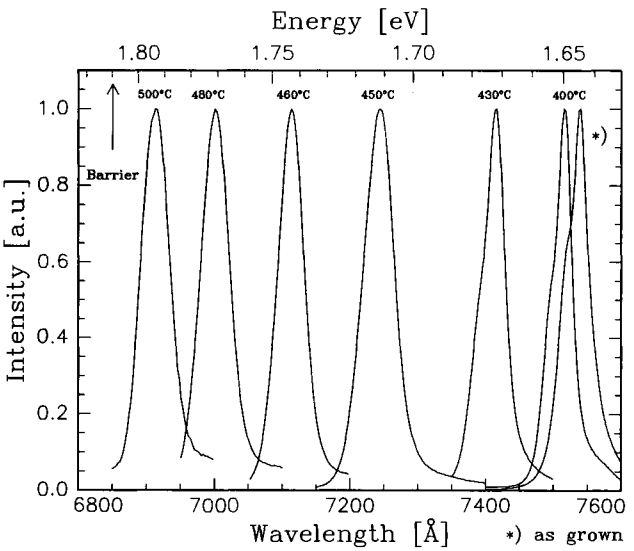

Fig. 1. Photoluminescence spectra of a 4.0 nm CdTe/$Cd_{0.86}Mn_{0.14}Te$ quantum well annealed at temperatures between 400 and 500 °C by RTA (annealing time 60 s). The right-hand emission line corresponds to a reference sample. The samples show a significant blue shift up to 150 meV. The barrier energy is at 1.810 eV.

0921-5107/93/$6.00
© 1993 – Elsevier Sequoia. All rights reserved

Of particular interest is the half-width of the emission lines, because this indicates the quality of the QW interfaces. For our samples the half-width increases a little from 9 to 13 meV. This still indicates good quality of the interdiffusion process even for samples annealed at high temperatures.

In Fig. 2 the blue shift is displayed explicitly against the corresponding annealing temperature. Evidently the blue shift increases strongly in the temperature region 420–470 °C and reaches a saturation for high annealing temperatures, demonstrating that the spectrum cannot shift any further than the energy of the barrier.

To extract more quantitative information about the interdiffusion process we apply a simple interdiffusion model to our results. Supposing the interdiffusion of Cd and Mn ions follows Fick's laws then the Mn content $c(x,t)$ can be described by error functions:

$$c(x,t)=c_0\left[1+\frac{1}{2}\,\mathrm{erf}\left(\frac{x-L_z/2}{2\Lambda_{\mathrm{Diff}}}\right)-\frac{1}{2}\,\mathrm{erf}\left(\frac{x+L_z/2}{2\Lambda_{\mathrm{Diff}}}\right)\right]$$

where $\Lambda_{\mathrm{Diff}}=(Dt)^{1/2}$ is the diffusion length and D the diffusion coefficient. The band gap of $Cd_{1-x}Mn_xTe$ alters with the Mn content x by [2]

$$E_g=(1.606+1.592x)\,\mathrm{eV}$$

With this the profiles of the conduction and the valence band are obtained assuming a valence band offset of 20% [3]. The energies of the groundstates of electrons and heavy holes was calculated numerically using $m_e=0.09\,m_0$ [4] as the effective electron mass and $m_{hh}=0.4\,m_0$ as the effective heavy hole mass. Figure 3 shows the results of the calculation for a 4.0 nm quantum well with an Mn content of 14% in the barrier. As long as the diffusion length is small compared with the well width, there is only a little dependence of the transition energy on the diffusion length. For diffusion lengths higher than 20 nm the energy is almost shifted to the barrier energy and does not depend strongly on the diffusion length anymore.

Thus from our measurements we can derive the diffusion length Λ_{Diff} for each annealing temperature. With $D_{\mathrm{Diff}}{}^2/t$ we obtain an estimate of the corresponding diffusion coefficient D.

Figure 4 displays the diffusion coefficient of CdTe/$Cd_{1-x}Mn_xTe$ quantum wells with well thicknesses of 4.0 and 10.0 nm *vs.* the reciprocal annealing temperature in a semilogarithmic plot. The temperature dependence of the diffusion coefficient D can be taken as a relation of the Arrhenius type:

$$D=D_\infty\exp\left(-\frac{E_a}{kT}\right)$$

where E_a can be interpreted as the activation energy, *i.e.* the energy necessary for the interchange of a Cd and a Mn ion.

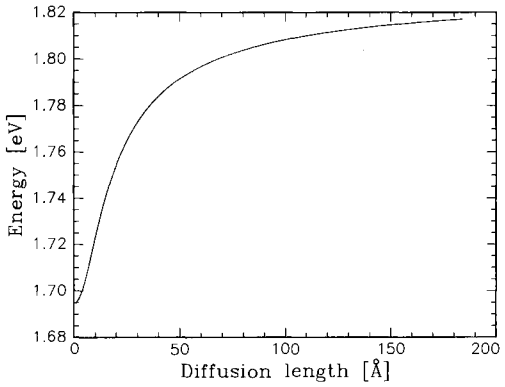

Fig. 3. Calculated energy shifts of a 4 nm $Cd_{0.86}Mn_{0.14}Te$/CdTe/$Cd_{0.86}Mn_{0.14}$ quantum well *vs.* the diffusion length.

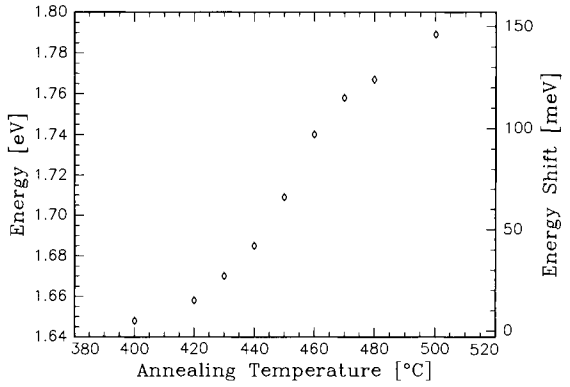

Fig. 2. Blue shift of the emission lines in Fig. 1 *vs.* annealing temperature. The energy level of the barrier is at 1.810 eV. Thus annealing at 500 °C leads to almost total interdiffusion of the Cd and Mn ions.

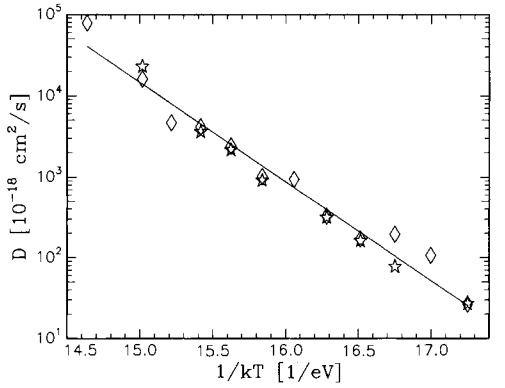

Fig. 4. The interdiffusion coefficients D of a CdTe/$Cd_{1-x}Mn_xTe$ quantum well against the reciprocal annealing temperatures (400–520 °C) for different quantum well thicknesses (◇ 100 Å; ☆ 40 Å). The activation energy $E_a=2.8$ eV of the interdiffusion process can be estimated from the slope of the curve.

In Fig. 4 the experimental data show a good linear relation, thus confirming the Arrhenius prediction. The curves were fitted linearly to estimate the activation energy E_a. We obtain an activation energy of $E_a = 2.8$ eV. This value lies a little above the activation energies for self diffusion in CdTe [5], which are reported to be between 2.0 and 2.7 eV.

In summary the $CdTe/Cd_{0.86}Mn_{0.14}Te$ quantum wells investigated show good diffusion behaviour offering the possibility of shifting the luminescence spectrum up to the barrier energy. Interdiffusion effects start to occur at an annealing temperature of 400 °C if annealed for 1 min. Annealing at 500 °C for 1 min leads to a blue shift near to the barrier energy. The quality of the interfaces remains good even for strongly interdiffused quantum wells. Furthermore the diffusion model discussed in this paper seems to describe the experimental data very well and provides an activation energy for the interdiffusion process of about 2.8 eV.

References

1 M. D. Camras, N. Holonyak, Jr., R. D. Burnham, W. Streifer, D. R. Scifres, T. L. Paoli and C. Lindström, *J. Appl. Phys., 54* (1983) 5637.
2 J. K. Furdyna, *J. Appl. Phys., 64* (4) (1988) R34.
3 B. Kuhn-Heinrich, W. Ossau, M. Popp, E. Bangert, A. Waag and G. Landwehr, in *Proc. 21st Int. Conf. Physics of Semiconductors, Peking, 1992*, p. 923.
4 Landolt-Börnstein, in O. Madelong (ed.), *Physics of II–VI and I–VII Compounds, Semimagnetic Semiconductors*, III/17b, Springer, Berlin, 1982.
5 B. L. Sharma, *Defects Diffusion Forum, 64/65* (1989) 77.

Materials Science and Engineering, B21 (1993) 277–280

Investigation of InGaAs/InP interdiffusion by simultaneous transmission electron microscopy and photoluminescence analysis

J. Oshinowo[a], A. Forchel[a], J. D. Ganière[b], P. Ruterana[c], P. A. Stadelmann[c], I. Gyuro[d], G. Laube[d] and E. Zielinski[d]

[a] *Technische Physik, University of Würzburg, Am Hubland, W-8700 Würzburg (Germany)*
[b] *Institut de Micro- et Optoélectronique, EPFL, CH-1015 Lausanne (Switzerland)*
[c] *Institut de Microscopie Electronique, EPFL, CH-1015 Lausanne (Switzerland)*
[d] *Alcatel SEL Research Center, W-7000 Stuttgart 40 (Germany)*

Abstract

We investigated the interdiffusion of InGaAs/InP quantum wells (QWs) due to rapid thermal annealing (RTA) by photoluminescence (PL) spectroscopy and wedge transmission electron microscopy (WTEM). After RTA at temperatures between 650 and 900 °C (annealing time 1 min) we observed large emission energy shifts of up to 210 meV. From the temperature dependence of the PL emission energy shifts, the interdiffusion lengths, interdiffusion coefficients and activation energies (*e.g.* of 2 eV) were determined using a simple model of ion intermixing. In addition the samples were characterized by WTEM to obtain a microscopic understanding of the interdiffusion process across the InGaAs–InP heterostructure interface. We obtained a transition region length of about 2.5 nm for an 11 nm QW, in qualitative agreement with the interdiffusion length obtained from PL spectroscopy. From WTEM analysis the variation in chemical composition across the interface was determined, suggesting lattice-matched interdiffusion.

1. Introduction

InGaAs/InP quantum wells (QWs) have been studied intensively owing to their interesting physical properties and the high potential for use in optoelectronic devices. As can be shown by simple models, the energy band gap in a QW depends on the QW width and composition. The layers can be modified by thermal or implantation induced interdiffusion of the matrix elements. This allows, for example, a controlled local increase in the gap energy which has been used to obtain, for example, buried laser structures without overgrowth [1, 2]. Interdiffusion processes in III–V semiconductors have been studied intensively owing to their interesting physical properties and their high potential for use in optoelectronic devices. In contrast to a variety of studies on interdiffusion in GaAs/AlGaAs, only a few reports on interdiffusion in InGaAs/InP are presently available [3, 4]. Interdiffusion in this system is generally more complex than in GaAs/AlGaAs systems because group III and group V elements participate in the interdiffusion process.

We investigated interdiffusion effects in InGaAs/InP heterostructures consisting of three InGaAs QWs with as-grown QW thickness of 3, 5 and 11 nm (from the top to the bottom) separated by InP barriers of 1000 nm. The top barrier thickness is 100 nm. The QWs were grown by low pressure metalorganic vapor phase epitaxy (MOVPE) on top of a 400 nm InP buffer layer. The samples were annealed for 1 min at temperatures between 650 and 900 °C. In order to suppress the evaporation of phosphorus, the samples were covered both sides by silicon wafers. The samples were heat treated in a rapid thermal annealing (RTA) system in a flowing nitrogen (N_2) atmosphere. The annealing temperature was controlled by a pyrometer with an accuracy of ±5 °C.

The as-grown and annealed samples were characterized by low temperature photoluminescence (PL) spectroscopy ($T = 2$ K) using an argon-ion laser for excitation (excitation power typically 2 mW) and a liquid nitrogen cooled germanium detector.

In addition the samples were characterized by wedge transmission electron microscopy (WTEM) [5] up to 300 keV. In the WTEM technique a high quality cleaved edge of the layer structure is used for transmission of the electron beam. Owing to the different atomic scattering factors, a material-specific interference pattern can be observed. This technique gives information simultaneously of the QW thickness, spatial extension of the interface and the chemical composition of layer structures. The spatial resolution of this method is about a few monolayers [6].

Figure 1 shows a PL spectrum of the as-grown InGaAs/InP QWs compared with a spectrum obtained from a sample annealed at 900 °C. The emission

0921-5107/93/$6.00

© 1993 – Elsevier Sequoia. All rights reserved

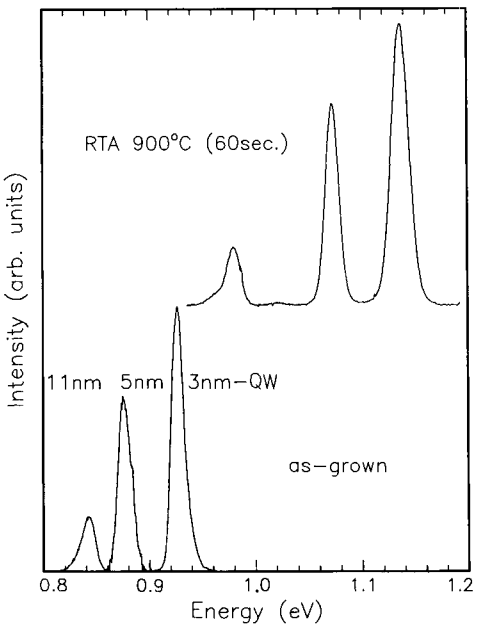

Fig. 1. Luminescence spectra ($T = 2$ K) obtained from an InGaAs/InP heterostructure consisting of 3, 5 and 11 nm thick InGaAs QWs before RTA (as-grown) and after RTA at 900 °C (annealing time 1 min).

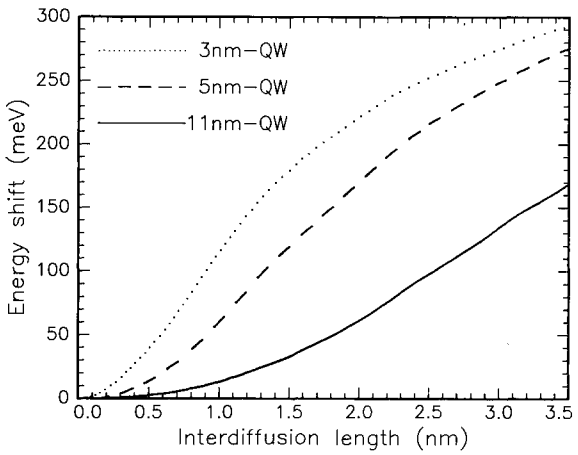

Fig. 2. Shifts in emission energy as a function of the interdiffusion length L_D calculated for 3, 5 and 11 nm $In_{0.53}Ga_{0.47}As$/InP QWs.

energy of the InGaAs/InP QWs can be increased significantly by RTA. Emission energy shifts of up to about 210 meV are obtained for the 3 and 5 nm QWs and 140 meV for the 11 nm QW after RTA compared with the as-grown sample. We observe no degradation of the quantum efficiency of the structures after RTA. This indicates that the quarternary (InGa)(AsP) interface, which is formed during the interdiffusion process, is not affected by non-radiative recombination centers.

We determined the interdiffusion coefficients of the InGaAs/InP QWs from the shifts in PL emission energy and the annealing time using a simple model of ion intermixing by thermal annealing [7, 8]. The In–Ga and As–P interdiffusion at the QW interface is obtained by assuming an error-function-type diffusion profile and lattice-matched intermixing. The assumption of lattice-matched intermixing correlates the gallium and arsenic fractions in the quaternary alloys formed in the interdiffusion by $2.2X_{Ga} = Y_{As}$ [9].

The energy levels for the ground state are obtained by solving the Schrödinger equation with the interdiffusion length L_D as a parameter [7, 8]. Figure 2 shows the shifts in emission energy as a function of the interdiffusion length L_D calculated for a 3, 5 and 11 nm $In_{0.53}Ga_{0.47}As$/InP heterostructure. By comparing the experimentally observed energy shifts with the results of the calculation, we can determine the interdiffusion length as a function of temperature. We obtain interdiffusion lengths of up to 3.0 nm for the 11 nm QW at 900 °C (*e.g.* $L_D = 2$ nm for the 3 and 5 nm QWs).

Given the annealing time τ, the interdiffusion coefficients D_{int} can be obtained from the ratio $D_{int} = L_D^2/\tau$ (τ is the annealing time, equal to 1 min). Figure 3 shows the interdiffusion coefficients D_{int} of the 3, 5 and 11 nm InGaAs/InP QWs as a function of the reciprocal annealing temperature. We obtain interdiffusion coefficients of about 10^{-15} cm^2 s^{-1} at 900 °C. According to the relation $D_{int} \sim \exp(-E_A/kT)$ the temperature dependence of the diffusion can be characterized by an activation energy. From the slope of the temperature dependences of D_{int} we determine activation energies $E_A = 2.0$ eV for the 5 and 11 nm QWs, and $E_A = 2.6$ eV for the 3 nm QW. These values are significantly smaller than the activation energies for GaAs/AlGaAs QWs ($E_A = 5$ eV).

In order to obtain a microscopic understanding of the interdiffusion process across the InGaAs/InP heterostructure interface independently of the PL evaluation, we carried out WTEM studies of as-grown and annealed samples. Figure 4 shows the WTEM images of the 11 nm InGaAs/InP QW heterostructure before RTA (a) and after RTA at 875 °C for 1 min (b). The left end of each image is the edge of the sample and the sample thickness increases from left to right linearly. The epitaxial layers were grown vertically and the InGaAs/InP QW is visible as a horizontal stripe. Equal interference thickness fringes are observed in the vertical direction and their positions are different for the InGaAs QW and InP barrier.

The as-grown 11 nm InGaAs/InP QW (see Fig. 4(a)) shows a sharp heterostructure interface with a small transition region of about 0.5 nm, indicating good compositional abruptness. Figure 4(b) shows the sample after annealing at 875 °C. The thickness fringes at the heterostructure interface are strongly inclined,

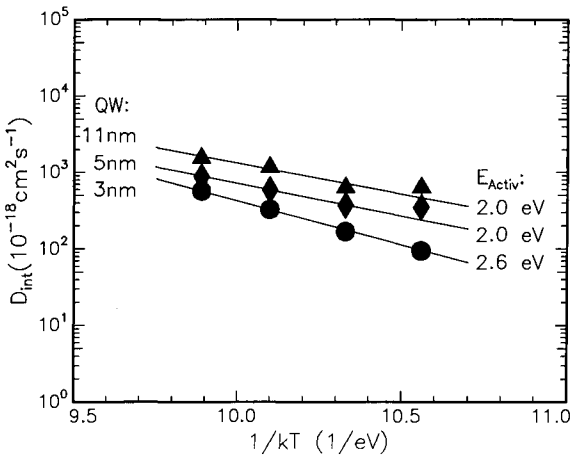

Fig. 3. Interdiffusion coefficients D_{int} obtained from an InGaAs/InP heterostructure consisting of 3, 5 and 11 nm thick InGaAs QWs as a function of the reciprocal annealing temperature. The activation energies derived from the slopes are indicated.

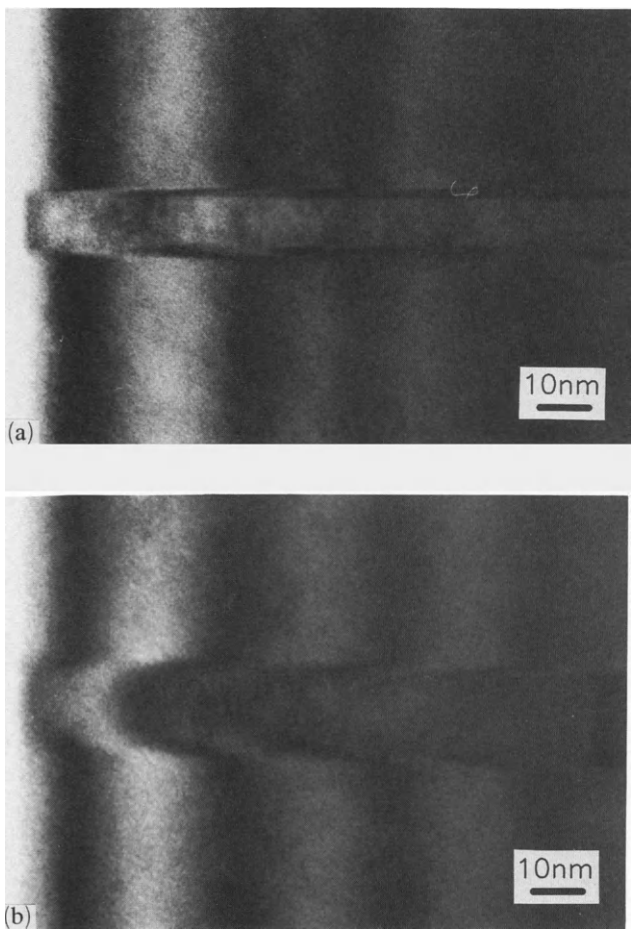

Fig. 4. Wedge transmission electron micrographs of an 11 nm thick InGaAs/InP heterostructure before RTA (a) and after RTA at 850 °C (b). The left end of each image is the edge of the sample. The InGaAs/InP QW is visible as a horizontal stripe. Equal thickness fringes are observed in the vertical direction and their positions are different for the InGaAs and InP layers.

indicating strong interdiffusion between the InGaAs and InP layer structure. A wide compositional transition region with a width of 2.5 nm is formed at both interfaces.

From the change in PL emission energy we obtain an interdiffusion length of 2.7 nm for the 11 nm QW at 875 °C, in qualitative agreement with the transition length obtained from WTEM.

In order to determine the variation in chemical concentration of the annealed structure, the equal thickness fringe profiles were calculated with the EMS simulation program [10] (using the dynamic theory of electron diffraction) and compared with the profiles obtained from experiment. The experimental intensity profiles are obtained by digitization of the WTEM image of the annealed 11 nm InGaAs/InP heterostructure. For different $In_{1-x}Ga_xAs_yP_{1-y}$ compositions, the interference profiles are calculated assuming lattice-matched intermixing (from $X_{Ga}=0$ to $X_{Ga}=0.47$ with an accuracy of 20%).

Figure 5 displays the intensity profiles as a function of sample thickness. The profiles from the experiment

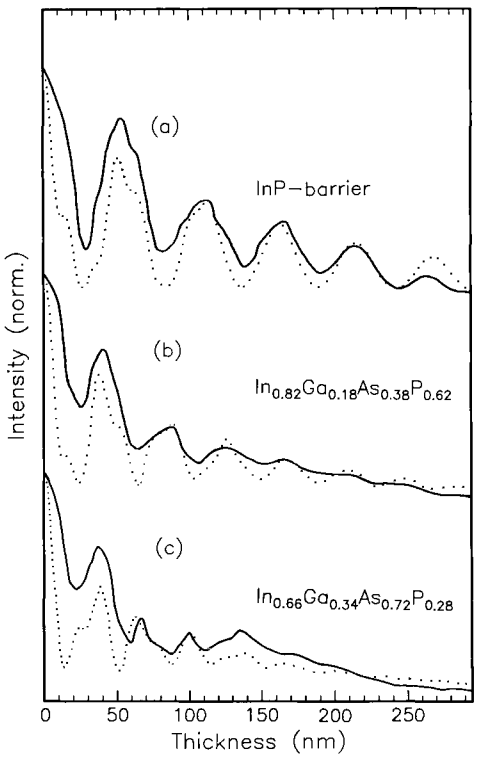

Fig. 5. Intensity profiles of interference patterns of an 11 nm InGaAs/InP heterostructure after RTA at 875 °C as a function of the sample thickness obtained from experiment (——) and the best fit simulation (·····). From the simulation the chemical composition of the $In_{1-x}Ga_xAs_yP_{1-y}$ layer is determined from three different layer thickness positions, (a) the InP barrier region, (b) half-widths of the intermixed transition region, and (c) half-widths of the quantum well.

are obtained from three different layer thickness positions from (a) the InP barrier region, (b) half-widths of the intermixed transition region and (c) half-widths of the QW. By comparing experimentally obtained profiles with simulated profiles we evaluate the positions of the maxima and minima for the InP composition (profile 5(a)), $In_{0.82}Ga_{0.18}As_{0.38}P_{0.62}$ composition (profile 5(b)) and $In_{0.66}Ga_{0.34}As_{0.72}P_{0.28}$ (profile 5(c)). In all cases lattice-matched interdiffusion across the heterostructure interface is seen to explain the data up to high annealing temperatures of 875 °C.

In summary, we investigated the thermal interdiffusion of InGaAs/InP QWs by photoluminescence spectroscopy and wedge transmission electron microscopy. From the change in PL emission energy we obtain an interdiffusion length of 2.7 nm for the 11 nm QW, in qualitative agreement with the transition region length obtained from WTEM. From analysis of the WTEM images the variation in chemical composition across the heterostructure interface is determined and lattice-matched interdiffusion is verified.

References

1 H. Nakashima, S. Semura, T. Ohta, Y. Uchida, H. Saito, T. Fukuzawa, T. Kuroda and K. L. I. Kobayashi, *IEEE J. Quantum Electron., 21* (1985) 629.
2 D. G. Deppe, G. S. Jackson, N. Holonyak, D. C. Hall, R. D. Burnham, R. L. Thornton, J. E. Epler and T. L. Paoli, *Appl. Phys. Lett., 50* (1987) 392.
3 H. Temkin, S. N. G. Chu, M. B. Panish and R. A. Logan, *Appl. Phys. Lett., 50* (1987) 956.
4 J. Oshinowo, A. Forchel, D. Grützmacher, M. Stollenwerk, M. Heuken and K. Heime, *Appl. Phys. Lett., 60* (1992) 2660.
5 H. Kakibayashi and F. Nagata, *Jpn. J. Appl. Phys., 25* (1986) 1644.
6 J. D. Ganière, F. K. Reinhart, R. Spycher, B. Bourqui, A. Catan, P. Ruterana, P. A. Stadelmann and P. A. Buffat, *J. Microsc. Spectrosc. Electron., 14* (1989) 407.
7 J. Cibert, P. M. Petroff, D. J. Werder, S. J. Pearton, A. C. Gossard and J. H. English, *Appl. Phys. Lett., 49* (1986) 223.
8 H. Leier, A. Forchel, G. Hörcher, J. Hommel, S. Bayer, H. Rothfritz, G. Weimann and W. Schlapp, *J. Appl. Phys., 67* (1990) 1805.
9 E. Kuphal, *J. Cryst. Growth, 67* (1984) 441.
10 P. A. Stadelmann, *Ultramicroscopy, 21* (1987) 131.

Materials Science and Engineering, B21 (1993) 281–283

Vacancy controlled interdiffusion in III–V heterostructures

W. P. Gillin, I. V. Bradley, S. S. Rao, K. P. Homewood, B. J. Sealy and L. K. Howard
Department of Electronic and Electrical Engineering, University of Surrey, Guildford, Surrey, GU2 5XH (UK)

A. D. Smith and A. T. R. Briggs
BNR Europe Ltd, London Road, Harlow, Essex, CM17 9NA (UK)

Abstract

Interdiffusion of both the group III and group V sublattices has been studied in the InGaAs/GaAs and InGaAs/InGaAsP systems respectively using photoluminescence and consecutive annealing. By measuring the diffusion coefficients between the temperatures of 1050 °C to 600 °C we have been able to determine the activation energies for diffusion in both sublattices and have found them to be equal (for temperatures above 650 °C) at 3.7 eV. From the effects of gallium and arsenic implantation on the interdiffusion of InGaAs/GaAs we have established that the diffusion is controlled by vacancies on both sublattices, and that except in the case of the group V diffusion below 650 °C the controlling vacancies are thermally created.

1. Introduction

The thermal stability of III-V heterostructures has long been a subject of much discussion, particularly in the GaAs/AlGaAs system. However, after many years there is still little agreement on the magnitude of activation energies for interdiffusion [1–5] and, due to this uncertainty in the activation energy, there is little consensus on the mechanisms responsible for interdiffusion. Within one material system there should only be discrete values for the activation energy of diffusion (corresponding to distinct physical processes), although the activation energy at any given temperature will depend on which process is dominant. Part of the reason for the wide range of activation energies measured is the use of small data sets, with many authors quoting an activation energy measured over narrow temperature ranges, often only about 100 °C [2, 3]. Whilst the absolute diffusion coefficients measured in such experiments may be of use when compared with those determined in other experiments in different temperature ranges, the measurement of the activation energies is unreliable.

In our experiments we have measured the activation energy for diffusion in different materials and under different conditions (such as following ion implantation) over a temperature range from 1050 °C to 600 °C. Whilst we could have fitted slightly different least squares fits to each of our data sets in a given material system, we believe that changes in the activation energy of 0.2 eV between two nominally identical wafers are physically unrealistic, and we have therefore used the best fit to all our data to obtain the activation energy and have attributed any deviations to the errors present in these experiments. Using this technique we have been able to establish that perturbations in the measured diffusion are due to changes in the pre-factor rather than to different processes.

2. Experimental method

The InGaAs/GaAs samples used in these experiments were grown by MBE at the DRA Malvern, whilst the $In_{0.66}Ga_{0.33}As/In_{0.33}Ga_{0.66}As_{0.7}P_{0.3}$ samples were grown by MOCVD at BNR Europe Ltd. Details of the growth are given in refs. 6 and 7 respectively. For the InGaAs/InGaAsP samples the structures were designed so that there was no concentration gradient on the group III sublattice to drive diffusion. Therefore, any change in the photoluminescence measured with annealing could be modelled using only diffusion on the group V sublattice without having to make any assumption as to the relative importance of the diffusion on the group III sublattice.

In order to determine the diffusion coefficients, samples from a single wafer were consecutively annealed at a given temperature with photoluminescence measurements performed after each anneal. The shift in photoluminescence observed was converted into a diffusion length by modelling the diffusion, assuming that Fick's second law was obeyed, with a diffusion coefficient that was independent of concentration, and then solving the Schrödinger equation for

0921-5107/93/$6.00

© 1993 - Elsevier Sequoia. All rights reserved

the resulting well shape. The diffusion coefficient was determined from the gradient of a plot of diffusion length squared against anneal time. This method has the advantage over performing a single anneal in that the diffusion coefficients obtained are more accurate as they are effectively averaged over up to ten data points, and, more importantly, because the diffusion is measured as a function of anneal time it is possible to observe time dependent effects following ion implantation. Further details of the diffusion experiments and the method used to analysis the results are given in refs. 6 and 7.

3. Results and discussion

Figure 1 shows a graph of the diffusion length squared against anneal time for a 100 Å $In_{0.2}Ga_{0.8}As$/GaAs single quantum well annealed at 900 °C (i) with no implant, (ii) following an implant of 10^{13} As^+cm^{-2} at 260 keV and (iii) a 10^{13} Ga^+cm^{-2} implant at 255 keV. These ion energies were chosen to place the peak of the atomic profiles at the centre of the quantum well. It can be seen that for the unimplanted sample all the data points lie on a straight line which passes through the origin. From this we can determine that the diffusion coefficient is constant with time and, in addition, it proves our assumption that the diffusion obeys Fick's law. However, following the gallium implantation, a very different behaviour is observed. The line obtained is still straight, but now passes through a point on the ordinate corresponding to a diffusion length of approximately 37Å. From the gradient of this line the diffusion coefficient is still identical to that measured for the unimplanted material. However, this result shows the need to measure the diffusion as a function of time. Had only a single anneal been performed, then the diffusion coefficient measured would be inaccurate and appear to be enhanced. The size of the offset has been found to be independent of the anneal temperatures used, and even at 750 °C the fast diffusion has always occurred during the first anneal. The effect of the collisional mixing caused by the ion beam has been modelled [6, 8] and has been shown to be too small to account for the observed offset. We therefore suggest that enhanced diffusion occurs during the first anneal as a result of the implantation damage which is subsequently annealed out.

Following arsenic implantation a very different behaviour is observed. There is still an intercept on the ordinate equal in magnitude to that measured for gallium implantation. This is expected as the damage profiles for the two implants are almost identical. However, following this initial intermixing there is a region of enhanced interdiffusion where the diffusion coefficient measured from the slope of the graph is an order of magnitude greater than that determined for the unimplanted sample. Following this initial fast region, the diffusion coefficient reduces towards that measured for the unimplanted samples.

An Arrhenius plot of the data obtained for the unimplanted, gallium implanted and fast diffusion regime in the arsenic implanted samples is shown in Fig. 2. From this it can be seen that the activation energy for the diffusion is 3.7 eV for all the samples,

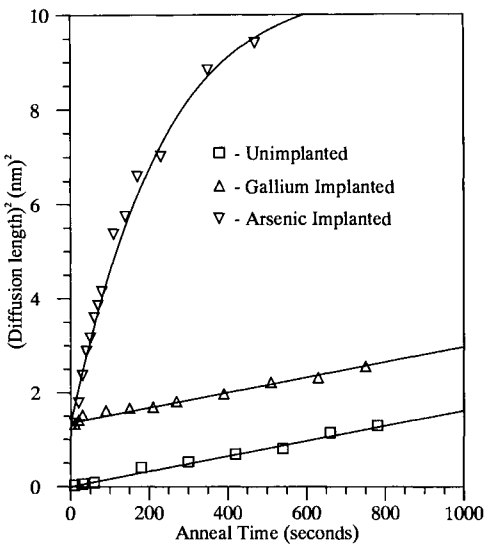

Fig. 1. A graph of diffusion length squared against anneal time for an unimplanted and gallium and arsenic implanted 100 Å $In_{0.2}Ga_{0.8}As$ quantum well in GaAs annealed at 900 °C.

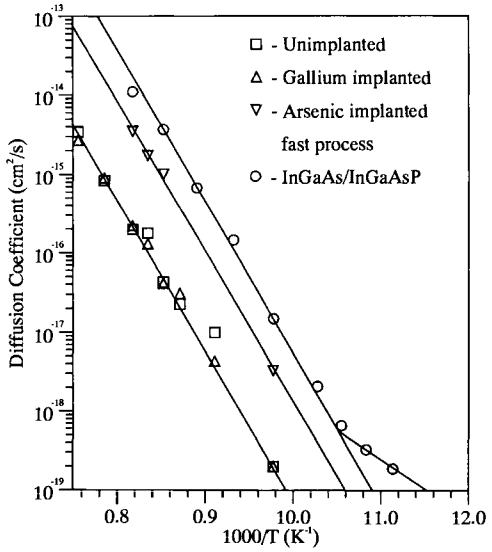

Fig. 2. An Arrhenius plot of the diffusion coefficients measured for $In_{0.2}Ga_{0.8}As$/GaAs with and without implantation and for an unimplanted InGaAs/InGaAsP quantum well.

even where there is an enhanced diffusion coefficient, and that the enhancement is caused by an increase in the pre-factor for the diffusion. In order to explain the relative behaviour of the different implants we propose that the diffusion is governed by the concentration of group III vacancies. Introducing excess gallium atoms is not expected to cause an increase in the group III vacancy concentration as gallium interstitials move onto group III lattice sites during annealing. However, following arsenic implantation, as the arsenic atoms move on to group V lattice sites, group III vacancies will be produced which can enhance the interdiffusion on the group III sublattice as they diffuse away from the implanted region. This is driven because in thermodynamic equilibrium $[V_{Ga}][V_{As}]$ has to remain constant, and so the arsenic atoms moving on to lattice sites reduce the concentration of group V vacancies and thus cause an increase in the group III vacancy concentration.

From similar annealing experiments on the InGaAs/InGaAsP system, we have also determined that plots of diffusion length squared against anneal time give straight lines which pass through the origin, and from these the diffusion coefficients were determined. This data is also contained in the Arrhenius plot given in Fig. 2. It can be seen that at temperatures between 650 °C and 950 °C, the activation energy for the group V diffusion is identical, within experimental error, to that determined for the group III diffusion. This is not unexpected if the mechanism for the diffusion is via vacancies on the group V sublattice, as the bonding for the two sublattices is identical and therefore the energy required to form a vacancy and the energy for that vacancy to move should be the same. However, the pre-factor for the group V diffusion is two orders of magnitude greater than that determined for the group III interdiffusion. This may be due to a number of factors such as the growth method or the substrate type (GaAs for the group III and InP for the group V). Also (from Fig. 2) at temperatures below 650 °C, a low activation energy process becomes significant with an activation energy of about 1.7 eV. This value is approximate due to the extremely small temperature range over which it has been determined. This low activation energy process can also be explained in terms of a vacancy diffusion process. If the sample is in thermal equilibrium then, at any given temperature, there is a concentration of thermally created vacancies. Provided that this thermally created vacancy concentration exceeds the grown-in concentration of vacancies, the activation energy for diffusion will consist of an energy of creation and an energy of diffusion. However, if the temperature is reduced to a value where the thermally created vacancy concentration is less than the grown-in concentration, the diffusion will be governed by the grown-in vacancies and the activation energy measured will correspond to the energy required to move a vacancy. We believe that this is the explanation for the results for the InGaAs/InGaAsP samples below 650 °C. Thus, the vacancy creation and mobility terms for the interdiffusion energy can be separated to produce a vacancy creation energy close to 2 eV. This is in agreement with the theoretically predicted value of Van Vechten [9].

4. Conclusions

We have shown that in InGaAs/GaAs and InGaAs/InGaAsP materials the diffusion mechanism for group III and group V diffusion, respectively, is governed by vacancies on the respective sublattices. We have also shown that in the InGaAs/InGaAsP system below 650 °C the concentration of grown-in vacancies becomes significant and that they govern the diffusion coefficient for intermixing. Further studies to reduce this grown-in vacancy concentration could result in a lowering of the prefactor for this process and thus improve thermal stability at low temperatures.

Acknowledgements

The authors would like to thank Dr D.J. Dunstan for many discussions and support during this work, and the SERC and DTI for help in funding aspects of the project.

References

1 P. Mei, H.W. Yoon, T. Venkatesan, S.A. Schwarz and J.P. Harbison, *Appl. Phys. Lett.*, *50* (25) (1987) 1823.
2 L.J. Guido, N. Holonyak, Jr., K.C. Hsieh, R.W. Kaliski, W.E. Plano, R.D. Burnham, R.L. Thornton, J.E. Epler and T.L. Paoli, *J. Appl. Phys.*, *61* (4) (1987) 1372.
3 T.E. Schlesinger and T. Kuech, *Appl. Phys. Lett.*, *49* (9) (1986) 519.
4 R.M. Cohen, *J. Electron. Mater.*, *20(6)* (1991) 425.
5 L.L. Chang and A. Koma, *Appl. Phys. Lett.*, *29* (3) (1976) 138.
6 I.V. Bradley, W.P. Gillin, K.P. Homewood and R.P. Webb, *J. Appl. Phys.*, *73* (4) (1993) 1686.
7 W.P. Gillin, S.S. Rao, I.V. Bradley, K.P. Homewood, A.D. Smith and A.T.R. Briggs, *Appl. Phys. Lett*, to appear in *63* (6), August 1993.
8 W.P. Gillin, I.V. Bradley, K.P. Homewood and R.P. Webb, *Solid State Communications*, *85* (3) (1993) 197.
9 J.A. Van Vechten, *J. Electrochem. Soc.*, *122* (3) (1975) 419.

Materials Science and Engineering, B21 (1993) 284–287

Simulation of lateral Al recoil atoms and damage defects gradients in a GaAs/GaAlAs quantum well created by masked ion implantation

M. M. Faye
LSCES/UCAD, Département de Physique, Fann-Dakar (Senegal)
C. Vieu
LMM/CNRS, 196 Ave H. Ravera, 92225 Bagneux (France)
L. Laânab, J. Beauvillain and A. Claverie
CEMES/CNRS, BP 4347, 31055 Toulouse (France)

Abstract

We have studied through computer simulations the effects of Ga^+ ion implantation through masked GaAlAs/GaAs/GaAlAs heterostructures presenting one single quantum well. The spatial distribution of the Al atoms responsible for the energy gap modifications has been calculated. Depth and lateral profiles in the quantum well of the Al recoil atoms extracted from the two dimensional distribution have elicited different types of situations encountered in collision mixing experiments. Finally, this work shows that computer simulation is of great importance for selecting the parameters to realize lateral nano-structures such as quantum wires or dots.

1. Introduction

Ion implantation is able to modify the shape and the composition of the layers at the heterointerfaces of semiconductor heterostructures. The layer disordering induced by the ion beam can modify the energy gap [1]. The great advantages of ion implantation, compared with other sources of disordering, are its reproducibility and the ability to govern the implantation parameters and so control the mixing rate. Localized ion implantation is a powerful tool for producing nanostructures (<50 nm) free from defects sandwiched between two highly irradiated areas [2]. Selective mixing is achieved by using a masking layer or by scanning a focused ion beam on to the surface of the target [2]. If a constituent element of the heterostructure is implanted (*e.g.* Ga or Al ions), a collision-induced mechanism, mainly caused by implantation damage, can take place [3]. So, to achieve good ballistic mixing in the GaAs/(Ga,Al)As system it is more judicious to use Ga ions because of their good nuclear efficiency with respect to the collisional mechanism.

In this paper we report on the simulation of Ga^+ ions implanted through a mask. Special attention was paid to the distribution of Al atoms in the structure after implantation which were responsible for the energy gap modulation. The structures investigated contained $Ga_{0.7}Al_{0.3}As/GaAs/Ga_{0.7}Al_{0.3}As$ single quantum wells (QW) of 4, 2 and 1 nm. We calculated the beam response function of Al recoil atoms and Al target vacancies to get the two-dimensional distribution of Al atoms after implantation. Depth Al profiles away from the mask edge and lateral Al profiles in the QW have been extracted from the two-dimensional distribution. Finally we show that, with a good choice of implantation parameters, it is possible to modify the heterostructure in predetermined proportions. Of course, the behavioral patterns depicted here are limited to a pure collisional disordering mechanism, no annealing of the defects is taken into account. However, it has been shown for a high dose regime ($>1\times10^{14}$ ions/cm^2) that all mixing occurs during implantation; the diffusion of the defects are frozen during annealing owing to their high concentration [3].

2. Point response function

Determination of the two-dimensional distribution begins with the calculation of the point response function which is defined by Giles and Gibbons as the result of the implantation at a single point [4]. This point response function can be calculated for implanted ions, substrate atom displacement or any other appropriate quantity. Several approaches have been proposed to calculate the point response func-

0921-5107/93/$6.00

© 1993 – Elsevier Sequoia. All rights reserved

tion. In the first approach, two-dimensional distributions are made with Gaussian profiles or with hybrid Edgeworth-Gaussian or Pearson-Gaussian profiles [5,6]. This approach has some limitations when the substrate is made of several planar layers. Monte Carlo simulations are also used to calculate the point response function, but this calculation requires a large number of ions to determine two-dimensional distributions.

When the substrate is made of several layers, or when the two-dimensional Monte Carlo code is not available, the third alternative, proposed by Giles and Gibbons [4], can be used. In this method, the point response function is taken to be the product of the vertical and the lateral projections. In our studies we estimated the point response function using the Giles and Gibbons method and the 1D-TRIM Monte Carlo computer code [7].

3. Two-dimensional distribution

The calculation of the two-dimensional distribution beneath an implantation mask is performed by convoluting the point response function with a function describing the geometry and opacity of the masking layer. This convolution can be calculated by analytical or numerical methods. The analytical solution is possible when an analytical point response function is available and when the masking layer is opaque with abrupt openings. Otherwise, it is better to use directly the point response function as given by computer simulation. This function is isolated using a grid with the same step in the target and point response function. The point response function is positioned in all the cells of the grid corresponding to the implanted surface. The calculation of the two-dimensional distribution then presents two levels of complexity depending on the nature of the masking layer. If the masking layer is opaque with abrupt openings the same response function is used at each grid point along the surface. If the geometry of the masking layer is arbitrary, the point response function is recomputed at each point across the surface.

In this work we studied the simple situation, *i.e.* the target had the same structure at each point along the surface apart from the presence of an abrupt and opaque mask, hence the same point response function is used. Figure 1 shows the two-dimensional distribution of the Al recoil atoms induced by the implantation of a 50 keV Ga^+ ion beam with a dose of 1×10^{14} ions/cm^2 in a 4 nm wide QW covered with an abrupt step-type mask of width 80 nm. For areas away from the edges, total overlap of the point response function induces a depth dependence the same as that observed for homogeneous implantations.

4. Heterointerface mixing by ion implantation

Figure 2 shows the total Al concentration for individual QW of 1, 2 and 4 nm for a 50 keV, 1×10^{14} Ga^+per cm^2 implantation. The total Al concentration is taken as the substrate Al concentration plus the Al recoil atoms minus the Al target vacancy concentrations.

The three QW show a high degree of mixing, but the heterointerfaces do not mix to the same extent. For this set of simulations, the interface close to the surface is more mixed than the deeper one. A decrease in the width of the QW leads to homogenization of the mixing. The asymmetry of the Al profile in the 1 nm QW (Fig. 2(c)) appears lower than in the 2 nm (Fig. 2(b)) or 4 nm (Fig. 2(a)) QW. The narrower the QW, the greater the mean Al concentration in the QW.

In many experimental studies of ion-induced intermixing, an error function shape is assumed to describe

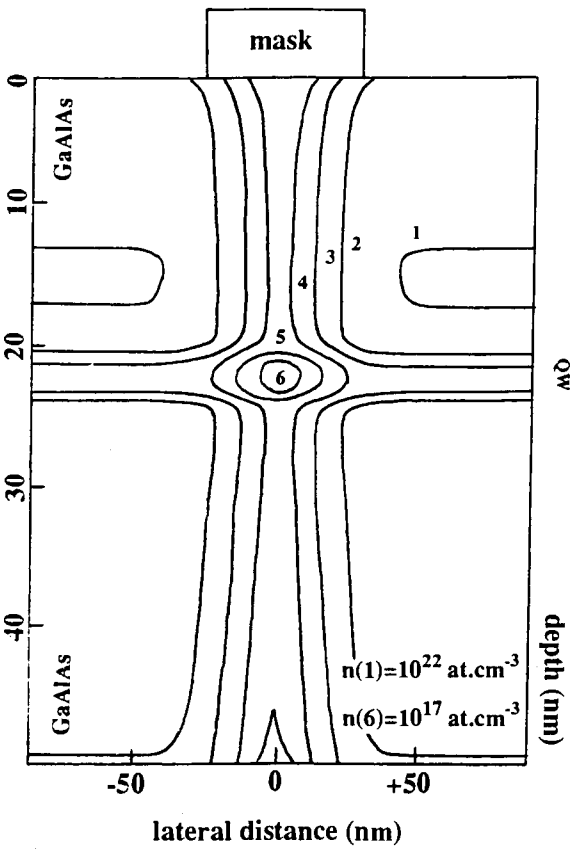

Fig. 1. Two-dimensional distribution of Al recoil atoms induced by the implantation of a 50 keV Ga^+ ion beam in a $Ga_{0.7}Al_{0.3}As$/GaAs(4 nm)/$Ga_{0.7}Al_{0.3}As$ QW covered with an abrupt and opaque mask.

the modulation of the Al concentration across the heterointerfaces [8]. Our results suggest that two different interdiffusion lengths should be considered to account for the differential disordering at each interface. The profiles obtained by our simulations indicate an interdiffusion length of about 0.5 nm. This value is lower than the experimental one extracted from photoluminescence measurements after annealing, for similar implantation conditions, which is about 1 nm [3].

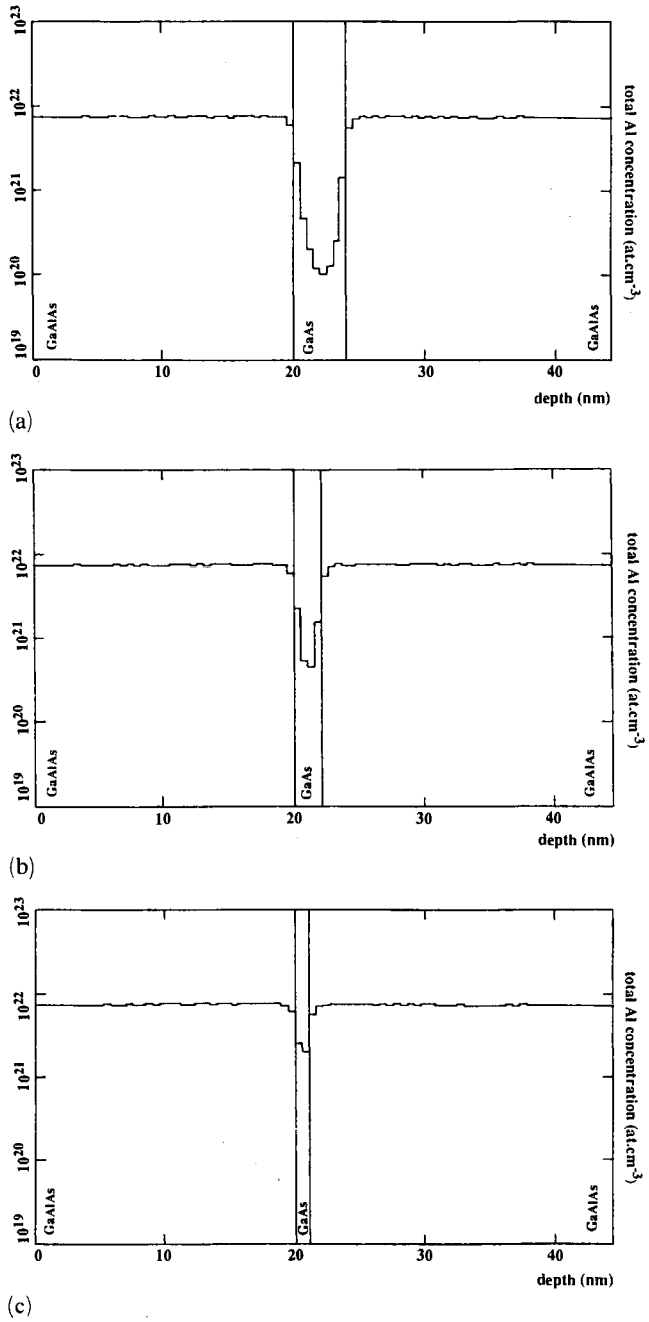

Fig. 2. A total Al depth profile obtained away from an abrupt and opaque mask edge owing to the implantation of a 50 keV Ga^+ ion beam with a dose of 1×10^{14} ions/cm^2 in $Ga_{0.7}Al_{0.3}As$/GaAs/$Ga_{0.7}Al_{0.3}As$ QW of: (a) 4 nm, (b) 2 nm and (c) 1 nm.

The comparison suggests that at this dose (1×10^{14} ions/cm^2) some interdiffusion is generated, during annealing, by short range diffusion of the defects. Out of the QW areas the Al profile presents small variations around the substrate Al concentration before implantation. A significant decrease in total Al concentration is observed close to the interface of the QW. For an implantation dose of 1×10^{15} ions/cm^2 the mean Al concentration in the QW after implantation reaches a value of 15%; this indicates strong disordering.

The diffusion of the implanted ions under the mask edges is responsible for the lateral extension of the Al recoil atoms in the part of the structure situated beneath the mask. Figure 3 shows the mean Al concentration in a 1 nm QW along the axis perpendicular to the implantation mask. We used a 50 keV Ga^+ ion beam with a dose of 1×10^{14} ions/cm^2 and the implantation mask is an abrupt step-type mask which is 100 nm wide. At the implantation mask edge the Al concentration is half of its value elsewhere. The Al concentration reaches 1.5% of its maximum value in the QW at about 20 nm from the mask edge. The width of the unmixed area situated beneath the mask depends on the ion beam and the implantation mask parameters. Decreasing the mask width or increasing the implantation dose leads to a decrease of the width of the unmixed area situated beneath the mask. In reported experiments on the fabrication of quantum wires by masked implantation, the lateral Al profile is often described by an error function [9]; we obtained similar results. For a Ga^+ implantation at 50 keV, Vieu *et al.* obtained a lateral interdiffusion length of 10 nm which characterizes the extension of the lateral Al profile under the mask [9]. Figure 3 gives a value of 8.5 nm which is in good agreement and indicates that the

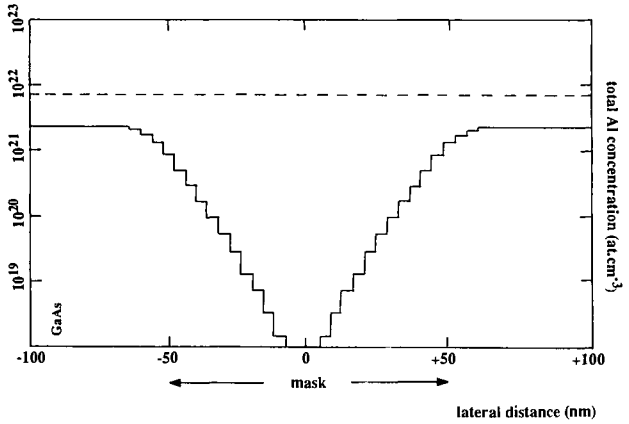

Fig. 3. Lateral profile of the total Al concentration after implantation of a 50 keV Ga^+ ion beam with a dose of 1×10^{14} ions/cm^2 in a $Ga_{0.7}Al_{0.3}As$/GaAs(1 nm)/$Ga_{0.7}Al_{0.3}As$ QW covered with an abrupt and opaque mask of 100 nm width. The dotted line indicates the Al concentration in the GaAlAs area before the implantation.

lateral interdiffusion of the defects during annealing is limited in these experiments.

5. Conclusion

We studied computer simulations of the implantation of Ga ions on masked GaAlAs/GaAs/GaAlAs heterostructures containing a QW. We estimated the point response function of the Al recoil atoms and the Al target vacancies created by the implantation. Two-dimensional total Al distribution in 4, 2 and 1 nm QW covered by an abrupt step-type mask were calculated and the depth distribution away from the mask edge and the lateral distribution of Al atoms in the QW were studied.

Our results tend to underestimate the mixing rate which is commonly observed experimentally after implantation. This suggests that some interdiffusion is activated by a short range diffusion of the defects during annealing. The simulations demonstrate that the interfaces of a QW present different mixing rates; especially in wide QW situations. The lateral extension of the mixing in the QW has also been investigated, our results are in good agreement with recent experiments on the fabrication of quantum wires by masked implantation.

Acknowledgments

This work was partly supported by the Délégation aux Affaires Scientifiques et Techniques, Sénégal.

References

1 D.G. Deppe and N. Holonyak, Jr., *J. Appl. Phys., 64* (1988) 5930.
2 M.M. Faye, L. Laânab, J. Beauvillain, C. Vieu, G. Benassayag and A. Claverie, *Proc. Mat. Res. Soc. Beams-Solids Interactions, Boston*, 1992, p. 783.
3 C. Vieu, M. Schneider, B. Descouts, Y. Gao, R. Planel and H. Launois, *J. Appl. Phys., 70* (1991) 1433.
4 M.D. Giles and J.F. Gibbons, *J. Electrochem. Soc., 132* (1985) 2476.
5 M.M. Faye, J. Beauvillain, Ph. Salles, L. Laânab, A. Yahia Messaoud, A. Martinez and A. Claverie, *J. Appl. Phys., 72* (1992) 5117.
6 A.M. Mazzone and G. Rocca, *IEEE Trans. Comput. Aided Design CAD-3*, 1984, p. 64.
7 J.P. Biersack and L.G. Haggmark, *Nucl. Instrum. Methods Phys. Res., 174* (1980) 257.
8 T.E. Schlesinger and T. Kuech, *Appl. Phys. Lett., 49* (1986) 519.
9 C. Vieu, M. Schneider, G. Benassayag, R. Planel, L. Birotheau, J.Y. Marzin and B. Descouts, *J. Appl. Phys., 71* (1992) 5012.

Strained InAs/$Al_xGa_{0.48-x}In_{0.52}As$ heterostructures: a tunable quantum well materials system for light emission from the near-IR to the mid-IR

Eric Tournié*
Max-Planck-Institut für Festkörperforschung, Heisenbergstraße 1, D-W-7000 Stuttgart 80 (Germany)

Klaus H. Ploog
Paul-Drude-Institut für Festkörperelektronik, Hausvogteiplatz 5–7, D-O-1086 Berlin (Germany)

Patrick Grunberg, Shata Kadret and André Joullié
Equipe de Microoptoélectronique de Montpellier (EM2), URA CNRS 392, Université de Montpellier II, U.S.T.L. Place Eugène Bataillon, F-34095 Montpellier cedex 5 (France)

Franz Daiminger, L. Butov** and Alfred Forchel
Technische Physik, Universität Würzburg, Am Hubland, D-W-8700 Würzburg (Germany)

Abstract

We report on spontaneous and stimulated emission from strained InAs quantum wells (QWs) embedded in an $Al_xGa_{0.48-x}In_{0.52}As$ matrix grown on InP substrates by solid-source molecular-beam epitaxy. By adjusting the QW width between 2 and 23 monolayers and/or the barrier composition between $Al_{0.48}In_{0.52}As$ and $Ga_{0.47}In_{0.53}As$, the low temperature photoluminescence can be tuned between 1.0 μm and 2.2 μm. Efficient room temperature luminescence is achieved up to 2.4 μm which is the longest wavelength reported for QWs grown on InP substrates. Finally, we demonstrate the first stimulated emission near 1.3 μm and 1.8 μm at 80 K in this materials system. These results thus enlarge the wavelength range of applications achievable with InP-based materials.

1. Introduction

The study of strained-layer heterostructures (SLHs) is currently attracting much attention because in addition to revealing fundamentals of epitaxy they exhibit unique physical properties (see for example ref. 1) which find applications in microwave as well as optoelectronic devices. One of the most remarkable benefits of SLHs manifests itself in the quantum well (QW) laser field where the peculiar valence-band configuration of compressively strained layers [2, 3] results in superior laser performance compared with lattice-matched devices [4]. The SL-QW systems investigated for laser applications are mostly GaInAs/GaAs, GaInP/AlGaInP/GaAs, GaInAs/GaInAsP/InP and, to a much lesser extent, GaInAs/AlInAs/InP [4]. A particular configuration of the last example, namely strained InAs QWs confined by $Al_{0.48}In_{0.52}As$ lattice matched to InP, has theoretically been credited with a high potential for laser emission near 1.5 μm [5]. In addition, the $Al_xGa_{0.48-x}In_{0.52}As$ solid solution is also lattice matched to InP for any value of x ($x \leqslant 0.48$) and its room temperature (RT) band gap energy can be tuned linearly from 0.75 eV ($x=0$) to 1.45 eV ($x=0.48$). It follows that strained InAs QWs confined by $Al_xGa_{0.48-x}In_{0.52}As$ layers can in principle give emission from the near-IR to the mid-IR, depending on the QW width and barrier composition. However, the large lattice mismatch ($\varepsilon \approx 3.2\%$) between InAs and InP renders the epitaxy of high-quality SL-QWs very difficult and such laser structures have not yet been investigated.

In this work we present a photoluminescence (PL) spectroscopy study of InAs QWs embedded in an $Al_xGa_{0.48-x}In_{0.52}As$ matrix grown on InP substrates by a modified solid-source molecular beam epitaxy (MBE) technique. We show that the spontaneous QW emission can be tuned effectively from the near-IR to the mid-IR wavelength range. In addition, we report on the first stimulated emission obtained near 1.3 μm and 1.8 μm at 80 K with this materials system.

*Present address: Fachbereich Materialwissenschaft, Technische Hochschule Darmstadt, D-W-6100 Darmstadt, Germany.
**Present address: Solid-State Physics Institute of the Russian Academy of Sciences, Chernogolovka 142432, Russia Federation.

0921-5107/93/$6.00
© 1993 – Elsevier Sequoia. All rights reserved

This paper is organized as follows. The sample structures and growth procedure are described in Section 2. The spontaneous emission results are reported and analysed in Section 3 while Section 4 deals with the stimulated emission measurements. Finally, a conclusion is drawn in Section 5.

2. Growth procedure

The samples under investigation were InAs single or multiple quantum wells (SQWs or MQWs) embedded in an $Al_xGa_{0.48-x}In_{0.52}As$ matrix. The SQWs were grown on n^+ (100) oriented InP substrates by solid-source MBE in a Riber 32P system. First, a 450–550 nm thick $Al_xGa_{0.48-x}In_{0.52}As$ buffer layer was grown at 450 °C under conventional As-stable conditions with an As_4 flux of $BEP_{As_4} \approx (5-10)\times 10^{-6}$ Torr and an As_4-to-group III flux ratio of approximately 15. Then the growth was stopped and the temperature was decreased to 380 °C for epitaxy of the InAs QW which was performed under virtual-surfactant conditions [6], *i.e.* the InAs growth occurred under In-stable conditions with $BEP_{As_4} \approx (2-5)\times 10^{-7}$ Torr and an As_4-to-In flux ratio of approximately 0.6. The InAs QW width varied between 2 and 23 monolayers (ML) in different samples. We have previously shown that this growth technique allows superior quality QWs to be obtained and enhances the critical thickness before defect generation [7]. Then, an approximately 160 nm thick $Al_xGa_{0.48-x}In_{0.52}As$ layer and an approximately 20 nm thick $Ga_{0.47}In_{0.53}As$ cap layer were grown at 450 °C under the same As_4 flux conditions as for the buffer layer. The MQWs were grown on (100) oriented semi-insulating InP substrates. The MQW structures, made of 3–10 periods of alternating 4–6 ML InAs/25–30 nm $Al_xGa_{0.48-x}In_{0.52}As$ layers, were sandwiched between buffer and cap layers as for the SQWs. The InAs films were also grown under virtual-surfactant conditions at 380 °C. The first 8 nm of the $Al_xGa_{0.48-x}In_{0.52}As$ barrier was grown at 380 °C under the same As_4 flux as for the buffer layer. Then the growth was stopped and the substrate temperature increased to 450 °C to complete the growth of the barrier layer. High-resolution double-crystal X-ray diffraction (HRXRD) was used to confirm that the $Al_xGa_{0.48-x}In_{0.52}As$ layers were lattice matched to the InP substrates and that the epitaxial structures were actually pseudomorphic.

3. Spontaneous emission

For the PL experiments the samples were mounted in an He-flow cryostat, the temperature of which was regulated between 4 K and 300 K. The excitation source was the 647.1 nm line of a Kr^+ laser. The emitted signal was focused on the entrance slit of a 1 m single pass spectrometer and detected with a cooled Ge or a cooled InAs detector. A standard lock-in technique was used as an amplifier.

In Figs. 1 and 2 we have plotted the PL spectra taken at low temperature (6 K) from representative $InAs/Al_{0.48}In_{0.52}As$ (Fig. 1) and $InAs/Ga_{0.47}In_{0.53}As$ (Fig. 2) SQWs. Note that they span the 1.0–2.2 μm

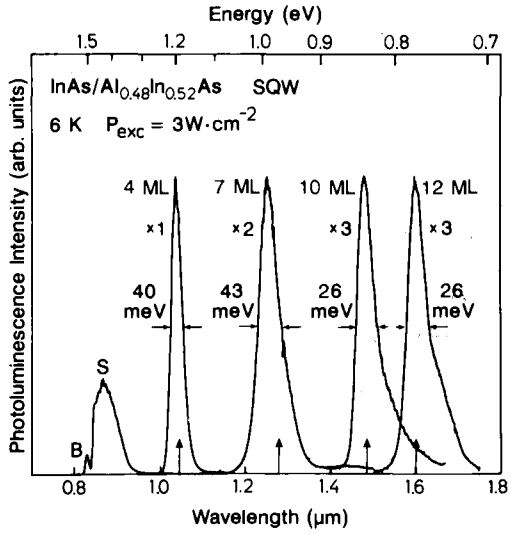

Fig. 1. Low temperature (6 K) PL spectra of $InAs/Al_{0.48}In_{0.52}As$ SQWs. The vertical arrows indicate the calculated positions of the e_1–hh_1 transitions.

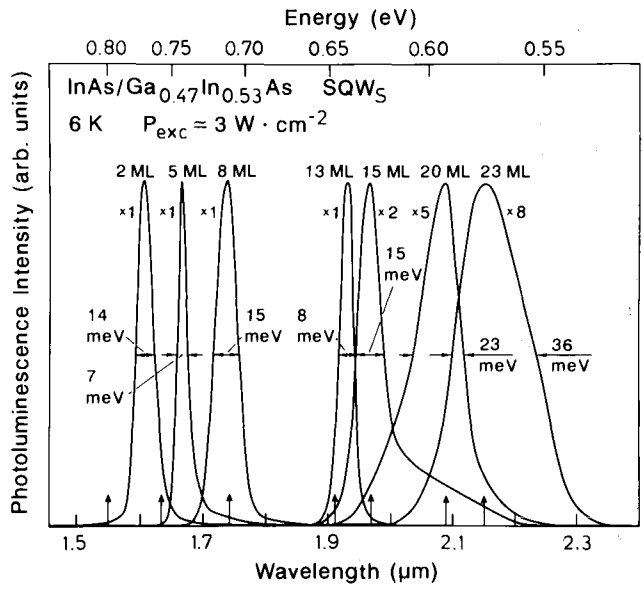

Fig. 2. Low temperature (6 K) PL spectra of $InAs/Ga_{0.47}In_{0.53}As$ SQWs. The vertical arrows indicate the calculated positions of the e_1–hh_1 transitions.

wavelength range. The long-wavelength shoulders observed from the 10 ML and 12 ML wide QWs in Fig. 1 and from the 15 ML wide QW in Fig. 2 saturate when the excitation power is increased, which identifies them as impurity-or defect-related emission features. The peaks labelled B and S in Fig. 1 arise from the $Al_{0.48}In_{0.52}As$ barrier layer and from the highly doped InP substrate respectively. The vertical arrows in Figs. 1 and 2 indicate the positions of the transitions between the confined electron state e_1 and the confined heavy-hole state hh_1 calculated with the envelope function model [8] assuming fully strained InAs QWs and using the parameters given in Table 1. Excellent agreement between calculated and experimental values is obtained except for the thinnest wells which are more sensitive to any interface fluctuation. However, when increasing the QW width above 8 ML in the InAs/$Al_{0.48}In_{0.52}As$ system and above 15 ML in the InAs/$Ga_{0.47}In_{0.53}As$ system the PL line broadens and becomes less intense (Figs. 1 and 2). This result is indicative of a slight structural deterioration as also observed by HRXRD. Nevertheless, the excellent agreement between experimental and calculated positions indicates that even the widest QWs are elastically strained, as confirmed by transmission electron microscopy [7]. It has to be noted that in Fig. 1 the barrier emission is much less intense than the QW emissions. In addition in Fig. 2 no barrier emission can be detected. Similar observations have also been reported with the InAs/$Al_{0.48}In_{0.52}As$ [11] and InAs/InP [12] systems. This finding points to the fact that the carrier-trapping process by the InAs SQWs is very efficient, even for SQWs as narrow as 2 ML, which is an important feature in view of the fabrication of light-emitter devices. Another general comment to be made is that the PL lines are narrower and more intense when the barrier material is $Ga_{0.47}In_{0.53}As$ than when it is $Al_{0.48}In_{0.52}As$ (Figs. 1 and 2). This is a direct consequence of the lower quality of the $Al_{0.48}In_{0.52}As$ ternary alloy compared with the $Ga_{0.47}In_{0.53}As$ ternary alloy. In fact, for comparable background doping (approximately 10^{15}–10^{16} cm^{-3}) the PL line of a bulk-like $Al_{0.48}In_{0.52}As$ layer is broader than the PL line of a bulk-like $Ga_{0.47}In_{0.53}As$ layer (approximately 30 meV *vs.* approximately 10 meV). Also, the deeper well formed with an $Al_{0.48}In_{0.52}As$ barrier layer than with a $Ga_{0.47}In_{0.53}As$ barrier layer results in a more pronounced value of broadening induced by a monolayer-fluctuation of the well width. However, owing to the growth conditions employed for the InAs QWs, we have achieved the narrowest PL line ever reported for InAs/$Al_{0.48}In_{0.52}As$ SQWs [13] as well as for any InAs QW grown on InP substrates [14], which is clear proof of the superior quality of our samples.

To evaluate further the potential of the InAs/$Al_xGa_{0.48-x}In_{0.52}As$ QW materials system for light-emitter application, we studied the variation of the PL emission as a function of the temperature. We observe that when the QWs are confined by $Al_{0.48}In_{0.52}As$ RT emission is obtained from QWs up to 7 ML wide. However, when the barrier material is $Ga_{0.47}In_{0.53}As$ we obtain RT emission from all samples, *i.e.* for InAs QWs up to 23 ML wide. Again, the different behaviour observed with the two kinds of barrier material reveals the difference in their quality. As an example, we show in Fig. 3 the PL spectra taken at RT from various 5 ML InAs/$Al_xGa_{0.48-x}In_{0.52}As$ 10 period MQWs. For the same QW width, changing the barrier composition from $Al_{0.48}In_{0.52}As$ to $Ga_{0.47}In_{0.53}As$ allows the emitted wavelength to be varied from 1.2 μm to 1.9 μm (Fig. 3). Also the more Ga the barrier contains, the brighter the PL line is. Furthermore, we note that the use of

TABLE 1. Parameters[a] used to calculate the e_1–hh_1 transition energies for strained InAs/$Al_xGa_{0.48-x}In_{0.52}As$ quantum wells, assuming $Q_c = \Delta E_c/\Delta E_g = 0.75$[b]

Parameter	InAs	$Ga_{0.47}In_{0.53}As$	$Al_{0.48}In_{0.52}As$
E_g (6 K) (eV)	0.47 (strained)	0.81	1.51
E_g (300 K) (eV)	0.41 (strained)	0.74	1.45
m_e (m_0)	0.023	0.041	0.071
m_{hh} (m_0)	0.26	0.33	0.35

[a]All values from ref. 9.
[b]Ref. 10.

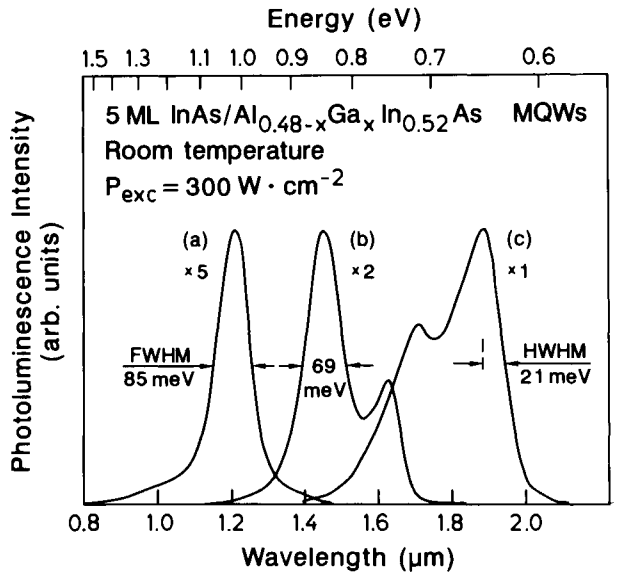

Fig. 3. Room temperature PL spectra of 5 ML InAs/$Al_xGa_{0.48-x}In_{0.52}As$ 10 period MQWs: (a) $Al_{0.48}In_{0.52}As$ barrier, (b) $Al_{0.24}Ga_{0.24}In_{0.52}As$ barrier, (c) $Ga_{0.47}In_{0.53}As$ barrier.

MQWs greatly enhances the PL efficiency, particularly at RT. This finding is easily explained in terms of retrapping of the carriers thermally spilled out of a well by the neighbouring wells. Finally, we show in Fig. 4 the RT spectrum taken from the widest (23 ML) InAs/$Ga_{0.47}In_{0.53}As$ SQW sample. Although the QW line is rather broad, its peak position (2.38 μm) fits very well with the calculated value indicated by the vertical arrow (any structural relaxation of this QW would give a red-shift by as much as 0.28 μm). This wavelength of 2.38 μm is, to our knowledge, the longest wavelength achieved up to now with QWs grown on InP substrates.

The PL data presented above show that the InAs/$Al_xGa_{0.48-x}In_{0.52}As$ QW materials system is well suited for giving emission in a wavelength range as wide as 1.0–2.4 μm. We now turn to the question of the stimulated emission.

4. Stimulated emission

In this work two preliminary structures, an MQW and an SQW, were tested for stimulated emission. The MQW structure consisted of three periods of alternating 6 ML InAs/27 nm $Al_{0.24}Ga_{0.24}In_{0.52}As$ layers clad by $Al_{0.48}In_{0.52}As$ layers. Optical pumping experiments were performed at 77 K with a mode-locked YAG laser delivering 100 ps wide pulses with a maximum peak energy density of 50 μJ cm^{-2} and a repetition rate of 82 MHz. Figure 5 shows the variation of the PL signal with the excitation power. When the excitation power is increased by a factor of 2, the emitted signal becomes narrow and its intensity increases by as much as 2×10^4 which is the signature of stimulated emission (no laser modes are resolved because the sample was not cleaved to form a Fabry–Pérot cavity). The maximum time-averaged excitation power is $P_0=4$ kW cm^{-2}, which can be transformed in an order of magnitude threshold-current density by $J_{th}\approx eP_0/h\nu\approx 3.5$ kA cm^{-2}. This rough estimate of J_{th} thus indicates that injection lasers can be made in the InAs/$Al_{0.24}Ga_{0.24}In_{0.52}As$ QW system. In addition, it has to be noted that the stimulated emission occurs in the technologically important wavelength region of 1.3 μm.

The SQW structure was made of a 10 ML InAs/$Ga_{0.47}In_{0.53}As$ SQW clad by stepped $Al_{0.24}Ga_{0.24}In_{0.52}As$/$Al_{0.48}In_{0.52}As$ barriers. Broad area (200 μm × 500 μm) laser diodes were then fabricated and tested under pulsed current injection at 80 K (800 ns pulse length, 1 kHz repetition rate). Figure 6 shows the output power *vs.* drive current for a typical diode. The threshold current density is $J_{th}=475$ A cm^{-2}. The inset in Fig. 6 shows a spectrum taken from the same diode at $J=1.1J_{th}$. It is centred at 1.836 μm with about ten clearly resolved longitudinal modes. No laser emission has yet been obtained at RT because of too weak confinement of the carriers at the InAs/$Ga_{0.47}In_{0.53}As$ interfaces. However, work is in progress in our laboratories to address this question and to characterize further these and other structures.

5. Conclusion

We have studied the spontaneous and stimulated emission from strained InAs QWs embedded in an $Al_xGa_{0.48-x}In_{0.52}As$ matrix grown on InP substrates. By adjusting the QW width and/or the barrier composition the spontaneous PL emission can be tuned between 1.0 μm and 2.2 μm at low temperature. Efficient PL emission is obtained up to 2.4 μm at room

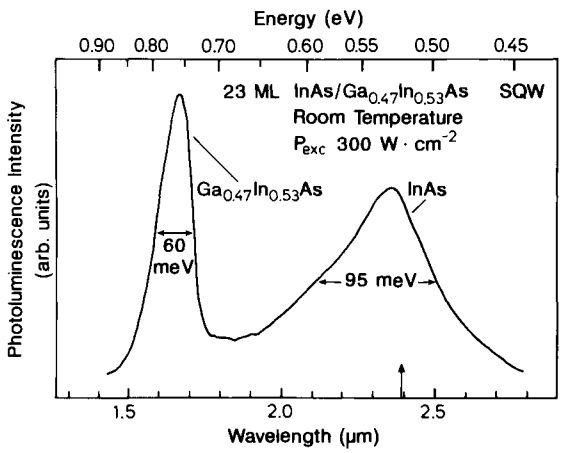

Fig. 4. Room temperature PL spectrum of the InAs/$Ga_{0.47}In_{0.53}As$ sample containing the 23 ML wide InAs SQW.

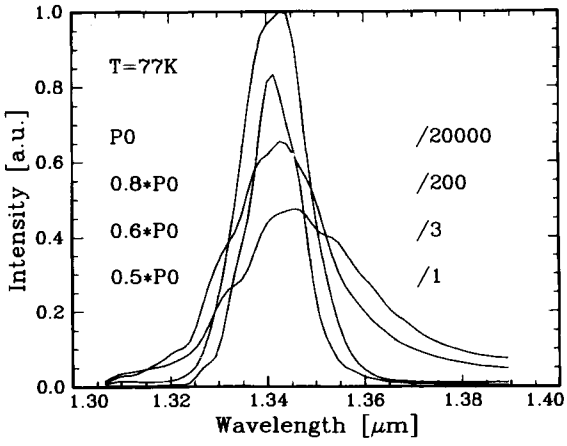

Fig. 5. PL signal taken at 77 K under various excitation power from a three period 6 ML InAs/27 nm $Al_{0.24}Ga_{0.24}In_{0.52}As$ MQW structure. The time-averaged excitation power is $P_0=$ 4 kW cm^{-2}. Each spectrum has been divided by the number indicated on its right-hand side.

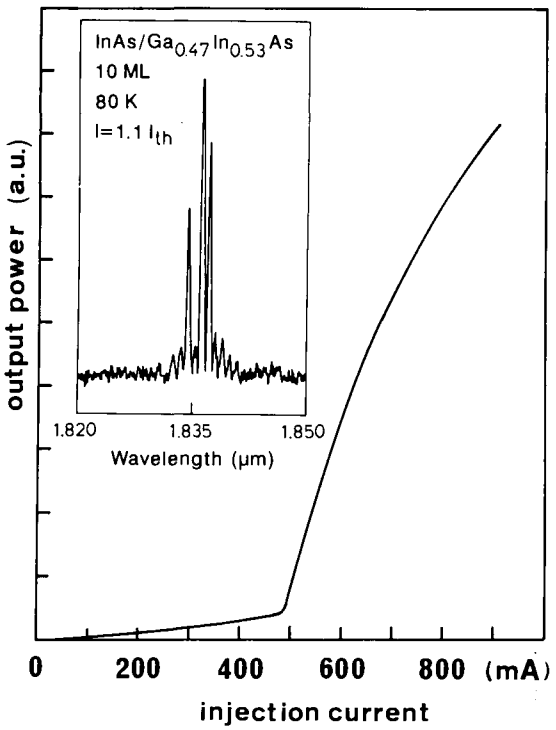

Fig. 6. Output power *vs.* drive current at 80 K for a broad area (200 μm × 500 μm) laser diode fabricated from a 10 ML InAs/$Ga_{0.47}In_{0.53}As$ SQW structure clad by stepped $Al_{0.24}Ga_{0.24}$-$In_{0.52}As/Al_{0.48}In_{0.52}As$ barriers. The inset shows the output spectrum at $J = 1.1J_{th}$.

temperature. Finally, for the first time stimulated emission was observed with the InAs/$Al_xGa_{0.48-x}$-$In_{0.52}As$ QW system near 1.35 μm and 1.85 μm. These results thus enlarge the wavelength range of applications achievable with InP-based materials.

Acknowledgments

Part of this work was sponsored by the GSI Darmstadt and by the Bundesministerium für Forschung und Technologie of the Federal Republic of Germany.

References

1 T. P. Pearsall (ed.), *Semiconductors and Semimetals*, Vols. 32 and 33, *Strained-Layer Superlattices*, Academic Press, San Diego, CA, 1990.
2 A. R. Adams, *Electron. Lett., 26* (1986) 249.
3 E. Yablonovitch and E. O. Kane, *J. Light. Technol., 4* (1986) 504; 961(E).
4 P. J. A. Thijs, *Proc. 13th IEEE Int. Semicond. Laser Conf., September 21–25, 1992, Takamatsu, Kagawa*, IEEE, New York, 1992, paper A1 and references therein.
5 E. Yablonovitch and E. O. Kane, *J. Light. Technol., 6* (1988) 1292.
6 E. Tournié and K. H. Ploog, *Appl. Phys. Lett., 62* (1993) 858.
7 E. Tournié, O. Brandt, K. H. Ploog and M. Hohenstein, *Appl. Phys. A, 56* (1993) 91.
8 G. Bastard, *Wave Mechanics Applied to Semiconductor Heterostructures*, Les Editions de Physique, Les Ulis, 1990.
9 Landolt-Börnstein, Vol. 22a, Springer, Berlin, 1987.
10 E. Tournié, O. Brandt and K. H. Ploog, *Semicond. Sci. Technol., 8* (1993) S236.
11 M.-H. Meynadier, J. L. de Miguel, M. C. Tamargo and R. E. Nahory, *Appl. Phys. Lett., 52* (1988) 302.
12 H. Banvillet, E. Gil, R. Cadoret, P. Disseix, K. Ferdjani, A. Vasson, A.-M. Vasson, A. Tabata, T. Benyattou and G. Guillot, *J. Appl. Phys., 70* (1991) 1638.
13 E. Tournié, O. Brandt and K. H. Ploog, *Appl. Phys. Lett., 60* (1992) 2877.
14 E. Tournié, H.-P. Schönherr, K. H. Ploog, C. Giannini and L. Tapfer, *Appl. Phys. Lett., 61* (1992) 846.

Chemical beam epitaxy and photoluminescence characteristics of InGaAsP/InP BRAQWET modulators

J. F. Carlin, B. Dwir, M. Glick, R. Monnard, A. Rudra, M. A. Dupertuis and F. K. Reinhart
Institute for micro- and optoelectronics, Ecole Polytechnique Fédérale de Lausanne, CH-1015 Lausanne (Switzerland)

Abstract

We report on the growth of barrier, reservoir and quantum well electron transfer (BRAQWET) structures using chemical beam epitaxy. The photoluminescence spectra of the structures are affected by the bias voltage. The QW emission line is extinguished at positive bias and the barrier emission line is extinguished at negative bias. These effects might be used for the BRAQWETs characterization.

1. Introduction

Barrier, reservoir and quantum well electron transfer (BRAQWET) modulators are drawing attention because of their potential for high speed operation. While significant results have been obtained with InGaAlAs/InP modulators [1], there have been very few attempts in the InGaAsP/InP material system [2] as a result of the much higher leakage current in these devices.

The BRAQWET structure studied here is described in Table 1 and the band diagram is shown in Fig.1. This structure is challenging for the growth technique since the tolerances on the GaInAsP layers composition and the doping levels are very tight (2% and 20% respectively). Chemical beam epitaxy (CBE) was chosen because of its reproducible control of InP based alloys and quantum wells (QWs) [3] and its potential for advanced device integration via selective area growth [4].

2. CBE Growth

All layers were grown at 0.5–2 μm/h using trimethylindium, triethylgallium, arsine and phosphine with a pressure regulated gas manifold and no carrier gas. The V/III ratio was maintained between 5 and 15. A silicon strip heater was used for n-type doping, since it is much less sensitive to contamination by alkyls than an ordinary effusion cell. Beryllium from a conventional effusion cell gave the appropriate p-type doping. To guarantee a specular surface together with higher InP growth rates, n-type S-doped (100) InP substrates with a 2° off-orientation toward (111)A were used.

Since the BRAQWET structure includes a succession of InP and GaInAsP layers of various compositions (Table 1), a detailed study of the growth kinetics of GaInAsP alloys was conducted [5] to identify the optimal growth parameters. In particular, the growth temperature (T_g) has a strong influence on the composition of these GaInAsP alloys as well as on their structural and optical properties, as pointed out by other groups [6,7]. A single growth temperature must be chosen to avoid long growth interruptions between the reservoir, QW and the barrier. We found that a growth temperature of 505 °C was a good choice because poor quality 1.26μm wavelength quaternary alloys were obtained above 510 °C and a high dependence of the alloy composition on T_g was observed at lower growth temperature. In this set of experiments, the growth temperature was controlled within ±2 °C by an infrared pyrometer having its measurement

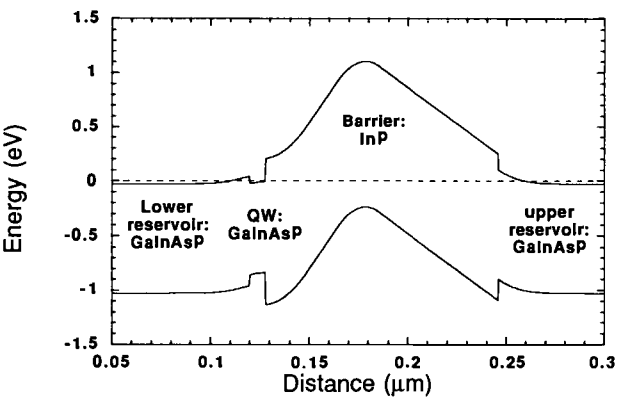

Fig.1. Band diagram of a BRAQWET structure.

0921-5107/93/$6.00

© 1993 – Elsevier Sequoia. All rights reserved

TABLE 1. Parameters of the BRAQWET growth

Function	Layer	Quaternary band-gap (nm)	Thickness (nm)	Doping level (cm^{-3})
Cap	n-InP		700	5.7×10^{17}
Reservoir	n-InGaAsP	1250	100	5.7×10^{17}
Barrier	InP		60	—
Barrier	p-InP		20	1.25×10^{18}
Barrier	InP		15	—
Barrier	n-InP		18	8×10^{17}
Quantum well	InGaAsP	1620	8	—
Spacer	InGaAsP	1250	7	—
Reservoir	n-InGaAsP	1250	113	5.7×10^{17}
Buffer	n-InP			5×10^{17}

window at 0.9 μm wavelength and regularly calibrated against InSb melting point (525 °C).

To achieve a control of the doping levels within 20%, frequent calibrations were performed by C-V profiling and Hall measurements. In addition, the different Si doping levels within the structure were obtained by changing the growth rates rather than the Si stripe current, to avoid temperature transients of the cell.

The BRAQWET structures show a typical surface defect density of 10^2 to 10^3 cm^{-2}. These defects are mostly because of dust contamination during the In bonding of the substrate prior to the growth.

3. Photoluminescence measurements under bias voltage

The 300K photoluminescence (PL) spectra obtained using a 1.96 eV laser excitation energy clearly show the QW and reservoir emission lines at 1500 nm and 1250 nm respectively. The balance between these lines can be dramatically modified by applying a bias voltage to the sample. As shown in Fig.2, a bias voltage of -0.5 V at the substrate side completely extinguishes the reservoir line, while $+0.5$ V extinguishes the QW line. The explanation of this phenomenon is not trivial since it includes behavior of both electrons and holes in a complex potential. We suppose that the PL is dominated by the holes behavior since they are the minority carriers in the sample.

It is important to notice that more than 90% of the 1.96 eV laser excitation is absorbed in the 0.7 μm-thick InP cap layer. The luminescence intensity of the InP cap (at 925 nm) was however lower than the one of the reservoir or QW, thus indicating that the luminescence occurs from holes generated in the InP cap and then trapped in the upper reservoir.

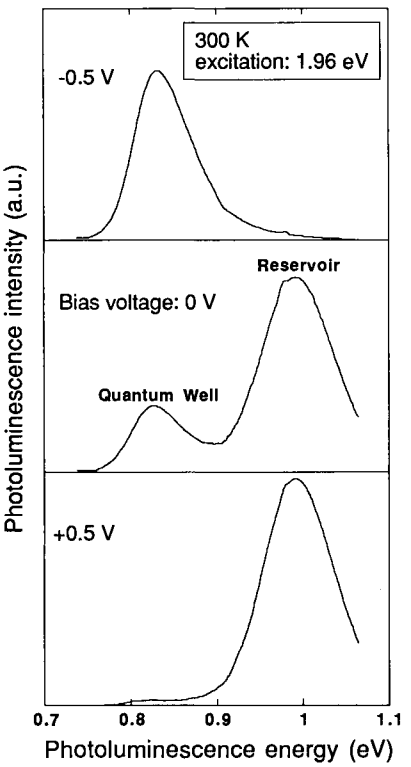

Fig.2. Effect of bias voltage on the photoluminescence spectra of a BRAQWET structure.

Our results can then be interpreted as follows:

- At $+0.5$ V bias, the holes remain and recombine in the upper reservoir, they cannot reach the QW region.
- At -0.5 V bias, the holes step over the valence band discontinuity between the upper reservoir and the barrier, cross the InP barrier and are trapped in the QW, where they recombine.

We also performed some PL measurements using a laser excitation energy of 1.17 eV. This wavelength is not absorbed in InP. Hole generation occurs in the upper reservoir, but the excitation light is only partially absorbed in this thin layer and hole generation also occurs in the QW and lower reservoir regions. In this case, the barrier emission line still extinguishes at -0.5 V bias but the extinction of the QW emission line happens at a higher voltage ($\approx$ 3 V). This is coherent with our previous interpretation; when the holes were generated near the surface, the extinction of the QW line occurred when they were prevented to reach the QW region, but now that generation also occurs in the QW region, the extinction of the QW line is more difficult to obtain. This might eventually occur when the holes are able to step over the valence band discontinuity between the QW and the barrier.

Improvements are still to be done in the understanding of these effects but PL under bias voltage could then be very helpful for the characterization of BRAQWET structures.

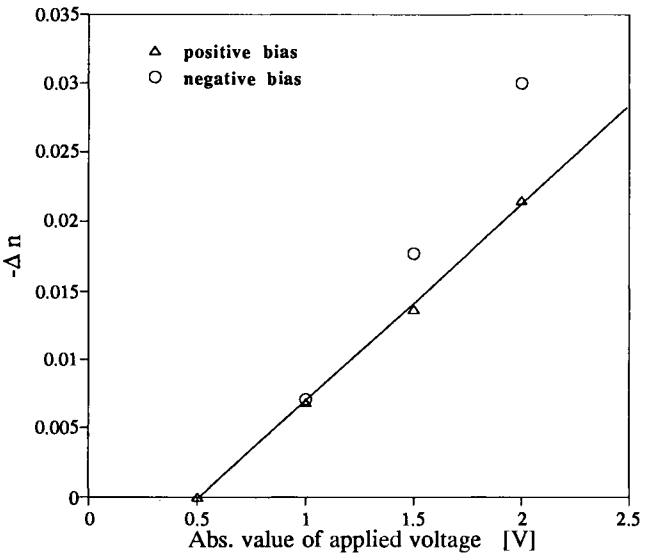

Fig.3. Change of the refractive index as a function of the applied bias.

4. Optical properties

The BRAQWET structures show the Franz-Keldysh effect in the reservoir and the quantum-confined Stark effect and band-filling effect in the QW, as it was measured by differential absorption spectra [8]. We show in Fig.3 the modulation of index of refraction in guided configuration at 20meV detuning from the photoluminescence peak as measured on a structure containing 5 BRAQWETs. These results are similar to those found in InGaAs/InAlAs material system [1]. The leakage current of our device is also similar ($\approx$ 40 mA/cm^2 at V = 0.5 V/QW) in spite of the lower conduction-band offset. This leakage current is two orders of magnitude lower than previously reported in this material system [2] as a result of the improvement of the BRAQWET structure [9].

5. Conclusion

We have adjusted the growth parameters to successfully obtain GaInAsP/InP BRAQWET structures. Room temperature photoluminescence under bias voltage might give information on the band diagram of the samples. We are trying to see whether the luminescence data can be easily correlated with more useful characteristics of the BRAQWETs, as for instance the QW dipping voltage. In this case, photoluminescence would be a rapid and powerful tool for BRAQWET characterization.

References

1 J.E. Zucker, T.Y. Chang, M.Wegener, N.J. Sauer, K.L. Jones and D.S. Chemla, *IEEE Photonic Technol. Lett.*, *2* (1990) 29.
2 N. Agrawal, D. Hoffman, D. Franke, K.C. Li, U. Clemens, A. Witt and M. Wegener, *Appl. Phys. Lett.*, *61* (1992) 249.
3 A. Rudra, J.F. Carlin, P. Ruterana, M. Gailhanou, J.L. Staehli and M. Ilegems, *J. Cryst. Growth*, *120* (1992) 338.
4 H. Sugiura, T. Nishida, R. Iga, T. Yamada and T. Tamamura, *J. Cryst. Growth*, *121* (1992) 579.
5 J.F. Carlin, A. Rudra and M. Ilegems, *J. Cryst. Growth*, 1993, to be published.
6 J.L. Benchimol, G. Leroux, H. Thibierge, C. Daguet, F. Alexandre and F. Brillouet, *J. Cryst. Growth*, *107* (1991) 978.
7 T.H. Chiu, M.D. Williams, T.K. Woodward, J.E. Cunningham, J.E. Zucker, T. Sizer, F.G. Storz, J.F. Ferguson and W.T. Tsang, *J. Cryst. Growth*, *124* (1992) 165.
8 M. Glick, B. Dwir, R. Monnard, F. Vasey, J.F. Carlin, A. Rudra, M.A. Dupertuis and F.K. Reinhart, *Proc. Europ. Conf. on Integrated Optics, Neuchatel, 1993*, pp. 14-24.
9 M. Nicolardot and M.A. Dupertuis, French Patent No. 91.13146 (extended to USA, Japan).

Second harmonic generation via excitations between valence sub-bands in p-type GaAs–AlAs and Si–SiGe quantum well structures

K. B. Wong, M. J. Shaw and M. Jaros
Department of Physics, The University of Newcastle upon Tyne, Newcastle upon Tyne (UK)

Abstract

We present full-scale calculations of the frequency dependence of second harmonic generation due to intervalence sub-band transitions in p-type GaAs–AlAs and Si–SiGe asymmetric quantum well structures (QWSs). We demonstrate that the response is dominated by excitations lying throughout the Brillouin zone and that the states involved are not predicted by semiclassical models. Significant light and heavy hole momentum mixing away from the zone center is responsible for the second harmonic generation.

1. Introduction

There has been a lot of interest [1, 2] in the study of optical response due to excitations between sub-bands in semiconductor quantum well structures (QWSs). The sub-band separations can be tuned over a significant range of energies spanning the mid-to-far IR range of wavelengths. In particular, in p-type QWSs it is easier to tune and optimize the optical response. This is because mixing between bulk light and heavy hole states exists in the valence sub-bands of QWSs and induces much stronger optical transitions than between conduction sub-bands. In this paper, we describe full-scale calculations of second harmonic generation spectra in both GaAs–AlAs and Si–SiGe QWSs in which the non-linearities arise owing to virtual optical transitions between valence sub-bands. Step-like wells were used to modify the confined state wavefunctions in order to enhance the second harmonic generation in the 3–5 μm (GaAs–AlAs) and 10–15 μm (Si–SiGe) range. Our study has two main motivations. Firstly, we identify the microscopic origin of the processes dominating the second-order susceptibility, $\chi^{(2)}(2\omega;\ \omega,\ \omega)$. Secondly, we are interested in showing how the band-structure effects the magnitude, directional and frequency dependence of $\chi^{(2)}$.

2. Theory

The expression for $\chi^{(2)}$ describing second harmonic generation using the density matrix theory [3] is

$$\chi_{\mu\alpha\beta}^{(2)}(-2\omega;\ \omega,\ \omega) = \frac{-ie^3}{\varepsilon_0 V 2\hbar m^3 2\omega^3} \sum_{lmn} \sum_{k} f_0(l,k) \times \left[\frac{p_{lm}^{\ \mu} p_{mn}^{\ \alpha} p_{nl}^{\ \beta} + p_{lm}^{\ \mu} p_{mn}^{\ \beta} p_{nl}^{\ \alpha}}{(\Omega_{ml} - i\Gamma_{mn} - i\Gamma_{nl} - 2\omega)(\Omega_{nl} - i\Gamma_{nl} - \omega)} + \frac{p_{lm}^{\ \alpha} p_{mn}^{\ \mu} p_{nl}^{\ \beta} + p_{lm}^{\ \beta} p_{mn}^{\ \mu} p_{nl}^{\ \alpha}}{(\Omega_{ml} + i\Gamma_{ml} + \omega)(\Omega_{nl} - i\Gamma_{nl} - \omega)} + \frac{p_{lm}^{\ \beta} p_{mn}^{\ \alpha} p_{nl}^{\ \mu} + p_{lm}^{\ \alpha} p_{mn}^{\ \beta} p_{nl}^{\ \mu}}{(\Omega_{ml} + i\Gamma_{lm} + \omega)(\Omega_{nl} + i\Gamma_{lm} + i\Gamma_{mn} + 2\omega)} \right] \quad (1)$$

where η is direction of the induced electric field vector by incident optical fields at frequency ω aligned in the α and β directions. In eqn. (1), Σ_{lmn} represents the summation of l, m and n over all possible sub-bands at wavevector k. Each combination of lmn represents the contribution from the virtual process $l \rightarrow n \rightarrow \mu \rightarrow l$. Ω_{ij} is the transition frequency between sub-bands i and j, and $p^{\delta}_{\ ij}$ is the corresponding momentum matrix element in the δ direction. Clearly, for a semiconductor system, the sub-band energy separations and momentum matrix elements will have a wavevector dependence, and the expressions for the susceptibilities include a summation over a set of randomly chosen sampling points in the superlattice Brillouin zone Σ_k. The bandstructure is evaluated by a semi-empirical relativistic pseudopotential calculation which

0921-5107/93/$6.00
© 1993 – Elsevier Sequoia. All rights reserved

accounts correctly for the details of the valence sub-bands throughout the Brillouin zone. The Fermi distribution function, $f_0(l, k)$, represents the thermal equilibrium populations of the states. A low concentration p-type doping in the structures considered has resulted in a Fermi level lying below the valence band edge. Relaxation processes have been included phenomenologically in the form of the damping terms Γ_{ij} in the frequency denominators of eqn. (1). This simple model provides a good description of the response at low intensities [4]. At higher intensities, where significant changes in population take place owing to optical pumping, a more sophisticated treatment of the relaxation mechanisms is required. We restrict ourselves to considering the low intensity behavior. In the absence of any accurate estimates of the damping constants a single linewidth was used for all transitions.

3. Results

3.1. GaAs–AlAs

The second-order susceptibility of a 5GaAs/$1Al_{0.5}Ga_{0.5}As$/14AlAs superlattice, with p-type doping in the barriers, was calculated using eqn. (1) in the manner described [4, 5] in our previous publications (5GaAs represents 5 monolayers, *i.e.* 2.5 lattice constants of bulk GaAs). A schematic level diagram of the structure is shown in Fig. 1, with principal zone center transition energies indicated. The frequency dependence of the five independent non-zero components of $\chi^{(2)}(-2\omega; \omega, \omega)$ was calculated at 0 K. The Fermi level was chosen to lie 65 meV below the superlattice valence band edge, and is shown in Fig. 1. The damping constant is set to 3 meV to represent a typical heterostructure linewidth. It can be seen that the dominant component is $\chi_{xyz}^{(2)}$, with a maximum value of 4.8×10^{-5} esu at a photon energy of 340 meV. From a simple particle-in-a-box model one might have expected that $\chi_{zzz}^{(2)}$ is dominant owing to processes of the type HH3→HH2→HH1→HH3 (where HHn refers to the nth heavy-hole sub-band). A detailed analysis of the individual processes which contribute to $\chi_{zyz}^{(2)}$ in our calculation indicates that processes of the type SO→HH1→C→SO are dominant (where SO represents the spin split-off state and C represents a low energy continuum state). Large contributions occur for such processes where the transitions SO→HH1 and C→SO are simultaneously resonant with ω, causing the denominator of the second term in eqn. (1) to be small. Our full bandstructure calculations, which include the effects of valence band mixing, thus predict a $\chi^{(2)}$ dominated by processes different to those expected intuitively for simple theory.

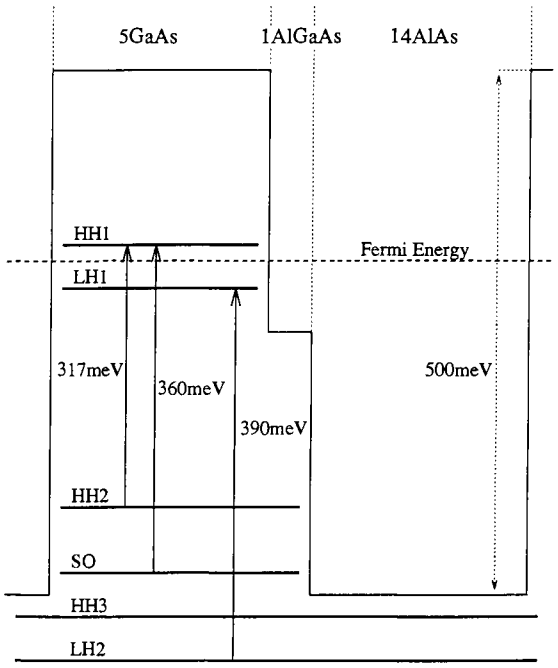

Fig. 1. Schematic energy band diagram of the 5GaAs/$1Al_{0.5}Ga_{0.5}As$/14AlAs superlattice valence band (5GaAs represents 5 monolayers, *i.e.* 2.5 lattice constants of GaAs). HHn represents the nth heavy-hole sub-band, LHn the nth light-hole sub-band, and SO the spin split-off sub-band. Zone center transition energies between some of the key states are shown.

From the above discussion it might be expected that the peak value of $\chi^{(2)}$ would occur at 360 meV, the zone-center SO→HH1 energy separation (see Fig. 1). However, the total susceptibility results from the summation of the contributions from k-points throughout the Brillouin zone. We find that the momentum matrix element, p_{ij}^{δ} in eqn. (1), is a rapidly varying function of k owing to the strong mixing of heavy and light hole sub-bands. p_{ij}^{δ} at the zone center is certainly not representative of the entire Brillouin zone. For instance, the SO→HH1 transition is stronger, and occurs at lower energies, at k-points lying away from the zone center. These points thus dominate the overall response, and result in the position of the peak of the spectrum at a lower energy of 340 meV (Fig. 2).

3.2. Si–SiGe

We also studied the second-order susceptibilities in an analogous Si–SiGe system. The light and heavy hole mixing is stronger in this strained-layer superlattice owing to strain induced momentum mixing [5]. This alters the non-linear optical interactions. The second-order susceptibility was evaluated in an $18Si_{0.85}Ge_{0.15}$/$2Si_{0.925}Ge_{0.075}$/40Si superlattice grown on a (001) Si substrate (40Si represents 40 monolayers, *i.e.* 10 lattice constants of Si). A schematic energy level diagram of

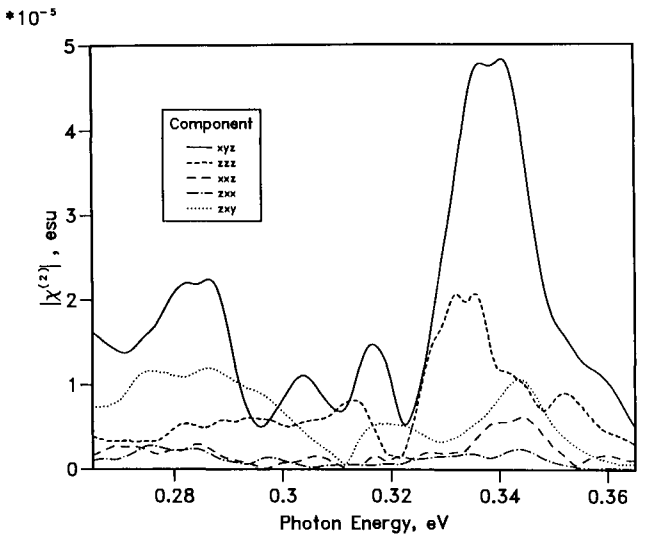

Fig. 2. The magnitude of the five independent components of $\chi^{(2)}(-2\omega;\ \omega,\ \omega)$ in esu, plotted against the photon energy in eV, for the p-type 5GaAs/1$Al_{0.5}Ga_{0.5}$As/14AlAs superlattice at 0 K. The component labels $\mu\alpha\beta$ are those in eqn. (1) where z is the superlattice growth direction.

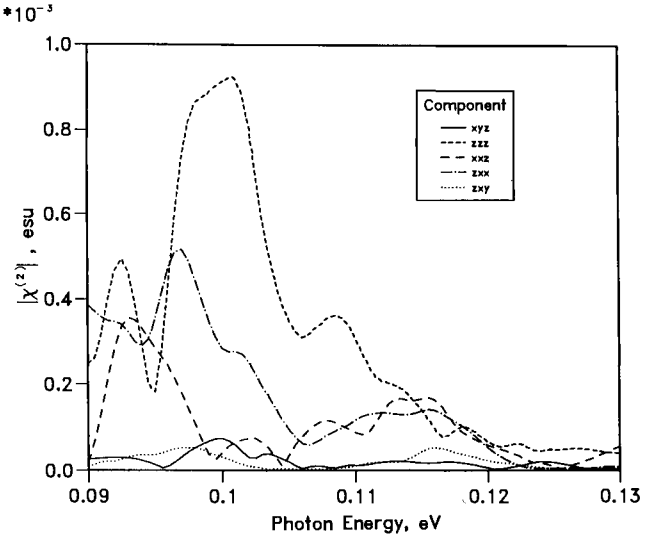

Fig. 4. The magnitude of the five independent components of $\chi^{(2)}(-2\omega;\ \omega,\ \omega)$ in esu, plotted against the photon energy in eV, for the p-type 18$Si_{0.85}Ge_{0.85}$/2$Si_{0.925}$/40Si superlattice at 0 K. The component levels $\mu\alpha\beta$ are those in eqn. (1) where z is the superlattice growth direction.

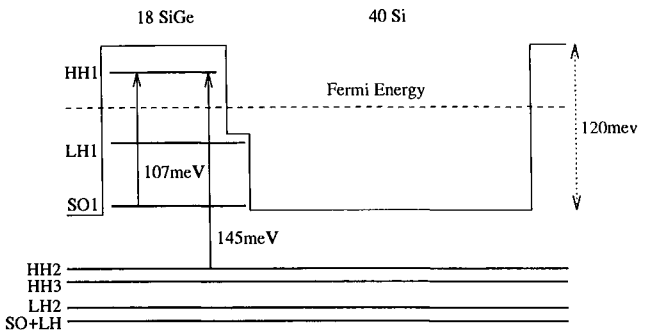

Fig. 3. Schematic energy band diagram of the 18$Si_{0.85}Ge_{0.15}$/2$Si_{0.925}Ge_{0.075}$/40Si superlattice valence band (40 Si represents 40 monolayers, *i.e.* 10 lattice constants of Si). Zone center transition energies between some of the key states are shown.

the structure is shown in Fig. 3, with principal zone center transition indicated. In Fig. 4 we present the frequency dependence of the five independent non-zero components of $\chi^{(2)}(-2\omega;\ \omega,\ \omega)$ evaluated at 0 K for the Fermi level chosen to lie 26 meV below the top of the uppermost valence sub-band. The damping constant used corresponds to a linewidth of 1.5 meV. A smaller value was chosen here merely to make it easier to resolve the individual peaks due to different processes and to obtain a better understanding of the role of bandstructure effects. However, it should be noted that the magnitude of $\chi^{(2)}$ increases as the magnitude of the damping constant decreases. This is generally true for all susceptibilities [6].

It is shown in Fig. 4 that the largest component is $\chi_{zzz}^{(2)}$, with a maximum value of 9.5×10^{-4} esu at a photon energy of 100 meV. The processes which dominate the contributions to this peak are identified to be C → SO → HH1 → C and SO → HH1 → C → SO. The states are labeled in the same manner as in the GaAs–AlAs system. There are two other satellite peaks near the central peak. The peak lying at an energy of 93 meV is dominated by the same processes. Apparently, the peak at a higher energy of 107 meV corresponds to the zone center SO → HH1 energy separation (see Fig. 3). However, we find two additional contributions apart from those mentioned above, namely C → HH2 → HH1 → C and HH2 → HH1 → C → HH2. The transition energy between HH1 and HH2 at the edge of the superlattice Brillouin zone (in the z-direction) is also 107 meV. In fact, the magnitude of such a peak cannot be predicted without including contributions from all the possible transitions associated with various excitations. The argument invoked above, namely that the momentum mixing is only strong away from the zone center can be applied here too. It results in an energy shift of the largest peak at 100 meV. Such shifts are even more prominent in components $\chi_{zxx}^{(2)}$ and $\chi_{xxz}^{(2)}$ which both peak at energies further away from the zone center transition energy of SO → HH1 (95 meV for $\chi_{zxx}^{(2)}$ and 92 meV for $\chi_{xxz}^{(2)}$ as shown in Fig. 4).

The strength of the optical transition matrix elements is an important factor in determining the magnitude of the peaks of second harmonic generation. It is

governed by the degree of light and heavy hole mixing in the states concerned. It is found that the mixing is strongest for state SO when the transition SO→HH1 occurs at 100 meV. We also find that the component $\chi_{zxx}^{(2)}$ has a large magnitude of 5×10^{-4} esu at 95 meV. $\chi_{zxx}^{(2)}$ decribes an induced electric field in the z-direction in response to fundamental fields applied in the x-direction (parallel to the interfaces). This component is therefore particularly useful for applications utilizing normal-incidence illumination of the IR detectors.

4. Conclusions

In conclusion, our results demonstrate that the intervalence sub-band excitations in p-type asymmetric QWSs can cause significant second harmonic generation. For example, $\chi^{(2)}(-2\omega;\ \omega,\ \omega)$ as large as 4.8×10^{-5} esu in the GaAs–AlAs system and 9.5×10^{-4} esu in the Si–SiGe system are predicted. It is found that the key transition SO→HH1 is responsible for the largest peak in $\chi^{(2)}$ for both sytems discussed above, but that the peaks correspond to different $\chi^{(2)}$ components in the two materials. The largest component $\chi_{xyz}^{(2)}$ in the GaAs–AlAs system becomes very small in the Si–SiGe system. Bandstructure effects are also shown to influence the directional properties of the non-linear optical response. Here the excitation process involving the SO state is different than in an intuitive picture of the type HH1–HH2–HH3. Finally, it is shown that the position of the peak response depends mainly on excitations lying away from the center of the Brillouin zone and involves higher lying sub-bands.

Acknowledgments

We would like to thank the United Kingdom Science and Engineering Research Council, the Office of Naval Research (USA), and ESPRIT-Basic Research European Community Programme for financial support.

References

1 B. F. Levine, K. K. Choi, C. G. Bethea, J. Walker and R. J. Malik, *Appl. Phys. Lett.*, 50 (1987) 1092.
2 C. Sirtori, F. Capasso, D. L. Sivco and A. Y. Cho, *Phys. Rev. Lett.*, 68 (1992) 1010.
3 P. N. Butcher and D. Cotter, *The Elements of Nonlinear Optics*, Cambridge University Press, 1990.
4 M. J. Shaw, D. Ninno, B. M. Adderley and M. Jaros, *Phys. Rev. B*, 45 (1992) 11031.
5 I. Morrison, M. Jaros and K. B. Wong, *Phys. Rev. B*, 18 (1987) 9693.
6 S. L. Chuang, S. Schmitt-Rink, B. I. Greene, P. N. Saeta and A. F. J. Levi, *Phys. Rev. Lett.*, 68 (1992) 102.

Materials Science and Engineering, B21 (1993) 300–303

An AlGaAs/GaAs OEIC structure for the integration of LEDs, MESFETs and photodetectors

D. Leipold, U. Kehrli, B. Delley, K. Thelen and B. D. Patterson
Paul Scherrer Institut, Badenerstr. 569, CH-8048 Zürich (Switzerland)

Abstract

An OEIC structure of AlGaAs/GaAs grown in one single step was designed to integrate LEDs, MESFETs and photodetectors. The bandgap of the LED is shifted so that the emitted light can efficiently be detected by the photodetector. The layer structure was optimised by a one-dimensional simulation in which the Poisson-, the continuity- and the drift-diffusion equations are solved self-consistently.

1. Introduction

In recent years there has been continuous interest in developing optoelectronic integrated circuits (OEICs) [1]. Several combinations of basic optoelectronic elements are regarded as an OEIC: photodetectors and transistors, light emitting structures with transistors and the combination of all these three elements. This last combination is of particular interest in the field of parallel data communication, smart pixel arrays and neural networks [2], and it is typically realised using sophisticated techniques like regrowth or selective growth [3]. We have investigated a layer structure grown in one step to realise this type of integration (Fig. 1). Our structure is compatible with simple mesa-etch processes. The structure was optimised using an in-house developed simulation program. In this paper we describe the layer design, then explain the bases of our simulation program and finally discuss the key characteristics of the structure.

2. Layer structure

A principal consideration in the design of OEICs is that the emitted light has a wavelength which can be detected efficiently by the photodetector. To achieve this, we use two pn-junctions with different bandgap material, one for emission and one for detection (Fig. 2). Amplifiers and switching functions are handled by an n-type MESFET structure. Efficient carrier confinement and a short gate length are necessary for a good MESFET performance. In order to be able to use contact photolithography to define short gates, the MESFET layers are placed on the top of the layer structure. Carrier confinement in the MESFET channel is normally realised by introducing a slightly p-doped buffer below the channel [4]. Here this buffer is also used as a light absorbing layer which, together with the MESFET channel, forms the pn-junction of the photodetector. When GaAs is used for the photodetector layers, the absorption edge is at 850 nm. The light emitted by the LED must therefore be shifted by at least the width of the emission spectrum to obtain an efficient absorption in the photodetector. This leads to a target emission wavelength of approximately 790 nm. For high-efficiency light emission, a single AlGaAs quantum-well heterostructure is used, which has been optimised for surface-emitting LEDs [5]. The LED is placed below the photodetector junction: *i.e.* all the layers together form an n-p-n structure (Fig. 2).

For the MESFET, the channel doping and thickness are chosen such that half the channel is depleted by the Schottky contact: *i.e.* the MESFET is a depletion-type transistor with a pinch-off voltage of 1.5 V. To reduce the depletion in the channel by the p-type buffer layer and to simultaneously maintain good carrier confinement, the p-doping of the buffer is graded. The thickness of the buffer layer, which also serves as the light-absorption layer, is chosen such that 70% of the incoming light is absorbed at the peak emission wavelength of the LED.

Several additional features of the layer structure are included to simplify the processing. The n-sides of all the LEDs are simultaneously connected through the n-substrate with a backside contact. To contact the p-sides of the LEDs and the photodetectors, a heavily-doped p + -layer is grown, such that ohmic contacts can be formed using a standard Schottky metallisation. The p + -layer is made quite thick in order to relax the etch-

0921-5107/93/$6.00

© 1993 – Elsevier Sequoia. All rights reserved

ing tolerance required to stop within it. On top of the MESFET structure, a heavily n-doped cap reduces the source and drain contact resistance. Good control of the channel thickness is necessary to achieve a homogeneous pinch-off voltage. Therefore, a thin AlGaAs etch stop layer is introduced between the cap layer and the channel (Fig. 1(b)).

3. Simulation

One-dimensional energy-band diagrams play an important role in the design of semiconductor devices.

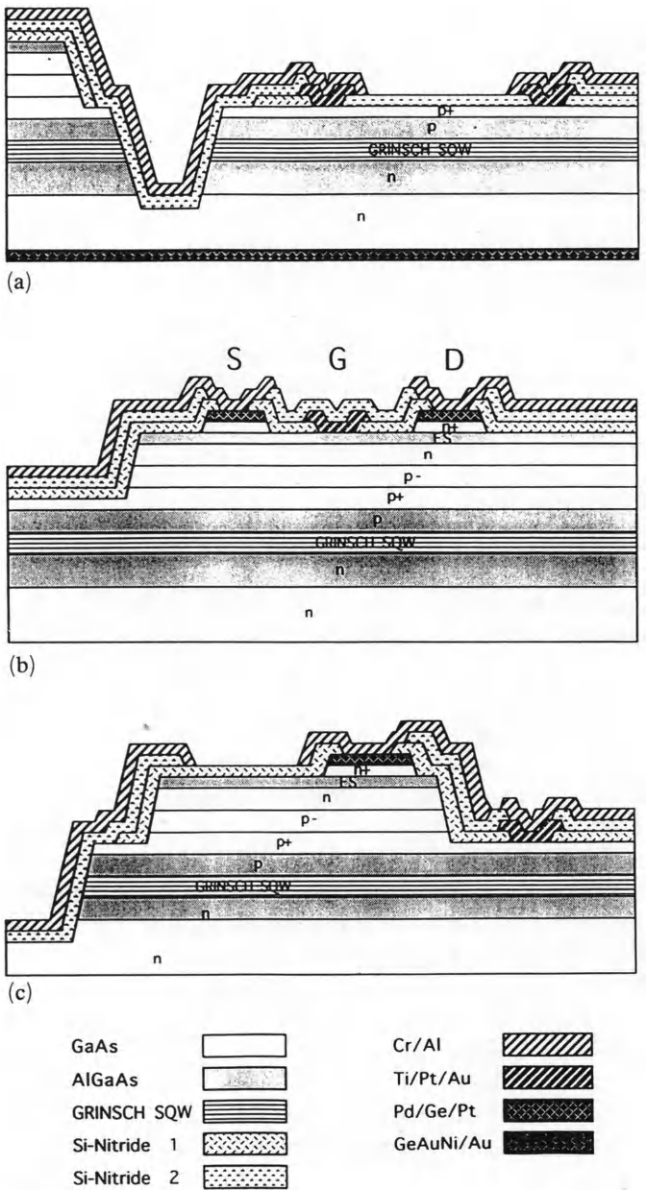

Fig. 1. Cross sections through all three devices fabricated in a two-mesa process using our material structure: (a) LED; (b) MESFET and (c) photodetector.

A program developed here provides accurate solutions of the drift-diffusion model for heterojunctions.

Neglecting quantum effects in narrow double heterojunctions, an accurate band diagram requires the self-consistent solution of Poisson's equation for the charge distribution as well as the current and continuity equations for electrons and holes. We assume: (i) complete ionisation of the nominal dopant concentration; (ii) the Boltzmann limit for the carrier concentrations; (iii) the validity of the Einstein relations relating diffusion constants to mobilities; (iv) the occurence of spontaneous emission, Auger processes and recombination at midgap traps (according to the Shockley–Read–Hall law) in the bulk and at surfaces.

Despite the fact that $Al_xGa_{1-x}As$ is a widely used material system, the best available data for the bandgap, density of states effective masses and intrinsic carrier concentration are not fully consistent [6, 7, 8]. We take the values for the bandgap from the literature [7]. The effective masses are renormalized by a single (concentration independent) factor C_{corr} to make the effective densities of states consistent with the intrinsic carrier concentration n_i of GaAs [8]. These values, and our best estimate of the conduction band offset ΔE_c are given in Table 1. The doping-dependent mobilities were estimated according to the data of Blakemore [6].

Our algorithm solves the equations

$$\frac{d}{dz}\varepsilon(z)\frac{d\Psi}{dz} = -q(p-n+D(z))$$

$$\frac{d}{dz}\mu_p p\frac{d\Phi_p}{dz} - R(n,p,z) = 0$$

$$-\frac{d}{dz}\mu_n n\frac{d\Phi_n}{dz} - R(n,p,z) = 0$$

$$p = n_i \exp\left\{\frac{q}{kT}(\Phi_p - \Psi)\right\}$$

and

$$n = n_i \exp\left\{\frac{q}{kT}(\Psi - \Phi_n)\right\}$$

by a full Newton algorithm with spectral representations in Legendre polynomials for the potentials Ψ, Φ_p and Φ_n in a sequence of sub-domains for each layer. This approach allows highly convergent solutions of the drift-diffusion equations in one dimension. Abrupt junctions and heterojunctions can be naturally represented by letting them fall at the border of a sub-domain. The boundary conditions between sub-domains are the continuity of the quasi-Fermi-

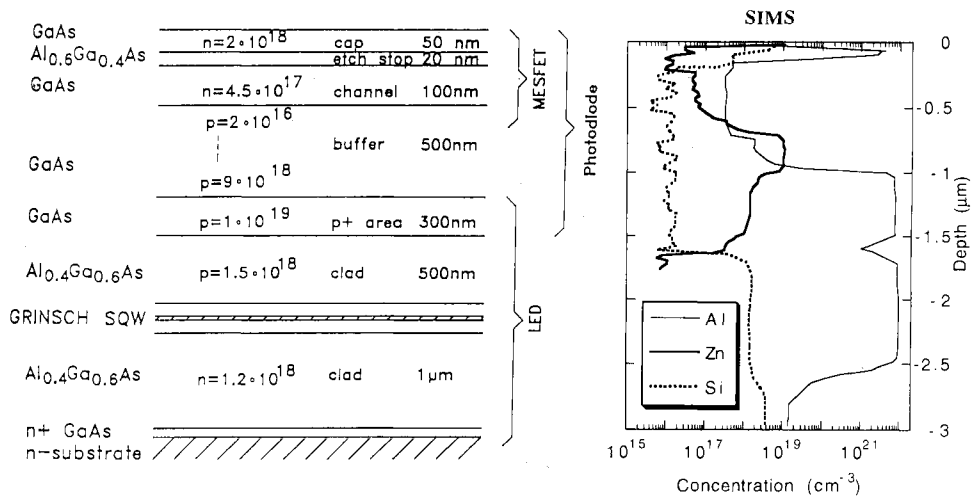

Fig. 2. Layer structure and corresponding SIMS data.

TABLE 1. Material parameters for $Al_xGa_{1-x}As$

Parameter	F	dF/dx	Units	Remarks
E_g	1424	1247	[mV]	Adachi
m_c	0.067	0.083	m_0	Adachi
m_h	0.62	0.14	m_0	Adachi
m_l	0.087	0.063	m_0	Adachi
C_{corr}	0.8655	0		To correct masses shown above (see text)
ε_r	13.18	3.12		Adachi
$n_i(0)$	2.1×10^6		cm^{-3}	Blackemore
$\Delta E_c/\Delta E_g$	$\frac{2}{3}$	0		Conduction band offset

potentials and the continuity of the current. If the interface charge density is zero, as we assume, the D-field is continuous. The static potential Ψ has a discontinuity which must be consistent with the band offsets across the heterojunction. Physically, the discontinuity of Ψ represents the atomically sharp dipole layer occurring between different materials. Although we have let the doping profile (chosen to be consistent with the measured SIMS profile (Fig. 2)) remain constant in the sub-domains, the algorithm can also treat continuously varying doping, mobilities, etc. In the present calculations, only direct generation–recombination processes were included. At the contact interface, we assumed a high recombination velocity due to midgap levels and flatband conditions, which represents an ideal ohmic contact. The capacitances of the pn-junctions are calculated by integration over the carrier concentration profile.

4. Discussion and conclusions

The layer design used in our OEIC structure has the advantage that all layers can be grown in a single epitaxial step, *i.e.* no regrowth is needed. The pn-junction between the MESFET channel and the p+ layer gives rise to a backgating capacitance which limits the cut-off frequency of the transistor. Our simulation yielded a backgating capacitance (Fig. 3) of 60 nF cm^{-2}, which leads to a capacitance of about 0.28 pF for a MESFET of gate length 2 mm and width 20 mm. This implies a cut-off frequency of approximately 3.5 GHz, assuming a channel resistance of 1 kW. The frequency response of the LED is limited to approximately 20 MHz by the spontaneous recombination rate [9]. The most critical device limiting the speed of the circuit is the photodetector. For an active area of 100×100 μm^2 and a reverse bias voltage of -5 V, we estimate a capacitance of 6 pF. For operation at 20 MHz, the load resistor for the photodiode must be less then 10 kΩ.

The p-buffer forms a depletion region into the n-type MESFET channel, leading to backgating effects in the MESFET characteristic. From our simulation data we derive a transconductance of 37 mS mm^{-1} V for this parasitic JFET. This gives rise to a reduction of the MESFET transconductance. The voltage which could be applied to a certain device is limited by the parasitic LED lying beyond each MESFET and photodetector. The problem of circuit design is further complicated by the common backside n-contact to all LEDs.

The OEIC structure presented allows the integration of LEDs, photodetectors and MESFETs by a simple two-mesa process. The speed of the circuits is

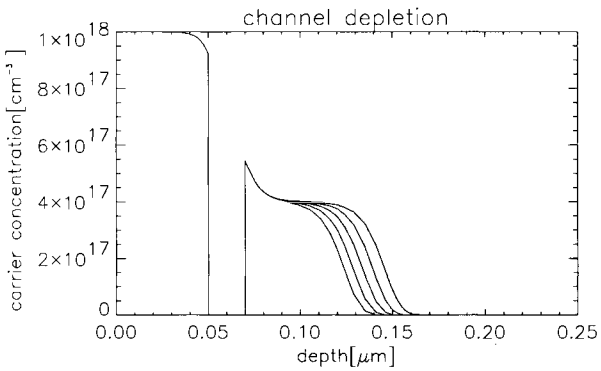

Fig. 3. Electron concentration profile of the photodetector/MESFET biased from −1.0 V to −5.0 V in 1.0 V steps.

mainly limited by the 20 MHz cut-off frequency of the LED. Some restrictions in the circuit design are caused by parasitic devices and the common contacts of the n-side of the LEDs. This OEIC process allows the integration of arrays of simple circuits such as smart pixels, data interconnects and optical neurons.

References

1 M. Dagenais, R. F. Leheny, H. Temkin and P. Bhattacharya, *J. Lightwave Technol., 8* (1990) 846.
2 S. Lin, A. Grot, J. Luo and D. Psaltis, *Appl. Optics, 32* (1993) 1275.
3 M.K. Hibbs-Brenner, S.D. Mukhrjee, B.L. Grung and J. Skogen, *LEOS Summer Topical Meeting on Smart Pixels, August, 1992, Integrated Optoelectronics* (1992) 27.
4 B. J. Van Zeghbroeck, W. Patrick, H. Meier and P. Vettiger, *IEEE Electron Dev. Lett., 8* (3) (1987) 118.
5 A. Ackaert, L. Buydens, F. De Pestel, P. Demeester and P. Van Daele, *Int. Symp. on GaAs and Related Compounds, Jersey, 1990*, Inst. Phys. Conf. Serv., Vol. 412, p.539.
6 J.S. Blakemore, *J.Appl. Phys., 35* (10) (1982) R123.
7 S. Adachi, *J.Appl. Phys., 58* (3) (1985) R1.
8 J. S. Blakemore, *J. Appl. Phys., 53* (1) (1982) 520.
9 K. Ikeda, S. Horiuchi, T. Tanaka and W. Susaki, *IEEE Trans. Electron. Dev., 4* (7) (1977) 1001.

AlGaInP/GaInAs/GaAs MODFET devices: candidates for optoelectronic integrated circuits

W. Pletschen, K. H. Bachem, P. J. Tasker and K. Winkler
Fraunhofer-Inst. of Applied Solid State Physics, Tullastr. 72, W-79108 Freiburg (Germany)

Abstract

Modulation doped field effect transistors (MODFETs) with a p^+-GaAs gate structure were fabricated from AlGaInP/GaInAs/GaAs heterostructures for the first time. Self-aligned devices with a gate length of 0.7 μm exhibit drain currents of 330 mA mm^{-1}, transconductances of 200 mS mm^{-1} and very small gate currents below 50 nA even at gate-source voltages of -5 V. Furthermore, large gate-drain diode breakdown voltages in excess of 30 V are observed. Short gatelength devices (0.3 μm) show a good r.f. performance with a current gain cut-off frequency of 60 GHz and a maximum frequency of oscillation of 140 GHz.

1. Introduction

$(Al_xGa_{1-x})_yIn_{1-y}P$ has been an interesting alloy system for optoelectronic devices for over two decades because one member of this family of alloys has the widest direct band gap (approximately 2.2 eV) of any III/V compound lattice matched to a binary III/V substrate, in this case to GaAs. Owing to the large effort undertaken so far, a variety of light-emitting devices has been developed, such as high performance injection lasers based on AlGaInP/GaAs heterojunctions lasing in the 600 nm range [1] and in the 900–1000 nm range [2]. Another advantage inherent to the AlGaInP/GaAs material system is the excellent etch selectivity between arsenides and phosphides, which simplifies laser fabrication compared with AlGaAs/GaAs based lasers. For these reasons a monolithic integration of AlGaInP/GaAs based electronic devices such as heterojunction bipolar transistors (HBTs) and modulation doped field effect transistors (MODFETs) with the laser diodes mentioned above is of substantial technological interest.

The Al-free alloy system GaInP/GaAs has recently proved to be an exellent candidate for the fabrication of NPN-HBTs [3] and low noise MODFETs [4]. However, no efforts have been undertaken so far to make use of the large conduction band offset, provided by the AlGaInP/GaAs system, for MODFET devices. The probable reason for this lack of activity is an "over-estimation" of the well known problems of preparing "perfect" interfaces between phosphides and arsenides. We have recently circumvented this interface problem via an interface design utilizing a thin AlGaAs layer (1.8 nm thick) placed between channel and AlGaInP barrier. This interlayer provides a sharp interface between the channel and barrier structure while pushing away the compositionally graded transition between arsenides and phosphides from the critical channel interface [5]. For these heterostructures we have indeed observed excellent electron transport properties.

In this paper we report preliminary results on AlGaInP/GaAs based MODFETs. For the investigation we have developed a novel device concept by combining the AlGaInP based active layer structure with a JFET-like design [6], in which the conventional Schottky gate is replaced by a p^+-GaAs gate structure to improve breakdown behaviour and to lower the gate current. By using sufficiently high hole concentrations, the GaAs gate structure behaves like a Schottky gate with artificially enhanced Schottky barrier.

2. Device fabrication

The devices were fabricated from AlGaInP/AlGaAs/GaInAs/GaAs layer structures grown on 2 in GaAs wafers by low-pressure metal-organic chemical vapour deposition as described elsewhere [5]. On top of these structures two additional layers were grown, a 5 nm thin GaInP etch stop and a heavily carbon doped p^+-GaAs layer ($p \approx 7 \times 10^{19}$ cm^{-3}). Carbon was used as dopant because of its stability against diffusion. Figure 1 shows a schematic diagram of our device and reveals the simple fabrication scheme, which makes use of standard contact lithography and selective wet

0921-5107/93/$6.00
© 1993 – Elsevier Sequoia. All rights reserved

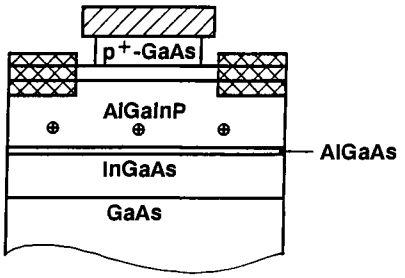

Fig. 1. Schematic view of the device structure.

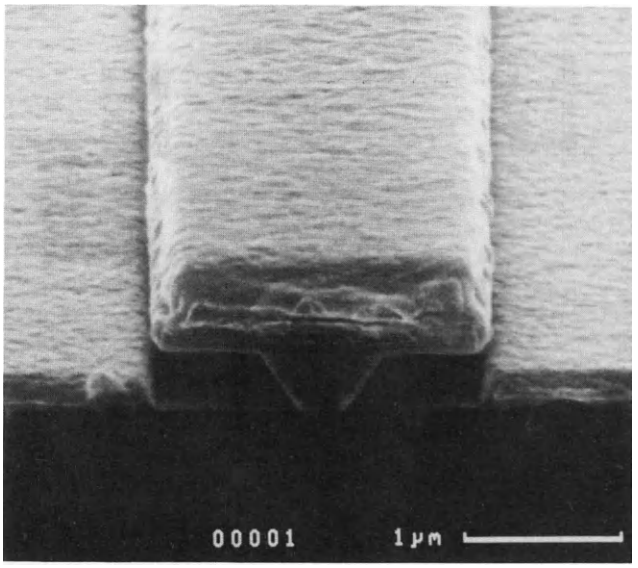

Fig. 2. Scanning electron micrograph of a FET with an effective gatelength of 0.3 μm (gate stripe 1 μm).

etching. Fabrication starts with the gate metallization (TiPtAu) followed by alloying at 380 °C. Subsequently, the p^+-GaAs layer is selectively etched off down to the GaInP etch stop in a phosphorus acid based etchant [7] using the gate metal as mask. In the next step NiGeAu is evaporated over the gate stripes to form self-aligned ohmic contacts for source and drain. After alloying these contacts, device isolation is carried out by boron implantation.

3. Results and discussion

The devices fabricated in this way have a mushroom shaped gate structure as demonstrated by the SEM photograph of Fig. 2. The undercut of the gate metal stripe can be controlled to give effective gatelengths in the submicrometre range because of the use of an etch-stop layer combined with sufficiently low etch rates. Typical d.c. results of a FET with an effective gatelength of 0.7 μm are shown in Figs. 3 and 4. Nearly ideal output characteristics (Fig. 3) without short channel effects are observed for these devices with drain currents of around 330 mA mm^{-1} and transconductances of 200 mS mm^{-1}. It is important to note that these FETs are capable of operating at drain-source voltages as high as 10 V. In addition, the gate current of these devices is much smaller than that of conventional FETs and does not exceed 50 nA even at gate-source voltages of -5 V. The breakdown characteristics at threshold are shown in Fig. 4 for both short- and long-gatelength devices. Long-gatelength (FAT-FET) devices show a one-to-one correlation between drain current and gate current at breakdown, which is indicative of breakdown of the gate-drain diode. The breakdown voltages in this case are above 30 V. In contrast, for short-gatelength devices the gate current near breakdown is a factor of 1000 smaller than the drain current. This reveals channel breakdown with breakdown voltages in excess of 15 V.

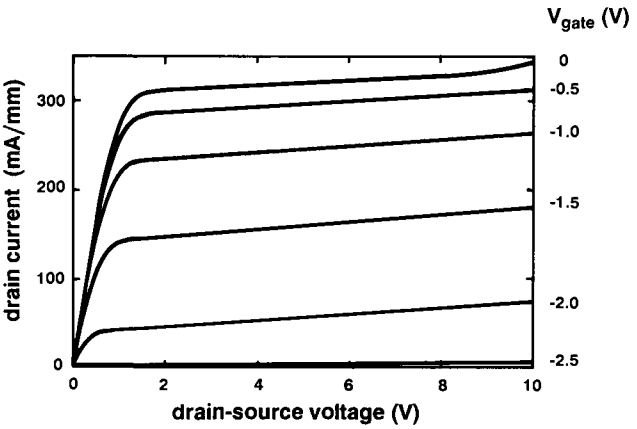

Fig. 3. Output characteristics of a FET with an effective gatelength of 0.7 μm (gate stripe 2 μm) and a gatewidth of 50 μm.

The values of drain current and transconductance are somewhat low and do not really demonstrate the full potential of this heterostructure system as expected from the Hall data [5]. This discrepancy is due to the fact that the device structure has not yet been optimized in terms of electron transport properties or channel–gate separation. In view of the non-optimized layer structure used, excellent r.f. data have been obtained for short-gatelength devices (Fig. 5). Typical cut-off frequencies of 60 GHz for current gain cut-off f_T and 140 GHz for power gain cut off f_{max} are demonstrated; these are the highest values for JFET-like devices reported to date. Note that an f_T of 100 GHz should be easily achievable by simply reducing the present channel–gate distance of 45 nm to about 25 nm.

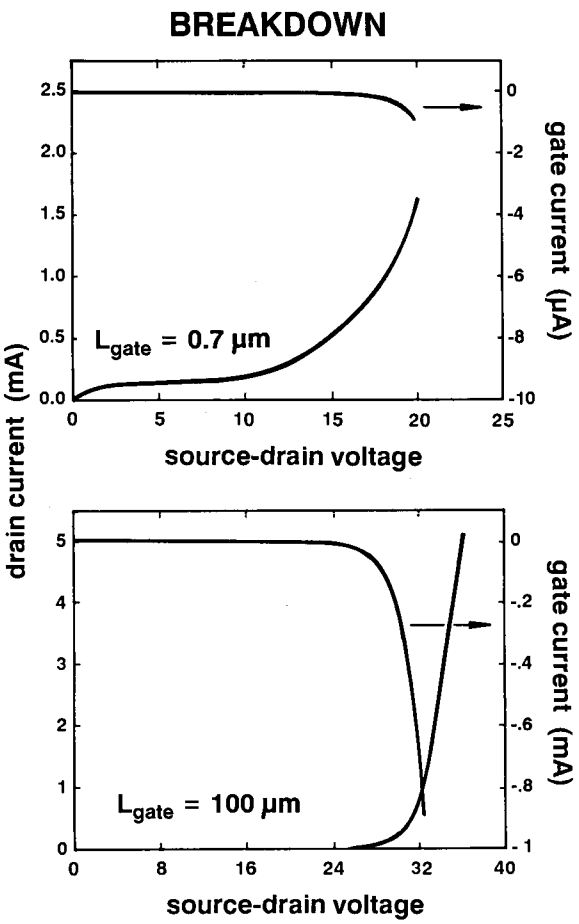

Fig. 4. Breakdown characteristics of the FET of Fig. 3 (top) and a FATFET with a gatelength of 100 μm (bottom).

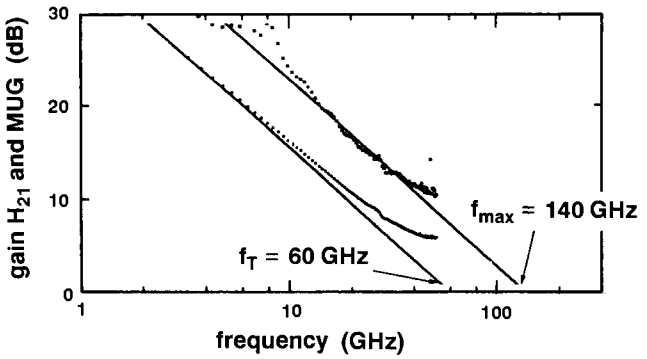

Fig. 5. R.f. figures of merit of a FET with an effective gatelength of 0.3 μm (gate stripe 1 μm) and a gatewidth of 240 μm.

4. Conclusions

Self-aligned AlGaInP/GaInAs/GaAs MODFET devices with a carbon doped p^+-GaAs gate structure have been fabricated and demonstrated to be an attractive alternative to conventional AlGaAs/GaAs MODFETs. The devices show good d.c. characteristics and exhibit large breakdown voltages, and are hence well suited for power applications. Furthermore, the devices already show excellent r.f. performance although the layer structure has not yet been optimized for high-speed operation. Slight modifications of the layer structure, such as a reduced channel-gate separation, are expected to improve the r.f. performance, transconductance and drain current. In conjunction with the etch selectivity mentioned above, our device concept leads to a simple fabrication scheme for MODFETs with submicrometre gates. The present device concept also fits well into the processing scheme of AlGaInP/GaAs based lasers, and thus should simplify the monolithic integration of electronic and optoelectronic devices.

Acknowledgment

The authors would like to thank J. Fleissner, C. Hoffmann and J. Wiegert for their assistance in preparing the devices.

References

1 P. Roentgen, W. Heuberger, G. L. Bona and P. Unger, *J. Cryst. Growth, 107* (1991) 724.
2 I. Yoshida, T. Katsuyama, J. Hashimoto and H. Hayashi, *Electron. Lett., 29* (1993) 654.
3 T. Kobayashi, F. Nakamura, K. Taira and H. Kawai, *Inst. Phys. Conf. Ser., 106* (1990) 357.
4 S. Kuroda, H. Suehiro, T. Miyata, S. Asai, I. Hanyu, M. Shima, N. Hara and M. Takikawa, *Proc. Int. Electron Devices Meet., San Francisco, CA, 1992*, IEEE, Piscataway, NJ, p. 324.
5 K. H. Bachem, D. Fekete, W. Pletschen, W. Rothemund and K. Winkler, *J. Cryst. Growth, 124* (1992) 817.
6 K. Ohata, M. Ogawa, H. Hida and H. Myamoto, *Inst. Phys. Conf. Ser., 74* (1984) 653.
7 T. Lauterbach, W. Pletschen and K. H. Bachem, *IEEE Trans. Electron Devices, 39* (1992) 753.

Materials Science and Engineering, B21 (1993) 307–311

Photoluminescence and electroluminescence processes in $Si_{1-x}Ge_x/Si$ heterostructures grown by chemical vapor deposition

J. C. Sturm, X. Xiao, Q. Mi, C. W. Liu, A. St. Amour and Z. Matutinovic-Krstelj
Department of Electrical Engineering, Princeton University, Princeton, NJ 08544 (USA)
L. C. Lenchyshyn and M. L. W. Thewalt
Simon Fraser University, Burnaby, B.C. V5A 1S6 (Canada)

Abstract

Well-resolved band-edge exciton photoluminescence has been observed in strained $Si_{1-x}Ge_x$ quantum wells on Si(100). A growth technique which provides material with a low density of non-radiative centers and a uniform microstructure is necessary for observing such luminescence. The luminescence exhibits a characteristic no-phonon line due to the alloy randomness, and a threefold splitting of the transverse optical phonon mode due to different nearest neighbor interactions. The luminescence has been observed from 2 to 300 K, and can also be electrically pumped (electroluminescence) to over 300 K, with peak emission from 1.3 to 1.5 μm.

1. Introduction

Very-large-scale integrated circuits are made in silicon because of the excellent manufacturability of silicon devices and resulting low defect density over large areas. The intrinsic electrical and optical properties of silicon are rather poor, however (low mobilities, indirect band gap, etc.). Therefore considerable effort has been focused over the last 10 years on developing a silicon-based heterojunction technology for overcoming these inherent limitations of silicon integrated circuits, with the most effective approach being that of commensurately strained $Si_{1-x}Ge_x$ alloys on Si(100) substrates. Heterojunction bipolar transistors made in this material system at present exhibit f_T values in excess of 90 GHz at room temperature [1].

Although the growth of strained $Si_{1-x}Ge_x$ on Si(100) has been actively pursued by many groups for nearly a decade, it is only within the past 3 years that well-resolved band-edge exciton luminescence has been observed in this material. In 1990, exciton photoluminescence (PL) was reported from a fairly thick strained layer with only 4 at.% Ge ($x=0.04$) [2]. In 1991, such PL was clearly observed for the first time in quantum wells (QWs) and superlattices (with $x \approx 0.2$) [3]. These latter samples were grown not by molecular beam epitaxy, as in most of the previous Si–Ge luminescence work, but rather by rapid thermal chemical vapor deposition (RTCVD). This paper reviews the RTCVD growth technique and the resulting Si–Ge layer PL and electroluminescence (EL) from 2 to 300 K and then finally suggests some future directions for continuing research.

2. Rapid thermal chemical vapor deposition

RTCVD is a straightforward combination of rapid thermal processing with conventional chemical vapor deposition (CVD) (Fig. 1). A single 100 mm silicon wafer is suspended on quartz pins inside a load-locked quartz reaction tube and is heated by a bank of tungsten–halogen lamps located outside the reactor chamber. The typical source gases are dichlorosilane, germane, diborane and phosphine in a hydrogen carrier, and growth temperatures vary from 500 to 1200 °C. (Unless otherwise noted, all results in this paper are for $Si_{1-x}Ge_x$ grown at 625 °C and Si at 700 °C, at a pressure of 6 Torr.) The reactor has several unusual features which are important to the growth of high quality films. First, although the reactor is not of an "ultrahigh vacuum" type (O-ring seals are used and only a mechanical rotary vane pump is used in normal operation), through the use of the load-lock and ultrahigh purity gas handling, high quality epitaxial layers with low oxygen concentrations (10^{18} cm^{-3} or less) can be achieved at growth temperatures as low as 550 °C. (Oxygen contamination (concentrations levels in excess of 10^{18} cm^{-3}) and related defects are a common problem in silicon-based CVD at temperatures below 900 °C.) Second, there is no possible source of extrinsic contamination (such as metal wafer heaters

0921-5107/93/$6.00

© 1993 – Elsevier Sequoia. All rights reserved

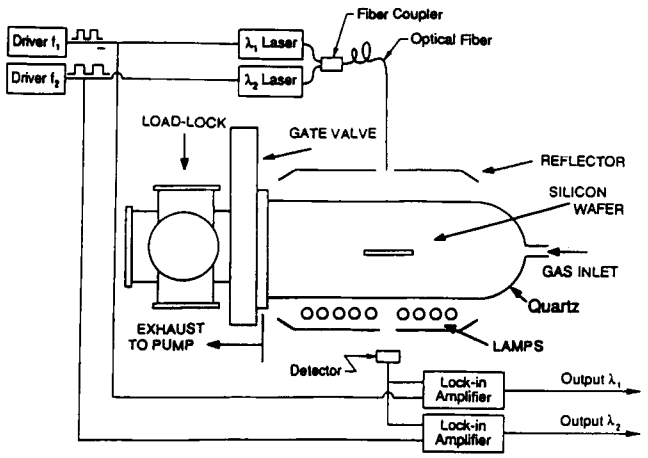

Fig. 1. Schematic cross-section of the RTCVD reactor with temperature measurement by IR transmission.

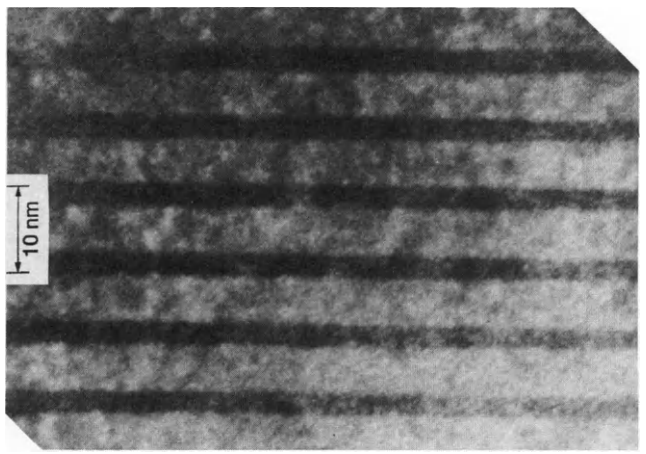

Fig. 2. Cross-section TEM of a Si(5 nm)/$Si_{0.8}Ge_{0.2}$(3 nm) MQW sample grown by RTCVD. All Si layers were grown at 700 °C and all $Si_{1-x}Ge_x$ layers at 625 °C.

and susceptors) inside the reactor chamber, so that films with very low densities of midgap states and high carrier lifetimes (*i.e.* low non-radiative recombination rates) can be grown. Third, the ability to change the sample temperature rapidly (about 100 K s^{-1}) gives the ability to optimize the growth temperature for each layer and interface. For example, substrate cleaning can be done at 1000 °C in H_2, $Si_{1-x}Ge_x$ can be grown at 625 °C or less (to avoid strain relaxation and island effects), and Si layers can be grown at a higher temperature (700 °C) to achieve a faster growth rate. (A catalytic reaction during $Si_{1-x}Ge_x$ growth allows a much higher growth rate (10–100 times) than with Si alone [4, 5].) Finally, the wafer temperature is measured *in situ* with an accuracy of a few kelvins, without the need for any adjustable parameters such as emissivity, by measuring the transmission of the substrate at 1.3 and 1.5 μm [6]. Figure 2 is a cross-section transmission electron micrograph (TEM) of a multiple quantum well (MQW) consisting of alternating layers of 5 nm Si and 3 nm $Si_{0.8}Ge_{0.2}$, where all Si layers were grown at 700 °C and all $Si_{1-x}Ge_x$ layers were grown at 625 °C. From this TEM it is evident that the interface abruptness is 1 nm or less. Furthermore, it is clear that repeatable temperatures can be achieved, as reflected in the constant thicknesses (and hence growth rates) of the multiple Si and $Si_{0.8}Ge_{0.2}$ layers, with the IR transmission technique for temperature measurement. Further growth details have been given in ref. 7.

3. Photoluminescence

Characteristic 2 and 77 K PL spectra of a single Si/$Si_{0.8}Ge_{0.2}$(33 Å)/Si QW is shown in Fig. 3. Although most of the carriers are generated deep in the substrate,

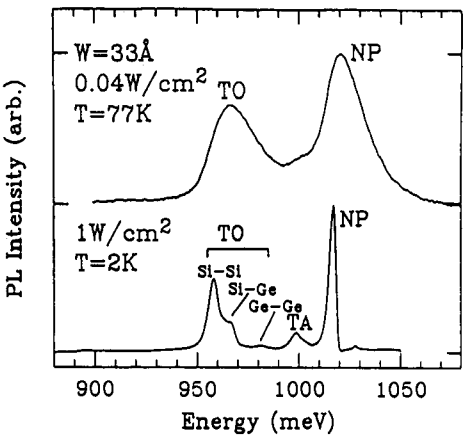

Fig. 3. 2 and 77 K PL spectra of an Si/strained $Si_{1-x}Ge_x$/Si QW of width 33 Å.

they can travel about 1 μm even at 2 K to the quantum well before generating luminescence [8]. By comparison with previous work in bulk unstrained $Si_{1-x}Ge_x$ [9], the PL features observed at 2 K may be easily identified. The highest energy signal is a no-phonon (NP) signal despite the fact that the alloy has an indirect band gap. This is due to the alloy randomness which breaks the translational symmetry of an ideal lattice, relaxing the requirement for conservation of crystal momentum. The lower energy features are momentum-conserving phonon replicas, the most significant of which is the transverse optical (TO). While a single TO line is seen in silicon, in the alloy three lines are seen because of the different nearest-neighbor modes (Si–Si, Si–Ge and Ge–Ge). The relative height of the different TO replicas depends on the composition as expected [9] but is different in narrow QWs compared with the bulk because of wavefunction pene-

tration into the barriers [3]. Except for thermal broadening, similar features are observed at 77 K. This shows that the NP signal is indeed an intrinsic property of the alloy and not due to any localization effects at low temperature (such as a bound exciton).

Similar spectra (except for a red shift due to an absence of quantum confinement) have been measured in wide structures with wider wells (*e.g.* 500 Å) [8]. This shows that the NP line is not due to any confinement effects. Similar spectra have also been obtained from ten isolated QWs (about 30 Å, $Si_{0.8}Ge_{0.2}$) and in $Si_{0.8}Ge_{0.2}/Si$ superlattices (period, about 40 Å), showing that superlattice effects are clearly not required to achieve luminescence (Fig. 4).

The temperature dependence is characterized first by a transition from a bound exciton to a free exciton in the range 10–20 K [3]. Above 30 K, there is little intensity change until over 100 K. Above 100 K, the PL decays exponentially with the onset of the decay, increasing with increasing valence band offset. Figure 5 shows the peak NP PL signal *vs.* temperature for two single QW samples, with $x=0.2$ and $x=0.35$. The decay at high temperatures is governed by the increased non-radiative recombination of carriers and has been found to be controlled by the thermal escape of carriers from the QW to a region of extremely low lifetime in the cladding Si layers, such as the top surface [10]. Therefore a large Ge fraction (about 0.3) is required to achieve room temperature luminescence.

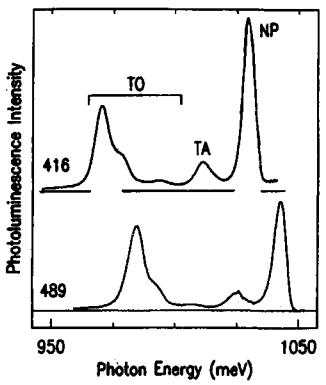

Fig. 4. Comparison of the PL spectra of a 50-period $Si_{0.8}Ge_{0.2}/Si$ (40 Å period) superlattice with that of ten isolated $Si_{0.8}Ge_{0.2}$ QWs (width, about 30 Å), $T=2$ K.

4. Electroluminescence

The band-edge recombination mechanism can also be electrically pumped by putting the $Si_{1-x}Ge_x$ QWs inside the i region of a p–i–n diode. Early results with $x \approx 0.2$ showed that this EL decayed sharply with increasing temperature above 100 K, consistent with the PL results in Fig. 5 [11]. By increasing x to 0.35 (ten QWs), the high temperature performance can be improved. Figure 6 shows the PL of such a structure before processing and EL of the finished device at a heat sink temperature of 80 K. The 4 K PL is not as well resolved as that presented in the earlier figures, possibly owing to some differences between each of the ten wells, some inhomogeneity, or electric field effects. Nevertheless the clear NP and TO replica signature of band-edge recombination is evident, and the NP energy corresponds approximately to that expected for the given composition. The 77 K PL is similar to that expected (*e.g.* Fig. 3), although the blue shift is not entirely understood [12]. The EL observed at a heat sink temperature of 80 K (junction temperature somewhat higher) also shows an NP peak together with a low energy TO shoulder, providing evidence that the EL and PL generation mechanisms are the same (*i.e.* band-edge recombination). At a heat sink temperature of 300 K, the NP peak is still clearly evident, with a peak at 1.3 μm (Fig. 7). Some emission from the Si cladding is also evident at this higher temperature, but it accounts for less than 10% of the emitted power. Above a threshold of about 10 mA, the light emission

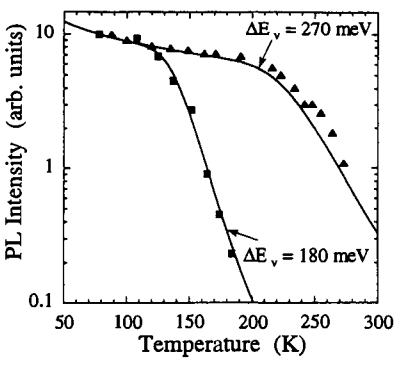

Fig. 5. NP luminescence *vs.* temperature for single $x=0.2$ (■) and $x=0.35$ (▲) QWs, —— model.

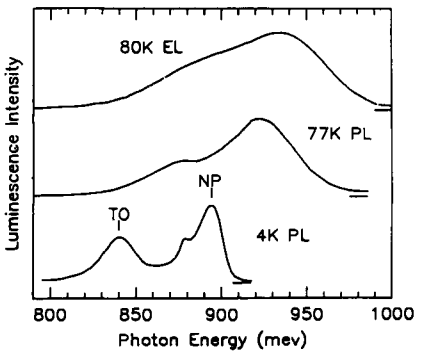

Fig. 6. 4 and 77 K PL spectra of the EL sample before processing, and the EL spectrum for 10 mA drive current and a heat sink temperature of 80 K.

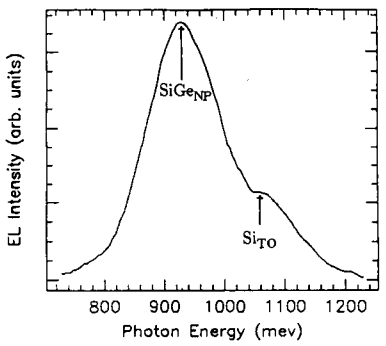

Fig. 7. EL spectra for a drive current of 10 mA at a heat sink temperature of 300 K.

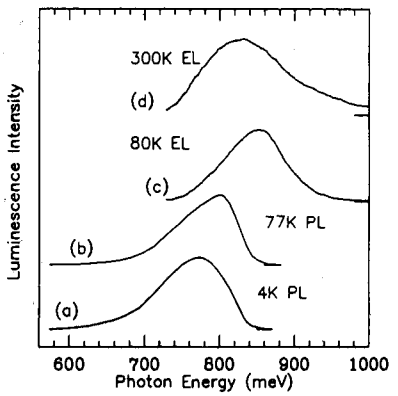

Fig. 8. PL (4 and 77 K) and EL (90 mA drive current; 80 and 300 K heat sink) for the 10 Å Ge layer.

from a 60 μm × 60 μm diode increases linearly with increasing current, with an estimated lower limit to the internal quantum efficiency at 60 mA of 0.03% [12].

We have also achieved a peak room temperature EL at 1.5 μm in a structure which consists of a single layer of Ge of 10 Å thickness, surrounded by Si cladding (Fig. 8). The exact microstructure of the sample is not yet known, and the layer may contain islands or have interdiffused with the silicon. Although the PL is of comparable strength with the $Si_{1-x}Ge_x$ ($x \leqslant 0.35$) shown earlier, the EL is an order of magnitude weaker. Furthermore, the broad linewidth of the 4 K PL (full width at half-maximum, 80 meV) prevents clear identification of the PL mechanism. It is possible that the EL and PL in this sample are due to defects and not to band-edge carriers.

5. Future directions

Further increases in light emission from $Si_{1-x}Ge_x/Si$ structures will require increasing the radiative recombination rate or decreasing the competing (and dominant) non-radiative recombination. One proposed approach for increasing the radiative rate is the use of short-period "zone-folded" Si/Ge superlattices. It has been proposed that such structures, created out of indirect-band-gap constituents, could yield a "quasi-direct" band gap superlattice [13, 14]. The interpretation of early PL results on such superlattices [15, 16] (and many other reports) were controversial [17], however, because of the broad linewidths, energies below expected band gaps and, in some cases, energies corresponding to known silicon dislocation luminescence. Recently, convincing evidence of band-edge PL in short-period Si/Ge superlattices of improved quality has been observed [18]. However, whether zone-folding effects were occurring and were responsible for the PL is not clear.

As an alternative to increasing the radiative rate, one can attempt to reduce the non-radiative rate. In principle this can be done by localizing excitons to prevent their finding non-radiative sites. Localization of bound excitons at shallow impurities (at 2 K, for example) is not acceptable because a bound exciton contains three carriers, and hence non-radiative Auger recombination occurs. Excitons may also be localized at areas where there are local fluctuations in band gap (locally higher Ge concentration), and the probability of such a region (about $(50\ \text{Å})^3$) containing impurities or defects is very low. At low pump densities we have obtained evidence of this localization, such as the low energy signal in Fig. 9. Note that the energy of the signal is less than that of the average band gap represented by the PL energies at higher pump powers (bound exciton signal). The radiative efficiency is indeed much larger (11% *vs.* 10^{-2}%) and the lifetime is much slower (greater than 1 ms *vs.* about 1 μs) compared with bound excitons at 2 K [19]. This feature saturates at only moderate pump powers, however, because of the finite number of such fluctuations. Intentionally creating such localizing regions with higher confining potential may be an option towards even higher efficiencies and higher temperatures.

Yet another approach involves growth on different substrate orientations. Because of the biaxial strain component in pseudomorphic layers, the crystal orientation strongly affects the band structure of the strained layer. For example, in strained $Si_{1-x}Ge_x$ on Si(100) the conduction band offset is close to zero, resulting in poor electron confinement in contrast with the well-confined holes. On Si(110), however, the different symmetry causes a larger reduction in the conduction band in the $Si_{1-x}Ge_x$, with the result that a positive conduction band offset and electron confinement to the $Si_{1-x}Ge_x$ well are expected [20]. We have recently succeeded in growing such pseudomorphic structures on Si(110) by RTCVD at 625 °C, and strong PL was observed (Fig. 10). Most significantly, a substantially larger NP line (compared with the TO line) is observed compared with that seen on (100) substrates (*e.g.* Figs.

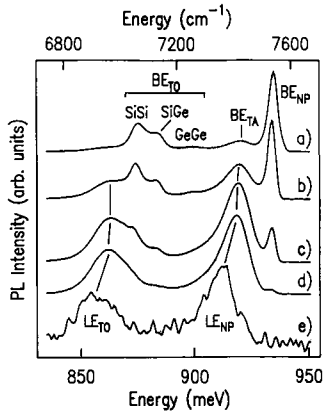

Fig. 9. 2 K luminescence for different pump powers for a single $Si_{0.8}Ge_{0.2}$ QW. At low pump power, a low energy (LE) feature (with a NP line and TO replica) due to excitons localized by alloy fluctuations is present, with an efficiency about 10^3 times higher than the regular band edge signal. BE represents the bound exciton signal, T = 2 K.

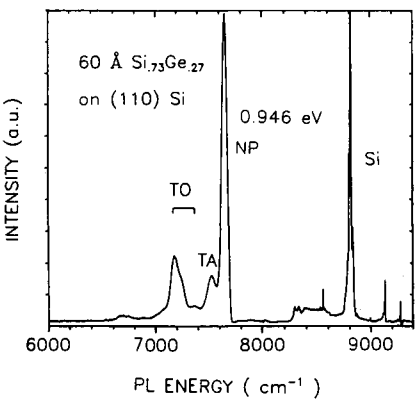

Fig. 10. 2 K luminescence from a single 60 Å quantum well of $Si_{0.7}Ge_{0.3}$ on Si(110) (a.u., arbitrary units).

3 and 4). Whether this effect is due to a higher electron density in the alloy region or other effects is not yet understood, however.

6. Summary

Well-resolved band-edge luminescence has been observed in $Si_{1-x}Ge_x/Si$ structures grown by RTCVD. The NP emission mechanism, which is due to alloy randomness, provides a radiative process which can be up to an order of magnitude larger than those found in silicon. Furthermore, the confining effect of a $Si_{1-x}Ge_x$ quantum well on carriers can prevent them from reaching non-radiative recombination sites and hence decrease the non-radiative recombination rate. Room-temperature EL at 1.3 μm can be achieved with an efficiency of about 0.03%. Further improvements will depend on increasing radiative mechanisms or decreasing non-radiative processes.

Acknowledgments

The assistance of J. McCaffrey of the National Research Council of Canada with the TEM is greatly appreciated. We gratefully acknowledge the support of the National Science Foundation; Office of Naval Research; N.J. Commission on Science and Technology (Princeton); Natural Sciences and Engineering Research Council; Simon Fraser University Centre for Systems Science and British Columbia Advanced Systems Institute.

References

1 A. Gruhle, H. Kibbel, U. Erben and E. Kasper, *Electron. Lett., 29* (1993) 415.
2 K. Terashima, M. Tajima and T. Tatsumi, *Appl. Phys. Lett., 57* (1990) 1925.
3 J. C. Sturm, H. Manoharan, L. C. Lenchyshyn, M. L. W. Thewalt, N. L. Rowell, J. P. Noel and D. C. Houghton, *Phys. Rev. Lett., 66* (1991) 1362.
4 B. S. Meyerson, K. J. Uram and F. R. Legoues, *Appl. Phys. Lett., 47* (1988) 721.
5 P. M. Garone, J. C. Sturm, P. V. Schwartz, S. A. Schwarz and B. J. Wilkens, *Appl. Phys. Lett., 56* (1990) 1275.
6 J. C. Sturm, P. M. Garone and P. V. Schwartz, *J. Appl. Phys., 69* (1991) 542.
7 J. C. Sturm, P. V. Schwartz, E. J. Prinz and H. Manoharan, *J. Vac. Sci. Technol. B, 9* (1992) 2011.
8 J. C. Sturm, X. Xiao, P. V. Schwartz, C. W. Liu, L. C. Lenchyshyn and M. L. W. Thewalt, *J. Vac. Sci. Technol. B, 10* (1992) 1998.
9 J. Weber and M. I. Alonso, *Phys. Rev. B, 40* (1989) 5683.
10 J. C. Sturm, X. Xiao, Q. Mi, L. C. Lenchyshyn and M. L. W. Thewalt, *Materials Research Society Symp. Proc.*, Vol. 298, Materials Research Society, Pittsburgh, PA, 1993, in press.
11 D. J. Robbins, P. Calcott and W. Y. Leong, *Appl. Phys. Lett., 59* (1991) 1350.
12 Q. Mi, X. Xiao, J. C. Sturm, L. C. Lenchyshyn and M. L. W. Thewalt, *Appl. Phys. Lett., 60* (1992) 3177.
13 U. Gnutzmann and K. Clausecker, *Appl. Phys., 3* (1974) 9.
14 S. Satpathy, R. M. Martin and C. G. van de Walle, *Phys. Rev. B, 38* (1988) 13 237.
15 H. Okumura, K. Miki, S. Misawa, K. Sakamoto, T. Sakamoto and S. Yoshida, *Jpn. J. Appl. Phys., 28* (1989) L1893.
16 R. Zachai, K. Eberl, G. Abstreiter, E. Kasper and H. Kibbel, *Phys. Rev. Lett., 64* (1990) 1055.
17 U. Schmid, N. E. Christensen and M. Cardona, *Phys. Rev. Lett., 65* (1990) 2610.
18 U. Menczigar, G. Abstreiter, J. Olajos, H. Grimmeiss, H. Kibbel, H. Presting and E. Kasper, *Phys. Rev. B, 47* (1993) 4099.
19 L. C. Lenchyshyn, M. L. Thewalt, J. C. Sturm, P. V. Schwartz, E. J. Prinz, N. L. Powell, J. P. Noel and D. C. Houghton, *Appl. Phys. Lett., 60* (1992) 3174.
20 C. G. van de Walle and R. M. Martin, *Phys. Rev. B, 34* (1986) 5621.

Materials Science and Engineering, B21 (1993) 312–316

Tunable infrared photoemission sensor on Si using epitaxial $ErSi_2$/Si heterostructures

I. Sagnes, Y. Campidelli, G. Vincent* and P. A. Badoz
France Telecom-CNET, BP 98, F-38243 Meylan (France)

Abstract

We study the internal photoemission response of an Ir/Si/$ErSi_2$ asymmetrical metal–silicon–metal heterostructure, or "tunable infrared photoemission sensor" (TIPS). The TIPS photoresponse results from the combination of both hole and electron photoemission, from one metallic film to the other, above or below the trapezoidal barrier formed by the epitaxial Si layer. Due to the asymmetry of the potential barrier, the effective barrier heights (EBHs) can be modulated by an external bias applied between the two metallic electrodes. This leads to a large dependence of the TIPS photoresponse on the applied bias. The experimental TIPS cutoff wavelength is shifted from around 1.4 μm to more than 6 μm with quantum efficiencies varying from 2.5% at 3 μm to 8.5% at around 1 μm when a positive bias of a few hundred meV is applied to the Ir electrode. The photoresponse of such a heterostructure is quantitatively fitted using the Fowler photoemission formalism, taking into account: (a) the respective absorption in each metallic film and (b) the four different photoemission processes. These fits allow the determination of the EBHs as a function of the applied bias and show that in an asymmetric heterostructure hot carriers, both holes and electrons, can cross a 200 nm thick epitaxial Si layer.

Silicide–silicon heterostructures are of increasing interest due to their applications in micro and optoelectronics, particularly in the field of near-infrared detectors. Two decades ago, Shepherd and Yang [1] proposed the use of internal photoemission of carriers over the silicide–silicon Schottky barrier for infrared detection. Since this work, large focal plane arrays based on PtSi/p-Si Schottky diodes with 6 μm cutoff wavelengths have been routinely fabricated [2] and recently, IrSi/p-Si Schottky photodetectors have been developed with cutoff wavelengths as long as 12 μm [3]. The Schottky photoresponse and the cutoff wavelengths are fully determined by the Schottky barrier height (SBH) at the metal–Si interface. The cutoff wavelength thus cannot be externally modified, except by lowering the Schottky barrier which rarely allows tuning ranges exceeding a few tens of meV. One could expect much larger modulation effects, however, in asymmetrical metal–semiconductor–metal heterostructures [4]. Indeed, when a bias is applied to such a heterostructure, the trapezoidal potential barrier (formed by the intermediate semiconductor band gap) is greatly modified, thus varying the spectral profile of the photoresponse.

In this paper, we characterize this new type of metal–silicon–metal infrared detector using the vertical Ir/Si/$ErSi_2$/Si_{sub} system. We show that the cutoff wavelength of such a tunable infrared photoemission sensor (TIPS) detector can indeed be modulated over a large wavelength range by applying a bias between the two metallic electrodes, resulting in quantum efficiencies comparable to the best obtained to date in single Schottky detectors. We also show that the experimental TIPS photoresponse exhibits a very different behaviour from that of a Schottky barrier detector, which can be quantitatively explained using a modified Fowler photoemission formalism [5].

The $ErSi_2$ and top Si films were epitaxially grown [6] under ultra high vacuum in a molecular beam epitaxy (MBE) chamber on 2-in. ⟨111⟩ Si 10^3 Ω cm wafers. The $ErSi_2$ films were grown by codeposition of Er and Si in the atomic ratio 1:2 at room temperature followed by a solid phase reaction at 850 °C. Extensive characterization by electron and X-ray diffraction, low energy electron diffraction, Rutherford backscattering and transmission electron microscopy show that the $ErSi_2$ films were epitaxial and monocrystalline [6]. The top Si layers were then epitaxially grown at 650 °C onto the silicide in the same MBE chamber [6]. Ir diodes of various areas were then defined using a standard liftoff technique on the epitaxial Si layer, the Ir film being evaporated at room temperature under high vacuum. Both Ir and $ErSi_2$ contacts were fabricated using ultrasonic wedge bonds to the Ir diode metallization (400×500 μm^2) and on a very large area Ir dot (acting as an ohmic contact to the underlying Er silicide) [7]

*Permanent address: Université Joseph Fourier, BP 53X, F-38041 Grenoble, France.

0921-5107/93/$6.00

© 1993 - Elsevier Sequoia. All rights reserved

respectively. The diodes were then mounted in a liquid nitrogen cryostat and illuminated by monochromatic light, with the internal photoemission current being measured using a lock-in amplifier (the experimental setup has been described previously) [8].

The TIPS basically consists of two back-to-back Schottky diodes [4] separated by a thin undoped Si layer. The thickness of this Si layer is adjusted so that the Si is fully depleted, resulting in a trapezoidal potential barrier between the two metallic films. The two metals are chosen so that they have different SBHs on silicon (an SBH on n-type Si of around 0.9 eV for Ir [9] and 0.3 eV for $ErSi_2$ [8]) and that the TIPS therefore exhibits a highly asymmetrical band structure. When the TIPS is illuminated at photon energies below the Si band gap energy, the photons are absorbed in both metal layers by the formation of excited carriers. A fraction of these excited carriers may overcome the trapezoidal potential barrier, giving rise to a photocurrent between the two electrodes [7].

Figure 1(a) shows the photoresponse of a single $ErSi_2$/n-Si Schottky diode *vs.* photon energy under front illumination. It is clearly seen in this figure that the photocurrent successfully follows the Fowler theory [5] over a more than 0.5 eV photon energy range (*i.e.* the photocurrent, normalized per incident photon, is proportional to $(h\nu-\varphi)^2$ where φ, the photoemission threshold, is the SBH). By a linear extrapolation of the curve to zero current, we unambiguously determine the $ErSi_2$/n-Si SBH to be $\varphi_n = 0.28$ eV. We also note that, by applying a bias between the metal and the Si, the photocurrent intensity and the threshold are not modified except for a slight shift of the threshold (due to the Schottky barrier lowering) which does not exceed a few tens of meV [8]. It should also be noted that far from the threshold (*i.e.* 0.5 eV above), the experimental photocurrent starts to deviate from the Fowler photocurrent. A fit over the whole photon energy range can therefore be obtained by assuming $I_{ph} \propto (h\nu-\varphi)^2 F_{fowler}$, where F_{fowler} is the "Fowler deviation coefficient" which is taken to be the ratio of the experimental photocurrent to the Fowler photocurrent. This "Fowler deviation coefficient" is equal to 1 over most of the photon energy range and decreases only at energies several 100 meV above the threshold.

Figure 1(b) shows the TIPS photoresponse, under back illumination, for different biases applied between the two metallic electrodes. This figure clearly demonstrates that:

(a) the TIPS photocurrent does not follow the usual Fowler theory and presents a pronounced dip around 0.75 eV,

(b) both the shape and the intensity of the TIPS photoresponse depend strongly on the applied bias, and

(c) at low applied bias the photocurrent becomes very weak, goes to zero and changes sign for a photon energy of around 1 eV. Note that the TIPS photoresponse is roughly independent of photon energy in the range 0.55–0.8 eV as opposed to that of a Schottky barrier photodetector.

As can be seen from a comparison of Figs. 1(a) and 1(b), the TIPS photoresponse exhibits a very different behaviour from that of a Schottky barrier detector. This indicates that the origin of the TIPS photocurrent is much more complex: indeed

(a) four different internal photoemission processes are simultaneously in competition, as we will see in the next paragraph, and

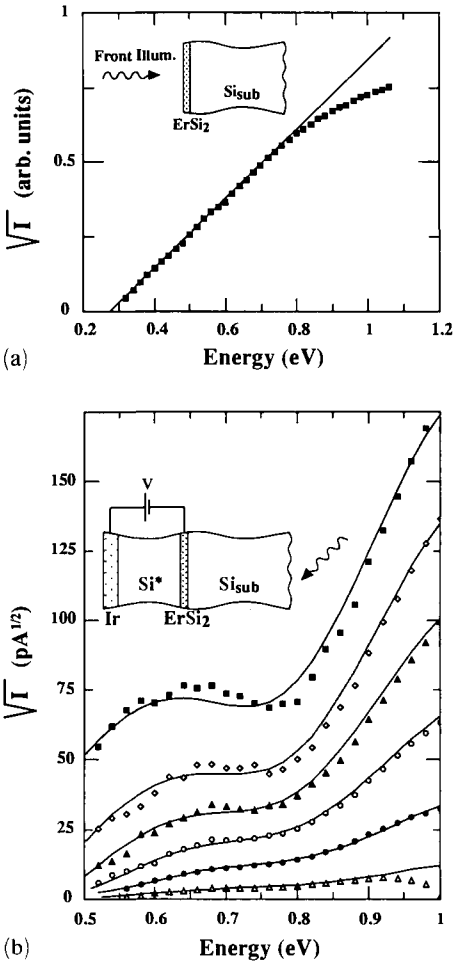

Fig. 1. (a) ■ Square root of the photocurrent *vs.* photon energy, measured at 77 K, for a single $ErSi_2$/n-Si Schottky diode (front illumination). —— Fowler plot $\sqrt{I} \propto (h\nu-\varphi)$ with $\varphi = 0.28$ eV. (b) Square root of the photocurrent of an Ir(20 nm)/Si*(200 nm)/$ErSi_2$(10 nm) TIPS, measured at 150 K, as a function of photon energy (back illumination) for different positive bias values applied between the Ir and the $ErSi_2$ electrodes: ■ 0.6 V, ◇ 0.5 V, ▲ 0.4 V, ○ 0.3 V, ● 0.2 V, △ 0.1 V. The solid lines are the theoretical curves obtained using the model described in the text derived from the Fowler formalism.

(b) due to its multilayer structure, the TIPS absorption is strongly dependent on the photon energy, which also must be taken into account.

Under illumination, the incident light is absorbed in both the Ir and $ErSi_2$ layers by the formation of electron–hole pairs. Four different internal photoemission processes may then occur, two of them being shown in Fig. 2. Electrons (photocurrent I_3) may be emitted from $ErSi_2$ over the potential barrier (whose effective barrier height (EBH) is the sum of the $ErSi_2$/n-Si SBH, φ_3, and the potential drop, ΔV, in the Si layer), cross the Si film against the built-in electric field and then be collected in the Ir electrode. Holes (photocurrent I_4) may be emitted from Ir below the trapezoidal barrier of EBH, $\varphi_4 + \Delta V$ (since in Fig. 2 increasing hole energy is directed to the bottom), cross the Si layer before being collected in the silicide. These two processes result in two photocurrents of the same sign and form the positive photocurrent (conventionally flowing from Ir to $ErSi_2$). The negative photocurrent results from the two remaining photoemission processes (which are not shown in Fig. 2 for the sake of clarity but mirror I_3 and I_4):

(1) electrons (photocurrent I_2) emitted over the Ir/n-Si Schottky barrier, φ_2, which drift down the electric field and are collected in the silicide;

(2) holes (photocurrent I_1) emitted below the $ErSi_2$/p-Si Schottky barrier, φ_1, which cross the Si layer before being collected in the Ir film.

The respective magnitude of these four photocurrents depends primarily on the photon energy but also on the temperature and sample crystalline quality. By applying a bias between the two metallic electrodes, the shape of the potential barrier is modified, mostly through variations in ΔV, thus strongly affecting the respective weight of the four contributions. This qualitatively explains why both the effective threshold and the intensity of the photocurrent may depend on the applied bias, as is experimentally observed.

Using the Abelès matrix method [10] and the complex refractive indices of Si, Ir and $ErSi_2$, it is possible to calculate the fraction of incident light absorbed in each metal in the TIPS structure as well as in single Ir/Si and $ErSi_2$/Si Schottky diodes. The Si and Ir refractive indices have been taken from the literature [11] whereas those of $ErSi_2$ have been obtained through reflection and transmission measurements [12]. Figure 3 shows the fraction of incident light energy which is absorbed in the $ErSi_2$ layer of the TIPS structure of Fig. 1(b). This figure clearly shows a strong dependence of the absorption on the direction of illumination and on the incident energy. Under back illumination, the $ErSi_2$ absorption exhibits a pronounced minimum around 0.75 eV which may qualitatively explain the photocurrent dip observed in Fig. 1(b). Indeed, in the TIPS structure, the epitaxial Si layer plays the role of a Fabry–Perot cavity: the Si thickness determines both the respective weight of absorption in each metallic film and the shape of the absorption curve. Contrary to the case of TIPS, it should be noted that in single Schottky diodes the fraction of light absorbed depends very little on the incident energy: in single $ErSi_2$/Si Schottky diodes, it is independent of energy while it increases roughly linearly with energy by a factor of around 2 in Ir/Si Schottky diodes over the 0.5–1 eV energy range.

At this point, it is clear that in order to quantitatively describe the TIPS photocurrent behaviour we must introduce a new model which takes into account the four photocurrents present in the TIPS structure as well as the fraction of incident light absorbed in each metallic film. Consequently, we assume that I_{ph}, normalized per unit incident photon, can be expressed

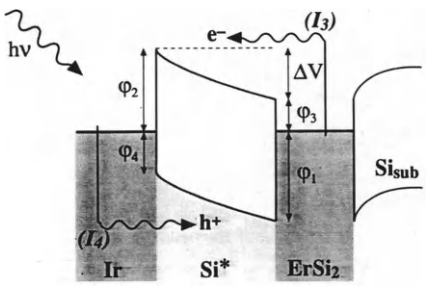

Fig. 2. Energy band diagram of the Ir/Si*/$ErSi_2$ TIPS with no applied bias. Two of the four photoemission processes are schematically indicated: electrons emitted from $ErSi_2$ over the trapezoidal potential barrier towards Ir (I_3) and holes emitted from Ir below the Si barrier towards $ErSi_2$ (I_4). The other two processes, I_1 and I_2, which are not shown in the figure, mirror I_3 and I_4.

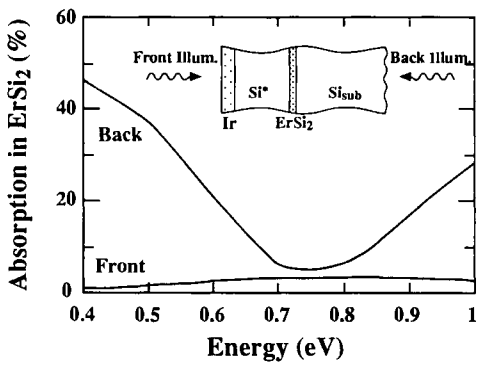

Fig. 3. Fraction of incident light absorbed in the $ErSi_2$ layer of the TIPS structure of Fig. 1(b) calculated using the Abelès matrix method. The inset shows a schematic drawing of the TIPS together with the two possible directions (back and front) of the illumination.

by the sum of the four contributions:

$$I_{ph} = \sum_{i=1}^{4} I_i$$

with every I_i given by

$$I_i = f_{abs}{}^i (h\nu - \varphi_{eff}{}^i)^2 F_{fowler}{}^i A_i$$

where $f_{abs}{}^i$ is the fraction of the incident light absorbed in the metal where the photocurrent is created, $(h\nu - \varphi_{eff}{}^i)^2$ comes from the usual Fowler theory, $\varphi_{eff}{}^i$ is an EBH (sum of the SBH, φ_i, and the potential drop in Si, ΔV), $F_{fowler}{}^i$ is the "Fowler deviation coefficient", and A_i is a constant which depends on the applied bias through the characteristics of the hot carrier transport in the TIPS structure. It should be noted that the "Fowler deviation coefficient" differs from unity far from the threshold only for a low SBH; a photocurrent saturation is always experimentally observed at high energies and is much more pronounced for the Ir/p-Schottky structure than for that of $ErSi_2$/n-Si.

Using this modified Fowler formalism, we fit the observed photocurrent dependence on the photon energy. To carry out this procedure, we solve for a set of adjustable parameters, *i.e.* values of the coefficients, A_i, and the EBHs, $\varphi_{eff}{}^i$, which may vary with the applied bias. The resulting fit is depicted by the solid lines in Fig. 1(b). First, we note a satisfying agreement for all photon energies and applied biases. We note that for a positive applied bias, a fit can be obtained only with dominant contributions from photocurrents I_3 and I_4. This suggests the existence of both electron and hole photocurrents in an asymmetric heterostructure. Furthermore, this indicates that transport of hot-electrons and -holes occurs in the epitaxial Si layer over distances as large as 200 nm in thickness. Second, this procedure allows accurate determination of the EBHs as a function of the applied bias. The values of $\varphi_{eff}{}^1$ and $\varphi_{eff}{}^2$, corresponding to the negative photocurrent, are found to be equal to the SBHs φ_1 and φ_2 respectively and independent of the applied bias except for the slight Schottky barrier lowering. This result is in agreement with standard photoemission observations in Schottky diodes [8]. On the other hand, the EBHs of the positive photocurrent are strongly affected by a positive bias as shown in Fig. 4. We emphasize that the EBH variation is more than an order of magnitude larger than that observed in usual Schottky barrier lowering. Furthermore, we also note that the potential drop ΔV, $\varphi_{eff}{}^i - \varphi_i$, is identical for both photocurrents. This symmetry is not surprising since the band gap of the epitaxial Si layer remains constant in the TIPS structure. The decrease in ΔV with positive bias, observed in Fig. 4, naturally explains the shift in the TIPS cutoff wavelength. The role played by the positive

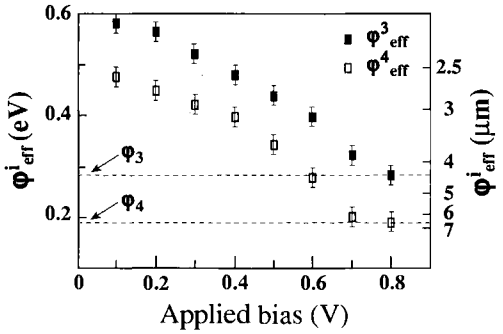

Fig. 4. Variation in $\varphi_{eff}{}^3$ (■) and $\varphi_{eff}{}^4$ (□) *vs.* positive bias applied to the TIPS structure of Fig. 1(b), as deduced from photocurrent fits using the modified Fowler formalism described in the text.

photocurrent in an asymmetric structure is therefore of critical importance to qualitatively explain the observed tunability. Similar laws (*i.e.* A_1, A_2 constant, strong dependence of A_3 and A_4 on the applied bias) were also found for the coefficients A_i which denote the respective weights of the different photocurrents. It should finally be noted that the A_1/A_2 and A_3/A_4 ratios are almost constant with the applied bias.

We have reported a new tunable infrared photosensor based on the photoemission of excited carriers in an asymmetrical metal-silicon-metal heterostructure. A detailed analysis of the TIPS photoresponse shows the existence of four different hole and electron photocurrents, two of them being related to hot carrier transport. Using a modified version of Fowler's formalism, which takes into account the optical absorption in the metallic layers, the origin of the tunability of the asymmetric TIPS has been explained by the EBH variation with the external applied bias (which is more than 10 times larger than the standard Schottky barrier lowering). All of the depicted characteristics combined with the possibility for monolithic integration with Si electronics offer tremendous versatility for this novel type of detector.

Acknowledgments

The authors would like to thank F. Chevalier and Y. Gamberini for their skilful help in sample preparations, Dr. P. Boucaud for critical reading of the manuscript and Drs. D. Bensahel, J. Y. Duboz and M. Mouis for fruitful discussions.

References

1 F. D. Shepherd and A. C. Yang, *IEDM Tech. Dig.* (1973) 310.
2 W. F. Kosonocky, F. V. Shallcross, T. S. Villani and J. V. Groppe, *IEEE Trans. Electron Devices, ED-22* (1985) 1564.

3 B. Y. Tsaur, C. K. Chen and B. A. Nechay, *IEEE Electron Device Lett., 11* (1990) 415.
4 P. A. Badoz and J. Y. Duboz, French Patent No. 90 03668, 1990; US Patent No. 07 672, 1991, 553.
5 R. H. Fowler, *Phys. Rev., 38* (1931) 45.
6 F. Arnaud d'Avitaya, P. A. Badoz, Y. Campidelli, J. A. Chroboczek, J. Y. Duboz, A. Perio and J. Pierre, *Thin Solid Films, 184* (1990) 283.
7 L. Pahun, Y. Campidelli, F. Arnaud d'Avitaya and P. A. Badoz, *Appl. Phys. Lett., 60* (1992) 1156.
8 J. Y. Duboz, P. A. Badoz, F. Arnaud d'Avitaya and E. Rosencher, *Phys. Rev., B40* (1989) 10607.
9 J. de Sousa Pires, P. Ali, B. Crowder, F. d'Heurle, S. Petersson, L. Stolt and P. A. Tove, *Appl. Phys. Lett., 35* (1979) 202.
10 F. Abelès, *Optical Properties of Solids*, North-Holland, Amsterdam, 1972, Chapter 3.
11 E. D. Palik, *Handbook of Optical Constants of Solids*, Academic Press, New York, 1985, pp. 296, 547.
12 I. Sagnes, G. Vincent and P. A. Badoz, *J. Appl. Phys., 72* (1992) 4295.

Materials Science and Engineering, B21 (1993) 317–320

A study of PbSe heteroepitaxy on Si(111) for IR optoelectronic applications

F. Nguyen-Van-Dau*, V. Mathet, P. Galtier, G. Padeletti, J. Olivier, D. G. Crété and P. Collot
Thomson CSF/LCR, Domaine de Corbeville, F-91404 Orsay (France)

Abstract

Molecular beam epitaxy was used to grow heteroepitaxial PbSe on Si(111) substrates with the aid of BaF_2 and CaF_2 buffer layers. The growth process was optimized with respect to transmission electron microscopy, atomic force microscopy and X-ray diffraction characterizations. A careful understanding of the initial stages of CaF_2/Si(111) growth allows the buffer layer thickness to be reduced to less than 100 Å, which definitely improves the compatibility of such structures with standard photolithographic technological procedures. Preliminary photovoltaic sensor performances are very promising for the use of such devices in non-cryogenically cooled conditions.

1. Introduction

Recently, there has been a growing interest in the heteroepitaxy of narrow gap semiconductors (NGSs) on Si substrates [1–4]. This is mainly due to the potential monolithic integration of IR detectors together with their Si read-out electronics. This would lead to cheaper and more reliable devices and would allow a higher level of integration than is possible using present hybrid technologies. Indeed, the high prices of IR imaging systems appear to be the main factor limiting the opening of new markets.

Lead salt compounds (LSCs) are particularly attractive for these applications of NGSs for several reasons. They can be epitaxially grown on Si substrates using very thin (less than 3000 Å) IIa fluoride buffer layers to overcome the significant lattice and thermal mismatches [1]. Integrated photovoltaic detector arrays using LSCs on Si have already been demonstrated [1]. Their performances, especially in the 3–5.5 μm atmospheric window range, are very close to those of state-of-the-art HgCdTe (MCT) hybrid devices. Their high dielectric constant ($\varepsilon_0 = 220$ for PbSe), which is detrimental for single detector devices, is no longer a problem in one- or two-dimensional array configurations where high working frequencies are not required.

In this paper, we present the main features associated with PbSe heteroepitaxy on Si(111) using $(Ba,Ca)F_2$ buffer layers. A careful optimization of the growth process on the basis of structural properties of the layers allows structures to be obtained which are compatible with standard photolithographic technological procedures.

The growth was performed by molecular beam epitaxy. Four effusion cells are necessary: CaF_2 and BaF_2 for the buffer layers, PbSe and Se in order to obtain slightly Se-rich and thus p-type PbSe (approximately 10^{17} cm^{-3}) active layers. Structural properties of the samples were investigated by transmission electron microscopy (TEM), atomic force microscopy (AFM), metallographic analysis and double crystal X-ray diffraction experiments. The electrical characteristics of the p-PbSe layers were obtained by Hall effect measurements.

2. Structural properties of $(Ba,Ca)F_2$ buffer layers

2.1. CaF_2 on Si(111)

Figure 1 shows AFM images of CaF_2(20 Å)/Si (Fig. 1(a)), CaF_2(57 Å)/Si (Fig. 1(b)), CaF_2(200 Å)/Si (Fig. 1(c)) and CaF_2(510 Å)/Si (Fig. 1(d)). Growth was performed at 570 °C. For the 20 Å thick layer, the surface is essentially flat. TEM analysis of this sample revealed that the layer is totally strained to the Si substrate. Thus, the growth mode appears to be pseudomorphic. For the 57 Å thick CaF_2/Si sample, triangular pits appear on the surface. Correlations with TEM experiments indicate that these pits are associated with threading dislocations which have nucleated at the surface [5]. The critical thickness t_c at this growth temperature is thus between 20 Å and 57 Å. The morphology of the 200 Å and 500 Å thick layers exhibits spiral shapes. These are associated with surface diffusion which strongly favours growth along

*Author to whom correspondence should be addressed.

0921-5107/93/$6.00

© 1993 – Elsevier Sequoia. All rights reserved

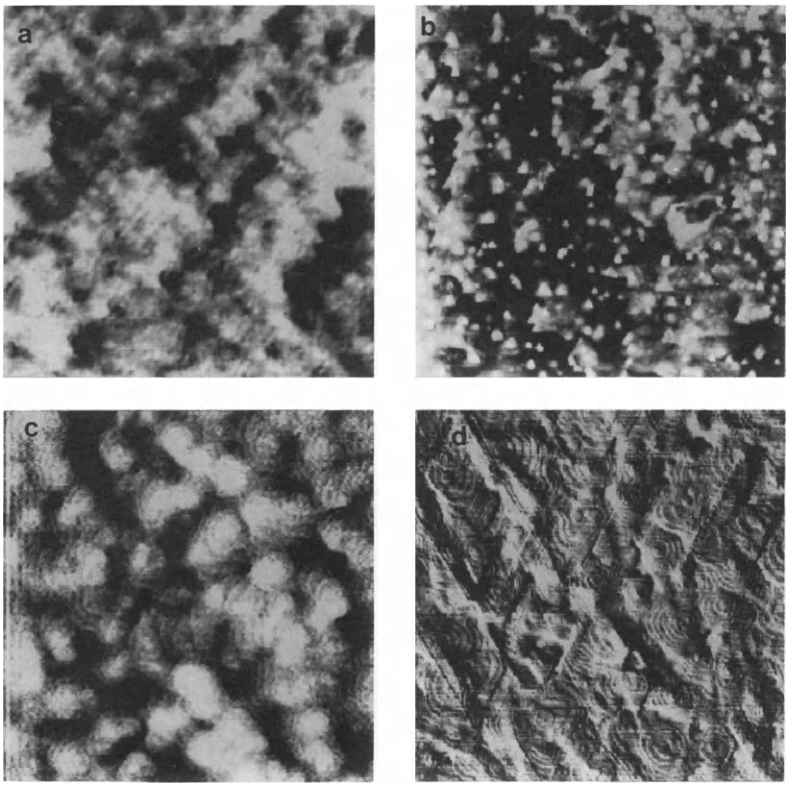

Fig. 1. AFM observations of the initial stages of CaF_2 growth on Si(111): (a) CaF_2(20 Å)/Si, observed zone 3 μm × 3 μm, total z range 20 Å. (b) CaF_2(57 Å)/Si, observed zone 5 μm × 5 μm, total z range 60 Å. (c) CaF_2(200 Å), observed zone 3 μm × 3 μm, total z range 70 Å. (d) CaF_2(510 Å)/Si, observed zone 5 μm × 5 μm, highpass filtered image.

the edges resulting from the emergence of threading dislocations at the surface [5, 6]. For the 500 Å thick layer, we observe extended spirals plus additional $\langle 1-10 \rangle$ oriented lines. We believe that, for these such thicknesses (500 Å), strains induced by thermal mismatch during cool down become sufficient to bend dislocations in their glide plane or to nucleate new dislocations [6]. Furthermore, the strong modifications of the CaF_2 surface morphology between 20 Å and 500 Å can be related to drastic changes in the residual strain resulting from a double relaxation mechanism (lattice and thermal mismatches) which we have discussed elsewhere [7]. Finally, we observe that an increase in the growth temperature leads to an increase in the roughness and the formation of islands instead of flat spirals above t_c [5].

2.2. BaF_2 on CaF_2/Si(111)

BaF_2 was grown at 340 °C on CaF_2(20–200 Å)/Si. The structural properties of the layers were characterized by metallographic analysis and TEM [7]. The threading dislocation density decreases with the layer thickness t, following a t^{-1} law which corresponds to a binary recombination process [7, 8]. High resolution TEM observations of the BaF_2–CaF_2 interface reveal that the important lattice mismatch (13.5%) is mostly accommodated by a grid of interfacial dislocations [5, 9]. The BaF_2 thickness was chosen to be around 0.3 μm to give a buffer layer as thin as possible, which allows epitaxy of PbSe with a reasonable dislocation density (approximately 10^8 cm^{-2}).

3. Structural and electrical properties of PbSe active layers

3.1. Structural properties of PbSe grown on BaF_2/CaF_2/Si(111)

The growth of the p-PbSe layer was performed at 250–300 °C on BaF_2(0.3 μm)/CaF_2(20–40 Å)/Si. Indeed, as we have already reported [7], if the CaF_2 thickness is greater than t_c, we observe the formation of blister shape defects [10].

Blister-free samples were characterized by TEM and double crystal X-ray diffraction. Plan-view TEM observations were performed using a "lift-off" preparation technique [7]. Samples are dipped in water for a few hours which dissolves the fluorides, owing to the hygroscopic character of these compounds. Then the PbSe layer is picked up and, if necessary, thinned again

using ion milling. This allows the surface and interface regions of the active layer to be observed separately. We find that typically approximately 3×10^9 cm^{-2} dislocations are emitted from the interface while 2 μm thick PbSe layers exhibit surface dislocation densities below 7×10^6 cm^{-2}. These low dislocation densities are illustrated in Fig. 2 which shows a cross-sectional TEM image of a PbSe/BaF_2/CaF_2/Si structure. Note that for these cross-sectional TEM observations, samples were prepared using conventional methods. In Fig. 3, we have plotted the full width at half-maximum (FWHM) of (333) PbSe X-ray diffraction peaks recorded on several samples *vs.* the PbSe layer thicknesses. These results confirm the reduction in dislocation density with thickness and are in good quantitative agreement with TEM measurements.

However, although the structural properties of this PbSe/BaF_2/CaF_2/Si heteroepitaxy are compatible with optoelectronic technologies, a major handicap of these structures is their fragility for almost any kind of wet treatment. This seems definitely to rule out the use of standard photolithographic techniques to fabricate detector arrays with such samples. Since the BaF_2 layer appeared to be the most reactive, we tried to avoid it and grow PbSe directly on an ultrathin CaF_2 buffer layer.

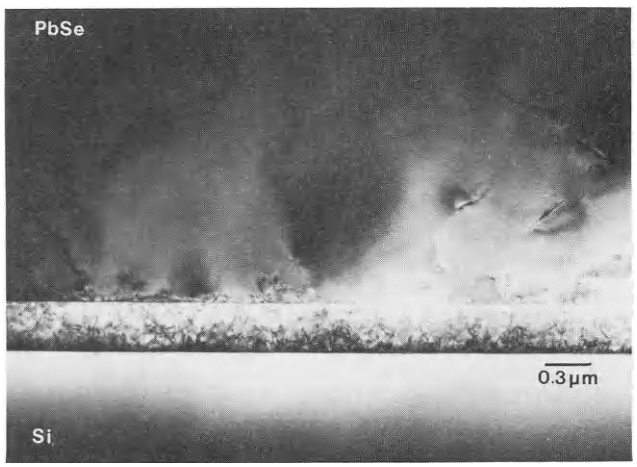

Fig. 2. ⟨1-10⟩ bright field cross-sectional TEM image of a PbSe/BaF_2/CaF_2/Si structure.

3.2. PbSe heteroepitaxy on CaF_2/Si(111)

Some p-PbSe layers were grown on CaF_2(80–100 Å)/Si. The PbSe growth conditions were not modified. Reflection high energy electron diffraction observations during growth reveal essentially the same patterns as observed during the growth of PbSe/BaF_2/CaF_2/Si structures, with a surface reconstruction appearing after growth during cool down of the sample. However, careful control of the CaF_2 growth conditions leading to flat surface morphologies, as described in Section 2.1, appears to be the most critical step in the growth process of these structures. Some results obtained by X-ray diffraction are presented in Fig. 3. No significant increase in the FWHM can be detected although almost all the lattice mismatch between PbSe and Si is accommodated during the active layer growth. TEM observations of these PbSe/CaF_2/Si structures are in progress. The first samples we prepared in this way exhibited a very high stability against wet treatments such as water, acetone or propanol. We believe these new structures are now fully compatible with standard photolithographic technological procedures.

3.3. Electrical properties

Figure 4 shows Hall mobilities *vs.* hole concentrations measured at 77 K on several samples of both kinds of structure. Note that carrier concentrations around 10^{17} cm^{-3} are close to optimum values for Schottky-based photodiode operation [11, 12]. Mobilities around 10000 cm^2 V^{-1} s^{-1} are close to state-of-the-art values reported for both bulk materials and thin films grown on BaF_2 substrates [13]. Moreover, no significant decrease in mobilities was found for PbSe/CaF_2/Si structures.

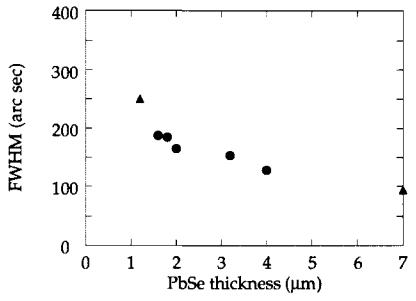

Fig. 3. Full width at half-maximum of (333) PbSe diffraction peaks recorded on PbSe/Si samples, PbSe/BaF_2/CaF_2/Si (●), PbSe/CaF_2/Si (▲).

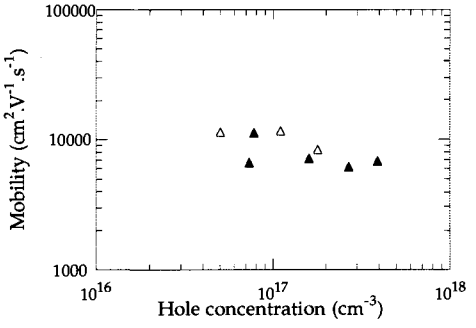

Fig. 4. Hall mobilities *vs.* hole concentrations measured on p-type PbSe/Si samples, p-PbSe/BaF_2/CaF_2/Si (△), p-PbSe/CaF_2/Si (▲).

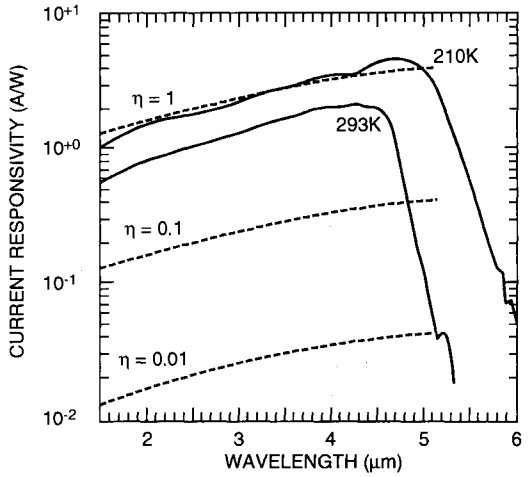

Fig. 5. Current responsivity of a PbSe/Si photovoltaic sensor.

4. Preliminary device results

A fully photolithographic technology is in current development in our laboratory. However, preliminary results have been obtained using shadow-masks. The photovoltaic sensors are made of a Pb Schottky contact and an Au ohmic contact. Owing to the mechanical softness of Pb, the Schottky contact is delineated using a polycrystalline BaF_2 insulating layer. Typical junction areas are 2.5×10^{-4} cm^{-2}. The principles of this technology are derived from Holloway's work [14, 15]. Figure 5 shows the current responsivity of a back-side illuminated photodiode measured at 293 K and 210 K. Corresponding quantum efficiencies are indicated on the figure, showing that very high values (close to unity) are obtained at 210 K. It should be noted that these values are probably slightly overestimated as the active area was taken as equal to the Pb-contact area, thus neglecting lateral diffusion of photocarriers. Anyway, we believe that these preliminary results are very promising for the use of such devices in non-cryogenically cooled conditions.

5. Conclusions

In this paper we have shown that a careful understanding of the microcrystalline properties of PbSe heteroepitaxy on fluoride covered Si(111) allows device compatible material to be obtained and opens a way to the fabrication of IR detector arrays using standard microelectronic techniques. Moreover, the perspective of a non-cryogenically cooled operating temperature is very promising in the course towards cheaper device production costs.

Acknowledgments

Dr. S. Ries is gratefully acknowledged for performing X-ray diffraction experiments. We wish to thank Dr. Zogg and his colleagues for fruitful discussions. This work was supported by the French Ministry of Defense under contract DRET No. 91.34.483.

References

1 J. Masek, T. Hoshino, C. Maissen, H. Zogg, S. Blunier, J. Vermeiren and C. Claeys, *Proc. SPIE, 1735* (1992) 54.
2 R. Sporken, M. D. Lange, J. P. Faurie and J. Petruzzello, *J. Vac. Sci. Technol. B, 9* (1991) 1651.
3 S. H. Shin, J. M. Arias, D. D. Edwall, M. Zandian, J. G. Pasko and R. E. DeWames, *J. Vac. Sci. Technol. B, 10* (1992) 1492.
4 W. Dobbelaere, J. De Boeck, P. Heremans, R. Mertens, G. Borghs, W. Luyten and J. Van Landuyt, *Appl. Phys. Lett., 60* (1992) 3256.
5 V. Mathet, G. Padeletti, J. Olivier, P. Galtier and F. Nguyen-Van-Dau, *Proc. 8th Oxford Conf. on Microscopy of Semiconducting Materials*, IOP, Bristol, 1993, in press.
6 J. Olivier, G. Padeletti, V. Mathet, F. Nguyen-Van-Dau and R. Bisaro, *Proc. 8th Oxford Conf. on Microscopy of Semiconducting Materials*, IOP, Bristol, 1993, in press.
7 V. Mathet, P. Galtier, F. Nguyen-Van-Dau, G. Padeletti and J. Olivier, *J. Cryst. Growth*, in press.
8 H. Kroemer, T. Y. Lui and P. M. Petroff, *J. Cryst. Growth, 95* (1989) 96.
9 S. Blunier, H. Zogg, C. Maissen, A. N. Tiwari, R. M. Overney, H. Haefke, P. A. Buffat and G. Kostorz, *Phys. Rev. Lett., 68* (1992) 3599.
10 H. Zogg, P. Maier and P. Norton, *Mater. Res. Soc. Symp. Proc., 56* (1986) 253.
11 W. Maurer, *Infrared Phys., 23* (1983) 257.
12 H. Preier, *Infrared Phys., 18* (1978) 43.
13 D. K. Hohnke and S. W. Kaiser, *J. Appl. Phys., 45* (1974) 892.
14 H. Holloway, in G. Haas and M. H. Francombe (eds.), *Physics of Thin Films*, Vol. 11, Academic Press, New York, 1980, p. 105.
15 H. Zogg, S. Blunier, T. Hoshino, C. Maissen, J. Masek and A. N. Tiwari, *IEEE Trans. Electron. Devices, 38* (1991) 1110.

Optical cross-sections and distribution of Fe^{2+} and Fe^{3+} in semi-insulating liquid encapsulated Czochralski grown InP:Fe

A. Seidl[a], F. Mosel[a], J. Friedrich[a], U. Kretzer[b] and G. Müller[a]

[a]*Institut für Werkstoffwissenschaften 6, Kristallabor, Universität Erlangen-Nürnberg, Martensstr. 7, D-91058 Erlangen (Germany)*

[b]*Freiberger Elektronikwerkstoffe GmbH, Berthelsdorfer Str. 113, D-09599 Freiberg (Germany)*

Abstract

Optical cross-sections σ_n and σ_p of the Fe correlated absorption in InP were evaluated from near-IR absorption spectra of n- and p-type Fe doped InP. The resulting σ_n and σ_p values were used to determine the Fe distribution in semi-insulating InP:Fe wafers, separated into both charge states Fe^{2+} and Fe^{3+}. By comparing the Fe distribution with a map of the resistivity, a clear correlation was found between the electronic properties and Fe in its neutral charge state.

1. Introduction

Semi-insulating InP-substrates with a resistivity $\rho \geq 10^7$ Ω cm are indispensable. For InP-based optoelectronic applications this property is usually achieved by doping with the deep acceptor Fe compensating the residual donor impurities. Since Fe is not uniformly incorporated during the liquid encapsulated Czochralski (LEC) process, the electrical and optical properties can vary significantly on a macroscopic and microscopic scale across InP wafers [1].

It is therefore of particular interest to develop a non-destructive quantitative technique for characterization of the Fe distribution and the correlated variation in resistivity. In a previous paper [2] we reported on measurement of the Fe content by an IR absorption technique and we demonstrated the possibility of determining the Fe content separated into both charge states Fe^{2+} and Fe^{3+} [3].

In this paper we report in more detail on the experimental determination of the optical cross-sections of the Fe^{2+} and Fe^{3+} charge states and present results of a separated Fe^{2+} and Fe^{3+} mapping which we have performed on a semi-insulating InP:Fe crystal. Furthermore we compare these results with a mapping of the resistivity determined using the contactless time dependent charge measurement (TDCM) technique.

2. Crystal growth and preparation

InP crystals doped with Fe, Fe + Zn and Fe + Te were grown with [100] orientation by the LEC technique in our laboratory [1]. The Zn and Fe contents of these crystals were analysed by atomic absorption spectrometry (AAS). The Te content was evaluated from Hall effect measurements. It must be considered that only about 70% of the incorporated Fe contributes to the electronic properties [1], whereas all of the Zn and Te content can be assumed to be electrically active. In the InP:Fe + Te crystal the Te content exceeds the Fe concentration by approximately one order of magnitude. The electrical properties are controlled by the shallow donor Te. Therefore, the Fermi level is positioned close to the conduction band which means that all Fe atoms are in the Fe^{2+} state (acceptor occupied by one electron). In the InP:Fe + Zn crystal all Fe atoms are in the Fe^{3+} state (neutral) because the Fermi level is located close to the valence band ([Zn] ≫ [Fe]).

For the characterization by IR absorption spectroscopy and by capacitance measurements, slices 2 mm thick were prepared by cutting the crystal parallel to the growth direction. More details of the preparation and characterization of these co-doped crystals are described in ref. 3.

3. Evaluation of optical cross-sections

The IR absorption coefficient α in semi-insulating InP:Fe is dominated by transitions from the occupied Fe^{2+} state to the conduction band as well as by transitions from the valence band to the neutral Fe^{3+} state [4]:

$$\alpha(\lambda) = \sigma_n(\lambda)[Fe^{2+}] + \sigma_p(\lambda)[Fe^{3+}] \quad (1)$$

0921-5107/93/$6.00

© 1993 - Elsevier Sequoia. All rights reserved

Provided that the optical cross-sections σ_n and σ_p are known as a function of the wavelength λ, it should be possible to evaluate the Fe^{2+} and Fe^{3+} concentrations by two independent absorption measurements at different wavelengths, where σ_n and σ_p differ significantly. We determined σ_n and σ_p by absorption spectra measurements of the co-doped InP:Fe + Zn and InP:Fe + Te samples. The measurements were performed at both 300 and 77 K.

For InP:Fe + Zn (p-type),

$$\alpha(\lambda) = \sigma_p(\lambda)[Fe^{3+}] + \alpha_0(p) \tag{2a}$$

whereas for InP:Fe + Te (n-type) the corresponding equation holds

$$\alpha(\lambda) = \sigma_n(\lambda)[Fe^{2+}] + \alpha_0(n) \tag{2b}$$

where $\alpha_0(p)$ and $\alpha_0(n)$ are the absorption coefficients due to the absorption by free carriers (holes and electrons respectively). This background absorption α_0 was measured using InP samples doped with Zn and Te only. Figure 1 shows the absorption spectra of both an InP:Fe + Zn and an InP:Zn sample of comparable hole concentration. The difference is caused by the Fe^{3+} related absorption. Since the total Fe content is known from chemical analysis, it is possible using eqn. (2a) to evaluate the optical cross-section $\sigma_p(\lambda)$. $\sigma_n(\lambda)$ was determined using the same procedure. The corresponding results for σ_n and σ_p as a function of photon energy are shown in Fig. 2 for 300 and 77 K. Our measurements are in good agreement with the qualitative photocapacitance measurements reported by several authors [5–7], but differ from the quantitative results of Takanohashi and Nakajima [4] by a factor of 10. The reasons for this discrepancy are still under investigation.

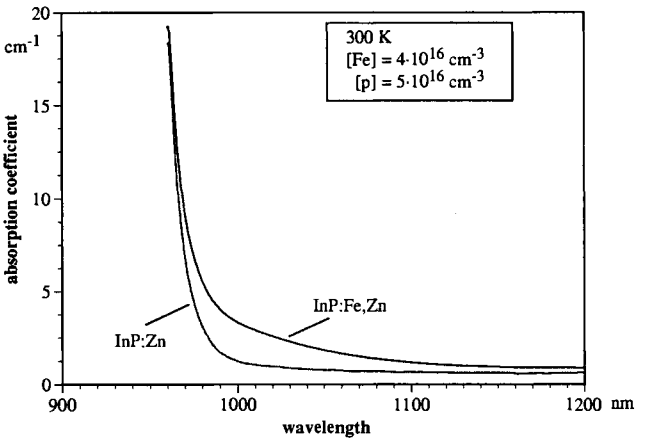

Fig. 1. Absorption coefficient α *vs.* wavelength λ for Zn doped and Fe + Zn doped InP samples of comparable hole concentrations. The additional absorption in InP:Fe + n is caused by Fe^{3+}. The concentrations were determined by AAS.

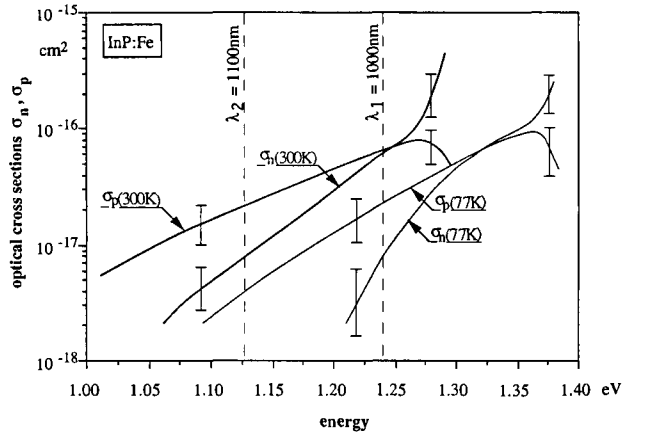

Fig. 2. Optical cross-sections σ_n and σ_p of InP:Fe evaluated from absorption measurements and from chemical analysis of the Fe content by AAS *vs.* photon energy.

4. Fe^{2+} and Fe^{3+} distribution in comparison with resistivity mapping

With the values of $\sigma_n(\lambda)$ and $\sigma_p(\lambda)$ we are able to evaluate the Fe^{3+} and Fe^{2+} concentrations in semi-insulating InP:Fe by taking measurements at two wavelengths $\lambda_1 = 1000$ nm and $\lambda_2 = 1100$ nm at room temperature. We can rewrite eqn. (1) and determine the Fe concentrations in its charge states:

$$[Fe^{3+}] = \frac{\sigma_n(\lambda_1)\alpha(\lambda_2) - \sigma_n(\lambda_2)\alpha(\lambda_1)}{\sigma_n(\lambda_1)\sigma_p(\lambda_2) - \sigma_n(\lambda_2)\sigma_p(\lambda_1)} \tag{3a}$$

$$[Fe^{2+}] = \frac{\sigma_p(\lambda_2)\alpha(\lambda_1) - \sigma_p(\lambda_1)\alpha(\lambda_2)}{\sigma_n(\lambda_1)\sigma_p(\lambda_2) - \sigma_n(\lambda_2)\sigma_p(\lambda_1)} \tag{3b}$$

In this way we determined the Fe^{2+} and Fe^{3+} concentrations in a slice cut parallel to the growth axis of a semi-insulating InP:Fe crysal grown in the [100] direction. Figures 3(a) and 3(b) show the resulting absorption mapping. The Fe^{2+} concentration (Fig. 3(a)) is quite homogeneous across the whole section and varies in the range $(1.5–2.5) \times 10^{16}$ cm^{-3}. The dark region at the end of the crystal is caused by FeP_2 precipitates. Here absorption spectroscopy does not give reasonable values. The Fe^{3+} concentration (Fig. 3(b)) in the precipitation-free region varies between 1.5×10^{16} and 1.5×10^{17} cm^{-3}. The Fe distribution reflects the convex shape of the solidification front, with the exception of the first part of the crystal. In the first-grown region the Fe concentration is higher in the centre than in the periphery of the crystal. This can be explained by growth kinetics and melt flow structure and is not discussed here in detail. Figure 3(c) shows the variation of the resistivity, measured by the TDCM technique

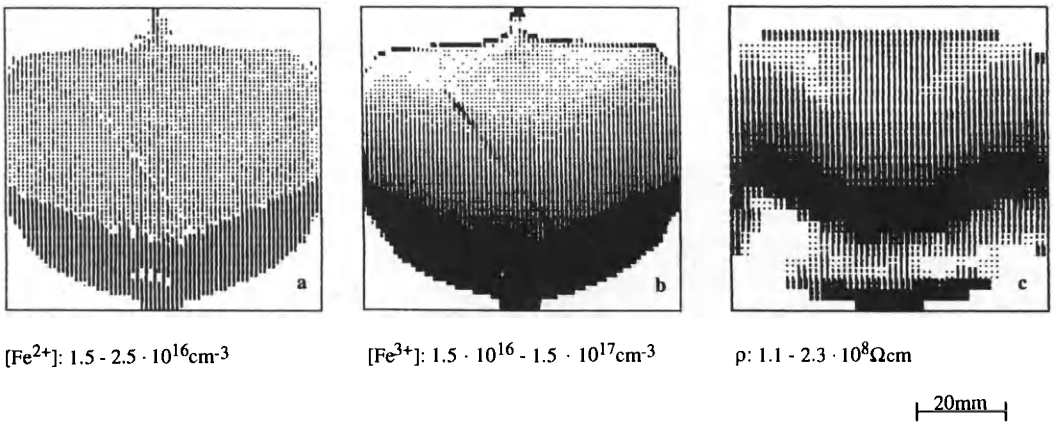

Fig. 3. Longitudinal section of a [100] Fe doped InP crystal grown by the LEC method: (a) distribution of Fe^{2+} evaluated by absorption mapping and eqn. (3b); (b) distribution of Fe^{3+} evaluated by absorption mapping and eqn. (3a); (c) distribution of resistivity measured by TDCM.

[8]. Within the precipitation-free region the resistivity varies from 1.1×10^8 to 2.3×10^8 Ω cm.

A quantitative evaluation of the axial concentration is plotted in Fig 4. The axial variation of the Fe^{3+} concentration can be explained by Fe segregation with a segregation coefficient $k_{Fe} = 0.001$. The increase in Fe^{2+} concentration is, by contrast, only small and should be equal to the compensated net donors $N_D - N_A$. From investigations of nominally undoped InP crystals we have determined the segregation coefficient for such impurities to behave like $k = 0.8$ [9], which also holds for the Fe^{2+} distribution. Nevertheless, as one can see from Fig. 4, the measured Fe^{2+} concentration is about half an order of magnitude higher than the impurity concentration $N_D - N_A$ of a nominally undoped reference crystal. However, the optical determination of the absolute Fe^{2+} concentration is not very precise in the concentration range below 1×10^{16} cm^{-3}.

The variation of the resistivity can be explained by the variation of the compensation ratio θ defined by

$$\theta = \frac{[Fe^{2+}] + [Fe^{3+}]}{N_D - N_A} \tag{4}$$

The carrier concentration in semi-insulating InP is given by an approximate solution of the charge balance equation

$$n = \frac{4}{(\theta - 1)} N_C \exp\left(\frac{E_{AA} - E_C}{kT}\right) \tag{5}$$

with N_C the density of states in the conduction band and $E_{AA} - E_C$ the energy difference between the Fe^{3+} state and the conduction band.

With $1/\rho = qn\mu$ and the electron mobility $\mu = 3000$ cm$^{2-1}$ V^{-1} s^{-1} at 300 K, which is typical in semi-

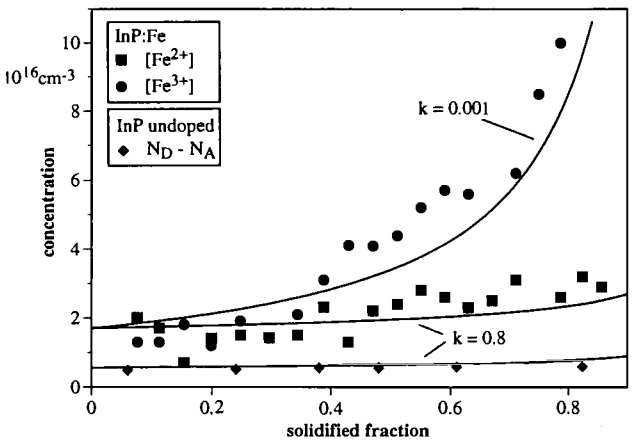

Fig. 4. Fe^{2+} and Fe^{3+} concentrations *vs.* the solidified fraction along the axis of the InP:Fe crystal of Fig. 3. Additionally, the net carrier distribution $N_D - N_A$ is shown in a comparable, nominally undoped InP cystal. The increase in Fe^{3+} and $N_D - N_A$ can be described by segregation coefficients of 0.001 and 0.8 respectively.

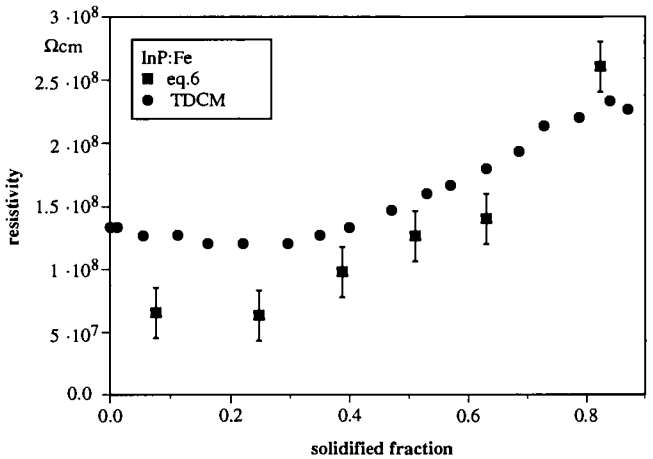

Fig. 5. Axial distribution of the resistivity measured by TDCM and calculated from eqns. (4)–(6) *vs.* solidified fraction.

insulating InP:Fe, eqn. (5) can be rewritten as

$$\rho = (\theta - 1)1.1 \times 10^7\ \Omega\ \text{cm} \qquad (300\ \text{K}) \qquad (6)$$

Figure 5 shows the resistivity along the crystal axis calculated using eqn. (6). θ was calculated from eqn. (4) using the experimentally determined concentrations from Fig. 4. The result is in good agreement with the resistivity measurements, if one considers the approximations, *e.g.* constant mobility.

5. Summary

Semi-insulating InP:Fe was investigated by near-IR absorption and resistivity measurements. The optical cross-sections σ_n and σ_p were determined in a range from near the band edge to 1200 nm. By measurements of the optical absorption coefficients at two wavelengths where σ_n and σ_p are significantly different, the distribution of Fe^{2+} and Fe^{3+} across whole wafers was determined. We showed that the non-uniform distribution of the specific resistivity is caused by variation in the compensation ratio.

Acknowledgment

The work was financially supported by the German TELEKOM within the project "InP based OEICs".

References

1 D. Hofmann, F. Mosel and G. Müller, in G. Grossmann and L. Ledebo (eds.), *Proc. Conf. on Semi-insulating III–V Materials, Malmö*, Hilger IOP, Bristol, 1988, p. 429.
2 F. Mosel, A. Seidl, D. Hofmann and G. Müller, *Appl. Surf. Sci., 50* (1991) 364.
3 F. Mosel, A. Seidl, D. Hofmann and G. Müller, *J. Electron. Mater., 20* (1991) 1091.
4 T. Takanohashi and K. Nakajima, *J. Appl. Phys., 65* (1989) 3933.
5 G. Bremond, A. Nouailhat and G. Guillot, *Solid State Commun., 41* (1982) 477.
6 P. Leyral, F. Litty, G. Bremond, A. Nouailhat and G. Guillot, in S. Makram-Ebeid and B. Tuck (eds.), *Proc. Conf. on Semi-insulating III–V Materials, Evian*, Shiva, Nantwich, 1982, p. 192.
7 C. Delerue, M. Lannoo, G. Bremond, G. Guillot and A. Nouailhat, *Europhys. Lett., 9* (1988) 373.
8 R. Stibal, J. Windscheif and W. Jantz, *Semicond. Sci. Technol., 6* (1991) 995.
9 G. Müller, *Phys. Scripta, T35* (1991) 201.

Materials Science and Engineering, B21 (1993) 325–328

Large negative persistent photoconductivity of bulk $GaAs_{1-x}P_x$ ($x = 0.02$–0.03) single crystals

T. Słupiński, G. Nowak, R. Bożek, A. Wysmołek and M. Baj

Institute of Experimental Physics, Warsaw University, Hoża 69, 00-681 Warsaw (Poland)

Abstract

It is known that n-type GaAs under hydrostatic pressure at low temperature exhibits negative persistent photoconductivity (NPPC) related to the EL2 defect. In this paper we present the observation of NPPC in $GaAs_{1-x}P_x$ bulk mixed crystals with $x = 0.02$–0.03 at ambient pressure. The growth of single crystals by the liquid encapsulated Czochralski method is described and discussed. Selected samples of $GaAs_{1-x}P_x$ with energy gap higher than that of GaAs by about 20–30 meV were investigated by optical absorption and photo-Hall measurements in the temperature range 10–60 K at ambient pressure.

1. Introduction

The reported negative persistent photoconductivity (NPPC) is an inherent property of n-type GaAs material at low temperature and with the energy gap increased by high hydrostatic pressure [1]. It can be observed if a sufficiently high concentration of EL2 native deep donor centres is present in GaAs, whose $[EL2]^{0/+}$ electronic level is responsible for the high resistivity of semi-insulating undoped GaAs, and which is also present in slightly doped n-type GaAs. Such unusual behaviour of semiconducting material, *i.e.* an increase in resistivity during illumination with an appropriate light, is a consequence of the existence of the acceptor state of the metastable configuration, EL2*, of the EL2 defect. In n-type GaAs at low temperatures (below about 45 K), illumination with 1.0–1.3 eV photons causes a transition from the normal to the metastable configuration of EL2, manifesting itself in the disappearance of the absorption spectrum characteristic of the $EL2^0$ state. Simultaneously, a new acceptor-like $[EL2^*]^{-/0}$ level appears within the conduction band at an energy of about $E_c + 0.02$ eV. A high hydrostatic pressure applied to a sample increases the energy gap and moves this level into the gap. Free electrons are then captured onto this level. Consequently, in n-type low-resistivity material this leads to NPPC, which lasts as long as the EL2 is not transferred to its normal configuration either by heating the sample above 45 K or illuminating with light of energy about 1.5 eV. We propose that observation of NPPC should be possible in mixed crystals, where the increase in energy gap is caused by an addition of GaP to GaAs, and not by a high pressure applied during measurements.

In the present paper we report the growth and investigations of bulk mixed crystals of $GaAs_{1-x}P_x$ specially designed for observation of the $[EL2^*]^{-/0}$ level. We describe the NPPC effect and finally we draw some conclusions concerning the homogeneity of our crystals.

Thin $GaAs_{1-x}P_x$ layers with $x = 0.3$–0.8 have been widely grown for LED applications for many years. However, growth of bulk $GaAs_{1-x}P_x$ crystals is a serious problem owing to the different compositions of solid and liquid phases at equilibrium in the GaAs–GaP high temperature mixture, and consequently segregation phenomena during crystal growth. Nevertheless, several attempts have been described in the literature.

Cerrina *et al.* [2] grew $GaAs_{1-x}P_x$ polycrystals with $x = 0.1$–0.4 by pulling from a Ga-rich solution. Saito and Seki [3] obtained $GaAs_{1-x}P_x$, $x = 0.1$–0.8 polycrystals by using a "synthesis solute diffusion"-like method also from Ga solution. Ga-rich conditions, usually utilized in solution growth, prevent a high EL2 defect concentration in GaAs crystals, since the EL2 defect is associated with excess arsenic in the crystal.

Also, near-stoichiometric methods have been used to grow bulk mixed crystals. For example Bachmann *et* al. [4] grew mixed single crystals of $Ga_xIn_{1-x}P_yAs_{1-y}$ with $x = 0$–0.07 and $y = 0$–0.8 by a gradient freezing method. Kimura *et al.* [5] used phosphorus as a complementary impurity to indium to reduce the dislocation density in GaAs liquid encapsulated Czochralski (LEC) crystals grown from melt alloyed with In and

InP. The concentration of P in their crystals was 0.1–1 mol.% and that of indium about 1%. Recently Jordan *et al.* [6] have grown $GaAs_{1-x}P_x$ crystals with $x=0.01$ (single crystal) and $x=0.13$ (polycrystal) by the horizontal Bridgman method with addition of GaP to the melt, aimed at basic investigations of antisite-related defects.

2. Crystal growth

Our idea was to grow $GaAs_{1-x}P_x$ crystal by the conventional LEC method used for GaAs growth, but with InP added to the melt before the process. In this case the large difference between segregation coefficients of phosphorus ($k_0=3$) and indium ($k_0=0.12$) [5, 6] leads to a much higher concentration of P than In in the seed part of the crystal. Since the concentration of phosphorus in a crystal must drop rapidly as the growth proceeds, an almost constant phosphorus concentration can be obtained if only a small fraction of liquid is solidified.

The input Ga + As + InP charge of about 1 kg contained 0.82 mol.% InP, corresponding to the expected 2.5 mol.% P and 0.1% In at the beginning of the crystal. To reduce the gradient of phosphorus concentration we kept the diameter of the crystal within 1–1.5 cm until the fraction of liquid solidified g reached 0.02. (100)-oriented GaAs seed and B_2O_3 encapsulating layer were used. Nitrogen pressures of 60 bar during *in situ* synthesis and melting, about 3 bar during melt homogenization and about 10 bar during growth was applied. The pulling speed of about 8 mm h^{-1} did not cause any problems with polycrystallization.

To reach a high EL2 defect concentration, a slightly As-rich melt was used with molar ratio [As]/[Ga] = 1.06 in the initial charge. The crystal was doped with tellurium to obtain a free electron concentration of a few times 10^{16} cm^{-3}.

Figure 1 shows the crystal shape and phosphorus contents both expected and obtained. The composition was measured by near band gap photoluminescence (PL). The results are 2.2 ± 0.2 mol.% P for fraction of liquid solidified $g=0.01$ and 1.9 ± 0.2% for $g=0.02$, assuming that the PL lines shift to higher energies at a rate $dE_G/dx=12$ meV per 1% [8]. The phosphorus composition x along the diameter of the initial part of the crystal was constant to within 0.4%. Concluding, the addition of 2–3 mol.% P to the crystal enlarged the energy gap by about 20–30 meV relative to GaAs.

3. Experimental results

To evaluate the total EL2 defect concentration in the crystal optical absorption measurements were

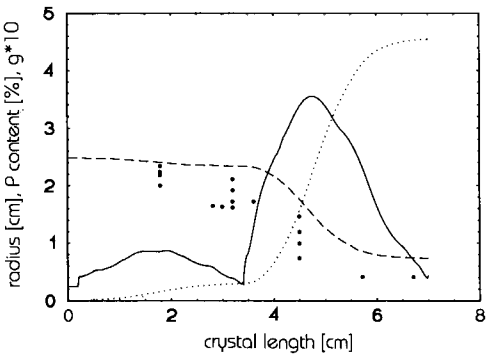

Fig. 1. Crystal radius (——), fraction of liquid solidified multiplied by 10 ($10g$ ·····), and expected phosphorus concentration (– – –) *vs.* crystal length. The points indicate the phosphorus content measured by near-band-gap photoluminescence.

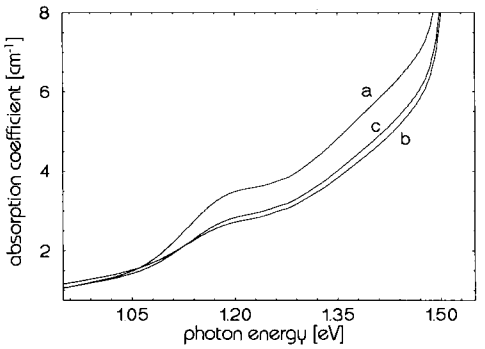

Fig. 2. Absorption spectra of $GaAs_{1-x}P_x$ at 10 K after cooling in the dark (curve a), after illumination with 1.05 μm (1.18 eV) light (curve b) and after subsequent illumination with 0.825 μm (1.5 eV) light (curve c).

taken in the photon energy range 0.7–1.55 eV at 10 K on a sample cut from the part corresponding to the fraction of liquid solidified $g=0.01$. The spectrum obtained after cooling the sample down in the dark (see Fig. 2, curve a) is typical of GaAs containing a neutral EL2 defect [9]. If practically all the absorption around 1.18 eV energy originates from neutral EL2, the concentration of the defect should be equal to about 2×10^{16} cm^{-3} [10]. Subsequent strong illumination with 1.05 μm light (1.18 eV) only partially quenched the EL2 absorption related to the transition of EL2 to its metastable EL2* configuration, see curve b. This is very similar to the case of n-type GaAs under hydrostatic pressure [11].

Since at high pressure the EL2 defect in GaAs recovers very rapidly from its metastable configuration under near-band-gap illumination, we attempted to check whether this phenomenon occurs at ambient pressure in $GaAs_{1-x}P_x$. In the sample previously illuminated with 1.5 eV photons only a few per cent absorption in the 1.18 eV region was restored (see Fig. 2, curve c), much less than in GaAs under pressure.

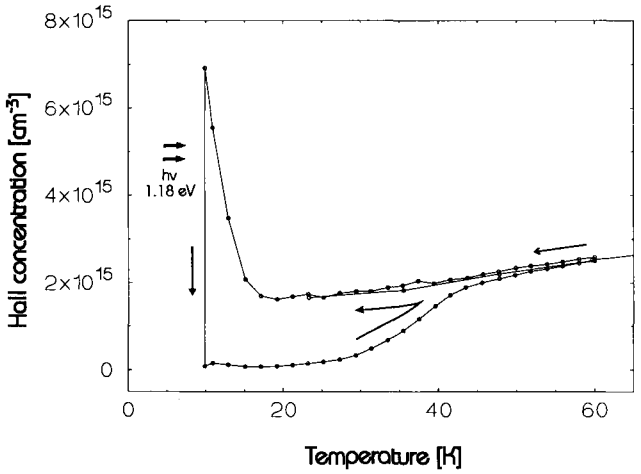

Fig. 3. Hall electron concentration measured as a function of temperature in $GaAs_{1-x}P_x$, $x=0.02$. The arrows indicate the direction of the temperature sequence during experiment. Illumination with 1.18 eV light at 10 K causes a persistent increase in resistivity, thus showing the NPPC effect.

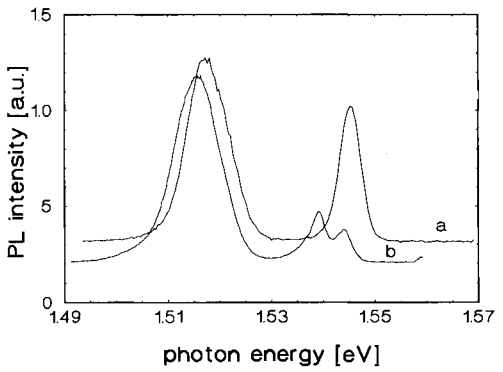

Fig. 4. An example of photoluminescence spectra observed for samples with fractions of liquid solidified of $g=0.01$ (curve a) and $g=0.02$ (curve b). The shift in line energy between the curves indicates changes in the energy gap. The double structure in the 1.54 eV energy range of curve b is discussed in the text.

To check the existence of NPPC we took resistivity and Hall effect measurements on a sample cut from the initial part of the crystal. Typical results are presented in Fig. 3. First we measured the Hall coefficient while cooling the sample to 10 K (the increase in Hall concentration observed at $T<15$ K probably results from a two-band conduction mechanism in conduction and shallow impurity bands [12]). The sample was then illuminated at 10 K with 1.1 μm wavelength light (1.13 eV), for 10 min, with a halogen lamp through an interference filter. The resistivity increased and the Hall electron concentration decreased by much more than one order of magnitude, thus showing a large NPPC effect. During subsequent heating of the sample the Hall concentration remained small up to about 40 K, when it returned to its original value before illumination. Successive cooling did not reveal any changes in comparison with the initial curve.

4. Discussion

The observed phenomena can be explained as follows. After cooling, illumination of the sample transformed the EL2 defect from its normal to the metastable configuration EL2*. Since the energy gap of $GaAs_{1-x}P_x$ for $x=0.02$ is higher than that of GaAs and since the acceptor level $[EL2^*]^{-/0}$ is already in the forbidden gap, it captures free electrons, thus decreasing the measured free electron concentration. After heating the sample over 40–45 K the EL2* defect returns to its normal coniguration, releasing previously captured electrons.

A similar large EL2 defect related NPPC effect was discovered earlier in GaAs under pressure $P>0.3$ GPa [1].

We observe some differences between the properties of GaAs under high pressure and $GaAs_{1-x}P_x$ at ambient pressure. Although incomplete photoquenching of EL2 (curves a and b in Fig. 2) is characteristic of n-GaAs under pressure, only partial photorecovery of the EL2 defect (curves b and c) is not consistent with the whole picture. There are at least two possible explanations for the above discrepancy: on an atomic scale nearby phosphorus atoms can modify some subtle properties of EL2 defects (*e.g.* photorecovery from metastable to normal state) or some large-scale fluctuations in P content can alter inhomogeneously the energy gap or can introduced mechanical stresses.

Such inhomogeneities in our crystal were clearly seen from PL measurements as a broadening of some lines in the spectrum. As shown in Fig. 4, curve b, around 1.54 eV, a double structure is present. This results from simultaneous observation of the PL signal from at least two domains with different phosphorus contents, and thus with different energy gaps. The difference in energy of these lines corresponds to about 0.4% difference in P content between the domains. The existence of such domains explains why for a given fraction of liquid solidified g we have various P contents, evaluated from PL lines measured for different laser spot positions, seen in Fig. 1. The average size of such domains should be of the order of the laser light spot (a few hundred micrometres).

The reason for the non-homogeneous phosphorus composition can be understood by considering the segregation of phosphorus (or rather GaP in GaAs + GaP liquid mixture) during growth. A segregation coefficient not equal to unity results in continuous

transport of excess dopant to ($k_0 > 1$) or from ($k_0 < 1$) the crystal–liquid interface. Various instabilities in such solute migration can cause irregularities of growth. Recently such behaviour was presented by Elliot *et al.* [13] for GaAs grown from As-rich melt. In our case the growth velocity was higher than that usually used for mixed material (equal to that for GaAs growth), thus amplifying the instabilities. A lower growth velocity should be helpful in decreasing the variations in phosphorus concentration.

We also tried to grow crystals of $GaAs_{1-x}P_x$ with higher x by the LEC method. Starting from the melt with 3 mol.% GaP we grew mixed crystals with initial composition $x = 0.09$. Unfortunately, only polycrystals were obtained. The probable reason for polycrystalline growth immediately after seeding is a rise in the crystallization temperature caused by the presence of GaP, and thus a high initial supercooling necessary for GaAs seed. Successive utilization of $GaAs_{1-x}P_x$ seeds with higher and higher phosphorus concentrations could be tried to obtain single-crystal growth, as has been done for $Ga_{1-x}In_xAs$ growth [14].

Initially, in our work we used InP as a source material for phosphorus. Later, GaP was added equally well to the charge, though to melt it completely (it could be easily seen on the melt surface), overheating of the melt by about 150 degrees was necessary.

5. Conclusions

Bulk $GaAs_{1-x}P_x$ single crystals with $x = 0.02$–0.03 can be grown by the LEC technique from GaAs melt with the addition of either InP or GaP. For a high crystallization rate of about 8 mm h^{-1} some inhomogeneities of phosphorus concentration can occur.

Such material enables investigations of the EL2* defect acceptor state without application of high hydrostatic pressure and thus allows, for example, uniaxial stress experiments.

The negative persistent photoconductivity is a material property of $GaAs_{1-x}P_x$ with $x > 0.02$ at temperatures below 45 K, with the EL2 defect concentration comparable with or greater than the free electron concentration and with the free electron concentration not higher than a few times 10^{16} cm^{-3}.

Acknowledgments

We are very much indebted to Dr. M. Sadowski for careful reading of the manuscript. The $GaAs_{1-x}P_x$ crystals were grown at the Laboratory of Physics of Crystal Growth in Warsaw. This work was supported by KBN (Poland) grants No. 2-0424-91-01 and 2-0179-91-01.

References

1 M. Baj, P. Dreszer and A. Babiński, *Phys. Rev. B*, 42 (1991) 2070.
2 F. Cerrina, D. Margadonna and P. Perfetti, *J. Cryst. Growth*, 18 (1973) 202.
3 T. Saito and Y. Seki, *J. Cryst. Growth*, 23 (1974) 217.
4 K. J. Bachmann, F. A. Thiel and S. Ferris, *J. Cryst. Growth*, 43 (1978) 752.
5 H. Kimura, A. T. Hunter, E.-H. Cirlin and H. M. Olsen, *J. Cryst. Growth*, 85 (1987) 116.
6 M. Jordan, T. Hangleiter and J.-M. Spaeth, *Semicond. Sci. Technol.*, 7 (1992) 738.
7 M. B. Panish and M. Ilegems, *Prog. Solid-State Chem.*, 7 (1972) 39.
8 D. J. Wolford, J. A. Bradley, K. Frey, J. Thompson and H. E. King, *Int. Conf. on Gallium Arsenid and Related Compounds, Inst. Phys. Conf. Serv.*, Vol. 65, Institute of Physics, Bristol, 1982, p. 477.
9 G. M. Martin, *Appl. Phys. Let.*, 39 (1981) 747.
10 M. Skowroński, J. Lagowski and H. C. Gatos, *J. Appl. Phys.*, 59 (1986) 2451.
11 M. Baj and P. Dreszer, *Phys. Rev. B*, 39 (1989) 10470.
12 D. C. Look, in *Electrical Characterization of GaAs Material and Devices*, Wiley, pp. 112–115.
13 A. G. Elliot, A. Flat and D. A. Vanderwater, *J. Cryst. Growth*, 121 (1992) 349.
14 W. A. Bonner, R. E. Nahory, H. L. Gilchrist and E. Berry, *Proc. Conf. on Semi-insulating III–V Materials, Toronto*, 1990, p. 199.

Materials Science and Engineering, B21 (1993) 329–332

Synthetic diamond: the optical band at 1.883 eV

M. H. Nazaré and L. M. Rino

Departamento de Física, Universidade de Aveiro, 3800 Aveiro (Portugal)

Abstract

The 1.883 eV absorption band is the dominant feature in high pressure synthetic diamonds grown using a nickel containing catalyst and without the presence of nitrogen getters. In absorption the optical band extends from 1.883 eV to about 2.2 eV and the dominant features are three sharp lines, with widths typically 2.5 meV, at 1.883 eV, 1.905 eV and 1.913 eV. For the first time the band is reported in photoluminescence and the results are consistent with the existence of three excited electronic states. We report on the temperature dependence of the band in absorption and use it to calculate the bandshape and to predict the shift of the lines expected to occur in ^{13}C diamond.

1. Introduction

Optical absorption bands with zero-phonon lines at 1.4 eV, 1.883 eV, 2.51 eV and 3.1 eV are typical of synthetic diamond grown using a nickel containing solvent catalyst [1]. While the 1.4 eV system is dominant in diamonds of low nitrogen content and has been associated [2] with Ni^+, with electronic configuration ($3d^9$, $S=1/2$), the 1.883 eV centre is stronger in diamonds grown without the presence of nitrogen getters, being dominant in diamonds with a nitrogen content greater than 50 ppm.

In absorption the optical band extends from 1.883 eV to about 2.1 eV and is made up of three sharp lines, with widths typically 2.5 meV, at 1.883 eV, 1.905 eV and 1.913 eV replicated twice with an energy interval of 61 meV. In synthetic diamond grown using 99% ^{13}C, the system appears to be shifted to higher energies by 3.8 meV, however the phonon energies in the band are the same as in ^{12}C diamonds [3].

In this paper we describe absorption and photoluminescence experiments which show that the three zero-phonon lines occur from a common ground state into three excited states. We report on the temperature dependence of the absorption band and analyse it in terms of vibronic coupling. We use the results to estimate the shift in energy expected in ^{13}C diamond.

2. Experimental details

The samples used in this work were synthetic diamond grown by the Japanese Institute for Research in Inorganic Materials using a nickel solvent catalyst and without the presence of nitrogen getters. Spectroscopic measurements were taken using a SPEX 1 m spectrometer, fitted with a 1200 grooves mm^{-1} grating. Light was detected using a RCA photomultiplier. Photoluminescence was excited using a xenon arc lamp coupled to a Kratos monochromator. Temperature data on the bandshape were obtained using an Air Products closed cycle cryostat.

3. Results and discussion

In Fig. 1(a) we show the visible absorption spectrum of a synthetic diamond recorded at 15 K. A luminescence spectrum is shown in Fig. 1(b). In absorption there are three zero-phonon lines at 1.883 eV, 1.903 eV and 1.913 eV. The three lines exhibit one-phonon replicas peaking at 61 meV from the zero-phonon line. In photoluminescence only the line at 1.883 eV is present at 15 K. At higher temperatures, namely above 110 K, the other two transitions can be detected but are not strong enough to allow quantitative analysis. Although the vibrational quanta observed in luminescence are higher than in absorption, the one-phonon side band peaking at 65 meV, its bandshape is the same in both the photoluminescence and absorption spectra and there is no evidence of Jahn–Teller effects. Therefore, the vibronic bandshape can be computed assuming that totally symmetric modes give the only significant vibronic coupling and that there are three independent progressions originating in a common ground state into three different excited states. Each vibronic progression is then given by [4]

$$\sum_{n=0} I_n(\omega) \qquad (1)$$

0921-5107/93/$6.00

© 1993 – Elsevier Sequoia. All rights reserved

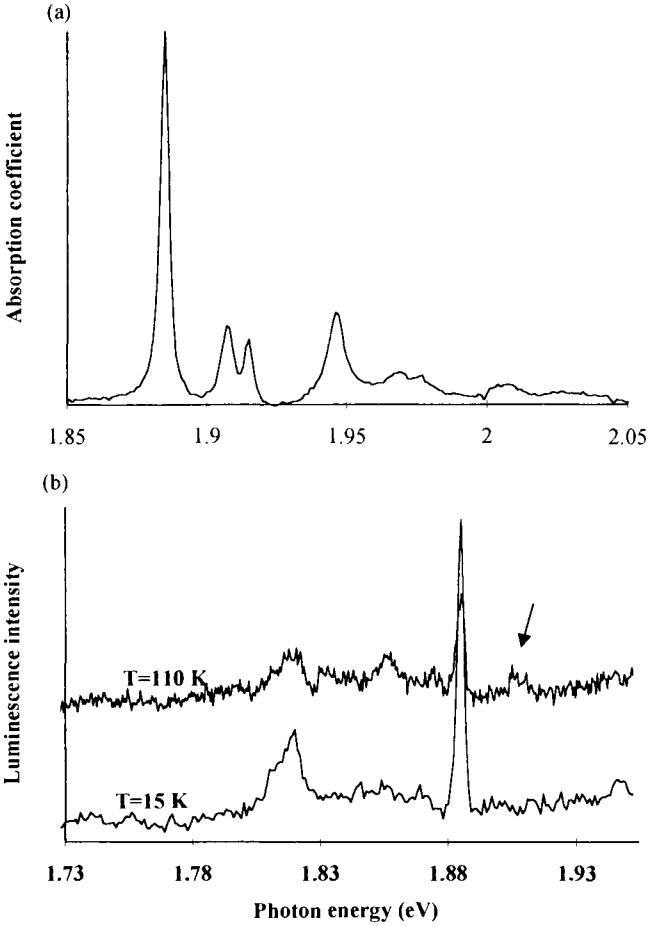

Fig. 1. (a) Absorption spectrum recorded at 15 K, from 1.85 eV to 2.05 eV of a high-pressure synthetic diamond. (b) Photoluminescence spectra of the same diamond recorded at two different temperatures, in the region of the 1.883 eV luminescence. The arrow indicates the position of the two zero-phonon lines not present at low temperatures.

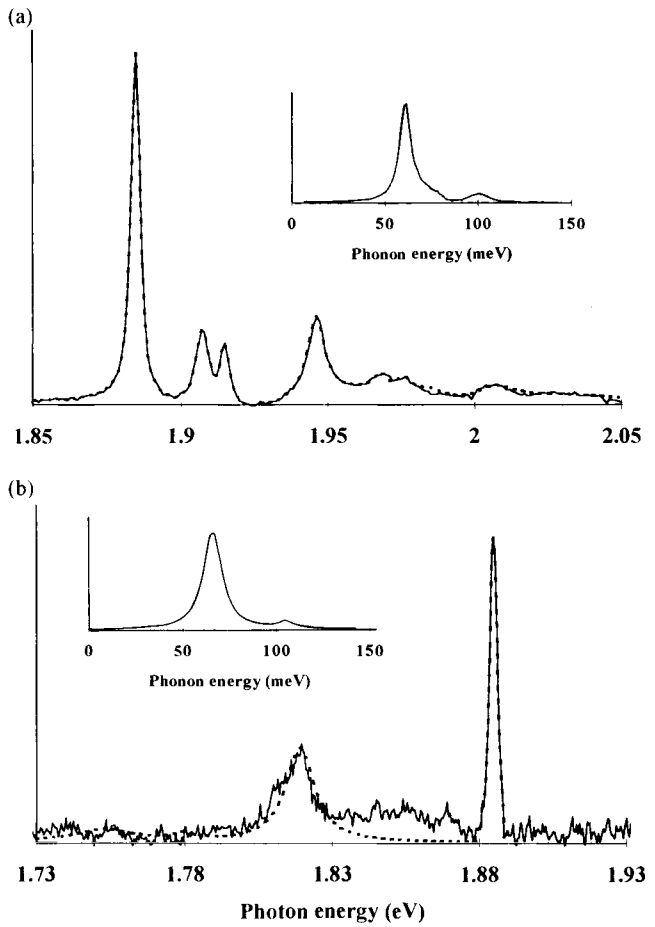

Fig. 2. Comparison of the measured (——) and calculated (- - -) bandshapes at 15 K for the 1.883 eV, 1.905 eV and 1.913 eV systems in (a) absorption and (b) photoluminescence. The insets show the phonon bandshape used.

where $I_n(\omega)$ is the transition probability for creating the nth phonon sideband at the frequency ω from the zero-phonon line (ZPL) and can be expressed in terms of the one-phonon transition probability as

$$I_n(\omega) = \int_0^{\omega_m} \mathrm{d}x I_1(x) I_{n-1}(\omega - x) \tag{2}$$

The relative weighting of the nth phonon sideband in the total bandshape is

$$\int \mathrm{d}\omega I_n = \exp(-S) S^n / n! \tag{3}$$

where S is the Huang–Rhys factor.

Experimentally S is obtained from the ratio of the one-phonon to the zero-phonon intensity. We used the theory above to simulate the measured absorption and luminescence bands, shown in Fig. 2. The measured absorption (luminescence) at a frequency ν has been converted to the transition probability dividing by ν (ν^3). The best fit to the absorption bandshape is obtained with Huang–Rhys factors of 0.7 for the 1.883 eV band and 0.85 for the other two bands. In luminescence at low temperature only the 1.883 eV state is populated, and the bandshape was computed considering only that state, using the same S value and the same one-phonon bandshape as for absorption but peaking at 65 meV instead of 61 meV; the result is shown in Fig. 2.

Vibronic theory predicts that the zero-phonon line intensity varies with temperature according to [4]

$$I_0(T) = \exp\left[-b \int_0^{\omega_m} \mathrm{d}\omega I_1(\omega)(2n(\omega) + 1) \right] \tag{4}$$

where $n(\omega)$ is the Bose–Einstein factor.

Assuming that the quadratic electron–phonon coupling to any two modes is proportional to the product of their linear interactions, the phonon

induced temperature dependences of the peak energy and width of the ZPL are

$$h\nu(T) = h\nu(0) + c\int \mathrm{d}\omega g(\omega) n(\omega) \tag{5}$$

$$\Gamma(T) = \mathrm{d}\int \mathrm{d}\omega g(\omega)^2 n(\omega)[n(\omega)+1] \tag{6}$$

where $g(\omega)$ is defined as a phonon density of states such that $g(\omega)/\hbar\omega$ is the change in energy in the adiabatic potentials of the modes with frequencies $\omega + \omega + \mathrm{d}\omega$. In addition, latticed expansion shifts the ZPL by

$$\Delta = -A_1(c_{11} + 2c_{12})\int_0^T \mathrm{d}T e(T) \tag{7}$$

here A_1 is the hydrostatic shift rate, c_{11} and c_{12} are the elastic constants of diamond, and $e(T)$ is the volume expansion coefficient.

According to Maradudin [4] $g(\omega)$ can be related to $I_1(\omega)$ by $g(\omega) = I_1(\omega)\omega^2$. However, in the present case we use a Debye spectrum of phonons to parameterize the temperature dependence of the peak position and width of the ZPL.

Figure 3 shows that the temperature dependence of the absorption integrated across the ZPL, of the energy of the ZPL and of the width, for the three systems at 1.883 eV, 1.903 eV and 1.913 eV, are fitted using the described model. Experiments in this laboratory enable us to use $A_1 = 0.65$ meV GPa^{-1}, in eqn. (7).

We now use the above results to calculate the shift that the zero-phonon lines are expected to exhibit in ^{13}C diamond and compare the calculated value with the measured value of 3.8 meV that the whole band exhibits when recorded in absorption in ^{13}C diamond [3].

The isotope shift of a ZPL arises through two different effects. One is the volume change of the lattice that induces a shift of [3, 5]

$$\Delta = A_1(c_{11} + 2c_{12}) \times 10^{-3} \text{ meV} \tag{8}$$

The second is the change in the vibrational frequency of the modes involving the motion of the carbon atoms and this produces a shift of

$$\Delta_1 = 1/2\left[\left(\sum_i \hbar\omega_i^{\mathrm{e}} - \sum_i \hbar\omega_i^{\mathrm{g}}\right)_{13} - \left(\sum_i \hbar\omega_i^{\mathrm{e}} - \sum_i \hbar\omega_i^{\mathrm{g}}\right)_{12}\right] \tag{9}$$

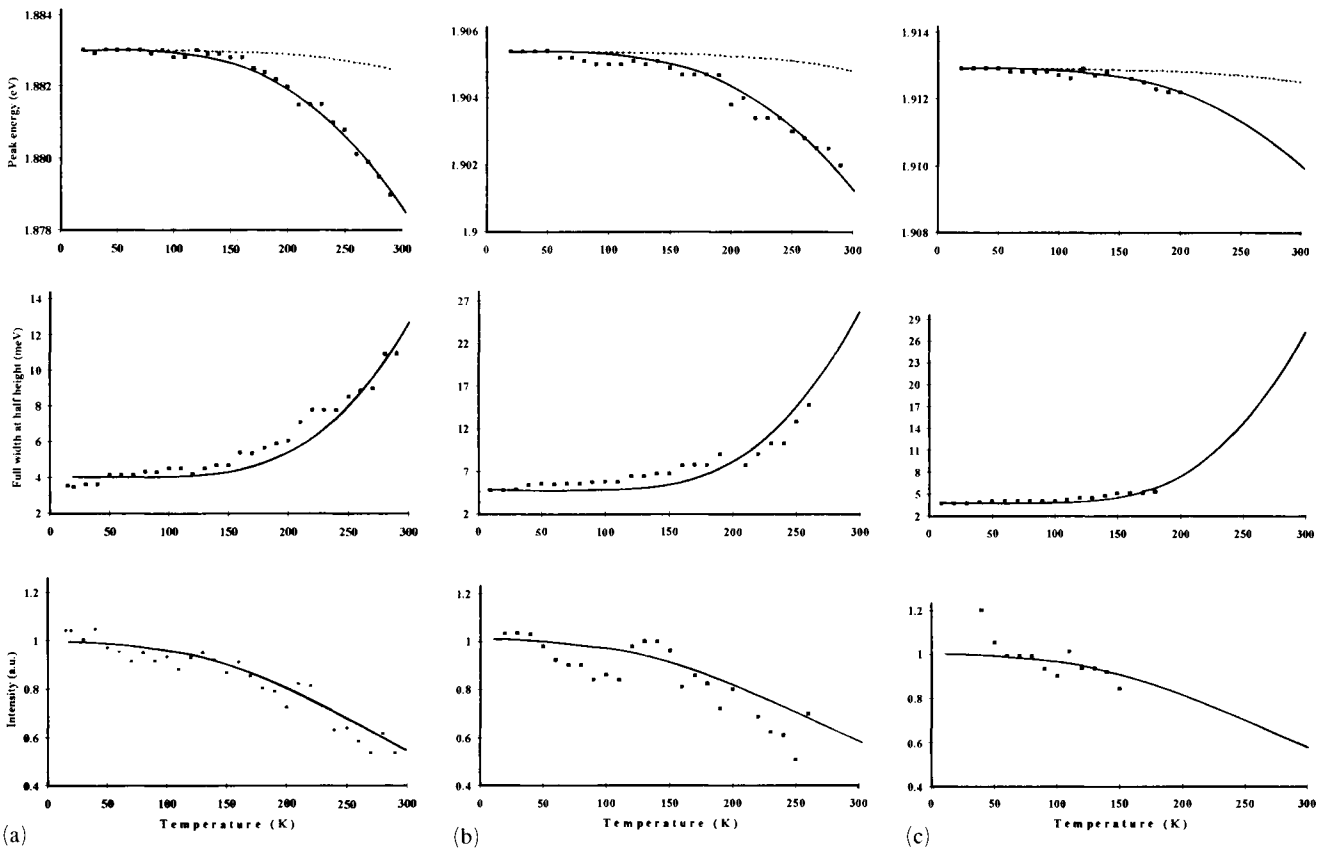

Fig,. 3. Temperature dependence of the intensity, the peak energy and the full width at half-height of the (a) 1.883 eV, (b) 1.905 eV and (c) 1.913 eV bands. The full lines show the fit to the data of the model described in the text.

or

$$\Delta_1 = 1/2\left[\int d\omega g^{13}(\omega) - \int d\omega g^{12}(\omega)\right] \quad (10)$$

so in principle we can use the temperature dependence of the ZPL energy to calculate Δ_1. Using eqn. (8) we find for the 1.883 eV line

$\Delta = 0.85$ meV

The dynamic shift presents more of a problem because, according to the published results [3], although the ZPL exhibits an isotope shift, the phonon energy is the same for both ^{13}C and ^{12}C diamond which means that the 61 meV mode does not involve motion of the lattice atoms. We have assumed that the 61 meV mode is localized and does not involve carbon and used the temperature dependence of the peak position to calculate a dynamic shift of

$\Delta_1 = 5.0$ meV

This gives a total shift of 5.85 meV, a value of the same sign and order of magnitude as the measured value, 3.8 meV. Given the uncertainties of the vibrational frequencies of the modes involved the results are acceptable.

4. Summary

We have described absorption and photoluminescence experiments which show that the 1.883 eV band involves electronic transitions from a common ground state into three excited states. Assuming vibronic coupling only to totally symmetric modes, we have computed the absorption bandshape and analysed the temperature dependence of the ZPL intensity.

Observing that the totally symmetric modes seen in the optical spectrum cannot be those responsible for the temperature dependence of the zero-phonon lines we used a Debye approximation to fit the results. As a result our estimates of the carbon-induced isotope changes are very rough, but have the same order of magnitude and sign as the observed value.

Acknowledgments

We are grateful to JNICT for partly financing the work. One of us (L.M.R.) acknowledges a travelling grant to CRIOLAB.

References

1 A. T. Collins, H. Kanda and R. C. Burns, *Philos. Mag. B, 61* (1990) 797.
2 M. H. Nazare, A. J. Neves and G. Davies, *Phys. Rev. B, 43* (1991) 14196.
3 A. T. Collins, G. Davies, H. Kanda and G. S. Woods, *J. Phys. C, 21* (1988) 1363.
4 A. A. Maradudin, *Solid State Phys., 18* (1966) 273.
5 W. F. Sherman, *J. Phys. C, 18* (1985) L973.

Materials Science and Engineering, B21 (1993) 333–337

Optical and transport properties in the electro-optical material $CdIn_2Te_4$

G. Couturier and B. Jean

LEMME, Université de Bordeaux I, 351 Cours de la Libération, 33405 Talence (France)

J. F. Lambert

Pôle de Recherche Aquitain pour les Matériaux dans l'Espace (PRAME), BP 11, 33615 St. Médard en Jalles (France)

P. Joffre

LCR, Thomson CSF, 91404 Orsay (France)

Abstract

Electrical and optical properties of the electro-optical semiconductor $CdIn_2Te_4$ are investigated. The temperature dependence of the fundamental gap has been measured in the range 77 K–500 K, reasons for the large optical absorption tails are also discussed. Conductivity measurements in a large range of temperatures reveal three different regions. A model for the conduction is proposed, as well as an energy diagram of the states in the forbidden band.

1. Introduction

$CdIn_2Te_4$ of the $A^{II}B_2^{III}C_4^{VI}$ class is often proposed as a potential electro-optical material for applications in the infrared region, the electro-optical coefficient r_{41} was announced to be as large as 50 pmV^{-1} [1]. We have recently shown that this high value probably resulted from some measurement artefacts due to the difficulty of making ohmic contacts. To take into account the nature of the Schottky contacts we have built a model based upon Jones' calculus to extract the actual r_{41} coefficient; our measurements and calculations lead to a value of $r_{41} = 1.5$ pmV^{-1} [2]. In measuring the electro-optical coefficient r_{41} we have also observed strange behavior in conductivity and optical transmission, in particular, non-reversibility of the conductivity after applying a large bias. Thus, this paper deals mainly with the temperature dependence of conductivity in various samples and after several thermal treatments in order to draw a transport model; a schematic energy diagram is proposed. An attempt is also made to explain the large optical absorption tails and to correlate them to the crystal composition.

2. Experimental procedure

Ingots of $CdIn_2Te_4$ with single crystal grains as large as 1 cm^3 were grown from an off-stoichiometric melt using a modified Bridgman–Stockbarger method. The stoichiometry was checked by electron probe microanalysis. Within the accuracy of the method, the expected stoichiometry was obtained at the bottom of the crystal. However, a slight increase in the In and decrease in the Cd concentrations (less than 1%) were observed along the crystal from bottom to top. This is in agreement with the phase diagram which predicts an increase in the off-stoichiometry in the growth direction [3].

X-ray diffraction confirms that $CdIn_2Te_4$ crystallizes in the tetragonal system (the lattice parameter c is twice the lattice parameter a, $a = c/2 = 6.23$ Å), and that it belongs to the I_4^-2m space group, in agreement with works published by Riede *et al.* [4], and not to the I_4^- group, as sometimes proposed. Results of reflectivity measurements and Raman spectroscopy are also consistent with the I_4^-2m space group [5]. Two configurations are then possible for Cd and In atoms in a unit cell, either the Cd and In are organized in planes, or Cd and In atoms are randomly distributed in the cationic sites. The X diffusion factors of Cd and In are so close that it is not possible to determine the exact configuration.

3. Optical and electrical properties

Measurements of the absorption spectrum of $CdIn_2Te_4$ were made in the temperature range 77–500 K around the absorption edge in order to:

0921-5107/93/$6.00

© 1993 – Elsevier Sequoia. All rights reserved

(1) determine the temperature dependence of the fundamental gap E_g and
(2) investigate the optical absorption tails below the gap.

As we have already mentioned [6], and in agreement with various authors [7, 8], the optical gap is assigned to indirect transitions; this is consistent with the square energy dependence of the absorption coefficient α above the gap. The fundamental gap E_g is deduced from the energy axis intercept of $\alpha^{1/2}$ in the high energy range. At room temperature E_g is close to 1.15 eV. A typical plot of the square root of α *vs.* the photon energy $\hbar\omega$ is shown in Fig. 1 (see curve (a) which correspond to crystals cut at the bottom of the ingots), in the following text these samples are quoted as # A.

The absorption coefficient α was deduced from the transmission ratio t_r using the classical relation:

$$\alpha = \frac{1}{d} \ln \left\{ \frac{2t_r R^2}{[(1-R)^4 + 4t_r^2 R^2]^{1/2} - (1-R)^2} \right\}$$

where d is the thickness. The reflectivity R was deduced from the values of t_r at large wavelengths ($\lambda > 1700$ nm) where the residual absorption is weak, in this case $t_r = (1-R)^2/(1-R^2)$. For well-polished crystals, the measured value of R is in good agreement with the calculated one from the relation $R = (1-n)^2/(1+n)^2$, with $n = 2.75$ [1, 9], giving a theoretical maximum of transmission $t_r = 0.64$; from optical measurements a value of $t_r \simeq 0.62$ is found.

As shown in Fig. 2, the temperature dependence of E_g is well described by the equation proposed by Varshni [10], *i.e.* $E_g(T) = E_{g0} - \gamma T^2/\beta + T$; most of the semiconductors have band gaps that fit well to this universal function; the constant β is a good approximation of the Debye temperature [11]. We found, respectively, $E_g = 1.26$ eV, $\gamma = 5.7 \times 10^{-4}$ eV K^{-1} and $\beta = 176$ K, which is related to the highest acoustical phonon energy. This value corresponds to a phonon wavenumber of 122 cm^{-1} (15 meV). It is smaller, and thus more consistent, than the highest optical phonon wavenumber of 192 cm^{-1} (23 meV) measured at the center of the Brillouin zone by reflectivity measurements [5].

In very pure indirect gap semiconductors, the absorption is composed of two parts beginning at two different energies; the upper part above the band gap is due to indirect transitions involving the creation of phonons whereas the lower part involves the absorption of phonons leading in some semiconductors (Si, Ge etc.) to a fine structure of the optical absorption tails [12, 13]. In the absence of exciton lines, the edge of absorption would be measured at an energy $(E_g - \hbar\Omega_m)$, where $\hbar\Omega_m$ is the highest phonon energy involved in indirect transitions. Thus, in $CdIn_2Te_4$ the absorption threshold would be located near 1.12 eV.

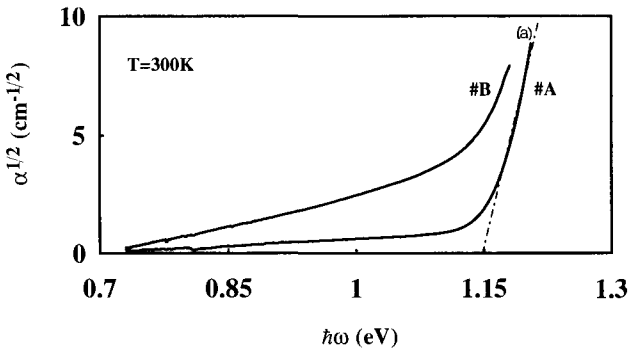

Fig. 1. Square root of the absorption coefficient of two $CdIn_2Te_4$ crystals, # A is cut in the lower part of the ingot and # B in the upper part.

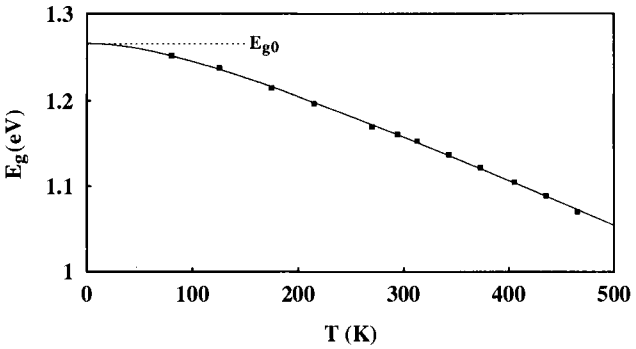

Fig. 2. The temperature dependence of the fundamental gap of $CdIn_2Te_4$. ■ Experimental values, —— calculated $E_g = E_{g0} - \gamma T^2/\beta + T$ ($E_{g0} = 1.26$ eV, $\gamma = 5.7 \times 10^{-4}$ eV K^{-1}, $\beta = 176$ K).

From an experimental point of view, it is rather difficult to determine the exact value of the absorption threshold because of the lack of accuracy of the reflectivity coefficient, $\Delta\alpha/\alpha \propto (1/\alpha)\Delta R/R$ at small values of α. However, in Fig. 1 it is clear that the absorption threshold (curve (a)) begins at a much lower energy than 1.12 eV. On the other hand no fine structure was observed even at the liquid nitrogen temperature.

The thickness of crystals used in optical transmission measurements was typically 0.8 mm. Thus a small change in the band gap is expected along the crystal according to the change of composition which becomes more off-stoichiometric and tends towards In_2Te_3. The fundamental gap of In_2Te_3 is about 1.13 eV [14], thus we can reasonably exclude this hypothesis to explain the optical tails. A possible cationic disorder, as mentioned above, can contribute to the formation of band tails and then to optical tails, as in amorphous semiconductors [15]. Band tails are associated with localized states and thus to a small mobility of carriers at the bottom of the conduction band. Transitions between defects and conduction and valence bands can also contribute to optical tails.

For samples # A, Hall measurements show that the electronic conductivity σ is n-type and is temperature activated (see the plots of $\log(\sigma)$ *vs.* $1000/T$ in Fig. 3(a)). Curve (a) corresponds to the first temperature scan (77 K → 400 K) and curve (b) to all other successive temperature scans.

The results may be divided into three regions. Region (1) corresponds to the beginning of the intrinsic domain where the activation energy is theoretically given by $E_{g0}/2 = 0.63$ eV, though this region is not completely reached at this value. In region (2), from 350 to 200 K, the activation energy ΔE is about 0.46 eV for the first temperature scan; ΔE is lowered to 0.43 eV for all other scans, see Fig. 3(b). In region (2) the mobility is about 100 $cm^2\ V^{-1}\ s^{-1}$. At room temperature the conductivity is 4×10^{-6} S cm^{-1} leading to a carrier concentration $n = N_c \exp[-(E_c - E_f)/kT] = 2.5 \times 10^{11}$ cm^{-3}, where N_c is the effective density of states, and E_c and E_f are the bottom of the conduction band and the Fermi level respectively, thus $(E_c - E_f) = 0.46$ eV. Assuming a theoretical effective mass for the electrons $m^* = 0.13\, m_0$ [16], we obtain a calculated value of n equal to 2.4×10^{10} cm^{-3}, an effective mass $m^* = 0.6\, m_0$ would be necessary to fit our results. In the third region, below 200 K, we probably observe a hopping transport of electrons through states near the Fermi energy. This would lead to a temperature dependence of the form $\sigma \propto \exp(-AT^{-1/4})$ [17], but it was not possible to test this relation; the same observation was made, for example, in amorphous SiO_2 [18].

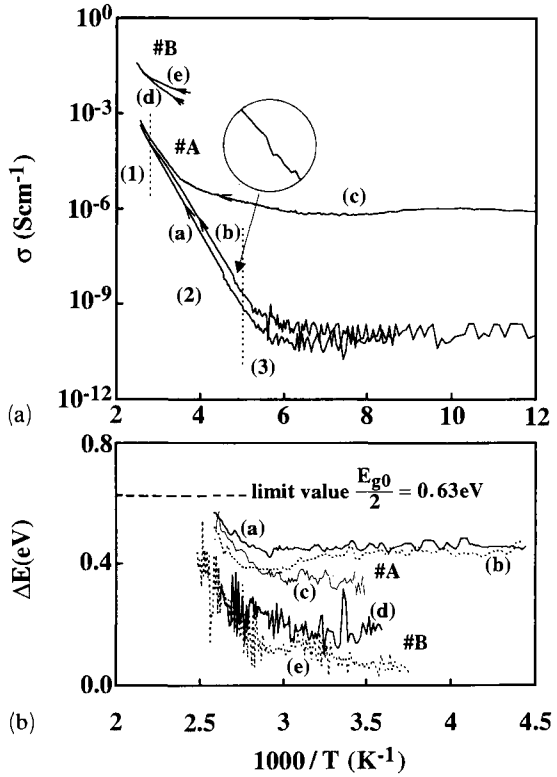

Fig. 3. (a) Conductivity *vs.* $1000/T$ for crystals # A (curves (a), (b) and (c)) and crystals # B (curves (d) and (e)); the zoom shows the conductivity step due to crossing the mobility edge. (b) Activation energy *vs.* $1000/T$ for crystals # A and # B.

As shown in Fig. 3(a), conductivity measurements in the low temperature range (below ≃ 210 K for curve (a)) are very noisy; this is consistent with conduction in localized states at the Fermi energy below 180 K and in the conduction band tail between 180 K and 210 K. The mobility in these states is probably very low and we were not able to measure it. The noise is not due to small values of conductivity. As a proof of this see, for instance, the conductivity noise of curve (c) below 290 K; explanations for this curve are given in the following. A small conductivity step (see the "zoom" in Fig. 3(a)) is probably due to a rapid increase in the mobility for electrons having an energy above the mobility edge, according to the concept of Mott and Davis [15].

After thermal stress performed by dissipating electric power of about 30×10^6 W m^{-3} for about one minute, followed by a relaxation time of about seven days, conductivity is drastically changed and then exhibits metal-like behavior in the low temperature range, see curve (c) in Fig. 3(a). In the regime of carrier ionization above ≃ 290 K, the activation energy is now smaller than 0.43 eV and takes a value of 0.35 eV. X-ray diffraction and microprobe analysis do not reveal any change of structure and composition within the accuracy of these methods.

Optical transmission and conductivity measurements performed with crystals # B cut in the upper part of the ingots are shown in Figs. 1 and 3. The absorption band tails are very large, and no peak is observed. As for crystals # A, the conductivity is also dependent on thermal annealings; it is weakly temperature-activated but we can no longer distinguish a single activation energy as in crystals # A, see curves (d) and (e) in Fig. 3(b). Although room temperature conductivity is three orders of magnitude higher than in crystals # A, the mobility is still close to 100 $cm^2\ V^{-1}\ s^{-1}$.

4. Discussion

Off-stoichiometric crystals enhance the formation of defects. Furthermore, a change of composition along the crystals probably leads to a non-homogeneous spatial distribution of these defects.

From conductivity measurements in crystals # A, it seems that the defects can be roughly described by a single level at about 0.46 eV below the bottom of the

conduction band, and at low temperature the Fermi level is pinned in these states where conduction takes place.

However, this is not very consistent with measurements performed after thermal stress followed by a long relaxation time. These latter results suggest that there are domains with higher concentrations of defects which are reorganized after thermal stress. A proof of this follows:

(1) The strong increase ($\times 10^4$) in residual conductivity at low temperature is only possible through a spatial rearrangement of defects leading to less distance between them and thus enhancing the residual conductivity.

(2) The fact that conductivity in the regime of carrier ionization is nearly the same at room temperature (see the curves (a) and (c) in Fig. 3(a)), shows that the total number of defects is not changed, only their spatial distribution. It is evident that the conduction of carriers in localized states is strongly dependent on their spatial distribution, whereas the conduction of these carriers in the extended states of the conduction band does not depend on their origin.

As shown in Fig. 4, it is possible to sketch a coarse energy diagram showing the conduction and valence bands, the band tails, the mobility edge and a narrow band of defects located at about 0.46 eV below the conduction band.

For crystals # B which have a more off-stoichiometric composition than crystals # A, conductivity and optical transmission measurements reveal a higher defect concentration which probably leads to a broader band of defect and larger band tails. Thus a single activation for conductivity cannot be found and large optical absorption tails are observed.

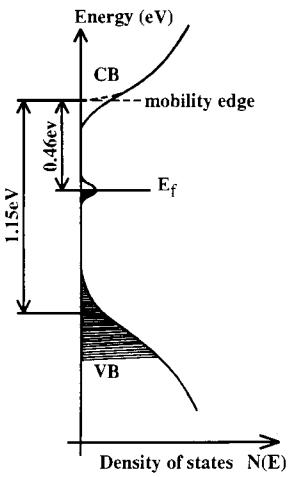

Fig. 4. Energy diagram of $CdIn_2Te_4$ showing the conduction and valence bands, the band tails and a narrow band at 0.46 eV below the bottom of the conduction band; at low temperature the Fermi level is pinned in the defect band.

Usually carrier mobility decreases as the carrier concentration increases, this is not the case in crystals # B. One possible explanation would be that electrons are separated from their parent donors as in GaAs/$Ga_{1-x}Al_xAs$ modulated structures. This is in agreement with the above hypothesis which supposes that the defects are not distributed in a homogeneous manner. Thus, if the mean free path of free carriers is smaller than the mean distance between diffusion centers, *i.e.* the defects, the mobility is not changed. This is what we observe.

5. Conclusion

We have measured the temperature dependence of the fundamental band gap of $CdIn_2Te_4$ and found that it obeys the classical law proposed by Varshni; an order of magnitude of the Debye temperature (176 K) is deduced. The large optical absorption tails are enhanced by the off-stoichiometric composition and are mainly attributed to defects and band tails; no fine structure was observed. At low temperature conductivity takes place through states near the Fermi energy. These states are spatially distributed in a non-homogeneous manner and can be rearranged after thermal treatment leading to a high increase in low temperature conductivity.

Acknowledgments

The authors are greatly indebted to Professor J. Salardenne for several helpful discussions.

References

1 A. L. Gentile, *Prog. Cryst. Growth Charac., 10* (1985) 241.
2 B. Jean, G. Couturier and P. Joffre, *Phys. Rev. B.*, submitted for publication.
3 L. Thomassen, D. R. Mason, G. D. Rose, J. C. Sarace and G. A. Schmitt, *J. Electrochem. Soc., 110* (1963) 1127.
4 V. Riede, H. Neumann, V. Krämer and M. Kittel, *Solid State Commun., 78* (1991) 211.
5 J. F. Lambert, *Thèse*, Université Bordeaux I, no. 875, 1993.
6 G. Couturier, B. Jean, J. F. Lambert, J. C. Launay and P. Joffre, *J. Appl. Phys., 73* (1993) 1813.
7 L. S. Koval, S. I. Radaustan and V. V. Sobolev, *Inorg. Mater., 8* (1972) 1776.
8 R. S. Becker, G. D. Zhou and J. Elton, *J. Phys. Chem., 90* (1986) 5866.
9 H. Neumann, W. Kissinger and F. Lévy, *Cryst. Res. Technol., 25* (1990) 1189.
10 Y. P. Varshni, *Physica, 39* (1967) 149.
11 C. D. Thurmond, *J. Electrochem. Soc., 122* (1975) 1133.
12 G. G. Macfarlane, T. P. Mclean, J. E. Quarrington and V. Roberts, *Phys. Rev., 108* (1957) 1377.

13 G. G. Macfarlane, T. P. Mclean, J. E. Quarrington and V. Roberts, *Phys. Rev., 111* (1958) 1245.
14 O. H. Hughes, P. M. Nikolic, C. J. Doran and S. S. Vujatovic, *Phys. Status Solidi (b), 71* (1975) 105.
15 N. F. Mott and E. A. Davis, in *Electronic Processes in Non-Crystalline Materials*, Oxford University Press, 1971, pp. 181–271.
16 V. I. Chizhikov, V. L. Panyutin, B. E. Ponedelnikov and A. E. Rozenson, *Phys. Status Solidi (b), 107* (1981) 347.
17 N. F. Mott, *Philos. Mag., 19* (1969) 835.
18 P. G. Le Comber and W. E. Spear, *Phys. Rev. Lett., 25* (1970) 509.

Materials Science and Engineering, B22 (1993) 1–8

Basic principles governing the surface atomic structure of zinc blende semiconductors

M. Lannoo
IEMN, Département ISEN (UMR CNRS 9929), 41 Boulevard Vauban, 59046 Lille (France)

Abstract

Six general rules are extracted from the large body of experimental and theoretical data on relaxation and reconstruction at semiconductor surfaces. They are justified on the basis of a tight-binding description of chemical bonding. Their application is detailed for the (111), (110) and (100) surfaces of covalent and compound tetrahedral semiconductors.

1. Introduction

The last 15 years have seen important progress in the knowledge of semiconductor surfaces. For the free surfaces essential results have been obtained concerning the lattice reorganization which results in surface relaxation or reconstruction. The details of the atomic structure are now well understood in many cases such as Si(111), Si(100), GaAs(110) and even, as we shall see, some polar surfaces of compound semiconductors. Total energy calculations have been quite helpful in this context. The situation is now mature enough that certain general features can be extracted. The aim of this work is thus to present some general rules governing relaxation and reconstruction at zinc blende semiconductor surfaces. These rules will be justified on the basis of simple physical arguments and discussed in the light of known experimental situations. For this we first recall briefly the nature of σ and π bonds in covalent systems and the notion of broken or dangling bonds. We then derive the general rules, first for covalent materials, then for non-polar and finally for polar surfaces of compounds (more details concerning this derivation can be found in ref. 1).

2. The nature of σ, π and dangling bonds

These notions have long been established in chemistry but it is of interest to summarize them here. They are based on a tight-binding description where the basis states are the s and p orbitals belonging to the outer valence shell of the atom. In the simplest version these are assumed to be orthonormal and the Hamiltonian matrix is restricted to nearest neighbours.

2.1. Covalent σ bonds

We consider a monoatomic covalent system in which there are n equivalent bonds, with interbond angle θ, between each atom and its neighbours. It is of interest to build hybridized atomic orbitals which point towards each of these neighbours [2]. For neighbour j this takes the form

$$\psi_j = \frac{\varphi_s + \lambda \varphi_j}{(1+\lambda^2)^{1/2}} \tag{1}$$

where φ_s is the s orbital and φ_j is the p orbital oriented along the bond with atom j ($j = 1-n$). Orthogonality between the ψ_j implies that $\lambda = (-1/\cos\theta)^{1/2}$. Of course this requires $n \leqslant 4$ so that $\cos\theta \leqslant 0$. The advantage is that the most important interactions occur between pairs of such hybrids involved in the same bond and pointing towards each other. In a first step, where one neglects other interactions (molecular model), such pairs can be treated independently and give rise to filled bonding states and empty antibonding states as in the H_2 molecule. This is what happens in tetrahedrally bonded covalent semiconductors with $n = 4$, $\cos\theta = -1/3$ (sp^3 hybrids). Figure 1 summarizes the situation and shows how further interactions broaden the bonding and antibonding states into the valence and conduction bands respectively. This can be considered as the prototype of σ bonds, which correspond to bonding with orbitals essentially pointing along the bonds.

2.2. π bonds

To illustrate the possible coexistence of σ and π bonds, we consider one plane of graphite. One first builds three equivalent hybrid orbitals per atom ($n = 3$,

0921-5107/93/$6.00 © 1993 – Elsevier Sequoia. All rights reserved

cos $\theta = -1/2$, sp^2 hybrids). These again lead to σ bonding with a filled (three electrons per atom) and an empty band. However, there remains one p orbital φ_π per atom perpendicular to the plane. Interaction between the φ_π will produce a broad band which, with one electron per atom, will be half filled. This leads to an extra contribution to the cohesive energy corresponding to π bonding. Usually π interactions are substantially smaller than σ interactions so that σ bonding is much stronger than π bonding.

2.3. *Dangling bonds*

The creation of vacancies or surfaces in covalent crystals implies the breaking of the bonds discussed before. For tetrahedrally bonded systems such broken bonds will correspond in the molecular model to sp^3 orbitals with no partner remaining at the corresponding atomic energy, midway between bonding and antibonding states. This feature will still remain valid beyond the molecular model, giving rise to the so-called dangling bond states in the gap region (Fig. 1).

The σ, π and dangling bonds have been described here for covalent bonding but remain valid in moderately ionic systems of similar nature. In such cases there can be different types of dangling bonds as will be discussed in detail later.

3. First set of rules

We discuss here rules which apply to covalent as well as partially ionic systems. Later we will introduce extra rules for ionic materials.

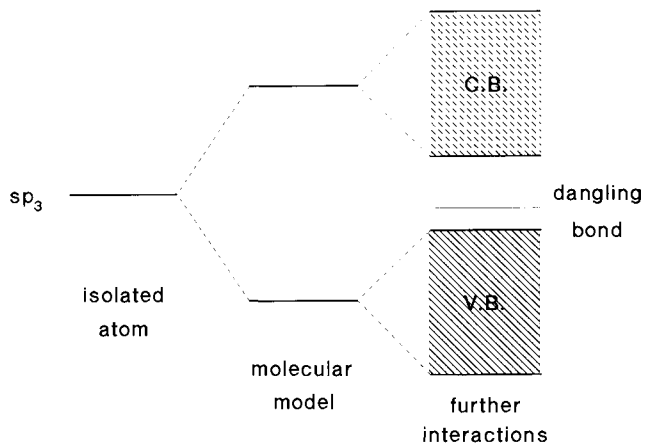

Fig. 1. Formation of bands from the molecular model showing the isolated atom sp^3 energy, its splitting into bonding and antibonding states and finally the broadening of these states into conduction and valence bands.

3.1. *Rule 1—Minimization of the number of dangling bonds*

Covalent and partly ionic semiconductors are characterized by strong nearest-neighbour bonds. A measure of this is provided by the cohesive energy per atom, of order 3–4 eV, which corresponds to what is gained in forming two bonds. This means that the breaking of such bonds requires an energy of about 1 eV per dangling bond. This is large enough to imply that the relaxation or reconstruction must be such as to minimize the number of dangling bonds in a way compatible with the geometrical constraints. This will reduce the number of dangling bonds to a value close to one per atom in most known cases.

3.2. *Rule 2—Preservation of bond lengths as far as possible*

The origin of this rule can be easily seen when one performs a second-order expansion of the total energy δE of a covalent system in terms of the atomic displacements with respect to the stable configuration. An approximate form is the so-called valence force field expression, the simplest version of which is

$$\delta E = \frac{k_r}{2} \sum_{\substack{\text{pairs} \\ ij}} (\mathrm{d}r_{ij})^2 + \frac{k_\theta r^2}{2} \sum_{\substack{\text{angles} \\ ijk}} (\mathrm{d}\theta_{ijk})^2 \qquad (2)$$

where the $\mathrm{d}r_{ij}$ and $\mathrm{d}\theta_{ijk}$ are changes in bond length and interbond angle respectively. The ratio k_θ/k_r of the force constants can be deduced from the phonon dispersion curves and turns out to be small, of order 0.04 for instance in the case of silicon [3]. Distortions in bond length thus cost much more energy than distortions in bond angles. This means that under the driving force for reconstruction the bonds close to the surface will react by keeping their length practically unchanged.

3.3. *Rule 3—Charge-dependent relaxation of trivalent atoms*

To illustrate this rule, consider an atom with one dangling bond in a covalent system. The dangling bond level E_{db} can be occupied by $n = 0$, 1 or 2 electrons. The change in total energy with respect to the neutral case ($n = 1$) contains a contribution $(n-1)E_{\mathrm{db}}$ resulting from the change in population. This leads to a population-dependent force $(n-1)\mathrm{d}E_{\mathrm{db}}/\mathrm{d}u$ on the trivalent atom, where u is the axial displacement away from the plane of its neighbours. We can get a fair estimation of this quantity from two extreme cases: (i) the atom is in the plane of its neighbours—then the dangling bond state is pure p with $E_{\mathrm{db}} = E_{\mathrm{p}}$; (ii) the atom lies in such a position that its interbond angles are $\theta = 90°$—then the hybrid orbitals become pure p and thus the dangling bond pure s at $E_{\mathrm{db}} = E_{\mathrm{s}}$. From this we get $\mathrm{d}E_{\mathrm{db}}/$

$du = 3(E_p - E_s)/2R$, where R is the bulk interatomic distance. An estimate for silicon [4, 5] gives $E_p - E_s \approx 4$ eV so that $dE_{db}/du \approx -1.7$ eV Å, which is a substantial value confirmed by detailed calculation [6, 7]. The resulting population-dependent force $(n-1)dE_{db}/du$ is equal to -1.7 eV Å^{-1} for $n=2$ and 1.7 eV Å^{-1} for $n=0$ and works in opposite directions. Considerations of gain in energy lead to the following third rule.

For empty dangling bonds the atom is lowered towards the basis of its three neighbours while the dangling bond energy E_{db} is raised towards E_p. For filled dangling bonds the atom is raised while E_{db} is lowered towards E_s.

This rule applies for the same reasons to compound semiconductors, where it will be extremely useful.

3.4. *Rule 4—Priority to σ bonds, then π bonds*

We have seen that σ bonds are much stronger than π bonds. The surface will therefore reorganize to allow for the maximum number of σ bonds and then π bonds if allowed by the topology.

4. Results for covalent surfaces

We discuss here three well-established situations, Si(111) 2×1, Si(111) 7×7 and Si(100), which illustrate the rules discussed above.

4.1. *Si(111) 2×1: the π-bonding chain model*

This metastable surface is obtained by cleavage at room temperature. For many years the most popular model for the 2×1 reconstruction was the buckling model [8] in which alternating rows of surface atoms are raised and lowered. However, the widely accepted model now is the π-bonding chain model of Pandey [9] which, as shown in Fig. 2, involves quite extensive atomic reorganization of the first two layers. The main characteristics are the following:

- keep the number of dangling bonds constant
- keep the bond lengths practically equal to the bulk value
- group the dangling bond atoms along chains of nearest neighbours.

The first two points are consequences of Rules 1 and 2 and would lead to small changes in energy with respect to the ideal surface. The third point illustrates Rule 4, since the parallel nearest-neighbour dangling bonds give rise to a half-filled band, leading to π bonding with substantial gain in energy calculated to be about 0.3 eV per atom [9]. An interesting point is that the change in topology can be obtained easily from the ideal 1×1 structure by simultaneously depressing a surface atom (1 in Fig. 2) into the second layer and raising a second-layer atom (2) into the surface layer. This breaks a subsurface bond (2–5) and establishes a new bond (1–5). The barrier for this process has been calculated and is smaller than 0.03 eV [10]. This explains why this structure could be created easily during the cleavage process and also why it transforms easily to a 1×1 during chemisorption.

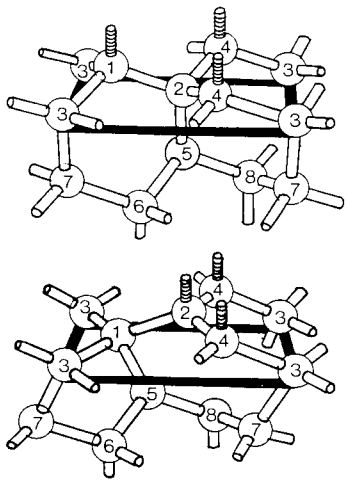

Fig. 2. Atomic structure of the Si(111) surface: unreconstructed surface (top) and Pandey's model [9] (bottom). The solid line represents the 2D unit cell.

4.2. *Si(111) 7×7: the dimer–adatom–stacking fault (DAS) model*

This reconstruction is obtained experimentally from the 2×1 by annealing the sample at 380 °C. It is only recently that a consensus has evolved about its structure [11]. The corresponding DAS model is illustrated in Fig. 3. Despite its complexity, it is of interest to check whether the general rules still retain some meaning.

Figure 3 shows that the non-reconstructed (111) 7×7 unit cell contains 49 atoms (lower plane). In the DAS model the dimerization leads to only 42 atoms in the first plane, of which 36 have their dangling bonds saturated by a bond with an adatom, leaving six dangling bonds per unit cell. Each of the 12 adatoms also have one dangling bond and each corner atom contributes to one dangling bond per unit cell. The number of dangling bonds has thus been reduced from 49 to 19. This represents a striking illustration of Rule 1 and is certainly at the origin of the stability of this structure. The extensive lattice reorganization is accompanied by very large angular distortions. Smaller but non-negligible (3–5.7%) stretching in bond lengths has been calculated [12] illustrating Rule 2. Recent first-principle calculations [13, 14] confirm the inherent stability of this model.

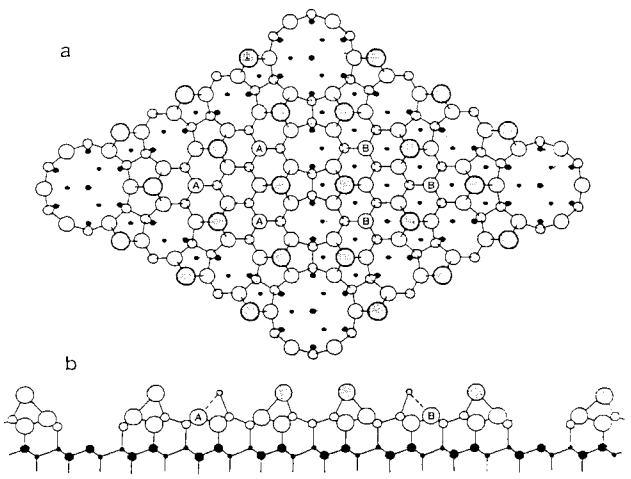

Fig. 3. The dimer-adatom-stacking fault reconstruction model.

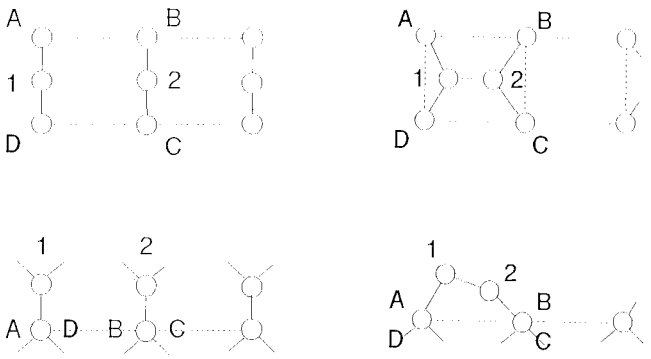

Fig. 4. Si(100) ideal surface (left): top view (top) and side view (bottom). Si(100) asymmetric dimer model (right): top view (top) and side view (bottom).

4.3. Si(100) 2 × 1: the dimer model

This case provides a remarkable illustration of the rules. The geometrical situation is pictured in Fig. 4. For each surface atom 1 and 2 two covalent bonds have been broken, a fact which, according to Rule 1, tends to make the ideal geometry highly unstable. To reduce the number of dangling bonds (Rule 1) and preserve bond lengths (Rule 2), one can move atoms 1 and 2 symmetrically with a pure angular distortion of their back bonds in order to allow for the formation of a σ bond between them which again will have the bulk bond length. This reduces the number of dangling bonds to one per atom and only costs angular energy. This view is confirmed by detailed analysis [15].

Starting from this symmetric dimer, there can be two possible extra contributions related to Rules 3 and 4. First, the interaction between the dangling bonds remaining on atoms 1 and 2 of the dimer can lead to some π bonding (Rule 4). However, another possibility would be to exploit Rule 3, building an asymmetric dimer by raising atom 1 and lowering atom 2. The lowered dangling bond state of atom 1 would be occupied by the two electrons while the raised state of atom 2 would be empty. Various calculations as well as experimental evidence reported in ref. 15 lead to the conclusion that the asymmetric dimer is more stable, *i.e.* Rule 3 dominates here over Rule 4.

5. Further rules for compound zinc blende semiconductors

Here we discuss two new rules which seem to account for most of the simple structures observed for III–V and II–VI compounds.

5.1. Rule 5—Filled anion dangling bonds (empty cation dangling bonds)

Here the basic argument is very simple. Anions are more electronegative than cations so that the anion dangling bond states lie at lower energy than the cation states, their distance in energy being a sizable fraction of the gap. Let us consider first surfaces with equal numbers of anion and cation dangling bonds. Since charge conservation requires that there are two electrons per pair of dangling bonds, one gains energy by completely filling the anion dangling bond states and emptying the corresponding cation states. This gain in energy is further amplified by the fact that Rule 3 now applies: indeed, the anion states being filled, the system is stabilized by outward anion relaxation which lowers the corresponding dangling bond states; symmetrically there is inward cation relaxation also leading to energy gain. The situation for the dangling bond states is pictured in Fig. 5 which, as discussed in the next section, is typical of what happens for non-polar surfaces of binary compounds.

The arguments given above seem strong enough to apply to more complex situations, *e.g.* when there are rebonding phenomena (dimerization). Here the rule takes the form that all bonding and anion dangling bond states must be filled and all antibonding and cation states must be empty. From the chemical point of view this rule means that, at least in III–V compounds, the stable situation for a trivalent anion corresponds to three electrons in bonding states and an s^2 lone pair.

5.2. Rule 6—The principle of local neutrality

This comes from the fact that it is necessary to avoid the existence of surface charges which would generate macroscopic electric fields. A simple way of satisfying this condition is to compensate the nuclear charges by the number of electrons engaged in the different bonds.

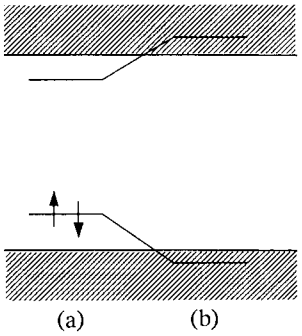

Fig. 5. Anion and cation dangling bond levels (a) before and (b) after atomic relaxation.

This starts from the bulk, where we can say that, in III–V compounds for instance, each anion has a nuclear charge $Z = 5$ compensated by 5/4 electrons in each of the four equivalent bonds, the same being true for each cation with $Z = 3$ and 3/4. This automatically ensures neutrality of each bulk plane. The difference for the surface planes is that this condition must be fulfilled with the appropriate population for the different types of bonds which can exist. We shall see several examples of this in detail in Section 7 on polar surfaces.

6. Non-polar (110) surfaces

Some of the early experiments [16, 17] concluded that the GaAs(110) surface was characterized by surface states in the gap. However, it was later made clear [18, 19] that such intrinsic states do not exist and that the previously observed pinning of the Fermi level was due to surface defects [18–22]. The structure of the ideal unrelaxed surface is shown in Fig. 6, which displays the corresponding unit cell together with the bonds with atoms belonging to the first inner plane. Calculations for this non-polar surface [23] predict two bands of interface states, one centred at $E_v - 0.25$ eV due to As dangling bonds, the other at $E_v + 1$ eV, well within the gap, due to Ga dangling bonds.

These theoretical results are in apparent contradiction with experiment since they predict gap states. Rule 6 is automatically satisfied if there are two electrons per pair of dangling bonds, which should populate the anion dangling states according to Rule 5. However, in such a case Rule 3 applies as discussed in the previous section, opening the gap between the two surface bands. The effect is strong enough for these bands to be pushed out of the gap in agreement with experiment. In addition, one expects respective upward and downward motion of the As and Ga atoms. This picture was first obtained from the tight-binding calculations of Chadi [24], who predicted the stable

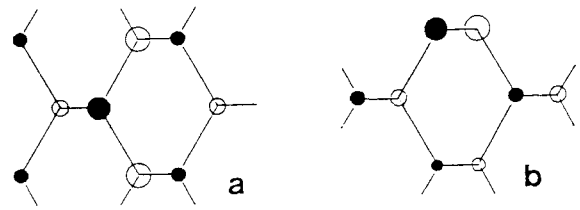

Fig. 6. GaAs(110) ideal surface atomic configuration: a, top view; b, side view.

configuration pictured in Fig. 7. Further calculations have shown that the corresponding dangling bond bands do not lie in the gap any more [25]. Finally, recent local density approximation (LDA) calculations [26] fully confirm the picture, yielding a value of 1.22 eV per unit cell for the surface energy compared with 1.21 eV experimentally and a photoelectric threshold of 4.94 eV compared with 5.15–5.75 eV experimentally.

The same picture holds true for the (110) surfaces of other III–V compounds [27]. This is further confirmed by the measured core level shifts, which have been shown to be fully consistent with filled (empty) anion (cation) dangling bonds [28].

7. Polar surfaces

We consider here in some detail the best-known cases of (100) and (111) polar faces of compounds.

7.1. The (100) surface

We follow here the work of Pashley [29], who derived the so-called electron-counting model and applied it to GaAs(001) and ZnSe(001). Scanning tunnelling microscopy (STM) studies [30, 31] have shown that the 2×4 reconstruction seen during growth arises from dimerization of the surface As atoms with every fourth dimer missing. These observations were in agreement with a previous calculation by Chadi [32] and we discuss now how they illustrate the different rules.

The first point is analogous to the Si(100) case where the formation of dimers satisfies Rules 1 and 2. Let us first assume that the GaAs(001) surface is completely covered with such dimers and calculate the net charge per As atom in the surface plane. Each As atom of this plane has the following number of electrons in each type of bond: $2 \times \frac{5}{4}$ in the normal back bonds, one in the dimer bond and two in its dangling bond according to Rule 5. With a nuclear charge of $+5$ it has a net excess number of electrons of $\frac{1}{2}$ or, equivalently, one per As dimer. According to Rule 6, such a net surface charge cannot correspond to the stable situation. One way to correct for this is to periodically remove dimers.

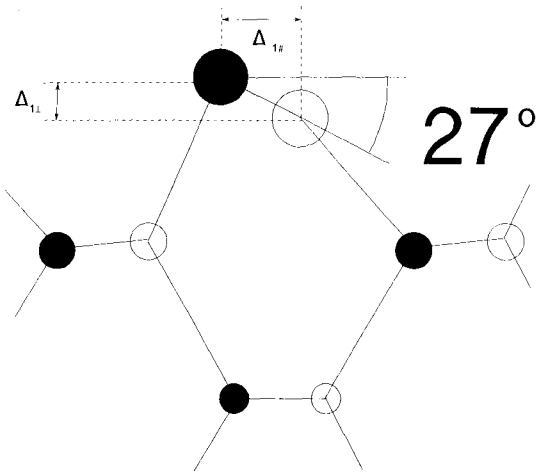

Fig. 7. Relaxed GaAs(110) surface: side view.

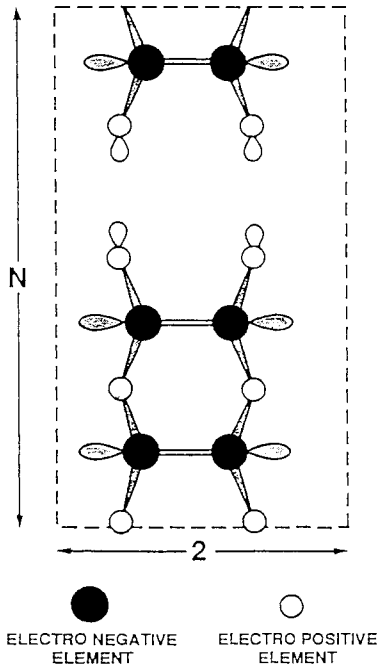

Fig. 8. The bonds and dangling bonds, both filled (shaded) and empty (open), for a $2 \times N$ unit cell on the (001) surface of a polar semiconductor with the zinc blende crystal structure, where the N-times periodicity arises from missing dimers.

Each missing dimer of Fig. 8 has four cation dangling bonds which must be empty (Rule 5), leading to a deficit of three electrons ($4 \times \frac{3}{4}$) per missing dimer. If D is the number of dimers and M the number of missing dimers, the overall neutrality of the surface (Rule 6) requires

$$D = 3M \tag{3}$$

The smallest unit cell that satisfies this condition is a (2×4) unit cell with three dimers and one missing dimer as observed experimentally [29]. The same analysis applied to II–VI compounds such as ZnSe shows that each Se of a surface plane fully covered by dimer bonds has $2 \times \frac{6}{4}$ electrons in the back bonds, one in the dimer bond and two in the dangling bond, *i.e.* a total of six, corresponding automatically to surface charge neutrality. It should thus be stable, as seems to be confirmed by experiment [29]. The same arguments predict a 4×2 unit cell for GaAs(001)-Ga, again consistent with experiment. Other confirmations are discussed in ref. 29 but will not be detailed here.

7.2. The (111) surfaces

In the case of GaAs, for instance, one has two possibilities: either the (111) (Ga-terminated) or $(\bar{1}\bar{1}\bar{1})$ (As-terminated) surface. A rich variety of patterns have been observed, such as (2×2), $(\sqrt{3} \times \sqrt{3})$, 3×3 and $(\sqrt{19} \times \sqrt{19})$. For GaAs$(\bar{1}\bar{1}\bar{1})$ we discuss the results of ref. 33 and for GaAs(111) those of refs. 34 and 35.

Let us first discuss the case where the surface is terminated by a layer of As atoms with one dangling bond per surface atom. The number of electrons per such atom is $3 \times \frac{5}{4}$ for each back bond plus two for the dangling bond (Rule 5), *i.e.* a net excess of $\frac{3}{4}$ electron per As atom. This means (Rule 6) that this surface cannot be stable. The symmetric situation holds for the Ga-terminated surface with a deficit of $\frac{3}{4}$ electron per atom.

A possibility of realizing the charge compensation implied by Rule 6 is the buckled vacancy model [34, 35] widely accepted for GaAs(111) (Ga-terminated). Consider the Ga-terminated case and assume that a Ga vacancy is created. This leaves three As atoms with a filled dangling bond (Rule 6), each one thus having an excess of $\frac{3}{4}$ electron. If we call N the number of normal Ga surface atoms and M the number of vacancies, one readily gets neutrality when

$$N = 3M \tag{4}$$

i.e. one vacancy per four sites. This result corresponds to the so-called buckled vacancy model of refs. 34 and 35.

However, the STM study of ref. 33 shows that the vacancy model can be ruled out for the As-rich GaAs$(\bar{1}\bar{1}\bar{1})$ surface and that an adatom model is to be preferred. The situation is as pictured schematically in Fig. 9, where an As-terminated plane with one dangling bond per atom is covered by one or more adatoms in the shaded regions. Let us consider first the case of one adatom at the centre of each such triangle. It makes three bonds with its neighbours and has one filled dangling bond. The number of electrons for such a four-atom unit is $3 \times \frac{5}{4}$ for the back bonds of each As

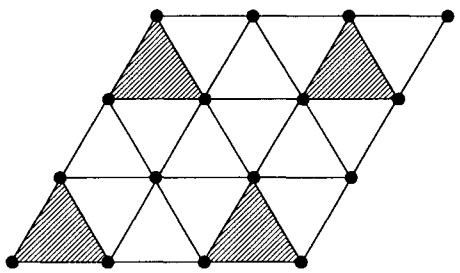

Fig. 9. 2×2 reconstruction of the As-rich GaAs($\bar{1}\bar{1}\bar{1}$) surface. The hatched triangles correspond to the regions where adatoms are located (see text). All atoms represented by black circles are As atoms belonging to the surface plane.

atom of the surface plane, six for the new bonds and two for the filled dangling bond. This total of $8+\frac{45}{4}$ is compensated by 4×5 nuclear charges, leading to a net deficit of $\frac{3}{4}$ electron. Thus, according to Rule 6, a stable possibility corresponds to one "normal" As atom for one adatom, *i.e.* exactly the periodicity of Fig. 9 which is the observed one. However, there is another possibility with three As adatoms forming a trimer, *i.e.* having equivalent bonds together and another bond with one of the three surface As atoms. There is thus a total of six new bonds and three filled dangling bonds, leaving $\frac{45}{4}+18-30$ excess electrons per such unit, *i.e.* again a deficit of $\frac{3}{4}$ electron. Thus from the point of view of Rule 6 the two cases are equally stable. Detailed calculations [33] show that As-rich conditions favour the trimers, which seems reasonable in view of the fact that one accommodates three times more adatoms, each one having a similar bonding configuration to the single adatom.

The (2×2) symmetry converts to $(\sqrt{19}\times\sqrt{19})$ after annealing at 500 °C for about 10 min, corresponding to a Ga-rich reconstruction. This structure is too complex to be discussed here but, according to ref. 33, it seems to be a case where Rules 5 and 6 might break down, at least locally for Rule 6. More work is certainly needed to explore this matter further.

8. Conclusions

We have shown that it is possible to establish fairly general rules which provide criteria for selecting possible relaxations or reconstructions. These rules apply to all the simple cases commonly studied but their use for complex structures such as Si(111) 7×7 or GaAs($\bar{1}\bar{1}\bar{1}$) $(\sqrt{13}\times\sqrt{13})$ still remains to be clarified. They can be extended to the case of chemisorbed layers but this is beyond the scope of the present work. A similar approach was recently proposed by Duke [36] but in a more chemical formulation. His rules can essentially be cast in the same form as the six rules presented here except for some dependence of the non-polar (110) surface bond length upon ionicity which was not considered here.

References

1 M. Lannoo and P. Friedel, in G. Ertl and R. Gomer (eds.), *Atomic and Electronic Structure of Surfaces: Theoretical Foundations, Springer Series in Surface Sciences*, Vol. 16, Springer, Berlin, 1991.
2 C. A. Coulson, *Valence*, Oxford University Press, Oxford, 1961.
3 M. Lannoo and G. Allan, *Phys. Rev. B, 25* (1982) 4089.
4 P. Vogl, H. P. Hjalmarson and J. P. Dow, *J. Phys. Chem. Solids, 44* (1983) 365.
5 D. N. Talwar and C. S. Ting, *Phys. Rev. B, 25* (1982) 2660.
6 W. A. Harrison, *Surf. Sci., 55* (1976) 1.
7 Y. Bar-Yam and J. D. Joannopoulos, *Phys. Rev. Lett., 56* (1986) 2203.
8 D. Haneman, *Phys. Rev., 121* (1961) 1093.
9 K. C. Pandey, *Phys. Rev. Lett., 47* (1981) 1913; *49* (1982) 223.
10 J. E. Northrup and M. L. Cohen, *J. Vac. Sci. Technol., 21* (1982) 333; *Phys. Rev. Lett., 49* (1982) 1349.
11 K. Takayanagi, Y. Tanishiro, M. Takahashi and S. Takahashi, *J. Vac. Sci. Technol. A, 3* (1985) 1502.
12 G. X. Qian and D. J. Chadi, *Phys. Rev. B, 35* (1987) 1288.
13 I. Stich, M. C. Payne, R. D. King-Smith, J. S. Lin and L. J. Clarke, *Phys. Rev. Lett., 68* (1992) 1351.
14 K. D. Brommer, M. Needels, B. E. Larson and J. D. Joannopoulos, *Phys. Rev. Lett., 68* (1992) 1355.
15 J. Pollmann, R. Kalla, P. Kruger, A. Mazur and G. Wolfgarten, *Appl. Phys. A, 41* (1986) 21.
16 D. E. Eastman and J. L. Freeouf, *Phys. Rev. Lett., 33* (1974) 1601; *34* (1975) 1624.
17 P. E. Gregory, W. E. Spicer and W. A. Harrison, *Appl. Phys. Lett., 25* (1974) 511.
18 J. van Laar and J. J. Sheer, *Surf. Sci., 8* (1967) 342; A. Huijser and J. van Laar, *Surf. Sci., 52* (1975) 202.
19 J. van Laar and A. Huijser, *J. Vac. Sci. Technol., 13* (1976) 769; J. van Laar, A. Huijser and T. van Rooy, *J. Vac. Sci. Technol., 14* (1977) 893.
20 W. E. Spicer, I. Lindau, P. E. Gregory, C. M. Garner, P. Pianetta and P. W. Chye, *J. Vac. Sci. Technol., 13* (1976) 233; P. E. Gregory and W. E. Spicer, *Phys. Rev. B, 13* (1976) 725.
21 W. E. Spicer, P. Pianetta, I. Lindau and P. W. Chye, *J. Vac. Sci. Technol., 14* (1977) 885.
22 W. Gudat and D. E. Eastman, *J. Vac. Sci. Technol., 13* (1976) 831.
23 J. R. Chelikowsky and M. L. Cohen, *Phys. Rev. B, 13* (1976) 826.
24 D. J. Chadi, *Phys. Rev. Lett., 43* (1979) 43.
25 J. R. Chelikowsky and M. L. Cohen, *Solid State Commun., 29* (1979) 267.
26 G.-X. Quian, R. M. Martin and D. J. Chadi, *Phys. Rev. B, 37* (1988) 1303.
27 C. B. Duke, C. Mailhiot, A. Paton, D. J. Chadi and A. Kahn, *J. Vac. Sci. Technol. B, 3*(4) (1985) 1087.
28 C. Priester, G. Allan and M. Lannoo, *Phys. Rev. Lett., 58* (1987) 1989.

29 M. D. Pashley, *Phys. Rev. B, 40* (1989) 10481.
30 M. D. Pashley, K. W. Haberern, W. Friday, J. M. Woodall and P. D. Kirchner, *Phys. Rev. Lett., 60* (1988) 2176.
31 M. D. Pashley, K. W. Haberern and J. M. Woodall, *J. Vac. Sci. Technol. B, 6* (1988) 1468.
32 D. J. Chadi, *J. Vac. Sci. Technol. A, 5* (1987) 834.
33 D. K. Biegelsen, R. D. Bringans, J. E. Northrup and L. E. Swartz, *Phys. Rev. Lett., 65* (1990) 452.
34 S. Y. Tong, G. Xu and W. N. Mei, *Phys. Rev. Lett., 52* (1984) 1963.
35 D. J. Chadi, *Phys. Rev. Lett., 52* (1984) 1911.
36 C. B. Duke, *Appl. Surf. Sci.*, in press.

LTMBE GaAs: present status and perspectives

Gerald L. Witt
AFOSR/NE, Bolling AFB, DC 20332 (USA)

Abstract

When GaAs is grown via MBE at 200 °C (compared to the normal 580–600 °C), the films manifest a remarkable set of structural, electrical and optical properties. As grown, LT GaAs (as it is commonly known) has an excess of As, contains a high concentration of point defects, displays hopping band conductivity and shows little, if any, photoluminescence. After a 600 °C anneal, the layers have a relaxed lattice constant, are highly resistive and contain a distribution of As precipitates. The point defect concentration diminishes by several orders of magnitude. The photo-induced carrier lifetime typically is of the order of 200 fs. This account will review what is known about these interesting materials, discuss models to explain the transport properties and mention potential applications.

1. Background

Between 1978 and 1983 a small number of papers appeared in which attempts were made to grow GaAs via MBE at temperatures lower than the usual range of 580–600 °C. The motivations for these explorations varied from the goal of reducing deep traps, to preserving abrupt doping profiles and overgrowing buried metals. In 1978 Murotani *et al.* [1] explored the properties of MBE GaAs grown at substrate temperatures down to 400 °C. The study included the first use of LT GaAs (500 °C) as a buffer layer beneath a GaAs power field effect transistor (FET). Two years later Stall *et al.* [2] also sought to use LT GaAs as a buffer layer. However, the overgrown normal GaAs channel layer was nonconducting, presumably owing to defect diffusion from the LT buffer. Metze and Calawa [3] demonstrated an abrupt decrease in mobility and carrier concentration when MBE GaAs is grown below 500 °C at normal growth rates. To compensate, they reduced the growth rate.

In 1988 Smith *et al.* [4] published a now widely referenced paper entitled "New MBE buffer used to eliminate backgating in GaAs MESFETs". Their buffer layer growth conditions (usually referred to as "LT GaAs") are as follows: As_4source, growth temperature of 200 °C, growth rate of 1 mm h^{-1} and As-stable growth condition. (As_4:Ga beam equivalent pressure (BEP) of 10:1).

2. Basic features of LT MBE GaAs

Table 1 contrasts the properties of LT and normal MBE GaAs. It is important to note that the "standard" LT MBE GaAs properties listed are for annealed samples. In the work of Smith *et al.* [4], this anneal took place *in situ* during the overgrowth of a 0.3 μm active channel. Effectively, this produces a 20 min anneal at 600 °C. It is important to distinguish between as-grown and annealed samples; they differ in many significant regards.

For growth temperatures above 190 °C, the as-grown layers are crystalline but have a lattice constant roughly 0.1% larger than that of the GaAs substrate. The variety and concentration of point defects are remarkable: $[As_{Ga}]^o \approx 10^{20}$ cm^{-3}, $[As_{Ga}]^+ \approx 5 \times 10^{18}$ cm^{-3}, $V_{Ga} \approx 5 \times 10^{18}$ cm^{-3}. There is evidence for As_i as well as for more complex local defects. The resistivity is of the order of 10^2 Ω-cm. The anti-site point defects are similar in many respects, though not all, to the important defect level EL2. There is essentially no photoluminescence signal.

Following an anneal of 10 min or more at 600 °C under As over pressure, the layers remain crystalline, have a relaxed lattice constant and show point defect concentrations two or three orders of magnitude less

TABLE 1. Comparison of normal and low temperature GaAs

	"Normal" MBE	"Standard" LT MBE
Structure	Crystalline	Crystalline
Stoichiometry	50:50	≈ 1 at.% excess As
Resistivity	≈ 0.3–20 Ω -cm	≈ 10^6 Ω-cm
Breakdown field	≈ 3×10^4 V cm^{-1}	≈ 5×10^5 V cm^{-1}
Trap density	< 10^{15} cm-3	≈ 10^{19} cm-3
Lifetime	≈ 1 ns	≈ 150 fs
Overgrowth	Excellent	Excellent

0921-5107/93/$6.00

© 1993 – Elsevier Sequoia. All rights reserved

than for as-grown samples. To within experimental sensitivity, the As concentration remains unchanged — roughly 1–1.5% excess above stoichiometry. The resistivity increases to 10^6–10^7 Ω-cm. The latter property contributes to the successful application in reducing back-gating.

GaAs of high quality can be grown epitaxially by MBE at normal temperatures on top of as-grown or previously annealed layers. (The overgrowth, of course, anneals the underlying GaAs.) This property is critical for many applications of this material. See Kamińska *et al.* [5] for a review of the properties of as-grown and annealed LT MBE GaAs. A summary of recent results can be found in [6].

Doping LT GaAs is difficult. Two factors appear to be involved. First, the very high density of electrically active point defects, even in annealed material, tends to compensate heavy dopant concentrations. For 200 °C material, dopant concentrations of about 10^{19} cm^{-3} would be required for activation. A second factor, on which there is not full agreement in published reports, is the failure of dopants such as Be or Si to enter the lattice substitutionally. See ref. 6 for a discussion of this issue.

There is one additional and important feature of annealed LT MBE GaAs — the presence of As precipitates [7]. With the growth and anneal conditions described above, the precipitates have an average diameter of 5–6 nm and a volume density of 10^{17} cm^{-3} [8]. This produces a two-phase material system which has been referred to as GaAs:As [9]: a term stressing the distinction, as mentioned earlier, which must be made between LT MBE GaAs with precipitates (usually annealed samples) and without precipitates (usually as-grown samples).

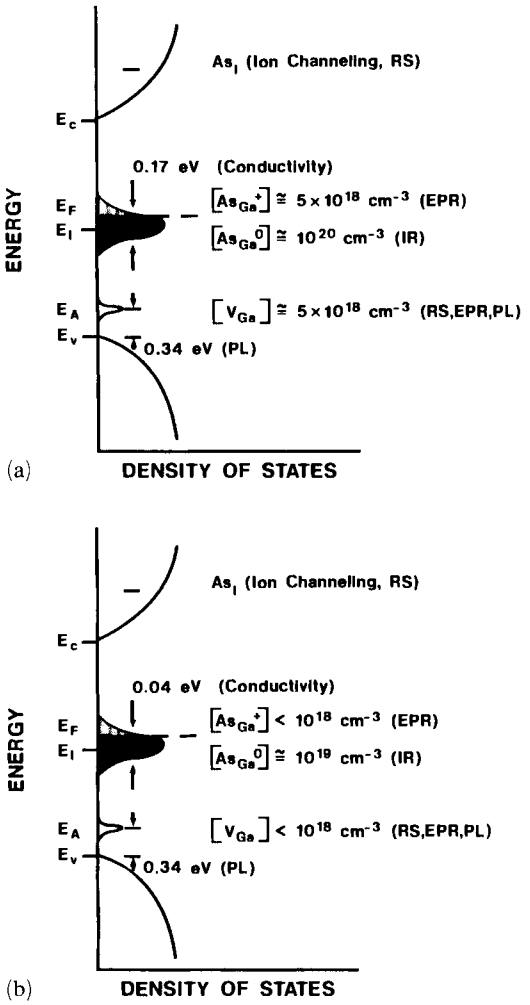

Fig. 1. (a) Energy band diagram based upon measured defect densites in as-grown LTMBE GaAs. (b) Energy band diagram for samples annealed for 10 min at 600 °C.

3. Models for LT MBE GaAs

The generally accepted model to account for the properties of as-grown LT GaAs is based upon the defects known to be present, see refs. 6 and 10. Figure 1(a) summarizes the basic features. The compensation mechanism is similar to that invoked for semi-insulating GaAs with the additional feature of hopping conductivity in the band of EL2-like levels near mid gap. Note that the density and role of As interstitials is not fully known, though they probably play a role in the expanded lattice constant and in the rate of defect diffusion.

Two models compete to explain the behavior of annealed material. The first is based on the defect model and is represented in Fig. 1(b). The defect densities indicated are, in part, near the limit of sensitivity for the relevant measurement techniques. This model does not explicitly include As precipitates in accounting for the transport properties of LT GaAs.

A second model has been offered to account for the properties of annealed samples containing precipitates [11]. Figure 2 illustrates the features of this model, usually referred to as the "buried Schottky barrier" model. According to this model, the As precipitates (principally hexagonal As, a semi-metal) form a Schottky barrier with respect to the matrix, depleting a portion of the surrounding space. If the doping density is high, or if the precipitates are sufficiently widely spread (as in Fig. 2(a)), the depletion zones do not overlap. This produces a material with a relatively high conductivity. For less heavily doped material, or for more closely spaced precipitates (as in Fig. 2(b)), the overlapping of precipitate depletion zones pinches off conducting paths. The lefthand figures show the electrostatic potential in either case. This model

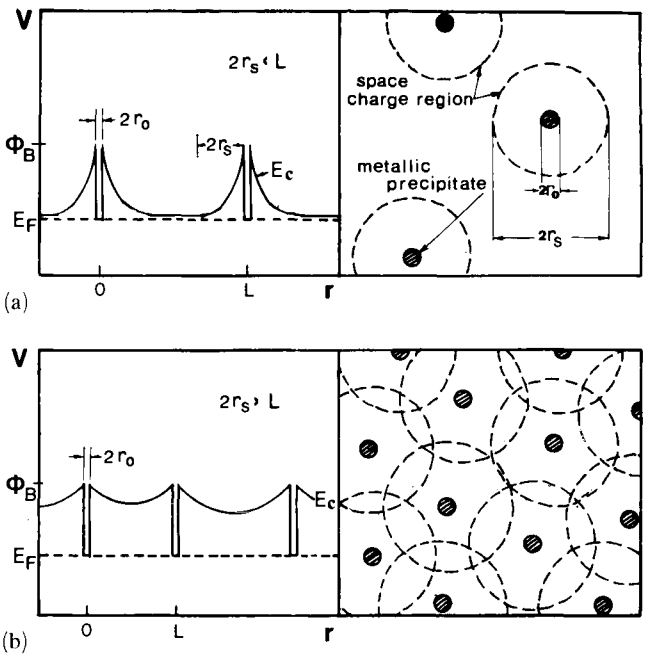

Fig. 2. Schematic diagram of the buried Schottky barrier model for LT GaAs that is subsequently annealed. N-type material is assumed.

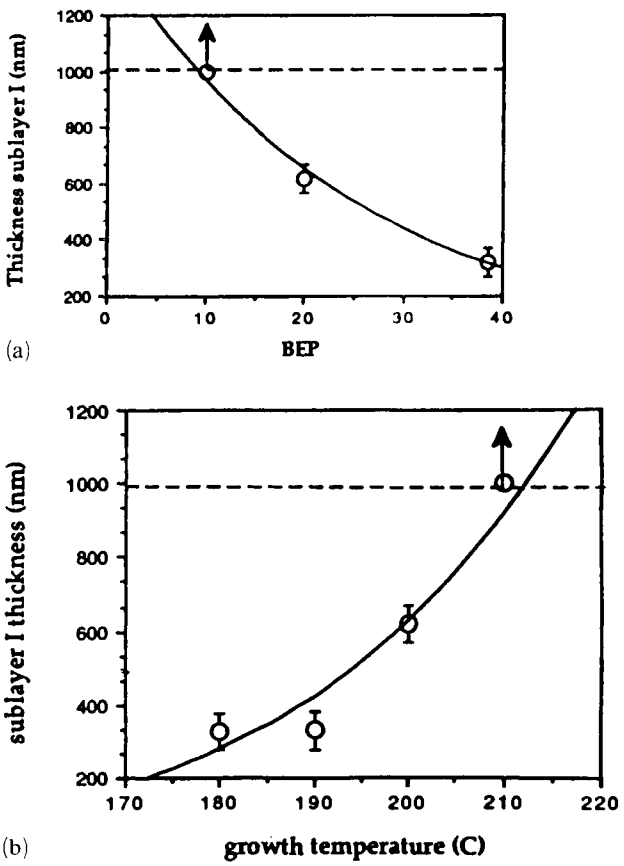

Fig. 3. Effects of varying growth conditions on the maximum thickness for crystalline LTMBE GaAs. In (a) the growth temperature is fixed at 200 °C while the As/Ga flux ratio (BEP) is varied. In (b) the BEP is fixed while the temperature is varied. The arrow at the highest growth temperature indicates that a thicker layer could have been grown had growth not been concluded.

assumes that the defect densities do not influence the transport properties in any significant way.

Each model has had some success in explaining certain experimental results. Neither fully accounts for the full span of electrical and optoelectronic properties of the material. A comprehensive model remains a key goal.

4. The effects of growth and annealing conditions

The preceding discussion has been based on what is referred to as "standard" LT GaAs. If any of the specified parameters are changed — growth temperature and rate, As/Ga ratio and anneal schedule — the properties of the material are altered significantly. Summaries of varying growth conditions are given in [12–14].

Figure 3 is taken from ref. 12. The maximum thicknesses for crystalline LT layer growth are shown. (The lattice expansion created by the LT conditions produces strain in the as-grown layers.) Figure 3(a) illustrates the importance of the As/Ga ratio during growth (BEP) at a growth temperature of 200 °C. For the conditions of "standard" LT growth, a crystalline layer of about 1 μm or less can be grown. Keeping the BEP fixed at 20, and varying the growth temperature, produces the data shown in Fig. 3(b). If appropriate growth conditions are not followed, for example for growth below 190 °C, extended line defects are produced [12]. Below 180 °C, polycrystalline material results. The remarks above apply specifically to 1 μm h^{-1} growth.

The growth parameters employed determine the non-stoichiometry of the LT GaAs (excess As). Annealing details — temperature and duration — then tailor the physical properties of LT MBE GaAs by relieving lattice strain, reducing point defects and coalescing the excess As into precipitates. Figure 4 shows the effects of varying one of these parameters for layers grown at 250 °C [8]. For a fixed duration anneal, increasing the anneal temperature causes the As precipitates to expand in diameter and move further apart.

The precipitates in annealed samples can be controlled to a large degree, both in terms of spatial distribution and density and size, by the incorporation of delta-doped layers, p-n junctions, heterointerfaces (*e.g.*

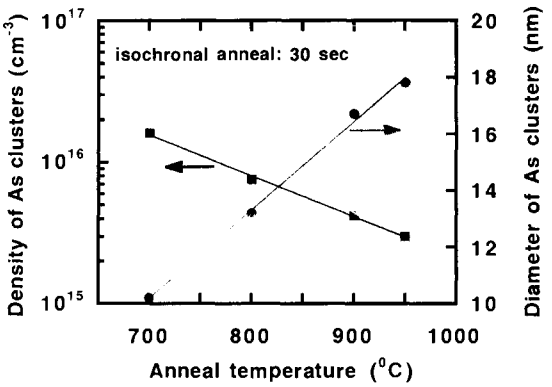

Fig. 4. Average diameter and density of As precipitates for various anneal temperatures with fixed growth temperature and anneal duration.

LT GaAs/AlGaAs) and so forth. This "precipitate engineering" enables the design of structures for various applications. An invited paper in this symposium, by Melloch [15], will address the subject.

5. Optical properties

It has been mentioned that as-grown LT GaAs (grown at 300 °C or lower) shows virtually no photoluminescence. A weak PL signal is recovered following an anneal at 800 °C. It is likely that these observations stem from the high density of fast traps found in as-grown LT samples and their reduced, but still substantial, concentrations in annealed samples.

Other notable properties of LT GaAs include the high electric field for dielectric breakdown and the very short recombination time for optically excited carriers (see Table 1). Despite the high concentration of defects, the mobility of the 200 °C LT GaAs, as-grown or annealed, is reasonably high — about 200 cm^2 V^{-1} s^{-1}. This combination of properties is quite unusual, leading to a variety of optoelectronic applications. An added attraction is the prospect of relatively easy monolithic integration into GaAs optoelectronic circuits.

Only one optoelectronic application will be mentioned here. Figure 5 presents the use of LT GaAs as a photoconductive switch [16]. The response time is typical of "standard" LT GaAs and varies depending upon the precise fabrication history. The response time and the responsivity are competitive with those obtained for other switch materials, such as radiation damaged InP and S-O-I. In an altered geometry, the same LT GaAs material has demonstrated switching of 1 kV in less than 5 ps. An invited paper in this symposium, by Whitaker [17], will more generally address optoelectronic applications.

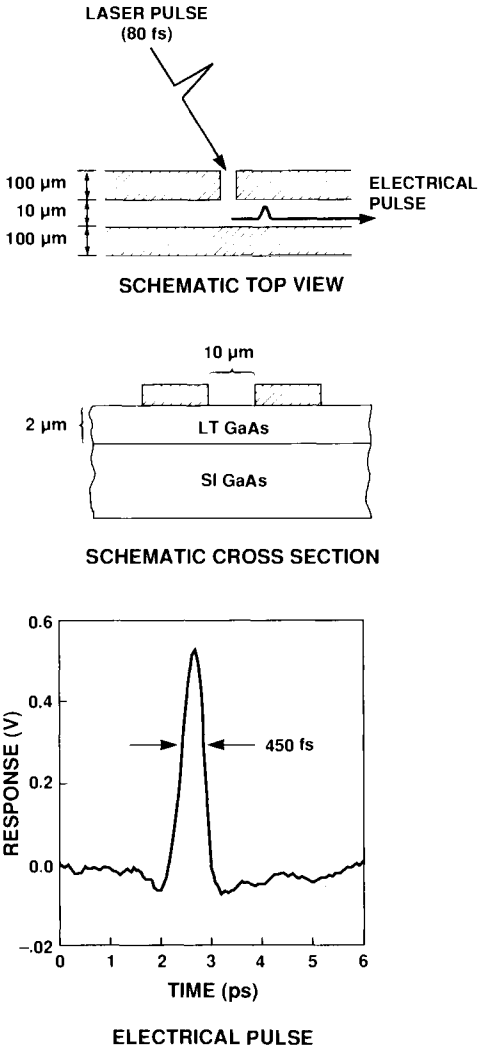

Fig. 5. A photoconductive switch exploiting the ultrafast photocarrier recombination time of LT GaAs. The laser pulse shorts the gap in the biased transmission line, creating an electrical pulse along the line. The 450 fs electrical pulse can be used for the testing of high speed electronic devices

6. Extensions of LT growth to other materials

What are the results of LT growth conditions for other compound semiconductors? The question is naturally prompted by basic scientific curiosity. More often than not the motivation is provided by potential applications. For example the need for advanced optoelectronic devices, matched to the technologically important (1.3 and 1.55) μm wavelengths, suggests a study of LT InGaAs lattice-matched to InP. Indeed this has been carried out, as indicated in Table 2 [18].

Space will not permit a full discussion of the varying results, many of them early results, obtained for these material systems. Several of the papers read at this meeting will address the subject.

TABLE 2. LT growth of other materials

Compound	ρ (Ω cm)	μ ($cm^2 V^{-1} s^{-1}$)	T_s (°C)	Anneal (°C)	Anneal time (min)	E_A (eV)
AlGaAs	10^{11}	0.1–10	250	600	20	0.14 (hole)
GaP/GaP	$>10^{10}$	10^6 (illum.)	190	700	60	—
GaP/GaP	10^8	—	190	—	—	—
InGaP/GaAs	$>10^9$ (illum.)	—	200	600	60	0.8
InGaP/GaAs	10^6 (illum.)	120	200	—	—	0.48
GaAs	10^7	—	230	600	10	0.8
InAlAs/InP	2×10^7	—	250	500	—	—
InAlAs/InP	10^8	—	100	500	60	—
InGaAlAs	10^5	—	400	—	—	—
InGaAs/InP	$\sim10^4$	10^3	100	500	No effect	0.032
InGaAs/InP	$\sim10^4$	10^4	600	500	No effect	0.032
InP	10^4	—	320	600	10	0.61
InP	10^{-2}	—	240	600	10	—

The case of LT InP is interesting. For InP grown via gas-source MBE at less than 350 °C, the samples are heavily n-type, saturating for lower growth temperatures at $n\cong4\times10$ cm^{-3} [19]. Optically detected magnetic resonance (ODMR) and PL have been used (Fig. 6), in conjunction with high pressure Hall measurements and free carrier absorption, to indicate clearly the reason for this behavior. The inset to Fig. 6(b) summarizes the results. First, the P-antisite defect is identified by ODMR. The suite of measurements indicate that the first excited state of P_{In} lies about 0.11 eV above the conduction band edge; the doubly ionized state lies 0.22 eV below E_C. This makes the Fermi level resonant with the conduction band for growth temperatures below 350 °C.

Another team [20] grew LT InP using GSMBE at 180 °C, then annealed the sample at 680 °C for 15 min. They report a dispersion of 3–7 nm diameter spots identified as α-white P, an insulator. No mention was made of the electrical properties of this sample.

A third experiment deals with bulk InP (nominally undoped LEC with $n\cong8\times10^{15}$–$9\times10^{15}cm^{-3}$)into which Cu was diffused then annealed [22]. Precipitates were observed with an average diameter of 0.09 μm and an average density of 1.4×10^{15} cm^{-3}. The precipitates were found to be Cu–In compounds, mostly hexagonal, all of which are known to be metallic. The high resistivity of the samples was explained by invoking the buried Schottky barrier model.

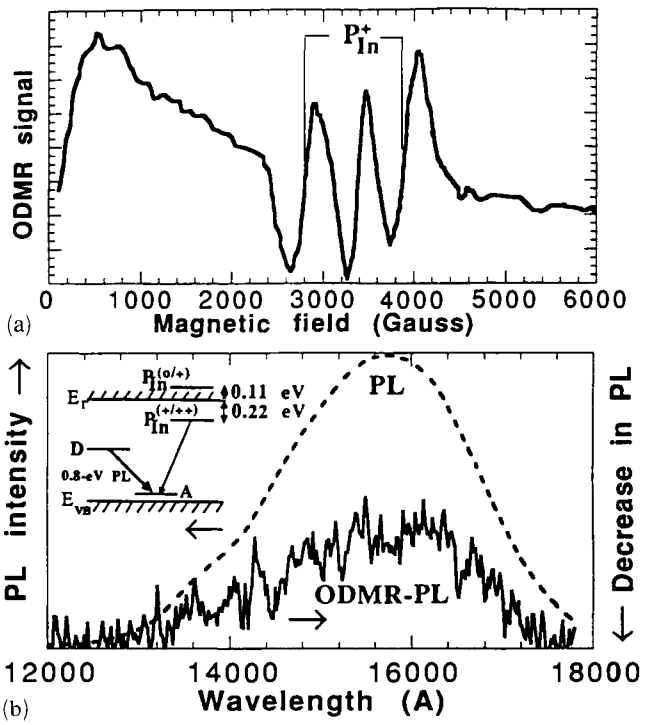

Fig. 6. (a) ODMR spectrum at 4 K for an InP sample grown at 310 °C and doped with Be. The spectrum displays the characteristic P_{In} doublet plus a singlet line, probably related to Be. (b) PL spectrum and spectral dependence of the anti-site ODMR signal, also at 4 K. The identity of the donor D and the acceptor A are not known, but probably related to Be.

7. Electronic applications of LT GaAs

Recall that the seminal paper [4] in the current study of LT GaAs dealt with an electronic application: the elimination of backgating for GaAs MESFETs. At least one company has incorporated an LT GaAs buffer layer in commercial millimeter wave integrated circuits. The electronic applications in general seek to exploit much the same set of attributes of LT GaAs as

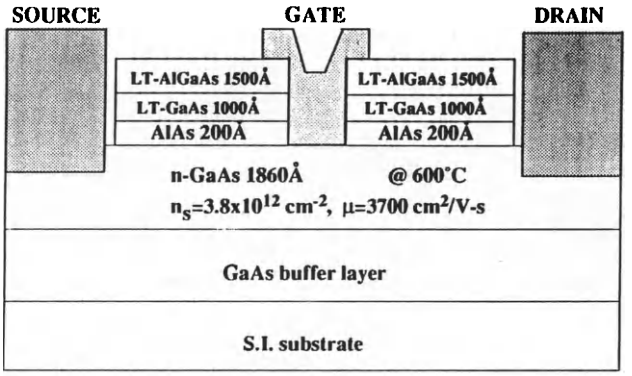

Fig. 7. Schematic cross-section diagram of a GaAs MESFET with LT passivation ($Al_{0.3}Ga_{0.7}As$/GaAs) and an overlapping gate structure, ref. 25.

mentioned in connection with optoelectronic uses, though in different ways. Here also the prospects of monolithic integration into GaAs circuits is attractive. A recent review has been made of device applications [22].

In addition to being used as a buffer layer — that is between the substrate and the active device layer — LT GaAs layers have been employed as a passivant on top of the active channel in FETs [23–25]. In either geometry, above or below the active layer, care must be taken to avoid contamination of the active layer by the outdiffusion of defects from the LT layer. For buffer layer purposes, this is often done by the incorporation of a normal GaAs buffer layer between the LT layer and the active layer. When incorporated on top of the active channel in a FET, the usual approach is to grow a thin (100 Å) layer of AlAs between the channel and the LT material.

The results reported in [23] and [24] both show an increase in the gate-to-drain breakdown voltage of about 60%. One consequence of this improvement is a record power density figure of 1.57 W mm^{-1} obtained from a GaAs MESFET with an LT GaAs passivation layer over the channel [24]. Figure 7 shows a recent design evolution for a device of this type [25]. An invited paper in this symposium, by Mishra [26], will give the details of this structure and discuss other recent electronic applications.

8. Concluding remarks

As a topic of basic materials science study, LT MBE GaAs and related materials are of fundamental interest. The unprecedented properties of these materials, particularly in the areas of point and extended defects, provide a new test-bed for experimentation and theory. Additional information has been gained on the propeties of "normal" compound semiconductors by these studies. The first clear identification of P_{In} in InP is an example. More has been learned of EL2, of central importance for producing semi-insulating bulk GaAs. There is reason to believe that more such contributions will follow. At the same time, many applications appear to be promising.

In concluding, I would like to list what I consider to be a number of key questions or demonstrations yet to be fully addressed. They are not listed in any particular order.

(a) A reliable, accurate, real-time method for the *in situ* measurement of growth temperature, useful down to at least 150 °C

(b) A (reasonably) comprehensive model explaining the electronic and optical properties of LT materials

(c) A full exploration of growth parameter space — growth temperature, growth rate and III/V ratio

(d) A full study of the interplay between growth and annealing parameters and the impact upon transport, etc.

(e) A determination as to whether or not precipitates (or alternatively what level of excess As) are required for a given set of electrical or optical requirements

(f) A study of the initial stages of nucleation of LT growth over a homo- or hetero- substrate

(g) R.f. data for electrical structures and devices

(h) A study of the stability and reliability of common LT structures

Acknowledgments

I wish to acknowledge the following for many fruitful conversations and permission to quote their results: A.R. Calawa, F.W. Smith, E.Weber, Z. Liliental-Weber, M. Melloch, D. Nolte, J.M. Woodall, D. Look, H. Grubin, U. Mishra, J. Ballingall, G. Mourou, J. Whitaker and C. Tu.

References

1 T. Murotani, T. Shimanoe and S. Mitsui, *J. Cryst. Growth, 45* (1978) 302.
2 R. Stall, C. Wood, P. Kirchner and L. Eastman, *Electron. Lett., 16* (1980) 171.
3 G. Metze and A. Calawa, *Appl. Phys. Lett., 42* (1983) 818.
4 F. Smith, A. Calawa, C.-L. Chen, M. Manfra and L. Mahoney, *Electron. Device Lett., 9* (1988) 77.
5 M. Kamińska and E. Weber, *Mater. Sci. Forum, 83–87* (1992) 1033.
6 D.C. Look, *Thin Solid Films, 231* (1993) 61.
7 M. Melloch, N. Otsuka, J. Woodall, A. Warren and J. Freeouf, *Appl. Phys. Lett., 57* (1990) 1531.
8 M. Melloch, D. Nolte, N. Otsuka, C. Chang and J. Woodall, *J. Vac. Sci. Technol. B, 11* (3) (1993) 795.

9 A. Warren, N. Katzennellenbogen, D. Grischkowsky, J. Woodall, M. Melloch and N. Otsuka, *Appl. Phys. Lett., 58* (1991) 1512.
10 D.C. Look, *J. Appl. Phys., 70* (1991) 3148.
11 A. Warren, J. Woodall, J. Freeouf, D. Grischowsky, D. McInturff, M. Melloch and N. Otsuka, *Appl. Phys. Lett., 57* (1990) 1331.
12 Z. Liliental-Weber, A. Claverie, P. Werner, W. Schaff and E. Weber, *Mater. Sci. Forum, 83–87* (1992) 1045.
13 K. Mahalingam, N. Otsuka, M. Melloch, J. Woodall and A. Warren, *J. Vac. Sci. Technol. B,* 9 (1991) 2328.
14 D. Eaglesham, L. Pfeiffer, K. West and D. Dykaar, *Appl. Phys. Lett., 58* (1991) 65.
15 M. Melloch, *Mater. Sci. Eng. B, 22* (1993) 31.
16 S. Gupta, M. Frankel, J. Valmanis, J. Whitaker, G. Mourou, F. Smith and A. Calawa, *Appl. Phys. Lett., 59* (1991) 3276.
17 J. Whitaker, *Mater Sci. Eng. B, 22* (1993) 61.
18 G. Maracas, *J. Electron. Mater.*, in press.
19 P. Dreszer, W. Chen, K. Seendripu, J. Wolk, W. Walukiewicz, B. Liang, C. Tu and E. Weber, *Phys. Rev. B, 47* (1993) 4111.
20 P. Claverie, J. Crestou and J. Garcia, *Appl. Phys. Lett., 62* (1993) 1638.
21 R. Leon, P. Werner, C. Eder and E. Weber, *Appl. Phys. Lett., 61* (1992) 2545.
22 F.W. Smith, *Proc. Mater. Res. Soc., 241* (1992) 3.
23 L.-W. Yin, J. Lee, R. Kolbas, R. Trew and U. Mishra, *IEEE Electron. Device Lett., 11* (1990) 561.
24 C.-L. Chen, L. Mahoney, M. Manfra, F. Smith, D. Temme and A. Calawa, *IEEE Electron. Device Lett., 13* (1992) 335.
25 L.-W. Yin, N. Nguyen, Y. Hwang, J. Ibbetson, R. Kolbas, A. Gossard and U. Mishra, *J. Electron. Mater.*, in press.
26 U. Mishra, *Mater. Sci. Eng. B, 22* (1993) 72.

Point defects in III–V materials grown by molecular beam epitaxy at low temperature

P. Hautojärvi, J. Mäkinen, S. Palko and K. Saarinen
Laboratory of Physics, Helsinki University of Technology, SF-02150 Espoo (Finland)
C. Corbel and L. Liszkay
Centre d'Etudes Nucléaires de Saclay, INSTN, F-91191 Gif-sur-Yvette (France)

Abstract

The present understanding of the point defects in GaAs and InP grown by molecular beam epitaxy at low temperature (LT) is briefly reviewed. New results on vacancies and ion-type acceptors obtained by positron annihilation are given. Depending on the growth temperature, Ga vacancies or small vacancy clusters are seen in LT GaAs in the concentration range 10^{18} cm^{-3}. No signal from Ga antisites is found. The LT InP layers contain vacancies, identified as In vacancies, in the concentration range 10^{18} cm^{-3}. Ion-type acceptors, probably In antisites, are also seen in concentrations of 10^{17} cm^{-3}. The annealed layer contains small vacancy clusters.

1. Introduction

Low temperature (LT) growth of thin III–V layers has recently attracted much attention as a potential technique to obtain semi-insulating layers [1, 2]. Such layers are strongly needed for various micro- and optoelectronic device and integrated circuit applications. The layers contain point defects in extremely high concentrations. To identify and understand their role in the electrical and optical properties of the LT layers is a new challenge for various defect spectroscopic techniques.

In LT GaAs and InP the main defects seem to be the group V antisite atoms As_{Ga} and P_{In}, which have been identified as native donors [3, 4]. However, there is little information on native acceptors. Vacancies and antisites of group III atoms are generally believed to be acceptors.

Positron annihilation is a unique method to identify vacancies [5–7]. In addition, as positive particles, positrons are also sensitive to ion-type acceptors. Here we present new information on the native acceptor defects in LT GaAs and InP by using positron annihilation.

In this paper the main properties of the point defects in LT GaAs and InP are briefly summarized in Sections 2 and 3. The positron beam spectroscopy of thin layers is described in Section 4. The results on LT GaAs and InP in Sections 5 and 6 show that the layers contain high concentrations of native vacancies (V) tentatively identified as V_{Ga} and V_{In}, respectively. LT InP layers also contain ion-type acceptors, most probably In antisites. The paper is summarized in Section 7.

2. Point defects in LT GaAs

The defect properties of LT GaAs depend strongly on the growth temperature T_g, which varies from 200 to 300 °C. Analysis by particle-induced X-ray emission (PIXE) shows an As excess in the layer depending on the growth condition. The As excess is up to 1.5 at.% at $T_g = 190$ °C and decreases monotonously as T_g increases. Layers grown at 300 °C or higher temperatures are stoichiometric within the sensitivity limit of 0.1 at.% of the PIXE method [2, 8]. Studies by Rutherford backscattering and channelling indicate that As interstitial complexes rather than isolated As interstitials are present [8].

The only well-identified defect, however, is the arsenic antisite As_{Ga} detected by the electron paramagnetic resonance (EPR) technique in its positive charge state As_{Ga}^{+} [3, 9]. Its concentration is $3–5 \times 10^{18}$ cm^{-3} at $T_g = 200$ °C and decreases by an order of magnitude when T_g is increased to 300 °C [10]. The neutral state As_{Ga}^{0} is observed by optical absorption in the near-IR region [11]. Its concentration is a maximum of 2×10^{20} cm^{-3} at $T_g = 190$ °C and decreases to 2×10^{19} cm^{-3} at $T_g = 270$ °C [2]. An open and controversial question is the photoquenching

0921-5107/93/$6.00
© 1993 - Elsevier Sequoia. All rights reserved

property of the As_{Ga} defect in the LT layers, which seems to be different from that of the As_{Ga} defect in semi-insulating bulk GaAs. Kaminska and Weber [2] have offered an interesting point of view. The strain in LT GaAs layers changes the local hyperfine field. The different properties of these two defects can be ascribed to differences in the local fields seen by the two defects rather than to differences in their nature. More generally, this question addresses the relation of the As_{Ga} antisite to the EL2 centre in GaAs.

Evidently As_{Ga} is the main native donor in LT GaAs. It is activated at concentrations well above 10^{18} cm^{-3}. To compensate the As_{Ga}^{+} centres, native acceptors are needed. Evidence of an intrinsic acceptor level at $E_v + 0.3$ eV has been given [12], which could be due to Ga vacancies. Yu *et al.* [13] have suggested that a complex seen by photolumiscence could be a V_{Ga}–As_i pair. Measurements of the localized IR vibration modes of Si atoms suggest that Si–V_{Ga} pairs are formed in Si-doped layers [14]. We show later in this paper that positron annihilation gives direct evidence of Ga vacancies at concentrations sufficiently high to account for the compensation.

The conductivity of the as-grown layer is due to hopping within a defect band of As_{Ga} antisites [15, 16]. After annealing of the layers at 600 °C, which always occurs in device applications, the normal conduction mechanism through thermally excited carriers appears. The layers have become semi-insulating but the carrier lifetime and mobility are still low.

The major annealing effect on the microstructure of the layers is the formation of As precipitates of size 6 nm to accommodate the As excess [17]. There is also a reduction in the concentration of As_{Ga}^{0} to below the detection limit of 10^{18} cm^{-3}. In addition, the As_{Ga}^{+} concentration drops to the level of 10^{17} cm^{-3} [9].

Two models have been suggested to explain the semi-insulating conductivity after annealing at 600 °C.

(1) The point defect concentration is still high enough to explain the low carrier lifetime and mobility. However, the question of the concentration of As_{Ga}^{0} and of other defects such as V_{Ga} remains open.

(2) The high resistivity is due to metallic As precipitates which act as buried Schottky junctions. The space charge regions generated by the Schottky barriers overlap in the matrix, which is thus completely depleted of free carriers [18].

3. Point defects in LT InP

The success in the case of LT GaAs layers has stimulated efforts to grow LT InP and understand its electrical and structural properties. The growth temperature ranges from 130 °C upwards. The interesting region is between 170 and 200 °C [19]. The amount of P excess is about 1 at.% at $T_g = 170$ °C and decreases with increasing growth temperature. The layers exhibit highly n-type conductivity except when they are passivated by hydrogen in the as-grown state [19, 20]. Beryllium doping does not compensate layers grown at $T_g < 300$ °C [4, 19, 20]. Layers annealed at 600 °C stay conductive, although the P excess precipitates into small particles of size 3–7 nm [21].

The electrical properties of LT InP layers indicate that the dominant intrinsic defect is present in concentrations of 10^{19} cm^{-3} [20]. EPR measurements are not possible owing to the high conductivity of the layers. Recently Dreszer *et al.* [4] have found two deep donor levels at 0.11 eV above 0.23 eV below the conduction band. Optically detected magnetic resonance (ODMR) combined with photoluminescence reveals that the two levels are the first and second ionization levels of the P antisite double-donor defect. The upper level being resonant with the conduction band gives rise to the high free-electron via auto-ionization. To explain the photoluminescence spectrum, the authors need to call for an unidentified donor level at 0.8 eV above the valence band.

We will see in Section 6 that in addition to the group V antisite atoms which seem to be the prevalent defects in LT InP, positron annihilation experiments indicate the presence of vacancies associated with the In sublattice in concentrations of 10^{18}–10^{19} cm^{-3}.

4. Positron annihilation technique

4.1. Positron dynamics in semiconductors

Energetic positrons in solids thermalize within a few picoseconds. In semiconductors the mean lifetime of free positrons is typically 250 ps. The motion and trapping of thermal positrons are in many respects analogous to those of free carriers apart from the "heavy" positron effective mass $m^*_+ \approx 1.5 m_e$. The positron diffusion coefficient at 300 K is around 2 cm^2 s^{-1} [22, 23]. The diffusion is limited mainly by acoustic phonons, leading to the $T^{-1/2}$ temperature dependence. Positrons feel electric fields and have a mobility of about 100 cm^2 V^{-1} s^{-1} t 300 K with a $T^{-3/2}$ dependence.

The Bloch state positron wavefunction is squeezed by the positron–ion repulsion into the interstitial regions between atoms. Thus an open-volume defect such as a vacant lattice cell is an attractive centre where positrons get trapped. Positron trapping is analogous to carrier capture [24]. The trapping rate κ is proportional to the defect concentration, $\kappa = \mu C_d$. The charge state of a vacancy has a strong effect on the trapping coefficient μ. For a neutral vacancy $\mu \approx 10^{14}$–10^{15} s^{-1}

independently of temperature. For a negative vacancy $\mu \approx 10^{15}$–10^{16} s^{-1} and it increases by an order of magnitude at low temperatures. Positive vacancies do not trap positive positrons. Minimum vacancy concentrations required to trap positrons during their lifetime are about 10^{15}–10^{16} cm^{-3}.

Owing to their different electronic environment, the annihilation characteristics of trapped positrons are different from those of free positrons in the bulk. The reduced electron density at a vacancy increases the positron lifetime by 10%–20%. Because of the smaller overlap of the trapped positrons with core electrons, the momentum distribution of the annihilating pairs becomes narrower. The change in the charge state of a defect causes measurable changes in the annihilation characteristics, thus giving the possibility to determine the ionization levels of the defect in the band gap [25].

Owing to coulombic interaction, a positron may also get trapped at weakly bound Rydberg states around negative ions. Thus information can also be obtained on ion-type acceptors [26].

4.2. Positron beam analysis

Positrons from a radioactive source first hit a separate moderator crystal which has a negative work function for positrons. Thermalized positrons close to the moderator surface are spontaneously emitted into a vacuum. They form a beam which is accelerated and guided to the sample. In an experiment monoenergetic positrons are implanted at various depths in the sample by varying the beam energy E typically from 0 to 30 keV. In GaAs this energy range scans depths from 0 to 1.5 μm. The positron-stopping profile is, however, rather wide [27], limiting the depth resolution of the technique. For reviews on positron beams see refs. 5 to 7.

Since the start signal from the positron emission is not available in a beam, the positron lifetime cannot be measured, but the 511 keV line of the annihilation radiation is recorded. This line shows considerable Doppler broadening due to the motion of annihilating pairs. It is customary to use a line shape parameter S (or W) defined as the ratio of the counts in the central (or wing) region of the annihilation line to the total number of counts in the peak. Owing to their high momentum, mainly core electrons contribute to the wing parameter W, whereas annihilations with the valence electrons fall predominantly in the energy region of the central parameter S. Both line shape parameters have characteristic values for each material, depending on the electron momentum distribution. When positrons are trapped at vacancy-type defects, the annihilations with core electrons are reduced with respect to the perfect lattice, increasing the S parameter and decreasing the W parameter. Hence the line shape parameters can be used to characterize vacancy defects in solids.

The measured line shape parameter as a function of beam energy, $S(E)$ (or $W(E)$), is a superposition of the characteristic values S_i for various annihilation states i. As an example, let us assume a defect layer in the near-surface region of a sample. There are annihilations at the surface (surf), in the defects (def) and in the bulk (bulk) and we have

$$S(E) = F_{\mathrm{surf}}(E) S_{\mathrm{surf}} + F_{\mathrm{def}}(E) S_{\mathrm{def}} + F_{\mathrm{bulk}}(E) S_{\mathrm{bulk}} \quad (1)$$

Here $F_i(E)$ denotes the fraction of annihilations in state i. To calculate the fractions $F_i(E)$, the positron diffusion equation must be solved. Analysis of the experimental results is carried out by varying the positron-trapping profile $\kappa(x) = \mu C_d(x)$ in the diffusion equation until a satisfactory fit between the experimental and calculated $S(E)$ is reached.

The line shape parameters S and W depend on the fractions of positrons in various states. To overcome this difficulty, a new defect-specific parameter R is defined as [28, 29]

$$R = \frac{|S - S_{\mathrm{bulk}}|}{|W - W_{\mathrm{bulk}}|} \quad (2)$$

If there are only two annihilation states, *e.g.* the bulk and a defect, R is independent of the fractions $F_i(E)$ and its value can be used to identify the defect.

5. Results on LT MBE GaAs

5.1. Samples

The GaAs layers were grown in a Varian 360 system under normal, As-stabilized conditions at a growth rate of 0.8 μm h^{-1} on semi-insulating GaAs substrates. A layer 4 μm thick was grown at 200 °C. Two other layers of thickness 2.5 μm were grown at 225 and 300 °C and doped with Be to around 8×10^{19} cm^{-3}. One sample was furnace annealed for 30 min in vacuum under face-to-face protection at successive temperatures of 300, 400 and 500 °C.

5.2. Results

Figure 1 shows the experimental Doppler-broadening parameter S as a function of the positron beam energy E in three layers grown at 200, 225 and 300 °C. As reference sample we use a piece of semi-insulating LEC-grown bulk GaAs wafer which is known to contain no positron traps. The change in $S(E)$ for $E < 5$ keV represents the transition from surface annihilations to annihilations in the layer. The flat part above

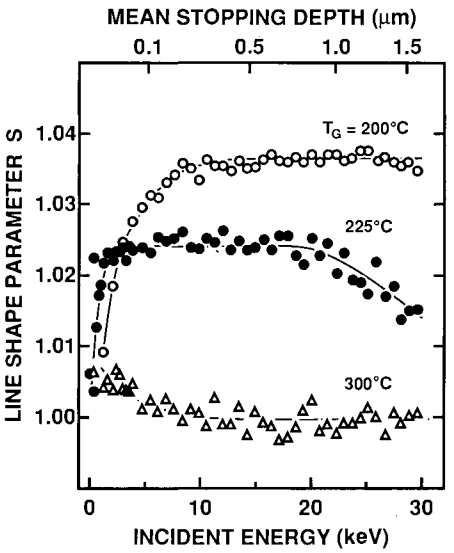

Fig. 1. Line shape parameter S as a function of positron beam energy in LT GaAs layers grown at various temperatures T_g. The $T_g = 300$ °C curve coincides with that of the semi-insulating GaAs crystal (not shown) used as reference.

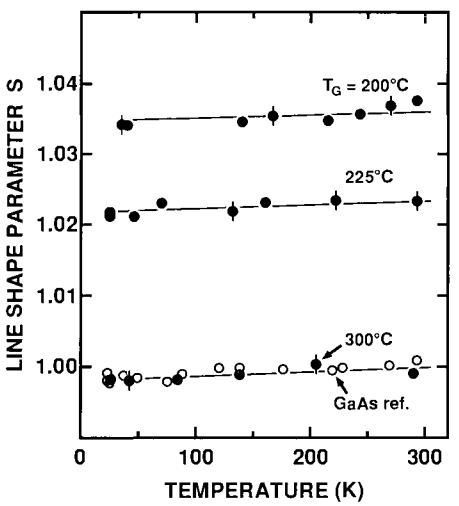

Fig. 2. Temperature dependence of S parameter measured at 15 keV positron energy in LT GaAs grown at various temperatures T_g.

5 keV is characteristic of layer annihilations. To facilitate comparisons, the level of the S parameter in the reference sample has been normalized to 1.00.

We can see a perfect overlap at the S parameter levels in the $T_g = 300$ °C layer and the reference sample. This means that no vacancies in the layer are seen. Also, the transition from the surface value to the layer value extends up to 10 keV, indicating free-positron diffusion.

The $T_g = 225$ °C has an S value of 1.023. This is well above the reference bulk level, which indicates the presence of vacancy-type defects in the layer. The very rapid increase from the surface S value to the plateau means that the positron diffusion length $L^+ \approx 100$ Å is very short compared with the free-positron diffusion length $L_+ \approx 1600$ Å [23]. This indicates a high concentration (about 10^{19} cm^{-3}) of defects trapping positrons, which means that all positrons between 3 and 20 keV annihilate when trapped. The S value of 1.023 is characteristic of the defects in the layer. This value is close to those found earlier for As and Ga monovacancies. Thus we can conclude that the dominant traps are monovacancies in this layer. The decrease in S above 20 keV is due to the increasing fraction of positrons, which at higher energies penetrate into the substrate with a negligible defect concentration compared with the overlayer.

The S value in the $T_g = 200$ °C layer is 1.040. This is even higher than the value for monovacancies. The increase in S between 0 and 5 keV gives an effective positron diffusion length $L_+ = 170$ Å. The corresponding positron trap concentration is between 10^{18} and 10^{19} cm^{-3}. Above 5 keV implantation energy the positron trapping is saturated and the $S = 1.037$ value is characteristic of the defects in this layer. The defects are divacancies or small vacancy clusters [28, 29]. We performed furnace annealing of this layer up to 500 °C. No changes in the $S(E)$ curves except at the surface ($E < 2$ keV) could be seen. This shows that the vacancy clusters are stable and difficult to anneal out. The high stability of vacancy clusters has also been observed earlier in ion-irradiated GaAs [28]. It is important to note that the total thickness of this layer is 4 μm, whereas positrons probe only the uppermost 1.5 μm region. Thus it is still open whether the region within the critical thickness (about 2 μm) from the substrate also contains vacancy clusters as the dominant defects.

Figure 2 shows the temperature dependence of the S parameters in the layers measured at 10 keV positron energy. The message is clear: no temperature dependence. This means that the vacancy signal is not reduced at low temperature by positron trapping at Rydberg states around negative ions. This is in contrast to what has been observed in electron-irradiated GaAs, where in addition to Ga vacancies, negative-ion-type acceptors identified as Ga antisites have also been observed [26]. We can conclude that the concentration of ion-type acceptors must be at least an order of magnitude less than that of vacancies.

To determine whether the vacancies in the $T_g = 225$ °C layer are in the Ga or As sublattice, we refer to their charge state. In semi-insulating GaAs, Ga vacancies are acceptors with a 2− or 3− charge, whereas As vacancies are positively charged [25]. Since positrons do not get trapped at positive defects, the traps can only be Ga vacancies. Such an identification

leads us to conclude that the vacancies act as native acceptors.

It is interesting that in the layer grown at 300 °C no Ga vacancies are seen. This means that the concentration of Ga vacancies is less than 10^{16} cm^{-3}. Von Bardeleben *et al.* have measured the concentration of As_{Ga}^{+} as a function of growth temperature. Their results show the same trend as for our V_{Ga}: when T_g is 300 °C or higher, the As_{Ga}^{+} concentration has decreased by more than one order of magnitude from the layers grown at 200 °C [10].

In conclusion, positron annihilation shows the existence of vacancies and vacancy clusters in concentrations of 10^{18}–10^{19} cm^{-3} in the Be-doped layer grown at 225 °C and in the undoped layer grown at 200 °C respectively. No signal from Ga antisites is observed. The vacancies are associated with V_{Ga} and so they can be the acceptors compensating the native As_{Ga} donors observed earlier by EPR. In the Be-doped layer grown at 300 °C the V_{Ga} concentration is below 10^{16} cm^{-3}.

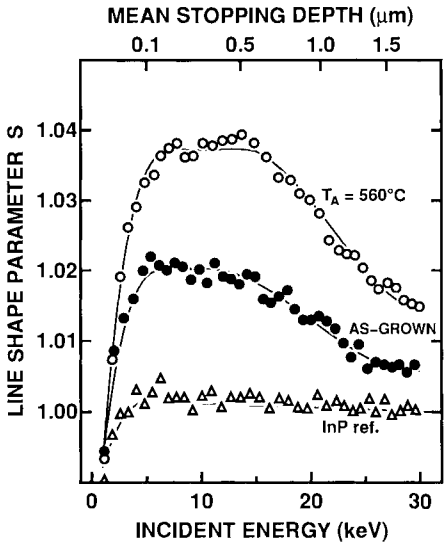

Fig. 3. Line shape parameter S as a function of positron beam energy in LT InP layers in as-grown state and after annealing at 560 °C. As reference sample an InP (Zn:2×10^{18} cm^{-3}) crystal has been used.

6. Results on LT MBE InP

6.1. Samples

Several InP layers were grown by gas source molecular beam epitaxy at Thomson, Corbeville. For details of the growth system see ref. 19. The growth temperature was 180 °C and the thickness of the layers 1.5 μm. The PH_3 flow rate was 8 or 22 sccm (standard cm^3 min^{-1}). Most of the layers were doped with Be to 5×10^{17} cm^{-3}. All the layers were n type with a carrier concentration of 5×10^{16} cm^{-3} even after annealing at 560 °C for 30 min. As a "defect-free" reference we used a Czochralski-grown InP (Zn: 2×10^{18} cm^{-3}) bulk wafer which, according to positron lifetime measurements, does not exhibit any positron trapping by defects.

6.2. Results

Figure 3 shows the experimental Doppler-broadening parameter S as a function of the positron beam energy E for three different samples. The InP(Zn) bulk crystal reference sample shows, after surface annihilations at 0–7 keV, a flat curve which corresponds to annihilations of free positrons in the bulk. This level has been normalized to 1.0. Both the as-grown and annealed layers show between 0 and 7 keV a transition from the surface annihilations to annihilations in the layer. The flat part from 7 to 15 keV is characteristic of layer annihilations. Above 15 keV an increasing fraction of positrons start to penetrate into the substrate, causing the S parameter to decrease towards the bulk value.

The transition from surface annihilations to layer annihilations can be used to estimate the effective positron diffusion length L_{eff}. For both LT layers we get $L_{eff} \approx 200$ Å, which is much lower than the diffusion length of free positrons, $L \approx 2000$ Å. The decrease in the diffusion length is due to trapping by defects and the trapping rate κ can be estimated [28] to be $\kappa = 100$–300 ns^{-1} in both layers. This is about two orders of magnitude higher than the free-positron annihilation rate, meaning that all positrons annihilate at defects. The value of S at 10–15 keV is thus characteristic of the defects (S_{def}) trapping positrons in the layer. For the as-grown layer $S_{def}/S_{bulk} = 1.023$, which is typical for monovacancies [30]. For the annealed layer the ratio $S_{def}/S_{bulk} = 1.037$ is too high for monovacancies and should correspond to divacancies or small vacancy clusters. The R parameter values of 1.0(1) and 1.4(1) respectively in the two layers also support this conclusion.

From preliminary electron irradiation experiments [30] we know that In vacancies produce parameters S_{vac}/S_{bulk} and W_{vac}/W_{bulk} which are about the same as found in the present as-grown layer, whereas P vacancies induce much smaller changes in S and W. Thus we associate the vacancies with the In sublattice.

According to calculations [31], the In vacancy is negative (2− or 3−) when the Fermi level is above the midgap position. For a negative vacancy the trapping coefficient μ is about 10^{15}–10^{16} s^{-1}. Using this value, we get the vacancy concentration $[V_{In}] \approx 10^{18}$–10^{19} cm^{-3}.

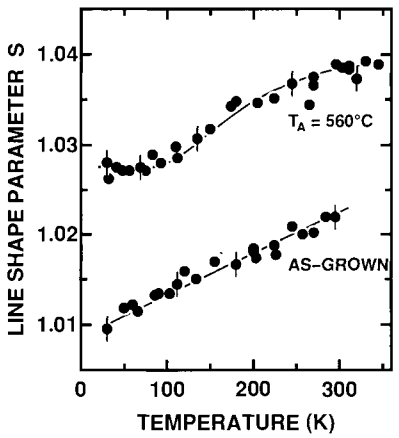

Fig. 4. Temperature dependence of S parameter measured at 12 keV positron energy in LT InP layer in as-grown state and after annealing at 560 °C.

Figure 4 shows the S parameter at 10 keV as a function of the measurement temperature. One can see a very strong decrease with decreasing T. This is in contrast with the expected behaviour of μ for a negative vacancy and means that at low temperature there are other ion-type negative centres which trap positrons at Rydberg states. The Rydberg states are shallow traps for positrons and the annihilation parameters are the same as in the bulk. When an increasing fraction of positrons annihilate at Rydberg states around negative ions, the S value decreases towards the bulk level. A rough analysis of the curves indicates that $C_{\text{ions}} \approx (0.1\text{–}0.5)C_{\text{vac}}$, *i.e.* 10^{17}–5×10^{18} cm^{-3}.

It would be natural to identify these ions as Be atoms which are the intentional acceptor impurities. However, Be atoms have no effect on the carrier concentration—$n = 5 \times 10^{16}$ cm^{-3} with or without Be doping—most likely owing to their association with oxygen impurities [19]. This means that they are unable to trap positrons. Only residual impurities or intrinsic defects can be considered. Residual impurities at a level of 10^{17}–10^{18} cm^{-3} are out of the question [19]. On the other hand, irradiation produces two types of positron traps, *i.e.* vacancies and negative ions [30]. This indicates that some intrinsic interstitial or antisite defects are acceptor type. It is likely that, as in the case of GaAs [26], the acceptors should have a double negative charge to trap positrons at Rydberg states. The most likely candidates are In_p antisites which, according to calculations [31], can be doubly negative when the Fermi level is above $E_c - 0.5$ eV.

It has been found previously from Hall measurements in n-type bulk InP that after heavy electron irradiation the Fermi level is pinned at an acceptor level located at $E_c - 0.3$ eV [32]. It is interesting that such a level is also observed in LT InP [20]. Earlier [30] and present positron results suggest that it may originate from a vacancy or an ion-type defect.

The effects of Be doping and variations in PH_3 flow during growth were also studied. The Be doping had no effect on the vacancies. The curves of as-grown layers with and without Be are superimposable. This is well understood if Be atoms are associated with oxygen [19]. An increase in the PH_3 flow from 8 to 22 sccm increased the vacancy signal slightly in the as-grown layers. It seems natural to have more In vacancies at higher P excess.

7. Summary

The As antisite is the well-identified native defect in LT GaAs observed earlier by EPR. As a midgap donor it plays the dominant role in the compensation. Positron annihilation gives information on acceptor-type defects, about which very little is known. Positrons detect vacancies in concentrations of 10^{18}–10^{19} cm^{-3} in Be-doped layers grown at 225 °C. The vacancy concentration drops below 10^{16} cm^{-3} when the growth temperature is 300 °C. The vacancies are identified as V_{Ga} and so they can be the native acceptors compensating the native As_{Ga} donors. On the other hand, multiple vacancies, divacancies or small clusters are observed in an undoped layer grown at 200 °C. No signal from Ga antisites is observed.

The P_{In} antisite has recently been identified in LT InP by ODMR. It is believed to be responsible via auto-ionization for the high free-electron concentration always found in as-grown layers. Positron annihilation results show that as-grown InP layers contain high concentrations (10^{18}–10^{19} cm^{-3}) of vacancy defects identified as negative In vacancies. In addition, ion-type acceptors, probably In antisites, in concentrations of 10^{17}–10^{18} cm^{-3} are observed. The annealed layer contains small vacancy clusters.

Acknowledgments

We are grateful to J. H. von Bardeleben, J. Garcia, K. Evans and C. Stutz for providing us with samples.

References

1 G. L. Witt, R. Calawa, U. Mishra and E. Weber (eds.), *MRS Symp. Proc., 241*, Pittsburgh, 1992.
2 M. Kaminska and E. R. Weber, *Mater. Sci. Forum, 83–87* (1991) 1033.
3 M. Kamiska, Z. Liliental-Weber, E. R. Weber, T. George, J. B. Kortright, F. W. Smith, B. Y. Tsaur and A. R. Calawa, *Appl. Phys. Lett., 54* (1989) 1881.

4 P. Dreszer, W. M. Chen, K. Seendripu, J. A. Wolk, W. Walukievicz, B. W. Liang, C. W. Tu and E. R. Weber, *Phys. Rev. B, 47* (1993) 4111.
5 P. Hautojärvi (ed.), *Topics in Current Physics*, Vol. 12, *Positrons in Solids*, Springer, Heidelberg, 1979.
6 L. Dorikens-Vanpraet, M. Dorikens and D. Segers (eds.), *Positron Annihilation*, World Scientific, Singapore, 1989.
7 P. J. Schultz and K. G. Lynn, *Rev. Mod. Phys., 60* (1988) 701.
C. Corbel, *Scanning Microsc., 12* (1987) 545.
8 K. M. Yu and Z. Liliental-Weber, *Appl. Phys. Lett., 59* (1991) 3267.
9 H. J. von Bardeleben, M. O. Manaresh, D. C. Look, K. R. Evans and C. E. Stutz, *Phys. Rev. B, 45* (1992) 3372.
10 H. J. von Bardeleben, Y. Q. Jia, J. P. Hirzt, J. C. Garcia, M. O. Manaresh, C. E. Stutz and K. R. Evans, in ref. 1, p. 69.
11 M. O. Manaresh, D. C. Look, K. R. Evans and C. E. Stutz, *Phys. Rev. B, 41* (1990) 10272.
12 M. Kaminska, E. R. Weber, Z. Liliental-Weber, R. Leon and Z. U. Rek, *J. Vac. Sci. Technol. B, 7* (1989) 710.
13 P. W. Yu, D. C. Reynolds and C. E. Stutz, *Appl. Phys. Lett., 61* (1992) 1432.
14 S. A. McQuaid, R. C. Newman, M. Missous and S. O'Hagen, *Appl. Phys. Lett., 61* (1992) 3008.
15 D. C. Look, Z.-Q. Fang and J. R. Sizelove, *Phys. Rev. B, 47* (1993) 1441.
16 D. C. Look, D. C. Walters, M. O. Manaresh, J. R. Sizelove, C. E. Stutz and K. R. Evans, *Phys. Rev. B, 42* (1990) 3578.
17 M. R. Melloch, N. Otsuka, J. M. Woodall, A. C. Warren and J. L. Freeouf, *Appl. Phys. Lett., 57* (1990) 1531.
18 A. C. Warren, J. M. Woodall, J. L. Freeout, D. Grischkowsky, M. R. Melloch and N. Otsuka, *Appl. Phys. Lett., 57* (1990) 1331.
19 J. Ch. Garcia, J. P. Hirtz, P. Maurel, H. J. von Bardeleben and J. C. Bourgoin, in ref. 1, p. 277.
20 B. W. Liang, Y. He and C. W. Tu, in ref. 1, p. 283.
B. W. Liang *et al., Appl. Phys. Lett., 60* (1992) 2104.
21 A. Claverie, J. Crestou and J. C. Garcia, *Appl. Phys. Lett., 62* (1993) 1638.
22 J. Mäkinen, C. Corbel, P. Hautojärvi, A. Vehanen and D. Mathiot, *Phys. Rev., 42* (1990) 1750.
23 E. Soininen, J. Mäkinen, D. Beyer and P. Hautojärvi, *Phys. Rev. B, 46* (1992) 13104.
24 M. J. Puska, C. Corbel and R. M. Nieminen, *Phys. Rev. B, 41* (1990) 9980.
25 K. Saarinen, P. Hautojärvi, P. Lanki and C. Corbel, *Phys. Rev. B, 44* (1991) 10585.
C. Corbel, M. Stucky, P. Hautojärvi, K. Saarinen and P. Moser, *Phys. Rev. B, 38* (1988) 8192.
26 C. Corbel, F. Pierre, K. Saarinen, P. Hautojärvi and P. Moser, *Phys. Rev. B, 45* (1991) 3386.
27 S. Valkealahti and R. M. Nieminen, *Appl. Phys. A, 35* (1984) 51.
28 K. Saarinen, P. Hautojärvi, J. Keinonen, E. Rauhala, J. Räisänen and C. Corbel, *Phys. Rev. B, 43* (1991) 4249.
29 E. Soininen, J. Mäkinen, P. Hautojärvi, C. Corbel, A. Freundlich and J. C. Grenet, *Phys. Rev. B, 46* (1992) 12394.
30 M. Törnqvist, J. Nissilä, F. Kiessling, C. Corbel, K. Saarinen, A. P. Seitsonen and P. Hautojärvi, unpublished results, 1993.
31 M. Alatalo, R. M. Nieminen, M. J. Puska, A. P. Seitsonen and R. Virkkunen, *Phys. Rev. B, 47* (1993) 6381.
A. P. Seitsonen, R. Virkkunen, M. J. Puska and R. M. Nieminen, unpublished results, 1993.
32 V. N. Brudnyi, V. D. Kuznetsov, S. A. Vorobiev and A. A. Tsoi, *Appl. Phys. A, 29* (1982) 219.

Gallium vacancy related defects in silicon doped GaAs grown at low temperatures

S. A. McQuaid, R. E. Pritchard and R. C. Newman

Interdisciplinary Research Centre for Semiconductor Materials, The Blackett Laboratory, Imperial College of Science, Technology and Medicine, Prince Consort Road, London SW7 2BZ (UK)

S. O'Hagan and M. Missous

Department of Electrical Engineering and Electronics and Centre for Electronic Materials, University of Manchester Institute of Science and Technology, PO Box 88, Manchester M60 1QD (UK)

Abstract

Point defects and complexes in silicon doped GaAs grown at low temperatures were investigated. Large differences between the donor and carrier concentrations imply that the crystals contain high concentrations of compensating defects. The detection of Si_{Ga}–V_{Ga} pairs confirms the expectation that they are gallium vacancies and their concentration appears to be controlled by the Fermi level or silicon concentration. The lattice expansion of the low temperature GaAs is related to the concentration of As_{Ga} antisite related defects which do not appear to affect significantly the electrical properties of the material. The annealing behaviour may be explained by the nucleation of Si clustering by V_{Ga} related defects.

1. Introduction

GaAs layers grown by molecular beam epitaxy (MBE) at low temperatures are extremely non-stoichiometric, containing up to 1.5% excess As atoms [1]. The crystal is therefore expected to contain interstitial As (As_i), As antisites (As_{Ga}) and gallium vacancies (V_{Ga}). Near band edge (approximately 1.2 eV) IR (NBE-IR) absorption has been detected in undoped material [1], characteristic of neutral As_{Ga}^0 related defects in concentrations of about 10^{20} cm^{-3}. In addition, approximately 5×10^{18} cm^{-3} singly ionized As_{Ga}^+ related defects were identified by electron paramagnetic resonance (EPR) [1–4], implying that similar concentrations of acceptor-like defects must have been present. Since V_{Ga} should be acceptors [5], it has been speculated that they are responsible [2]. Doping with a shallow donor impurity should lead to an increase in the concentration of V_{Ga} relative to As_{Ga}. There is no proven method for the detection of V_{Ga} but recently we reported [6] the detection of Si_{Ga}–V_{Ga} donor–acceptor second-neighbour pairs in silicon doped ($[Si] \approx 10^{19}$ cm^{-3}) LT GaAs by IR localized vibrational mode (LVM) spectroscopy, in concentrations of around 2×10^{18} cm^{-3}. In this work we correlate the results of LVM and NBE-IR absorption with electrical properties of this material both in its as-grown state and after thermal anneals.

2. Experiment

Two 3 μm thick low temperature (LT) GaAs layers were grown consecutively in a VG V90H MBE system on (100) oriented semi-insulating (SI) substrates. The Ga, Si and As cell temperatures were set for a growth rate of 1 $\mu m\ h^{-1}$, a doping level of 1×10^{19} cm^{-3} and an As_4-to-Ga beam equivalent pressure (BEP) ratio of approximately 3. Substrate temperatures T_g of 250 and 210 °C were maintained throughout growth of the first (number 273) and second (number 274) layers. Samples with van der Pauw geometry were prepared from each layer. Indium contacts were alloyed at temperatures close to T_g for each sample, and Hall measurements were taken at room temperature. LVM absorption spectra were obtained using a Bruker IFS 120 interferometer operated at a resolution of 0.1 cm^{-1} and with the sample at 20 K. Diffraction of X-rays from (400) crystal planes was recorded for each sample using a Bede QC1 double-crystal diffractometer. Samples were cooled to 77 K in the dark and NBE-IR absorption was measured using a PE $\lambda 9$

0921-5107/93/$6.00

© 1993 – Elsevier Sequoia. All rights reserved

spectrometer. Isochronal (1 h) anneals up to about 800 °C were performed in evacuated ampoules together with crushed GaAs. Hall samples were subjected to 1 min isochronal anneals in air over the same temperature range.

3. Results

LVM absorption spectra (Fig. 1) revealed a sharp line at 383.9 cm^{-1} due to isolated Si_{Ga} donors, with weaker lines at 378.4 and 373.5 cm^{-1} corresponding to the less abundant heavier isotopes $^{29}Si_{Ga}$ and $^{30}Si_{Ga}$. The strengths of absorption due to Si_{Ga} donors were very similar in the two layers and corresponded to concentrations $[Si_{Ga}] \approx 1.4 \times 10^{19}$ cm^{-3} (Table 1) using the previously reported calibration [7]. Weak LVM absorption was also detected [6] due to $^{28}Si_{Ga}$–V_{Ga} donor–acceptor pairs (Fig. 1) giving rise to three lines at 366.7, 367.5 and 397.8 cm^{-1}. The integrated absorptions due to Si_{Ga}–V_{Ga} pairs were again similar in both layers, being approximately 13% of the absorption due to isolated Si_{Ga} donors in each case. Assuming that the dipole moment of Si_{Ga} is unaffected by the pairing, values of $[Si_{Ga}$–$V_{Ga}]$ were estimated to be approximately 2×10^{18} cm^{-3} (Table 1). No other Si-related LVM absorption was detected and the total concentration of Si ($[Si_{Ga}]_T = [Si_{Ga}] + [Si_{Ga}$–$V_{Ga}]$) was comparable with the intended doping level. These observations represent the most direct evidence for the presence of V_{Ga} in high concentrations in LT GaAs.

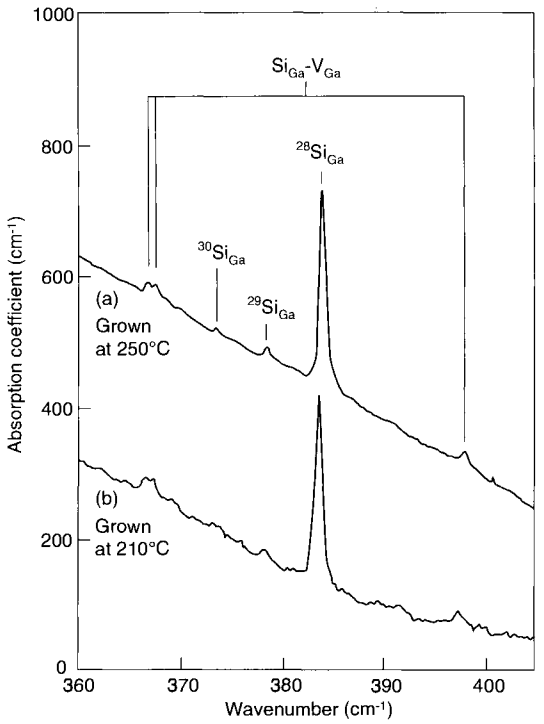

Fig. 1. IR LVM absorption (at 20 K) due to Si impurities in samples (a) 273 and (b) 274 grown at 250 °C and 210 °C respectively.

Both samples were n-type, with carrier concentrations less than 10% of the intended doping level, implying that approximately 90% of the donors were compensated (Table 1). Values of carrier mobility were consistent with the implied compensation, indicating free carrier transport rather than the hopping conduction identified in undoped LT GaAs [1]. Assuming each V_{Ga} defect traps three electrons in n-type material, the measured carrier concentrations and intended doping level of $(1 \pm 0.5) \times 10^{19}$ cm^{-3} imply a value of $[V_{Ga}]_T/[Si_{Ga}]_T \approx (30 \pm 3)\%$ where $[V_{Ga}]_T$ represents the sum of the concentrations of isolated and paired vacancies. These values of $[V_{Ga}]_T$ are in agreement with an extended extrapolation of the results of previous thermodynamic calculations [8]. The Coulombic attraction between negatively charged V_{Ga} and positively charged Si_{Ga} would be consistent with pair formation and the relative disposition of the LVM lines. If all V_{Ga} defects form pairs, which would be double acceptors, during growth then $[Si_{Ga}$–$V_{Ga}]/[Si_{Ga}]$ is estimated as $(42 \pm 3)\%$ and $(48 \pm 1)\%$ for layers 273 and 274 respectively. These ratios are almost equal, as were the ratios of $[Si_{Ga}$–$V_{Ga}]/[Si_{Ga}]$ deduced from LVM measurements for each layer. However, the absolute values implied by the electrical measurements are larger by a factor of about 3. This apparent discrepancy can be explained if only about 30% of V_{Ga} defects in the layers are in the form of pairs or alternatively if the dipole moment associated with LVM absorption of Si_{Ga}–V_{Ga} pairs is smaller than that of isolated Si_{Ga} donors by a factor of about 2, leading to reduced absorption by a factor of 4.

To investigate whether significant concentrations of isolated V_{Ga} were present in the as-grown layers, a sample prepared from layer 273 was heated at a temperature close to T_g for about 500 h, much longer than the growth time (1 h). No significant change in

TABLE 1. A summary of the properties of Si-doped LT GaAs layers grown at 250 and 210 °C

		Layer 273 $T_g = 250$ °C	Layer 274 $T_g = 210$ °C
Hall effect	n (cm^{-3})	7.9×10^{17}	3.3×10^{17}
	μ ($cm^2 V^{-1} s^{-1}$)	455	390
X-ray diffraction	$\Delta a/a$	$< 5 \times 10^{-5}$	1.1×10^{-4}
LVM absorption	$[Si_{Ga}]$ (cm^{-3})	1.4×10^{19}	1.4×10^{19}
	$[Si_{Ga}$–$V_{Ga}]$ (cm^{-3})	2×10^{18}	2×10^{18}
IR absorption	$[As_{Ga}]$ (cm^{-3})	5.3×10^{18}	9.1×10^{18}

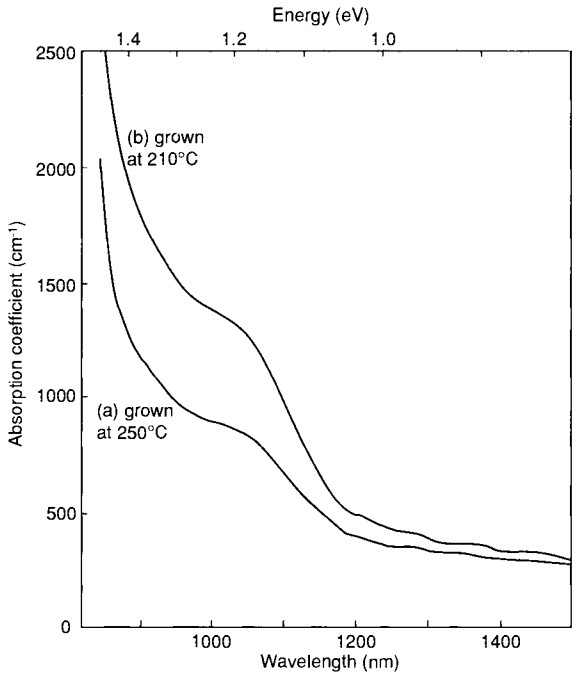

Fig. 2. Near band edge IR absorption due to As_{Ga} antisite related defects in samples which were cooled to 77 K in the dark. The spectra are shown for samples prepared from layers (a) 273 and (b) 274 grown at 250 °C and 210 °C respectively.

$[Si_{Ga}-V_{Ga}]$ was observed, suggesting either that the concentration of isolated V_{Ga} is much smaller than $[Si_{Ga}-V_{Ga}]$ or that the diffusivity of vacancies at T_g is negligible. In the latter case it would be inferred that V_{Ga} had been introduced preferentially near Si_{Ga} donors during growth.

The X-ray rocking curve of the material grown at the lower temperature (210 °C) exhibited two distinct Bragg peaks corresponding to a lattice expansion in the epitaxial layer of $\Delta a_0/a_0 = 1.1 \times 10^{-4}$ (Table 1). However, only a single peak was resolved for the material grown at the higher temperature (250 °C), indicating that the lattice mismatch was smaller than approximately 5×10^{-5}. As already discussed, the Si site occupancy, vacancy concentrations and electrical compensation were very similar in the two layers, so the origin of strain in the crystal would not appear to be strongly related to any of these defects or properties. NBE-IR absorption due to As_{Ga}-related defects in samples prepared from each layer (including the substrate) was measured and the relatively weak absorption due to EL2 defects in substrate material was subtracted to yield the absorption in the LT GaAs layers (Fig. 2). The As_{Ga} concentration, estimated [3] as approximately 10^{19} cm^{-3} in layer 274, was around twice that in layer 273 (Table 1).

The effects of anneals on LVM spectra and electrical properties were the same for the two layers [9]. Above about 300 °C, $[Si_{Ga}]$ decreased and reached a minimum value of approximately 3×10^{18} cm^{-3} at about 500 °C and there was a corresponding drop in electron concentration. Although $Si_{Ga}-V_{Ga}$ pairs appear to be stable up to about 700 °C in plastically deformed material [10], $[Si_{Ga}-V_{Ga}]$ decreased, coinciding with the apparent loss of donors, and was undetectable above about 400 °C. Over the same temperature range the Hall mobility increased, indicating that acceptors must have been lost from solution as well as donors.

4. Discussion

The lattice expansion and $[As_{Ga}]$ in the present n-type LT GaAs grown at 210 °C was about an order of magnitude smaller than for undoped LT GaAs grown at similar temperatures [1]. The difference is probably due to the smaller (1/3) BEP ratio during growth of the present layers. The lattice expansion appears to correlate with $[As_{Ga}]$ and to be independent of either [Si] or $[V_{Ga}]$. The results of LVM and electrical measurements are consistent although the ratio of isolated V_{Ga} relative to those in $Si_{Ga}-V_{Ga}$ pairs remains uncertain and may be as high as 3. Apparent values of $[Si_{Ga}-V_{Ga}]$ and $[V_{Ga}]$ were almost the same in both layers, despite the large difference in magnitude of As-rich non-stoichiometry. In the present n-type material, V_{Ga} appear to trap approximately 10^{19} cm^{-3} carriers while a smaller concentration could account for the detection of approximately 5×10^{18} cm^{-3} ionized antisites in undoped material. It would appear that $[V_{Ga}]$ is a function of the Fermi level or [Si] rather than the degree of non-stoichiometry. During anneals, donors and compensating defects appear to be lost from solution. We speculate that $(Si_{Ga}-V_{Ga})^{2-}$ pairs may be attracted to a second and even a third isolated Si_{Ga}, resulting in the formation of small Si clusters, although the migration mechanism is not known. A similar process might also account for the photoluminescence results of Suezawa *et al.* [11]. Furthermore, since the anneal temperature (approximately 300 °C) of As_{Ga} related defects in undoped LT GaAs [1] is the same as that for Si_{Ga} in the present samples, it is possible that V_{Ga} defects nucleate As precipitates which form during anneals [12].

Acknowledgment

We acknowledge the Science and Engineering Research Council (UK) for financial support.

References

1 M. Kaminska and E. R. Weber, in G. Davies, G. G. DeLeo and M. Stavola (eds.), *Proc. 16th Int. Conf. on Defects in Semiconductors*, Trans. Tech., Zurich, 1992, p. 83.

2 M. Kaminska, E. R. Weber, Z. Liliental-Weber, R. Leon and Z. U. Rek, *J. Vac. Sci. Technol. B, 7* (1989) 710.
3 M. Kaminska and E. R. Weber, in E. M. Anastassakis and J. D. Joannopoulos (eds.), *Proc. 20th Int. Conf. on the Physics of Semiconductors*, World Scientific, Singapore, 1990, p. 473.
4 H. J. von Bardeleban, M. O. Manasreh, D. C. Look, K. R. Evans and C. E. Stutz, *Phys. Rev. B, 45* (1992) 3372.
5 G. A. Baraff and M. Schlüter, *Phys. Rev. Lett., 55* (1985) 1327.
6 S. A. McQuaid, R. C. Newman, M. Missous and S. O'Hagan, *Appl. Phys. Lett., 61* (1992) 3008.
7 R. Murray, R. C. Newman, M. J. L. Sangster, R. B. Beall, J. J. Harris, P. J. Wright, J. Wagner and M. Ramsteiner, *J. Appl. Phys., 66* (1989) 2589.
8 T. Y. Tan, H.-M. Tou and U. M. Gösele, *Appl. Phys. A, 56* (1993) 1.
9 S. A. McQuaid, R. C. Newman, M. Missous and S. O'Hagan, *J. Cryst. Growth, 127* (1993) 515.
10 H. Ono and R. C. Newman, *J. Appl. Phys., 66* (1989) 141.
11 M. Suezawa, A. Kasuya, Y. Nishina and K. Sumino, *J. Appl. Phys., 69* (1993) 1618.
12 M. R. Melloch, N. Otsuka, J. M. Woodall, A. C. Warren and J. L. Freeouf, *Appl. Phys. Lett., 57* (1990) 1531.

EL2-like defects in low temperature GaAs

G. Kowalski, A. Kurpiewski and M. Kamińska
Institute of Experimental Physics, University of Warsaw, Warsaw (Poland)
E. R. Weber
University of California, Berkeley, CA (USA)

Abstract

Two different techniques, namely optical absorption and X-ray diffraction, were extensively used to study arsenic antisite (As_{Ga}) defects in low temperature (LT) GaAs. A standard temperature and illumination cycle following the ground-to-metastable and reverse transitions was employed in both experiments. Similarities between EL2 and the defects in question were found, leading to the establishment of three types of As_{Ga}-related centres in LT GaAs. The underlying role of the strained lattice in LT GaAs layers was pointed out by the X-ray experiment.

1. Introduction

Arsenic antisite (As_{Ga}) defects in low temperature (LT) GaAs, like EL2-type defects in bulk semi-insulating (SI) GaAs, are of great importance in connection with commercial applications of these materials. Much attention has been devoted in recent experimental studies to their similarities and differences. A characteristically high concentration (about 10^{20} cm^{-3}) of arsenic antisite defects in LT GaAs has been determined by optical absorption [1], well above the intrinsic defect concentration (EL2) in SI GaAs (about 10^{16} cm^{-3}). The near-IR absorption spectrum of LT GaAs has been found [2] to be very similar to that of bulk GaAs, both ascribed to As_{Ga}-type defects, but some differences are clearly noticeable. The characteristic fine structure at about 1.05 eV, well known for EL2 [3], is absent and the intracentre absorption band is substantially broadened in LT GaAs. The state of the crystal lattice in both bulk and LT GaAs plays an important role in the interpretation and understanding of the defect behaviour in these materials. In as-grown LT GaAs layers a lattice mismatch has been recorded [4] and studied by the X-ray diffraction technique [5].

2. Samples

Samples of {100}-oriented LT GaAs layers were grown by molecular beam epitaxy (MBE) on SI GaAs substrates. The growth temperature was in the range 190–220 °C. Various layer thicknesses between 1.5 and 3.5 μm were chosen for our experiments.

3. Optical experiments

Absorption and transient experiments were performed using a "Cary" spectrophotometer and with an additional illumination set-up consisting of an SPM1 monochromator and a 150 W tungsten halogen lamp. The samples were kept in an APD closed-cycle cryostat which allowed temperature stabilization in the range 10–300 K.

The absorption spectra of bulk and LT GaAs samples generally resemble one another, but the characteristic structure of EL2 absorption is slightly broadened and the fine structure (zero-phonon line and its replicas) is not observed in LT GaAs crystals. Both spectra are metastable, but in contrast with bulk crystals where the EL2 absorption can be totally quenched, there exists a non-metastable part of the centres in LT GaAs.

The excitation spectra to the metastable state of EL2 in bulk GaAs and As_{Ga}-related defects in LT GaAs are shown in Fig. 1. As can be seen, the maximum of the metastable transition efficiency for As_{Ga}-related defects in LT GaAs is shifted from the well-known value of 1050 nm to 900 nm.

The absorption transients due to the metastable transition of EL2 in bulk GaAs and As_{Ga}-related defects in LT GaAs are shown in Fig. 2 together with the fitted curves. The samples were illuminated with

0921-5107/93/$6.00
© 1993 – Elsevier Sequoia. All rights reserved

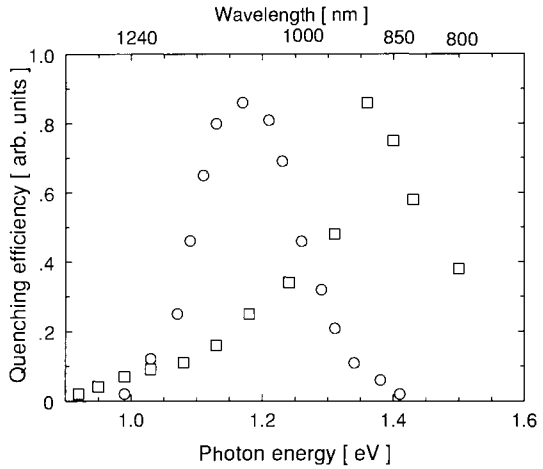

Fig. 1. Quenching efficiency for SI GaAs (○) and LT GaAs (□) as a function of photon energy.

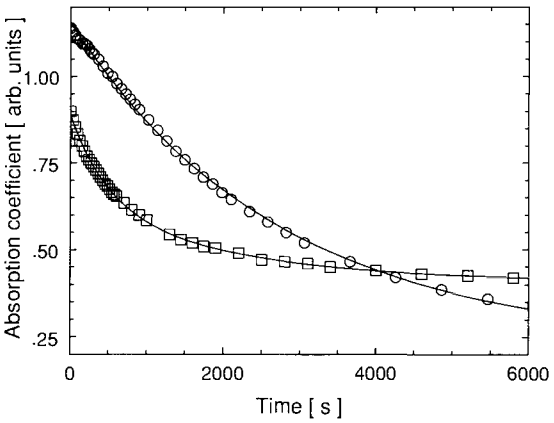

Fig. 2. Transients of metastable transitions in SI GaAs (○) and LT GaAs (□). Absorption coefficients were measured at a wavelength of 1000 nm.

monochromatic light of wavelength 900 nm and absorption coefficient changes were measured at 1000 nm.

The EL2 defects in the SI GaAs transients were found to be exponential, *i.e.* they obeyed the equation

$$A = a\exp(-bt) + c$$

where A is the absorption coefficient, t, is the time and a, b and c are constants. In contrast, the transients of the As_{Ga}-related defects in LT GaAs are described by the equation

$$A = d\exp(-et) + f\exp(-gt) + h$$

where A is the absorption coefficient, t is the time and d, e, f, g and h are constants. The time constants b and e are almost equal, while g is an order of magnitude greater. The c limit is equal to the background value for the quenched EL2 absorption band, while h is much greater. This suggests the existence of three types of As_{Ga}-related centres in LT GaAs: those identical to EL2 known from bulk crystals (slow), metastable centres with a larger time constant (fast) and non-metastable centres. All centres were found to recover to the ground state after a temperature increase above 140 K.

4. X-ray experiments

The high resolution X-ray double-crystal technique has already been employed successfully in experiments on both EL2 defects in SI GaAs [6] and As_{Ga}-related defects in LT GaAs [5]. For the X-ray experiment a double-crystal spectrometer set for [400] Cu Kα_1 or [800] Cu Kβ_1 Bragg reflection was used. This set-up was combined with a liquid nitrogen continuous flow cryostat for sample cooling and light illumination, enabling us to follow repeated ground-to-metastable and reverse transitions of As_{Ga}-related defects. At all subsequent stages of the experiment repeated series of rocking curves were recorded (*e.g.* Fig. 3) showing two characteristic Bragg peaks from the LT GaAs layer and the SI GaAs substrate. At all stages the lattice parameter values for the LT GaAs layers were larger than the substrate values. The room temperature average peak-to-peak distance indicates a $\Delta a/a \approx 8 \times 10^{-4}$ difference in the relative lattice parameter, thus confirming previous measurements [4]. A slight shift towards larger $\Delta a/a$ and a small broadening of the layer peak were observed after cooling in the dark to 80 K. After sample illumination a marked broadening of the layer peak full width at half-maximum (FWHM) was recorded, resulting in an increase of more than 100% in the FWHM as compared with the state before illumination. After prolonged illumination (more than 15 min) an even greater increase was noticed [5]. Reversing the cycle, *i.e.* raising the temperature to above 140 K for the sample after illumination, resulted in recovery of the previous height, position and FWHM of the layer peak. The complete set of rocking curves recorded in this type of experiment thus shows the successive state transitions of the As_{Ga}-related defects from ground to metastable and back to ground. In terms of the crystal lattice it points to different overall lattice strains (mismatches) across the layer. Computer simulations (Fig. 3) using dynamical theory revealed lattice mismatch profiles [5] with reduced $\Delta a/a$ close to the free surface and increased $\Delta a/a$ in the proximity of the substrate interface. Previous experiments [7] showed that the layer was subjected to tetragonal distortion, with the lattice parameter component parallel to the interface equal to the substrate values and the perpendicular component ({100} direction) in

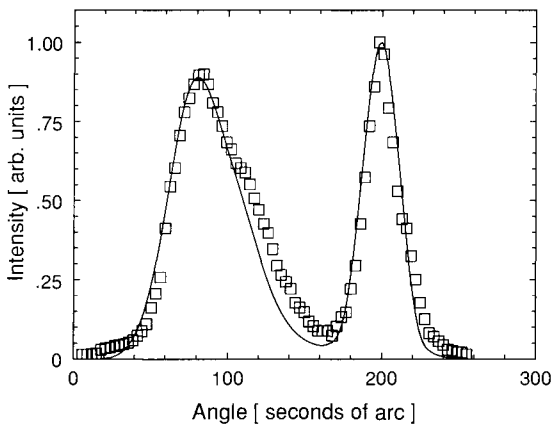

Fig. 3. Measured (□) and calculated (——) [400] Cu Kα_1 Bragg reflection rocking curves for LT GaAs in the metastable state. Note the strong asymmetry of the layer peak resulting from the lattice mismatch gradient in the layer.

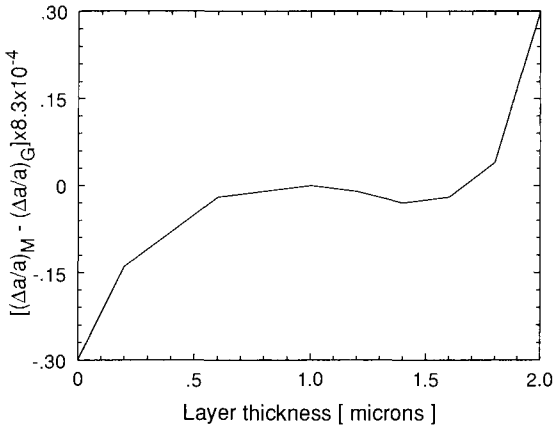

Fig. 4. Difference between metastable ($(\Delta a/a)_M$) and ground ($(\Delta a/a)_G$) state relative lattice parameters of LT GaAs.

the form of a strain gradient spanning from low to high values towards the interface. To visualize the overall change in lattice mismatch, the difference between the ground and metastable (before and after illumination) strain profiles is shown in Fig. 4 for one of the samples measured in our experiment. It is clearly seen that three different regions are present across the layer: one close to the free surface where the lattice parameter approaches the substrate values, a middle region with overall slightly changed values and a third region close to the interface with high values of $\Delta a/a$. Approximate "borders" can be drawn between them, giving $\frac{1}{4}$, $\frac{1}{2}$ and $\frac{1}{4}$ of the layer thickness respectively for this particular sample. This is somewhat arbitrary and may differ from sample to sample and is subject to local non-uniformity of the defect distribution.

5. Discussion

The results of the experiments presented underline the similarities and differences in the ground and metastable configurations of the defects in SI GaAs and LT GaAs. The differences can be summarized as follows. The LT GaAs absorption spectra cannot be fully quenched [1] (non-metastable defects), different maximum positions in the transition efficiency spectra for the two defects occur [8] and, most strikingly, there is a difference in the time transients of the defect transitions into the metastable state. The last observation leads to the conclusion that two kinds of quenchable antisite defects exist in LT GaAs, *i.e.* "fast" and "slow". The time constant of the "slow" defects is the same as for EL2. Comparison of the optical and X-ray experiments points also to the suggestion that the different "types" of centres are in some way spatially separated across the layer, bearing in mind the statistical nature of the defect distribution. The underlying "force" behind most of the differences between EL2 in SI GaAs and As_{Ga}-related defects in LT GaAs is the strained lattice of the LT layer. Near the free surface of the layer the lattice parameter is relaxing towards the substrate values (SI GaAs) during transition to the metastable state and this relaxation can assist the transition. We think that such a mechanism can account for the "fast"-type centres. The middle part of the layer with its mismatch value in between the two extremes is probably the region where "slow" centres are located. The transition in this part of the layer does not change the lattice parameter significantly and is similar to the slight changes observed for EL2 in SI GaAs [5]. We believe that the part of the layer close to the interface, where a large build-up of strain was recorded, is mostly occupied by unquenchable (non-metastable) As_{Ga}-related defects. All three regions are of course subject to local statistical variations in strain, thus implying that the proposed spatial delimitation is in a way arbitrary, though supported strongly by experimental results. The role played by lattice deformation and its influence on EL2 defects has already been established in experiments with hydrostatic pressures [9]. Although the deformation of the lattice was quite the opposite in those experiments, *i.e.* compression rather than expansion, it still points to the way that this type of problem in LT GaAs should be approached.

References

1 M. Kaminska and E. R. Weber, in E. M. Anastassakis and J. D. Joannopoulos (eds.), *Proc. 20th Int. Conf. on the Physics of Semiconductors, Thessaloniki, 1990*, World Scientific, Singapore, 1991, p. 473.

2 M. Kaminska, E. R. Weber, K. M. Yu, R. Leon, T. George, F. W. Smith and A. R. Calawa, in A. G. Milnes and C. J. Miner (eds.), *Semi-insulating III–V Materials, Toronto, 1990*, Adam Hilger, Bristol, 1990, p. 111.
3 M. Kaminska, M. Skowronski, J. Lagowski, J. M. Parsey and H. C. Gatos, *Appl. Phys. Lett., 43* (1983) 302.
4 M. Kaminska, Z. Liliental-Weber, E. R. Weber, T. George, J. H. B. Kortraight, F. W. Smith, B.-Y. Tsaur and A. R. Calawa, *Appl. Phys. Lett., 54* (1989) 1881.
5 G. Kowalski, M. Leszczynski, A. Kurpiewski, M. Kaminska, T. Suski and E. R. Weber, *MRS Symp. Proc., 241* (1992) 125.
6 G. Kowalski and M. Leszczynski, *Appl. Phys. Lett., 59* (1991) 1.
7 G. Kowalski and M. Leszczynski, unpublished results, 1989.
8 A. Kurpiewski, M. Palczewska, M. Kaminska and E. R. Weber, *Appl. Phys. Lett.*, in press.
9 M. Baj, P. Dreszer and A. Babinski, *Phys. Rev. B, 43* (3) (1991) 2070.

Materials Science and Engineering, B22 (1993) 31–36

GaAs, AlGaAs, and InGaAs epilayers containing As clusters: semimetal/semiconductor composites

M. R. Melloch[a], J. M. Woodall[b], N. Otsuka[a], K. Mahalingam[a], C. L. Chang[a] and D. D. Nolte[a]

[a]*Purdue University, West Lafayette, IN (USA)*

[b]*IBM T. J. Watson Research Center, Yorktown Heights, NY (USA)*

Abstract

A new kind of semiconductor composite material is demonstrated with a dispersion of semimetallic particles with properties common to high-quality single crystals. These materials are arsenides such as GaAs, AlGaAs, and InGaAs containing arsenic clusters. These composites are formed by incorporating excess As in the semiconductor, which precipitate with anneal. The incorporation of the excess As is accomplished by molecular beam epitaxy at low substrate temperatures. We demonstrate that the cluster densities can be controlled with the coarsening anneal. Furthermore, we demonstrate that heterojunctions and doping can be used to control the positioning of the As clusters.

1. Introduction

Everyone is well aware of the virtues of composite materials. However, with some exceptions, these virtues are usually only associated with those properties useful for mechanical applications. Attempts to engineer new and useful electronic and photonic properties in semiconductor materials through metal/semiconductor composites has met with limited success. The reason is simple: useful crystalline devices usually require semiconductors with relatively low defect densities, while most compositing techniques render semiconductors highly defective. Recently, we have demonstrated a new kind of semiconductor composite material with a dispersion of semimetallic particles with some properties common to good quality single crystals. These materials are arsenides, such as GaAs, AlGaAs and InGaAs, containing arsenic clusters, which we designate as GaAs:As [1], AlGaAs:As [2] or InGaAs:As [3].

These semimetal/semiconductor composites exhibit several interesting properties. The As clusters act as internal Schottky barriers, and therefore the depletion regions surrounding the As clusters compensate for p- and n-dopants in GaAs:As and AlGaAs:As [4]. This is the reason that GaAs:As is so effective in eliminating sidegating when used as a buffer layer below field-effect transistors [5–7]. In addition, layers that are grown at normal substrate temperatures on top of GaAs:As exhibit extremely high electrical quality [7]. The As clusters should be very efficient recombination centres, and in conjunction with other defects in the film make GaAs:As a very fast photoconductor. Several pulse generation systems have been demonstrated using GaAs:As as a photoconducting switch [8–10]. GaAs:As responds to light below the bandgap of GaAs due to internal photoemission from the As clusters [11, 12]. This internal photoemission has been used to make a 1.3 μm GaAs PiN photodetector [13]. Recently we have observed a large room temperature electro-optic effect in GaAs:As and AlGaAs:As; almost a 60% differential transmission has been obtained for a 1 μm thick $Al_{0.25}Ga_{0.75}As$:As epilayer [14, 15]. Using this electro-optic effect, along with charge storage on As clusters, we have demonstrated holographic storage in AlGaAs:As [16].

2. Composite formation

The starting point for forming these composite materials is to incorporate excess As into the epilayers. This is accomplished using molecular beam epitaxy (MBE) with typical group III and As fluxes, but at a reduced substrate temperature, typically in the range of 200 to 300 °C. This results in an incorporation of as much as 2% excess As in the epilayer in the form of point defects, and an expansive lattice strain of approximately 0.1% [17, 18]. Owing to this strain there is a critical thickness beyond which there is a breakdown in the crystallinity of the growing film, this critical thickness being a function of the amount of excess As incorporated [19]. The dimer As_2 or the tetramer As_4 can be used as the arsenic flux [20, 21]. Upon annealing this

0921-5107/93/$6.00

© 1993 – Elsevier Sequoia. All rights reserved

material the excess As precipitates, forming a high-quality III–V matrix containing As clusters [1], with a corresponding order of magnitude reduction in the lattice strain. It has been observed that even though a considerable amount of the excess As has precipitated, there are still in the neighbourhood of 10^{18} cm^{-3} As antisites after an anneal of 600 °C for 10 min [22, 23]. Therefore our typical precipitation anneals are in the range of 700 to 950 °C.

The total energy of these two-phase systems is reduced by an increase in size and hence decrease in density of the clusters due to a reduction in total precipitate-to-matrix interfacial area [15, 24]. Therefore the final average cluster size and corresponding density is controlled by the temperature and duration of the coarsening anneal, while the amount of excess As in the epilayer is controlled by the substrate temperature during MBE. This is illustrated in Fig. 1, where the average As cluster size and density are plotted as a function of coarsening anneal temperature for a GaAs sample that contained 0.9% excess As. The data in Fig. 1 were determined using transmission electron microscopy (TEM). It is clear from Fig. 1 that the control of the density with the coarsening anneal is routine. For a given density of As clusters the average size of the As clusters is determined by the excess As in the film. Therefore complete control of both the density and average size of the clusters requires setting the excess As in the starting epilayer by use of the substrate temperature during MBE [2] followed by the coarsening anneal. Arsenic clusters have been observed in GaAs [1], AlGaAs [2] and InGaAs [3, 25] after this technique of low-temperature MBE followed by an anneal.

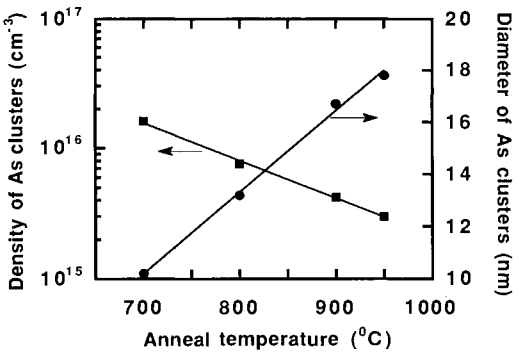

Fig. 1. Arsenic cluster density and average diameter as a function of anneal temperature for isochronal anneals of 30 s with a GaAs sample containing 0.9% excess As.

The As clusters act as internal Schottky barriers, and hence there will be a depletion region surrounding each cluster. In n- or p-doped material, if these depletion regions overlap, the material will be highly resistive. We have seen that the density and hence spacing between As clusters can be controlled with the coarsening anneal. Therefore, by annealing doped material, the clusters will eventually be spaced far enough apart that the depletion regions can be accommodated, leaving conducting regions between clusters [26]. This is illustrated in Table 1 for samples from a GaAs epilayer that contained 1.5% excess As and were doped n-type at 5×10^{18} cm^{-3}. (Note that as-grown all the Si atoms will be on Ga sites [27].) In Table 1, the 600 °C anneal was for 1 h and the higher temperature anneals were for 30 s. On a sample at each anneal, a Hall bar was fabricated to ascertain the density and mobility of the carriers, and TEM imaging was used to obtain cluster average size and density information. As can be seen in Table 1, the material begins to exhibit n-type conductivity as the depletion regions no longer overlap. For the sample annealed at 900 °C for 30 s, a carrier density of 1×10^{18} cm^{-3} and mobility of 1320 cm^2 V^{-1} s^{-1} were measured. This mobility is comparable to that obtained for high-quality highly stoichiometric GaAs doped at 1×10^{18} cm^{-3}.

3. Cluster formation at heterojunctions

Arsenic clusters can be readily formed in GaAs and AlGaAs. If a GaAs/AlGaAs heterojunction is present during cluster coarsening there will be a preferential

TABLE 1. Effect of annealing on As cluster coarsening, carrier mobility and density for a sample doped n-type with silicon at 5×10^{18} cm^{-3}. The 600 °C anneal was for 1 h, all other anneals were for 30 s

Anneal temperature (°C)	Average cluster diameter (Å)	Average inter-cluster spacing (Å)	Cluster density ($\times 10^{16}$ cm^{-3})	Cluster volume fraction	Electron density ($\times 10^{18}$ cm^{-3})	Mobility (cm^2 V^{-1} s^{-1})
600	55	180	17	0.015	—	—
700	70	225	8.7	0.015	0.12	680
800	150	475	0.93	0.016	0.75	1180
900	200	675	0.325	0.013	1.1	1320

coarsening of the clusters to the lower bandgap GaAs regions [24, 28, 29]. This is due to the differences in interfacial energy between the As cluster and semiconductor matrices. (An As cluster in GaAs has a lower interfacial energy than an As cluster in AlGaAs, since the Ga–As bond is weaker than the Al–As bond.) Therefore at a GaAs/AlGaAs heterojunction, there is a preferential growth of the clusters on the GaAs side during cluster coarsening. This is illustrated in Figs. 2(a) and 2(b) for a sample consisting of 10 nm GaAs layers surrounded by 100 nm AlGaAs layers after anneals at 700 °C for 5 min (Fig. 2(a)) and 700 °C for 1.5 h (Fig. 2(b)). We know that after MBE of the structure in Fig. 2 there is approximately the same amount of excess As in the 10 nm GaAs and 100 nm AlGaAs layers [2]. After the 700 °C anneal for 5 min (Fig. 2(a)), enough coarsening has occurred to give a much higher density of clusters in the 10 nm GaAs layers than in the 100 nm AlGaAs regions. With further coarsening, as occurs during the 700 °C anneal for 1.5 h (Fig. 2(b)), there is further transfer of the excess As from the AlGaAs regions to the GaAs regions.

It is also possible to form GaAs wells that are free of As clusters but that have clusters in the surrounding AlGaAs layers [30]. The two keys to accomplish this reversal in positioning of the As clusters are first to grow a film where there is excess As in the AlGaAs regions but no excess As in the GaAs wells, and second to place an As diffusion barrier between the GaAs and AlGaAs regions. The first task is accomplished by growing the GaAs regions using migration-enhanced epitaxy (MEE), which results in highly stoichiometric GaAs even at low substrate temperatures [31], and growing the AlGaAs using MBE at low substrate temperatures to incorporate 1–2% excess As. The second task is accomplished by placing thin AlAs layers between the AlGaAs and GaAs regions, which act as As diffusion barriers [32]. The results of this technique are illustrated in Fig. 3. The white lines in Fig. 3 are the AlAs layers, of which only the lower AlAs layer is indicated. Clearly seen in Fig. 3 is a high concentration of As clusters (about 9) in the AlGaAs regions with very few As clusters (1 or 2) in the GaAs regions and none in the AlAs layers. Note that the clusters in the lower thick GaAs region, which was grown by MBE and hence has excess As as-grown, are much larger in diameter than the clusters in the AlGaAs layers, due to the AlAs layers constraining the size of the clusters in the AlGaAs layers.

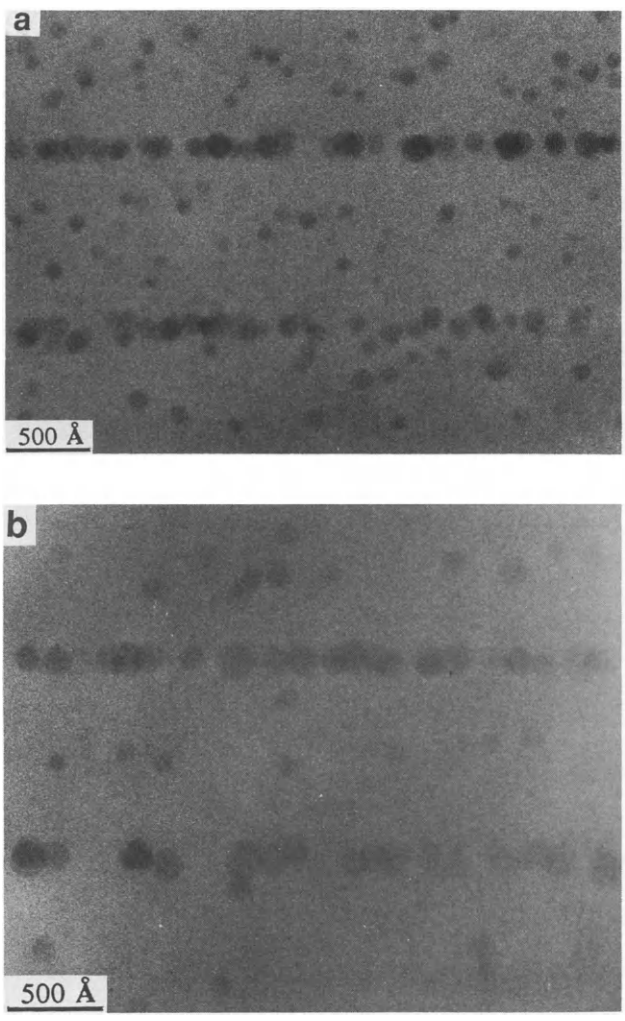

Fig. 2. Arsenic clusters in a structure consisting of 10 nm GaAs layers surrounded by 100 nm AlGaAs layers after anneals of (a) 700 °C for 5 min and (b) 700 °C for 1.5 h.

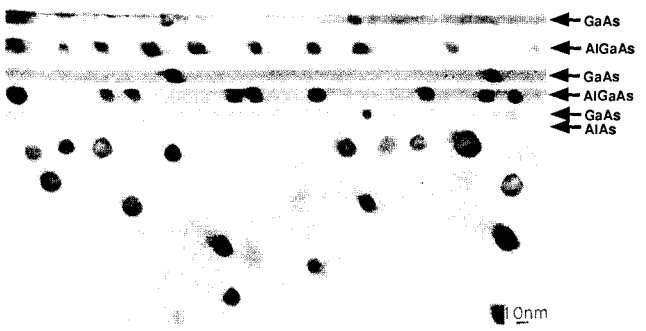

Fig. 3. TEM image of a film structure grown at 260 °C using As_4 and annealed for 30 s at 700 °C. The white lines are AlAs layers (the lowest one is marked) and were either 6 nm or 12 nm thick. The region below the marked AlAs layer is a GaAs temperature transition region. The three GaAs wells in the image are indicated with arrows. The AlAs layers and the GaAs regions between the AlAs layers were grown by MEE and as-grown are highly stoichiometric. The $Al_{0.2}Ga_{0.8}As$ layers and the GaAs temperature transition layer were grown by MBE and as-grown have a large excess of As.

4. Controlling cluster formation with doping

During annealing, some very interesting phenomena are observed if the layers are doped, owing to the fact that the As clusters act as Schottky barriers and hence are charged [33–35]. This is illustrated in Figs. 4, 5(a) and 5(b). Figure 4 is a transmission electron micrograph of a sample that was grown at 250 °C and annealed for 30 s at 800 °C. In Fig. 4, the white lines are 5 nm AlAs layers that serve as markers for the TEM imaging; the other regions are GaAs. There are four GaAs regions of interest in Fig. 4. The first GaAs region, in the lower part of the figure between the lower two AlAs markers, contains a growth interruption of 3 min duration. The growth interruption was accomplished by closing the shutter to the Ga effusion cell while maintaining the As flux. In Fig. 4 the growth interruption is seen to have no effect on the As cluster formation. The next GaAs region contained three planes of Si atoms, an n-type dopant, every 100 nm. These planes were formed by closing the shutter in front of the Ga effusion cell while maintaining the As flux, opening the Si effusion cell for 3 min to deposit 5×10^{12} cm^{-2} Si atoms, then resuming the Ga flux. In Fig. 4, the As clusters are seen to coarsen preferentially on these planes of Si atoms. The next GaAs region contained three planes of 5×10^{12} cm^{-2} Be atoms, a p-type dopant, using the same procedure as just described. In Fig. 4, the As clusters are seen to coarsen preferentially between the planes of Be atoms. Finally, the last GaAs region, which has an AlAs marker only on the bottom, contained a plane of In atoms, an isoelectronic site in GaAs. In Fig. 4, the plane of In atoms is seen to have no affect on the As cluster coarsening, although the amount of excess As in this region is lower than in others, probably due to As escaping from the surface during the anneal.

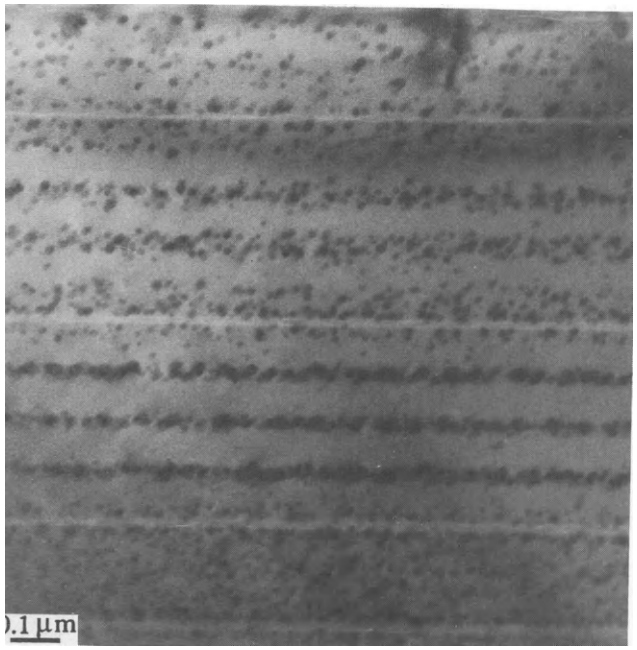

Fig. 4. TEM image of a film structure grown at 250 °C using As_2 and annealed for 30 s at 800 °C. The white lines are 5 nm AlAs layers. Between the lower two AlAs layers is a 200 nm GaAs region that contained a 3 min growth interruption in the centre. There is no apparent effect on the As cluster coarsening due to the growth interruption. The next 400 nm region is a GaAs layer that contained three planes of Si dopants. The As clusters are lined up on the planes of Si dopants. The next 400 nm region is a GaAs layer that contained three planes of Be dopants. The As clusters are seen to coarsen preferentially between the planes of Be dopants. The final top GaAs layer contained a plane of In. There is no apparent effect on the As cluster formation due to the plane of In atoms.

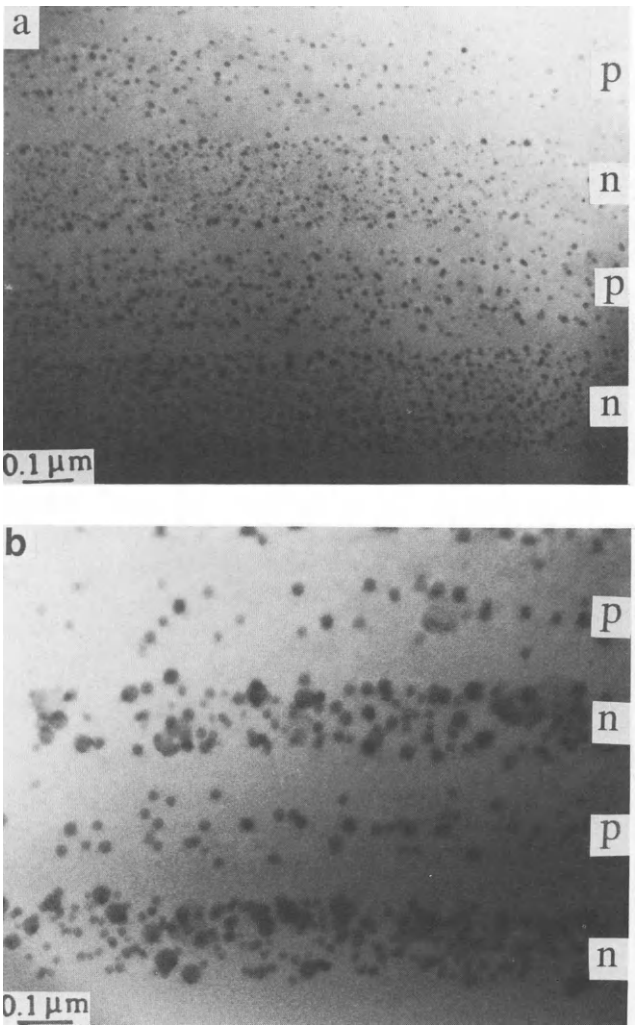

Fig. 5. TEM image of a series of 200 nm GaAs regions uniformly doped with Si at 1×10^{18} cm^{-3} followed by a 200 nm GaAs region uniformly doped with Be at 1×10^{18} cm^{-3}, and subsequently annealed at (a) 700 °C for 30 s and (b) 950 °C for 30 s.

To investigate further the effect of doping on cluster coarsening, a film structure was grown consisting of 200 nm GaAs regions uniformly doped with Si at 1×10^{18} cm^{-3} followed by 200 nm GaAs regions uniformly doped with Be at 1×10^{18} cm^{-3} [34]. Figure 5(a) is a sample from this film annealed for 30 s at 700 °C, and Fig. 5(b) is a sample that was annealed for 30 s at 950 °C. As the As clusters coarsen, there is a preferential coarsening of the clusters from the p-GaAs to the n-GaAs regions.

The above observations of the effects of doping on the cluster coarsening are due to the Schottky nature of the As clusters. An As cluster in n-GaAs will be negatively charged. Therefore, if the cluster thermally emits an As interstitial (As_i), there will be a coulombic attraction between the cluster and the As_i. An As cluster in p-GaAs will be positively charged and so there will be a coulombic repulsion between the cluster and an As_i. Therefore As clusters will be inherently more stable in n-type GaAs than p-type GaAs. Furthermore, an As cluster will be very unstable in a region where there is an electric field.

There is one more interesting phenomenon observed with the formation of As clusters in the presence of dopants. As-grown at low temperature, heavily n-doped GaAs will still be conducting, since As interstitials and As antisites are deep donors. Therefore As clusters readily form with annealing, since the formation of clusters depletes the semiconductor and drives the Fermi level to mid-gap. In contrast, as-grown at low temperature heavily p-doped material is insulating because the deep donor As interstitials and As antisites compensate the material, so the Fermi level is already at midgap. For a GaAs sample grown at 220 °C and doped with Be at 2×10^{19} cm^{-3} we have found that no As clusters form with annealing. Arsenic cluster formation in such a heavily p-doped sample would quickly lead to p-type conduction, since the As in clusters would be much less effective in compensating this material. The result would be that the Fermi level would move from midgap towards the valence band. This represents an increase in energy, which is not offset by the lowering in energy caused by cluster formation. Hence As clusters will not form in heavily p-doped material.

5. Conclusions

In this paper we have described a new composite material consisting of clusters of the semimetal As in arsenide semiconductor matrices. These composites are formed by incorporating excess As in the semiconductor, which precipitates with annealing. The incorporation of the excess As is accomplished by MBE at low substrate temperatures [1]; however, it has been observed recently that the excess As can be incorporated using ion implantation [36]. We have demonstrated that the cluster densities can be controlled with the coarsening anneal. Furthermore, we have demonstrated that heterojunctions and doping can be used to control the positioning of the As clusters.

Acknowledgment

This work was partially supported by the US Air Force Office of Scientific Research under grant numbers F49620-93-1-0031 and F49620-93-1-0388.

References

1 M. R. Melloch, N. Otsuka, J. M. Woodall, A. C. Warren and J. L. Freeouf, *Appl. Phys. Lett.*, *57* (1990) 1531.
2 K. Mahalingam, N. Otsuka, M. R. Melloch, J. M. Woodall and A. C. Warren, *J. Vac. Sci. Technol.*, *B9* (1991) 2328.
3 J. M. Woodall, G. D. Pettit, C. L. Chang, N. Otsuka, M. R. Melloch, D. Yan and F. H. Pollak, *Appl. Phys. Lett.*, in press.
4 A. C. Warren, J. M. Woodall, J. L. Freeouf, D. Grischkowsky, D. T. McInturff, M. R. Melloch and N. Otsuka, *Appl. Phys. Lett.*, *57* (1990) 1331.
5 F. W. Smith, A. R. Calawa, C.-L. Chen, M. J. Mantra and L. J. Mahoney, *IEEE Electron. Dev. Lett.*, *9* (1988) 77.
6 B. J.-F. Lin, C. P. Kocot, D. E. Mars and R. Jaeger *IEEE Trans. Electron. Dev.*, *37* (1990) 46.
7 M. R. Melloch, D. C. Miller and B. Das, *Appl. Phys. Lett.*, *54* (1989) 943.
8 F. W. Smith, H. W. Lee, V. Diadiuk, M. A. Hollis, A. R. Calawa, S. Gupta, M. Frankel, D. R. Dykaar, G. A. Mourou and T. Y. Hsiang, *Appl. Phys. Lett.*, *54* (1989) 890.
9 S. Gupta, P. K. Battacharya, J. Pamaulapati and G. Mourou, *Appl. Phys. Lett.*, *57* (1990) 1543.
10 A. C. Warren, N. Katzenellenbogen, D. Grischkowsky, J. M. Woodall, M. R. Melloch and N. Otsuka, *Appl. Phys. Lett.*, *58* (1991) 1512.
11 D. T. McInturff, J. M. Woodall, A. C. Warren, N. Braslau, G. D. Pettit, P. D. Kirchner and M. R. Melloch, *Appl. Phys. Lett.*, *60* (1992) 448.
12 D. T. McInturff, J. M. Woodall, A. C. Warren, N. Braslou, G. D. Pettit, P. D. Kirchner and M. R. Melloch, *Appl. Phys. Lett.*, *62* (1993) 2367.
13 A. C. Warren, J. H. Burroughes, J. M. Woodall, D. T. McInturff, R. T. Hodgson and M. R. Melloch, *IEEE Electron. Dev. Lett.*, *12* (1991) 527.
14 D. D. Nolte, M. R. Melloch, J. M. Woodall and S. J. Ralph, *Appl. Phys. Lett.*, *62* (1993) 1356.
15 M. R. Melloch, D. D. Nolte, N. Otsuka, C. L. Chang and J. M. Woodall, *J. Vac. Sci. Technol.*, *B10* (1993) 795.
16 D. D. Nolte, M. R. Melloch, S. E. Ralph and J. M. Woodall, *Appl. Phys. Lett.*, *61* (1992) 3098.
17 M. Kaminska, E. R. Weber, Z. Liliental-Weber, R. Leon and Z. U. Rek, *J. Vac. Sci. Technol.*, *B7* (1989) 710.
18 R. J. Matyi, M. R. Melloch and J. M. Woodall, *Appl. Phys. Lett.*, *60* (1992) 2642.
19 Z. Liliental-Weber, W. Swider, K. M. Yu, J Kortright, F. W. Smith and A. R. Calawa, *Appl. Phys. Lett.*, *58* (1991) 2153.

20 M. R. Melloch, K. Mahalingam, N. Otsuka, J. M. Woodall and A. C. Warren, *J. Cryst. Growth, 111* (1991) 39.
21 R. A. Puechner, D. A. Johnson, K. T. Shiralagi, D. S. Gerber, R. Droopad and G. N. Maracas, *J. Cryst. Growth, 111* (1991) 43.
22 M. O. Manasreh, D. C. Look, K. R. Evans and C. E. Stutz, *Phys. Rev. B, 41* (1990) 10272.
23 Z.-Q. Fang and D. C. Look, *Appl. Phys. Lett., 61* (1992) 1438.
24 M. R. Melloch, N. Otsuka, K. Mahalingam, A. C. Warren, J. M. Woodall and P. D. Kirchner, *Mater. Res. Soc. Proc.*, Vol. 241, Materials Research Society, Pittsburgh, PA, 1992, p. 113.
25 J. P. Ibbetson, J. S. Speck, A. C. Gossard and U. K. Mishra, *Appl. Phys. Lett., 62* (1993) 2209.
26 A. C. Warren, J. M. Woodall, P. D. Kirchner, X. Yin, F. Pollak, M. R. Melloch, N. Otsuka and K. Mahalingam, *Phys. Rev. B, 46* (1992) 4617.
27 S. A. McQuaid, R. C. Newman, M. K. Missous and S. O'Hagan, *Appl. Phys. Lett., 61* (1992) 3008.
28 K. Mahalingam, N. Otsuka, M. R. Melloch, J. M. Woodall and A. C. Warren, *J. Vac. Sci. Technol., B10* (1992) 812.
29 K. Mahalingam, N. Otsuka, M. R. Melloch and J. M. Woodall, *Appl. Phys. Lett., 60* (1992) 3253.
30 M. R. Melloch, C. L. Chang, N. Otsuka, K. Mahalingam, J. M. Woodall and P. D. Kirchner, *J. Cryst. Growth, 127* (1993) 499.
31 Y. Horikoshi, M. Kawashima and H. Yamaguchi, *Jpn. J. Appl. Phys., 25* (1986) L868.
32 L.-W. Yin, Y. Hwang, J. H. Lee, R. M. Kolbas, R. J. Trew and U. K. Mishra, *IEEE Electron. Dev. Lett., 11* (1990) 561.
33 M. R. Melloch, N. Otsuka, K. Mahalingam, C. L. Chang, P. D. Kirchner, J. M. Woodall and A. C. Warren, *Appl. Phys. Lett., 61* (1992) 177.
34 M. R. Melloch, N. Otsuka, K. Mahalingam, C. L. Chang, J. M. Woodall, D. Pettit, P. D. Kirchner, F. Cardone, A. C. Warren and D. D. Nolte, *J. Appl. Phys., 72* (1992) 3509.
35 J. P. Ibbetson, J. S. Speck, A. C. Gossard and U. K. Mishra, *Appl. Phys. Lett., 62* (1993) 169.
36 A. Claverie, F. Namavar and Z. Liliental-Weber, *Appl. Phys. Lett., 62* (1993) 1271.

Materials Science and Engineering, B22 (1993) 37–40

Semi-insulating GaAs made by As implantation and thermal annealing

A. Claverie
CEMES-LOE/CNRS, BP 4347, F-31055 Toulouse (France)

F. Namavar
Spire Corporation, 1 Patriots Park, Bedford, MA 01730-2396 (USA)

Z. Liliental-Weber
MSD, Lawrence Berkeley Laboratory, 1 Cyclotron Road, Berkeley, CA 94720 (USA)

P. Dreszer
University of California, Berkeley, CA, 94720 (USA)

E. R. Weber
MSD, Lawrence Berkeley Laboratory and University of California, Berkeley, CA 94720 (USA)

Abstract

We have demonstrated that it is possible to regrow amorphous layers created by high dose As implantation in GaAs by thermal annealing in order to obtain arsenic precipitates distributed in a GaAs matrix similarly to that observed in low temperature GaAs. The characteristics of the As precipitates can be monitored through appropriate selection of the implantation and annealing conditions. Electrical measurements show that dielectric-like resistivity of surface or buried GaAs layers can be obtained by this method. Results on the growth of epilayers on these semi-insulating regions are also reported.

1. Introduction

Several recent studies on the so-called low temperature (LT) GaAs grown by molecular beam epitaxy (MBE) have shown this material to be very interesting because of its semi-insulating (SI) properties [1, 2]. These SI properties result from the ability of this material to incorporate a large (several per cent) amount of group V atoms in excess of the regular stoichiometry of the GaAs crystal [3]. Although some controversy still exists, one of the models which explains the SI properties is related to the presence of small precipitates of As in annealed LT GaAs [4]. A theoretical model gives an attractive explanation for the relation between precipitate sizes and densities and the resulting electronic properties by assuming that the metallic precipitates act as buried Schottky barriers and that overlapping of depletion regions occurs for large enough sizes and densities [5]. Although extremely promising, the so-called LT process is limited to MBE growth. This method allows a device to be grown on top of the SI layer and hence to be "vertically" isolated from the substrate. It is also of great importance to isolate such a device from its neighbors and this explains the need for "lateral" isolation. While up to now all these layers have been grown by MBE at low temperatures, it is of interest to explore other ways of fabricating this new type of material. In principle, any process leading to the formation of a well-controlled high density of As precipitates in a GaAs crystal should be able to render the material insulating. Ion implantation is a good tool to introduce a required concentration of impurities (usually a dopant) within a material. It may be used through mask openings, so that localized areas of the material may be selected and implanted. However, the problems are *a priori* very different from those encountered with MBE. Amorphization of the GaAs crystal invevitably occurs as a result of the high dose As implantation and a thermal anneal is needed to regrow the amorphous layer by solid phase epitaxy (SPE). The goal of this paper is to show that ion implantation can be used to fabricate SI GaAs of comparable structure and resistivity to the LT-MBE-grown material.

0921-5107/93/$6.00

© 1993 – Elsevier Sequoia. All rights reserved

2. General procedure

Implantation conditions are chosen so that the resulting As concentration in the layers, defined as $(N_{As} - N_{Ga})/(N_{Ga} + N_{As})$, has a maximum of several per cent. For a typical 200 keV implantation with 1×10^{16} ions cm^{-2} a maximum of 2% excess As is predicted from range calculations (TRIM) [6] at a depth of about 90 nm. It is also predicted that the excess of As concentration is comparable with those found in LT GaAs from the surface to a depth of about 200 nm. The only difference between these two materials is that the As-implanted layer is rendered amorphous by the bombardment (Fig. 1(a)). The widths of these amorphous layers are in agreement with the "critical damage energy density" model, which was previously used to describe GaAs amorphization kinetics [7], and hence they can be predicted by calculations. To recrystallize these layers, thermal annealing is needed. This process occurs through SPE, *i.e.* displacement of the crystalline–amorphous (c–a) interface toward the surface. Figure 1(b) shows such a regrown layer after a 600 °C, 30 min anneal. In the regrown layer precipitates are always found whose density and sizes depend on the implantation and annealing conditions. For short-time annealings voids have also been found in some cases, but they disappear during further annealing [8]. Few defects are seen in this layer, most of them being dislocations interacting in the vicinity of the former interface. However, the situation is different in the deeper region beneath the former c–a interface, where many dislocation loops are found. Their density decreases with increasing distance from the interface and larger precipitates are also seen attached to these defects. The mechanism by which these dislocations form is well documented for ion-implanted silicon [9] and these defects are known to be interstitial dislocation loops formed through agglomeration upon annealing of interstitial (implanted plus recoiled) atoms remaining beneath the c–a interface after implantation. These defects are generally termed end-of-range (EOR) defects. In cases where these defects are detrimental to devices, it is possible to optimize the implantation conditions to minimize their density [10].

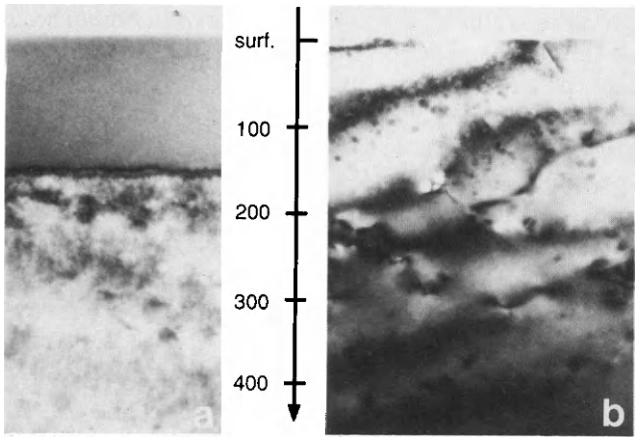

Fig. 1. (a) Bright field (220) cross-sectional transmission electron microscopy (XTEM) image showing the amorphous layer created by the 200 keV, 1×10^{16} As^+ cm^{-2} bombardment. (b) Same layer after 30 min, 600 °C thermal annealing. Note the different types of defects that appear depending on the depth.

3. Formation and crystallography of the precipitates

Precipitates are always found in such regrown layers with sizes that depend on the annealing temperature and time. Their sizes range from 3 to 20 nm for a typical 600 °C, 30 min annealing and they are depth distributed in good agreement with calculations of the As profile in the as-implanted material. Microdiffraction experiments with a transmission electron microscope (see Fig. 2) show the presence of extra spots in the diffraction pattern, which are identified as being due to rhombohedral As (metallic) in a particular orientation relationship (OR). Analysis of such diffraction patterns shows that the OR is given by (0003)pp//

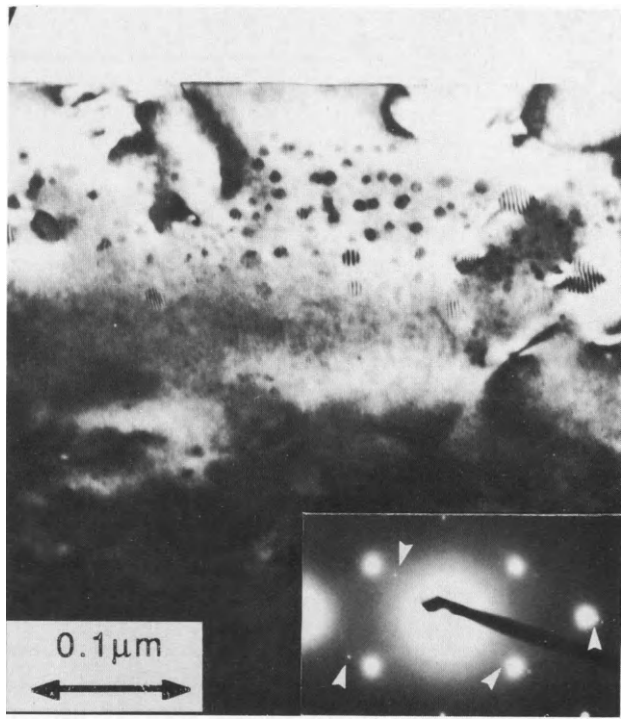

Fig. 2. XTEM image showing the upper part of the layer after 200 keV, 1×10^{16} As^+ cm^{-2} plus 400 keV, 2×10^{16} As^+ cm^{-2} and thermal annealing at 600 °C for 30 min. Note that the precipitates are homogeneously distributed. The inset shows the associated microdiffraction pattern. The extra spots due to the precipitates are shown by arrows in the pattern.

(111)m and [1210]pp//[011]m when the As structure is given in a hexagonal unit [9]. This represents the highest symmetry ($3m$) and the lowest energy (interfacial or elastic) attainable by the association of these two materials. This is indeed the same orientation relationship as the one observed in defect-free LT GaAs [11] and, as expected, four orientational variants are observed for the precipitates. In the region that was formerly beneath the c–a interface, larger precipitates are also seen connected to extended defects, dislocations or EOR defects. They are shown to be of the same structure but of different ORs. These ORs are due to the local strain and to the reduction in symmetries near the core of the defects [12]. However, this observation shows that As precipitation occurs *after* the clustering of EOR defects. Similarly, in the regrown layer a few large precipitates are only found connected to growth defects. This also shows that As precipitation occurs *after* the SPE regrowth of the amorphous layer [9].

4. Electrical characteristics

Preliminary Hall measurements of annealed As-implanted samples have shown that they are semi-insulating, similarly to annealed LT GaAs. Polaron profiling has shown a decreased carrier concentration in the layer, which agrees reasonably well with As profile simulations [13]. A test structure as shown in Fig. 3 was used to study lateral isolation of the unimplanted region and vertical isolation with the substrate by applying an a.c. voltage on the contacting probes in different regions of the samples. While the unimplanted regions (AA′) exhibit a turn-on voltage of about 5 V with no apparent breakdown, in the implanted regions (BB′) the maximum 1600 V available was not sufficient to cause breakdown in the film. With respect to vertical isolation, breakdown was observed at about 100 V in the unimplanted regions

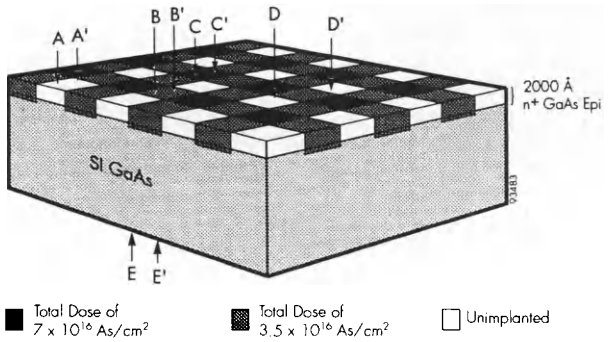

Fig. 3. Schematic diagram of the test structure used to evaluate the electrical isolation quality of As-implanted GaAs buffer layers.

(AE), while in the As-implanted regions (BE) the value of the breakdown voltage was higher than 1000 V. Subsequently, the breakdown electric field was estimated to be about 5×10^7 V cm^{-1}. This high breakdown field strength indicates that the As-implanted GaAs has insulating properties comparable with those of high quality dielectrics.

5. Epilayer growth on As-implanted substrates

After annealing of the As implanted material to recover crystallinity up to the surface, epilayers can be grown by metal organic chemical vapour deposition (MOCVD). The temperature at which this growth takes place and the time needed for growing a layer 1 μm thick (23 min at 720 °C) cause the implanted region to receive a much higher energetic annealing during the epigrowth compared with that required for the SPE regrowth of the amorphous layer. Consequently, the structure of the As-rich region is changed during the epigrowth. Precipitates have reduced densities and larger sizes and their depth positions are more spread out than after the first annealing. The EOR defect density is also reduced for the same reasons and the dislocations remaining in the implanted region have a simpler structure than before. These dislocations are mostly found in the interfacial region between the implanted and the epigrown layers. Small precipitates (a few nanometers in diameter) are also found decorating the interface. Moreover, the absence of precipitates in the epilayer suggests that excess As does not diffuse easily through the interface, a result that may be due to its contamination before growth. However, the structure of the implanted region is shown to be the result of intensive diffusion and competition of all the single-defect species (As, Ga, V, etc.) that are emitted or trapped by the extended defects during energetic annealing. Indeed, As precipitates, voids and EOR defects are reservoirs of single defects that compete for growth and shrinkage during annealing. However, an epilayer of relatively good overall quality can be grown on the implanted layer with a reduction in dislocation density of the order of 10 between the implanted and the epigrown layers (Fig. 4). This is to stress that epilayers of reduced dislocation densities will be obtained only after optimization of the annealing conditions of the implanted layer prior to MOCVD growth.

6. Conclusions

We have shown that it is possible to fabricate materials by ion implantation and subsequent thermal

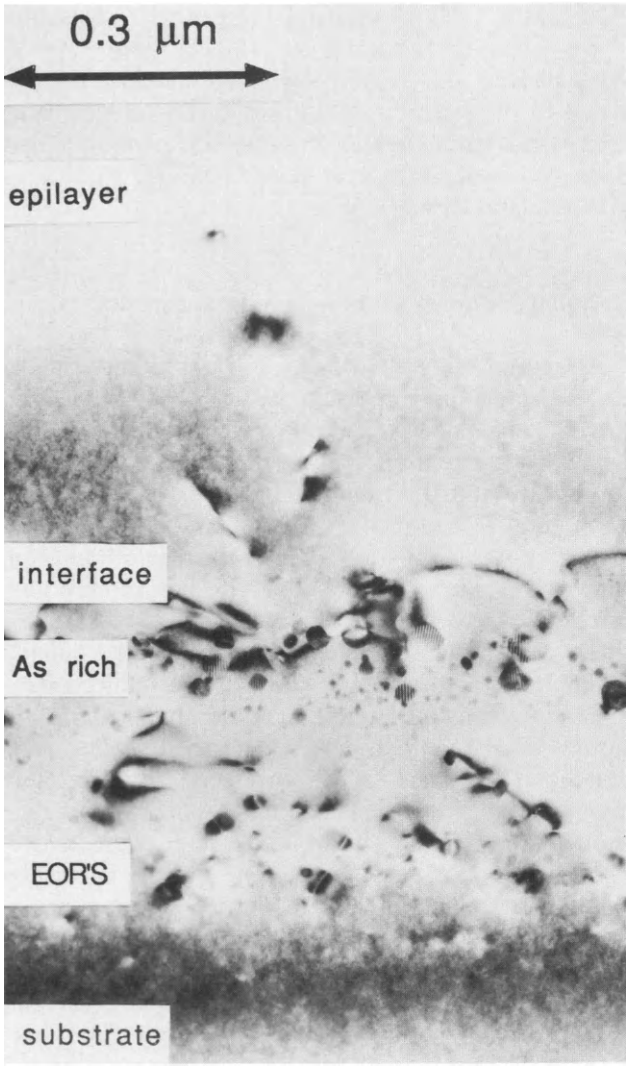

Fig. 4. XTEM image showing the epilayer grown on top of the implanted layer. Note the band of precipitates in the As-rich region. Growth conditions: $T = 720\,^{\circ}C$, $V = 11\ A\ s^{-1}$.

annealing whose structural characteristics are comparable with those found in LT GaAs. A careful choice of implantation and annealing conditions leads to the formation of As precipitates in the GaAs matrix. The density and size of arsenic precipitates can be controlled by varying the implantation dose and annealing time respectively, while the thickness of the As-rich layer can be monitored through the implantation energy. Preliminary electrical measurements on these layers show that a resistivity at least as high as that of LT-MBE-grown materials may be obtained. When As implantation is carried out through mask openings, selected regions may be protected or implanted and the implanted regions can provide lateral as well as vertical isolation in GaAs device structures. Moreover, regular or doped GaAs epilayers can be grown on top of such SI GaAs layers with a good overall crystalline quality. Formation of insulating GaAs layers by this technique may improve the performance and packing density of GaAs integrated circuits, leading to advanced novel III–V-compound-based technologies for high speed and radiation-hardened circuits.

Acknowledgments

Work at Spire was funded by an Army SBIR contract. Spire would like to acknowledge the guidance and technical assistance of Sam DiVita.

References

1 F. W. Smith, A. R. Calawa, C. L. Chen, M. Manfra and L. J. Mahoney, *IEEE Electron-Device Lett., 9* (1988) 77.
2 A. S. Brown, U. K. Mishra, C. S. Chou, C. E. Hooper, M. A. Melendess, M. Thompson, L. E. Larson, E. S. Rosenbaum and M. J. Delaney, *IEEE Electron-Device Lett., 10* (1989) 565.
3 K. M. Yu and Z. Liliental-Weber, *Appl. Phys. Lett., 57* (13) (1990) 1331.
4 M. R. Melloch, N. Otsuka, J. M. Woodall, A. C. Warren and J. L. Freeouf, *Appl. Phys. Lett., 57* (1990) 1531.
5 A. C. Warren, J. M. Woodall, J. L. Freouf, D. Grischkowsky, D. T. McIntueff, M. R. Melloch and N. Otsuka, *Appl. Phys. Lett., 57* (13) (1990) 1331.
6 J. F. Ziegler, J. P. Biersack and U. Littmark, TRIM–Transmission of Ions in Matter, 1991. See also *The Stopping and Range of Ions in Solids*, Pergamon, New York, 1985.
7 J. Beauvillain, A. Claverie and K. Akmoum, *J. Phys. III (Fr.), 2* (1992) 407.
8 Z. Liliental-Weber, F. Namavar and A. Claverie, *Ultramicroscopy, 279* (1993) 381.
9 A. Claverie, Z. Liliental-Weber and F. Namavar, *Appl. Phys. Lett., 62* (11) (1993) 1271.
10 L. Laanab, C. Bergaud, M. Faye, A. Martinez and A. Claverie, *MRS Symp. Proc.*, 1992, in press.
11 A. Claverie and Z. Liliental-Weber, *Philos. Mag. A, 4* (1992) 981–1002.
12 Z. Liliental-Weber, A. Claverie, P. Werner, W. Schaff and E. R. Weber, *Mater. Sci. Forum, 83–87* (1992) 1045.
13 F. Namavar, A. Claverie and Z. Liliental-Weber, *MRS Symp. Proc.*, 1993, in press.

Electro-optical measurement of low temperature GaAs

K. P. Korona, M. Kamińska and J. M. Baranowski
Institute of Experimental Physics, Warsaw University, Hoz☆☆a 69, 00-681 Warsaw (Poland)
E. R. Weber
University of California, Berkeley, CA 94720 (USA)

Abstract

Photocurrent, conductivity and Hall effect studies, performed on GaAs grown by molecular beam epitaxy at low substrate temperatures, are reported. Experiments, conducted on as-grown and 300–600 °C annealed layers, showed domination of arsenic antisite (EL2-like) defects in photocurrent spectra and transport properties of low temperature GaAs. Parameters describing hopping conductivity, and the dependence of these parameters on temperature of annealing, are discussed. Persistent negative photoconductivity was observed. EL2 defect concentration in samples annealed at 600 °C was estimated to be of the order of 10^{18} cm^{-3}. Hall measurements on photoexcited carriers showed unexpectedly high mobility, of the order of 10^4 cm^2 V^{-1} s^{-1} at temperatures in the range 100–200 K.

1. Introduction

One of the most important features of GaAs layers grown by molecular beam epitaxy (MBE) at low substrate temperature is the unusually high arsenic content (of the order of 1% more than gallium). This causes a high concentration of arsenic antisite defects (of the order of 10^{20} cm^{-3}). This number of defects is sufficiently high to create a deep defect band. It has been shown that in as-grown low temperature (LT) GaAs layers, hopping conductivity exists between arsenic antisite defects [1, 2]. The objective of this work was to investigate basic transport properties, such as conductivity and photoconductivity, between deep defect bands of LT GaAs layers.

2. The samples

LT MBE GaAs layers were grown at a temperature of 190 °C under As rich conditions in the MIT Lincoln Laboratory by Drs. F. W. Smith and R. Calawa. Layers of 2.0–2.5 μm thickness were grown on a semi-insulating substrate. Two samples had an extra 0.5 μm layer of AlAs, intended to provide better electrical insulation from the substrate. The samples were annealed in the MBE system at temperatures from 300 to 600 °C. As calculated from the near-IR optical absorption spectra, using Martin's calibration curve [3], the concentration of arsenic antisite defects in the as-grown samples was 1×10^{20} cm^{-3}. In samples annealed at 400 °C, this concentration was about five times lower. Annealing at higher temperatures caused a decrease in EL2-like defect concentration to such a level that optical detection was impossible.

3. Results and discussion

The photocurrent spectrum in Fig. 1, identified as the photoionization spectrum of an EL2 defect, is dominated by the photoionization band at $h\nu = 1.1$ to 1.5 eV. At low temperature (12 K) this band could be

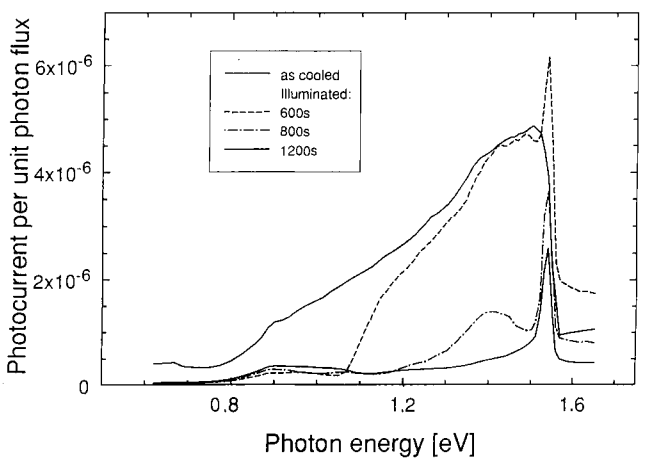

Fig. 1. Photocurrent spectra of LT GaAs measured at $T = 12$ K before and after illumination with $h\nu = 1.3$ eV light.

0921-5107/93/$6.00
© 1993 - Elsevier Sequoia. All rights reserved

quenched by illumination with white or monochromatic $h\nu = 1.3$ eV light. The band recovered at temperatures higher than 130 K. This implies that the metastable behavior of this band is the same as the behavior of the EL2 band in standard SI GaAs.

Conductivity measurements were performed in the range 12–300 K. As an example, results for a sample annealed at 450 °C are presented in Fig. 2. Two straight lines, for activation energies of 0.76 and 0.056 eV, have been plotted. The activation energy corresponds well with thermal excitation of electrons from EL2 to the conduction band. This transport mechanism dominated at temperatures higher than 250 K. It is probable that, in this temperature range, the main part of the current flowed through the substrate, whereas at lower temperatures the concentration of electrons in the conduction band decreased and the substrate became more insulating than the layer. Below 250 K hopping conductivity was observed. In the range 140–240 K, the conductivity had a well determined activation energy $E_a = 0.056$ eV. At temperatures below 140 K the conductivity changed slowly, in agreement with the theory developed by Mott [5] and Shklovskii and Efros [6]. The curve in this region had dependence

$$\sigma = \sigma_0 \exp(-(T_0/T)^{1/4}) \tag{1}$$

This formula is characteristic of hopping conductivity at low temperatures [5, 6]. The parameter T_0 is given by $T_0 = \beta/g(\mu)a$ where a is a localization parameter of the defect wave function, β is a numerical coefficient equal to 21.2 and $g(\mu)$ is the density of states at the Fermi level.

At higher temperatures the following relationship is expected:

$$\sigma = \sigma_{03} \exp\left(\frac{\varepsilon_3}{kT}\right) \tag{2}$$

where

$$\sigma_{03} = \sigma_0 \exp\left(\alpha \frac{2}{aN^{1/3}}\right) \tag{3}$$

with α as a numerical coefficient equal to 1.73, N as the concentration of hopping centers and ε_3 as an average difference of energies between two impurities caused by Coulomb interaction between ionized centers. The numerical coefficients α and β were calculated by Shklovskii and Efros [6].

By fitting eqn. (3) to the experimental data, energies ε_3 for all samples were determined. It was found that ε_3 values were of the order of 100 meV and decreased for samples annealed at higher temperatures. According to Shklovskii and Efros theory, ε_3 should increase with $N^{-1/3}$. Taking N as the EL2 concentration, known for some samples from optical absorption measurements, an experimental dependence of ε_3 on $N^{-1/3}$ was found. Using this dependence, concentrations of EL2 for the remaining samples were calculated and found to be high (about 10^{18} cm^{-3}) even for samples annealed at 600 °C. The dependence of conductivity on temperature for one of the samples annealed at 600 °C, with a fitted hopping conductivity curve, is shown in Fig. 3.

Based on eqn. (3), the conductivity σ_{03} was examined. The wave function localization parameter a was found to be equal to 5.2 Å (for shallow impurities it is equal to about 100 Å).

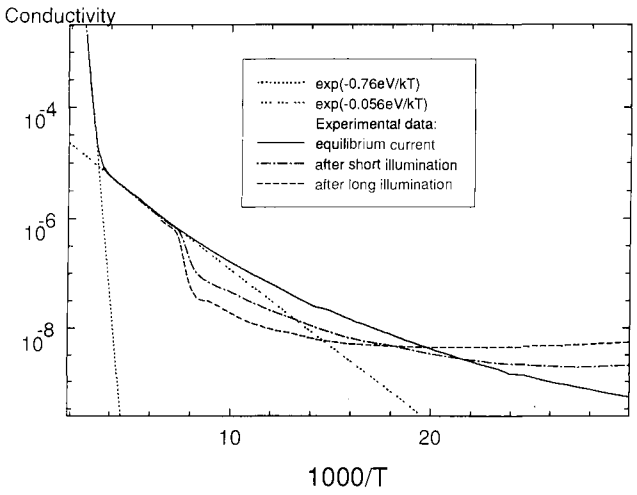

Fig. 2. Conductivity σ *vs.* $1000/T$ in equilibrium conditions and after illumination with $h\nu = 1.3$ eV light at low temperature. The two straight lines represent conductivities with activation energy of 0.76 eV and 0.056 eV respectively.

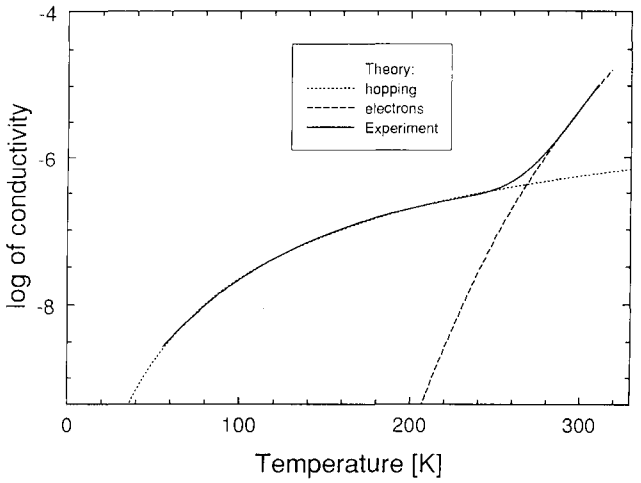

Fig. 3. Analysis of hopping and electronic conductivity of LT GaAs annealed at 600 °C.

Measurements were made of conductivity after illumination. For temperatures below 130 K a significant difference was observed between conductivity after illumination and dark conductivity (see Fig. 2). In as-grown layers the current after illumination was higher than the dark current, whereas in all annealed samples the current after illumination dropped to a value 30 times lower than that of the dark current. This persistent negative photoconductivity suggests that a part of the conducting centers had disappeared. Indeed, based on the experimental relation of N to $g(\mu)$ (determined for annealed samples), the concentrations of hopping centers after illumination were calculated. It was found that in all the samples these concentrations decreased after illumination. This is consistent with a model of EL2 centers participating in the hopping process. Recovery at 130 K, characteristic of EL2, confirms this model. We also conclude that transformation of EL2 to a metastable state removes the EL2 centers from hopping conductivity.

Hall measurements were carried out on samples without AlAs layers. Hall mobility was found to be infinitesimal (in agreement with hopping theory [6]). However, after LT GaAs illumination, a dramatic increase of mobility was observed, owing to transport by electrons excited in the conduction band. Monochromatic light, with an energy of $h\nu = 1.9$ or 1.3 eV, was used. Electron–hole pairs were created by 1.9 eV light, whereas 1.3 eV light excited electrons from EL2 defects to the conduction band.

In the case of our two transport mechanisms, the Hall voltage V_H and transverse resistance R_{xy} are as follows:

$$V_H = \frac{UBs}{l} \frac{n^*\mu^2\rho_0 e}{1 + n^*\mu\rho_0 e} \tag{4}$$

$$R_{xy} = \frac{B}{d} \frac{n^*\mu^2\rho_0 e}{(1 + n^*\mu\rho_0 e)^2} \tag{5}$$

where n^* is the concentration and μ the mobility of excited electrons, ρ_0 is the equilibrium resistivity of the sample. Based on the measured dependence of V_H, R_{xy} and ρ_0 on temperature, and using eqns. (4) and (5), the excited carrier concentrations n^*, and mobilities μ as a function of temperature, were calculated. Mobility of the excited carriers *vs.* temperature for an as-grown sample is shown in Fig. 4(a). It was observed that, whilst using 1.9 eV light, the photoexcited electron mobility had a temperature dependence as in standard n-type GaAs. The peak value of mobility, 20 000 cm^2 V^{-1} s^{-1} was found at 130 K. Such a high mobility was not expected in a material with 10^{20} cm^{-3} defects and about 10^{18} cm^{-3} ionized centers. This effect is probably explained by spatial correlation of ionized EL2

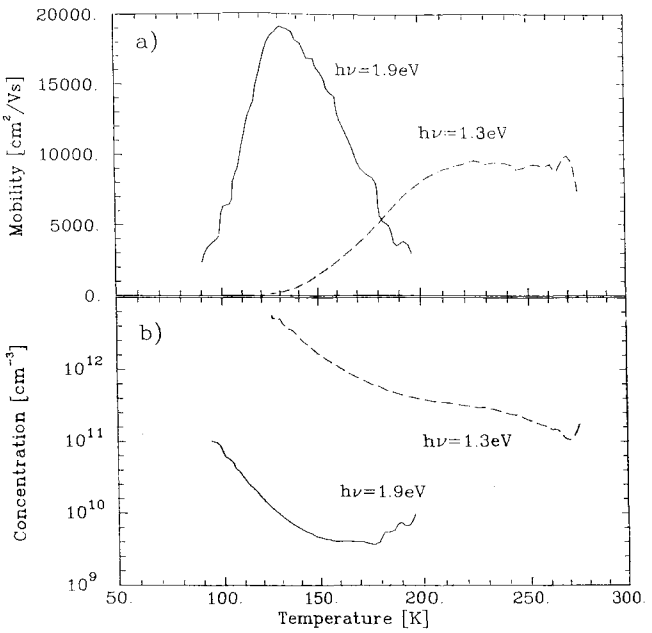

Fig. 4. Dependence of (a) mobility and (b) concentration of photoexcited electrons in as-grown LT GaAs.

(EL2$^+$) centers. The sublattice of ions should not scatter electrons as effectively as single ions do [7]. This conclusion is also supported by the observation that illumination with light $h\nu = 1.3$ eV led to a rapid decrease in mobility with decrease in temperature. Light of $h\nu = 1.3$ eV chaotically ionized EL2 centers and effectively destroyed spatial correlation of ions.

Figure 4(b) shows the dependence of concentration of photoexcited electrons on temperature. The activation energy of photoexcited carrier concentration was determined as $E = 0.07 \pm 0.02$ eV. This value corresponds to the activation energy of cross section electron capture of EL2 [8]. Therefore, at higher temperatures, photoexcited electrons are more effectively captured by EL2 and the value of electron concentration decreases.

For samples annealed at 450 °C the dependences of mobility and concentration on temperature were similar.

Samples annealed at 600 °C had very low mobility (below 100 cm^2 V^{-1} s^{-1}).

4. Conclusions

In summary, this paper presents conductivity, photoconductivity and Hall effect measurement results, performed on LT GaAs. All these results confirmed the dominating role of arsenic antisites (EL2 defects) in this material. Based on hopping analysis, EL2 concentration equal to about 10^{18} cm^{-3} was calculated for

layers annealed at 600 °C. Persistent negative photoconductivity due to EL2 transformation to the metastable state was observed. In as-grown and slightly annealed layers, unusually high mobility of photoexcited carriers was observed, suggesting that spatial correlation of charged EL2 centers existed.

Acknowledgments

This work was supported by KBN grant number 2 0424 91 01.

References

1 M. Kamińska, E. R. Weber, K. M. Yu, R. Leon, T. George, F. W. Smith and A. R. Calawa, in A. G. Milnes and C. J. Miner (eds.), *Semi-insulating III–V Materials*, Adam Hilger, Bristol, 1990, p. 111.
M. Kamińska and E. R. Weber, *Proc. 16th Int. Conf. on Defects in Semiconductors*, Trans. Tech. Publ., Switzerland, 1992, p. 1033.
2 D. C. Look, D. C. Walters, M. O. Manasreh, J. R. Sizalove, E. C. Stutz and K. R. Evans, *Phys. Rev. B, 42* (1990) 3578.
3 G. M. Martin, *Appl. Phys. Lett., 39* (1981) 747.
4 M. Kamińska, M. Skowronski, J. Lagowski, J. M. Parsey and H. C. Gatos, *Appl. Phys. Lett., 43* (1983) 302.
5 N. F. Mott, *Philos. Mag., 19* (1969) 835.
6 B. I. Shklovskii and A. L. Efros, *Properties of Doped Semiconductors*, Springer, 1984.
7 J. Mycielski, *Solid State Commun., 60* (1986) 165.
8 D. V. Lang and R. A. Logan, *J. Electron. Mater., 4* (1975) 1053.

Materials Science and Engineering, B22 (1993) 45–54

Extended defects and precipitates in LT-GaAs, LT-InAlAs and LT-InP

Alain Claverie

Centre d'Elaboration des Matériaux et d'Etudes Structurales (CEMES-LOE)/CNRS, BP 4347, F-31055 Toulouse (France)

Zuzanna Liliental-Weber

Materials Science Division, Lawrence Berkeley Laboratory, 1 Cyclotron Road, Berkeley, CA 94720 (USA)

Abstract

We review the main structural characteristics of low temperature molecular beam epitaxially produced GaAs (LT-GaAs), LT-InAlAs, and LT-InP. These materials exhibit almost identical behaviours with respect to growth and annealing conditions. For too low growth temperatures or too high As pressures, defects are seen in these layers with characteristic pyramidal shapes which result from multiple twinning. The increase in the strain energy stored in the layers that are slightly mismatched on the substrate is responsible for the formation of these defects. On annealing the excess group V atoms dispersed in the matrix condense to form precipitates except in LT-InAlAs. Sizes and orientation relationships of the precipitates depend on the crystalline quality of the layers. An important difference between LT-GaAs and LT-InP is that As precipitates are metallic while the structure in which P condenses is thought to be insulating.

1. Introduction

Arsenides grown by low temperature molecular beam epitaxy (LTMBE), typically at 200–300 °C, such as GaAs (LT-GaAs), LT-AlGaAs, and LT-InAlAs, have been recently shown to be very promising materials because of the semi-insulating (SI) properties they exhibit after a short period of annealing at 600 °C or higher [1–4]. These SI properties result from the ability of these materials to incorporate a large amount of group V atoms (*i.e.* As) in excess of the regular stoichiometry of the crystals. Subsequently, LT-GaAs and LT-InAlAs were investigated as photodetectors, and response recovery times as short as a few hundred femtoseconds were observed in these layers [5, 6]. More recently, LT-InP was also grown by gas source MBE (GSMBE), although the electrical characteristics of these layers appear more complicated [7, 8].

In addition to having good insulating properties with respect to surrounding doped regions, such layers must also be perfectly crystalline. Since a device is likely to be grown on the top, the LT layers should be preferably epitaxially grown on the buffer layer and should provide a clean and well-oriented surface for further growth of a device.

Generally the SI properties of these layers are observed after annealing for, say, 10 min at 600 °C, and the structural changes that take place on annealing are to be considered to explain the observed properties. However, the optimal range of MBE parameters over which SI properties, fast response, and good crystallinity may be obtained is evidently quite narrow, if any. In this paper we will review some of the recent results that have been obtained concerning the structural characteristics of as-grown and annealed layers of LT-GaAs, LT-InAlAs, and InP. For an extensive report on LT-GaAlAs layers, see the excellent paper by Melloch *et al.* in this conference [9].

2. LT-GaAs

2.1. As-grown layers

MBE growth of GaAs is normally performed at a substrate temperature of 600 °C. When it is grown in the 200 °C range under As overpressure, perfectly monocrystalline layers or defective layers can be obtained, and this depends strongly on the temperature and beam equivalent pressure (BEP). In monocrystalline layers, energy-dispersive X-ray analysis by transmission electron microscopy (TEM) [10] as well as particle-induced X-ray emission experiments [11, 12] have shown that these layers are As rich, with an excess of As concentration usually in the 1%–1.5% range, depending on the growth conditions. Electron paramagnetic resonance experiments and IR spectroscopy reveal a high concentration of antisite defects up to $(1.5\text{–}2)\times10^{20}$ cm^{-3} [13], *i.e.* corresponding to $(3\text{–}4)\times10^{20}$ excess As cm^{-3} ($As_{Ga}=A_{Si}+V_{Ga}$). Convergent beam electron diffraction (CBED) [14, 15] and

0921-5107/93/$6.00

© 1993 – Elsevier Sequoia. All rights reserved

ion channelling experiments [12] tend to show that a substantial fraction of the excess As atoms are located in interstitial positions close to the substitutional As atoms with a projected displacement of about 0.3 Å into the ⟨110⟩ channel. As a result of the incorporation of such an amount of excess As in the layer, the cell parameter of LT-GaAs is slightly different from that of perfect stoichiometric GaAs. This was proved by using X-ray diffraction [10, 16]. Shifts in diffraction peaks indicate larger lattice parameters in the LT layers than in the substrate with a variation in $\Delta a/a$ as large as 0.1%. Detailed CBED studies [14, 15] of LT-GaAs showed that the layers are under compressive strain in the area close to the interface with the substrate and that the crystallographic symmetry of the layer can even be described as tetragonal.

It follows that the growth of a LT-GaAs layer on a GaAs layer on a GaAs substrate is somehow similar to that of a mismatched layer on a substrate. Some discrepancy in the substrate temperature measurement is often observed in different laboratories; therefore the same nominal growth temperature can really mean ±30–50 °C difference. Generally, samples grown at 200 °C or higher on In-bonded Mo blocks with a BEP of 10 and a growth rate of 1 μm h^{-1} exhibit high crystalline perfection up to 3 μm thickness. With increasing thickness, extended defects are found as revealed by high resolution electron microscopy (HREM); Fig. 1. These defects consist mostly of stacking faults and microtwins on (111) planes, which ultimately change the growth direction in some part of the layer. Because of the statistical distribution of partial dislocations at the edge of the stacking faults, growth directions are also altered from one area to the next, and this is evidenced by the observation of small angle grain boundaries in the material. As the thickness increases, specific defects, called pyramidal defects, are formed [17, 18]. They are thought to be the result of further development of the defective region shown in Fig. 1. The pyramidal defects (Fig. 2) often appear as

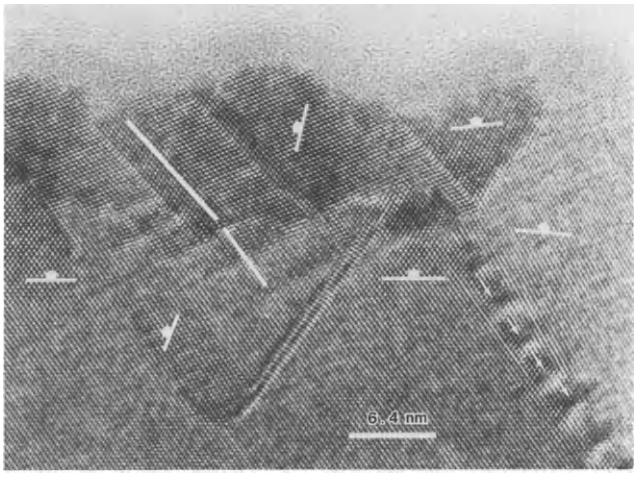

Fig. 1. HREM image showing the defective region near the surface of an LT-GaAs layer grown at 200 °C with a BEP of 40. Arrows point toward the ⟨001⟩ nominal growth direction.

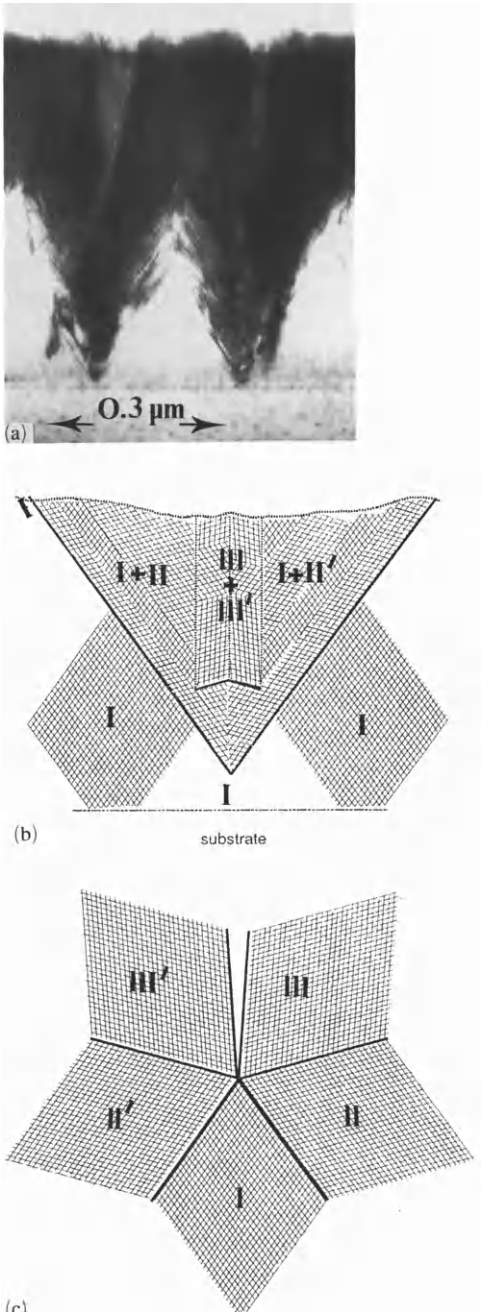

Fig. 2. (a) Cross-sectional TEM (XTEM) image along ⟨110⟩ of a typical pyramidal defect, (b) schematic representation of the crystallographical features of the defect, and (c) five twins used for the scheme.

bunches of microtwins and stacking faults surrounding a core that is thought to be polycrystalline or at least highly defective. In addition to microtwins, a large number of dislocations are also found in the layer so that small angle boundaries are also seen within the twin systems. Boundaries between GaAs grains are sometimes filled with hexagonal As [11]. An interesting observation is that in the process the growth direction is changed, since the transmission electron diffraction (TED) patterns taken along [100] consist of a superposition of ⟨100⟩, ⟨110⟩ and ⟨112⟩ GaAs patterns plus extra spots identified as hexagonal As [11, 19]. Figure 2 also shows a schematic view of an "idealized" pyramidal defect, as can be deduced from TEM and microdiffraction experiments [19]. The main feature of this defect is that it can be described by multiple twinning of the GaAs structure. These defects are also observed when samples of a given thickness are grown at lower temperatures or with higher BEP. With a lower growth temperature, the thickness of the defect-free material is reduced and pyramidal defects are formed. The measurement of this critical thickness as a function of growth parameters is required to understand the mechanism responsible for the breakdown of crystallinity in the LT layers [11, 17, 20].

In Fig. 3(a) the thickness of the monocrystalline sublayer is shown as a function of growth temperature for a BEP of 20. The Ga pressure was 4×10^{-7} Torr, the As pressure was then 8×10^{-6} Torr, and the temperature was varied from 180 °C to 210 °C at 10 °C intervals. This graph shows that at 180 °C only a 320 nm thick monocrystalline layer can be grown; when this thickness is exceeded, defects are generated. At a temperature of 200 °C, an approximately 600 nm thick monocrystalline layer can be grown and, at 210 °C, the entire 1 μm thick layer is monocrystalline, *i.e.* the critical thickness is larger than the thickness of the layer. In a previous paper [11], we have shown that increasing the growth temperature decreases the amount of extra As that can be incorporated in the layer. This provides evidence of the relation between As incorporation, straining of the layer, and breakdown of crystallinity: the lower the growth temperature, the more As can be incorporated, and the thinner the layer of high crystalline perfection that can be grown. At a given temperature (here at 200 °C), an increase in the BEP ratio leads to a decrease in the critical thickness, to defect formation (dislocations and stacking faults) and finally to polycrystalline growth. The dependence of the monocrystalline layer thickness on As pressure is shown in Fig. 3(b). This graph demonstrates that the thickness of the defect-free sublayer can be increased, *e.g.* from 320 nm to 1 μm (or presumably even higher), when the BEP (or the growth rate) is reduced [21].

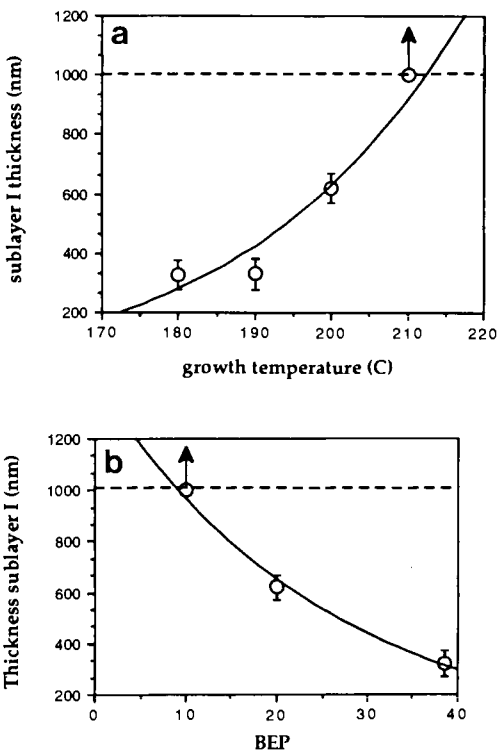

Fig. 3. (a) Thickness of the defect-free layer as a function of growth temperature for a BEP of 20. (b) Thickness of the defect-free layer as a function of BEP for a growth temperature of 200 °C.

Different mechanisms have been already proposed to explain this breakdown of crystallinity [11, 17, 20, 22]: (1) nucleation of misoriented GaAs at strain-induced nucleation sites resulting from the high concentration of As in the layer, (2) low growth temperature, where kinetics factors in MBE may become predominant, and (3) strain which induces As agglomeration on the surface during growth.

The breakdown of monocrystalline growth observed here is due to the strain caused by the excess As incorporated in LT-GaAs. Pseudomorphic growth of strained layers is possible only up to a certain critical thickness, at which the introduction of misfit dislocations, usually by a glide mechanism from the surface down to the strained interface, is thermodynamically favourable. This is required to reduce the strain energy stored in the layer. However, at very low growth tempertures, dislocation mobility is low. When the critical thickness is exceeded, this mechanism cannot operate fast enough so that strain energy has to be released through surface mechanisms. Surface roughening [23] is also likely to occur on these surfaces. This roughness may be a good explanation for the formation of stacking faults, twins, and, later on, pyramidal defects. As atoms can condense directly on (111) facets

with a structure close to that of (0001) planes in hexagonal As. If cubic GaAs grows on the top of As, the mirror symmetry of the basal plane of the latter gives a 50% chance that the GaAs will be twinned with respect to its last orientation. Finally, dislocations which are inevitably formed in the process also change the average growth direction.

2.2. *Annealed LT-GaAs layers*

For LT-GaAs, the concentration of the different antisite defects (which act as middle-gap-type defects) evidenced in the as-grown material falls close to or below the experimental limits on annealing [13], while the material becomes more insulating than before annealing. Although some controversy still exists, the SI properties have been proposed to be related to the presence, after short annealing times, of small precipitates of As in the perfect GaAs crystal. In this connection, the "Schottky barrier model" was proposed by Warren *et al.* [24], to explain the observed SI properties of the LT layers.

Figure 4 is a set of typical images obtained from annealed layers grown at slightly different temperatures. In all these layers, high densities of precipitates are evidenced in TEM images. The total precipitate volume is found to be consistent with the concentration of excess As in the as-grown layers, *i.e.* increases with decreasing temperature. HREM images and associated

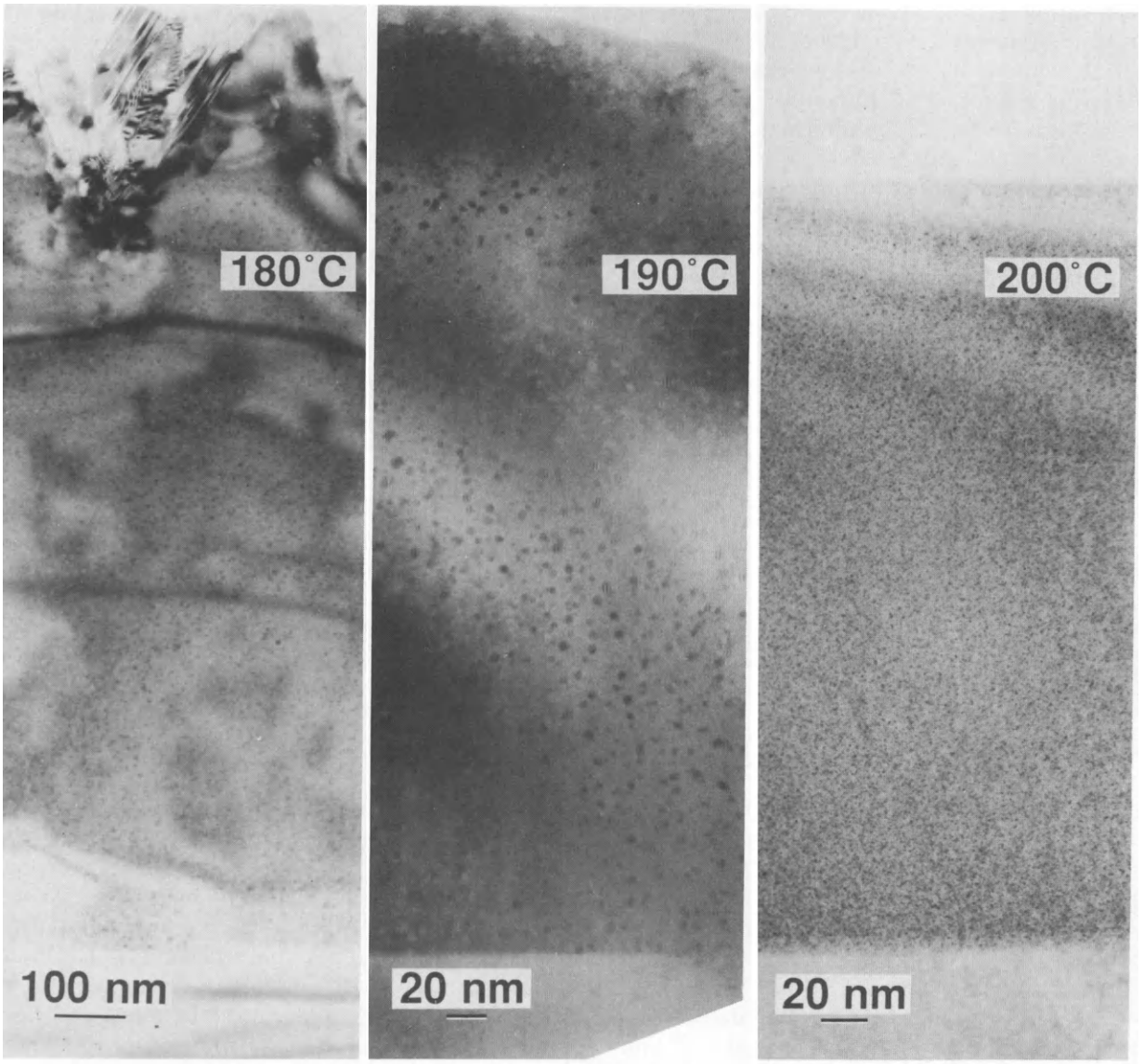

Fig. 4. Set of XTEM micrographs showing the precipitates obtained after the same annealing on samples grown at different temperatures.

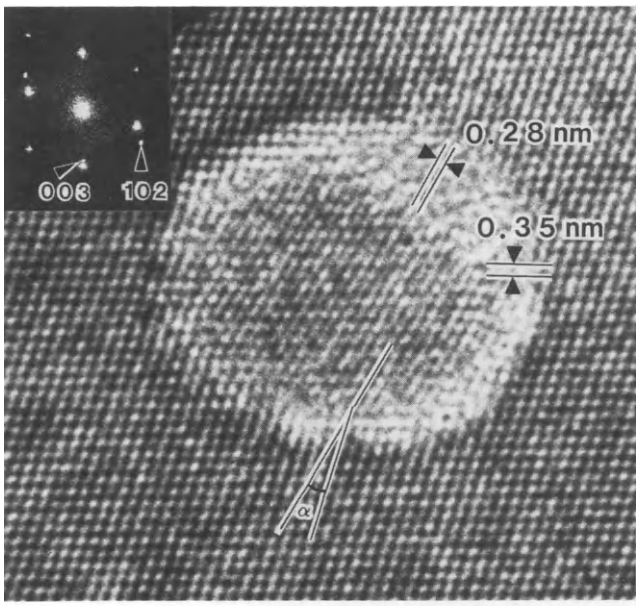

Fig. 5. HREM image of a typical precipitate in $3m$ orientation relationship (OR) with the matrix. The optical Fourier transform is also shown.

Fourier transforms (Fig. 5) clearly show that the structure of the precipitates is rhombohedral (but often referred as to hexagonal As for crystallographic convenience), with a simple relationship: $(0003)_{pp}//(\bar{1}1\bar{1})_m$ and $[\bar{1}2\bar{1}0]_{pp}//[011]_m$. This As structure proves that the precipitates are metallic and that the hypothesis of Warren *et al.* [24] holds. The observed OR is $3m$ and, since it is the highest symmetry attainable by combining cubic and hexagonal structures, it provides the lowest interfacial and elastic energies. It is stable, and any temperature increase will not change it. As expected, four variants of this OR are observed, and they are needed to explain the quite complicated diffraction patterns observed for these samples [25, 26].

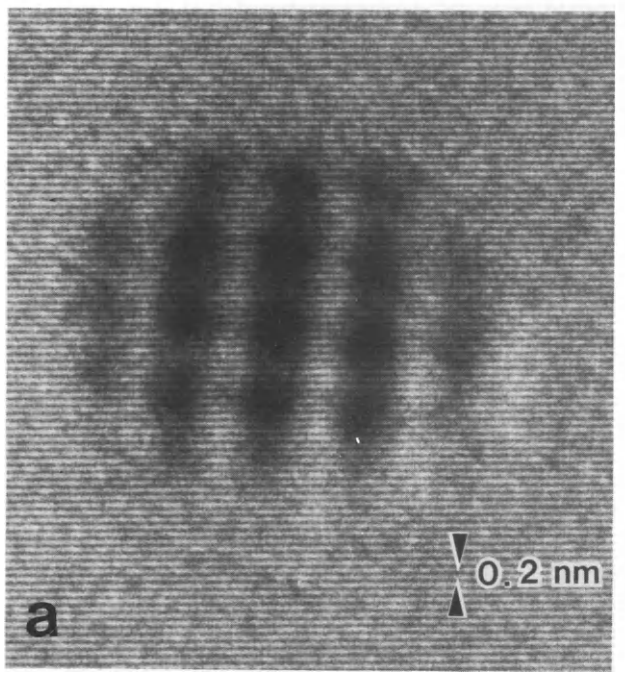

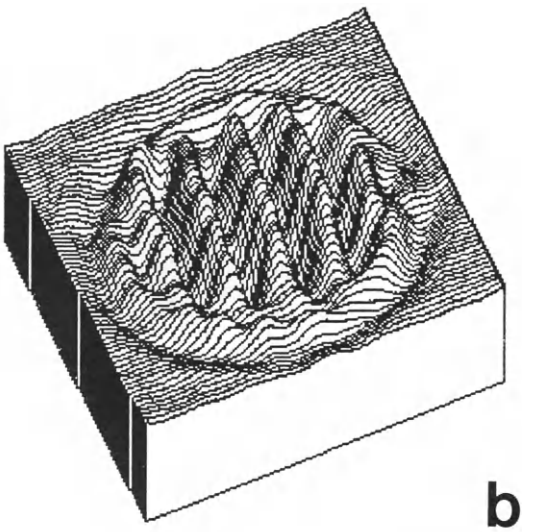

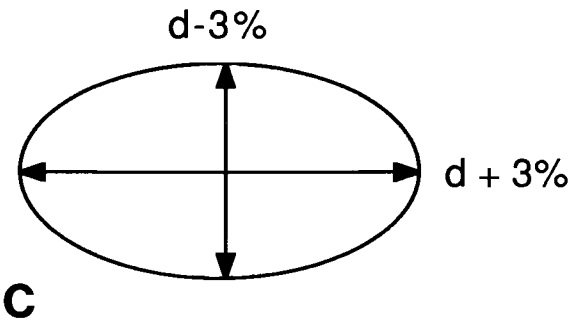

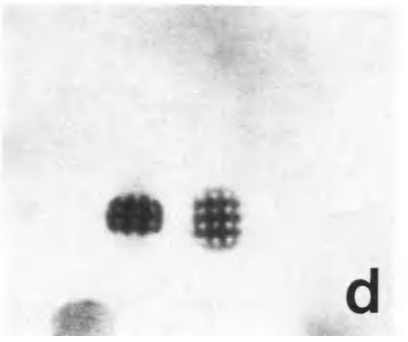

Fig.6. (a) HREM image (800 keV) of a precipitate seen near its ⟨001⟩ projection. When imaging the two sets of moiré fringes, only one set of lattice fringes can be imaged. (b) Microdensitometric traces of the experimental image used for strain measurements. (c) Anisotropic strain revealed within the precipitate. (d) Two variants in orthogonal orientations relieving stress.

Moreover, it can be shown that the precipitates and the surrounding matrix are strained (Fig. 6) but that the overall matrix stress is relaxed from one precipitate to the other owing to the random distribution of the four different variants [26, 27]. This means that an LT layer after annealing can be virtually stress free and that an active device or another LT layer can be grown on the top of it with no problem.

As previously mentioned, depending on growth conditions the crystalline quality of the LT layer may be not as good. Figure 7 depicts such a defective layer after annealing. It was grown at 200 °C but with a high BEP ratio of 40 for a Ga base pressure of 4×10^{-7} Torr. This layer consists of three different sublayers of about 1/3 of the total thickness. From the buffer layer up to the surface, the sublayers are denoted by I, II and III. Sublayer I consists of an otherwise defect-free GaAs monocrystal with almost homogeneous distribution of As precipitates. Only the area adjacent to the lower interface has smaller precipitates. They are hexagonal As precipitates in the $3m$ OR, always found in defect-free layers. At a thickness of about 0.35 μm, the first dislocations appear (sublayer II). They are generally correlated with the presence of larger precipitates, which sometimes exhibit a different OR. Figure 8 shows HREM images of such precipitates in a thick area of the sample. Moiré fringes characteristic of the precipitate spacings are clearly seen. Fourier analysis of these images shows that the structure of these precipitates is also hexagonal but that their ORs are of lower symmetry, *i.e.* 2 *mm* or *m* [18, 22]. Thus, many variants are possible and give rise to different contrasts in images. It is obvious that the presence of these precipitates is related to the dislocations visible in the same regions. The largest precipitates are pinned on dislocations or nodes because these defective regions may provide active sites for nucleation of the As phase. However, because of the special arrangement of atoms in the vicinity of these defects, the cubic symmetry may be lost. As a result, the precipitates grow faster (no or limited incubation stage) and with a high energy (or low symmetry) OR because of the lack of symmetry near the core of a defect. After this transition region, denoted by sublayer II, stacking faults and twin systems on each (111) plane are formed (sublayer III). In this region, similar to that shown in Fig. 1, no As precipitates are seen. Dislocation loops associated with stacking faults and twins are thought to incorporate As directly during growth, and hence precipitation does not occur in their vicinity.

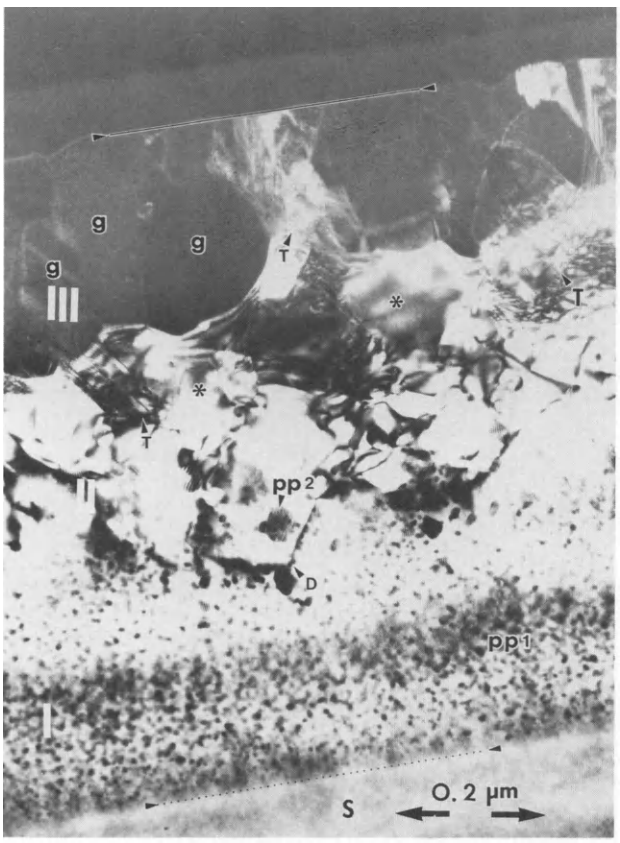

Fig. 7. XTEM image showing an LT layer grown above its critical thickness. There are three distinct regions indicated by I, II and III.

We have recently performed XTEM characterization of monocrystalline LT-GaAs after isochronal annealings at various temperatures [18]. The results are shown in Fig. 9. An intriguing behaviour of the precipitates is seen. While the precipitates increase in size and decrease in density for increasing temperature, as expected for a competitive emission–capture phenomenon, they tend to be depth distributed within layers, while the average distance between these horizontal As-rich layers increases for increasing temperature, *i.e.* for increasing precipitate size. Although not fully explained at the moment, this behaviour is probably linked to charge effects between the depletion regions surrounding the precipitates. This reminds us of the observation of the depth distribution of precipitates in GaAlAs/GaAs structures or in locally doped GaAs [9].

3. LT-InAlAs

The structural quality of ternary compounds, such as $In_{0.52}Al_{0.48}As$ grown at low temperatures on InP, reminds us very much of the structure of LT-GaAs and is described in detail elsewhere [28, 29]. We found that the amount of As incorporated into the layers increases with decreasing temperature, with the crystalline quality of the layers being good for temperatures higher than 200 °C. The layers grown at the lowest

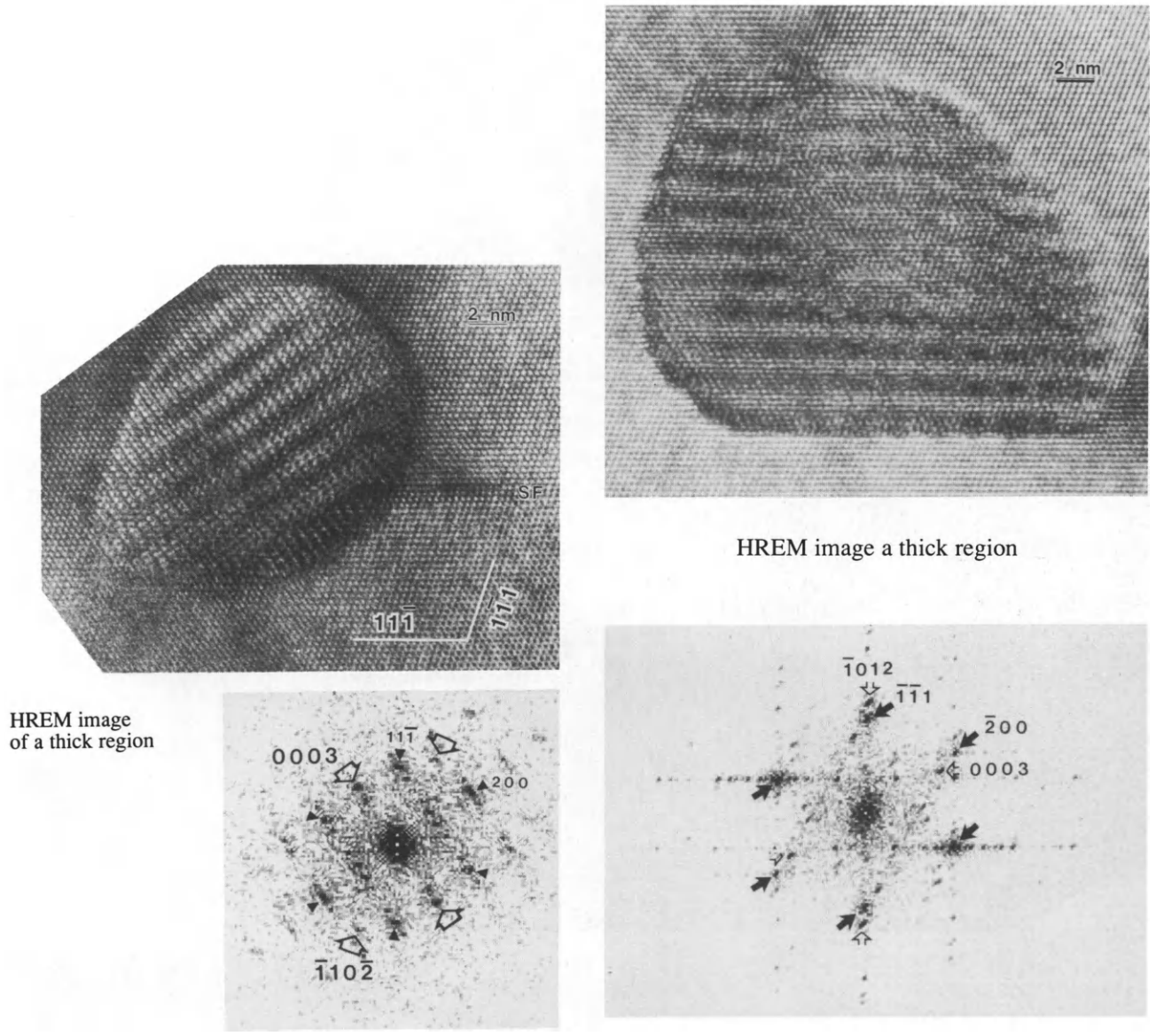

Fig. 8. Large precipitates seen in defective regions with no pyramidal defects for ORs of (a) $2mm$ and (b) m.

temperature (150 °C) have a high density of pyramidal defects, with inclusions of hexagonal As grains (Fig. 10). At 200 °C, however, the amount of excess As is lower than expected, and wavy streaks of diffuse scattering are seen in electron diffraction patterns. These streaks are due to small ordered domains of the CuPt type on the group III atoms. Contrary to LT-GaAs, annealing of these layers does not lead to the formation of As precipitates, but further studies are needed to trace the behaviour of As in $In_{0.52}Al_{0.48}As$ on annealing. We have to note, however, that the shortest recombination times of 400 fs [4] were obtained on samples with pyramidal defects but also with As grains between the defects.

4. LT-InP

In principle, the same route might have been used to fabricate SI-InP, *i.e.* growth at low temperature and P overpressure to include extra group V atoms in the layers. Previous work has shown that it is possible to

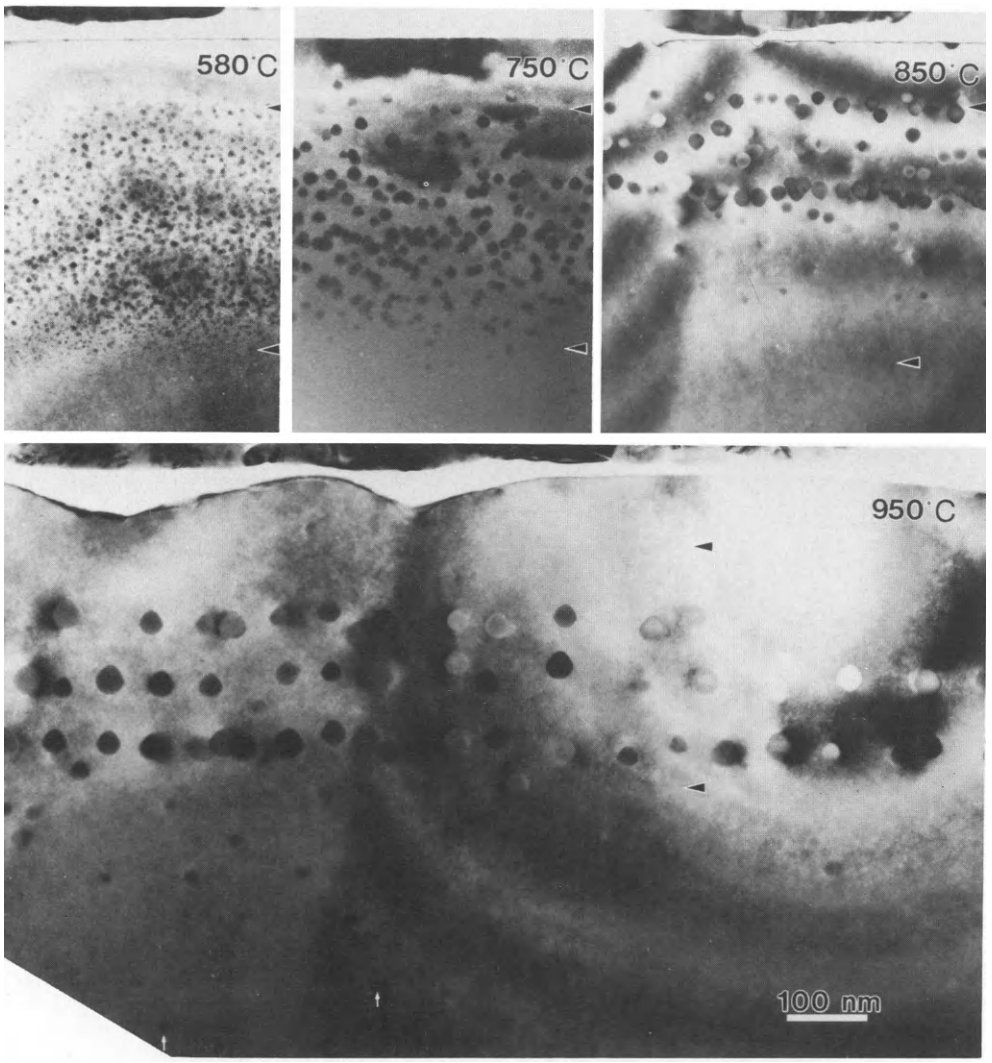

Fig. 9. Isochronal annealing of a GaAs layer grown at 210 °C with a BEP of 20. A cap layer was grown on top of the LT layer (shown by arrows), the same sample was further annealed at temperatures as shown. The depth distribution of precipitates should be noted.

grow monocrystalline layers at growth temperatures in the 170–500 °C range. As observed for arsenides, the lower the growth temperature the larger the amount of excess P in the layer [30]. This incorporation of excess P may result in a polycrystalline or even amorphous layer if the amount of excess P is larger than a certain threshold. This is clearly seen by lowering the growth temperature from 170 °C to room temperature. However, an intriguing fact is that, contrary to GaAs, LT-InP becomes more conductive (n type) [7, 8] when annealed at 600 °C for a few minutes. TEM has been used to study the structural changes that take place in monocrystalline InP grown by GSMBE at low temperature on annealing at about 600 °C. The partial relaxation of the crystal observed by X-rays is due to the formation of small precipitates (3–7 nm) [31]. Electron diffraction experiments show that the structure of these precipitates is cubic, with a simple cube-to-cube OR with the substrate (Fig. 11). Although the various allotropic forms of P, whose space groups are not all determined, make it very difficult to identify their structure, these precipitates are most probably of α white cubic P, which is known to be insulating. This is indeed a very important point, because, in arsenides, rhombohedral As precipitates are indeed metallic and therefore the material exhibits SI properties. While middle-gap defects also exist in as-grown LT-InP samples, they condense on annealing to a non-metallic structure. As a result (possibly), the annealed material turns conductive.

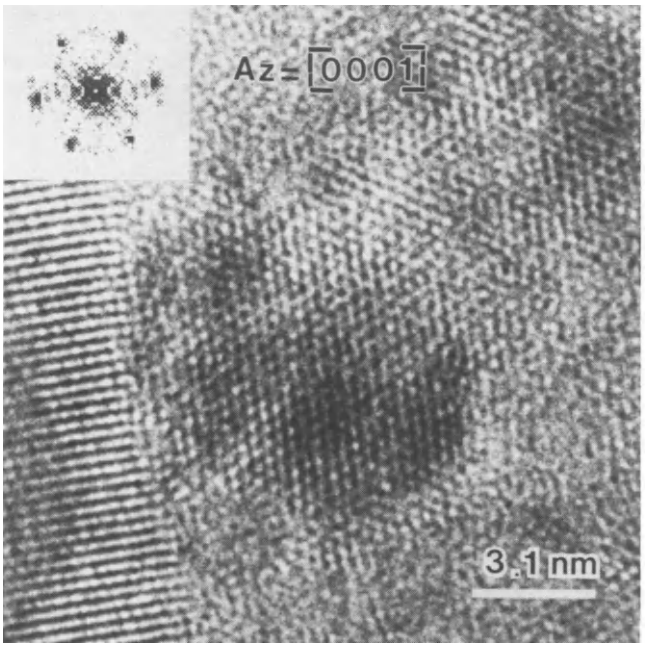

Fig. 10. Small grain of hexagonal As between two InAlAs grains of different orientations. The Fourier transform revealing sixfold symmetry is also shown. The sample was grown at 150 °C and not annealed.

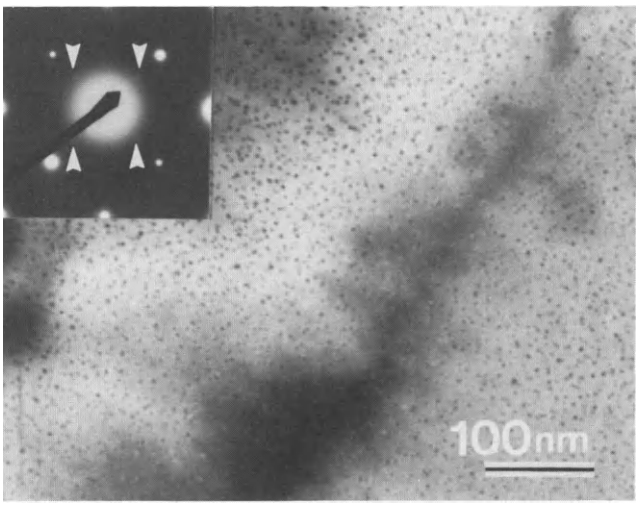

Fig. 11. Uniform distribution of precipitates in LT-InP after annealing at 580 °C for 30 min. The diffraction pattern revealing a cube-to-cube OR is also shown.

5. Conclusions

We have tried to review the main structural characteristics of LT-GaAs, LT-InAlAs, and LT-InP. These materials clearly belong to the same "family" and exhibit almost identical behaviours with respect to growth and annealing conditions. The new properties of these materials are due to their ability to include group V atoms in excess of the regular stoichiometry of the crystals. These excess atoms in both antisite and interstitial positions increase the lattice parameter of the crystal up to a certain threshold that depends on the strain energy already stored in the layer and hence depends on the layer thickness. The only difference with regular mismatched layers lies in the fact that, owing to the low growth temperatures, the usual mechanisms for stress relief, dislocation transfer, and/or formation of misfit dislocations cannot operate. Instead, defects are formed on the surface and develop with further growth of the layers. These defects are called pyramidal defects and are the result of multiple twinning of the structure together with As segregation in the hexagonal structure. On annealing, a large number of these interstitials condense to form precipitates, except in InAlAs, and we do not have an explanation for this. In monocrystalline LT-GaAs and LT-InP layers, the precipitates condense in their stable structures and reach orientations that minimize the interfacial energies. In LT-GaAs, stress in the matrix is relieved through the distribution of precipitate variants. In defective layers, however, precipitation does not occur for too high pyramidal defect densities because As interstitials are not available but are already in a crystalline form. Large precipitates with orientations of lower symmetries are found connected to dislocations, because these defects provide nucleation sites for the excess As to condense.

Since all these structural characteristics dramatically depend on temperature ±10 °C, it is obvious that growth temperatures are not transferable from one laboratory to the next. The same behaviour is expected for electrical or transport properties.

Acknowledgments

This work was partly supported by AFOSR-ISSA-90-0009. The authors would like to thank W. Swider at LBL and J. Crestou at CEMES for the excellent TEM sample preparation. Use of the Facility of the Materials Science Division and the National Center for Electron Microscopy in Berkeley, supported by the US Department of Energy under Contract DE AC03-76SF00098, is greatly appreciated. Thanks are also due to our colleagues, F. W. Smith, A. R. Calawa, R. Mariella, C. Kocot, and W. Schaff for providing us with LT-GaAs samples, S. Gupta, P. K. Bhattacharya, G. Mourou for the InAlAs samples, and J. C. Garcia and J. P. Hirtz at Thomson, France, for the LT-InP materials. Fruitful discussions with E. R. Weber, P. Werner, U. Dahmen,

A. Rocher, and J. C. Bourgoin are greatly acknowledged. A.C. is grateful to NATO for having provided him with financial support during his one-year stay in Berkeley in 1991.

References

1 F. W. Smith, A. R. Calawa, C. L. Chen, M. Manfra and L. J. Mahoney, *IEEE Electron. Device Lett.*, *9* (1988) 77.
2 A. S. Brown, U. K. Mishra, C. S. Chou, C. E. Hooper, M. A. Melendess, M. Thompson, L. E. Larsson, E. S. Rosenbaum and M. J. Delaney, *IEEE Electron Device Lett.*, *10* (1989) 565.
3 K. Mahalingam, N. Otsuka, M. R. Melloch, J. M. Woodall and A. C. Warren, *J. Vac. Sci. Technol. B*, *9* (1991) 2328.
4 S. Gupta, P. K. Bhattacharya, J. Pamulapati and G. Mourou, *Appl. Phys. Lett.*, *57* (15) (1990) 1543.
5 F. W. Smith, H. Q. Le, V. Diaduk, M. A. Hollis, A. R. Calawa, S. Gupta, M. Frankel, D. R. Dykaar, G. A. Mourou and T. Y. Hsiang, *Appl. Phys. Lett.*, *54* (1989) 890.
6 S. Gupta, P. K. Bhattacharya, J. Pamulapati and G. Mourou, *Appl. Phys. Lett.*, *57* (15) (1990) 1543.
7 J. C. Garcia, J. P. Hirtz, P. Maurel, H. J. von Bardeleben and J. C. Bourgoin, *Mater. Res. Soc. Symp. Proc.*, *241* (1992) 277.
8 B. W. Liang, P. Z. Lee, D. W. Shih and C. W. Tu, *Appl. Phys. Lett.*, *60* (17) (1992) 2104.
9 M. R. Melloch, J. M. Woodall, N. Otsuka, K. Mahalingam, C. L. Chang and D. D. Nolte, *Mater. Sci. Eng.*, *B22* (1993) 31 and references cited therein.
10 M. Kaminska, E. R. Weber, Z. Liliental-Weber, T. George, J. B. Kortright, F. W. Smith, B. Y. Tsaur and A. R. Calawa, *J. Vac. Sci. Technol. B*, *7* (1989) 710.
11 Z. Liliental-Weber, W. Swider, K. M. Yu, J. B. Kortright, F. W. Smith and A. R. Calawa, *Appl. Phys. Lett.*, *58* (19) (1991) 2153.
12 K. M. Yu and Z. Liliental-Weber, *Appl. Phys. Lett.*,*59* (1991) 3267.
13 M. Kaminska and E. R. Weber, in E. M. Anastaskis and J. D. Joannopoulos (eds.), *The Physics and Semiconductors*, World Scientific, Singapore, 1990, p. 473.
14 Z. Liliental-Weber, A. Ishikawa, M. Teriauchi and M. Tanaka, *Mater. Res. Soc. Symp. Proc.*, *208* (1991) 183.
15 Z. Liliental-Weber, T. Kaneyama, M. Teriauchi and M. Tanaka, *J. Cryst. Growth*, in press.
16 Z. Liliental-Weber, K. M. Yu and D. Look, *J. Electron. Mater.*, in press.
17 Z. Liliental-Weber, *Mater. Res. Soc. Symp. Proc.*, *198* (1990) 371.
18 Z. Liliental-Weber, *Mater. Res. Soc. Symp. Proc.*, *241* (1992) 101.
19 A. Claverie and Z. Liliental-Weber, unpublished results, 1992.
20 D. J. Eaglesham, L. N. Pfieffer, K. W. West and D. R. Dykaar, *Appl. Phys. Lett.*, *58* (1991) 65.
21 Z. Liliental-Weber, A. Claverie, P. Werner, W. Schaff and E. R. Weber, *Mater. Sci. Forum, Defects Semicond.*, *83–87* (1992) 1045.
22 A. Claverie, Z. Liliental-Weber and E. R. Weber, in A. K. Sreedhar, W. S. Khokle and S. C. Jain (eds.), *Proc. IWPSD, New Delhi, 1992*, p. 120.
23 D. J. Eaglesham, G. Gilmer, D. C. Jacobson, K. West, L. N. Pfeiffer, S. M. Yalisove, D. Adams and O. Karpenko, *Mater. Res. Soc. Symp. Proc.*, *312*, in press.
24 A. C. Warren, J. M. Woodall, J. L. Freouf, D. Grischkowsky, M. R. Melloch and N. Otsuka, *Appl. Phys. Lett.*, *57* (13) (1990) 1331.
25 A. Claverie and Z. Liliental-Weber, *EMSA Proc.*, *1991*, San Fransisco Press, p. 900.
26 A. Claverie and Z. Liliental-Weber, *Philos. Mag. A*, *65* (1992) 981.
27 A. Claverie and A. Rocher, *Proc. EUREM 92, 1992*, p. 109.
28 A. Claverie, K. M. Yu, W. Swider, Z. Liliental-Weber, M. O'Keefe, R. Kilaas and P. K. Bhattacharya, *Appl. Phys. Lett.*, *60* (8) (1992) 989.
29 A. Claverie, Z. Liliental-Weber, P. Wener, W. Swider, P. K. Bhattacharya, S. Gupta and G. Mourou, *Mater. Res. Soc. Symp. Proc.*, *241* (1992) 289.
30 J. C. Garcia, A. Claverie, J. Mimila-Arroyo and J. C. Bourgoin, *Proc. 7th Int. Conf. on Semi-Insulating Materials, Ixtapa, April 1992, J. Cryst. Growth*, in press.
31 A. Claverie, J. Crestou and J. C. Garcia, *Appl. Phys. Lett.*, *62* (14) (1993) 1638.

Interfacial barrier characteristics of LT-GaAs on low doped GaAs layers

K. M. Lipka[a], B. Splingart[a], X. Zhang[a], M. Poese[a], K. Panzlaff[b] and E. Kohn[a]

[a] *Department of Electron Devices and Circuits, University of Ulm, Oberer Eselsberg, W-89069 Ulm (Germany)*

[b] *Department of Optoelectronics, University of Ulm, Oberer Eselsberg, W-89069 Ulm (Germany)*

Abstract

As-grown (σ-conductive) and annealed (semi-insulating (SI)) low temperature (LT)-GaAs/n-GaAs and LT-GaAs/p-GaAs double layers have been analysed by conductivity profiling. The σ-LT-GaAs/GaAs junction represents an N_T^+/GaAs junction with no noticeable depletion effects in the σ-LT-GaAs. The SI-LT-GaAs/GaAs junction is an SI(n^-)-GaAs/GaAs junction with depletion effects in LT-GaAs. The Fermi-level of the LT-GaAs lies in all cases above the n-GaAs free surface potential and is estimated to satisfy $0.18\ \text{eV} < |E_c - E_F| < \Phi_s$.

1. Introduction

GaAs grown at extremely low temperatures (LT-GaAs) contains a large amount of excess As, which occupies mostly Ga sites leading to a high As_{Ga} antisite defect density and a large donor trap density related to the two charge states near midgap [1]. In addition, the presence of acceptor antisite levels has also been reported [2]. Depending on the growth conditions and post-growth annealing the material is either weakly conductive (σ-LT-GaAs) or semi-insulating (SI-LT-GaAs).

It is believed that the carrier transport in as-grown LT-GaAs is caused by thermally activated hopping in an EL2-like deep donor band [3]. The SI properties are explained in two ways: firstly by the compensation of deep acceptor and donor levels [2] and secondly by the formation of overlapping Schottky-barrier-like depletion regions around As precipitates of high density. These precipitates are formed during the post-growth annealing process. Furthermore, the activation of shallow donors and acceptors is inhibited up to high densities [4, 5]. A decrease in the density of antisite defects after annealing has been reported; their final density should, however, still be determined by the solubility limit.

In this way LT-GaAs will in general act like a heavily deep donor doped (N_T^+) material with a Fermi level pinned near midgap and a high free carrier recombination rate. If LT-GaAs is in contact with ordinary GaAs, a depletion layer is therefore expected in p-GaAs as well as in n-GaAs material. However, to n-GaAs the junction should be an n^-/n junction with a fast recombination of those carriers which diffuse from the n region into the n^- region (and which do not therefore contribute to the conduction in the structure), while to p-GaAs a pn junction is expected.

2. Method and experimental procedure

LT-GaAs/GaAs interfacial properties have been investigated by differential etching (Δ etching). In these experiments the differential resistance of LT-GaAs/GaAs double-layer structures was determined by I–V profiling at low fields in the linear regime.

The etching was performed using an NH_4OH:H_2O_2:H_2O solution (1:1:200 by volume) with an etching rate of 130 nm min^{-1}. The etching depth was controlled by a Tencor α-step instrument and the resistance was measured by a Tektronix curve tracer. The mobilities of the doped GaAs layers were obtained by Hall measurements.

In these experiments the following general cases can be distinguished.

(1) If both layers exhibit conductivity of the same type, a monotonic increase in the resistance is expected:

$$R(x) = \begin{cases} \left[\dfrac{W}{L}\left(\dfrac{d_1 - x}{\rho_1} + \dfrac{d_2 - d_1}{\rho_2}\right) + G_{sub}\right]^{-1} & 0 \leqslant x \leqslant d_1 \\ \left(\dfrac{W}{L}\dfrac{d_2 - x}{\rho_2} + G_{sub}\right)^{-1} & d_1 \leqslant x \leqslant d_2 \end{cases} \quad (1)$$

0921-5107/93/$6.00

© 1993 - Elsevier Sequoia. All rights reserved

Here, d_1 and d_2 denote the two layer thicknesses, ρ_1 and ρ_2 the two resistivities and W and L the sample width and length. The conductivity $\sigma(x)$ is easily calculated from the gradient $\mathrm{d}(1/R)/\mathrm{d}x$. The parallel conductance G_{sub} of the SI substrate appears as a small additional constant:

$$\rho^{-1} = \sigma = q\mu n \tag{2}$$

If $\sigma(x)$ is given by the free carrier concentration n (eqn. (2)), and the mobility $\mu(x)$ is known, the shallow donor profile $N(x)$ can readily be calculated.

(2) On profiling through an insulating layer, the resistance will stay constant during etching through this layer.

(3) In case of δ charges in such a structure a stepwise increase in the resistance will be observed at their position.

(4) A more complex behaviour will be expected if the structure includes depletion layers. These regions may be caused by a surface potential and/or by an interface potential as in the case of a pn junction. Of specific interest here are the n^-n and n^-p junctions and in particular the N_T^+-n and N_T^+-p cases.

(a) In the case of an n^-n junction a continuous increase in the resistance will be observed when profiling across the interface owing to a gradual substitution of the interface potential by the surface potential.

(b) In the case of an N_T^+ top layer, because of the high density of N_T, only thin depletion layers and a small deep trap conduction are expected in this layer. In addition to the typical $1/x$ increase in the resistance caused by reducing the undepleted part of this layer, an abrupt change in the resistance will be observed when the top layer is removed and the interface conduction band potential ϕ_{int} is suddenly substituted by the free surface potential ϕ_s. Two cases can be distinguished:

(i) $|\phi_s| > |\phi_{int}|$ resistance increases
(ii) $|\phi_s| < |\phi_{int}|$ resistance decreases

The Fermi level can be assumed in the upper part of the band gap throughout the structure.

(c) In the case of an n^-p junction, the resistance will continuously decrease while profiling through the interface, where the interface potential is gradually replaced by the surface potential.

(d) In the N_T^+p junction case, the resistance will change abruptly following the arguments for the N_T^+n junction. However, now the Fermi level in the N_T^+ layer is located in the upper part of the band gap, whereas the Fermi level in the p material is located in the lower part. Therefore, $|\phi_s| < |\phi_{int}|$ will apply.

Thus, the absence of presence of depletion effects in the upper LT-GaAs layer will tell us whether this material acts predominantly as n^- material or N_T^+ material. In the N_T^+ material case the sudden resistance changes at the interface will enable us to estimate the location of the Fermi level and therefore the band line-up.

3. Device fabrication

The n layers and p layers had been grown in a Riber 32P molecular beam epitaxy (MBE) system on (100) liquid encapsulated Czochralski (LEC) GaAs substrates, using standard GaAs MBE growth parameters. While the p-type GaAs layers had been nominally undoped, the n-type layers were Si doped. LT-GaAs top layers had been grown at 200 °C and 250 °C substrate temperatures, determined from thermocouple readings. The amount of excess As was estimated (on a relative scale) by the lattice mismatch to bulk GaAs, which was obtained by X-ray diffraction. The as-grown LT-GaAs layers were in general σ-LT-GaAs layers.

SI properties of the LT-GaAs had been obtained by annealing at 500 °C for 10 min under an N_2 atmosphere. As outdiffusion had been prevented by GaAs face-to-face annealing. Because of the annealing, As outdiffusion into the underlying GaAs is expected. Therefore thick double layers have been analysed. Since a wide range of conductivities had to be measured, the size of the samples was chosen to be of the order of 1 mm^2.

Contacts were made by Ge–Au evaporation and alloying at 420 °C for 30 s under an N_2 atmosphere. It had been verified by X-ray diffraction that the lattice mismatch between the LT-GaAs and the substrate was not affected. Therefore it was concluded that the material remained its as-grown properties. Before metal deposition, tapered windows were etched through the LT-GaAs layer to ensure that both layers are contacted. These contacts served also as etching masks and an Au overlayer was evaporated onto the contacts for etch protection.

An overview of the investigated structures is shown in Table 1.

4. Results

4.1. LT-GaAs on n-GaAs (sample A)

This sample may represent, although thick layers are used, the case of a metal–insulator–semiconductor field effect transistor structure. The Δ etch resistance profile is shown in Fig. 1(a). Since the conductivity of the n layer is much higher than the conductivity of the LT-GaAs layer, the resistivity of the LT-GaAs cannot be calculated. Therefore both σ-LT-GaAs as well as SI-GaAs appear as insulating layers. Etching into the n-GaAs results in a linear conductivity profile for this

TABLE 1. Investigated structures on an SI LEC GaAs substrate

Samples	A (M97/92) A1: unannealed A2: annealed	B (M32/93) B1: unannealed B2: annealed	C (EM4391) C1: unannealed C2: annealed	D (M74/92) D1: unannealed D2: annealed	Layer
Growth temperature	200 °C	200 °C	260 °C	200 °C	LT-GaAs
Thickness	1.5 μm	1.5 μm	2 μm	1.5 μm	
Lattice mismatch	4.13×10^{-4}		1.18×10^{-4}	2.3×10^{-4}	
Growth temperature	600 °C	600 °C	600 °C	600 °C	GaAs
Thickness	3 μm	1 μm	1 μm	1 μm	
Carrier concentration	$n = 3 \times 10^{16}$ cm^{-3}	$n = 4 \times 10^{15}$ cm^{-3}	$p \approx 10^{13}$ cm^{-3}	$p \approx 10^{13}$ cm^{-3}	
Aspect ratio w/l	1	2	1	2.5	

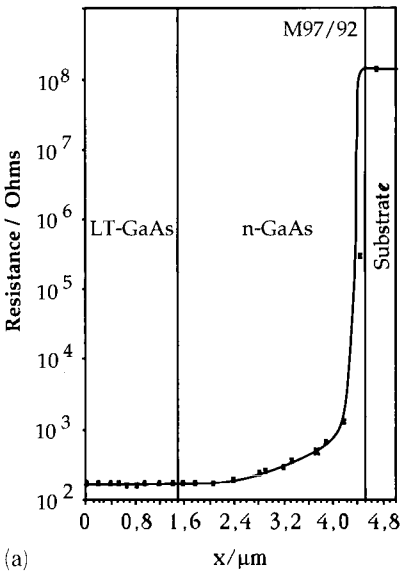

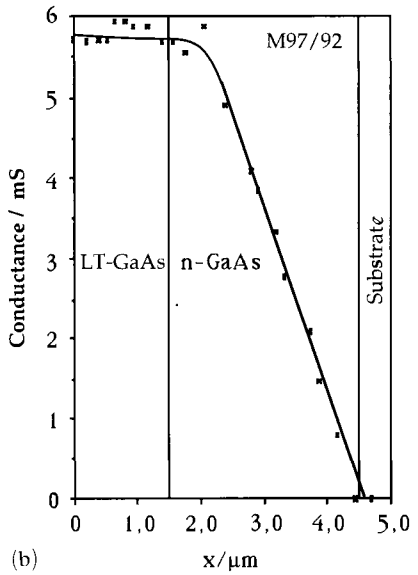

Fig. 1. (a) Resistance profile for sample A1; (b) conductance profile for sample A1.

layer (Fig. 1(b)) from which a constant doping concentration $N = 3.04 \times 10^{16}$ cm^{-3} is extracted, using the Hall mobility $\mu = 4090$ cm^2 V^{-1} s^{-1} (and in agreement with the Hall concentration). At the interface no discontinuity indicative of an interface barrier could be resolved.

4.2. LT-GaAs on n$^-$-GaAs (sample B)

To improve the resolution in the LT-GaAs and at the interface, the doping concentration of the n layer was reduced by roughly one order of magnitude. The profiles of the as-grown sample (B1) and the annealed sample (B2) are shown in Figs. 2 and 3.

4.2.1. σ-LT-GaAs on n$^-$-GaAs (sample B1)

Since the LT-GaAs layer resistance is still difficult to determine, σ has been inferred from layers grown under identical conditions on SI substrates and p$^-$-doped GaAs.

A steep increase in the resistance is observed on profiling across the LT-GaAs–GaAs interface. This steep increase cannot be related to a doping concentration as in the case of Section 4.1. This indicates therefore a sudden depletion by the free surface potential. This is consistent with the fact of σ-GaAs being an only narrowly depleted N_T^+ layer interfacing with the n-GaAs layer with a lower interfacial barrier than that of the free surface (which is estimated to satisfy $|\phi_{int}| < |\phi_s| \approx 0.6$ eV). This indicates a rather shallow location of one of the donor states of the As_{Ga} antisite.

4.2.2. SI-LT-GaAs on n$^-$-GaAs (sample B2)

On profiling this sample, at first no change in resistance is seen as expected for SI-LT-GaAs. However, after approximately 500 nm a gradual increase is observed, followed by a sudden increase after removal of the LT-GaAs layer. Obviously, after etching off 500 nm, the free surface potential reaches through the SI-LT-GaAs into the n$^-$-GaAs layer, gradually depleting

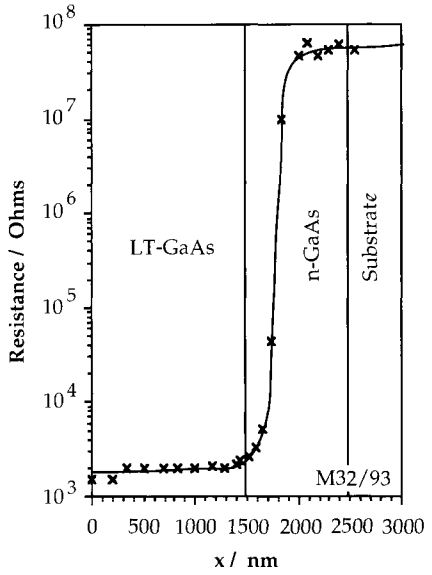

Fig. 2. Profile of sample B1.

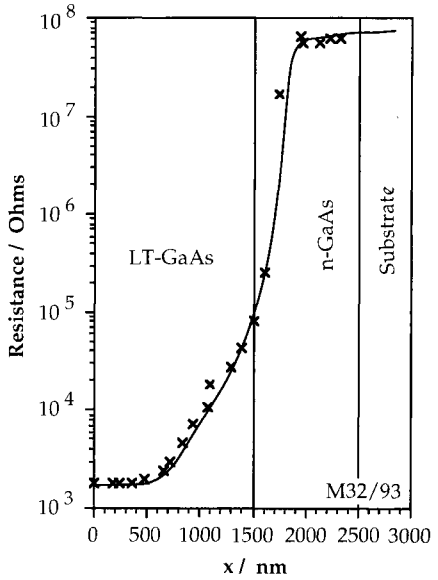

Fig. 3. Profile of sample B2.

this layer until it is totally substituting the interfacial barrier, which is made visible by the sudden resistance increase as also found in sample B1.

This allows the following conclusion to be made.

(1) The SI-LT-GaAs used here acts like an effectively low doped n^- layer, which can partially be depleted of donor charge (which might be shallow or deep).

(2) The interfacial barrier to the n^- layer is again smaller than the surface barrier. This locates the SI-LT-GaAs layer Fermi level in the upper half of the band gap such that $0.18\ \text{eV} < |E_c - E_F| < 0.6\ \text{eV}$.

4.3. LT-GaAs on p^- GaAs (samples C and D)

Two LT-GaAs layers, grown at two different temperatures and therefore different lattice mismatches and excess As contents on nominally undoped p^--GaAs (buffer) layers, were investigated. The net doping concentration $p \approx 1 \times 10^{13}\ \text{cm}^{-3}$. The Fermi level position in the p^--GaAs layer is therefore approximately $|E_F - E_v| \approx 0.35$ eV and the total sheet charge N_s in this layer is approximately $10^9\ \text{cm}^{-2}$.

4.3.1. σ-LT-GaAs on p^--GaAs (sample C1)

The profile for the as-grown sample is shown in Fig. 4. One can see that the total resistance R of the as-grown sample is of the order of $10^8\ \Omega$. While the LT-GaAs layer is etched off, the resistivity increases further by a factor of 2. This translates into a specific σ-LT-GaAs conductivity $\rho = 2.2 \times 10^4\ \Omega$ cm. Despite this low conductivity the layer is not depleted by the surface potential or the interface potential, confirming that it represents a heavily N_T^+-doped layer with hopping-like conductivity (no attempt has, however, been made to determine the exact conductivity mechanism).

When the interface is reached, the conductivity decreases suddenly by an order of magnitude. This means, that the p^--GaAs layer, which was depleted by the interface barrier, becomes suddenly undepleted when in contact with the free surface.

Etching further reveals, a $1/x$ increase in R from which a carrier concentration $p = 5 \times 10^{13}\ \text{cm}^{-3}$ is deduced. This is in good agreement with Hall measurement results on undoped buffer layers, grown under identical conditions.

Etching through the entire structure into the LEC substrate results in a final resistance $R_{sub} \approx 8 \times 10^7\ \Omega$. This is lower than the resistance before profiling and has been obtained consistantly. Thus, the σ-LT-GaAs layer is well shielded from the substrate by a depleted p^- layer.

It is therefore inferred that the interface represents an N_T^+-p^- GaAs junction.

4.3.2. SI-LT-GaAs on p^--GaAs (samples C2 and D2)

Etching the first 1000 nm yields an SI-LT-GaAs conductivity $\rho = 1.5 \times 10^8\ \Omega$ cm, the slope of the resistance profile being slightly positive (Fig. 5). However, on etching further, the slope inverts and the resistance decreases gradually. Thus, the surface potential starts to reach through the SI-LT-GaAs and starts to undeplete the p^--GaAs layer. This behaviour is similar to that of the case in Section 4.2.2. Again, the SI-LT-GaAs layer acts like an effectively low doped layer, which can be depleted of donor charge. Etching further results again in the undepletion of the p^--GaAs layer.

Again, the starting resistance is higher than that for the substrate alone. Thus, here also the LT-GaAs layer is well shielded by the depleted p^- layer.

The same characteristics have been obtained from sample D2 as shown in Fig. 6. In this sample the excess As content in the as-grown sample has been lowered (noticeable from the smaller mismatch). However, after annealing, the layer still converted to the SI characteristics as seen from the resistance profile.

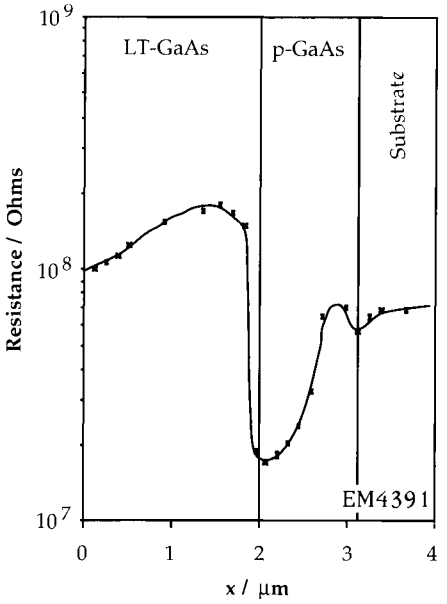

Fig. 4. Profile of sample C1.

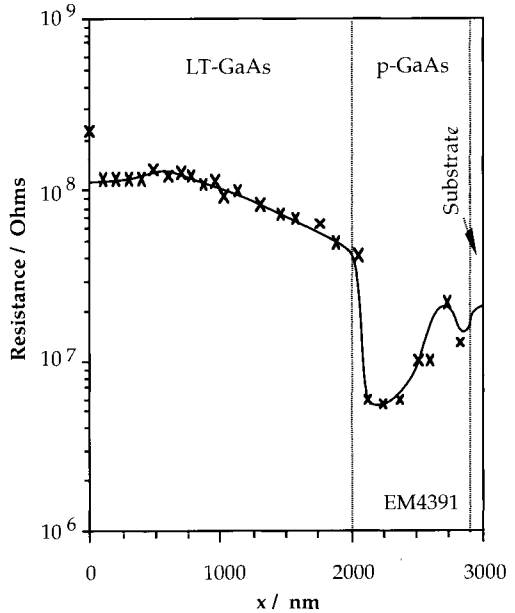

Fig. 5. Profile of sample C2.

5. Discussion and conclusion

The series of experiments shows that LT-GaAs acts as an n-type material. As-grown σ-LT-GaAs is best described as an N_T^+ deep donor doped material. Although having a deep Fermi level position, it is essentially undepleted.

Annealed (under the conditions as listed in Section 3) its resistivity to increases above 10^7 Ω cm. Nevertheless, surface depletion effects as in low doped n-type material are observed. This might be explained as follows. Excess As segregates into clusters and reduces the N_T density. The clusters act as metallic Schottky barriers and deplete most of the volume. A small undepleted volume remains, so that the layer appears overall low doped. However, no major through-connected conduction paths exist. This view is consistent with the observation of free carrier transport through such annealed material [6] and the conclusion that in this case the SI-LT-GaAs was not fully depleted but the resistivity was nevertheless controlled by the As clusters. Recently a Fermi level position for annealed SI-LT-GaAs was inferred at $E_c - E_f = 0.44$ eV [7], which is thought to be the Fermi level position in the neutral regions between neighbouring As precipitates.

It should, however, be noted that during this investigation all data were taken at room temperature and that no attempt had been made to identify the nature of the carrier transport.

The Fermi level position of the material is estimated to satisfy $0.18\ \text{eV} < |E_c - E_F| < \Delta\phi_s$. Assuming a free surface potential $\Delta\phi_s = 0.6$ eV, the Fermi level is

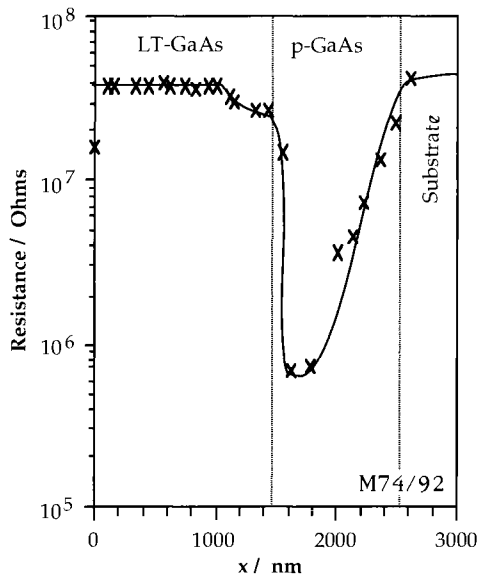

Fig. 6. Profile of sample D2.

estimated to be more then 80 meV above the previously reported position at $E_v + 0.75$ eV [8] and is also estimated to be above the deep level commonly associated with the EL2 As_{Ga} antisite defect. It seems to be controlled by a different charging state of the As_{Ga} antisite defect, being essentially shallower than the EL2 level. This finding of a rather shallow Fermi level position is consistent with mesurements on LT-GaAs passivated or unpassivated n channels, where a higher saturation current is measured before the LT-GaAs passivation is removed (data to be published elsewhere).

On connecting LT-GaAs with low doped n-GaAs, interfacial carrier depletion effects have been observed. A depletion region is formed in the n^--GaAs layer, caused by the outdiffusion of carriers into the LT-GaAs. However, these carriers are lost to the conduction, because they recombine extremely rapidly in the LT-GaAs. The depletion region in the n^--GaAs was determined to be smaller than the depletion region caused by the free surface potential, which leads to the above Fermi level position estimate for LT-GaAs.

When LT-GaAs is contacted to p material the behaviour of a pn junction is seen. In our case the entire p layer is depleted by the interfacial barrier potential. After removing the LT-GaAs and substituting the interfacial barrier potential by the free surface potential, the p layer becomes at least partially undepleted. For this reason the resistance decreased abruptly when profiling through the interface.

σ-LT-GaAs on p-GaAs exhibited the depletion characteristics of an N_T^+ p junction with virtually no depletion in the σ-LT-GaAs but only a small conductivity in this layer. In case of the SI-LT-GaAs/p^--GaAs junction a depletion region is observed in the p-GaAs as well as in the SI-LT-GaAs. In the SI-LT-GaAs materials investigated here, an apparent net carrier concentration n of the order of 10^{16} cm^{-3} is observed.

Acknowledgments

The authors would like to thank H. Grubin (Scientific Research Associate), U. Mishra (UCSB) and D. Theron (IEMN, Lille) for many stimulating discussions, and G. Maracas (ASU) for the first sample of LT-GaAs leading to this project. Many thanks are also expressed to D. Sowada (Department of Optoelectronics, University of Ulm) for the X-ray diffraction measurements. This work was supported by the European Commission ESPRIT project 6849 TAMP-FETS.

References

1 M. Kaminska, Z. Liliental-Weber, E. R. Weber, T. George, J. B. Kortright, F. W. Smith, B.-Y. Tsaur and A. R. Calawa, *Appl. Phys. Lett., 54* (1989) 1881.
2 F. W. Smith, *Mater. Res. Soc. Symp. Proc., 241* (1992) 3.
3 M. Kaminska, E. R. Weber, Z. Liliental-Weber, R. Leon and Z. U. Rek, *J. Vac. Sci. Technol. B, 7* (4) (1989) 710.
4 A. C. Warren, J. M. Woodall, J. L. Freeouf, D. Grischkowsky, D. T. Mcinturff, M. R. Melloch and N. Otsuka, *Appl. Phys. Lett., 57* (1990) 1331.
5 M. R. Melloch, N. Otsuka, J. M. Woodall, A. C. Warren and J. L. Freeouf, *Appl. Phys. Lett., 57* (1990) 1531.
6 M. Kaminska, E. R. Weber, K. M. Yu, R. Leon, T. George, F. W. Smith and A. R. Calawa, *Semi-insulating III–V Materials 2, Toronto, 1990*, p. 111.
7 K. Xie and C. R. Wie, *Mater. Res. Soc. Symp. Proc., 241* (1992) 33.
8 D. C. Look, D. C. Walters, M. O. Manasreh, J. R. Sizelove, C. E. Stutz and K. R. Evans, *Phys. Rev. B, 42* (1990) 3578.

Optoelectronic applications of LTMBE III-V materials

John F. Whitaker

Center for Ultrafast Optical Science, University of Michigan, 2200 Bonisteel Blvd, Rm. 1006, Ann Arbor, MI 48109-2099 (USA)

Abstract

A review of the application of semiconductor layers grown at low substrate temperatures to ultrafast optoelectronics is presented. The films, grown by molecular beam epitaxy primarily around 200 °C and subsequently annealed, are demonstrated to have high resistivity, high mobility, an ultrashort carrier lifetime, and a high dielectric breakdown. This combination of properties makes the low-temperature-grown materials perfectly suited for use in high-speed optoelectronic devices. A number of issues which influence the application of these materials, such as growth temperature, use of an annealing process, layer thickness, and optical wavelength, are considered. Examples of low-temperature-grown semiconductor optoelectronic devices, including ultra-high-bandwidth photoconductive detectors, high-sensitivity, high-bandwidth MSM photodetectors, and optical temporal analyzers are demonstrated. While the discussion concentrates on low-temperature-grown GaAs, the lattice-mismatched ternary compound $In_xGa_{1-x}As/GaAs$ is also considered in the context of detection of the longer wavelengths used in optical communications.

1. Introduction

With the development of technology for future optical communications networks, including soliton transmission in fibres, high-speed laser diodes, fibre lasers and erbium-doped fibre amplifiers comes the suggestion that, within a decade, operating speeds for communications systems will exceed 100 Gbit s^{-1}. This, along with the fact that sources of short-duration optical pulses will be used for ranging, medical imaging, the generation of short bursts of ultraviolet and X-ray radiation, the generation and reception of submillimetre-wave radiation and many other applications, will lead to a significant demand for detectors that can reproduce optical waveforms in the electrical domain. Furthermore, since ultrashort electrical waveforms can be used in the characterization of electronic components such as transmission lines, high-speed devices and integrated circuits, the need for ultrafast response photoswitches [1] which convert d.c. electrical signals to very brief impulses will also be strong. Each of these optoelectronic applications can be best served by a semiconducting material which has a high resistivity, high responsivity (mobility), short carrier lifetime and high dielectric breakdown. When prepared correctly, layers of GaAs and other III–V semiconductors grown by molecular beam epitaxy at low substrate temperatures (*i.e.* LT-GaAs) have been demonstrated to exhibit all of these criteria simultaneously.

The first photoconductive (PC) detectors on GaAs [2] used a substrate doped with chromium and were demonstrated to have carrier lifetimes as short as 100 ps. When excited by sub-picosecond pulsed lasers, transients with rise times of less than one picosecond could be produced from these detectors. Such waveforms, which appeared virtually as step functions on picosecond time-scales (Fig. 1), had spectra with components in the THz regime, and the signals were applied in the qualitative characterization of materials and electronic components such as transmission lines and devices [3, 4]. However, for almost every modern application, from detectors to sampling gates to test-signal generators, the capability of generating a short electrical pulse is required. For optical applications,

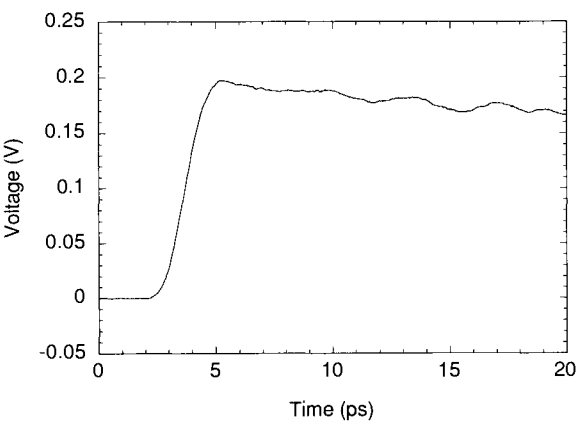

Fig. 1. Photoconductive response of Cr:GaAs. The step-like function is formed due to the long photo-excited carrier lifetime of the semiconductor.

0921-5107/93/$6.00

© 1993 – Elsevier Sequoia. All rights reserved

one wishes to reproduce as faithfully as possible the signal being detected, while for electrical applications, the ability to compute an accurate Fourier transform of a pulsed signal which does not have a long "tail" (which might be corrupted by reflections) is imperative.

A number of approaches have been investigated to achieve short fall times in the response of a detector. These include the identification of photoconductive materials which have very short carrier lifetimes, the fabrication of detector patterns that rely on asymmetric excitation of long carrier lifetime materials [5], and the fabrication of pulse-shaping networks to change the step output of a Cr:GaAs detector into a pulse [6]. Fast-lifetime materials utilized have included amorphous silicon [7], films of CdTe [8], O^+ ion-implanted silicon-on-sapphire (SOS) [9] and proton-bombarded GaAs [10] and InP [11]. While the materials that rely on damage and deep-level trapping/recombination centres for their fast response can have very short lifetimes, they also typically have a poor sensitivity to the energy in the excitation pulses, owing to their low mobilities. The materials with higher mobilities do not have the fastest, sub-picosecond relaxation times. The geometrical approaches to producing short pulses have been moderately successful, although they are arguably more difficult to implement. Historically, despite the deficiencies of radiation-damaged SOS, photoconductive detectors fabricated on this material have been used more than any other source to produce picosecond electrical pulses.

2. Ultrashort carrier lifetime

In the past several years of its development, LT-GaAs has been found to possess characteristics superior to any other photoconductor. Typically, the optimum GaAs layer for optoelectronics is grown by molecular beam epitaxy at low substrate temperatures ($\approx$ 190–210 °C) at a growth rate of 1 μm h^{-1} [12]. This substrate temperature, the group III–V flux ratio, the growth rate, the film thickness and perhaps even other more subtle parameters are all important in determining the growth mechanism and quality of the epitaxial layers. All the GaAs samples represented in this investigation have been grown by Lincoln Laboratory [13] and General Electric [14] using the typical parameters described here and in the references.

Numerous studies have demonstrated that as-grown LT-GaAs contains $\geqslant$ 1% excess arsenic, producing a large concentration of As antisite-related defects (10^{18}–10^{20} cm^{-3}), and that it also has a $\approx$ 0.1% larger lattice constant than its bulk GaAs substrate [15, 16]. The as-grown phase of LT-GaAs is known to have relatively low resistivity and mobility, so that even though it possesses a fast carrier response, it is not an outstanding photoconductor. When annealed (typically at 600 °C for 10–15 min), the LT-GaAs displays a marked decrease in defects, and As precipitates with an average diameter of 60 Å are observed by TEM to form within the single crystal host [13, 14]. The crystallinity of the layer helps to maintain a high mobility, while the overlapping depletion regions of the metallic arsenic precipitates lead to a high resistivity. The material is then in a state that makes it ideal as a photoconductor, since besides its high resistivity and responsivity, it has a fast carrier response from the trapping/recombination sites [17] (perhaps with some contribution from the structural precipitate defects [18]) and a high dielectric breakdown as well [19]. What makes this material truly outstanding as a photoconductor, however, is that when it is optimally fabricated each of the above properties is superior to those of virtually all other materials. This is relevant not only for optical detection applications, but also for the characterization of electronics at the highest possible frequencies, since the $\approx$ 100 fs carrier response of LT-GaAs allows the generation of extremely short duration broadband electrical test signals [20].

Since the carrier lifetime of the LT-grown materials is so short, measurement techniques that have a temporal resolution high enough to characterize this response and the resulting high-bandwidth of LT-GaAs optoelectronic devices are necessary. While time-resolved photoluminescence would seem to be the most direct approach for determining carrier lifetimes, the high density of deep-level defects present in LT-GaAs, along with the high degree of non-radiative recombination of excited carriers in the material, makes this difficult [21]. Two alternative, but well-known, high-resolution characterization techniques are used in the investigations described here: one which measures the optical response of LT-grown materials to excitation by a pulsed laser source, and another which determines the electrical response of a detector fabricated on an LT-grown material and illuminated by a short laser pulse.

The laser source primarily employed here is a solid state mode-locked titanium-doped sapphire (Ti:sapphire) oscillator with 65 fs duration pulses (FWHM), 350 mW average power, and 90 MHz repetition rate. The pulse train from the laser is divided at a beam splitter, with part of the energy going into a pump beam and the rest to a probe beam. The pump pulses excite carriers in the LT-grown material under test through pair-breaking by above-bandgap energy photons. This carrier injection induces an absorption change in LT-GaAs through band filling, band gap renormalization and free carrier absorption [22]. This pump-induced change in absorption, $\Delta\alpha(t)$, and the

corresponding change in reflection, evolve along with the carrier population due to a number of phenomena. Because most of these processes occur on a slow timescale, however, the relaxation decay of the reflection and the transmission (or $\Delta\alpha$) are influenced mainly by trapping/recombination at deep levels [23].

Figure 2 shows the normalized fractional transmissivity changes for two as-grown and two annealed LT-GaAs samples grown at 190 and 200 °C. The carrier lifetime can be determined from the decay of the pulses to $1/e$ of their peak amplitudes. These times are found to be extremely short, between 180 and 260 fs, regardless of whether the material was annealed or not. This, along with other research [17], appears to provide evidence that the fast response of LT-GaAs may not be due to the precipitates, which are present only in the post-annealed material, but that deep levels arising from the excess arsenic or other point or structural defects are mainly responsible. Several studies also confirm that this ultrashort carrier lifetime cannot be sustained as the growth temperature is increased [23]. For instance, by the time growth temperatures are increased only to 250–300 °C, carrier lifetimes measured by this technique are typically > 50 ps.

The second measurement technique mentioned above, external electro-optic sampling (EOS), provides some information about the carrier lifetime of the LT-grown materials, but more importantly it is the only technique which can directly measure the sub-picosecond electrical response of a detector fabricated from LT-GaAs and related materials. It is not possible to resolve accurately an electrical signal having a rise time of less than even 10 ps with any conventional instrumentation available today. However, using short laser pulses and the very fast Pockels effect in an electro-optic probe tip, it is possible to produce a measurement system with a bandwidth of 1 THz [24].

The simplest detectors that are made have a gap within a planar transmission line or between two coplanar lines, fabricated on top of a fast photoconductor. The detector pattern most commonly used is a set of two parallel gold alloy metal lines, 20 μm wide and separated by 20 μm, with a d.c. bias across the lines that is as high as 20–30 V. The lasers pulses, of ≈ 20 μm diameter, uniformly illuminate a spot between the lines to generate the electrical impulses. The electrical signals excited by the pump pulses are coupled from the detector to the transmission line and are readily measured using the EOS probe (Fig. 3). This photoconductive detector has very low capacitance, and thus the limitations on the shortness of the signal which can be generated arise from the duration of the laser pulse used or the lifetime of the photogenerated carriers. Radiation, skin-effect ohmic losses and modal dispersion lead to a rapid degradation of short impulses as they travel down the transmission line between the detector and the probe, however, often limiting the measurements to a resolution of around 500 fs. From Fig. 3 it can be seen that the determination of the carrier lifetime is limited compared with the pump–probe experiment. However, for the measurement of the impulse response of optoelectronic devices, the external EOS technique is invaluable.

3. LT-GaAs photodetectors and photoswitches

The previous section demonstrated that LT-GaAs, whether as-grown or annealed, has a tremendous

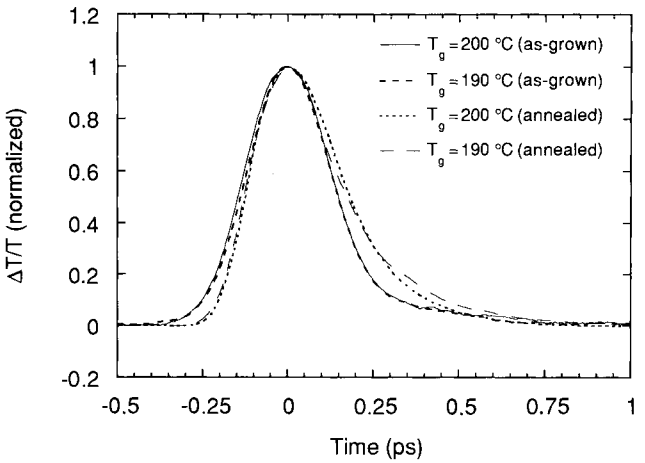

Fig. 2. Normalized fractional transmissivity of as-grown and annealed LT-GaAs layers grown at 190 and 200 °C. The data indicate photo-excited carrier lifetimes of less than 300 fs in each case.

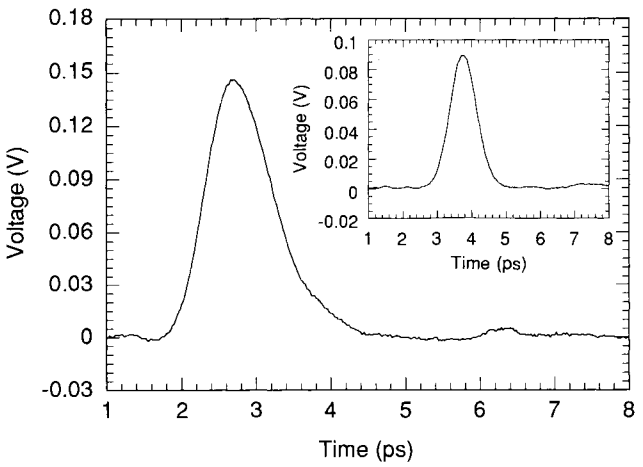

Fig. 3. Typical photoconductive response of simple detector gaps fabricated on annealed GaAs and (inset) as-grown LT-GaAs samples. The pulse widths are less than 1 ps in duration, while the trailing edge returns to the baseline with virtually no tail in a comparable time.

ability to respond to optical signals on a very short time-scale. Besides reproducing as closely as possible the temporal characteristics of an arbitrarily shaped optical signal, however, an ideal photodetector should, in general, be responsive to optical signals that may be very weak and also have a low conductivity or dark current in the absence of illumination. As mentioned in Section 2, the resistivity of the as-grown LT-GaAs layers is relatively low, typically 10^5–10^6 Ω cm, as compared to the resistivity after annealing, which is 10^7–10^8 Ω cm. This leads to higher dark currents in detectors fabricated on unannealed LT-GaAs, as well as lower switching efficiencies and a diminished responsivity. For detector applications, even though a substrate of as-grown LT-GaAs provides a high-bandwidth device (Fig. 3, inset), its high conductivity hinders, and in some cases makes impossible, its use as a photoconductor.

While the most obvious approach is to exclusively utilize annealed LT-GaAs in detectors, several other experimental aspects independent of the annealing conditions have to be considered. The most important of these issues are the thickness of the LT-grown layer being employed in the detector and the wavelength of light that is being detected. For instance, the $1/e$ penetration depth of the 800 nm light is around 1 μm, while that for 630 nm photons from a short-pulse dye laser is only about 0.3 μm. The ramifications for detection using a 1 μm thick layer of LT-GaAs at these two wavelengths are shown in Fig. 4. While the 630 nm light is absorbed only in the LT-grown layer with the short carrier lifetime, the 800 nm light penetrates through the LT-GaAs and into the substrate, resulting in an electrical waveform that has the long lifetime characteristics of intrinsic GaAs, like the behaviour seen in Fig. 1. This indicates that, for detection of long-wavelength light, either a thicker LT-semiconductor layer must be grown, or a thin layer must be lifted off its substrate and grafted onto an insulator. This liftoff and grafting has been demonstrated by several groups [25, 26], and it gives LT-GaAs another advantage over other materials in optoelectronic applications, *i.e.* that a semiconductor with a fast carrier response can be bonded into circuits where a fast photoconductor could otherwise not be located. The high-frequency characteristics of several novel transmission line structures have been determined due to this flexibility of the LT-GaAs layers [27].

The benefits of a detector fabricated on a thicker LT-grown layer are substantiated in Fig. 5. Here the wavelength remains fixed at 800 nm, while detectors fabricated on layers of different thickness, specifically 1 and 4.5 μm, are excited. Again, the penetration of longer wavelengths is found to degrade the response of a detector on a thin LT-GaAs layer. However, with a thick layer of LT-GaAs, the light penetration into the long lifetime substrate is negligible, and the response of the detector is very fast. The switching responsivity of the detectors is also found to be improved, by about a factor of three, when more of the light is absorbed in the LT-GaAs layer, *i.e.* when it is thicker. Therefore, a faster, more sensitive, optoelectronic device is realized when a thicker layer of LT-grown material is used for these simple, straight gap detectors.

The final characteristic of a detector which must be addressed is its ability to detect weak optical signals. Until the development of LT-GaAs, research on high-speed photodetectors concentrated on metal–semiconductor–metal (MSM) Schottky barrier photodiodes, with a device having 105 GHz, 3 dB bandwidth and a

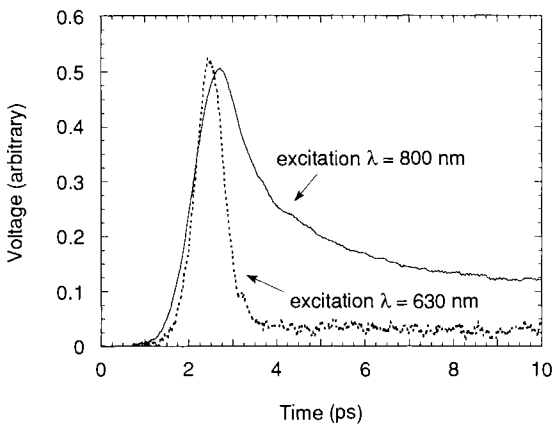

Fig. 4. Photoconductive response of a detector gap fabricated on a 1 μm thick LT-GaAs layer for laser excitation wavelengths of 630 and 800 nm. The longer wavelength penetrates farther into the detector structure, exciting long-lifetime carriers in the intrinsic GaAs substrate.

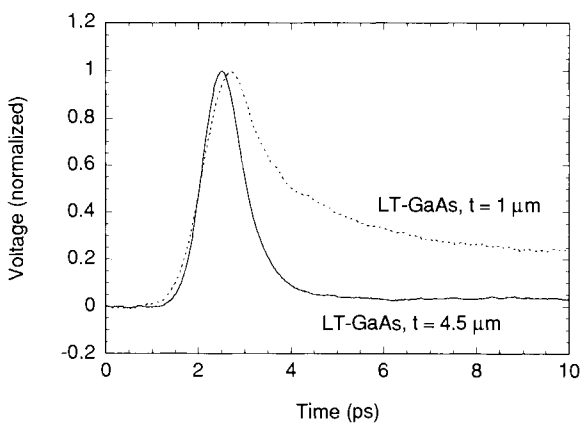

Fig. 5. Photoconductive response of simple detector gaps fabricated on 1 μm and 4.5 μm thick LT-GaAs layers for laser excitation wavelengths of 800 nm. The light is mainly absorbed in the short-lifetime material only when the layer is substantially thicker than the penetration depth.

0.1 A W^{-1} responsivity being the best demonstrated [28]. With the small spacing of interdigitated fingers on this MSM detector, the short transit time of photo-excited carriers allows the metal electrodes to have an enhanced collection efficiency, increasing the conduction current. However, the slow recombination of the carriers in the undoped GaAs substrate and the low mobility of the holes limits the bandwidth of this detector.

When a finely spaced interdigitated pattern—designed so that the transit time is made equal to the carrier lifetime—is fabricated on the high-resistivity, annealed LT-GaAs, a photoconductive detector with a characteristic ultrahigh bandwidth and a responsivity normally associated with a photodiode can be produced. Such an MSM detector fabricated on LT-GaAs with 200 nm finger widths and spacings and an active area of 7 μm × 7 μm is seen in Fig. 6. As with the simple detector gaps, it is defined between two coplanar metal lines. With an incident optical energy of 0.04 pJ $pulse^{-1}$, this LT-GaAs detector has demonstrated a 3 dB bandwidth of 375 GHz with a responsivity of 0.1 A W^{-1}, making it the fastest high-sensitivity detector reported [29]. The dark current at a 1 V bias is 100 pA, and for a higher optical fluence of 22 pJ $pulse^{-1}$ the on-state resistance of the detector is as low as 30 Ω.

This ability to drive the detector to such a low resistance state also allows the interdigitated gaps to be employed as sampling gates. In one investigation [23], two MSM structures were integrated on one wafer of LT-GaAs (Fig. 7, inset), where one behaved as the detector (in the shunt position), and one served as a sampling gate. The standard pump–probe configuration is again utilized, with the delay between the excitation and sampling pulses plotted against the signal amplitude. The MSM detector, which can measure even very weak optical transients, acts as a correlator if both the detected signal and the sampling gate signal are the same (Fig. 7), and as a time domain optical waveform analyzer if the transient illuminating the detector has an arbitrary pulse shape.

4. Low-temperature-grown $In_xGa_{1-x}As$

While all of the detectors reported in this review are excited using laser pulses at $\lambda = 800$ or 630 nm, the main commercial applications for high-speed detectors will be found in the operating regimes of fibre optic communications systems, around 1.3 and 1.5 μm. While LT-GaAs has actually been found to absorb 1.3 μm light [30], it is also desirable to investigate whether other LT-grown materials could be used in high-bandwidth detectors for communications. To reach the bandgap associated with 1.5 μm light, a material such as $In_{0.53}Ga_{0.47}As$, which is sensitive down to 1.7 μm, is needed. Unfortunately, even though $In_{0.53}Ga_{0.47}As$ grown on InP has been demonstrated to have a carrier lifetime of 2.5 ps when grown at 180 °C [23], it has a very low resistivity and thus is not a candidate for use in high-speed infrared detectors. It has been recently discovered, however, that LT-$In_xGa_{1-x}As$ grown lattice-mismatched on GaAs, with InAs mole fractions as high as 35%, does have a moderately high resistivity to go along with a picosecond carrier lifetime [23]. As

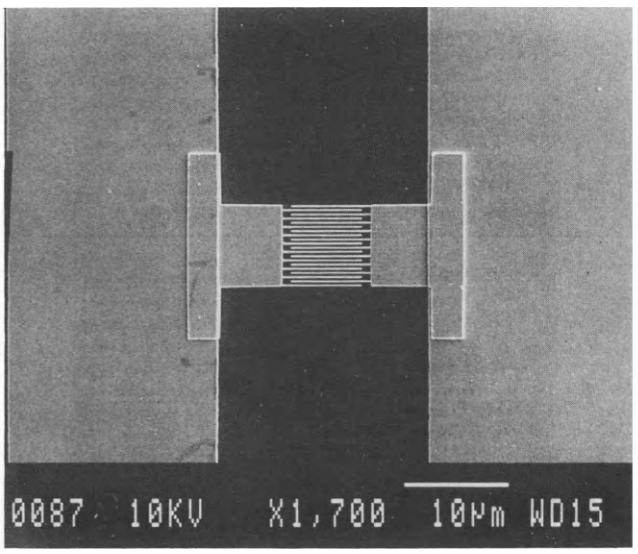

Fig. 6. Interdigitated MSM detector gap on annealed LT-GaAs with finger widths and spacings of 200 nm and area of 50 μm^2 (magnified 1700 ×). Extremely high sensitivities with high bandwidths are combined in this structure.

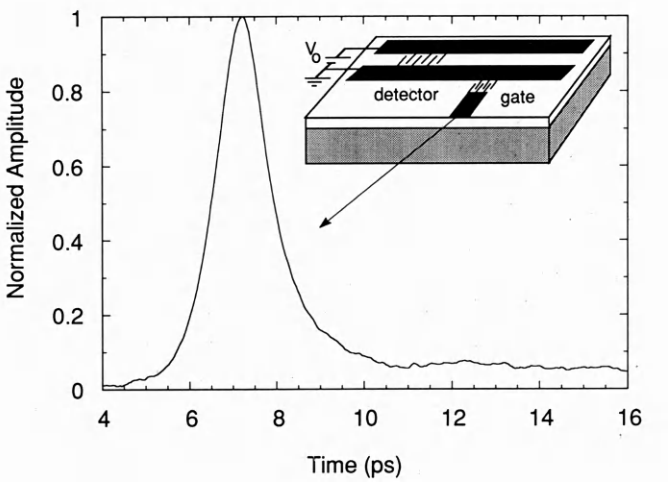

Fig. 7. Electrical response of two interdigitated photoconductive gaps fabricated on annealed LT-GaAs for use as integrated detector and sampling gate (inset). The FWHM response is 1.4 ps.

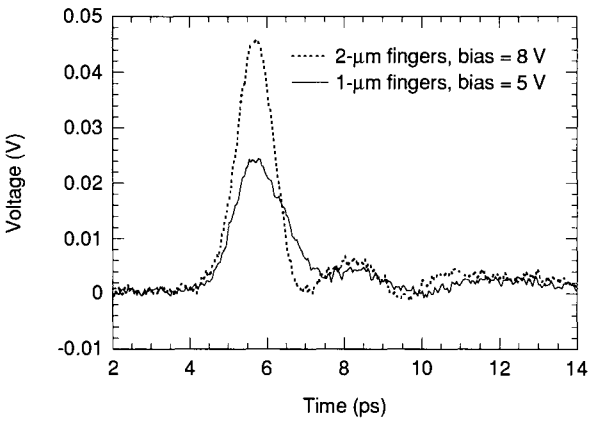

Fig. 8. Photoconductive response of interdigitated detectors fabricated on LT-$In_{0.35}Ga_{0.65}As$ on GaAs, with 1 μm and 2 μm features, for a laser excitation wavelength of 800 nm.

in the LT-GaAs system, the carrier lifetime for the LT-$In_xGa_{1-x}As$ is shortest (≈ 1 ps) at the lowest growth temperatures used (< 200 °C), and it increases (to > 10 ps) at higher growth temperatures (250–400 °C). Annealing of the material also leads to the formation of precipitates, although compared with LT-GaAs, the behaviour of LT-$In_xGa_{1-x}As$ is much more difficult to predict, since the anneal relaxes the strain and some of the structural defects which arise from the lattice mismatch.

Thus far, 1 μm thick layers of LT-$In_xGa_{1-x}As$ having both $x = 0.25$ and $x = 0.35$ have been grown and tested for carrier response and utility as a detector substrate [31]. While the 25% InAs mole fraction material appears to have a resistivity advantage, its bandgap is too large to detect radiation with $\lambda > 1.1$ μm directly. The LT-$In_{0.35}Ga_{0.65}As$ does have a cutoff at 1.3 μm, however, and thus applications are now concentrating on the use of LT-$In_xGa_{1-x}As$ with this composition. In one preliminary experiment using LT-$In_{0.35}Ga_{0.65}As$, an interdigitated pattern having finger widths and separations of 1 μm and an area of 13 $\mu \times 20$ μm was fabricated [31]. The layer used was grown at a temperature of ≈ 125 °C and was thus of poor crystal quality (in fact, it was believed to be amorphous). Nevertheless, a picosecond duration response was observed from this detector (Fig. 8), albeit with a depressed responsivity of 3×10^{-4} A W^{-1}. The fabrication of a larger pattern, having 2 μm finger widths and separations, allowed the use of a larger voltage bias (8 V, or 40 kV cm^{-1}), and thus an even larger detector response was obtained. With optimization of the material properties, and other improvements such as the use of antireflection coatings, it is believed that LT-$In_xGa_{1-x}As$ can form the foundation of a family of long-wavelength, high-sensitivity, high-bandwidth detectors.

5. Conclusions

The behaviour of the carrier lifetime of LT-grown layers, as well as the influence of wavelength, layer thickness, and annealing conditions on LT-GaAs detectors, have been reviewed. The ultrafast carrier response of LT-GaAs and $In_xGa_{1-x}As$ has been demonstrated to be of tremendous utility for high-bandwidth optoelectronic applications. Advanced detection and gating devices based on MSM interdigitated structures fabricated on LT-GaAs have also been shown to have superior performance compared to similar semiconductor devices. The potential for using LT-$In_xGa_{1-x}As$/GaAs in high-speed, long-wavelength detector applications for optical communications systems has also been established.

Acknowledgments

Many past and present staff members and graduate students at the University of Michigan contributed to the work reported here, including S. L. Williamson, S. Gupta, J. A. Nees, T. Brock, G. A. Mourou, H.-H. Wang, H.-J. Cheng, Y. Chen and J. Kim. We thank F. W. Smith of Lincoln Laboratory and J. M. Ballingall of General Electric for their expert preparation of the LT-grown semiconductor films used. This research has been supported by AFOSR contract no. AFOSR-90-0214 (University Research Initiative) and by the National Science Foundation through the Center for Ultrafast Optical Science under STC PHY 8920108.

References

1 D. H. Auston, *Appl. Phys. Lett.*, *26* (1975) 101.
2 C. H. Lee, *Appl. Phys. Lett.*, *30* (1977) 84.
3 T. Y. Hsiang, J. F. Whitaker, R. Sobolewski, D. R. Dykaar and G. A. Mourou, *Appl. Phys. Lett.*, *51* (1987) 1551.
4 M. K. Jackson, M. Y. Frankel, J. F. Whitaker, G. A. Mourou, D. Hulin, A. Antonetti, M. Van Hove, W. De Raedt, P. Crozat and H. Hafdallah, *Appl. Phys. Lett.*, *61* (1992) 1187.
5 D. Krökel, D. Grischkowsky and M. B. Ketchen, *Appl. Phys. Lett.*, *54* (1989) 1046.
6 M. Y. Frankel, S. Gupta, J. A. Valdmanis and G. A. Mourou, *Electron. Lett.*, *25* (1989) 1363.
7 W. C. Nunnally and R. B. Hammond, in C. H. Lee (ed.), *Picosecond Electronics*, Academic Press, Orlando, 1984, p. 373.
8 M. C. Nuss, D. W. Kisker, P. R. Smith and T. E. Harvey, *Appl. Phys. Lett.*, *54* (1989) 57.
9 F. E. Doany, D. Grischkowsky and C. -C. Chi, *Appl. Phys. Lett.*, *50* (1987) 460.
10 B. Lambsdorff, J. Kuhl, J. Rosenzweig, A. Axmann and J. Schneider, *Appl. Phys. Lett.*, *58* (1991) 1881.
11 A. G. Foyt, F. J. Leonberger and R. C. Williamson, *Appl. Phys. Lett.*, *40* (1982) 448.
12 F. W. Smith, S. Gupta, H. Q. Le, V. Diadiuk, M. A. Hollis, A. R. Calawa, M. Frankel, D. R. Dykaar, G. A. Mourou and T. Y. Hsiang, *Appl. Phys. Lett.*, *54* (1989) 890.

13 S. Gupta, M. Y. Frankel, J. A. Valdmanis, J. F. Whitaker, G. A. Mourou, F. W. Smith and A. R. Calawa, *Appl. Phys. Lett., 59* (1991) 3276.
14 H. H. Wang, J. F. Whitaker, A. Chin, J. Mazurowski and J. M. Ballingall, *J. Electron. Mater.*, in press.
15 M. Kaminska, Z. Liliental-Weber, E. R. Weber, T. George, J. B. Kortright, F. W. Smith, B.-Y. Tsaur and A. R. Calawa, *Appl. Phys. Lett., 54* (1989) 1881.
16 A. C. Warren, J. M. Woodall, J. L. Freeouf, D. Grischkowsky, D. T. McInturff, M. R. Melloch and N. Otsuka, *Appl. Phys. Lett., 57* (1990) 1331.
17 Z. Liliental-Weber, H. J. Cheng, S. Gupta, J. F. Whitaker, K. Nichols and F. W. Smith, *J. Electron. Mater.*, in press.
18 A. C. Warren, N. Katzenellenbogen, D. Grischkowsky, J. M. Woodall, M. R. Melloch and N. Otsuka, *Appl. Phys. Lett., 58* (1991) 1512.
19 M. Y. Frankel, J. F. Whitaker, G. A. Mourou, F. W. Smith and A. R. Calawa, *IEEE Trans. Electron. Dev., 37* (1990) 2493.
20 M. Y. Frankel, J. F. Whitaker and G. A. Mourou, *IEEE J. Quantum Electron., 28* (1992) 2313.
21 H. M. van Driel, X.- Q. Zhou, W. W. Rühle, J. Kuhl and K. Ploog, *Appl. Phys. Lett., 60* (1992) 2246.
22 B. R. Bennett, R. A. Soref, and J. A. del Alamo, *IEEE J. Quantum Electron., 26* (1990) 113.
23 S. Gupta, J. F. Whitaker and G. Mourou, *IEEE J. Quantum Electron., 28* (1992) 2464.
24 J. A. Valdmanis and G. Mourou, *IEEE J. Quantum Electron., 22* (1986) 69.
25 E. Yablonovitch, D. Hwang, T. Gmitter, L. Florez and J. Harbison, *Appl. Phys. Lett., 56* (1990) 2419.
26 H. J. Cheng and J. F. Whitaker, in J. Shah (ed.), *Ultrafast Electronics and Optoelectronics*, OSA, Washington, in press.
27 H. J. Cheng and J. F. Whitaker, in *IEEE MTT-S International Microwave Symposium Digest*, IEEE, New York, Vol. 3, 1993, p. 1355.
28 B. J. van Zeghbroeck, W. Patrick, J.-M. Halbout and P. Vettiger, *IEEE Electron. Dev. Lett., 9* (1988) 527.
29 Y. Chen, S. Williamson, T. Brock, F. W. Smith and A. R. Calawa, *Appl. Phys. Lett., 59* (1991) 1984.
30 A. C. Warren, J. H. Burroughes, J. M. Woodall, D. T. McInturff, R. T. Hodgson and M. R. Melloch, *IEEE Electron. Dev. Lett., 12* (1991) 527.
31 L. F. Lester, K. C. Hwang, P. Ho, J. Mazurowski, J. M. Ballingall, J. Sutliff, S. Gupta, J. F. Whitaker and S. L. Williamson, *IEEE Photon. Tech. Lett., 5* (1993) 511.

Subpicosecond electric field dynamics in low-temperature-grown GaAs observed by reflective electro-optic sampling

T. Dekorsy[a], X. Q. Zhou[b], K. Ploog[b] and H. Kurz[a]

[a]*Institute of Semiconductor Electronics, RWTH Aachen, Sommerfeldstr. 24, D-52074 Aachen (Germany)*

[b]*Max-Planck-Institut für Festkörperforschung, Heisenbergstr. 1, D-70506 Stuttgart 80 (Germany)*

Abstract

For the first time we investigate the subpicosecond electric field and coherent LO phonon dynamics in as-grown and post-growth annealed low-temperature (LT) GaAs by reflective electro-optic sampling (REOS) with femtosecond time-resolution. This technique allows a direct observation of the screening of built-in surface fields after pulsed optical excitation of free carriers and the built-up of an electric field due to the different mobilities of electrons and holes (photo Dember effect) in this high resistivity material. After trapping of mobile carriers the decay of the signal gives an accurate measure of the carrier lifetime in trapped states. The observed differences in annealed and as-grown LT GaAs are related to the microscopic form of excess arsenic and the density of point defects. The generation of coherent LO phonons allows the determination of the LO phonon frequency and lifetime in as-grown and annealed LT GaAs. Besides a red-shift of the LO phonon in as-grown LT GaAs we observe an additional local-mode below the LO frequency, which gives evidence for structural defects.

1. Introduction

LT-GaAs has recently attracted interest due to its application in optoelectronic devices, *e.g.* ultrafast optical switches [1] and long-wavelength photodetectors [2]. The fast response of LT-GaAs-based optical switches is closely related to a relatively high carrier mobility and a short mobile carrier lifetime in the subpicosecond time range, as determined from time-resolved luminescence upconversion measurements [3]. This extremely short carrier lifetime is mainly attributed to the trapping of free carriers in As clusters of annealed LT-GaAs. Although the lifetime of mobile carriers can be determined via their radiative decay, the carrier lifetime in the trapped states is not easily accessible using standard methods, such as deep-level transient spectroscopy (DLTS), photoluminescence and photocurrent measurements. Time-resolved reflectivity measurements performed on annealed LT-GaAs also only give information on the mobile carrier lifetime [4]. Knowledge of the carrier recombination rate in trapped states is of great technological importance, since this parameter basically determines the high-frequency performance of LT-GaAs based devices.

We apply reflective electro-optic sampling (REOS) with a time resolution of approximately 50 fs for the investigation of LT-GaAs. REOS is a powerful tool for the investigation of time-dependent electric fields and the carrier transport parameters involved after pulsed optical excitation [5]. In addition, this method is a unique technique for studying the macroscopic polarization associated with coherently generated LO phonons [6]. Since the crystalline quality of as-grown and post-growth annealed LT-GaAs is good enough to exhibit a linear electro-optic effect (Pockels effect), it is possible to detect internal electric field changes directly by a purely optical method.

2. Reflective electro-optic sampling

The REOS technique enables the direct detection of electric field changes perpendicular to the surface of the sample. Signal contributions due to isotropic changes in the refractive index after optical excitation can be ruled out. A pump and a probe beam, both derived from a colliding-pulse mode-locked (CPM) ring dye laser ($E = 2$ eV, $\tau = 50$ fs), are focused nearly collinearly on the LT-GaAs grown on a (100) GaAs substrate (Fig. 1(a)). The probe beam is polarized along the [001] crystal direction. The reflected probe beam is split into its orthogonal components $R_\perp$ and $R_\parallel$ via a polarizing beam splitter (Fig. 1(b)). The amplified difference signal $\Delta R = R_\perp - R_\parallel$ is recorded with a 4 MHz ADC and further averaged with a high-performance computer unit. The temporal resolution is achieved via a time-calibrated retroreflector mounted on a shaker, thus varying the pump to

0921-5107/93/$6.00

© 1993 – Elsevier Sequoia. All rights reserved

probe time delay at a frequency of 50–100 Hz. This technique allows fast averaging over 10^5 scans in approximately 10 min providing a resolution of $\Delta R \approx 10^{-7}$. For large time delays (> 10 ps) we apply a conventional lock-in technique, where the time delay is achieved via a stepper delay stage.

The difference in reflectivity along the $[0\bar{1}\bar{1}]$ and $[0\bar{1}1]$ crystal orientations is directly proportional to the electric field along $z=[100]$, *i.e.* $\Delta R(\Delta t)/R_0 = (n_0^3 r_{41})/(n_0^2 - 1)E_z(\Delta t)$, where R_0 is the unperturbed reflectivity, n_0 is the isotropic refractive index, r_{41} is the electro-optic coefficient of GaAs (1.6×10^{-10} cm V^{-1} for crystalline GaAs [7]) and E_z is the longitudinal surface field.

3. Electric field and carrier dynamics

Our LT-GaAs samples are grown by molecular beam epitaxy at 200 °C. We investigated one as-grown sample and one annealed at 600 °C for 10 min. The decay time of the radiative recombination has been determined to be 1 ps for electrons and holes by luminescence upconversion and correlation spectroscopy in the annealed sample, which corresponds to the time constant for trapping [3]. The REOS signals of annealed LT-GaAs are depicted in Fig. 2 for two different excitation densities. The signals reveal a fast initial rise on the time-scale of the pump pulse, which is caused by fast initial screening of the built-in electric fields. This ultrafast screening generates a burst of coherent phonons within the surface space charge field, which is clearly observed as a periodic modulation.

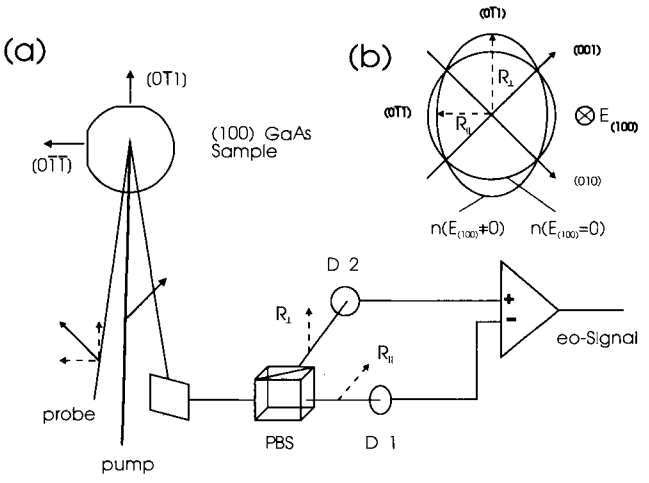

Fig. 1. Experimental REOS setup. (a) Pump–probe geometry with electro-optic sensitive detection (PBS polarizing beam splitter; D1, D2 detectors); (b) optical indicatrix of the (100)-oriented GaAs surface in the case of zero and non-zero longitudinal electric field. $R_\perp$ and $R_\parallel$ are the split components of the reflected probe beam.

The amplitude of this initial field screening is a factor of 2 smaller than the signals of low-doped ($N_D = 10^{16}$ cm^{-3}) crystalline samples [5]. This is a result of the high resistivity of LT-GaAs corresponding to maximum electric field changes of about 20 kV cm^{-1}. We assume only the screening of the surface space charge field set up by Fermi-level pinning to be responsible for the observed field changes, since the field contribution due to multiple overlapping depletion regions of As precipitates [8] within the absorption length contribute with negative and positive signs to the REOS signal. Thus the observed electro-optic field changes are not enhanced due to a large absolute field amplitude, as observed in near-bandgap electro-absorption measurements [9]. The fast decay and sign reversal within the first picosecond is attributed to the build-up of a photo Dember field, which is caused by a higher electron than hole mobility [10]. This effect has not been observed in doped crystalline GaAs at comparable excitation densities, since the screening dynamics of the high electric surface fields is more dominant [5]. The direct temporal resolution of the Dember effect is justified by an analysis of the excitation density dependence of the signals. The ratio of the excitation densities N_1/N_0 is 4. The ratio of the initial field screening is 2, as expected from an $N^{1/2}$ dependence of screening below the saturation density for screening. The ratio of the Dember field contribution is proportional to N_1/N_0 [10]. We confirm the observation of the Dember field by additional c.w.-illumination of the sample, which results in a reduced screening amplitude but no reduction of the Dember field contribution.

4. Carrier lifetime in trapped states

The open question of the carrier lifetime in trapped states is addressed by the measurement of the decay of

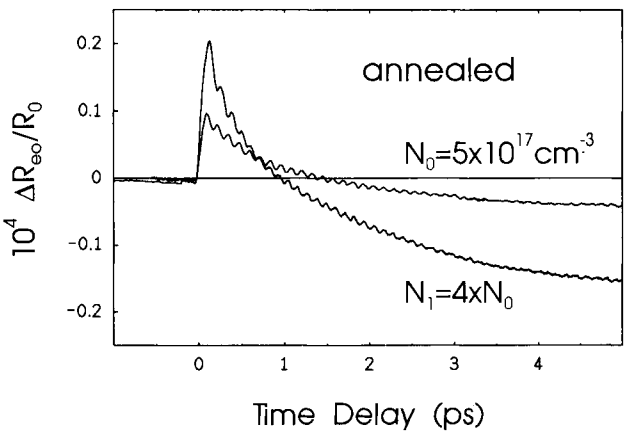

Fig. 2. REOS signals of annealed LT-GaAs at the excitation densities of 5×10^{17} cm^{-3} and 2×10^{18} cm^{-3}.

the REOS signals after the transport dynamics are frozen out, due to trapping of mobile carriers, and the electric field evolves towards its unperturbed value. As shown in Fig. 3, the signal decay of the as-grown sample is clearly mono-exponential, with $\tau = 125 \pm 2$ ps. The annealed sample exhibits two time constants, $\tau_1 = 7 \pm 2$ ps and $\tau_2 = 160 \pm 10$ ps, as determined from numerical fits to the data. These time constants are independent of the excitation density in the range 5×10^{17} cm^{-3} to 2×10^{18} cm^{-3}. We attribute the slow time constant in both samples to carrier recombination in As_{Ga} antisites, which is influenced by the lower point defect density in the annealed sample. The fast recombination rate in the annealed sample is related to the recombination in As clusters of metallic character.

5. Coherent LO phonon dynamics

Coherent LO phonons are generated by ultrafast initial field changes on a time-scale shorter than the LO phonon period (≈ 113 fs) and are observed as a periodic modulation of the signals [6]. Analysis of the decay of the oscillatory signal part gives the LO phonon lifetime and frequency, which both reveal details of the crystalline quality of the samples. Figure 4 depicts the Fourier spectra of the time-resolved coherent oscillations. The annealed sample exhibits an LO mode centred at 8.78 THz (292.7 cm^{-1}), which is close to the Γ_{15}-LO phonon frequency in crystalline GaAs. This underlines the good crystalline quality of annealed LT-GaAs. The spectrum of the as-grown sample exhibits a large red shift of the LO phonon of 0.09 THz (3 cm^{-1}), due to a reduction of the displacement field of the LO phonon. The observed red shift in our sample is 6 times larger than the recently reported one [11] and is related to the higher excess arsenic in our sample. Additionally, we observe a mode at 8.4 THz (280 cm^{-1}) in as-grown LT-GaAs, which vanishes after annealing. This mode is attributed to a local mode of amorphous arsenic [12]. The TO phonon is not excited by the ultrafast field screening mechanism responsible for the coherent phonon excitation.

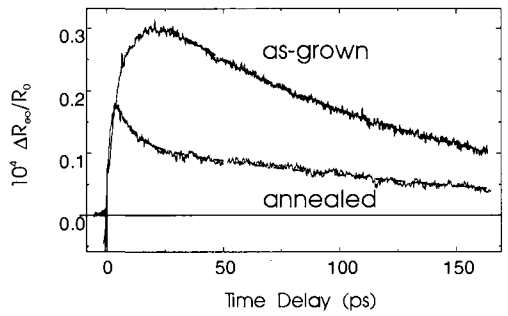

Fig. 3. Long delay time REOS measurements on annealed and as-grown LT-GaAs. The dashed curves (----) are numerical fits to the data.

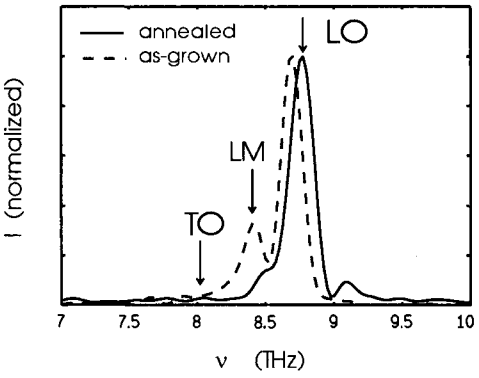

Fig. 4. Fourier spectra of coherent phonon signals from annealed and as-grown LT-GaAs. The arrows indicate the spectral position of the TO and LO phonons in crystalline GaAs, and of the local mode in as-grown LT-GaAs.

6. Conclusions

We have reported for the first time on picosecond and sub-picosecond dynamics of electric fields, carrier lifetimes and coherently excited LO phonons in LT-GaAs observed via reflective electro-optic sampling. We found a superposition of screening and the photo Dember effect in the transport dynamics of high-resistivity annealed LT-GaAs. The recombination of carriers in trapped states is observed via the evolution of the electric field towards its unperturbed value. For as-grown LT-GaAs we observe a strict mono-exponential decay of 125 ps, due to recombination at As_{Ga} antisites. For annealed LT-GaAs the presence of an additional short time constant of 7 ps is related to the presence of As precipitates. We estimate the high-frequency performance of LT-GaAs based devices to be in the range of 5 GHz. The analysis of coherent LO phonon dynamics gives evidence for structural defects in as-grown LT-GaAs like As_{Ga} antisites and amorphous arsenic. In conclusion, REOS is a highly promising technique for the characterization and future development of low-temperature-grown III–V compounds.

References

1 S. Gupta, P. K. Battacharya, J. Pamaulapati and G. Mourou, *Appl. Phys. Lett.*, *57* (1990) 1543.
2 A. C. Warren, J. H. Burroughs, J. M. Woodall, D. T. McInturff, R. T. Hodgson and M. R. Melloch, *IEEE Electron. Device Lett.*, *EDL-12* (1991) 527.

3 X. Q. Zhou, H. M. van Driel, W. W. Rühle, Z. Gogolak and K. Ploog, *Appl. Phys. Lett., 61* (1992) 3020.
4 S. Gupta, M. Y. Frankel, J. A. Valdmanis, J. F. Whitaker, G. A. Mourou, F. W. Smith and A. R. Calawa, *Appl. Phys. Lett., 59* (1991) 3276.
5 T. Dekorsy, T. Pfeifer, W. Kütt and H. Kurz, *Phys. Rev. B, 47* (1993) 3842.
6 T. Pfeifer, T. Dekorsy, W. Kütt and H. Kurz, *Appl. Phys. A, 55* (1992) 482.
7 A. Yarif, *Introduction to Optical Electronics*, Holt, Rinehart and Winston, New York, 1971.
8 A. C. Warren, J. M. Woodall, J. L. Freeouf, D. Grischkowsky, M. R. Melloch and N. Osuka, *Appl. Phys. Lett., 57* (1990) 1331.
9 D. D. Nolte, M. R. Melloch, J. M. Woodall and S. J. Ralph, *Appl. Phys. Lett., 62* (1993) 1356.
10 T. S. Moss, *Optical Properties of Solids*, Butterworth Scientific, London, 1959.
11 T. A. Grant, H. Shen, J. R. Flemish, L. Fotiadis and M. Dutta, *Appl. Phys. Lett., 60* (1992) 1453.
12 R. J. Nemanich, G. Lucovsky, W. Pollard and J. D. Joannopoulos, *Solid State Commun., 26* (1978) 137.

Materials Science and Engineering, B22 (1993) 72–77

Applications of GaAs grown at a low temperature by molecular beam epitaxy

Umesh K. Mishra
ECE Department, University of California, Santa Barbara, CA 93016 (USA)

Abstract

GaAs based semiconductors grown at low temperature by molecular beam epitaxy have several interesting properties which can be exploited for a variety of applications, both electronic and opto-electronic. The material exhibits a range of resistivity from highly conductive to highly resistive based on the growth temperature and subsequent annealing temperature. The most important applications of low-temperature-grown (LTG) GaAs and AlGaAs use the highly resistive form of the material. This paper summarizes the applications of LTG (Al)GaAs in microelectronics.

1. Electronic materials properties

The material characteristics of low-temperature-grown (LTG) GaAs have been studied by various groups owing to its potential application as a semi-insulating epitaxial layer [1]. The growth of GaAs at about 200 °C by molecular beam epitaxy (MBE) is highly non-stoichiometric with approximately 1%–2% excess arsenic being incorporated in solid solution during growth [2]. Following high temperature anneals (at about 600 °C) the excess arsenic forms precipitates embedded in the GaAs matrix [3]. Amongst other interesting properties, the annealed material is found to be highly resistive. In one model, the high resistivity is explained qualitatively by viewing arsenic precipitates as buried Schottky barriers (BSB) with overlapping depletion regions [4]. This attractively simple model is supported indirectly by the activation of dopants following precipitate coarsening at high temperatures [5]. The metallic nature of the precipitates is also supported by recent scanning tunneling microscopy results [6]. For such a model, the transport properties should quantitatively reflect the observed microstructural features. By combining the temperature dependence of I–V data with microstructure data obtained by transmission electron microscopy (TEM), Ibbetson *et al.* [7] showed that transport in annealed LTG GaAs is consistent with thermally assisted tunneling of electrons from metallic As precipitates. The temperature of growth and the anture of the anneal is found too crucial in determining the magnitude of current transport through the LT GaAs. A simple one-dimensional calculation (no fitting parameters) is found to agree well with the experimental data.

To study transport at high fields, an n^+/LTG-i/n^+ structure was used, as shown in Fig. 1. The LTG layer was grown at 230 °C. The sample was cleaved and annealed separately in a rapid thermal annealer for 30 s at 600, 650, 700 and 750 °C. A mesa structure diode was fabricated, with alloyed AuGe/Ni/Au contacts.

The results are summarized in schematic form in Fig. 2. There is evidence for two transport mechanisms. At low temperatures (below 200 K) the temperature dependence of the I–V data is attributed to defect-associated hopping conduction. This behavior has previously been shown to dominate the transport in unannealed LTG GaAs [8]. This result suggests that there is a significant residual concentration of point

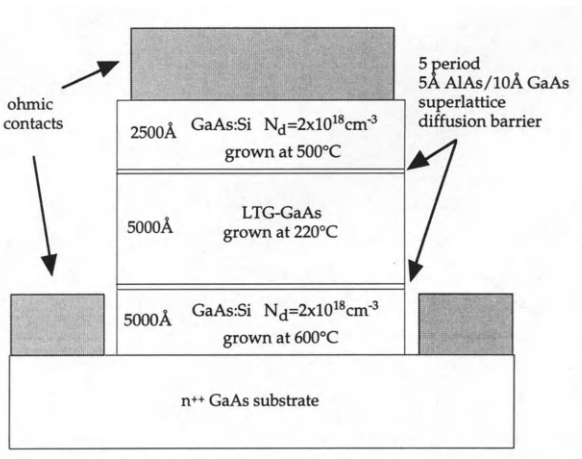
ohmic contacts
5 period 5Å AlAs/10Å GaAs superlattice diffusion barrier
2500Å GaAs:Si N_d=2x10^{18}cm^{-3} grown at 500°C
5000Å LTG-GaAs grown at 220°C
5000Å GaAs:Si N_d=2x10^{18}cm^{-3} grown at 600°C
n^{++} GaAs substrate

Fig. 1. Schematic diagram of the growth architecture used to study transport through LTG GaAs annealed at different temperatures.

0921-5107/93/$6.00

© 1993 – Elsevier Sequoia. All rights reserved

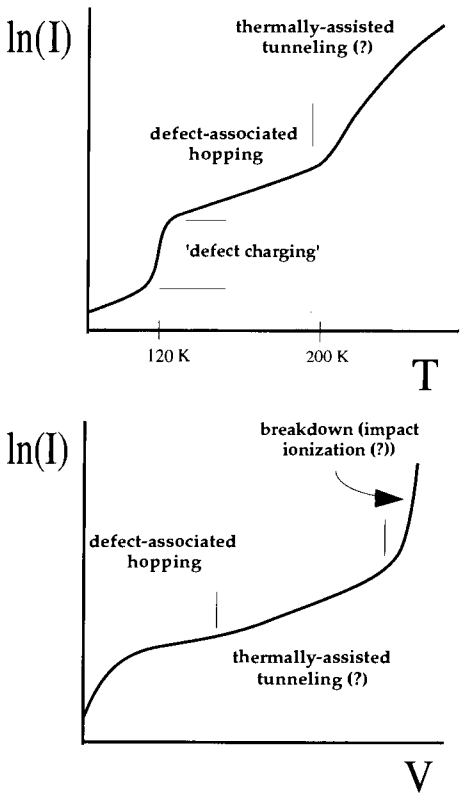

Fig. 2. Schematic diagram summarizing data obtained from I–V measurements as a function of temperature. Behavior attributed to hopping conduction associated with point defects is observed in all samples. The high temperature (above 200 K) behavior is consistent with tunneling emission from metallic As precipitates.

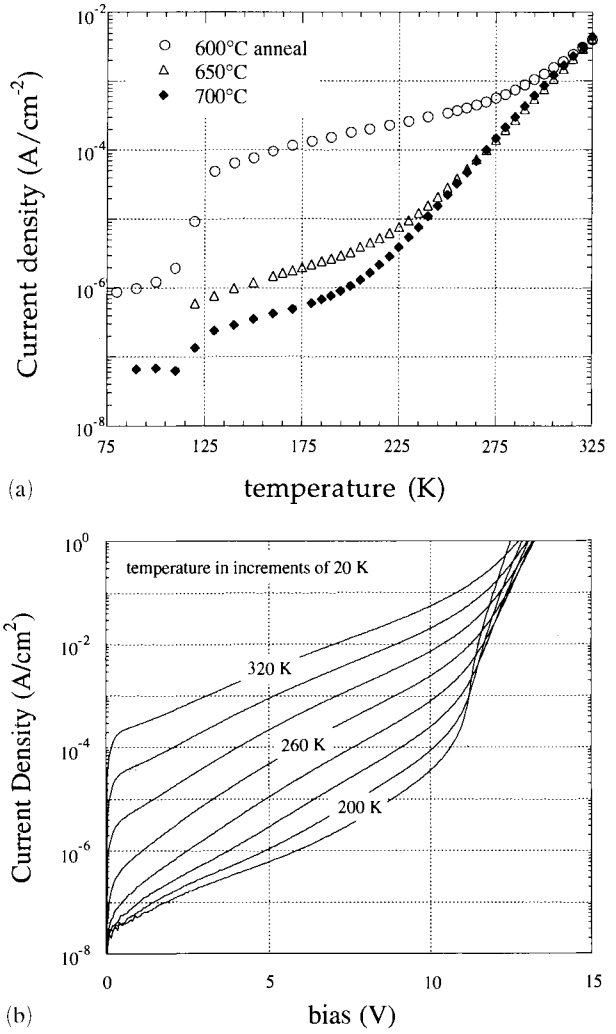

Fig. 3. (a) Current measured at 5 V bias as a function of temperature for samples annealed at 600, 650, and 700 °C. As the annealing temperature increases, the contribution due to hopping conduction decreases. (b) I–V measurements taken at various temperatures (200–320 K) for the sample annealed at 700 °C. For $T > 200$ K hopping conduction is negligible and the current is exponentially dependent on the applied bias.

defects in the LTG GaAs layer that has not precipitated out of solution even for annealing temperatures as high as 750 °C. Indeed, for the sample annealed at 600 °C, hopping conduction dominates the transport for nearly all measurement temperatures. Figure 3(a) shows the temperature dependence for samples annealed at different temperatures. As expected, the hopping conduction contribution to transport decreases as T_{anneal} increases, consistent with continued precipitation of As-related point defects.

Except for the sample annealed at 600 °C, transport at temperatures above 200 K is clearly dominated by a mechanism other than hopping conduction. In Fig. 3(b) the I–V data at various $T > 200$ K for the sample annealed at 700 °C are summarized. The current exhibits an approximately exponential dependence on the voltage, suggesting transport over a potential barrier, which in the model is assumed to be the barrier between the As precipitates and the GaAs. Assuming that the precipitates are metallic, the one-dimensional band diagram for the structure is shown in Fig. 4, showing an equivalent single junction, which is essentially two back-to-back Schottky diodes. Figures 4(a) and 4(b) show the relevant junction parameters such as barrier height ϕ_b and average junction width D for zero and non-zero applied bias respectively. The average junction width can be measured by TEM. For the sample annealed at 700 °C, TEM analysis yielded a precipitate density of 1.7×10^{16} cm^{-3}, and an average precipitate diameter of 107Å, from which an average junction width of 285 Å was obtained. Since even a relatively high residual doping of 1×10^{18} cm^{-3} results in a maximum band-bending between Schottky barriers of only approximately 0.1 eV, it is reasonable to neglect free carrier conduction in the material between precipitates.

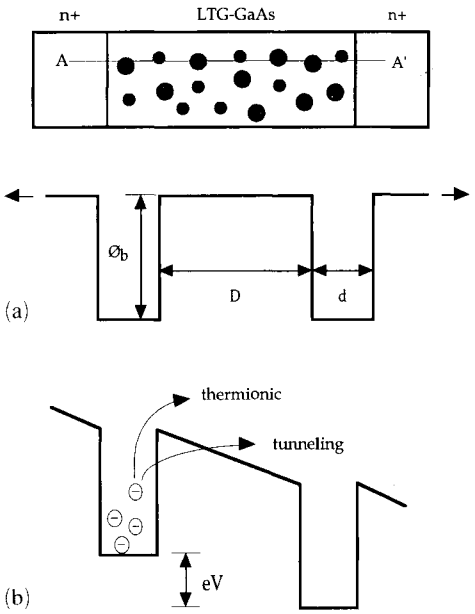

Fig. 4. Schematic diagram showing the one-dimensional potential energy profile assuming the As precipitates act as buried Schottky barries at (a) zero bias, and (b) non-zero bias. In this model the LTG GaAs is a series of metal/semiconductor/metal junctions, and current flow is due to thermionic emission and tunneling emission from the As precipitate.

The current through the reverse biased Schottky barrier taking into account both thermionic emission over the barrier and tunneling emission below the barrier tip is given by [9]

$$J = \frac{qmkT}{2\pi h^3} \int_0^\infty \exp\left(-\frac{E}{kT}\right) P(E,\varepsilon)\, dE$$

where $P(E,\varepsilon)$ is the transmission probability for an electron with energy. E. $P(E,\varepsilon)$ explicitly contains the field dependence since the potential energy profile of the barrier changes with the applied field and is calculated numerically based on tranmission matrices. Figure 5(a) shows the calculated and experimentally obtained current as a function of the junction field at 300 K for a barrier height of 0.6 eV, and the temperature dependence of the current is shown in Fig. 5(b) illustrating good agreement between the model and the experimental data.

2. Applications

The properties of LTG material that have been found to be the most useful are the relatively high electron mobility, extremely low lifetime and the extremely high resistivity. The first two properties lead to a fast rise time and extremely fast fall times for electronic

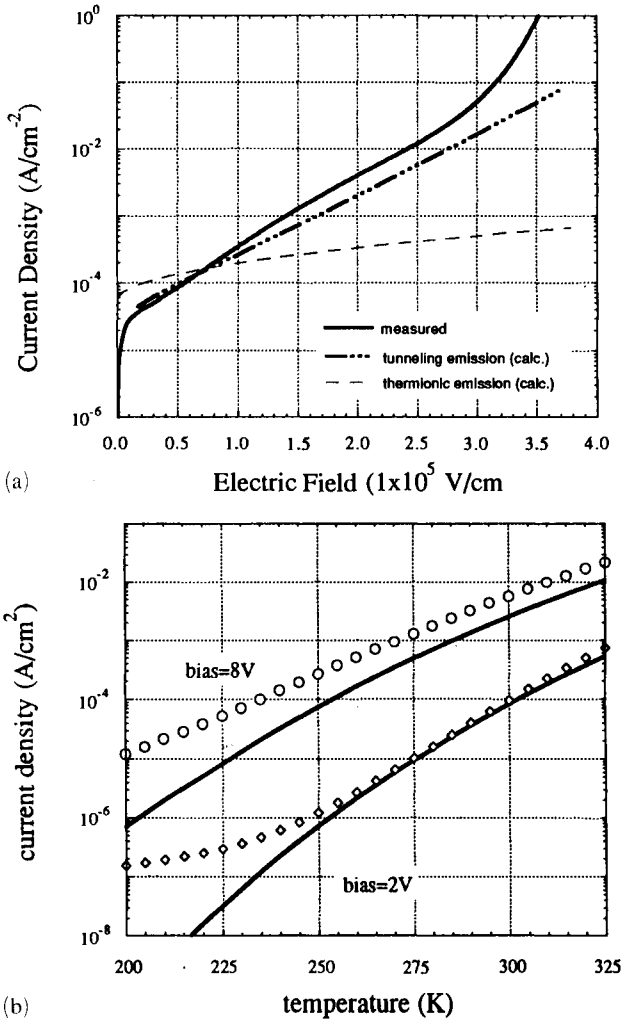

Fig. 5. (a) Measured current–field dependence compared with calculations due to thermionic emission and tunneling emission current flow. A Schottky barrier height of 0.6 eV was used in the calculations. (b) Comparison between the observed temperature dependence and that calculated using the tunneling emission model.

pulses generated by modulating the conductivity of a gap in LTG material with a short pulse laser [10]. Record pulse widths of less than 450 fS have been obtained. The high resistivity of the material has been used in several applications.

(i) The first was as a buffer layer for a GaAs MESFET by Smith *et al.* [1].

(ii) Next, it was used as a surface layer in a MISFET type structure to enhance the breakdown voltage of a GaAs FET [11].

(iii) MESFETs with LT GaAs as a surface passivant have displayed a reduced $1/f$ noise at frequencies below 100 Hz [12].

(iv) It has been proposed as a lateral isolation layer in a LOCOS like process for highly dense integrated circuits [13].

(v) Most recently it has been used for heterodyne generation of high power millimeter-wave signals [14].

In this paper we concentrate on the microwave power MESFET with LTG. GaAs as a surface insulator as this is the application which is the most developed.

3. Microwave power MESFET

The product of the maximum drain current and the gate-drain breakdown voltage is a good indication of the microwve power performance of a device. Whereas an arbitrary value of drain current can be obtained by simply changing the channel epitaxial layer, a design that leads to a high gate-drain breakdown voltage is much more elusive. Recently incorporation of LTG GaAs as a surface passivant along with an overlapping gate structure has demonstrated a dramatic improvement in the gate-drain breakdown voltage [11, 15]. However, the mechanism through which the LTG passivating layer improves the breakdown voltage is not completely understood. Yin *et al.* [16] have fabricated and studied the temperature dependence of the gate-drain diode of a GaAs MESFET with LTG AlGaAs/GaAs passivation and an overlapping gate structure. By studying the observed anomalous decrease in the breakdown voltage at low temperature a qualitative explanation of how the LTG passivant improves the gate-drain breakdown voltage is obtained.

The epitaxial structure and device cross-section are shown in Fig. 6. The growth temperature of the LTG GaAs and AlGaAs was 200 °C and the anneal was carried out *in situ* at 600 °C. The mobility and sheet charge concentration were determined from Van der Pauw measurement to be 3700 $cm^2\ V^{-1}\ s^{-1}$ and $3.8 \times 10^{12}\ cm^{-2}$ respectively. The fabrication process of the device began with the definition of the mesa by wet chemical etching of the patterned sample. Next, the source-drain regions were defined and reactive ion-etching (RIE) with Cl_2 was used to remove the insulating layers and expose the channel. AuGe/Ni/Au ohmic contacts were defined by lift-off and subsequent rapid thermal annealing at 375 °C for 15 s, resulting in a contact resistance of 0.3 Ω mm. The foot of the gate was then defined and again RIE with Cl_2 was used to etch away the LTG layers down to the channel. Finally, the overlapping gate mask was aligned to the defined gate foot print and the gate was then formed by lift-off of Ti/Au metals.

The temperature characteristics of the gate-drain diode of a GaAs MESFET with 1.2 μm gate length and LTG AlGaAs/GaAs passivation is shown in Fig. 7. At 300 K, the diode shows a high breakdown voltage of 34 V. However, as the temperature is lowered, the breakdown voltage first decreases monotonically, then saturates at about 10 V at 77 K. In comparison, Fig. 8 shows the temperature dependence behavior of a gate-drain diode in a conventional GaAs MESFET ($N_d = 3 \times 10^{17}\ cm^{-3}$). In the conventional device, the observed dependence of the breakdown voltage with temperature is very small.

The strong temperature dependence of the breakdown voltage observed in the MESFET with LTG GaAs passivation can be explained using the existing breakdown model [17, 18]. In the low gate voltage range, the I–V characteristics shown in Fig. 9 agree with the transport model of thermionically assisted tunneling between precipitates proposed by Ibbetson *et al.* [7]. The electrons propagate from the gate metal onto the LTG GaAs passivation layer by tunneling via the assistance of the local electric field and the temperature. However, since the electric field drops off rapidly away from the gate metal, the injected electrons

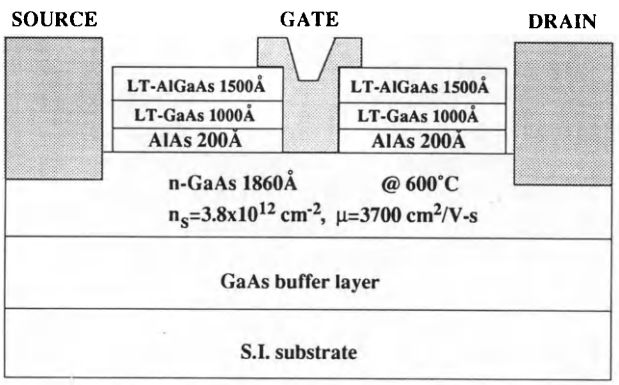

Fig. 6. Schematic representation of the cross-section profile of a GaAs MESFET with LTG $Al_{0.3}Ga_{0.7}As$/GaAs passivation and overlapping gate structure.

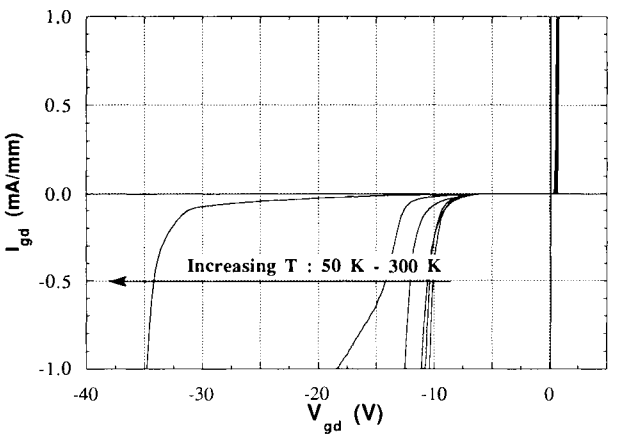

Fig. 7. Gate-drain diode characteristics at different temperatures of an LTG $Al_{0.3}Ga_{0.7}As$/GaAs n-GaAs MESFET.

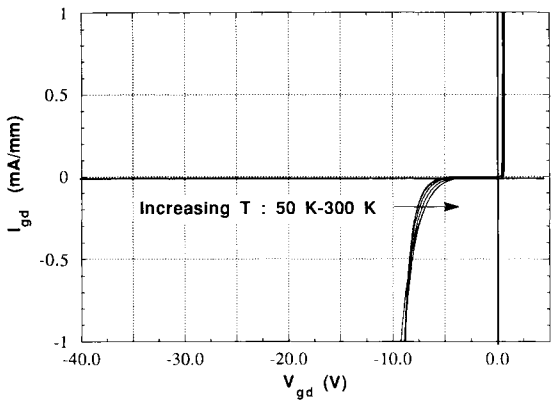

Fig. 8. Gate-drain diode characteristics of a conventional GaAs MESFET.

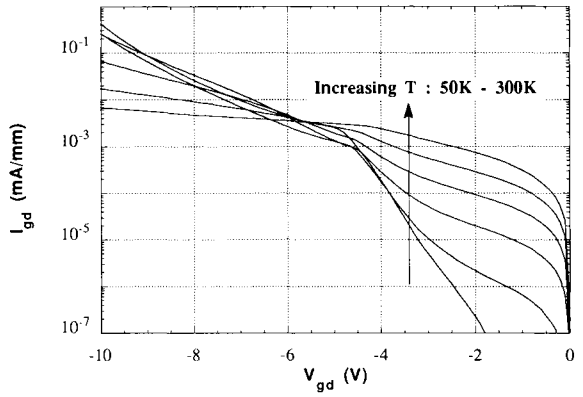

Fig. 9. Semilog plot of the gate-drain diode characteristics.

are localized to the precipitates that are close to the gate metal. The resulting excess of negative charges in the vicinity of the metal drain edge would redistribute the associated electric field. Consequently the peak electric field at the edge of the gate is alleviated. As the temperature is lowered, the number of electrons that can thermionically field emit into the precipitates and from precipitate to precipitate is significantly reduced, thus the LTG GaAs becomes less effective in reducing the field. At low temperature (77 K), this field alleviation mechanism becomes relatively ineffective, thus the breakdown voltage saturates to that of a conventional GaAs MESFET. Figure 10 shows schematically the electric field distribution with field alleviation by the charged precipitates. The most conservative hypothesis we can draw is that, since the trap response at low temperature is similar to the high frequency trap response, the r.f. breakdown may be close to the breakdown voltage at 77 K. Even so, a large benefit results as explained below.

To obtain the maximum output power from MESFETs, the devices are usually biased at half of the breakdown voltage, thereby allowing the r.f. signal to

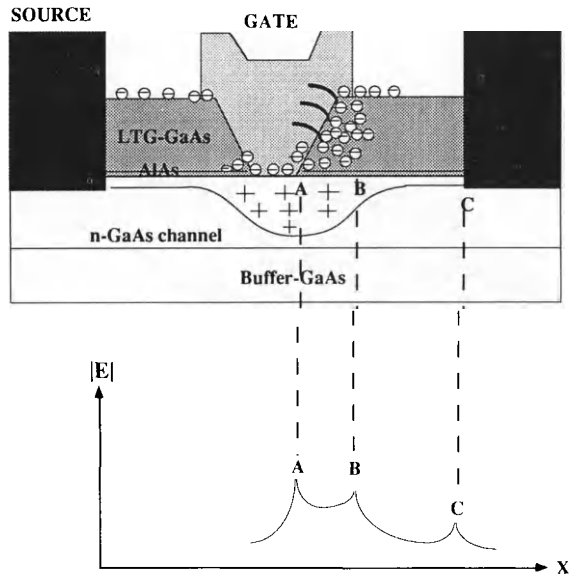

Fig. 10. Field redistribution by trapped electrons at the gate metal edge at 300 K.

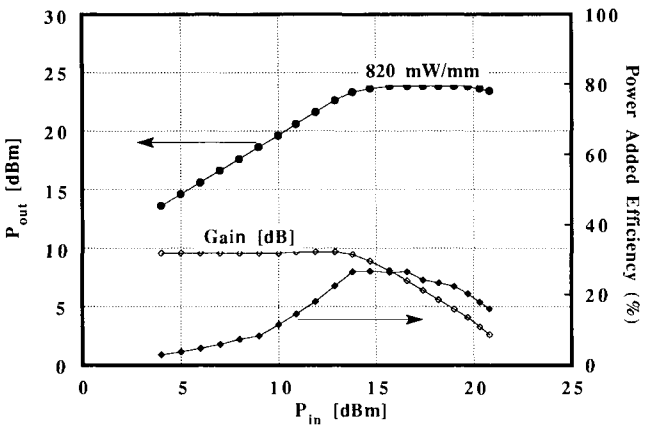

Fig. 11. Output power and power-added efficiency *vs.* input power at 4 GHz for a 1.2 μm × 200 μm device.

swing from zero to the r.f. breakdown voltage BV_{rf}. However, the static electric field at the gate edge for LTG passivated devices is low even at a gate-drain bias as high as BV_{rf} ($BV_{rf} \leqslant BV_{dc}$). We therefore expect that a full r.f. swing of $2BV_{rf}$ is accommodated in these devices, doubling (at the minimum) the r.f. power from passivated devices compared with conventional GaAs MESFETs. The power measurement of the device shown in Fig. 11 supports the above hypothesis.

4. Conclusion

Researchers have only begun to understand the properties of GaAs and AlGaAs grown at a low temperature by MBE. The various states of the material

based on growth and annealing conditions and its associated properties have the potential of being exploited in a wide variety of electronic and opto-electronic applications. Already the available power from MESFETs with LTG (Al)GaAs is impressive and over 1.5 W mm^{-1} power density is expected in the near future. There is no reason why the technology cannot be applied to GaAs based HEMTs and provide additional advantage. The unexpected advantage of reduced $1/f$ noise and millimeter-wave power generation are examples of how new applications rapidly develop as understanding of the material improves. There is no indication of such progress slowing down.

Acknowledgments

This work was supported by the AFOSR, California MICRO Grant (HP) and the NSF (PYI award).

References

1 F. W. Smith, A. R. Calawa, C.-L. Chen, M. J. Manfra and L. J. Mahoney, *IEEE Electron. Device Lett.*, *9* (1988) 77.
2 M. Kaminska, Z. Liliental-Weber, E. R. Weber and T. George, *Appl. Phys. Lett.*, *54* (1989) 1881.
3 M. R. Melloch, N. Otsuka, J. M. Woodall, A. C. Warren and J. L. Freeouf, *Appl. Phys. Lett.*, *57* (1990) 1531.
4 A. C. Warren, J. M. Woodall, J. L. Freeouf, D. Grischkowsky, D. T. McInturf, M. R. Melloch and N. Otsuka, *Appl. Phys. Lett.*, *57* (1990) 1331.
5 A. C. Warren, J. M. Woodall, P. D. Kirchner, X. Yin, F. Pollak, M. R. Melloch, N. Otsuka and K. Mahalingham, *Phys. Rev. B*, *46* (1992) 4617.
6 A. Vaterlaus, R. M. Feenstra, P. D. Kirchner, J. M. Woodall and G. D. Pettit, *J. Vac. Sci. Technol., B*, *127* (1993) 1502.
7 J. P. Ibbetson, N. X. Nguyen, J. S. Speck, A. C. Gossard and U. K. Mishra, paper presented at the *MRS Spring Meet., San Francisco, CA, March 1993, J. Electron. Mater.*, in press.
8 D. C. Look, D. C. Walters, M. O. Manasreh, J. R. Sizelove, C. E. Stutz and K. R. Evans, *Phys. Rev. B*, *42* (1991) 3578.
9 J. G. Simmons, *J. Appl. Phys.*, *34* (1963) 1793.
10 S. Gupta, G. Mourou, G. W. Smith and A. R. Calawa, *Mater. Res. Soc. Symp. proc.*, *241* (1991) 205.
11 L.-W. Yin, Y. Hwang, J. H. Lee, R. M. Kolbas, R. J. Trew and U. K. Mishra, *IEEE Electron. Device Lett.*, *11* (12) (1990) 561–563.
12 A. D. Van Rheenen, Y. Lin, C.-L. Chen and F. W. Smith, paper presented at the *MRS Spring Meet., San Francisco, CA, March 1993, J. Electron Mater.*, in press.
13 U. K. Mishra and R. M. Kolbas, *Mater. Res. Soc. Symp. Proc.*, *241* (1991) 159.
14 E. R. Brown, K. A. McIntosh, F. W. Smith, M. J. Manfa and C. L. Den, paper presented at the *MRS Spring Meet., San Francisco, CA, March 1993, J. Electron. Mater.*, in press.
15 C.-L. Chen, L. J. Mahoney, M. J. Manfra, F. W. Smith, D. H. Temme and A. R. Calawa, *IEEE Electron. Device Lett.*, *13* (6) (1992) 335–337.
16 L. W. Yin, N. Z. Nguyen, Y. Hwang, J. P. Ibbetson, R. M. Kolbas, A. C. Gossard and U. K. Mishra, paper presented at the *MRS Spring Meet., San Francisco, CA, March 1993.*
17 T. M. Barton and P. H. Ladbrooke, *Solid-State Electron.*, *29* (1986) 908–813.
18 R. J. Trew and U. K. Mishra, *IEEE Electron. Device Lett.*, *12* (10) (1991) 524–526.

Temperature measurements of LT GaAs diodes

R. Westphalen*, B. Boudart, D. Théron, X. Wallart, Y. Druelle and Y. Crosnier
Institut d'Electronique et de Microélectronique du Nord, Université des Sciences et Technologies de Lille, Bât. P3, 59655 Villeneuve d'Ascq (France)

Abstract

We have grown low temperature (LT) GaAs by molecular beam epitaxy in order to study its insulating properties. The LT GaAs exhibits trap filled limited (TFL) conduction. The TFL conduction mechanism is correlated with the measurement of a double peak on X-ray diffraction patterns. Therefore, it is connected to the presence of an excess of arsenic. Diodes realized on LT GaAs were fabricated and measured from 77 K to room temperature. The dependence of the low field resistivity and the breakdown voltage *vs.* temperature is analysed. The variation with the layer thickness is also shown. In contrast to diodes realized on GaAs grown at higher temperature, the breakdown voltage exhibits excellent uniformity.

1. Introduction

Low temperature (LT) GaAs has raised much interest in recent years because the backgating and sidegating effects on metal–semiconductor field effect transistor (FET) integrated circuits have been strongly reduced by growing an LT GaAs buffer layer [1, 2]. The material analysis reveals an excess of arsenic in GaAs layers grown in the temperature range 200–300 °C. The material behaves as an insulator [3]. After annealing, arsenic precipitates appear in the GaAs [4, 5]. Annealed LT GaAs has been used as an insulator for the realization of metal–insulator–semiconductor (MIS) structures. FETs realized on these structures exhibit very high breakdown voltages and high output power densities [6]. In the work reported in this paper, we have grown LT GaAs, realized MIS diodes and studied their I–V characteristics as a function of temperature. The growth conditions are described. The evolution of the resistivity and the breakdown voltage is presented and discussed in terms of the trap filled limit (TFL) model.

2. Material growth

The GaAs layers were grown in a RIBER 2300 molecular beam epitaxy system. For determining the growth conditions of the LT GaAs, the arsenic pressure is maintained at 10^{-5} Torr ($\pm 10\%$). Only the growth temperature is varied. *In situ* reflection high energy electron diffraction (RHEED) patterns reveal a specific (1×1) reconstruction for LT GaAs if an excess of arsenic is incorporated. At lower growth temperatures, the RHEED pattern becomes spotty after a few monolayers, indicating the poorer quality of this material. At higher growth temperatures (up to 500 °C), the $C(4 \times 4)$ pattern remains unchanged. This allows us to determine an approximate temperature range for the growth of LT GaAs. After growth, double X-ray diffraction is carried out so as to measure the strain induced by the arsenic excess. LT GaAs is strained on GaAs which gives rise to a double peak on double X-ray diffraction patterns. The shift $\Delta\theta$ of the angle between the two peaks can be related to the relative variation in the vertical lattice parameter $a_\perp$. The results obtained for substrates with different kinds of back sides are shown in Fig. 1. For all samples, the temperature measurements are performed with a thermocouple located in the high vacuum behind the substrate near the heating filament. We think that the large variations in $\Delta a_\perp / a_\perp$ for the same temperature come from the variations from one growth to another of the arsenic pressure or the actual growth temperature. However, we see the tendency of decreasing strain (and therefore the arsenic excess) as the temperature increases. We have also observed that the temperature measured with the thermocouple is not the same when a double-side-polished substrate is replaced by a rough back side substrate. To obtain the same excess of arsenic in the LT GaAs layers on the one-side-polished substrates the measured temperature has to be lowered by around 100 °C. The difference in the measured

*Author to whom correspondence should be addressed.

0921-5107/93/$6.00
© 1993 – Elsevier Sequoia. All rights reserved

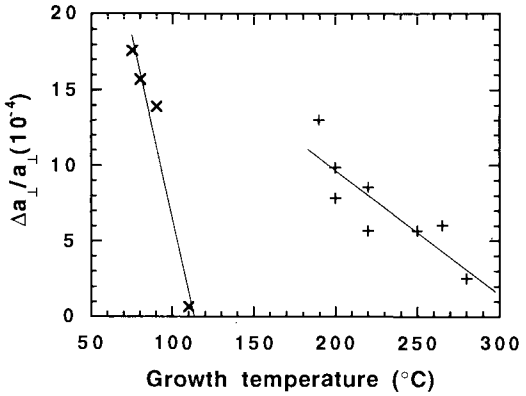

Fig. 1. Lattice mismatch of LT GaAs *vs.* growth temperature: +, polished back side substrates; ×, rough back side substrates.

growth temperatures comes from the lower reflectivity of the rough back side of the substrates. For the fabrication of devices the LT GaAs layers are annealed at 600 °C for 10 min. The double X-ray diffraction pattern then displays only one peak, indicating the reduction of stress due to the formation of arsenic precipitates.

3. Metal–insulator–semiconductor diode fabrication and measurements

LT GaAs layers have been grown on n^+ substrates in order to realize MIS diodes of area 100×100 μm^2. Two types of diodes have been realized. Some have on top a Ti/Pt/Au Schottky contact; the others have on top an ohmic contact. The back side of the substrate is connected by an Ni/AuGe/Ni ohmic contact. The diodes are isolated by a MESA structure.

I–V measurements performed on ohmic structures with a 1 μm LT GaAs layer exhibit very symmetrical characteristics (Fig. 2(a)). In contrast, Schottky structures display a higher breakdown voltage under reverse bias than under forward bias, because of the presence of the Schottky barrier. No transient conduction was observed. The *I–V* characteristics reveal TFL breakdown [7]. This breakdown mechanism is only observed on layers containing an excess of arsenic. If no arsenic excess is detected, the forward breakdown voltage has the usual value of around 0.6 V. Therefore, the excess of arsenic results in this TFL breakdown. The breakdown voltage of LT GaAs MIS diodes exhibits an excellent uniformity on a given wafer. In contrast, the same device made on GaAs grown at 250 °C (on a rough back side substrate) presents wide variations of the breakdown voltage (between 13 and 22 V for a 1 μm GaAs layer). We believe that such a difference comes from the different nature of the breakdown mechanism in LT GaAs compared with GaAs grown at

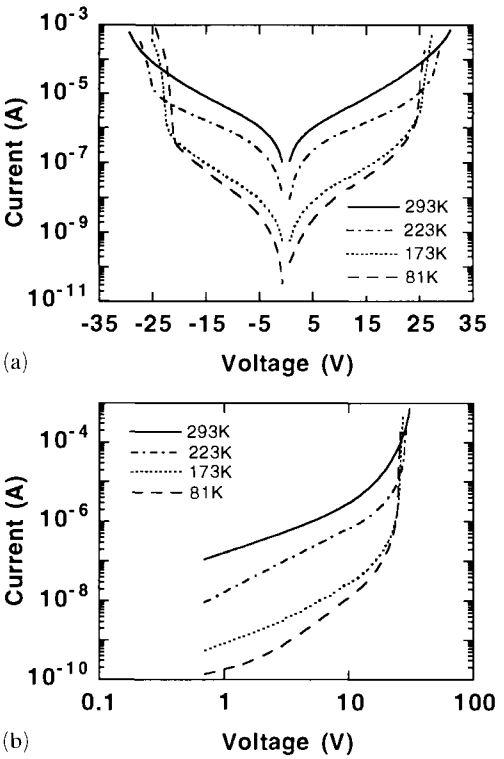

Fig. 2. Temperature dependence of the *I–V* characteristics of MIS diodes where LT GaAs is used as the insulator: (a) log–linear scale; (b) log–log scale.

higher temperature. However, it could also probably come from the intermediate value of the temperature (250 °C) used for non-uniform samples. On LT GaAs, the breakdown is a volumetric behaviour of the layer and does not depend on the interface states or on the processing of the metal–semiconductor interface.

Temperature measurements have been performed on the ohmic structures (with a 1 μm LT GaAs layer). The results are shown in Fig. 2(a). The temperature dependence exhibits two different behaviours depending on the biasing voltage. At low voltages where the material behaves as a highly resistive material, the current density decreases when the temperature is lowered. This phenomenon is attributed to the freeze out of the free electrons in the conduction band. At high voltages, the breakdown occurs as a result of the achievement of the TFL. We see that the breakdown voltage increases slightly with the temperature. Therefore, at high temperatures, the trap density to be filled is higher. This is consistent with a greater number of free electrons in the conduction band.

4. Discussion

The TFL conduction has been studied by Lampert and Mark [8]. In their model, three *I–V* dependences

are possible. First, at low electric fields, there is an ohmic region ($I \propto V$). At higher fields, space charge conduction has to be taken into account. In that case, $I \propto V^2$. The conduction corresponds to a perfect insulator. The breakdown occurs when traps are present. The traps are progressively filled as the voltage increases. As they are completely filled, suddenly all excess electrons injected in the material take part in the conduction. This results in a drastic increase in the current.

In our case, we see the successive behaviours. The ohmic law is observed at very low voltages and then space charge conduction occurs. This is seen especially at low temperatures (Fig. 2(b)). The breakdown occurs at a value which does not depend very much on the temperature (between 25 and 30 V). According to the theory of current injection in solids, this value can be related to the number of traps to be filled:

$$V_{TFL} = (q/2\varepsilon) p_{t,0} L^2$$

where $p_{t,0}$ is the ionized trap density, *i.e.* the number of traps to be filled, and L the thickness of LT GaAs layer. We assume a similar dielectric constant ε for the LT GaAs as used for GaAs grown at 600 °C. From $V_{TFL} = 25$ V, we calculate that $p_{t,0} = 3.5 \times 10^{16}$ cm^{-3}. Assuming that LT GaAs contains a high density of N_{dd} of deep donors and a lower density N_A of acceptors and that $N_{dd}^+ = N_A^- = N_A$, $p_{t,0}$ corresponds to N_{dd}^+, that is to the number of acceptors. This result seems to be acceptable. We have also used the theory of current injection in solids in order to determine the activation energy of the observed traps. In this approach, we have simply modelled the current density as qnv_{sat}, where n is the free electron density and v_{sat} is the saturation velocity. However, our results cannot be explained by this model because the found energy depends on the temperature.

We have also investigated the dependence of the breakdown voltage on the LT GaAs layer thickness. According to the TFL model, the breakdown voltage should vary linearly with L^2. We observe a linear dependence (Fig. 3) indicating a breakdown occurring at an electric field of around 300 kV cm^{-1}. Such a linear dependence has already been observed [9]. It is attributed either to a non-uniform trap distribution in the material with a lower density near the surface or to the presence of several traps. However, this electric field is in the range of the breakdown field of GaAs. Therefore we think that avalanche breakdown cannot be excluded from the breakdown mechanism. The temperature variation of the breakdown voltage is also consistent with the avalanche breakdown. We believe therefore that a correct description of the breakdown behaviour of LT GaAs should include both possible mechanisms.

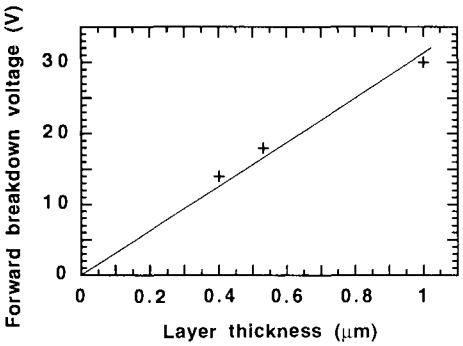

Fig. 3. Forward breakdown voltage *vs.* LT GaAs layer thickness.

5. Conclusion

We have realized MIS diodes using GaAs grown at low temperature as an insulator in order to measure its insulating properties. The conduction of LT GaAs diodes is very characteristic of this material and is connected to the presence of an excess of arsenic in the material. Therefore, it can be easily distinguished from normal GaAs. The breakdown voltage is very homogeneous on the wafer. Temperature measurements reveal a dependence of the I–V characteristics which is in agreement with the TFL conduction mechanism. From the breakdown voltage, the number of traps to be filled can be deduced. The obtained value of 3.5×10^{16} cm^{-3} is demonstrated to correspond to the number of acceptors located in the LT GaAs. However, the field achieved at breakdown are high enough to cause the onset of avalanche breakdown in the LT GaAs.

Acknowledgment

This work has been carried out with the financial help of the ESPRIT Basic Research project TAMP-FETS (6849).

References

1 F. W. Smith, A. R. Calawa, C.-L. Chen, M. J. Manfra and L. J. Mahoney, *IEEE Electron Device Lett.*, 9 (2) (1988) 77.
2 C.-L. Chen, F. W. Smith, A. R. Calawa, L. J. Mahoney and M. J. Manfra, *IEEE Trans. Electron Devices*, *36* (9) (1989) 1546.
3 M. Manserah, D. Look, K. R. Evans and C. E. Stutz, *Phys. Rev. B*, *41* (1990) 10272.
4 Z. Liliental-Weber, W. Swider, K. M. Yu, J. B. Kortright, F. W. Smith and A. R. Calawa, *Appl. Phys. Lett.*, *58* (19) (1991) 2153.
5 M. R. Melloch, N. Otsuka, J. M. Woodall, A. C. Warren and J. L. Freeouf, *Appl. Phys. Lett.*, *57* (15) (1990) 1531.

6 C.-L. Chen, F. W. Smith, B. J. Clifton, L. J. Mahoney, M. J. Manfra and A. R. Calawa, *IEEE Electron Device Lett., 12* (6) (1991) 306.
7 B. Wu, A. Verma, J. Gamelin, H. Sohn and S. Wang, *Mater. Res. Soc. Symp. Proc., 241* (1992) 45.
8 A. Lampert and P. Mark, *Current Injection in Solids*, Academic Press, New York, 1970.
9 L.-W. Yin, J. Ibbetson, M. M. Hashemi, W. Jiang, S.-Y. Hu, A. C. Gossard and U. K. Mishra, *Mater. Res. Soc. Symp. Proc., 241* (1992) 181.

Materials Science and Engineering, B22 (1993) 82–85

Noise studies of HFETs on low temperature grown GaAs buffers and of MESFETs with low temperature grown GaAs passivation

A. D. van Rheenen and Y. Lin
Electrical Engineering Department, University of Minnesota, Minneapolis, MN 55455 (USA)
S. Tehrani
Motorola Inc., Phoenix Corporate Research Laboratories, Tempe, AZ 85284 (USA)
C.-L. Chen and F. W. Smith
Lincoln Laboratory, Massachusetts Institute of Technology, Lexington, MA 02173 (USA)

Abstract

We report measurements of the low-frequency noise of HFETs built on low temperature grown (LTG) GaAs buffer and superlattice buffer layers. A distinct generation–recombination noise source with activation energy of 0.70 eV was observed in devices built on the LTG GaAs buffer. In addition, both structures exhibited a trap whose activation energy depended on the gate-to-source voltage. This dependence is believed to be due to interactions between electrons in the channel and traps in the AlGaAs supply layer. We also report measurements of the low-frequency noise and phase noise of MESFETs with an LTG GaAs passivation layer and of conventional MESFETs without the passivation. We found the phase noise of the LTG GaAs MESFETs to be significantly lower at small offset frequencies and to have a weaker frequency dependence. A similar reduction in the low-frequency noise was observed. This supports the idea that the LTG GaAs passivation reduces the number of traps with large activation energies.

1. Introduction

Since the introduction of the low temperature grown (LTG) GaAs in 1988 [1] the interest in different applications of this material has been growing. Initially, it was used exclusively as a buffer layer between the substrate and the active layer in order to help reduce the effect of backgating. Later applications focused on increasing the gate-drain breakdown voltage [2] and on surface passivation [3]. Earlier noise measurements examined the influence of an LTG GaAs buffer on the low-frequency noise performance of MESFETs [4] and pseudomorphic HFETs [5]. In this paper we review some of these results and present recent results [6] regarding the effects of the LTG GaAs on the low-frequency noise and phase noise of MESFETs when the material is used as a passivation layer on top of the conducting channel.

2. Low-frequency noise in HFETs

We studied the low-frequency noise in identical, planar doped, pseudomorphic heterojunction FETs (HFETs) built on an LTG GaAs buffer layer and built on an AlAs/GaAs superlattice buffer. The spectra consisted of generation–recombination (g–r) contributions, with their typical $1/(1+\omega^2\tau^2)$ shape, superimposed on the $1/f$ contribution. From a measurement of the knee-frequency $(1/2\pi\tau)$ as a function of temperature we extracted the activation energies of the traps responsible for the g–r processes. The results are summarized in Fig. 1. The main difference is the additional trap at 0.70 eV we observed in the HFETs on the LTG GaAs buffer layer. Because the FETs were biased in saturation the gate-to-drain potential is large enough to pinch off the channel, forcing the electrons to travel close to the buffer layer making possible interactions with the traps in the buffer layer. The activation energy we observed might very well be the Schottky barrier height due to As precipitates in the LTG GaAs buffer.

In both types of FET we observed a trap whose activation energy depended on the applied gate-to-source voltage. We show these results in Fig. 2. We propose that this trap is located in the AlGaAs supply layer and interacts with electrons in the InGaAs channel. When the gate voltage is made more negative the AlGaAs conduction band is pulled up at the gate and the trap level in the AlGaAs band gap follows the conduction band and moves up, closer to the first quantization

0921-5107/93/$6.00

© 1993 – Elsevier Sequoia. All rights reserved

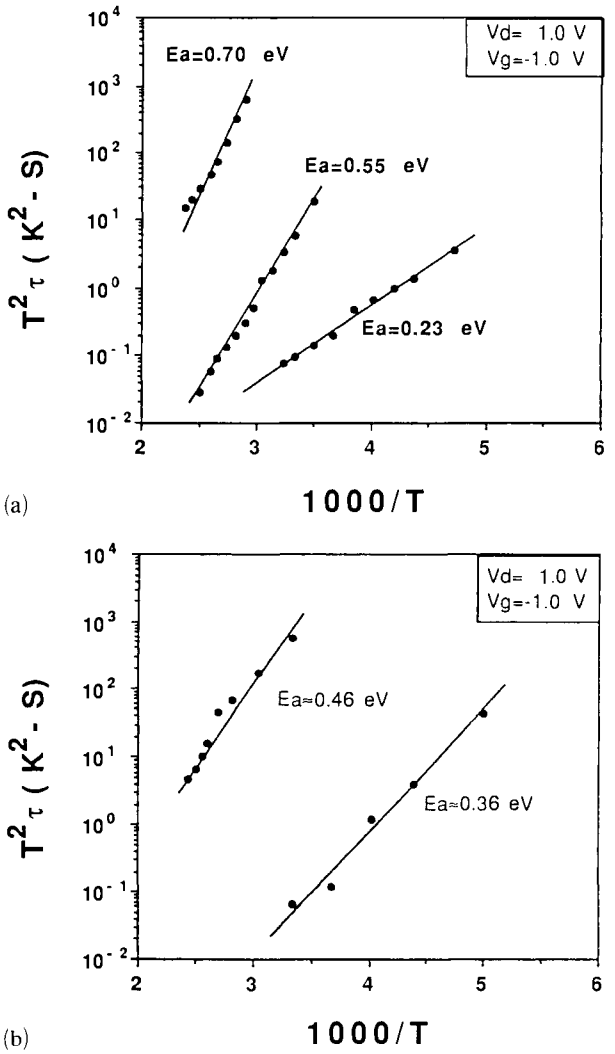

Fig. 1. Arrhenius plot of the activation energy at $V_{ds} = 1.0$ V and $V_{gs} = -1.0$ V for HFETs on (a) an LTG GaAs buffer and (b) a superlattice buffer.

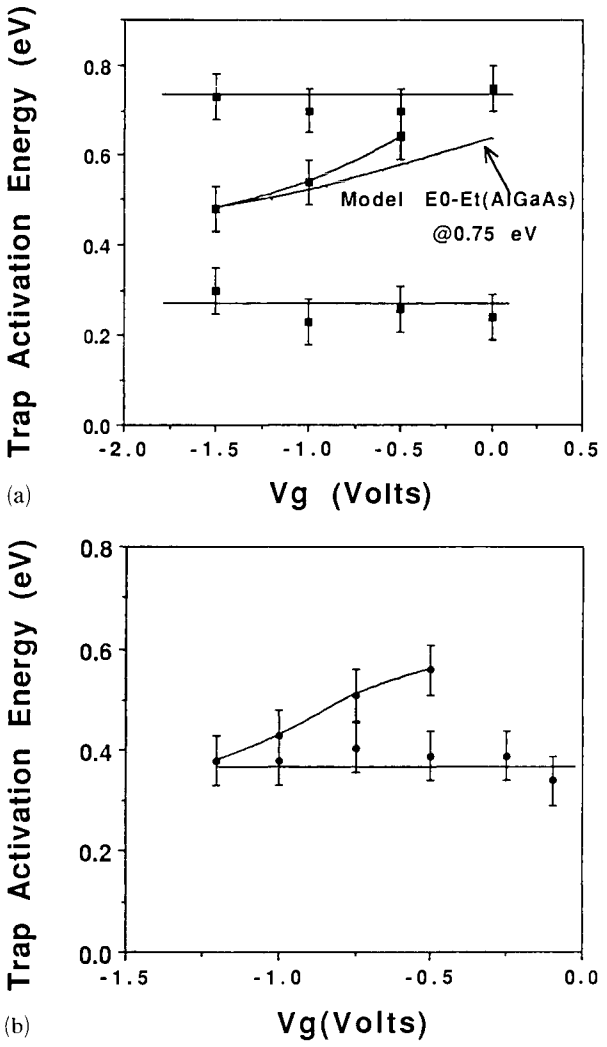

Fig. 2. Trap activation energies *vs.* V_{gs} for HFETs on (a) an LTG GaAs buffer and (b) a superlattice buffer. Results from the computer simulation are also shown in (a). Similar results were observed in (b).

level in the InGaAs channel well. To test the explanation we simultaneously solved the Schroedinger equation and Poisson's equation to obtain the band diagram. In this model we included a trap in the AlGaAs, located 0.75 eV below the conduction band, and calculated the energy difference between this level and the first quantization level. These results are also shown in Fig. 2.

3. Phase noise in MESFETs

An overlapping-gate MESFET with an LTG GaAs passivation layer [3] (henceforth referred to as an LTG-MESFET) and a conventional GaAs MESFET (henceforth referred to simply as a MESFET) were used for the experiments. The 2000 Å thick LTG GaAs passivation layer was grown *in situ* on top of the conducting channel by molecular beam epitaxy. No dielectric passivation layer was deposited onto either the MESFET or the LTG-MESFET. The nominal gate length is 1 μm.

The phase noise of the devices was measured in the saturation regime using a 1 GHz carrier. The drain current was 60 mA and the drain-to-source voltage was 2.5 V. As illustrated in Fig. 3, the phase noise of the LTG-MESFET displays a flatter frequency dependence than the MESFET, which shows $1/f$ dependence, and is 15 dB lower at 1 Hz from the carrier and 10 dB higher at 100 kHz from the carrier. The lower near-carrier noise can be attributed to the passivation of surface states by addition of the LTG GaAs layer. To test this assertion we took low-frequency noise measurements on single devices when

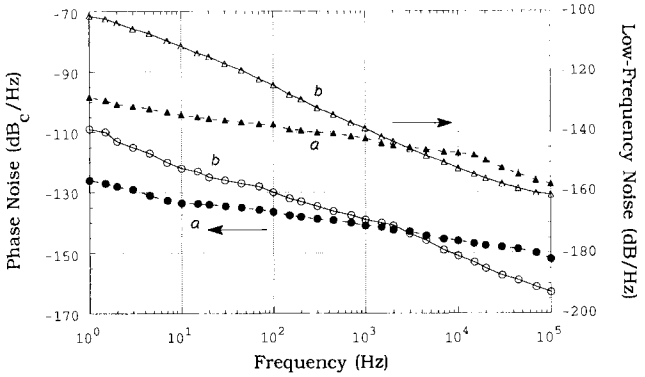

Fig. 3. Room-temperature phase noise measurements (▲ ●) and low-frequency noise measurements (△ ○) of devices biased in the saturation regime with $I_{ds}=60$ mA: ● ○, LTG-MESFET; ▲ △, MESFET triangles.

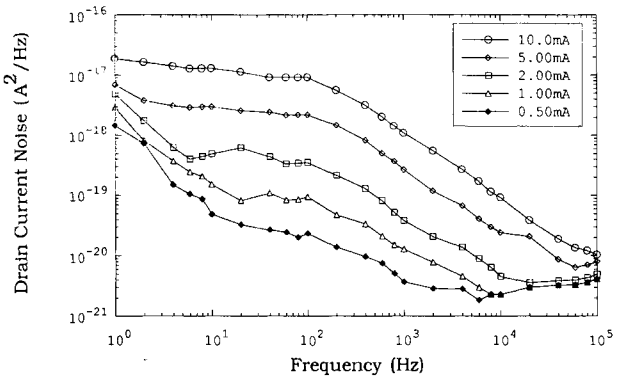

Fig. 4. Noise spectra of the LTG-MESFET in the ohmic regime for different drain currents. The gate voltage was kept constant at 0 V.

they were biased in saturation as well as the ohmic regime.

4. Channel noise

In Fig. 3 we show the spectral intensity of the low-frequency drain-current fluctuations of the LTG-MESFET and MESFET in the saturation regime for a drain current of 60 mA and a drain-to-source voltage of 2.5 V. Two apparent differences between the devices are the spectral shape and the magnitude of the noise. The MESFET exhibits a $1/f$-shaped spectrum whereas the LTG device has a weaker dependence on the frequency.

The low-frequency noise measurements were consistent with the phase noise results. At 1 Hz, the LTG GaAs passivation reduced the phase noise and amplitude noise by 16 and 26 dB respectively.

The low-frequency noise spectra for the LTG-MESFET biased in the ohmic regime are shown in Fig. 4. The gate bias was kept at 0 V while the drain current was varied from 0.5 to 10 mA. Further analysis identified two distinct contributions: one that varies quadratically with the current (typical of a resistor) and may be associated with the conducting channel, and one that varies linearly with current (typical of a diode). The quadratic component has a frequency dependence that is weaker than $1/f$ and can in fact be modeled as a McWorther-style [7] spectrum which is typical of a collection of trapping sites with a distribution proportional to the inverse of the trapping time constants:

$$S_I(f)=(A/f)[\arctan(f/f_1)-\arctan(f/f_2)]$$

where A is a constant proportional to the number of traps that are active, f is the frequency and $1/f_1$ and $1/f_2$ are the limits of the distribution of the trapping time constants. Such a spectrum is flat for frequencies smaller than f_1, rolls off as $1/f^2$ for frequencies larger than f_2, and behaves as $1/f$ for $f_1<f<f_2$. The component that increases linearly with operating current can be modeled as having a $1/f$ dependence.

Similar measurements on the MESFETS in the ohmic regime reveal spectra that are almost perfectly $1/f$ like. The fact that this component is not observed in the LTG-MESFETS leads us to believe that the $1/f$ noise is not fundamental in nature. This component could not have been masked in the LTG-MESFETS because the observed noise is smaller than in the MESFETs. Hence, these $1/f$ shaped spectra could also be a manifestation of a McWorther-style spectrum with a larger range of trapping time constants.

The difference between the MESFET and the LTG-MESFET is the addition of LTG GaAs passivation layer. It appears that the LTG GaAs passivation layer modifies the distribution of the surface traps, resulting in a shift of the distribution of trapping time constants. One can view this as shifting the upper limit of the trapping time distribution to smaller values, *i.e.* deactivating the deeper traps that have long time constants. This interpretation is supported by Fig. 5, which compares the channel noise of the two MESFETs operating at 5 mA (ohmic regime) with two different gate voltages. The observed knee in the LTG-MESFET spectra is the upper limit of the trapping time constants. The $1/f$ part of the spectral intensity for the LTG-MESFET is slightly larger than for the MESFET. (The spectra are measured in the ohmic regime at the same current so that comparison is warranted.) In addition, since the magnitude is a measure of the number of traps that are active, slightly more traps are active in the LTG-MESFET than in the MESFET. From these two observations we conclude that for devices operating in the ohmic regime, the addition of the LTG passivating layer removes traps with larger

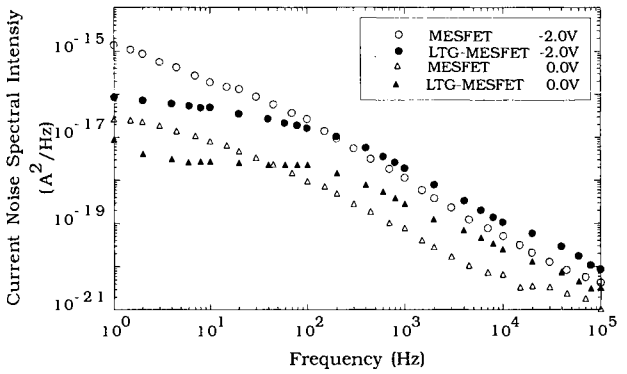

Fig. 5. Ohmic-regime noise spectra ($I_{ds} = 5$ mA) of the LTG-MESFET and MESFET for two different gate voltages.

activation energies and adds (only marginally) traps with smaller activation energies.

5. Conclusion

Three different activation energies were observed in HFETs grown on an LTG GaAs buffer layer. There is a distinct trap with an activation energy of 0.70 eV possibly related to As precipitates in the buffer region. The other two traps are thought to be located in the AlGaAs supply layer, one (DX center) which interacts with carriers in the AlGaAs layer (parallel conduction) and one which interacts with carriers in the channel, displaying a gate voltage dependence of the activation energy.

Including the LTG GaAs layer as a passivating layer on top of the device seems to reduce the phase noise at low off-set frequencies. This is supported by measurements of the low-frequency noise. A noise reduction of 15 dB was observed when the MESFET and LTG-MESFET were biased in saturation with a drain current of 60 mA. Further noise measurements taken when the devices were biased in the ohmic regime revealed that the passivation layer seems to deactivate the traps with larger activation energy and increase only marginally the density of the shallower traps.

References

1 F. W. Smith, A. R. Calawa, C. L. Chen, M. J. Mantra and L. J. Mahoney, *IEEE Electron. Device Lett., 9* (1988) 77.
2 R. J. Trew and U. K. Mishra, *IEEE Electron. Device Lett., 12* (1991) 524.
3 C. L. Chen, L. J. Mahoney, M. J. Manfra, F. W. Smith, D. H. Temme and A. R. Calawa, *IEEE Electron. Device Lett., 13* (1992) 335.
4 A. N. Birbas, B. Brunn, A. D. van Rheenen, A. Gopinath, C.-L. Chen and F. W. Smith, *IEE Proc. G Circuits, Devices, Systems, 138* (1991) 175.
5 S. Tehrani, A. D. van Rheenen, M. M. Hoogstra, J. A. Curless and M. S. Peffley, *IEEE Trans. Electron. Device, 39* (1992) 1070.
6 Y. Lin, A. D. van Rheenen, C.-L. Chen and F. W. Smith, Paper presented at the *MRS Spring Meet., San Francisco, CA, April 12–16, 1993*, in *J. Electron. Mater.*, in press.
7 A. L. McWorther, in R. H. Kingston (ed.), *Semiconductor Surface Physics*, University of Philadelphia Press, Philadelphia, PA, 1956, p. 207.

Materials Science and Engineering, B22 (1993) 86–88

Electrical conduction in low temperature grown InP

K. Khirouni and H. Maaref

Département de Physique, Faculté des Sciences de Monastir, 5000 Monastir (Tunisia)

J. C. Bourgoin

Groupe de Physique des Solides de l'Université Paris 7, Centre National de la Recherche Scientifique, Tour 23, 2 place Jussieu, 75251 Paris Cedex 05 (France)

J. C. Garcia

Laboratoire Central de Recherche, Thomson-CSF, Domaine de Corbeville, BP 10, 91401 Orsay (France)

Abstract

Electric conduction has been studied *vs.* frequency ω and temperature T in InP layers grown at low temperature. The T and ω behaviours of the conductivity are found to be typical of a hopping process in a partially defect filled band, very similar to that observed in disordered materials. We have demonstrated the location of the Fermi level. The results are analysed in terms of a recent theory developed by Emin (D. Emin, *Phys. Rev. B, 46* (1992) 9419).

1. Introduction

Low temperature (LT) grown semiconductor layers are technologically interesting for their semi-insulating as well as short lifetime properties. If it is admitted that short minority carrier lifetimes are a consequence of the high defect concentration these layers contain, this is not the case for their electrical properties, *i.e.* for the way electron conduction takes place. The mechanism which renders these layers semi-insulating is of prime importance to evaluate the degree of insulation and carrier mobility. Basically, two mechanisms are proposed. The first one states that the disappearance of free carriers is achieved by compensation with deep defects. The second mechanism involves overlapping of depleted zones [1, 2] developed around As precipitates which are formed following the annealing that renders semi-insulating LT GaAs layers [3–5].

The way electrical conduction takes place is a means to determine which mechanism is operative. In the first case, owing to the large defect concentration, the residual conduction occurs via electron hopping between defect sites located in a partially filled defect band. In the second case, the decrease in conductivity has to be ascribed to a reduced geometrical section of the conductance channel. A conduction via hopping therefore indicates that the semi-insulating character of the material is a consequence of the compensation of free carriers by defects. In LT GaAs a detailed study of conductivity and Hall effect *vs.* temperature has shown that the conduction is indeed governed by hopping [6, 7]. However, the analysis of the data is not straightforward because it is difficult to separate the components of the conductivity due to hopping and to the thermal activation of carrier in the conduction band. A direct way to test the existence of hopping consists to study the frequency ω dependence of the conductivity. Indeed, hopping conductivity is proportional to ω^s with $s \approx 0.8$–1 [8]. This behaviour has been observed in many situations, from heavily compensated semiconductors to amorphous materials.

The aim of this communication is to describe the result of such study in case of an LT grown material. We choose to present data here for the case of LT InP [9, 10] for which very few conductivity data have yet been reported [11, 12].

2. Material

The InP layers have been grown at 180 °C on a semi-insulating InP substrate by molecular beam epitaxy. The In source is solid while the P source is obtained by PH_3 dissociation in a low pressure Mo cracker cell. The P:In flux ratio is equal to 10. Some of the layers have been annealed at 550 °C *in situ* under a P flux. All layers are finally subjected to a 450 °C treatment for 1 min when ohmic contacts realized by In alloying are deposited.

0921-5107/93/$6.00

© 1993 – Elsevier Sequoia. All rights reserved

3. Results

As shown in Fig. 1, at low temperature, *i.e.* in the range 77–200 K, the conductivity of the unannealed layers varies linearly *vs.* ω^s with $s = 0.9$ in the frequency range investigated (100 Hz–100 kHz). At higher temperatures, the data deviate from linearity in the low ω range. Similar data (Fig. 2) are obtained for annealed layers. However, in this case $s = 1$ and deviation from linearity at low frequency is observed above 77 K.

4. Discussion

Because the frequency behaviour of the conductivity is typical of a hopping mechanism at least in low temperature and high frequency ranges, we analyse the data in terms of hopping between independent pairs of polarized centres assuming the distance between traps is not correlated with their energy difference and the carrier transfer is adiabatic [13]. As shown in Figs. 1 and 2, reasonable fits with Emin's theory [13], which gives the ω dependence of the conductivity the expression

$$\sigma(\omega) = \sigma_0 \left(\frac{\omega T}{\omega_0 T_0}\right) \left[1 - \left(\frac{\omega_0}{\omega}\right)^{1/3} \frac{T}{T_0}\right]^{-2}$$

are obtained using the different values for the parameters σ_0, ω_0 and T_0 given in Tables 1 and 2.

The validity of the model in the low temperature range is verified by the fact that the ratio $\omega_0^{1/3}/T_0$ is T and ω independent. Also, the temperature dependence of the conductivity can be fitted by Emin's formula using the same parameters. However, the theory foresees a resonance at a frequency

$$\omega = \omega_0 \left(\frac{T_0}{T}\right)^3$$

which has not been observed experimentally.

In the low frequency and high T ranges the increase in conductivity is consistent with a change of mechanism. As shown in Fig. 3, the plots of σ *vs.* T^{-1} strongly suggest that σ is thermally activated. The associated activation energies are 45 meV and 102 meV for the annealed and unannealed layers respectively. We can therefore conclude that hopping conduction occurs in partially filled defect bands located around these energies. The effect of annealing is to move the Fermi level towards the conduction band.

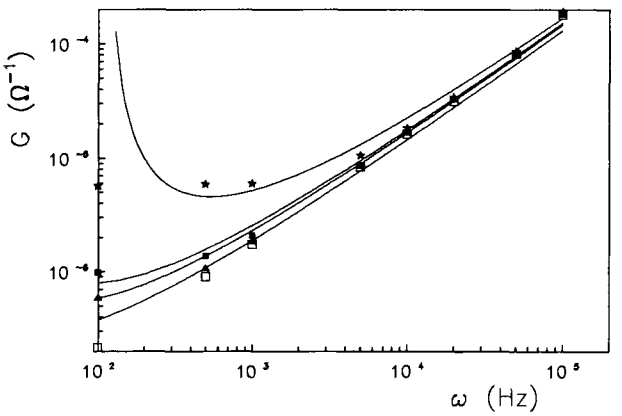

Fig. 1. Conductance *vs.* frequency in unannealed layers at different temperatures: ★, 300 K; ■, 270 K; ▲, 240 K; □, 200 K; ——, fits with Emin's theory.

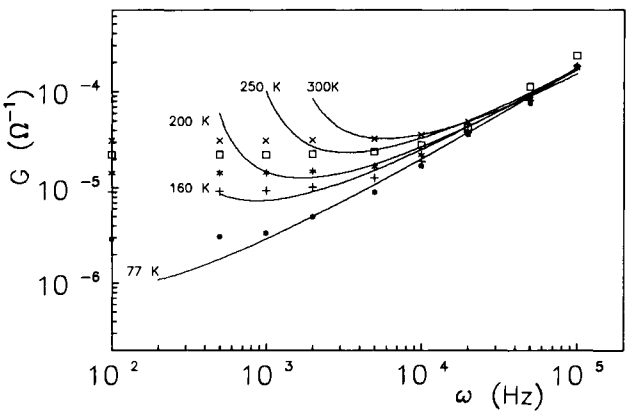

Fig. 2. Conductance *vs.* frequency in annealed layers at different temperatures: ●, 77 K; +, 160 K, ⋆, 200 K; ×, 300 K; ——, fits with Emin's theory.

5. Conclusions

The electronic conduction in LT InP is due to a hopping process in a partially filled defect band. The

TABLE 1. Values of the parameters in Emin's formula for the unannealed layer

T (K)	200	240	210	300
$\omega_0^{1/3} T_0^{-1}$ ($Hz^{1/3} K^{-1}$)	0.010	0.010	0.010	0.016
$\sigma_0 \omega_0^{-1} T_0^{-1} \times 10^{-12}$ ($s\,\Omega^{-1}\,m^{-1}\,K^{-1}$)	6.0	5.5	5.0	4.5

TABLE 2. Values of the parameters in Emin's formula for the annealed layer

T (K)	77	160	200	250	300
$\sigma_0 \omega_0^{-1} T_0^{-1} \times 10^{-12}$ ($s\,\Omega^{-1}\,m^{-1}\,K^{-1}$)	20.0	8.5	6.0	4.5	3.0
$\omega_0^{1/3} T_0^{-1}$ ($Hz^{1/3} K^{-1}$)	0.035	0.035	0.035	0.035	0.035

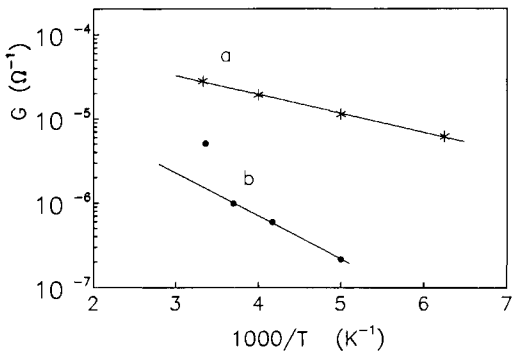

Fig. 3. Plot of conductance *vs.* the inverse of the temperature at low frequency in annealed layers (curve a) and unannealed layers (curve b).

Fermi level, which defines the level of filling, moves towards the conduction band as a result of annealing. The location of the defect band, about 45 meV below the conduction band after annealing, is apparently too shallow to be ascribed to P antisites which are located about 300 meV below the conduction band [14]. This implies that acceptor defects have been removed by this annealing. One cannot therefore expect to obtain a good semi-insulating material after annealing, the Fermi level being too close from the conduction band.

References

1 A. Y. Polyakov, M. Stam, A. G. Milnes, R. G. Wilson and Z. Q. Fang, *J. Appl. Phys., 72* (1992) 1320.
2 A. C. Warren, J. M. Woodall, J. L. Freeouf, D. Grischkowsky, D. T. McInturff, M. R. Melloch and N. Otsuka, *Appl. Phys. Lett., 57* (1990) 1331.
3 K. M. Yu and Z. Lilental-Weber, *Appl. Phys. Lett., 59* (1991) 3267.
4 J. B. Ibbetson, J. Speck, A. C. Gossard and U. K. Mishra, *Appl. Phys. Lett., 62* (1993) 169.
5 R. J. Matyi, M. R. Melloch and J. M. Woodall, *Appl. Phys. Lett., 60* (1992) 2642.
6 Z. Q. Fang and D. C. Look, *Appl. Phys. Lett., 61* (1992) 1438.
7 D. C. Look, D. C. Walters, M. O. Manasreh, J. R. Sizelove, C. E. Stutz and K. R. Evans, *Phys. Rev. B, 42* (1990) 3578.
8 M. F. Mott and E. A. Davies, *Electronic Process in Non-Crystalline Materials*, Clarendon, Oxford, 1979.
9 J. C. Garcia, J. P. Hirtz, P. Maurel, H. J. von Bardeleben and J. C. Bourgoin, *Mater. Res. Soc. Symp. Proc., 241* (1991) 277.
10 J. C. Garcia, A. Claverie, J. Mimila-Arroyo and J. C. Bourgoin, in *Proc. Conf. on Semi-insulating III–V Materials, Ixtapa, Mexico, 1992*, to be published.
11 B. W. Liang, P. Z. Lee, D. W. Shih and C. W. Tu, *Appl. Phys. Lett., 60* (1992) 2104.
12 K. Khirouni, H. Maaref, J. C. Bourgoin and J. C. Garcia, *Appl. Phys. Lett., 62* (25) (1993).
13 D. Emin, *Phys. Rev. B, 46* (1992) 9419.
14 H. P. Gislason, H. Sun, F. Rong and G. D. Watkins, in E. M. Anastassakis and J. D. Joannopoulos (eds.), *Proc. 20th Int. Conf. on Physics of Semiconductors*, World Scientific, Singapore, 1990, p. 666.

Materials Science and Engineering, B22 (1993) 89–92

Low temperature molecular beam epitaxy of Al(Ga)InAs on InP and its application to high electron mobility transistor structures

H. Künzel, J. Böttcher and A. Hase*

Heinrich-Hertz-Institut für Nachrichtentechnik Berlin G.m.b.H., D-10587 Berlin (Germany)

C. Heedt

Universität-Gesamthochschule-Duisburg, D-47048 Duisburg (Germany)

H. Hoenow

Humboldt Universität zu Berlin, D-10099 Berlin (Germany)

Abstract

In this paper we summarize basic material properties of low temperature (LT) molecular beam epitaxy (MBE) grown Al(Ga)InAs. A lower MBE growth temperature limit for these alloys is given by the incorporation of excess arsenic occurring near a growth temperature of 100 °C. The specific resistivity increases with the Al content, and its growth temperature dependence is correlated with the incorporation of deep traps. *In situ* annealing of LT-Al(Ga)InAs layers was found to have virtually no effect on the electrical properties. In GaInAs/AlInAs high electron mobility transistor structures LT-MBE was applied to the buffer, spacer, and gate layers to improve device characteristics.

1. Introduction

Low temperature (LT) molecular beam epitaxy (MBE) growth is known to influence significantly the incorporation behaviour of impurities in III–V compounds. In contrast to LT growth of Ga(Al)As, only very limited results are available for InP-based materials. For AlInAs here incorporation of excess As and a slight degradation of the semi-insulating behaviour were found to occur at LT growth conditions [1]; LT-GaInAs, on the contrary, is characterized by high electrical conductivity in conjunction with a similar concentration of excess arsenic [2]. Only minor interest has been devoted so far to the exploitation of LT growth for Al(Ga)InAs-based device structures (*e.g.* ref. 3).

2. Molecular beam epitaxy growth procedure

MBE growth of Al(Ga)InAs layers was performed under slightly As-stabilized conditions. A beam equivalent pressure V:III ratio of 15 in conjunction with growth rates of 0.8–1.3 μm h^{-1} were used. The substrate temperature T_s was varied between 100 and 550 °C. More details on the growth process are given in ref. 2. *In situ* annealing experiments were performed immediately after growth under the same As flux as applied during the growth process. The temperature was ramped to 500 °C which is markedly lower than usually applied with LT-GaAs because it is limited by In desorption from the surface. The LT-Al(Ga)InAs grown layers were kept at these annealing conditions for 1 h in each case.

3. Electrical characteristics of LT-Al(Ga)InAs

For the standard growth temperature of 500 °C the specific resistivity of Al(Ga)InAs is found to increase monotonically with the Al content. For this particular T_s value the alloy composition dependence of the resistivity of nominally undoped material is shown in Fig. 1. Over the entire composition range a strong variation from above 10^7 Ω cm for AlInAs to 0.3 Ω cm for GaInAs can be noticed. The effect of T_s on the specific resistivity for a representative quaternary composition ($x_{Ga} = 0.18$) is also shown. A common trend for the whole material system is a decrease in the specific resistivity at the higher T_s values as well as in the low T_s range. For the particular alloy shown the resistivity is characterized by a maximum near 400 °C. For the two ternary constituents the dependence on T_s is less

*On leave from: Universität Stuttgart, Pfaffenwaldring 57, W-70550 Stuttgart, Germany.

0921-5107/93/$6.00

© 1993 – Elsevier Sequoia. All rights reserved

pronounced. For AlInAs semi-insulating behaviour is found over the entire T_s range investigated in agreement with ref. 1. For GaInAs, on the contrary, the resistivity appears to be almost insensitive to the growth temperature down to 450 °C whereas below this value a decrease by roughly one order of magnitude can be noticed as well. At $T_s = 200$ °C highly conductive material with a resistivity of less than 10^{-1} Ω cm is obtained which is caused by dramatically enhanced residual carrier concentration levels as a result of electron emission from a non-shallow donor level of increasing density and thus decreasing activation energies [2].

4. Doping behaviour of LT-AlInAs:Si

The influence of T_s on the transport properties was studied on Si-doped AlInAs. High quality material grown at 500 °C is evidenced by the achieved mobilities (*e.g.* 900 $cm^2 V^{-1} s^{-1}$ at $n = 2 \times 10^{17}$ cm^{-3}), being comparable with data published elsewhere [4]. The doping behaviour was found to be strongly affected by T_s in that the carrier concentration decreases with decreasing T_s for a fixed Si flux. This finding is illustrated in Fig. 2 for two different doping levels. For the chosen doping level of 1.3×10^{17} cm^{-3} the electron density can be seen to decrease below the detection limit at $T_s < 400$ °C. At the slightly higher doping level of 2×10^{17} cm^{-3} a similar trend can be noticed except for the lower temperature regime where the carrier density tends to saturate at a level of about 5×10^{16} cm^{-3}. This behaviour cannot be reasonably explained by a deepening effect of the donor level in this range since Hall measurements indicate only a minor degree of carrier freeze-out between 300 and 77 K which suggests the Si impurity level to be of shallow nature. In addition, secondary ion mass spectrometry (SIMS) measurements clearly demonstrate that a constant Si concentration is incorporated in the grown material as would be expected for a low vapour pressure dopant. As will be shown below, the decrease in electron concentration with T_s can be ascribed only partially to an increasing concentration of deep electron traps present in material grown at reduced T_s. Consequently, the observed doping behaviour may be primarily explained by assuming the presence of a compensating acceptor. By modelling the measured temperature dependence of the carrier concentration an additional deep compensating acceptor level was derived [5]. It should, however, be mentioned that excess incorporation of neutral Si atoms has also been proposed as a potential mechanism [6].

5. Deep levels in LT-Al(Ga)InAs

The specific resistivity behaviour in the T_s range from about 400 to 600 °C which is characterized by an increase towards 400 °C is correlated with an increased incorporation of electron traps of two different levels, TDE1 and TDE2, in AlInAs [7]. Lowering the growth temperature results in an increase in the corresponding activation energies as well as of the total trap concentration. The latter quantity increases from approximately 1×10^{16} to 3×10^{16} cm^{-3} when T_s is reduced from 550 to 350 °C and is mainly determined

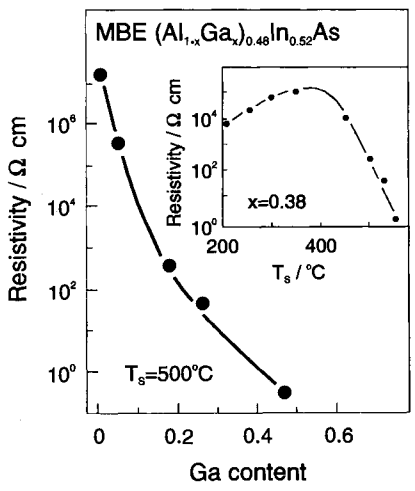

Fig. 1. Specific resistivity of Al(Ga)InAs as function of the alloy composition. The growth temperature dependence of the specific resistivity of Al(Ga)InAs ($x_{Ga} = 0.18$) is also shown.

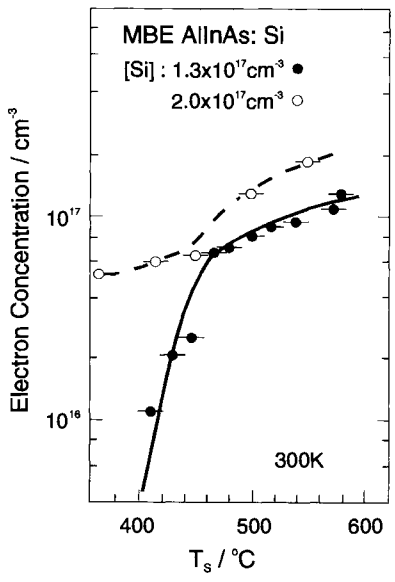

Fig. 2. Growth temperature dependence of the Hall carrier concentration for n-AlInAs:Si with two different doping levels applied.

by the deeper of the two detected trap levels, TDE1. The concentration of this trap level was found to vary between different MBE systems whereas the other trap level, TDE2, remains fairly unchanged. The deep level concentration governs the electrical properties of undoped AlInAs; semi-insulating behaviour due to electron trapping is obtained as long as the residual carrier concentration is below the deep level concentration. This may explain why some researchers have reported n-type conductivity, accessible by Hall measurements, in AlInAs with growth near the higher temperature limit. The increasing trap concentration encountered with reduction in T_s qualitatively accounts for the increase in specific resistivity for substrate temperatures down to 400 °C. Also in quaternary material (alloys with $x_{Ga}=0.05$ and 0.18 were investigated) two traps labelled QE1 and QE2 were detected. The energetic levels with respect to the conduction band edge for QE1 and QE2 were 360 and 600 meV and 270 and 480 meV for $x_{Ga}=0.05$ and 0.18 respectively. Within the accuracy of the measurement it can be concluded that the activation energies, and thus the trap levels, are identical for the ternary [7] and the quaternary compositions investigated here. Increasing the Ga content results in a decrease in the total trap concentration N_t, predominantly because of a reduction in the QE1 concentration which is reduced by a factor of 3 for $x_{Ga}=0.18$. This continuous reduction in N_t with increasing x_{Ga} causes the composition-dependent decrease in the specific resistivity towards the Ga-rich alloy compositions.

6. Annealing behaviour of LT-Al(Ga)InAs

The influence of *in situ* annealing on the electrical properties was investigated for the ternary constituents. For undoped LT-AlInAs no measurable effect of annealing on the semi-insulating behaviour could be detected, suggesting that annealing only insignificantly influences the electrical characteristics as also confirmed by the results on LT-GaInAs. Hall data for GaInAs grown at 150 °C are given in Table 1. The increase in conductivity attained under LT MBE conditions is evidenced by a carrier concentration of 6.5×10^{17} cm^{-3} associated with a mobility which is reduced by a factor of almost 10 compared with that for 500 °C growth. The material resistivity can be deduced to be hardly influenced on annealing as the measured decrease in the electron concentration is compensated by an increase in mobility. The same behaviour was found on AlInAs grown at reduced T_s. To ease deep level transient spectroscopy (DLTS) measurements these layers were intentionally doped with Si. While the Si concentration for the samples presented in Table 1 amounted to 2.0×10^{17} cm^{-3}, as verified by SIMS measurements, reduced carrier concentrations are detected at $T_s=400$ °C (see above). Annealing of this material did not result in a notable change in either the Hall data or the trap characteristics. Merely a minor decrease in carrier concentration and mobility together with some increase in the trap concentration seem to occur.

7. Application of LT-AlInAs to high electron mobility transistor structures

The growth temperature offers a degree of freedom for optimizing the MBE process to give device layer structures of superior performance. The employment of LT MBE grown AlInAs in high electron mobility transistor (HEMT) structures may serve here to exemplify the capability of this approach. Growth of AlInAs layers at lower temperature was shown previously to give significantly smoother surfaces [8] which is of great importance for buffer layer applications. The leakage current of Schottky diodes on AlInAs gate layers was found to be reduced by about two orders of magnitude with growth at 350 °C rather than 500 °C [9]. Another technological topic is Si segregation which appears to be a problem in inverted and single quantum well (SQW) type HEMTs which, in contrast to "normal" HEMT structures, are designed with the donor layer placed below and at both sides of the channel respectively. Table 2 summarizes basic elec-

TABLE 1. Electrical characteristics of as-grown and annealed LT-GaInAs and AlInAs:Si grown at reduced T_s

Material	T_s (°C)	Annealing conditions		n ($\times10^{17}$ cm^{-3})		μ (cm^2 V^{-1} s^{-1})		E_a (meV)		N_t (cm^{-3})
		Time	Temperature	300 K	77 K	300 K	77 K	TDE1	TDE2	
GaInAs	150	—	—	6.5	6.1	1140	890	—	—	—
GaInAs	150	60	500	1.4	1.1	3310	3260	—	—	—
AlInAs:Si	400	—	—	1.7	1.5	740	660	326	557	3.5×10^{15}
AlInAs:Si	400	60	500	1.6	1.3	620	480	322	513	5.5×10^{15}

TABLE 2. Electrical characteristics of inverted and single quantum well high electron mobility transistors as a function of the (lower) spacer growth temperature (data for normal high electron mobility transistors are given for comparison)

HEMT	T_s^{spacer} (°C)	$n_{300K}^{(2)}$ ($\times 10^{12}$ cm^{-2})	μ_{300K} (cm^2 V^{-1} s^{-1})	$n_{77K}^{(2)}$ ($\times 10^{12}$ cm^{-2})	μ_{77K} (cm^2 V^{-1} s^{-1})
Normal	500	3.1	9.560	3.1	27.870
Inverted	500	3.4	5.440	3.5	10.180
Inverted	300	2.7	7.990	2.8	24.850
SQW	500	4.1	7.390	4.6	12.850
SQW	300	4.7	10.549	5.1	33.701

tronic properties of related HEMT structures, with the normal HEMT structure grown at 500 °C serving as reference. In all the structures investigated a 20 nm thick gate layer and a 10 nm thick contact layer doped to 1×10^{18} cm^{-3} were used. In the normal and inverted structures the electrons were supplied by an Si δ-doped plane with a donor density of 5×10^{12} cm^{-2}. The thicknesses of the channel and the spacer layer were chosen to be 20 nm and 2 nm respectively. The Hall data of the inverted HEMT grown entirely at 500 °C clearly reveal deterioration of the structure indicated by enhanced electron concentration in the channel for which Si segregation seems to be a plausible reason and reduced mobilities. Exclusive growth of the spacer layer at low T_s (300 °C) results in a marked improvement in the mobility, approaching the value of the normal HEMT structure which does not suffer from Si segregation. From this effective suppression of Si segregation by use of reduced growth temperature for the spacer layer can be concluded. The same finding holds for SQW-type structures, the thicknesses of the channel and spacer layers of which were 20 nm and 7 nm respectively. Doping was introduced asymmetrically with 6×10^{12} cm^{-2} and 2.8×10^{12} cm^{-2} for the upper and lower supply regions respectively. Again, for the structure grown entirely at 500 °C, degradation of the mobility is obvious, whereas growth of the lower spacer at 300 °C again results in substantially improved mobilities of as high as 10 550 cm^2 V^{-1} s^{-1} and 33 700 cm^2 V^{-1} s^{-1} at 300 K and 77 K respectively, in conjunction with an electron concentration of 5×10^{12} cm^{-1}. Further optimization of the structure by modifying the dopant distribution to minimize parallel conduction gave mobilities of 10 700 and 41 800 cm^2 V^{-1} s^{-1} (at 300 and 77 K).

8. Summary

LT MBE growth of Al(Ga)InAs lattice matched to InP was studied. The substrate temperature dependence of the specific resistivity as well as the Si donor incorporation behaviour can be qualitatively explained in terms of the deep electron trap concentration deduced by DLTS. *In situ* post-growth annealing of LT-GaInAs as well as LT-AlInAs at 500 °C was shown not to change the electrical properties significantly. The usefulness of LT material is exemplified by the improvement in the electrical characteristics of inverted and SQW HEMTs with an LT-AlInAs lower spacer to prevent Si segregation into the channel.

Acknowledgment

This work was partially funded by the DBP Telekom under the "OEIC Project".

References

1 R. A. Metzger, A. S. Brown, W. E. Stanchina, M. Lui, R. G. Wilson, T. V. Kargodorian, L. G. McCray and J. A. Henige, *J. Cryst. Growth, III* (1991) 445.
2 H. Künzel, J. Böttcher, R. Gibis and G. Urmann, *Appl. Lett., 61* (1992) 1347.
3 H. Künzel, N. Grote, P. Albrecht, J. Böttcher and C. Bornholdt, *Electron. Lett., 28* (1992) 844.
4 G. J. Davies, T. Kerr, C. G. Tuppen, B. Wakefield and D. A. Andrews, *J. Vac. Sci. Technol. B, 2* (1984) 219.
5 H. Hoenow, H.-G. Bach, H. Künzel and C. Schramm, *20th Int. Conf. on GaAs and Related Compounds, Freiburg, Germany, 1993*, in press.
6 M. Higuchi, T. Ishikawa, K. Imanishi and K. Kondo, *J. Vac. Sci. Technol. B, 9* (1991) 2802.
7 H. Hoenow, H.-G. Bach, J. Böttcher, F. Gueissaz, H. Künzel, F. Scheffer and C. Schramm, *4th Int. Conf. on InP and Related Materials, Newport, RI, 1992*, p. 136 (IEEE Catalog no. 92CH3104-4; Library of Congress no. 91-77922, 1992).
8 H. Künzel, W. Passenberg, J. Böttcher and C. Heedt, *Microelectron. Eng., 15* (1991) 569.
9 H. Künzel, J. Böttcher, R. Gibis, H. Hoenow and C. Heedt, *J. Cryst. Growth, 127* (1993) 519.

Photo-induced current transient spectroscopy of $Al_{0.48}In_{0.52}As$ semi-insulating layers grown on InP by molecular beam epitaxy

A. Kalboussi, G. Marrakchi*, A. Tabata and G. Guillot

Laboratoire de Physique de la Matière (URA CNRS 358), Institut National des Sciences Appliquées de Lyon, Bât 502, 20 avenue Albert Einstein, 69621 Villeurbanne Cédex (France)

G. Halkias and K. Zekentes

Foundation for Research and Technology, Hellas-IESL, 71110 Heraklion, Crete (Greece)

A. Georgakilas and A. Cristou

University of Maryland, CALCE Electronic Packaging Research Center, College Park, MD 20742 (USA)

Abstract

Deep levels in undoped semi-insulating $In_{0.52}Al_{0.48}As$ layers grown by molecular beam epitaxy on iron-doped InP have been studied by photoluminescence and photo-induced current transient spectroscopy. The effect of the growth temperature T_g in the range from 300 °C to 530 °C has been investigated. The results show that low T_g causes the material quality to deteriorate and leads to formation of a higher concentration of deep traps. It is shown that optimized material quality can be obtained for InAlAs layers on InP substrates with T_g around 530 °C with sufficiently high resistivity, reduced trap density and good structural properties which is appropriate for fabrication of high electron mobility transistors.

1. Introduction

InP-based InGaAs/InAlAs high electron mobility transistors (HEMTs) are among the highest speed devices available today [1]. It has been shown that InAlAs alloy grown by molecular beam epitaxy (MBE) becomes semi-insulating in a wide range of growth conditions [2]. Thus the lattice-matched $In_{0.52}Al_{0.48}As$ (denoted by InAlAs hereafter) must be used as buffer layer in the $In_xGa_{1-x}As$/InAlAs HEMT structures on InP. The electrical and structural properties of this alloy material affect strongly the performance of HEMTs. Traps present into the InAlAs buffer layer and/or at the interfaces can be the origin of the kink effect observed on the I–V characteristics of HEMTs [3]. However, if the trap defects are associated with the crystal defect as shown by Claverie *et al.* [4], these layers cannot be used for the development of high performance devices. Some contradictory results about MBE grown high quality InAlAs layers have been reported by several researchers [2, 5–10]. However, it is clearly established that, on using MBE, the growth temperature T_g deeply affects the material's quality. In this paper, we present the influence of the InP pre-growth thermal desorption temperature T_T and of the growth temperature T_g on the optical and electrical properties of MBE grown InAlAs. The range of T_g investigated was 300–530 °C. This work is mainly focused on the study of deep levels responsible for the semi-insulating character of the InAlAs material by photo-induced current transient spectroscopy (PICTS) as a function of T_g. On combining photoluminescence (PL) and PICTS results, a strong dependence of the properties of InAlAs layers on the growth temperature has been found.

2. Experimental details

The MBE growth was performed on (001) semi-insulating iron-doped InP substrates in the temperature range from 300 °C to 530 °C. Undoped InAlAs layers of 1.5–2.0 μm thickness were grown for all the samples. The InAlAs was grown with composition around that required for lattice matching to InP ($x_{In} = 0.52$). The growth rate was 0.85 μm h^{-1} and the As_4/III beam flux equivalent pressure ratio was 26. The growth parameters of the five samples S1–S5 are given in Table 1.

*Author to whom correspondence should be addressed.

TABLE 1. Molecular beam epitaxy growth parameters and photoluminescence results at 5 K of semi-insulating InAlAs samples

Sample	T_g (°C)	T_T (°C)	FWHM[a] (meV)	I_{PL}	x_{In}	P_{In}/P_{Ga}	d (μm)	Resistivity ($\times 10^6$ Ω cm)
S1	300	500	25	1	0.56	2.81	2	—
S2	440	530	28	5×10^3	0.56	2.76	1.4	0.20
S3	480	530	23	4×10^3	0.54	2.76	1.65	1.30
S4	500	500	33	6×10^3	0.53	2.81	2	0.025
S5	530	530	15	7×10^4	0.56	2.95	1.65	4.95

[a]FWHM, full width at half-maximum.

The PL spectra have been measured at 5 K using argon laser excitation and classical detection techniques by a germanium liquid nitrogen cooled detector and lock-in treatment. Structural characterizations of the same layers have been made by double-crystal X-ray diffraction (DCXD), scanning electron microscopy (SEM) and transmission electron microscopy (TEM) and have been reported in detail elsewhere [11, 12].

Details on the PICTS theory and the experimental arrangements for digital PICTS measurements used in this work have reported elsewhere [13, 14]. Only the experimental conditions will be given here. The ohmic contacts have been made by evaporating 1500 Å semi-transparent indium layers followed by a rapid thermal annealing at 320 °C for 20 s. Light pulses (duration, 100 ms; repetition rate, 1 Hz) provided by an He–Ne laser (1.96 eV) were used as an excitation source and focused on the sample. The photocurrent and photo-induced transient current were measured through a sampling resistor and amplified with a high speed preamplifier. The entire transient was recorded digitally at each temperature and stored on floppy disk. PICTS peaks occur in the spectrum when the emission rate of trapped carriers corresponds to the rate window set by the chosen values of t_1 and t_2. In the following experiments, the t_2/t_1 ratio is kept at 10 and the sampling time t_1 was varied between 1 and 20 ms.

3. Results and discussion

The growth temperature T_g was found to be a very critical parameter for the structural, optical and electrical properties of InAlAs. This is illustrated by Table 1 and Fig. 1 where the FWHM and the PL near-band-gap edge intensity at 5 K are given as a function of T_g. It is evident that on increasing the InAlAs growth temperature the optical quality of InAlAs is improved: the FWHM decreases (15 meV for S5) and the PL intensity increases (10^5 times higher signal intensity for S5 compared with S1). The FWHM value of 15 meV

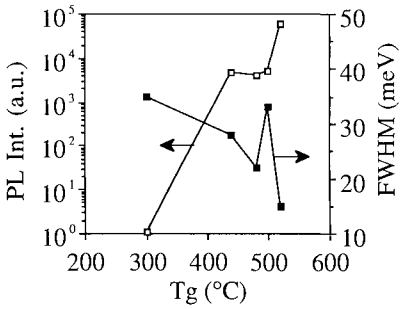

Fig. 1. Variations in the PL intensity and FWHM at 5 K for InAlAs samples grown at different temperatures.

appears to be indicative of a good material quality and defect-free layers [11, 12].

PL deep level bands are present in the energy range 1.2 eV–0.7 eV. The presence of deep level emission appears to be very sensitive to the growth temperature. There is a tendency to reduced deep level PL bands when T_g increases from 300 °C to 530 °C. A deep emission peaking at about 0.85 eV is always detected whatever T_g. In the S5 sample, this band is the only band detected in the deep energy emission range. It seems typical of an intrinsic defect of the InAlAs material situated at about 0.6 eV from the conduction or valence band. In fact PICTS results will reveal the presence of such deep level located at this energy.

The influence of the InP substrate thermal cleaning temperature T_T is less evident from the optical results but we can qualitatively state that there is a trend to improved material quality when T_T is increased (see Table 1 and variations in the FWHM with T_T).

These results are very well correlated with SEM, TEM and DCXD observations [11, 12]. The InAlAs surface morphology was found to be dramatically dependent on T_g and T_T [15]. Very smooth surfaces have been obtained for $T_g = T_T = 530$ °C and significant surface degradation has been observed either for $T_T = 500$ °C or for T_g lower than 500 °C [15].

From all these characterization results, it appears that the PL FWHM values are mainly correlated with

the concentration of extended defects in the InAlAs layers while the PL intensity and X-ray FWHM are mainly correlated with point defects and alloy clustering (due to the growth temperature). The sample grown with the optimum conditions ($T_g = T_T = 530$ °C) has a FWHM of 15 meV at 5 K which is very near the state-of-the-art value (10–12 meV from refs. 16 and 17) and presents a very strong signal intensity.

Figure 2 shows PICTS spectra obtained from samples S1, S4 and S5. The S2 and S3 samples exhibit the same PICT spectra as sample S5. In sample S1, five levels labelled A, B, C, D and E with different amplitudes are detected at 0.19 eV, 0.36 eV, 0.56 eV, 0.6 eV and 0.82 eV respectively. In samples S2, S3 and S5 two levels labelled P_1 and P_2 are situated at 0.59 eV and 0.66 eV are detected, while S4 exhibits only one level named P and detected at 0.38 eV.

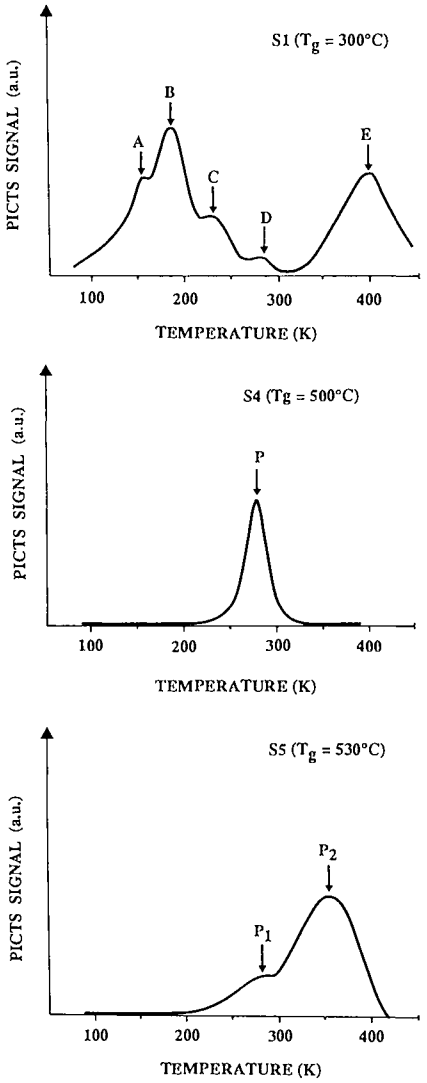

Fig. 2. PICTS spectra of samples S5, S4 and S1 grown respectively at 530 °C, 500 °C and 300 °C.

The apparent activation energies and capture cross-sections corresponding to the PICTS peaks observed in all the samples and deduced from an Arrhenius plot of T^2/e_n *vs.* $1/T$ are reported in Table 2.

In order to have a qualitative interpretation of the PICTS peaks amplitude evolution, we have paid attention to keep the experimental conditions unchanged. In this case, we can consider that the variation in the PICTS peak amplitude is roughly proportional to the corresponding level concentration. Figure 3 shows the evolution of the PICTS peak amplitudes of the P_1 and P_2 traps detected in S2, S3 and S5 samples as a function of growth temperature T_g. It is clearly evidenced that the concentrations of these levels decrease when T_g increases and reach a minimum at 530 °C. In studied temperature range, we observe a clear correlation between the PL intensity and the concentration of point defects (Figs. 1 and 3), showing that they certainly act as non-radiative centres. The PL emission

TABLE 2. Apparent activation energies and capture cross-sections of the deep levels detected by photo-induced current transient spectroscopy

Sample	T_g (°C)	Trap label	Activation energy (eV)	Capture cross-section (cm^2)
S1	300	A	0.19	3×10^{-17}
		B	0.36	1×10^{-13}
		C	0.56	1×10^{-11}
		D	0.60	2×10^{-13}
		E	0.82	5×10^{-14}
S2	440	P1	0.59	6×10^{-14}
		P2	0.65	7×10^{-15}
S3	480	P1	0.58	2×10^{-13}
		P2	0.67	6×10^{-14}
S4	500	P	0.38	4×10^{-17}
S5	530	P1	0.59	7×10^{-13}
		P2	0.66	2×10^{-15}

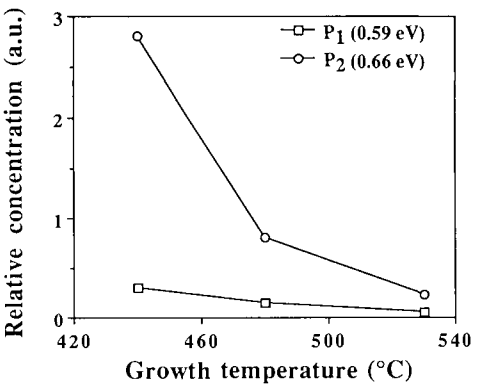

Fig. 3. Evolution of the PICTS signal for P_1 and P_2 traps as a function of the growth temperature.

band detected at 0.85 eV in all the studied samples can be correlated with the deep level observed by PICTS at 0.59 eV in all the samples except for the sample S4. In this case, the amplitude of the 0.38 eV PICTS peak is higher than the total sum of the peak amplitudes in samples S3 and S5. Therefore, the 0.59 eV deep level is probably present in sample S4 with a much lower concentration than the 0.38 eV level and it cannot be clearly observed by PICTS. Several researchers [18, 19] have observed by deep level transient spectroscopy (DLTS) in MBE n-type silicon doped InAlAs a level having the same parameters as the level which we observed by PICTS at 0.59 eV in undoped InAlAs samples. Consequently, this deep level is an electron trap related to a native defect. The appearance of the 0.38 eV level and the disappearance of the 0.66 eV level in the sample S4 is correlated with the increase in the FWHM in this sample and can be explained by the decrease in the InP substrate thermal cleaning temperature ($T_T = 500$ °C). The 0.66 eV level seems to be related to the InP substrate. Indeed, when the substrate temperature T_T decreases from 530 °C to 500 °C, the 0.66 eV level disappears (samples S1 and S4). This indicates that this level probably originates at the substrate-epilayer interface. Hong *et al.* [19] have found by DLTS an electron trap at 0.71 eV labelled EA4 and they suggested that this level is related to the InAlAs–InP interface. Taking into account the error estimated by Hong *et al.* of 0.07 eV in the determination of activation energies and the deviation in the indium composition x_{In}, we can assume that the level detected in this work at 0.66 eV corresponds to the 0.71 eV level observed by Hong *et al.* The C and E levels situated at 0.56 eV and 0.82 eV respectively in sample S1 have also been detected in MBE n-type samples by DLTS [18, 19]. Thus, these levels are electron traps which are annihilated when T_g is higher than 300 °C, whereas the A level situated at 0.19 eV in sample S1 could be a hole trap because it is indetectable by DLTS measurements in n-type samples.

4. Conclusion

Semi-insulating behaviour of undoped MBE InAlAs grown at $T_g < 530$ °C is investigated by the study of deep levels. We show that the trap concentrations increase when T_g decreases. For $T_g = 300$ °C five defects are present in the material; however, only two defects remain for $T_g = 530$ °C. PL results reveal a direct correlation between defect density and optical properties. Very good optical and structural properties are obtained with thermal treatment and a growth temperature both equal to 530 °C.

Acknowledgments

This work has been supported by ESPRIT Basic Research 3086 Project. A. Tabata wishes to acknowledge the CAPES (Brazil) for financial support.

References

1 F. I. Ng, D. Pavlidis, Y. Kwon, T. Brock, J. I. Davies, G. Clarke and P. K. Rees, *Proc. 4th Int. Conf. on InP and Related Materials, Newport, RI, April 1992*, IEEE, New York, 1992, p. 18.
2 G. J. Davies, T. Kerr, C. G. Tuppen, B. Wakefield and D. A. Andrews, *J. Vac. Sci. Technol. B, 2* (1984) 219.
3 L. F. Palmateer, P. J. Tasker, W. J. Schaff, L. D. Nguyen and L. F. Eastmann, *Appl. Phys. Lett., 54* (1991) 2139.
4 A. Claverie, K. M. Yu, W. Swider, Z. Lilienthal-Weber, M. O'Keefe, P. Kilaas, J. Pamulapati and P. K. Bhattacharya, *Appl. Phys. Lett., 60* (1992) 989.
5 J. Massies, J. F. Rochette, P. Etienne, P. Delescluse, A. M. Huber and J. Chevrier, *J. Cryst. Growth, 64* (1983) 101.
6 A. Chin, P. Battacharya, W. P. Hong and W. Q. Li, *J. Vac. Sci. Technol. B, 6* (1988) 665.
7 A. S. Brown, M. J. Delaney and J. Singh, *J. Vac. Sci. Technol. B, 7* (1989) 384.
8 J. P. Praseuth, L. Golstein, P. Henoc, J. Primot and G. Danan, *J. Appl. Phys., 61* (1987) 215.
9 J. E. Oh, P. K. Bhattacharya, Y. C. Chen, O. Aina and M. Mattingly, *J. Electron. Mater., 19* (1990) 435.
10 E. Tournié, Y. H. Zhang, N. J. Pulsford and K. Ploog, *J. Appl. Phys., 70* (1991) 7362.
11 A. Georgakilas, A. Cristou, G. Halkias, K. Zekentes, N. Kornilias, C. Papavassiliou, A. Dimoulas, F. Peiro, A. Cornet, S. Ababou, A. Tabata and G. Guillot, *Proc. SOTAPOCS XVI, 181st Electrochemical Society Meet., St. Louis, MO, May 1992*, Electrochemical Society, Pennington, NJ, to be published.
12 A. Georgakilas, K. Zekentes, K. Tsagaraki, P. Lefebvre, J. Allegre and A. Christou, *Proc. 4th Int. Conf. on InP and Related Materials, Newport, RI, April 1992*, IEEE, New York, 1992, p. 101.
13 C. Hurtes, M. Boulou, A. Mitonneau and D. Bois, *Appl. Phys. Lett., 32* (1978) 821.
14 O. Yoshie and M. Kamihara, *Jpn. J. Appl. Phys., 22* (1983) 621.
15 F. Peiro, A. Cornet, J. R. Morante, A. Georgakilas and G. Halkias, *Proc. SOTAPOCS XVI, 181st Electrochemical Society Meet., St Louis, MO, May 1992*, Electrochemical Society, Pennington, NJ, to be published.
16 W. P. Hong, A. Chin, N. Debbar, J. Hinckley, P. Bhattacharya, J. Singh and R. Clarke, *J. Vac. Sci. Technol. B, 5* (1988) 800.
17 A. S. Brown, U. K. Mishra, J. A. Henige and M. J. Delaney, *J. Vac. Sci. Technol. B, 6* (1988) 678.
18 P. S. Whitney, W. Lee and C. G. Fonstad, *J. Vac. Sci. Technol. B, 5* (1987) 796.
19 W. P. Hong, S. Dhar, P. K. Bhattacharya and A. Chin, *J. Electron. Mater., 16* (1987) 271.

Low temperature chemical beam epitaxy of gallium phosphide/silicon heterostructures

J. T. Kelliher, J. Thornton and N. Dietz
Department of Materials Science and Engineering, North Carolina State University, Raleigh, NC 27695-7919 (USA)
G. Lucovsky
Department of Physics, North Carolina State University, Raleigh, NC 27595-7919 (USA)
K. J. Bachmann*
Department of Chemical Engineering, North Carolina State University, Raleigh, NC 27695-7919 (USA)

Abstract

The low temperature epitaxial growth of GaP on (001) Si by chemical beam epitaxy (CBE) was investigated with the aim of using GaP epilayers for the dielectric isolation of silicon circuits. Optimum CBE of GaP on silicon, using *t*-butyl phosphine (TBP) and triethylgallium (TEG) as source vapors, is obtained at 310 °C. GaP nucleates on silicon highly selectively with regard to deliberately SiO_2 and SiC coated surface regions. This behavior is due to the higher catalytic activity of the GaP surface compared with a silicon dioxide surface with regard to TBP pyrolysis. The efficiencies of incorporating phosphorus and gallium at the GaP surface are substantially different and require flux ratios $R_{TBP:TEG} \geq 25$ for stoichiometric GaP deposition. Atomic force microscopy reveals a typical surface roughness of 75 Å for a film thickness of 2000 Å. Although the GaP growth occurs initially without interfacial reactions, upon prolonged growth (layer thickness more than 300 Å), transport of oxygen and carbon through the GaP film to the GaP–Si interface results in the growth of an SiO_2/SiC layer between the silicon substrate and the GaP film, which is desirable in the context of dielectric isolation but requires modifications of the growth conditions in the context of opto-electronics.

1. Introduction

The room temperature band gaps of 2.25 and 1.11 eV and electron affinities of 4.3 and 4.01 eV for gallium phosphide and silicon respectively, suggest large offsets in the valence band edges and sizable discontinuities in the conduction band edges of heterostructures between these two materials. Also, their lattice constants, $a(GaP) = 5.451$ Å and $a(Si) = 5.431$ Å, match at room temperature within 0.37%. Therefore, GaP is an attractive choice for the dielectric isolation of Si circuits which are built in the top layer of Si/GaP/Si heterostructures. Furthermore, the discontinuities in the band edges of Si/GaP junctions, may become useful in the context of scaling of heterostructure transistors and of the investigation of confinement effects. In addition, GaP/Si heterostructures have attracted considerable attention in the context of opto-electronic applications [1, 2], and may permit the future extension of the range of available substrate diameters for epitaxial growth of other compounds and alloys on GaP, for example of non-linear optical materials such as $ZnGeP_2$ and $ZnSi_xGe_{1-x}P_2$ [3, 5]. In the context of the above mentioned potential use in microelectronics, a low thermal budget is an important aspect, demanding either low temperature or rapid thermal processing. Low temperature processing is favored because of the large mismatch in the thermal expansion coefficients, 5.3×10^{-6} K^{-1} for GaP and 2.33×10^{-6} K^{-1} for Si. Therefore, we have chosen chemical beam epitaxy (CBE) and UV photon enhanced chemical beam epitaxy (UVPECBE), which achieve epitaxial growth at low substrate temperature [1].

2. Experimental conditions

The work described in this paper was performed using a CBE system which is described in more detail elsewhere [6]. It consists of a growth chamber pumped by three turbomolecular pumps to a background pressure of 10^{-9} Torr, a load-lock and by-pass chamber that are both separately pumped. The substrate is

*Author to whom correspondence should be addressed.

0921-5107/93/$6.00
© 1993 – Elsevier Sequoia. All rights reserved

located in a boron nitride block and is heated by a quartz lamp. A central port is provided for illumination of the substrate by UV light emitted from a 1 kW mercury lamp or a nitrogen laser.

In order to test for selectivity and to create a reference surface for film thickness measurements, after an initial RCA cleaning procedure, the silicon substrate wafers are coated by 3500 Å thermal SiO_2. They are subsequently patterned by photolithography to expose well defined bare Si surface areas. For tests of the selectivity of GaP deposition with regard to SiC, several patterned wafers were carbonized to grow an approximately 100 Å thick SiC layer on the exposed silicon. Then the SiO_2 was removed by etching to expose a negative pattern of bare silicon surrounded by SiC. Prior to use, all wafers receive another standard RCA cleaning procedure and brief buffered HF etch. They were immediately loaded into the CBE growth chamber. After establishing ultrahigh vacuum conditions, heating was initiated. When the substrate reached a temperature of 160 °C, the *t*-butyl phosphine (TBP) flow was switched to the growth chamber. The triethylgallium (TEG) flux is switched to the CBE chamber when the desired substrate temperature is reached to commence GaP nucleation and growth. Reversing the sequence, *i.e.* exposing the silicon surface first to the TEG and then adding the TBP flux, results in the formation of silicon carbide which prevents the nucleation of an epitaxial GaP film.

3. Results

Auger electron spectroscopy establishes that no growth occurs on the SiO_2 so that the film thickness can be established by Dektak measurements using the SiO_2 as a reference surface. The validity of these measurements was checked independently by cross-sectional transmission electron microscopy. Also, CBE of GaP on the carbonized silicon wafers occurs highly selectively on the clean silicon surface and not on the SiC. X-ray diffraction experiments show the expected (400) and (111) Si substrate reflections for (100) and (111) surfaces respectively, which nearly coincide with the GaP reflections with the same Laue indices. The only additional GaP reflections recorded are (200) and (222) respectively, in accord with the selection rules $h+k+l=2n+l$ or $h+k+l=4n$ for $Fd3m$ and $h+k$, $k+l, (l+h)=2n$ and $h+l=2n$ for $F43m$.

Rutherford backscattering experiments on GaP films grown at different ratios $R_{TBP:TEG}$ of *t*-butyl phosphine and triethylgallium flows to the surface reveal that the films are phosphorus deficient below a critical flux ratio. Two-phase growth including gallium-rich droplets in the films occurs at $R_{TBP:TEG} < 25$ for (100) substrates [6] and at $R_{TBP:TEG} < 10$ for (111) substrates. Figures 1(a) and 1(b) show scanning electron microscopy images of the Si (001) surface after 5 and 10 min exposure to both TBP and TEG fluxes at $R_{TBP:TEG} = 25$. They reveal the formation of two distinct nucleation features of circular and irregular cross-sections respectively. Further information on these features is obtained by atomic force microscopy (AFM) and scanning tunneling microscopy (STM) studies. Figures 2(a) and 2(b) show AFM and STM line scans of 10 μm length across the surface of the partially GaP-covered silicon substrate after 10 min of exposure to both TBP and TEG fluxes. In addition to a relatively flat surface, the AFM scan reveals the presence of needles of typically 50 nm height. AFM images show that these whiskers have a density comparable with the density of the circular features observed by

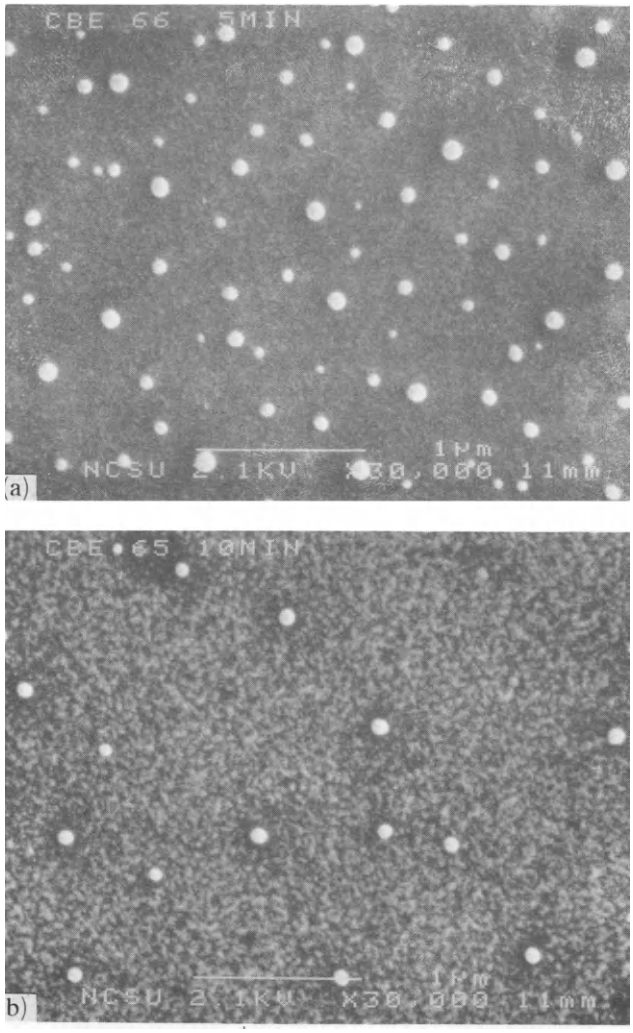

Fig. 1. Scanning selectron micrographs of partially gallium phosphide covered silicon (100) surfaces after exposure to both TBP and TEG fluxes at $R_{TBP:TEG} = 25$ for (a) 5 min and (b) 10 min.

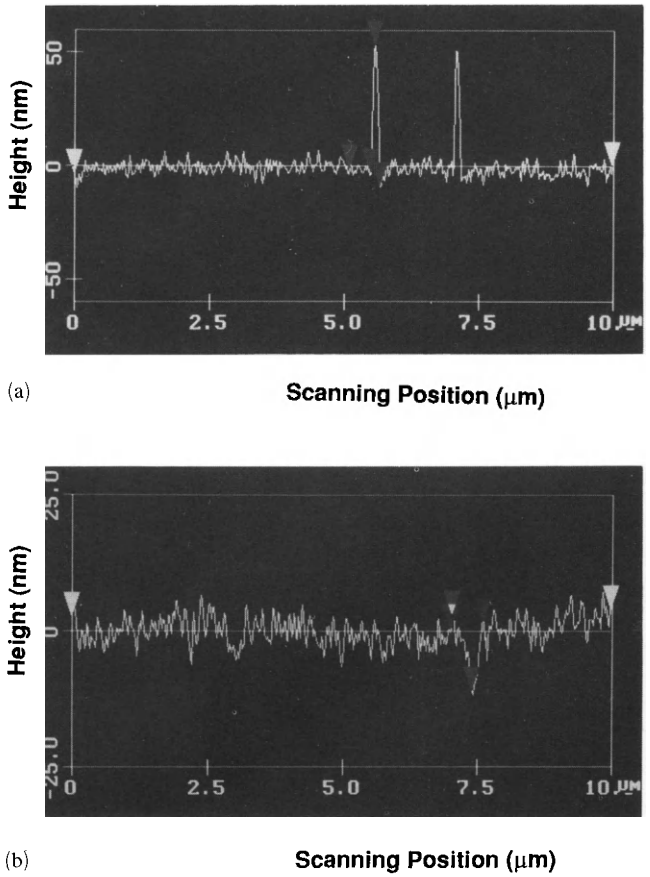

Fig. 2. (a) AFM and (b) STM line scans across partially gallium phosphide covered silicon surfaces after exposure to both TBP and TEG fluxes at $R_{V:III} = 25$ for 10 min.

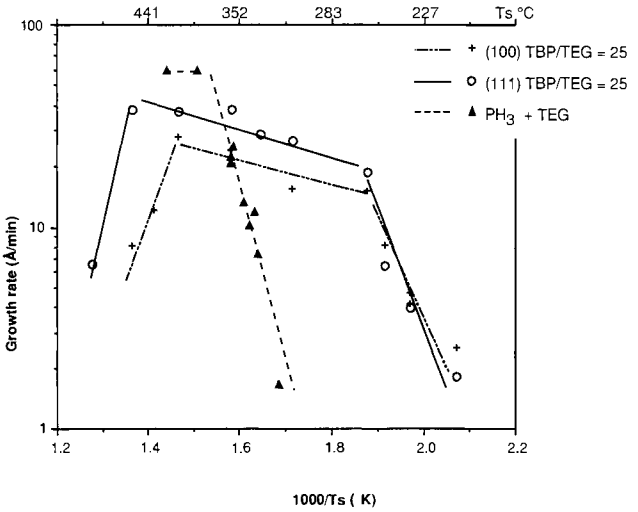

Fig. 3. Growth rate *vs.* reciprocal temperature for CBE of GaP on Si(100) and Si(111) surfaces using TBP and TEG as source materials ($R_{TBP:TEG} = 25$); ——, results of ref. 1 using PH_3 and TEG as source materials.

SEM. More extensive SEM studies show that the density of these needles decreases with increasing growth time, *i.e.* their vertical growth stops after a transient period of time so that they become embedded into the film without loss of epitaxy as detected by X-ray diffraction. The surface roughness determined by AFM on 2000 Å thick GaP films is typically 75 Å.

Figure 3 shows a plot of the growth rate v_g(GaP) at $R_{TBP:TEG} = 25$ as a function of reciprocal substrate temperature. There are three regions, where the growth rate (I) increases, (II) slightly decreases and (III) steeply decreases with decreasing substrate temperature. The transitions between regions I and II occur on (001) and (111) Si at approximately 410 and 510 °C respectively. The transition between regions II and III occurs at approximately 260 °C for both surface orientations. For comparison, we show as a dashed line in Fig. 3 the results of Yoshimoto *et al.* [1] for GaP growth on Si(100) by CBE using TEG and PH_3 as source materials.

Secondary ion mass spectrometry (SIMS) analyses of GaP epilayers, grown at 310 °C and a TBP:TEG flow ratio of 25 for less than or equal to 30 min, show a monotonic decrease in the signals at mass over charge (m/e) ratios of 12 and 16 on sputtering with Cs^+ through the GaP film into the Si substrate. For longer growth times, an increase in these signals is observed in the interfacial region. The signals at $m/e = 12$ and $m/e = 16$, normalized to the signal at $m/e = 31$, increase in the interfacial region because the phosphorus ($m/e = 31$) concentration decreases while the carbon ($m/e = 12$) and oxygen ($m/e = 16$) concentrations first increase and, on sputtering into the silicon substrate, settle at a constant background level. Out of 54 SIMS analyses, performed for films representing 14 different combinations of flow rate ratios, growth times, substrate temperatures and orientations, we observed that the normalized signal at $m/e = 16$ rises consistently before the normalized signal at $m/e = 12$.

Figure 4(a) shows a plot of the signals at $m/e = 12$ and $m/e = 40$ *vs.* sputtering time for an epilayer deposited at 310 °C for 3 h at a TBP:TEG flow rate ratio of 25. Note that the $m/e = 40$ signal is at a constant background level throughout the GaP film and increases sharply at the GaP–Si interface. The $m/e = 12$ signal decreases linearly inside the GaP film and shows a maximum in the interfacial region. Figure 4(b) shows a plot of the absolute value of the signal at $m/e = 12$ at the Si–GaP interface as a function of the square root of the growth time t_g. There is an induction period about 30 min long during which no enhancement of this signal at the interface is observed. On completion of this period, the carbon concentration rises steeply and assumes an approximately linear $\sqrt{t_g}$ dependence after approximately 1 h of growth.

4. Discussion

The X-ray diffraction results show that the GaP films grow with the same surface orientation as the underlying silicon substrate on both (100) and (111) Si, *i.e.* they exhibit a least sharp fiber texture. The efficiencies of phosphorus and gallium incorporation on the GaP surface are substantially different, as indicated by the large values of $R_{TBP:TEG}$ required for stoichiometric growth. In the temperature regime where the growth rate is only a weak function of temperature, and for sufficiently high values of $R_{TBP:TEG}$, both TBP and TEG molecules impinging onto the substrate are pyrolyzed into fragments at comparable rates and sustain the growth of a contiguous single-phase GaP film. The key to understanding of the selectivity of the nucleation and growth process, and of the morphology observed during nucleation, is the catalytic enhancement of the decomposition rate of TBP by the different solid surfaces. For GaP and SiO_2, a considerable difference in the catalytic activity with regard to TBP decomposition is well established [7]. It has been related to the formation of complex bonds in the initial step of thermal decomposition between TBP molecules which carry lone pairs and gallium sites in the GaP surface which act as electron acceptors [8]. The selectivity with regard to SiO_2 arises from the absence of surface sites for complex bonding for TBP on an SiO_2 surface. Although silicon surfaces have not been investigated in this context thus far, their catalytic activity is expected to lie in between those of GaP and SiO_2 surfaces, enhancing three-dimensional growth of the GaP nuclei on the silicon surface in accordance with the results of the SEM, AFM and STM imaging.

In view of the difference in the catalytic activities of the silicon and the GaP surfaces, the silicon surface may be more highly supersaturated by gallium compared with phosphorus even at a TBP:TEG flux ratio that assures nearly stoichiometric GaP growth, once a contiguous GaP epilayer is formed. Thus two-phase deposition conditions may exist in the initial stage of nucleation, providing a possible explanation for the observation of whisker growth as part of the nucleation process. It is well known that the growth of whiskers by a vapor–liquid–solid (VLS) mechanism, for compound semiconductors that decompose into constituents with vastly different vapor pressures, can be supported by the less volatile constituents acting as a solvent [9]. For III–V compounds, these are group III droplets that exist at the whisker tips and are consumed in the course of the VLS growth process which terminates after some period of time in accordance with the above discussed observations. Of course, this does not prove that a VLS mechanism is indeed established. The STM scan, Fig. 4(b), indicates a reversed contrast at approxi-

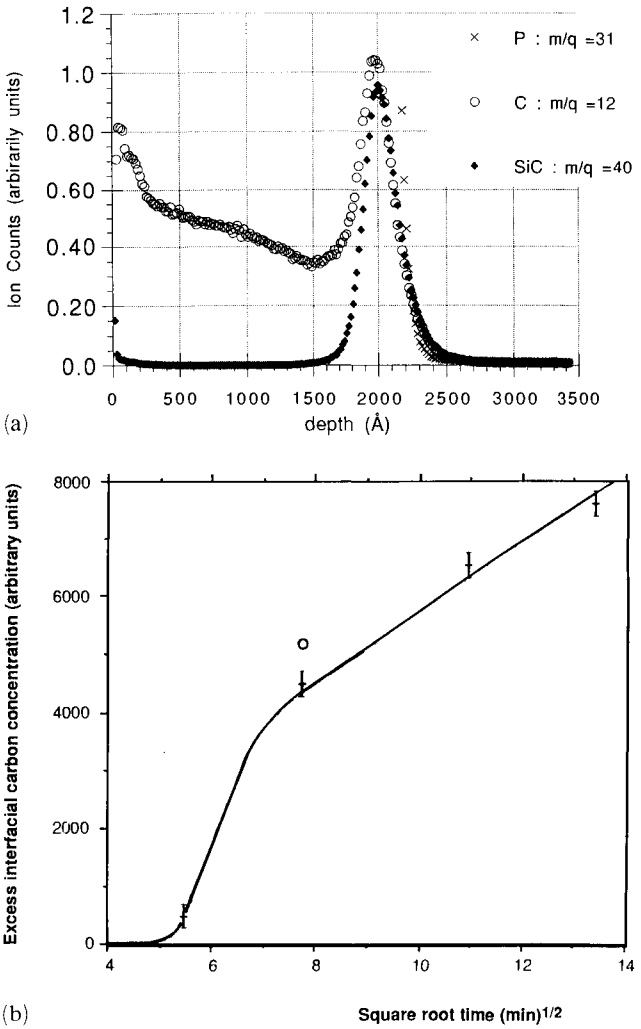

Fig. 4. (a) SIMS profiles at $m/e = 12$ (○) and $m/e = 40$ (◆) for a GaP epilayer grown by CBE on a (100) silicon substrate at $R_{TBP:TEG} = 25$ for 180 min at 310 °C. (b) Interfacial carbon concentration *vs.* square root of time of exposure of an Si(100) surface to both TBP and TEG fluxes at 310 °C and $R_{TBP:TEG} = 25$.

mately the density of the whiskers detected by AFM and SEM. Because of the low solubility of carbon in liquid gallium, a lower conductivity of the GaP grown from Ga solution is expected. However, although the reduction in conductivity reduces the tunneling current compared with surrounding carbon-doped regions of the film and would be consistent with a VLS growth mechanism for the whiskers, the observed reversal of contrast cannot be understood as an effect of reduced conductivity alone. Therefore, further investigations are needed to develop a better understanding of this phenomenon.

The different slopes in the three temperature ranges shown in Fig. 3 may be interpreted in terms of different hindrances in the crystal growth kinetics. The decrease

in v_g with increasing temperature in region I can be interpreted in terms of either an increasing desorption rate of adsorbed species which participate in the surface reaction, or of the uncontrolled partial carbonization of the surface, preventing the nucleation of a contiguous GaP film, or both. SEM images of films grown in this temperature regime reveal an open structure, that is GaP grows only on parts of the substrate surface, leaving other parts completely uncovered. However, the participation of the desorption kinetics in determining the overall temperature dependence of v_g is not precluded by these observations. The break between regions II and III in the dashed curve for GaP growth on Si by CBE, using PH_3 as phosphorus source, at a higher temperature and the decrease in v_g with a larger activation energy E_a than for the growth of GaP, using *t*-butyl phosphine is in accord with the higher energy of the H–PH_2 bond compared with the (*t*-butyl)–PH_2 bond. However, the observed slopes are not explained by these bond energies alone, and additional studies are needed to determine the details of the surface kinetics in all three temperature regimes.

The results shown in Figs. 4(a) and 4(b) can be interpreted in terms of diffusion-controlled steady state growth of an amorphous SiC film at the Si–GaP interface after an induction period needed to establish a sufficient supersaturation of carbon at the silicon surface to nucleate the SiC interlayer. Since the induction period allows the formation of a contiguous GaP film, the subcutaneous formation of an SiC/SiO_2 composite interlayer does not interfere with further homo-epitaxial growth at the front surface of the GaP film. The formation of amorphous SiC interlayers has been reported on the basis of cross-sectional high resolution transmission electron microscopy of GaP/Si heterostructures grown by metal–organic chemical vapor deposition (MOCVD) [2]. The slope of the $\sqrt{t}$ section in Fig. 4(b) results in a diffusion constant of carbon in GaP at 310 °C of approximately 2×10^{-14} cm^2 s^{-1}. Since the composite SiO_2 and SiC interlayer is expected to have high resistivity, an average dielectric constant smaller than that of GaP, and an average thermal expansion coefficient below the thermal expansion coefficients of GaP and Si, its presence is not necessarily detrimental in the context of dielectric isolation, provided that it can be located well removed from critical silicon device locations. This will be possible, for example, by the provision of an Si/GaP superlattice after a few hundred ångströms of GaP growth, acting as a filter which prevents carbon transport to the underlying silicon surface. In view of the above discussed conditions during the initial nucleation period, the provision of planar superlattices requires the complete sealing of the silicon surface by an initial atomic layer epitaxy (ALE) step. The feasibility of ALE is well established for both GaP [10] and Si [11].

In the context of optoelectronic applications, it may be necessary to avoid the formation of a subcutaneous SiC film completely. Therefore, we are currently pursuing remote plasma enhanced chemical vapor deposition (RPCVD) as an alternative growth method. We have already shown that silicon films can be grown on the (100) GaP surface by RPCVD at about 300 °C [12]. We have also established that GaP can be grown by RPCVD with *in situ* generation of phosphine fragments from solid red phosphorus in a helium–hydrogen plasma at substantially lower substrate temperatures than under the conditions of open tube MOCVD [13]. However, this work employed trimethylgallium as source material, leading to substantial carbon doping of the epitaxial films. Therefore, we have redesigned the RPCVD reactor to accept carbon-free halide sources. The optimum temperature range for this growth method is presently not yet established, but it is expected to be higher than under the above discussed conditions of CBE.

5. Conclusion

GaP films were grown by CBE at 310 °C on Si(100) and Si(111) with excellent selectivity with regard to SiO_2 and SiC covered surface areas. After an induction period which permits the growth of a contiguous GaP film, transport of oxygen and carbon to the GaP–Si interface results in the formation of a composite interlayer of SiO_2 and SiC which is desirable for dielectric isolation, but is limiting in the context of opto-electronic applications.

Acknowledgments

This work has been supported by NSF grants DMR 9282201 and CDR 8721505.

References

1 M. Yoshimoto, K. Ozasa and H. Matsunami, *J. Appl. Phys., 70* (1991) 5708.
2 J. M. Olson, M. M. Al-Jassim, A. Kibbler and K. M. Jones, *J. Cryst. Growth, 77* (1986) 512.
3 G. C. Xing, K. J. Bachmann, G. S. Solomon, J. B. Posthill and M. L. Timmons, *J. Cryst. Growth, 94* (1989) 381.
4 G. C. Xing, K. J. Bachmann, J. B. Posthill and M. L. Timmons, *J. Appl. Phys., 69* (1991) 4286.
5 G. C. Xing, K. J. Bachmann, J. B. Posthill and M. L. Timmons, *J. Cryst. Growth, 113* (1991) 113.

6 J. T. Kelliher and K. J. Bachmann, *Mater. Res. Soc. Symp. Proc., 282* (1992) 51.
7 S. H. Li, N. I. Buchan, C. A. Larsen and G. B. Stringfellow, *J. Cryst. Growth, 96* (1989) 906.
8 S. H. Li, C. A. Larsen, N. I. Buchan, G. B. Stringfellow, W. P. Kosar and D. W. Brown, *J. Appl. Phys., 65* (1989) 5161.
9 E. I. Givargizov, in A. A. Chernov (ed.), *Modern Crystallography III, Springer Series in Solid-State Sciences*, Vol. 36, Springer, Berlin, 1984, p. 343.
10 Y. Sakuma, K. Kodama and M. Ozeki, *Appl. Phys. Lett., 56* (1990) 827.
11 D. Lubben, R. Tsu, T. R. Bramblett and J. E. Greene, *J. Vac. Sci. Technol. A, 9* (1991) 3003.
12 S. Habermehl, N. Dietz, G. Lucovsky and K. J. Bachmann, unpublished results, 1993.
13 S. W. Choi, G. Lucovsky and K. J. Bachmann, *J. Vac. Sci. Technol. B, 10* (1992) 1070.

Author Index of Volume 21, Issues 2–3

Abraham, P., 257
Agne, M., 217
Albrecht, T. F., 249
Allen, E. M., 130
Alvarcz, A.-L., 262
Anderson, N. G., 237
Arena, C., 189
Asonen, H., 211
Aulombard, R. L., 169

Bachem, K. H., 304
Bacher, G., 274
Badoz, P. A., 312
Baj, M., 325
Barbusse, D., 257
Baudet, M., 185
Beauvillian, J., 284
Bedel, E., 157
Böhm, G., 153
Bolognesi, C. R., 201
Böttcher, J., 194
Bozek, R., 325
Bradley, I. V., 281
Briggs, A. T. R., 281
Briot, N., 169
Briot, O., 169
Bru, C., 177
Bruggeman, F., 244
Burkhard, H., 174
Butov, L., 288
Buydens, L., 253

Camassel, J., 244
Campidelli, Y., 312
Carlin, J. F., 293
Cavenett, B. C., 205
Claverie, A., 284
Cloitre, T., 169
Collot, P., 317
Couturier, G., 333
Crété, D. G., 317

Daiminger, F., 288
Dang, L. S., 224
Delly, B., 300
Demeester, P., 253
Deveaud, B., 185
Dinges, H. W., 174
Döscher, M., 270
Dreybrodt, J., 198
Dücker, M., 270
Dupertuis, M. A., 293
Dwir, B., 293

Ebeling, K. J., 228
Emery, J. Y., 241
Esquivias, I., 232

Faller, F., 198
Faye, M. M., 284
Finders, J., 161
Fleissner, J., 232
Fontaine, C., 157
Forchel, A., 198, 274, 277, 288
Fourcade, R., 257
Fraisse, B., 244, 257
Friedrich, J., 321

Galtier, P., 317
Ganière, J. D., 277
Gauer, C., 201
Genova, F., 189
Gentile, P., 224
Georgakilas, A., 177
Geunais, B., 185
Geurts, J., 161
Gibbon, M. A., 130
Gil, B., 169
Gillin, W. P., 281
Glick, M., 293
Gnoth, D., 161
Göbel, E. O., 249, 266
Goldstein, L., 241
Grey, R., 253
Grunberg, P., 288
Guillot, G., 177
Gyuro, I., 277

Haas, H., 224
Hackbarth, T., 228
Halkias, G., 177
Hamdani, F., 257
Hamilton, B., 130
Hase, A., 194
Hegarty, J., 253
Heime, K., 161
Heinecke, H., 120
Henrion, W., 270
Hincelin, G., 165
Homewood, K. P., 281
Howard, L. K., 281

Jalonen, M., 237
Jaros, M., 296
Jean, B., 333
Joffre, P., 333
Jones, A. C., 169
Joullié, A., 288
Jowett, J. M., 130
Juillaguet, S., 244

Kadret, S., 288
Kehrli, U., 300
Keuter, M., 161
Klen, W., 153
Kohl, A., 161, 244
Koidl, P., 262
Kotthaus, J. P., 201
Kretzer, U., 321
Kroemer, H., 201
Künzel, H., 194
Kurbel, R., 217
Kurz, H., 244

Laânab, L., 284
Lambert, B., 185
Lambert, J. F., 333
Lambrecht, A., 217
Landwehr, G., 274
Lange, H., 270
Larkins, E. C., 232
Lascaray, J. P., 257
Laube, G., 277
Lefebvre, K. R., 237
Leipold, D., 300
Lenchyshyn, L. C., 307
Leo, K., 244
Lindner, A., 181
Liu, C. W., 307
Liu, Q., 181
Lorberth, J., 266
Lösch, R., 174
Lutgen, S., 249

Magnea, N., 224
Maier, M., 232
Mallard, R. E., 130
Marschner, T., 249, 266
Mathet, V., 317
Matutinovic-Krstelj, Z., 307
Maurin, M., 257
Mellet, R., 165
Mi, Q., 307
Moloney, M. H., 253
Monéger, S. 177
Monnard, R., 293
Monteil, Y., 257
Mosel, F., 321
Müller, G., 321
Müller, J., 270
Müller, M., 266
Müller, R., 161
Munoz-Yague, A., 157

Näppi, J., 211
Nazaré, M. H., 329
Nguyen, C., 201
Nguyen-Van-Dau, F., 317
Nickel, H., 174
Nishizawa, J., 107
Nowak, G., 325

Olivier, J., 317
Oshinowo, J., 277

Ovtchinnikov, A., 211

Padeletti, G., 317
Panzlaff, K., 228
Patterson, B. D., 300
Pauli, M., 270
Pautrat, J. L., 224
Pelekanos, N. T., 224
Pessa, M., 211, 237
Peyre, H., 244
Phillipp, F., 266
Pletschen, W., 304
Ploog, K. H., 288
Ponchet, A., 241
Pougnet, A. M., 165
Prior, K. A., 205
Prost, W., 181

Quedeweit, U., 181

Ralston, J. D., 232, 262
Rao, S. S., 281
Reinhart, F. K., 293
Reithmaier, J. P., 198
Rigo, C., 189
Rino, L. M., 329
Rocher, A., 241
Rochus, S., 153
Röhr, T., 153
Rosenzweig, J., 232
Rouillard, Y., 185
Royo, F., 244
Rudra, A., 293
Ruterana, P., 277

Sagnes, I., 312
Scheffer, F., 181
Schlapp, W., 174
Schmitz, J., 262
Scholz, F., 147
Schönfelder, A., 232
Schramm, C., 194
Schwedler, R., 244
Scriba, J., 201
Sealy, B. J., 281
Seidl, A., 321
Shaw, M. J., 296
Simon, A., 201
Simon, J. C., 185
Słupiński, T., 325
Smith, A. D., 281
St. Amour, A., 307
Stadelmann, P. A., 277
Stagg, J. P., 130
Starck, C., 241
Stoehr, M., 257
Stolz, W., 249, 266
Sturm, J. C., 307

Tabata, A., 177
Tapfer, L., 249
Tarricone, L., 189
Tasker, P. J., 232, 304
Tegude, F. J., 181
Thelen, K., 300
Thewalt, M. L. W., 307
Thrush, E. J., 130
Toivonen, M., 237
Tönnies, D., 274
Toudic, Y., 185
Tournié, E., 288
Tränkle, G., 153
Tuttle, G., 201

Valiente, I., 185
Veuhoff, E., 120
Vieu, C., 157, 284
Vincent, G., 312

Waag, A., 274
Wagner, J., 262
Walther, M., 153
Wang, S. Y., 205
Weimann, G., 153
Weisser, S., 232
Winkler, K., 304
Wipiejewski, T., 228
Wixforth, A., 201
Woitok, J., 161
Wolter, K., 244
Wong, K. B., 296
Woodhead, J., 253
Wysmołek, A., 325

Xiao, X., 307

Zahzouh, M., 165
Zeeb, E., 228
Zekentes, K., 177
Zhang, G., 211
Zielinski, E., 277

Subject Index of Volume 21, Issues 2–3

Absorption
  absorption coefficient and exciton oscillator strengths in InGaAs/InP multi-quantum wells, 189
  optical cross-sections and distribution of Fe^{2+} and Fe^{3+} in semi-insulating liquid encapsulated Czochralski grown InP:Fe, 321
Alloys
  blue diode lasers and visible optoelectronic devices, 205
  chemical beam epitaxy and photoluminescence characteristics of InGaAsP/InP BRAQWET modulators, 293
Aluminium
  aluminium-free 980 nm laser diodes, 211
Aluminium antimonide
  intersubband transitions in InAs/AlSb quantum wells, 201
  optical properties of GaSb–AlSb heterostructures grown by molecular beam epitaxy, 185
Aluminium arsenide
  second harmonic generation via excitations between valence sub-bands in p-type GaAs–AlAs and Si–SiGe quantum well structures, 296
Amorphous silicon
  characterization of the heterostructure between hetero-epitaxially grown β-$FeSi_2$ and (111) silicon, 270
Annealing
  simulation of lateral Al recoil atoms and damage defects gradients in a GaAs/GaAlAs quantum well created by masked ion implantation, 284
Stoichiometry of III–V compounds, 107
  vacancy controlled interdiffusion in III–V heterostructures, 281

Beryllium
  p-dopant incorporation and influence on gain and damping behaviour in high-speed GaAs-based strained MQW lasers, 232

Cadmium telluride
  optical investigation of interdiffusion in CdTe/CdMnTe quantum wells, 274
  quantum confined Stark Effect (QCSE) and self-electro-optic effect device (SEED) in II–VI heterostructures, 224
Chemical beam epitaxy
  absorption coefficient and exciton oscillator strengths in InGaAs/InP multi-quantum wells, 189
  chemical beam epitaxy and photoluminescence characteristics of InGaAsP/InP BRAQWET modulators, 293
  chemical beam epitaxy of high purity InP using tertiarybutylphosphine and 1,2 bis-phosphinoethane, 165
  ESPRIT MORSE: research for novel metal–organic precursors, 147
  evaluation of III–V growth technologies for optoelectronic applications, 120
Chemical vapour deposition
  photoluminescence and electroluminescence processes in $Si_{1-x}Ge_x$/Si heterostructures grown by chemical vapor deposition, 307
Crystal growth
  synthetic diamond: the optical band at 1.883 eV, 329

Defects
  stoichiometry of III–V compounds, 107
Diamond
  synthetic diamond: the optical band at 1.883 eV, 329
Diode lasers
  aluminium-free 980 nm laser diodes, 211
  blue diode lasers and visible optoelectronic devices, 205
  growth of InAlGaAs multilayer structures for high power and submilliamp vertical cavity lasers, 228
  shadow mask MBE for the fabrication of lead chalcogenide buried heterostructure lasers, 217
Doping and impurity implantation
  effects of deep levels and Si-doping on GaInP material properties investigated by means of optical methods, 181
Doping effects
  AlGaInP/GaInAs/GaAs MODFET devices: candidates for optoelectronic integrated circuits, 304
  p-dopant incorporation and influence on gain and damping behaviour in high-speed GaAs-based strained MQW lasers, 232
  simulation of lateral Al recoil atoms and damage defects gradients in a GaAs/GaAlAs quantum well created by masked ion implantation, 284

Electrical conductivity
  optical and transport properties in the electro-optical material $CdIn_2Te_4$, 333
Electrical measurements
  AlGaInP/GaInAs/GaAs MODFET devices: candidates for optoelectronic integrated circuits, 304
Electrical properties
  optical characterization of extremely high purity ZnSe grown by metal–organic vapour phase epitaxy using dimethylzinc–triethylamine adduct, 169
Electron microscopy
  investigation of InGaAs/InP interdiffusion by simultaneous transmission electron microscopy and photoluminescence analysis, 277
Electron spectroscopy
  absorption coefficient and exciton oscillator strengths in InGaAs/InP multi-quantum wells, 189
  improved method for GaAs–(Ga,Al)As epitaxial regrowth, 157
Electron states
  effects of deep levels and Si-doping on GaInP material properties investigated by means of optical methods, 181
  intersubband transitions in InAs/AlSb quantum wells, 201
Electronic band structure
  optical and transport properties in the electro-optical material $CdIn_2Te_4$, 333
Electronic properties
  optical cross-sections and distribution of Fe^{2+} and Fe^{3+} in semi-insulating liquid encapsulated Czochralski grown InP:Fe, 321
Electronic sub-band structure
  second harmonic generation via excitations between valence sub-bands in p-type GaAs–AlAs and Si–SiGe quantum well structures, 296

Ellipsometry
spectroscopic ellipsometry: a useful tool to determine the refractive indices and interfaces of $In_{0.52}Al_{0.48}As$ and $In_{0.53}Al_xGa_{0.47-x}As$ layers on InP in the wavelength range 280–1900 nm, 174
Epilayers
determination of residual strain by reflectivity, X-ray diffraction and Raman spectroscopy in ZnSe epilayers grown on GaAs(001), InP(001) and GaSb(001) by metal–organic vapour phase epitaxy, 257
improved method for GaAs–(Ga,Al)As epitaxial regrowth, 157
improvements in the heteroepitaxial growth of GaAs on Si by MOVPE, 266
optical characterization of extremely high purity ZnSe grown by metal–organic vapour phase epitaxy using dimethylzinc–triethylamine adduct, 169
p-dopant incorporation and influence on gain and damping behaviour in high-speed GaAs-based strained MQW lasers, 232
tunable infrared photoemission sensor on Si using epitaxial $ErSi_2$/Si heterostructures, 312
Epitaxy of thin films
characterization of the heterostructure between heteroepitaxially grown β-$FeSi_2$ and (111) silicon, 270
Etching
MBE regrowth of GaAs/AlGaAs structures on RIE patterned substrates, 153
Excitons
absorption coefficient and exciton oscillator strengths in InGaAs/InP multi-quantum wells, 189
influence of the cap layer thickness on the optical properties of near surface GaInAs/GaAs quantum wells, 198

Field effect transistor
AlGaInP/GaInAs/GaAs MODFET devices: candidates for optoelectronic integrated circuits, 304
an AlGaAs/GaAs OEIC structure for the integration of LEDs, MESFETs and photodetectors, 300

Gallium antimonide
determination of residual strain by reflectivity, X-ray diffraction and Raman spectroscopy in ZnSe epilayers grown on GaAs(001), InP(001) and GaSb(001) by metal–organic vapour phase epitaxy, 257
optical properties of GaSb–AlSb heterostructures grown by molecular beam epitaxy, 185
Gallium arsenide
AlGaInP/GaInAs/GaAs MODFET devices: candidates for optoelectronic integrated circuits, 304
aluminium-free 980 nm laser diodes, 211
an AlGaAs/GaAs OEIC structure for the integration of LEDs, MESFETs and photodetectors, 300
characterization of heterointerfaces and surfaces in InSb on GaAs and in InAs/AlSb quantum wells, 262
determination of residual strain by reflectivity, X-ray diffraction and Raman spectroscopy in ZnSe epilayers grown on GaAs(001), InP(001) and GaSb(001) by metal–organic vapour phase epitaxy, 257
experimental and theoretical studies of multi-quantum well structures for unipolar avalanche multiplication, 237
growth of InAlGaAs multilayer structures for high power and submilliamp vertical cavity lasers, 228
improved method for GaAs–(Ga,Al)As epitaxial regrowth, 157
improvements in the heteroepitaxial growth of GaAs on Si by MOVPE, 266
influence of the cap layer thickness on the optical properties of near surface GaInAs/GaAs quantum wells, 198
large negative persistent photoconductivity of bulk $GaAs_{1-x}P_x$ ($x = 0.02$–0.03) single crystals, 325
MBE regrowth of GaAs/AlGaAs structures on RIE patterned substrates, 153
p-dopant incorporation and influence on gain and damping behaviour in high-speed GaAs-based strained MQW lasers, 232
second harmonic generation via excitations between valence sub-bands in p-type GaAs–AlAs and Si–SiGe quantum well structures, 296
strain effects on carrier lifetimes in InGaAs/(Al)GaAs multiple quantum wells, 253
Gallium phosphide
large negative persistent photoconductivity of bulk $GaAs_{1-x}P_x$ ($x = 0.02$–0.03) single crystals, 325
Germanium
photoluminescence and electroluminescence processes in $Si_{1-x}Ge_x$/Si heterostructures grown by chemical vapor deposition, 307
second harmonic generation via excitations between valence sub-bands in p-type GaAs–AlAs and Si–SiGe quantum well structures, 296

Heteroepitaxy
a study of PbSe heteroepitaxy on Si(111) for IR optoelectronic applications, 317
Heterostructures
AlGaInP/GaInAs/GaAs MODFET devices: candidates for optoelectronic integrated circuits, 304
characterization of heterointerfaces and surfaces in InSb on GaAs and in InAs/AlSb quantum wells, 262
characterization of the heterostructure between heteroepitaxially grown β-$FeSi_2$ and (111) silicon, 270
intersubband transitions in InAs/AlSb quantum wells, 201
MBE regrowth of GaAs/AlGaAs structures on RIE patterned substrates, 153
optical properties of GaSb–AlSb heterostructures grown by molecular beam epitaxy, 185
photoluminescence and electroluminescence processes in $Si_{1-x}Ge_x$/Si heterostructures grown by chemical vapor deposition, 307
quantum confined Stark effect (QCSE) and self-electro-optic effect device (SEED) in II–VI heterostructures, 224
shadow mask MBE for the fabrication of lead chalcogenide buried heterostructure lasers, 217
simulation of lateral Al recoil atoms and damage defects gradients in a GaAs/GaAlAs quantum well created by masked ion implantation, 284
strained $InAs/Al_xGa_{0.48-x}In_{0.52}As$ heterostructures: a tunable quantum well materials system for light emission from the near-IR to the mid-IR, 288
tunable infrared photoemission sensor on Si using epitaxial $ErSi_2$/Si heterostructures, 312
vacancy controlled interdiffusion in III–V heterostructures, 281

Indium
strain effects on carrier lifetimes in InGaAs/(Al)GaAs multiple quantum wells, 253
Indium antimonide
characterization of heterointerfaces and surfaces in InSb on GaAs and in InAs/AlSb quantum wells, 262

Indium arsenide
intersubband transitions in InAs/AlSb quantum wells, 201
strained InAs/$Al_xGa_{0.48-x}In_{0.52}As$ heterostructures: a tunable quantum well materials system for light emission from the near-IR to the mid-IR, 288
Indium phosphide
absorption coefficient and exciton oscillator strengths in InGaAs/InP multi-quantum wells, 189
chemical beam epitaxy and photoluminescence characteristics of InGaAsP/InP BRAQWET modulators, 293
chemical beam epitaxy of high purity InP using tertiarybutylphosphine and 1,2 bis-phosphinoethane, 165
determination of residual strain by reflectivity, X-ray diffraction and Raman spectroscopy in ZnSe epilayers grown on GaAs(001), InP(001) and GaSb(001) by metal–organic vapour phase epitaxy, 257
growth and characterization of $In_{0.53}Ga_{0.47}As/In_xGa_{1-x}As$ strained-layer superlattices, 244
investigation of InGaAs/InP interdiffusion by simultaneous transmission electron microscopy and photoluminescence analysis, 277
investigation of MOVPE-grown $In_{0.53}Ga_{0.47}As$/InP multi-quantum wells by Raman spectroscopy and X-ray diffractometry, 161
large negative persistent photoconductivity of bulk $GaAs_{1-x}P_x$ ($x = 0.02$–0.03) single crystals, 325
lateral thickness modulations in alternate tensile–compressive strained GaInAsP multilayers grown by gas source molecular beam epitaxy, 241
optical cross-sections and distribution of Fe^{2+} and Fe^{3+} in semi-insulating liquid encapsulated Czochralski grown InP:Fe, 321
room temperature photoreflectance as a powerful tool to characterize the crystalline quality of InAlAs layers grown on InP substrates, 177
selective and non-planar epitaxy of InP/GaInAs(P) by MOCVD, 130
spectroscopic ellipsometry: a useful tool to determine the refractive indices and interfaces of $In_{0.52}Al_{0.48}As$ and $In_{0.53}Al_xGa_{0.47-x}As$ layers on InP in the wavelength range 280–1900 nm, 174
Indium sulphide
strained InAs/$Al_xGa_{0.48-x}In_{0.52}As$ heterostructures: a tunable quantum well materials system for light emission from the near-IR to the mid-IR, 288
Infrared detectors
a study of PbSe heteroepitaxy on Si(111) for IR optoelectronic applications, 317
shadow mask MBE for the fabrication of lead chalcogenide buried heterostructure lasers, 217
strained InAs/$Al_xGa_{0.48-x}In_{0.52}As$ heterostructures: a tunable quantum well materials system for light emission from the near-IR to the mid-IR, 288
tunable infrared photoemission sensor on Si using epitaxial $ErSi_2$/Si heterostructures, 312
Integrated technology
AlGaInP/GaInAs/GaAs MODFET devices: candidates for optoelectronic integrated circuits, 304
Interdiffusion
investigation of InGaAs/InP interdiffusion by simultaneous transmission electron microscopy and photoluminescence analysis, 277
optical investigation of interdiffusion in CdTe/CdMnTe quantum wells, 274
vacancy controlled interdiffusion in III–V heterostructures, 281
Interface vibrations
characterization of heterointerfaces and surfaces in InSb on GaAs and in InAs/AlSb quantum wells, 262
Interfaces
MBE growth and properties of high quality Al(Ga)InAs/GaInAs MQW structures, 194
Interfacial strain
growth and characterization of $In_{0.53}Ga_{0.47}As/In_xGa_{1-x}As$ strained-layer superlattices, 244
Ion implantation
simulation of lateral Al recoil atoms and damage defects gradients in a GaAs/GaAlAs quantum well created by masked ion implantation, 284
vacancy controlled interdiffusion in III–V heterostructures, 281
Ions
optical cross-sections and distribution of Fe^{2+} and Fe^{3+} in semi-insulating liquid encapsulated Czochralski grown InP:Fe, 321
Iridium
tunable infrared photoemission sensor on Si using epitaxial $ErSi_2$/Si heterostructures, 312
Iron
optical cross-sections and distribution of Fe^{2+} and Fe^{3+} in semi-insulating liquid encapsulated Czochralski grown InP:Fe, 321

Lasers
aluminium-free 980 nm laser diodes, 211
ESPRIT MORSE: research for novel metal-organic precursors, 147
lateral thickness modulations in alternate tensile–compressive strained GaInAsP multilayers grown by gas source molecular beam epitaxy, 241
MBE growth and properties of high quality Al(Ga)InAs/GaInAs MQW structures, 194
p-dopant incorporation and influence on gain and damping behaviour in high-speed GaAs-based strained MQW lasers, 232
shadow mask MBE for the fabrication of lead chalcogenide buried heterostructure lasers, 217
Layered compounds
evaluation of III–V growth technologies for optoelectronic applications, 120
Light emitting diodes
an AlGaAs/GaAs OEIC structure for the integration of LEDs, MESFETs and photodetectors, 300
Luminescence
MBE regrowth of GaAs/AlGaAs structures on RIE patterned substrates, 153
optical investigation of interdiffusion in CdTe/CdMnTe quantum wells, 274
photoluminescence and electroluminescence processes in $Si_{1-x}Ge_x$/Si heterostructures grown by chemical vapor deposition, 307

Metal–organic chemical vapour deposition
selective and non-planar epitaxy of InP/GaInAs(P) by MOCVD, 130
Metal–organic molecular beam epitaxy
evaluation of III–V growth technologies for optoelectronic applications, 120
Metal–organic vapour phase epitaxy
determination of residual strain by reflectivity, X-ray diffraction and Raman spectroscopy in ZnSe epilayers grown on

GaAs(001), InP(001) and GaSb(001) by metal-organic vapour phase epitaxy, 257
effects of deep levels and Si-doping on GaInP material properties investigated by means of optical methods, 181
ESPRIT MORSE: research for novel metal-organic precursors, 147
evaluation of III-V growth technologies for optoelectronic applications, 120
growth and characterization of $In_{0.53}Ga_{0.47}As/In_xGa_{1-x}As$ strained-layer superlattices, 244
improvements in the heteroepitaxial growth of GaAs on Si by MOVPE, 266
investigation of MOVPE-grown $In_{0.53}Ga_{0.47}As/InP$ multi-quantum wells by Raman spectroscopy and X-ray diffractometry, 161
metal-organic vapour-phase epitaxial growth of symmetrically strained (GaIn)As/Ga(PAs) superlattices, 249
optical characterization of extremely high purity ZnSe grown by metal-organic vapour phase epitaxy using dimethylzinc-triethylamine adduct, 169
spectroscopic ellipsometry: a useful tool to determine the refractive indices and interfaces of $In_{0.52}Al_{0.48}As$ and $In_{0.53}Al_xGa_{0.47-x}As$ layers on InP in the wavelength ragne 280-1900 nm, 174

Molecular beam epitaxy
a study of PbSe heteroepitaxy on Si(111) for IR optoelectronic applications, 317
evaluation of III-V growth technologies for optoelectronic applications, 120
experimental and theoretical studies of multi-quantum well structures for unipolar avalanche multiplication, 237
growth of InAlGaAs multilayer structures for high power and submilliamp vertical cavity lasers, 228
improved method for GaAs-(Ga,Al)As epitaxial regrowth, 157
lateral thickness modulations in alternate tensile-compressive strained GaInAsP multilayers grown by gas source molecular beam epitaxy, 241
MBE growth and properties of high quality Al(Ga)InAs/GaInAs MQW structures, 194
MBE regrowth of GaAs/AlGaAs structures on RIE patterned substrates, 153
optical investigation of interdiffusion in CdTe/CdMnTe quantum wells, 274
optical properties of GaSb-AlSb heterostructures grown by molecular beam epitaxy, 185
room temperature photoreflectance as a powerful tool to characterize the crystalline quality of InAlAs layers grown on InP substrates, 177
shadow mask MBE for the fabrication of lead chalcogenide buried heterostructure lasers, 217
strained $InAs/Al_xGa_{0.48-x}In_{0.52}As$ heterostructures: a tunable quantum well materials system for light emission from the near-IR to the mid-IR, 288

Multilayer materials
growth of InAlGaAs multilayer structures for high power and submilliamp vertical cavity lasers, 228
lateral thickness modulations in alternate tensile-compressive strained GaInAsP multilayers grown by gas source molecular beam epitaxy, 241

Narrow band-gap semiconductors
a study of PbSe heteroepitaxy on Si(111) for IR optoelectronic applications, 317

Nitrogen
synthetic diamond: the optical band at 1.883 eV, 329

Non-planar epitaxy
selective and non-planar epitaxy of InP/GaInAs(P) by MOCVD, 130

Optical absorption
large negative persistent photoconductivity of bulk $GaAs_{1-x}P_x$ ($x = 0.02$-0.03) single crystals, 325
optical and transport properties in the electro-optical material $CdIn_2Te_4$, 333
quantum confined Stark effect (QCSE) and self-electro-optic effect device (SEED) in II-VI heterostructures, 224

Optical measurements
characterization of the heterostructure between heteroepitaxially grown β-$FeSi_2$ and (111) silicon, 270
effects of deep levels and Si-doping on GaP material properties investigated by means of optical methods, 181
optical investigation of interdiffusion in CdTe/CdMnTe quantum wells, 274

Optical properties
chemical beam epitaxy of high purity InP using tertiarybutylphosphine and 1,2 bis-phosphinoethane, 165
experimental and theoretical studies of multi-quantum well structures for unipolar avalanche multiplication, 237
influence of the cap layer thickness on the optical properties of near surface GaInAs/GaAs quantum wells, 198
MBE growth and properties of high quality Al(Ga)InAs/GaInAs MQW structures, 194
MBE regrowth of GaAs/AlGaAs structures on RIE patterned substrates, 153
metal-organic vapour-phase epitaxial growth of symmetrically strained (GaIn)As/Ga(PAs) superlattices, 249
optical and transport properties in the electro-optical material $CdIn_2Te_4$, 333
optical characterization of extremely high purity ZnSe grown by metal-organic vapour phase epitaxy using dimethylzinc-triethylamine adduct, 169
optical properties of GaSb-AlSb heterostructures grown by molecular beam epitaxy, 185
quantum confined Stark effect (QCSE) and self-electro-optic effect device (SEED) in II-VI heterostructures, 224
spectroscopic ellipsometry: a useful tool to determine the refractive indices and interfaces of $In_{0.52}Al_{0.48}As$ and $In_{0.53}Al_xGa_{0.47-x}As$ layers on InP in the wavelength range 280-1900 nm, 174
strain effects on carrier lifetimes in InGaAs/(Al)GaAs multiple quantum wells, 253

Optoelectronic devices
blue diode lasers and visible optoelectronic devices, 205
ESPRIT MORSE: research for novel metal-organic precursors, 147
evaluation of III-V growth technologies for optoelectronic applications, 120
investigation of MOVPE-grown $In_{0.53}Ga_{0.47}As/InP$ multi-quantum wells by Raman spectroscopy and X-ray diffractometry, 161

Optoelectronic materials
growth and characterization of $In_{0.53}Ga_{0.47}As/In_xGa_{1-x}As$ strained-layer superlattices, 244

Optoelectronics
a study of PbSe heteroepitaxy on Si(111) for IR optoelectronic applications, 317
optical characterization of extremely high purity ZnSe grown by metal-organic vapour phase epitaxy using dimethylzinc-triethylamine adduct, 169

optical cross-sections and distribution of Fe^{2+} and Fe^{3+} in semi-insulating liquid encapsulated Czochralski grown InP:Fe, 321
selective and non-planar epitaxy of InP/GaInAs(P) by MOCVD, 130
spectroscopic ellipsometry: a useful tool to determine the refractive indices and interfaces of $In_{0.52}Al_{0.48}As$ and $In_{0.53}Al_xGa_{0.47-x}As$ layers on InP in the wavelength range 280–1900 nm, 174

Phonons
characterization of heterointerfaces and surfaces in InSb on GaAs and in InAs/AlSb quantum wells, 262
Photoconduction
large negative persistent photoconductivity of bulk $GaAs_{1-x}P_x$ ($x = 0.02$–0.03) single crystals, 325
Photodetectors
an AlGaAs/GaAs OEIC structure for the integration of LEDs, MESFETs and photodetectors, 300
Photoelectron spectroscopy
tunable infrared photoemission sensor on Si using epitaxial $ErSi_2$/Si heterostructures, 312
Photoluminescence
chemical beam epitaxy and photoluminescence characteristics of InGaAsP/InP BRAQWET modulators, 293
influence of the cap layer thickness on the optical properties of near surface GaInAs/GaAs quantum wells, 198
investigation of InGaAs/InP interdiffusion by simultaneous transmission electron microscopy and photoluminescence analysis, 277
photoluminescence and electroluminescence processes in $Si_{1-x}Ge_x$/Si heterostructures grown by chemical vapor deposition, 307
room temperature photoreflectance as a powerful tool to characterize the crystalline quality of InAlAs layers grown on InP substrates, 177
strain effects on carrier lifetimes in InGaAs/(Al)GaAs multiple quantum wells, 253
synthetic diamond: the optical band at 1.883 eV, 329
vacancy controlled interdiffusion in III–V heterostructures, 281
Photoluminescence spectroscopy
improved method for GaAs–(Ga,Al)As epitaxial regrowth, 157
Photoreflectance spectroscopy
room temperature photoreflectance as a powerful tool to characterize the crystalline quality of InAlAs layers grown on InP substrates, 177
Precursors
chemical beam epitaxy of high purity InP using tertiarybutylphosphine and 1,2 bis-phosphinoethane, 165
ESPRIT MORSE: research for novel metal–organic precursors, 147
Process and device modelling
an AlGaAs/GaAs OEIC structure for the integration of LEDs, MESFETs and photodetectors, 300
experimental and theoretical studies of multi-quantum well structures for unipolar avalanche multiplication, 237
simulation of lateral Al recoil atoms and damage defects gradients in a GaAs/GaAlAs quantum well created by masked ion implantation, 284
p–n Junctions
blue diode lasers and visible optoelectronic devices, 205

Quantum wells
absorption coefficient and exciton oscillator strengths in InGaAs/InP multi-quantum wells, 189
chemical beam epitaxy and photoluminescence characteristics of InGaAsP/InP BRAQWET modulators, 293
experimental and theoretical studies of multi-quantum well structures for unipolar avalanche multiplication, 237
improved method for GaAs–(Ga,Al)As epitaxial regrowth, 157
influence of the cap layer thickness on the optical properties of near surface GaInAs/GaAs quantum wells, 198
intersubband transitions in InAs/AlSb quantum wells, 201
investigation of InGaAs/InP interdiffusion by simultaneous transmission electron microscopy and photoluminescence analysis, 277
investigation of MOVPE-grown $In_{0.53}Ga_{0.47}As$/InP multi-quantum wells by Raman spectroscopy and X-ray diffractometry, 161
lateral thickness modulations in alternate tensile–compressive strained GaInAsP multilayers grown by gas source molecular beam epitaxy, 241
MBE growth and properties of high quality Al(Ga)InAs/GaInAs MQW structures, 194
optical investigation of interdiffusion in CdTe/CdMnTe quantum wells, 274
optical properties of GaSb–AlSb heterostructures grown by molecular beam epitaxy, 185
p-dopant incorporation and influence on gain and damping behaviour in high-speed GaAs-based strained MQW lasers, 232
quantum confined Stark effect (QCSE) and self-electro-optic effect device (SEED) in II–VI heterostructures, 224
second harmonic generation via excitations between valence sub-bands in p-type GaAs–AlAs and Si–SiGe quantum well structures, 296
selective and non-planar epitaxy of InP/GaInAs(P) by MOCVD, 130
simulation of lateral Al recoil atoms and damage defects gradients in a GaAs/GaAlAs quantum well created by masked ion implantation, 284
strain effects on carrier lifetimes in InGaAs/(Al)GaAs multiple quantum wells, 253
strained $InAs/Al_xGa_{0.48-x}In_{0.52}As$ heterostructures: a tunable quantum well materials system for light emission from the near-IR to the mid-IR, 288

Raman scattering
characterization of heterointerfaces and surfaces in InSb on GaAs and in InAs/AlSb quantum wells, 262
Raman spectroscopy
investigation of MOVPE-grown $In_{0.53}Ga_{0.47}As$/InP multi-quantum wells by Raman spectroscopy and X-ray diffractometry, 161
Rapid thermal annealing
investigation of InGaAs/InP interdiffusion by simultaneous transmission electron microscopy and photoluminescence analysis, 277
Rutherford backscattering
characterization of the heterostructure between heteroepitaxially grown β-$FeSi_2$ and (111) silicon, 270

Schottky barrier
quantum confined Stark effect (QCSE) and self-electro-optic effect device (SEED) in II–VI heterostructures, 224
Semiconductors
aluminium-free 980 nm laser diodes, 211
Silicon
a study of PbSe heteroepitaxy on Si(111) for IR optoelectronic applications, 317

characterization of the heterostructure between heteroepitaxially grown β-$FeSi_2$ and (111) silicon, 270
effects of deep levels and Si-doping on GaInP material properties investigated by means of optical methods, 181
improvements in the heteroepitaxial growth of GaAs on Si by MOVPE, 266
photoluminescence and electroluminescence processes in $Si_{1-x}Ge_x$/Si heterostructures grown by chemical vapor deposition, 307
second harmonic generation via excitations between valence sub-bands in p-type GaAs–AlAs and Si–SiGe quantum well structures, 296
tunable infrared photoemission sensor on Si using epitaxial $ErSi_2$/Si heterostructures, 312
Stoichiometry
stoichiometry of III–V compounds, 107
Stoichiometry and homogeneity
optical and transport properties in the electro-optical material $CdIn_2Te_4$, 333
Structural properties
metal–organic vapour-phase epitaxial growth of symmetrically strained (GaIn)As/Ga(PAs) superlattices, 249
Superlattices
growth and characterization of $In_{0.53}Ga_{0.47}As/In_xGa_{1-x}As$ strained-layer superlattices, 244
metal–organic vapour-phase epitaxial growth of symmetrically strained (GaIn)As/Ga(PAs) superlattices, 249
Surface morphology
chemical beam epitaxy of high purity InP using tertiarybutylphosphine and 1,2 bis-phosphinoethane, 165
improvements in the heteroepitaxial growth of GaAs on Si by MOVPE, 266

Ternary compounds
aluminium-free 980 nm laser diodes, 211
effects of deep levels and Si-doping on GaInP material properties investigated by means of optical methods, 181
growth and characterization of $In_{0.53}Ga_{0.47}As/In_xGa_{1-x}As$ strained-layer superlattices, 244
large negative persistent photoconductivity of bulk $GaAs_{1-x}P_x$ ($x = 0.02$–0.03) single crystals, 325
room temperature photoreflectance as a powerful tool to characterize the crystalline quality of InAlAs layers grown on InP substrates, 177
strain effects on carrier lifetimes in InGaAs/(Al)GaAs multiple quantum wells, 253
Thermal annealing
improvements in the heteroepitaxial growth of GaAs on Si by MOVPE, 266
Thermal processing
room temperature photoreflectance as a powerful tool to characterize the crystalline quality of InAlAs layers grown on InP substrates, 177
Transport properties
optical and transport properties in the electro-optical material $CdIn_2Te_4$, 333
vacancy controlled interdiffusion in III–V heterostructures, 281

Vapour pressure
stoichiometry of III–V compounds, 107
Vibration of atoms
synthetic diamond: the optical band at 1.883 eV, 329

X-ray spectroscopy
investigation of MOVPE-grown $In_{0.53}Ga_{0.47}As$/InP multiquantum wells by Raman spectroscopy and X-ray diffractometry, 161
metal–organic vapour-phase epitaxial growth of symmetrically strained (GaIn)As/Ga(PAs) superlattices, 249

Zinc selenide
blue diode lasers and visible optoelectronic devices, 205
determination of residual strain by reflectivity, X-ray diffraction and Raman spectroscopy in ZnSe epilayers grown on GaAs(001), InP(001) and GaSb(001) by metal–organic vapor phase epitaxy, 257
optical characterization of extremely high purity ZnSe grown by metal–organic vapour phase epitaxy using dimethylzinc–triethylamine adduct, 169

Author Index of Volume 22, Number 1

Allegre, J., 61
Ard, C. K., 78
Azema, A., 16

Bachmann, K. J., 97
Baranowski, J. M., 41
Bassani, F., 23
Baumann, A. E., 97
Benz, K. W., 31
Bhatti, M. T., 97
Bicknell-Tassius, R. N., 86
Böttcher, J., 89
Boudart, B., 78
Bourgoin, J. C., 86
Brown, P., 82

Calatayud, J., 61
Capper, P., 78
Chang, C. L., 31
Chen, C. L., 82
Chen, Y. P., 68
Chibani, L., 45
Claverie, A., 37, 45
Collet, J., 89
Corbel, C., 16
Coutal, C., 16
Cox, R. T., 23
Cristou, A., 93
Crosnier, Y., 78
Cuniot, M., 1
Cuzin, M., 55

Dekorsy, T., 68
Dietz, N., 97
Dreszer, P., 37
Drigo, A. V., 37
Druelle, Y., 78
Durose, K., 82
Dutton, D., 78

Ebe, H., 27

Faschinger, W., 41
Faurie, J. P., 68

Garcia, J. C., 86
Gaucherel, P., 16
Georgakilas, A., 93
Gilabert, A., 16
Gouaichault-Brugel, N., 89
Guillot, G., 93

Hage-Ali, M., 45
Halkias, G., 93
Harris, J. E., 78
Hase, A., 89
Hautojärvi, P., 16
Hauzenberger, F., 41
Heedt, C., 89
Hill, R., 97
Hoenow, H., 89
Hommel, D., 86
Huant, S., 23
Hynes, K. M., 97

Iwase, Y., 93

Jones, C. L., 78
Juza, P., 41

Kalboussi, A., 93
Kamińska, M., 27, 41
Kelliher, J. T., 97
Khirouni, K., 86
Koebel, J. M., 45
Kohn, E., 55
Korona, K. P., 41
Kowalski, G., 27
Künzel, H., 89
Kurpiewski, A., 27
Kurtz, E., 86
Kurz, H., 68

Lajzerowicz, J., 55
Landwehr, G., 86
Lange, M. D., 68
Lannoo, M., 1
Lefebvre, P., 61
Leo, G., 37
Liliental-Weber, Z., 37, 45
Lin, Y., 82
Linke, H., 31
Lipka, K. M., 55
Lischka, K., 41
Liszkay, L., 16
Lucovsky, G., 97

Maaref, H., 86
Mackett, P., 78
Mahalingam, K., 31
Mäkinen, J., 16
Mandray, A., 23
Marfaing, Y., 1
Marrakchi, G., 93
Mathieu, H., 61
Mathy, F., 55
McQuaid, S. A., 23
Melloch, M. R., 31
Meyer, B. K., 31
Miles, R. W., 97
Mishra, U. K., 72
Missous, M., 23

Namavar, F., 37
Nardo, L., 89
Newman, R. C., 23
Nolte, D. D., 31

Ohmori, M., 93
Ohno, R., 93
Omling, P., 31
Otsuka, N., 31
O'Hagan, S., 23
O'Keefe, E. S., 78

Palko, S., 16
Panzlaff, K., 55
Pesek, A., 41
Ploog, K., 68
Poese, M., 55
Pritchard, R. E., 23
Pugnet, M., 89

Roustan, J. C., 16
Rzepka, E., 1

Saarinen, K., 16
Salk, M., 31
Saminadayar, K., 23
Schmitt, K., 86
Siffert, P., 45
Sitter, H., 41
Sivananthan, S., 68
Smith, F. W., 82
Splingart, B., 55
Sporken, R., 68
Stoquert, J. P., 45

Tabata, A., 93
Takigawa, H., 27
Tatarenko, S., 23
Tehrani, S., 82
Théron, D., 78
Thornton, J., 97
Traverse, A., 37
Triboulet, R., 1, 16
Turnbull, A., 82

Verger, L., 55
van Rheenen, A. D., 82

Waag, A., 86
Wallart, X., 78
Weber, E. R., 27, 37, 41
Westphalen, R., 78
Whitaker, J. F., 61
Wit, G. L., 9
Woodall, J. M., 31

Zajicek, H., 41
Zekentes, K., 93
Zhang, X., 55
Zhou, X. Q., 68

Subject Index of Volume 22, Number 1

Aluminium arsenide
  extended defects and precipitates in LT GaAs, LT-InAlAs and LT-InP, 45
Annealing
  applications of GaAs grown at a low temperature by molecular beam epitaxy, 72
  extended defects and precipitates in LT-GaAs, LT-InAlAs and LT-InP, 45
  interfacial barrier characteristics for LT-GaAs on low doped GaAs layers, 55
  optoelectronic applications of LTMBE III–V materials, 61
  point defects in III–V materials grown by molecular beam epitaxy at low temperature, 16
  subpicosecond electric field dynamics in low-temperature-grown GaAs observed by reflective electro-optic sampling, 68
Arsenic
  GaAs, AlGaAs and InGaAs epilayers containing As clusters: semimetal/semiconductor composites, 31
  semi-insulating GaAs made by As implantation and thermal annealing, 37

Chemical beam epitaxy
  low temperature chemical beam epitaxy of gallium phosphide/silicon heterostructures, 97
Clusters
  GaAs, AlGaAs and InGaAs epilayers containing As clusters: semimetal/semiconductor composites, 31
Conductivity
  electro-optical measurement of low temperature GaAs, 41

Deep level transient spectroscopy
  low temperature molecular beam epitaxy of Al(Ga)InAs on InP and its application to high electron mobility transistor structures, 89
Defects
  EL2-like defects in low temperature GaAs, 27
  extended defects and precipitates in LT-GaAs, LT-InAlAs and LT-InP, 45
  gallium vacancy related defects in silicon doped GaAs grown at low temperatures, 23
  point defects in III–V materials grown by molecular beam epitaxy at low temperature, 16
  subpicosecond electric field dynamics in low-temperature-grown GaAs observed by reflective electro-optic sampling, 68
Dielectric properties
  low temperature chemical beam epitaxy of gallium phosphide/silicon heterostructures, 97
Diodes
  temperature measurements of LT GaAs diodes, 78
Doping effects
  gallium vacancy related defects in silicon doped GaAs grown at low temperatures, 23

Electric field effect
  subpicosecond electric field dynamics in low-temperature-grown GaAs observed by reflective electro-optic sampling, 68
Electrical conductivity
  electrical conduction in low temperature grown InP, 86
Electrical measurements
  electro-optical measurement of low temperature GaAs, 41
Electrical properties
  low temperature molecular beam epitaxy of Al(Ga)InAs on InP and its application to high electron mobility transistor structures, 89
  LTMBE GaAs: present status and perspectives, 9
Electron states
  electrical conduction in low temperature grown InP, 86
Electronic properties
  electrical conduction in low temperature grown InP, 86
Epilayers
  GaAs, AlGaAs and InGaAs epilayers containing As clusters: semimetal/semiconductor composites, 31
  semi-insulating GaAs made by As implantation and thermal annealing, 37

Field effect transistor
  noise studies of HFETs on low temperature grown GaAs buffers and of MESFETs with low temperature grown GaAs passivation, 82

Gallium
  gallium vacancy related defects in silicon doped GaAs grown at low temperatures, 23
Gallium arsenide
  applications of GaAs grown at a low temperature by molecular beam epitaxy, 72
  basic principles governing the surface atomic structure of zinc blende semiconductors, 1
  EL2-like defects in low temperature GaAs, 27
  electro-optical measurement of low temperature GaAs, 41
  extended defects and precipitates in LT-GaAs, LT-InAlAs and LT-InP, 45
  GaAs, AlGaAs and InGaAs epilayers containing As clusters: semimetal/semiconductor composites, 31
  gallium vacancy related defects in silicon doped GaAs grown at low temperatures, 23
  interfacial barrier characteristics for LT-GaAs on low doped GaAs layers, 55
  LTMBE GaAs: present status and perspectives, 9
  noise studies of HFETs on low temperature grown GaAs buffers and of MESFETs with low temperature grown GaAs passivation, 82
  optoelectronic applications of LTMBE III–V materials, 61
  point defects in III–V materials grown by molecular beam epitaxy at low temperature, 16
  semi-insulating GaAs made by As implantation and thermal annealing, 37
  subpicosecond electric field dynamics in low-temperature-grown GaAs observed by reflective electro-optic sampling, 68
  temperature measurements of LT GaAs diodes, 78
Gallium phosphide
  low temperature chemical beam epitaxy of gallium phosphide/silicon heterostructures, 97

Hall effect
electro-optical measurement of low temperature GaAs, 41
Heat treatment
applications of GaAs grown at a low temperature by molecular beam epitaxy, 72
LTMBE GaAs: present status and perspectives, 9
temperature measurements of LT GaAs diodes, 78
Heterostructures
low temperature chemical beam epitaxy of gallium phosphide/silicon heterostructures, 97

Indium phosphide
electrical conduction in low temperature grown InP, 86
extended defects and precipitates in LT-GaAs, LT-InAlAs and LT-InP, 45
low temperature molecular beam epitaxy of Al(Ga)InAs on InP and its application to high electron mobility transistor structures, 89
photo-induced current transient spectroscopy of $Al_{0.48}In_{0.52}As$ semi-insulating layers grown on InP by molecular beam epitaxy, 93
point defects in III–V materials grown by molecular beam epitaxy at low temperature, 16
Integrated technology
applications of GaAs grown at a low temperature by molecular beam epitaxy, 72
Interfaces
interfacial barrier characteristics for LT-GaAs on low doped GaAs layers, 55
Ion implantation
semi-insulating GaAs made by As implantation and thermal annealing, 37
Iron
photo-induced current transient spectroscopy of $Al_{0.48}In_{0.52}As$ semi-insulating layers grown on InP by molecular beam epitaxy, 93

Metal-insulator-semiconductor structures
temperature measurements of LT GaAs diodes, 78
Models of surface and interface atomic displacement
basic principles governing the surface atomic structure of zinc blende semiconductors, 1
Molecular beam epitaxy
applications of GaAs grown at a low temperature by molecular beam epitaxy, 72
electro-optical measurement of low temperature GaAs, 41
extended defects and precipitates in LT-GaAs, LT-InAlAs and LT-InP, 45
interfacial barrier characteristics for LT-GaAs on low doped GaAs layers, 55
low temperature molecular beam epitaxy of Al(Ga)InAs on InP and its application to high electron mobility transistor structures, 89
LTMBE GaAs: present status and perspectives, 9
photo-induced current transient spectroscopy of $Al_{0.48}In_{0.52}As$ semi-insulating layers grown on InP by molecular beam epitaxy, 93
point defects in III–V materials grown by molecular beam epitaxy at low temperature, 16
temperature measurements of LT GaAs diodes, 78

Noise processes and phenomena
noise studies of HFETs on low temperature grown GaAs buffers and of MESFETs with low temperature grown GaAs passivation, 82

Optical absorption
EL2-like defects in low temperature GaAs, 27
Optical measurements
electro-optical measurement of low temperature GaAs, 41
Optical properties
LTMBE GaAs: present status and perspectives, 9
photo-induced current transient spectroscopy of $Al_{0.48}In_{0.52}As$ semi-insulating layers grown on InP by molecular beam epitaxy, 93
subpicosecond electric field dynamics in low-temperature-grown GaAs observed by reflective electro-optic sampling, 68
Optoelectronics
applications of GaAs grown at a low temperature by molecular beam epitaxy, 72
optoelectronic applications of LTMBE III–V materials, 61

Passivation
noise studies of HFETs on low temperature grown GaAs buffers and of MESFETs with low temperature grown GaAs passivation, 82
Phonons
subpicosecond electric field dynamics in low-temperature-grown GaAs observed by reflective electro-optic sampling, 68
Photoelectronic materials
optoelectronic applications of LTMBE III–V materials, 61
Photoluminescence
photo-induced current transient spectroscopy of $Al_{0.48}In_{0.52}As$ semi-insulating layers grown on InP by molecular beam epitaxy, 93

Schottky barrier
interfacial barrier characteristics for LT-GaAs on low doped GaAs layers, 55
Semiconductors
basic principles governing the surface atomic structure of zinc blende semiconductors, 1
GaAs, AlGaAs and InGaAs epilayers containing As clusters: semimetal/semiconductor composites, 31
Silicon
basic principles governing the surface atomic structure of zinc blende semiconductors, 1
gallium vacancy related defects in silicon doped GaAs grown at low temperatures, 23
low temperature chemical beam epitaxy of gallium phosphide/silicon heterostructures, 97
low temperature molecular beam epitaxy of Al(Ga)InAs on InP and its application to high electron mobility transistor structures, 89
Structural properties
LTMBE GaAs: present status and perspectives, 9
Superlattices
noise studies of HFETs on low temperature grown GaAs buffers and of MESFETs with low temperature grown GaAs passivation, 82
Surface roughnesses
low temperature chemical beam epitaxy of gallium phosphide/silicon heterostructures, 97
Surfaces
basic principles governing the surface atomic structure of zinc blende semiconductors, 1

Ternary compounds
GaAs, AlGaAs and InGaAs epilayers containing As clusters: semimetal/semiconductor composites, 31

photo-induced current transient spectroscopy of $Al_{0.48}In_{0.52}As$ semi-insulating layers grown on InP by molecular beam epitaxy, 93
Thermal annealing
Semi-insulating GaAs made by As implantation and thermal annealing, 37
Thermal processing
electrical conduction in low temperature grown InP, 86
Thermal properties
gallium vacancy related defects in silicon doped GaAs grown at low temperatures, 23
Transport properties
optoelectronic applications of LTMBE III–V materials, 61

X-ray spectroscopy
EL2-like defects in low temperature GaAs, 27
temperature measurements of LT GaAs diodes, 78